NOVA SCHOOL OF SCIENCE & TECHNOLOGY

U.PORTO

universidade de aveiro

DEPARTAMENT OF CHEMISTRY

NEW ADVANCED HYBRID MATERIALS FOR SEPARATION OF FLUORINATED GREENHOUSE GASES

JULIO EDUARDO SOSA PARRA

Chemical Engineer

DOCTORATE IN SUSTAINABLE CHEMISTRY

NOVA University Lisbon

September. 2025

NOVA SCHOOL OF SCIENCE & TECHNOLOGY

DEPARTAMENT OF CHEMISTRY

NEW ADVANCED HYBRID MATERIALS FOR SEPARATION OF FLUORINATED GREENHOUSE GASES

JULIO EDUARDO SOSA PARRA

Chemical Engineer

Adviser: Ana Belén Pereiro Estévez
Principal Investigator, NOVA School of Science and Technology, NOVA University Lisbon

Co-advisers: João Miguel Mendes de Araújo
Assistant Professor, NOVA School of Science and Technology, NOVA University Lisbon

Examination Committee:

Chair: Ana Isabel Nobre Martins Aguiar de Oliveira Ricardo,
Full Professor, NOVA School of Science and Technology, NOVA University Lisbon

Rapporteurs: Ana Maria Soto Campos,
Full Professor, University of Santiago de Compostela

Félix Llovell Ferret,
Associate Professor, Universitat Revira i Virgili

Adviser: Ana Belén Pereiro Estévez,
Principal Investigator, NOVA School of Science and Technology, NOVA University Lisbon

Members: Liliana Sofia Carvalho Tomé,
Assistant Professor, University of Coimbra

Andreia Filipa Ribeiro de Oliveira Peixoto
Assistant Researcher, Faculty of Sciences, University of Porto

Ana Isabel Nobre Martins Aguiar de Oliveira Ricardo,
Full Professor, NOVA School of Science and Technology, NOVA University Lisbon

Filipe Ribeiro Ferreira da Silva,
Associate Professor with habilitation, NOVA School of Science and Technology, NOVA University Lisbon

DOCTORATE IN SUSTAINABLE CHEMISTRY

NOVA University Lisbon
September, 2025

New Advanced Hybrid Materials for Separation of Fluorinated Greenhouse Gases

Copyright © Julio Eduardo Sosa Parra, NOVA School of Science and Technology, NOVA University Lisbon.

The NOVA School of Science and Technology and the NOVA University Lisbon have the right, perpetual and without geographical boundaries, to file and publish this dissertation through printed copies reproduced on paper or on digital form, or by any other means known or that may be invented, and to disseminate through scientific repositories and admit its copying and distribution for non-commercial, educational or research purposes, as long as credit is given to the author and editor.

À minha esposa, família e amigos, deixo o meu sincero agradecimento pelo apoio incondicional.

ACKNOWLEDGMENTS

I would like to express my sincere gratitude to the Fundação para a Ciência e a Tecnologia (FCT) for the financial support provided through grant 2022.11909.BD, which made possible the development of project New advanced hybrid materials for separation of fluorinated Greenhouse gases and the achievement of the results presented in this thesis. To my host institutions, the NOVA School of Science and Technology and the Associated Laboratory for Green Chemistry (LAQV-REQUIMTE), for providing the infrastructures, equipment, services, and resources required to carry out this work. I am also grateful to all the people I had the opportunity to meet in these institutions, whose constant availability and support were essential to overcoming the many challenges encountered along the way.

My deepest gratitude goes to my wife, whose understanding, unconditional support, and unwavering strength have been the cornerstone of this academic journey. Her patience during long hours of study, encouragement in moments of doubt, and constant belief in my abilities provided me with the motivation to persevere. Beyond being my partner, she has been my confidante, my source of inspiration, and calm during challenges. This work would not have been possible without her love, sacrifice, and unwavering presence by my side.

To my parents, siblings, and nephews, for teaching me to face adversity with determination and for instilling in me the values that have guided my personal and professional development. Their unwavering support, love, and belief in my abilities have been a constant source of strength and inspiration, motivating me to pursue my goals with confidence and resilience.

To my family Orlando, Zoraida, Edison, Aurora, and María Lilia, for their constant affection and unconditional support throughout my academic formation.

I would like to express my sincere gratitude to Professor Ana, who was the first person to believe in me academically and see potential in me that I had not even recognized myself. Her high standards, always accompanied by dedication and commitment, pushed me to give my best and have been crucial in achieving the results of this dissertation. I am especially thankful for the opportunity to be her PhD student and for teaching me that research goes far beyond technical knowledge: it also involves learning to think critically, being independent, and facing challenges with courage. Her advice, words of encouragement during the most difficult moments, and her constant example of rigor and passion for science have been a true source of inspiration. Thanks to her support, I have grown not only as a researcher but also as a person

I am especially grateful to Professor João for his guidance through insightful discussions, valuable advice, and constant encouragement, particularly during the most challenging stages of this dissertation. His dedication, patience, and motivation have been a true source of inspiration, and his support has allowed me to grow not only as a researcher but also as a person.

A very special thanks to Professor Rui Ribeiro, for his generosity in sharing knowledge, for his valuable observations and corrections, and for his constant support during this process. Likewise, to Professor Mota, for his corrections, guidance, and significant contribution to my academic development.

To my colleagues and friends, who made this path more enriching and enjoyable:

- Tiago Ferreira, for reminding me of the value of friendship, punctuality, and effort as fundamental principles for achieving any goal.
- Henrry, for his unconditional friendship, his constant presence, and for teaching me, through his perseverance and determination, that consistency and commitment are key to achieving any goal.
- My PhD colleagues Tiago Santos and Thiago Carvalho, for their understanding, companionship, generosity, and for always being willing to share their knowledge.

I would like to express my sincere gratitude to Jhoana, Camila, Daniela, and Patricia, as well as to all the members of the Laboratory of Alternative Fluids for Green Chemistry, for the coffees, conversations, and shared experiences that made life in the lab more enjoyable.

A very special thanks to Elena Gabirondo, for her friendship, her generosity in sharing knowledge, and above all, for teaching me that science goes far beyond the laboratory. Through her, I have discovered a world of details that inspire and fascinate, especially in the face of the challenges that research presents.

I would also like to sincerely acknowledge the technicians Nuno Costa and Carla, whose professionalism, constant support, and availability greatly facilitated the development of the analyses and contributed significantly to the quality of the results obtained.

Finally, I extend my heartfelt gratitude to the university secretaries Isabel Rodríguez, Maria do Carmo, and Maria José, whose indispensable work ensures the proper functioning of the institution and whose support has been fundamental in the administrative management of this process.

“Life is like a journey across the sea. There are days of calm and days of storm. What truly matters is being a good captain of our own ship.” (Jacinto Benavente).

ABSTRACT

Greenhouse gas (GHG) emissions are among the primary drivers of climate change. These gases include carbon dioxide (CO_2), methane (CH_4), and fluorinated gases (F-gases). The release of these GHGs into the atmosphere can be extremely harmful, particularly in the case of certain F-gases, whose global warming potential can be up to 22,000 times higher than that of a CO_2 molecule.

These compounds are widely used in industries that meet technological and human comfort needs, such as refrigeration and air conditioning, the production of electrical insulators, and the manufacturing of superconductors for circuits used in artificial intelligence applications. The extensive use of F-gases and their high climatic impact highlight the need for effective strategies for their mitigation and substitution with more sustainable alternatives.

A promising strategy for the capture and recovery of these gases at the end of their life cycle involves their separation and reuse using advanced absorbents and adsorbents, including ionic liquids (ILs), deep eutectic solvents (DES), and porous solid matrices such as Activated Carbons (ACs), Metal-Organic Frameworks (MOFs), Porous Organic Polymers (POPs), and zeolites.

Absorbents, due to the presence of anions and cations in their structure, can establish specific interactions with the fluorine atoms present in F-gases, enabling efficient capture and storage within the free volumes of the material. On the other hand, adsorbents possess critical structural properties, such as high surface area, controlled porosity, and specific functional groups, that facilitate selective adsorption and separation of gas mixtures, optimising the recovery of individual components. The rational design of these materials allows not only the maximisation of capture capacity but also the improvement of selectivity and stability during operational cycles, representing a key tool for GHGs mitigation in industrial applications.

In this doctoral thesis, ILs were investigated as advanced absorbents for the capture and separation of F-gases, together with DESs as sustainable and cost-effective alternatives. The study combines experimental measurements with theoretical modeling to analyze the absorption behavior of fluorinated gases of industrial relevance. Particular emphasis was placed on the role of cation and anion chemistry in governing gas solubility, selectivity, and absorption equilibria, enabling the identification of robust structure–property relationships.

To support and rationalize the experimental findings, COSMO-RS calculations were employed to screen and analyze approximately 600 cation–anion combinations, providing molecular-level insight into the dominant interactions controlling absorption, including electrostatic, dispersive, and polarity

effects. These predictions were further evaluated through process simulations using a combined COSMO-RS/Aspen Plus approach, allowing the translation of molecular thermodynamic behavior into process-level performance. This multiscale methodology provided valuable information on absorption and separation equilibria, solvent regeneration, and operational feasibility, highlighting the potential of ILs and DESs as tunable and efficient media for fluorinated gas capture.

In parallel, a wide range of solid porous materials, including commercial activated carbons, bio-carbons derived from treated residual biomass, MOFs, and POPs, were systematically investigated for the adsorption and selective separation of F-gases. Activated carbons and bio-carbons exhibited high adsorption capacities, pressure-dependent selectivities, and excellent regenerability, with their performance strongly governed by microporosity, pore size distribution, and surface chemistry. MOFs and POPs, including dye-derived POPs, demonstrated outstanding molecular selectivity due to their highly ordered pore architectures and precisely tailored surface functionalities, enabling advanced gas separation tasks.

The results of this thesis confirm the feasibility of different advanced materials for the capture, separation, and recovery of fluorinated gases, offering a promising approach for industrial and environmental applications.

Keywords: F-gases, ILs, ACs, MOFs, POPs, COSMO-RS, Aspen Plus, Gas separation, Porous solid matrices.

RESUMO

As emissões de gases com efeito de estufa (GEE) são um dos principais fatores que contribuem para as alterações climáticas. Estes gases incluem dióxido de carbono (CO_2), metano (CH_4) e gases fluorados (F-gases). A libertação destas moléculas na atmosfera pode ser extremamente prejudicial, particularmente no caso de certos F-gases, cujo potencial de aquecimento global pode ser até 22,000 vezes superior ao de uma molécula de CO_2.

Esses compostos são amplamente utilizados em indústrias relacionadas com às necessidades tecnológicas e de conforto humano, como refrigeração e ar condicionado, produção de isolantes elétricos e fabricação de supercondutores para circuitos usados em aplicações de inteligência artificial. O uso extensivo de gases fluorados e seu alto impacto climático destacam a necessidade de estratégias eficazes para sua mitigação e substituição por alternativas mais sustentáveis.

Uma estratégia promissora para a captura e recuperação desses gases no final do seu ciclo de vida envolve a sua reclamação, separação e reutilização usando absorventes avançados e adsorventes, incluindo líquidos iónicos (ILs), solventes eutéticos profundos (DES) e matrizes sólidas porosas, como carvão ativados (ACs), estruturas metal-orgânicas (MOFs), polímeros orgânicos porosos (POPs) e zeólitos.

Os absorventes, devido à presença de aniões e catiões na sua estrutura, podem estabelecer interações específicas com os átomos de flúor nas moléculas de F-gases, permitindo a captura e o armazenamento eficientes nos volumes livres do material. Os adsorventes, por outro lado, possuem propriedades estruturais importantes tais como alta área superficial, porosidade controlada e grupos funcionais específicos que facilitam a adsorção seletiva e a separação de misturas de gases, otimizando a recuperação de componentes individuais. O desenho racional desses materiais permite não apenas a maximização da capacidade de captura, mas também a melhoria da seletividade e estabilidade durante os ciclos operacionais, representando uma ferramenta fundamental para a mitigação de GEE em aplicações industriais.

Nesta tese de doutoramento, investigaram-se ILs como absorventes avançados para a captura e separação de F-gases, juntamente com DESs como alternativas sustentáveis e economicamente viáveis. O estudo combina medições experimentais com modelação teórica para analisar o comportamento de absorção de gases fluorados de relevância industrial. Foi dado especial destaque ao papel da química dos catiões e aniões na solubilidade dos gases, na seletividade e nos equilíbrios de absorção, permitindo a identificação de relações robustas entre estrutura e propriedades.

Para apoiar e racionalizar os resultados experimentais, foram utilizados cálculos COSMO-RS para avaliar e analisar aproximadamente 600 combinações catião–anião, fornecendo uma visão ao nível molecular das interações dominantes que controlam a absorção, incluindo efeitos electrostáticos, dispersivos e de polaridade. Estas previsões foram posteriormente avaliadas através de simulações de processo utilizando uma abordagem combinada COSMO-RS/Aspen Plus, permitindo a tradução do comportamento termodinâmico molecular em desempenho a nível de processo. Esta metodologia multinível forneceu informação valiosa sobre os equilíbrios de absorção e separação, regeneração dos solventes e viabilidade operacional, destacando o potencial dos ILs e DESs como meios ajustáveis e eficientes para a captura de gases fluorados.

Paralelamente, foi investigada de forma sistemática uma ampla gama de materiais sólidos porosos, incluindo carvões ativados comerciais, biocarvões derivados de biomassa residual tratada, MOFs e POPs, para a adsorção e separação seletiva de F-gases. Os carvões ativados e biocarvões demonstraram elevadas capacidades de adsorção, seletividades dependentes da pressão e excelente regenerabilidade, com o seu desempenho fortemente condicionado pela microporosidade, distribuição do tamanho dos poros e química superficial. Os MOFs e POPs, incluindo POPs derivados de corantes, apresentaram uma seletividade molecular excecional devido às suas arquiteturas de poros altamente ordenadas e funcionalidades superficiais cuidadosamente ajustadas, permitindo a realização de tarefas avançadas de separação de gases.

Os resultados desta tese confirmam a viabilidade de diferentes materiais porosos avançados para a captura, separação e recuperação de gases fluorados, oferecendo uma abordagem promissora para aplicações industriais e ambientais.

Palavras chave: Gases fluorados, ILs, MOFs, POPs, COSMO-RS, Aspen Plus, Separação de Gases, Materiais Porosos.

CONTENTS

CHAPTER 1 INTRODUCTION 1

1.1 Global Context 3

1.2 Absorption 6

1.2.1 Absorption equilibrium 7

1.2.2 Thermodynamic Modeling of Gas–Liquid Phase Equilibria 9

1.3 Adsorption 11

1.3.1 Classification of Porous Materials and Adsorption Behaviour 12

1.3.2 Adsorption models 14

1.4 Green Absorbents and Porous Solid Adsorbents for Gas Capture and Separation 17

1.4.1 Ionic liquids (ILs) and deep eutetic solvents (DES) 17

1.4.2 Hybrid materials 22

1.4.3 Activated Carbons (ACs) 22

1.4.4 Zeolites 26

1.4.5 Metal–Organic Frameworks (MOFs) 27

1.4.6 Porous Organic Polymers (POPs) 28

1.5 Objectives of the Thesis 29

1.6 Scientific outputs 30

1.7 References 32

CHAPTER 2 F-GASES ABSORPTION WITH IONIC LIQUIDS AND DEEP EUTECTIC SOLVENTS: DESIGN AND PROCESS SIMULATION USING COSMO-RS 43

2.1 Introduction 45

2.2 Non-Random Two-Liquid (NRTL) thermodynamic model 49

2.3 Absorption of fluorinated greenhouse gases using fluorinated ionic liquids 50

2.3.1 Experimental section 50

2.3.2 Results and discussion 54
2.3.3 Conclusions 64
2.4 Absorption of fluorinated greenhouse gases in deep eutectic solvents 65
2.4.1 Experimental section 65
2.4.2 Results and discussion 71
2.4.3 Conclusions 100
2.5 Process evaluation of fluorinated ionic liquids as F-gas absorbents 101
2.5.1 Computational details 103
2.5.2 Results and discussion 111
2.5.3 Conclusions 124
2.6 Design of ionic liquids for fluorinated gas absorption: COSMO-RS selection and solubility experiments 125
2.6.1 Materials and methods 125
2.6.2 Results and discussion 130
2.6.3 Conclusions 154
2.7 References 155
CHAPTER 3 HYBRID MATERIALS FOR THE SORPTION OF F-GASES 167
3.1 Introduction 169
3.2 Sorption of fluorinated greenhouse gases in silica-supported fluorinated ionic liquids 171
3.2.1 Experimental section 171
3.2.2 Results and discussion 176
3.3 Conclusions 202
3.4 References 203
CHAPTER 4 POROUS SOLID MATRICES FOR ADSORPTION AND SEPARATION OF GHGS 209
4.1 Introduction 211
4.2 Materials Characteristics 216
4.2.1 Textural properties 216
4.2.2 Fourier-transform infrared spectroscopy (FTIR) 216
4.2.3 Thermal gravimetric analysis (TGA) 216

4.2.4 Elemental analysis (EA) 217
4.2.5 Photoelectron spectra (XPS) 217
4.2.6 Scanning Electron Microscopy with Energy Dispersive Spectroscopy (SEM-EDS) .. 217
4.2.7 Crystallographic analyses were conducted by X-ray powder diffraction (XRPD) 217
4.3 Adsorption equilibrium of GHGs 218
4.4 Isosteric Heat of Adsorption and Henry's Constant 219
4.5 Prediction of the Adsorption and Selectivity of GHGs Using Ideal Adsorption Solution Theory (IAST) 220
4.6 Adsorption of fluorinated greenhouse gases on activated carbons: evaluation of their potential for gas separation 220
4.6.1 Experimental section 221
4.6.2 Results and discussion 222
4.6.3 Conclusions 257
4.7 Exploring the potential of biomass-derived carbons for the separation of fluorinated gases with high global warming potential 258
4.7.1 Experimental section 258
4.7.2 Results and discussion 259
4.7.3 Conclusions 294
4.8 Coconut shell derived activated carbon for effective separation of greenhouse gases 295
4.8.1 Experimental Section 296
4.8.2 Results and discussion 296
4.8.3 Conclusions 321
4.9 Exploring the Potential of Metal–Organic Frameworks for the Separation of Blends of Fluorinated Gases with High Global Warming Potential 322
4.9.1 Experimental section 322
4.9.2 Results and discussion 323
4.9.3 Conclusions 340
4.10 Porous Organic Polymers for the adsorption of fluorinated gases 341
4.10.1 Experimental section 341
4.10.2 Results and discussion 342

4.10.3 Conclusions 359
4.11 References 361
CHAPTER 5 POROUS MATERIALS FOR THE CAPTURE AND SEPARATION OF SF_6, THE MOST POTENT GHG 379
5.1 Introduction 381
5.2 Toth Isotherm Model 385
5.3 Performance Criteria for the Selection of Adsorbent Materials 386
5.4 Porous Materials for Selective Capture and Storage of Sulphur Hexafluoride (SF_6) 387
5.4.1 Experimental section 388
5.4.2 Results and discussion 388
5.4.3 Conclusions 406
5.5 Capture and separation of sulphur hexafluoride: the most powerful greenhouse gas 406
5.5.1 Experimental section 407
5.5.2 Results and discussion 407
5.5.3 Conclusion 422
5.6 References 423
CHAPTER 6 CONCLUDING REMARKS AND FUTURE PERSPECTIVES 433
6.1 General conclusion 435
6.2 Future work 437

LIST OF FIGURES

Figure 1.1.1 The global warming potential of greenhouse gases studied in this work [6]. 3

Figure 1.2.1 Gas-liquid phase equilibrium diagrams at constant P and T on: a) the equilibrium relationship between the partial pressure of component A in the vapour phase (P_A) and its mole fraction in the liquid phase (x_A); and b) the gas–liquid equilibrium curve that shows the mole fraction of component A in the vapour phase (y_A) as a function of its mole fraction in the liquid phase (x_A)..... 8

Figure 1.3.1 Schematic representation of the adsorption phenomenon on a porous solid [49]. 11

Figure 1.3.2 The classification of materials by their porosity, according to IUPAC terminology [51]. 12

Figure 1.3.3 Classification of different types of adsorption isotherms [50]. 13

Figure 1.4.1 Some cations and anions commonly present in the structure of ionic liquids. 18

Figure 1.4.2 Classification of ionic liquids and their key applications [66]. 19

Figure 1.4.3 Comparison between the ideal solid-liquid behaviour of the mixtures of two solids (A+B) and the DES diagram [75]. 21

Figure 1.4.4 Activated carbon production: physical vs. chemical activation. 23

Figure 2.3.1 Schematic diagram of the experimental set up (MSB: magnetic suspension microbalance where PCI is the PC interface for data acquisition, T is the Pt100 temperature sensor, PT represents the Omegadyne pressure transducer and MKS is the MKS Baratron pressure transducer). 52

Figure 2.3.2 Comparison of data of CO_2 absorption in $[C_2C_1Im][N(CF_3SO_2)_2]$ obtained in this work and obtained by other authors [66]..... 54

Figure 2.3.3 Comparison of the absorption of R-32 and R-134a in the ILs studied in this work and in conventional organic solvents [67–70]. Absorption was determined at 303.15 K and equilibrium pressures of 0.1 MPa (for R-32) or 0.3 MPa (for R-134a). 55

Figure 2.3.4 Absorption (full symbols) and desorption (empty symbols) isotherms of : a) R-32, b) R-134a, and c) R-125, refrigerants in different ILs, determined at 303.15 K and equilibrium pressures ranging from 0.02 to 0.5 MPa. Solid lines are the NRTL model calculations. 56

Figure 2.3.5 Sorption isotherms of : a) R-32, b) R-134a and c) R-125 refrigerants in ILs studied in this work and by other authors [73,74] with different number of fluorine atoms in the anion and with different lengths of the hydrogenated chain in the cation. Isotherms were determined at 303.15 K (except for R-134a in $[C_6C_1Im][N(CF_3SO_2)_2]$, which was determined at 298.15 K) and equilibrium pressures ranging from 0.02 to 0.5 MPa..... 58

Figure 2.3.6 Henrry's law constants (in MPa) determined for the absorption of R-32, R-125, and R-134a in the ILs studied in this work and in others reported in the literature [56,57,59,73,74,76–78], at 298.15 K or 303.15K 61

Figure 2.3.7 Ideal selectivities of ILs studied in this work and ILs available in the literature [57,59,74,76] for the separation of the refrigerants mixtures: a) R-134a + R-125, b) R-32 + R-125 and c) R-134a + R-32 (where an ampliation of the selectivities range of 1 - 2 was incorporated for a better visualization) at 303.15 K and equilibrium pressures ranging from 0.01 to 0.5 MPa. 64

Figure 2.4.1 Matrix of the DESs studied in this work, resulting from the mixture of a FIL with a perfluorinated acid at molar ratios 1:1, 1:2 or 2:1. 68

Figure 2.4.2 Schematic diagram of the experimental setup used in this work. TC: temperature controller, VREF: gas cylinder of subsystem 1, P1: manometer of subsystem 1, P2: manometer of subsystem 2, Cell: high-pressure absorption cell, and VP: vacuum pump. 70

Figure 2.4.3 ^{1}H NMR of : a) $[N_{4444}][C_4F_9SO_3]$, b) n-perfluoropentanoic acid and c) $[N_{4444}][C_4F_9SO_3]$:$C_4F_9CO_2H$ at molar ratios of 1:1, d) 2:1 , and e) 1:2. 73

Figure 2.4.4 ^{19}F NMR of: a) $[N_{4444}][C_4F_9SO_3]$, b) n-perfluoropentanoic acid, c) $[N_{4444}][C_4F_9SO_3]$:$C_4F_9CO_2H$ at molar ratio of 1:1, d) 2:1, and e) 1:2. 73

Figure 2.4.5 ^{1}H NMR of : a) $[C_2C_1Im][C_8F_{17}SO_3]$, b) n-perfluoropentanoic acid, c) $[C_2C_1Im][C_8F_{17}SO_3]$:$C_4F_9CO_2H$ at molar ratio of 1:1, d) 2:1 and e) 1:2. 74

Figure 2.4.6 ^{19}F NMR of : a) $[C_2C_1Im][C_8F_{17}SO_3]$, b) n-perfluoropentanoic acid, c) $[C_2C_1Im][C_8F_{17}SO_3]$:$C_4F_9CO_2H$ at molar ratio of 1:1, d) 2:1, and e) 1:2. 74

Figure 2.4.7 DSC curves at 5 K/min of: a) $[N_{1112(OH)}][C_4F_9CO_2]$:$C_4F_9SO_3H$ (1:1), b) $[C_2C_1Im][C_8F_{17}SO_3]$:$C_4F_9CO_2H$ (1:1) and c) $[C_2C_1Im][C_8F_{17}SO_3]$:$C_4F_9CO_2H$ (2:1). 77

Figure 2.4.8 Density of each DES as a function of temperature. 79

Figure 2.4.9 Comparison of experimental data of R-134a absorption in $[C_2C_1Im][N(CF_3SO_2)_2]$ obtained in this work at 303.15 K and obtained by other authors. Data from Lepre *et al*., 2019 [30] and Sosa *et al*., [29] was obtained at 303.15 K and data from Shiflett *et al.*, 2007 [88] was obtained at 298.2 K... 80

Figure 2.4.10 Absorption isotherms of R-134a in all tested DESs prepared in a molar fraction 1:1, determined at 303.15 K and equilibrium pressures up to 0.6 MPa. 80

Figure 2.4.11 Absorption equilibrium isotherms: a) R-32, b) R-125 and c) R-134a on $[N_{4444}][C_4F_9SO_3]$:$C_4F_9CO_2H$ and $[C_2C_1Im][C_8F_{17}SO_3]$:$C_4F_9CO_2H$ at molar ratios of 1:1, 2:1, and 1:2, at 303.15 K. The dashed lines represent the isotherms fitting with the NRTL model. 82

Figure 2.4.12 Absorption equilibrium isotherms of : a) R-32, b) R-125 and c) R-134a on $[N_{4444}][C_4F_9SO_3]$:$C_4F_9CO_2H$ and $[C_2C_1Im][C_8F_{17}SO_3]$:$C_4F_9CO_2H$ at molar ratios of 1:1, 2:1, and 1:2, at 313.15 K. The dashed lines represent the isotherms fitting with the NRTL model. 82

Figure 2.4.13 Absorption equilibrium isotherms of: a) R-32, b) R-125 and c) R-134a on $[N_{4444}][C_4F_9SO_3]$:$C_4F_9CO_2H$ and $[C_2C_1Im][C_8F_{17}SO_3]$:$C_4F_9CO_2H$ at molar ratios of 1:1, 2:1, and 1:2, at 323.15 K. The dashed lines represent the isotherms fitting with the NRTL model. 83

Figure 2.4.14 Absorption (full symbols) and desorption (open symbols) equilibrium isotherms of R-32, R-125, and R-134a on $[N_{4444}][C_4F_9SO_3]$:$C_4F_9CO_2H$ (2:1) at 323.15 K. 83

Figure 2.4.15 Absorption equilibrium isotherms of : a) R-32, R-125, and R-134a in $[N_{4444}][C_4F_9SO_3]$:$C_4F_9CO_2H$ (1:1), b) $[C_2C_1Im][C_8F_{17}SO_3]$:$C_4F_9CO_2H$ (1:1), c) $[N_{4444}][C_4F_9SO_3]$:$C_4F_9CO_2H$ (2:1), d) $[C_2C_1Im][C_8F_{17}SO_3]$:$C_4F_9CO_2H$ (2:1), e) $[N_{4444}][C_4F_9SO_3]$:$C_4F_9CO_2H$ (1:2) and f) $[C_2C_1Im][C_8F_{17}SO_3]$:$C_4F_9CO_2H$ (1:2), at 303.15 K. The dashed lines represent the isotherms fitting with the NRTL model. 84

Figure 2.4.16 Absorption equilibrium isotherms of a) R-32, R-125, and R-134a in $[N_{4444}][C_4F_9SO_3]$/$C_4F_9CO_2H$ (1:1), b) $[C_2C_1Im][C_8F_{17}SO_3]$/$C_4F_9CO_2H$ (1:1), c)

[N_{4444}][$C_4F_9SO_3$]/$C_4F_9CO_2H$ (2:1), d) [C_2C_1Im][$C_8F_{17}SO_3$]/$C_4F_9CO_2H$ (2:1), e) [N_{4444}][$C_4F_9SO_3$]/$C_4F_9CO_2H$ (1:2) and f) [C_2C_1Im][$C_8F_{17}SO_3$]/$C_4F_9CO_2H$ (1:2) (Panel F), at 313.15 K. The dashed lines represent the isotherms fitting with the NRTL model. 85

Figure 2.4.17 Absorption equilibrium isotherms of: a) R-32, R-125, and R-134a in [N_{4444}][$C_4F_9SO_3$]/$C_4F_9CO_2H$ (1:1), b) [C_2C_1Im][$C_8F_{17}SO_3$]/$C_4F_9CO_2H$ (1:1), c) [N_{4444}][$C_4F_9SO_3$]/$C_4F_9CO_2H$ (2:1), d) [C_2C_1Im][$C_8F_{17}SO_3$]/$C_4F_9CO_2H$ (2:1), e) [N_{4444}][$C_4F_9SO_3$]/$C_4F_9CO_2H$ (1:2) and f) [C_2C_1Im][$C_8F_{17}SO_3$]/$C_4F_9CO_2H$ (1:2) at 323.15 K. The dashed lines represent the isotherms fitting with the NRTL model. 86

Figure 2.4.18 Absorption equilibrium isotherms in mass fraction (*w*) of : a) R-32, b) R-125 and R-134a (Panel C) on [N_{4444}][$C_4F_9SO_3$]/$C_4F_9CO_2H$ and [C_2C_1Im][$C_8F_{17}SO_3$]/$C_4F_9CO_2H$ at molar ratios of 1:1, 2:1, and 1:2 at 303.15 K. 87

Figure 2.4.19 Absorption equilibrium isotherms in mass fraction (*w*) of : a) R-32, R-125, and R-134a in [N_{4444}][$C_4F_9SO_3$]/$C_4F_9CO_2H$ (1:1), b) [C_2C_1Im][$C_8F_{17}SO_3$]/$C_4F_9CO_2H$ (1:1), c) [N_{4444}][$C_4F_9SO_3$]/$C_4F_9CO_2H$ (2:1), d) [C_2C_1Im][$C_8F_{17}SO_3$]/$C_4F_9CO_2H$ (2:1), e) [N_{4444}][$C_4F_9SO_3$]/$C_4F_9CO_2H$ (1:2) and f) [C_2C_1Im][$C_8F_{17}SO_3$]/$C_4F_9CO_2H$ (1:2) at 303.15 K. 88

Figure 2.4.20 Henry's law constants (in MPa) determined for the absorption of R-32, R-125 and R-134a at 303.15 K, 313.15 K, and 323.15 K. 90

Figure 2.4.21 Henry's law constants (in MPa) determined for the absorption of R-32, R-125 and R-134a in the systems studied in this work, and in selected ILs reported in the literature [29], at 303.15 K. 92

Figure 2.4.22 Ideal selectivities of the systems studied in this work towards: a) R-32 over R-125, b) R-134a over R-125 and c) R-134a over R-32 at 303.15 K. 96

Figure 2.4.23 Ideal selectivities of the systems studied in this work towards: a) R-32 over R-125, b) R-134a over R-125, and c) R-134a over R-32 at 313.15 K. 97

Figure 2.4.24 Ideal selectivities of the systems studied in this work towards: a) R-32 over R-125, b) where an amplification of the selectivities range of 0−2 and pressures range of 0-0.4 was incorporated for better visualization), R-134a over R-125 and c) R-134a over R-32 (panel C) at 323.15 K. 97

Figure 2.4.25 Ideal selectivities, determined from the Henry's constants, of the systems studied in this work at: a) 303.15 K, b) 313.15 K, and c) 323.15 K. 99

Figure 2.4.26 Ideal selectivities, determined from the Henry's constants, of the systems studied in this work, and of selected ILs reported in the literature, at 303.15 K [29]. 100

Figure 2.5.1 Complete process scheme used in Aspen Plus v10. 111

Figure 2.5.2 Validation of Henry's law constant prediction: [C+A] model using COSMO-based/Aspen calculations at T = 298 K using COSMO-RS model [96]. 112

Figure 2.5.3 Experimental molar solubility of HFC in FILs and comparison with the values predicted in COSMO-based/Aspen Plus approach at T = 298 K at HFC partial pressure of: a) 0.02 bar; and b) 1 bar. 113

Figure 2.5.4 HFC recovery as a function of L/G ratio (in mass unit) at T = 298 K and HFC partial pressure of 0.02 bar for systems: a) R-134a and b) R-32 for a RADFRAC column in equilibrium mode. 114

Figure 2.5.5 HFC recovery as a function of L/G ratio at T = 298 K and HFC partial pressure of 1 bar for systems: a) R-134a and b) R-32 for a RADFRAC column in equilibrium mode. 114

Figure 2.5.6 HFC recovery for different FIL/ILs tested on this work at T = 298 K, L/G=6 and HFC partial pressure of 0.02 and 1 bar for systems: a) R-134a and b) R-32 for a RADFRAC column in equilibrium mode. 115

Figure 2.5.7 HFC recovery as a function of the temperature using equilibrium and rate-based mode of RADFRAC column at L/G=6 and 1 bar of partial pressure for the systems: (a) R-134a-[C_2C_1Im][CF_3SO_3]; and (b) R-134a-[C_2C_1py][$C_4F_9SO_3$]. 116

Figure 2.5.8 HFC recovery as a function of the temperature using equilibrium and rate-based mode of RADFRAC column at L/G=6 and 1 bar of partial pressure for the systems: (a) R-32-[C_2C_1Im][CF_3SO_3]; and (b) R-32-[C_2C_1py][$C_4F_9SO_3$]. 117

Figure 2.5.9 HFC recoveries in rate-based mode as a function of the viscosity (T=298.15 K) for the FIL/ILs tested on this work at L/G=6 and 1 bar of partial pressure. 118

Figure 2.5.10 HFC recoveries in rate-based mode vs recoveries in equilibrium mode for all the systems studied in this work at 298.15 K, L/G=6 and HFC partial pressures of: (a) 0.02 bar; and (b) 1 bar. .. 119

Figure 2.5.11 HFC recoveries in rate-based mode as a function of L/G ratio (in mass units) at different total pressures on the absorption column in the complete process (see Figure 2.5.1) using $[C_2C_1Im][CF_3SO_3]$ as absorbent for the systems: (a) R-134a; and (b) R-32. 120

Figure 2.5.12 HFC recoveries in rate-based mode as a function of L/G ratio (in mass units) at different total pressures on the absorption column in the complete process using R-134 as solute for the systems: (a) $[C_2C_1Im][N(CF_3SO_3)_2]$; and (b) $[C_8C_1Im][N(CF_3SO_3)_2]$. 120

Figure 2.5.13 HFC recoveries in Rate-Based mode as a function of L/G ratio (in mass units) at different total pressures on the absorption column in the complete process using R-32 as solute for the systems: (a) $[C_2C_1Im][N(CF_3SO_3)_2]$; and (b) $[C_8C_1Im][N(CF_3SO_3)_2]$. 121

Figure 2.5.14 Absorption column diameters as a function of L/G ratio (in mass units) and total pressure for R-134a-$[C_2C_1Im][CF_3SO_3]$ system. 121

Figure 2.5.15 Absorption column diameters as a function of L/G ratio (in mass units) and total pressure for R-32-$[C_2C_1Im][CF_3SO_3]$ system. 122

Figure 2.5.16 HFC recovery on the desorption column as a function of the pressure on it for R-134a-$[C_2C_1Im][CF_3SO_3]$ system at 423.15 K of temperature in the reboiler. 122

Figure 2.6.1 Physical properties obtained in the literature [107,108,109,110,111] for $[P_{2444}][C_2C_2PO_4]$, $[P_{66614}][CNPyr]$ and $[P_{66614}][C_2NO_2]$ where: a) density (ρ) and b) viscosity (η). 129

Figure 2.6.2 Validation of Henry's law constants (bar) of solutes in ILs, calculated by COSMO-RS determined using experimental vapor pressure of the different solutes at room temperature with C+A model. 131

Figure 2.6.3 Henry's law constants (bar) screening of: a) R-134a and b) R-32 in >600 different ILs at T = 298 K calculated by COSMO-RS method. The blue color highlights the cations and anions studied in this work and the red color highlights the ILs studied in our previous works [29,30]. 135

Figure 2.6.4 Effect of cation on the excess enthalpy, entropy, and Gibbs free energy of R-134a + IL equimolar mixture calculated using COSMO-RS at T = 298 K. The blue color highlights the cations and anions studied in this work, the red color highlights the ILs studied in our previous work [29,30]. .. 139

Figure 2.6.5 Effect of cation on the excess enthalpy, entropy, and Gibbs free energy of R-32 + IL equimolar mixture calculated using COSMO-RS at T = 298 K. The blue color highlights the cations and anions studied in this work, the red color highlights the ILs studied in our previous work [29]. 140

Figure 2.6.6 The intermolecular interaction (misfit-electrostatic, van der waals and hydrogen-bonding) contributions to excess molar enthalpies of R-134a + IL equimolar mixtures calculated using COSMO-RS (C+ A model). The blue color highlights the cations and anions studied in this work, the red color highlights the ILs studied in our previous work [29,30]. 142

Figure 2.6.7 The intermolecular interaction (misfit-electrostatic, van der waals and hydrogen-bonding) contributions to excess molar enthalpies of R-32 + IL equimolar mixtures calculated using COSMO-RS (C+ A model). The blue color highlights the cations and anions studied in this work, the red color highlights the ILs studied in our previous work [29]. 143

Figure 2.6.8 Comparison of experimental absorption data for R-134a in $[P_{2444}][C_2C_2PO_4]$ as a function of pressure, using the volumetric and the gravimetric methods at different working temperatures.... 144

Figure 2.6.9 Absorption equilibrium isotherms of F-gas in: a) $[P_{2444}][C_2C_2PO_4]$; b) $[P_{66614}][C_2NO_2]$; and c) $[P_{66614}]$[CNPyr] at 303.15 K. The dashed lines represent the fitting using the NRTL model. 146

Figure 2.6.10 Absorption equilibrium isotherms of F-gas in: a) $[P_{2444}][C_2C_2PO_4]$; b) $[P_{66614}][C_2NO_2]$; and c) $[P_{66614}]$[CNPyr] at 313.15 K. The dashed lines represent the fitting using the NRTL model. . 146

Figure 2.6.11 Absorption equilibrium isotherms of F-gas in: a) $[P_{2444}][C_2C_2PO_4]$; b) $[P_{66614}][C_2NO_2]$; and c) $[P_{66614}]$[CNPyr] at 323.15 K. The dashed lines represent the fitting using the NRTL model. . 147

Figure 2.6.12 Comparison of the absorption equilibrium isotherms, in mass fraction unit, for the F-gas in ILs of this work ($[P_{2444}][C_2C_2PO_4]$, $[P_{66614}][C_2NO_2]$ and $[P_{66614}]$[CNPyr]) and ILs studied in our previous work [29,30] at 303.15 K where: a) R-134a and b) R-32. 151

Figure 2.6.13 Comparison of Henry constants versus mass solubility the F-gas in ILs studied in this work ($[P_{2444}][C_2C_2PO_4]$, $[P_{66614}][C_2NO_2]$ and $[P_{66614}]$[CNPyr]) and ILs studied in our previous work [29,30] at 303.15 K and 0.1 MPa where: a) R-134a and b) R-32..... 153

Figure 2.6.14 Ideal selectivity at 303.15 K, determined from the Henry's constants, for the ILs studied in this work and ILs available in the literature [29,30] for the separation of the refrigerant mixtures R-32/R-134a. 154

Figure 3.2.1 Fumed silica (A) and ionic liquid (B) used to prepare the IL/silica composites (C)..... 173

Figure 3.2.2 Nitrogen sorption isotherms at 77 K for the silica/IL composites. 177

Figure 3.2.3 Electron scanning microscopy image and energy-dispersive X-ray spectroscopy spectrum of SiO_2 (panels A and B), $[C_2C_1Im][C_4F_9SO_3]$ (panels C and D), and $SiO_2/[C_2C_1Im][C_4F_9SO_3]$ (panel E and F)..... 178

Figure 3.2.4 Electron scanning microscopy image and energy-dispersive X-ray spectroscopy spectrum of SiO_2 (panels A and B), $[C_2C_1Im][N(CF_3SO_2)_2]$ (panels C and D), and $SiO_2/[C_2C_1Im][N(CF_3SO_2)_2]$ (panels E and F)..... 179

Figure 3.2.5 Electron scanning microscopy image and energy-dispersive X-ray spectroscopy spectrum of SiO_2 (panels A and B), $[C_2C_1Im][C_1CO_2]$ (panels C and D), and $SiO_2/[C_2C_1Im][C_1CO_2]$ (panels E and F)..... 180

Figure 3.2.6 Sorption equilibrium isotherms, at 303.15 K, of R-32 (panel A), R-125 (panel B), and R-134a (panel C) on the fumed silica, composites studied in this work, and on pure ILs studied previously [19]. 181

Figure 3.2.7 Sorption equilibrium isotherms, at 303.15 K, of R-32 (panel A), R-125 (panel B), and R-134a (panel C) on SiO_2 and SiO_2/IL composites studied in this work. The dashed lines represent the data fitting to the Sips equation..... 181

Figure 3.2.8 Sorption (full symbols) and desorption (empty symbols) of R-32 (panel A), R-125 (panel B), and R-134a (panel C) on SiO_2 and SiO_2/IL composites at 303.15 K. 182

Figure 3.2.9 Sorption equilibrium isotherms, at 303.15 K, of R-32 (panel A), R-125 (panel B), and R-134a (panel C) on silica and silica/IL composites studied in this work, and on pure ILs studied previously (with a correction factor of 0.4 to account to the percentage of ILs in the composites, 40% weight) [19]. 185

Figure 3.2.10 Sorption of R-32, R-125, and R-134a at 303.15 K on $SiO_2/[C_2C_1Im][C_1CO_2]$ (panel A), $SiO_2/[C_2C_1Im][CF_3SO_3]$ (panel B), $SiO_2/[C_2C_1Im][N(CF_3SO_2)_2]$ (panel C), $SiO_2/[C_2C_1Im][N(C_2F_5SO_2)_2]$ (panel D), $SiO_2/[C_2C_1Im][N(C_4F_9SO_2)_2]$ (panel E), $SiO_2/[C_2C_1Im][C_4F_9CO_2]$ (panel F), $SiO_2/[C_2C_1Im]$ $[C_4F_9SO_3]$ (panel G), $SiO_2/[C_2C_1py]$ $[C_4F_9SO_3]$ (panel H), $SiO_2/[C_2C_1Im][C_8F_{17}SO_3]$ (panel I), and SiO_2 (panel J)..... 186

Figure 3.2.11 Comparison of the sorption of R-32 (panel A), R-125 (panel B), and R-134a (panel C) at 303.15 K on SiO_2/IL composites prepared with ILs with different functional groups in the anion. ... 188

Figure 3.2.12 Comparison of the sorption of R-32 (panel A), R-125 (panel B), and R-134a (panel C) at 303.15 K on SiO_2/IL composites prepared with ILs with different functional groups in the cation. .. 188

Figure 3.2.13 Comparison of the sorption of R-32 (panel A), R-125 (panel B), and R-134a (panel C) at 303.15 K on SiO_2/IL composites prepared with ILs with different sizes (or absence) of the perfluorinated chain in the anion. 189

Figure 3.2.14 Comparison of the sorption of R-32 (panel A), R-125 (panel B), and R-134a (panel C) at 303.15 K on SiO_2/IL composites prepared with ILs with linear or ramified perfluorinated chain in the anion. 189

Figure 3.2.15 Henry's law constants (in $MPa \cdot g \cdot mmol^{-1}$) determined for the sorption of R-32, R-125, and R-134a, at 303.15 K, in the SiO_2/ILs composites studied in this work and pure ILs studied previously [19]. 192

Figure 3.2.16 Characteristic curves obtained by adsorption potential theory (APT) using the experimental sorption data of R-32, R-125, and R-134a at 303.15 K on SiO_2/$[C_2C_1Im][C_1CO_2]$ (panel A), SiO_2/$[C_2C_1Im][CF_3SO_3]$ (panel B), SiO_2/$[C_2C_1Im][N(CF_3SO_2)_2]$ (panel C), SiO_2/$[C_2C_1Im][N(C_2F_5SO_2)_2]$ (panel D), SiO_2/$[C_2C_1Im][N(C_4F_9SO_2)_2]$ (panel E), SiO_2/$[C_2C_1Im][C_4F_9CO_2]$ (panel F), SiO_2/$[C_2C_1Im]$ $[C_4F_9SO_3]$. 194

Figure 3.2.17 Sorption equilibrium isotherms of R-32 (panel A), R-125 (panel B), and R-134a (panel C) at 303.15 K on the studied SiO_2/IL composites. The dashed lines represent the fittings with the Dubinin–Astakhov (D–A) equation. 195

Figure 3.2.18 IAST predictions for the sorption of R-404A (panel A) and R-407F (panel B). 197

Figure 3.2.19 Selectivity of SiO_2 and the SiO_2/composites to the separation of the mixture R-32 / R-125 as a function of pressure at 303.15 K from the commercial R-410A refrigerant ($y_{R-32} = 0.7$ and $y_{R-125} = 0.3$)..... 198

Figure 3.2.20 Selectivity of SiO_2 and the SiO_2/composites to the separations of: R-32/R-125 (panel A); R-134a/R-32 (panel B); and R-134a/R-125 (panel C), as a function of pressure at 303.15 K from the commercial refrigerant R-407F ($y_{R-32} = 0.47$, $y_{R-125} = 0.21$, and $y_{R-134a} = 0.32$). 200

Figure 3.2.21 Selectivities, determined from the Henry's constants, of SiO_2 and composites studied in this work, and of ILs previously studied [19] at 303.15 K. 201

Figure 4.6.1 Schematic diagram of the manometric/calorimetric device. 222

Figure 4.6.2 Pore size distribution of AC1 (green triangles), AC2 (pink diamonds), BAC (blue circles), and Ecosorb (red squares), determined by deconvolution of the N_2 adsorption isotherm at 77 K using standard methods based on the Non-Localized Density Functional Theory (NLDFT)..... 223

Figure 4.6.3 Nitrogen adsorption isotherm at 77 K for AC1 (green triangles), AC2 (pink diamonds), BAC (blue circles), and Ecosorb (red squares) carbons. 224

Figure 4.6.4 Adsorption equilibrium isotherms of R-32 on AC1 (green triangles), AC2 (pink diamonds), BAC (blue circles), and Ecosorb (red squares), at 283.15 K (A, B), 303.15 K (C, D), and 323.15 K (E, F). The dashed lines represent the data fittings with the dimensionless form of Toth's model (eqn. 4.6.15). The right-hand-side plots use a logarithmic pressure scale. 225

Figure 4.6.5 Adsorption equilibrium isotherms of R-125 on AC1 (green triangles), AC2 (pink diamonds), BAC (blue circles), and Ecosorb (red squares), at 283.15 K (A, B), 303.15 K (C, D), and 323.15 K (E, F). The dashed lines represent the fittings with the dimensionless form of Toth's model (eqn. 4.6.15). The right-hand-side plots use a logarithmic pressure scale. 226

Figure 4.6.6 Adsorption equilibrium isotherms of R-134a on AC1 (green triangles), AC2 (pink diamonds), BAC (blue circles), and Ecosorb (red squares), at 283.15 K (A, B), 303.15 K (C, D), and 323.15 K (E, F). The dashed lines represent the fittings with the dimensionless form of Toth's model (eqn. 4.6.15). The right-hand-side plots use a logarithmic pressure scale. 227

Figure 4.6.7 Isosteric heats of adsorption of R-32 (A), R-125 (B), and R-134a (C) at 323.15 K on AC1 (green triangles), AC2 (pink diamonds), BAC (blue circles), and Ecosorb (red squares). 228

Figure 4.6.8 Determination of αT for R-32 adsorption on AC2. The molar volume of the adsorbed phase, $v_a(T)$, is such that a plot of $W \equiv v_a q$ as a function of $\phi \equiv RT \ln(f_s/f)$ produces a single characteristic curve with minimum data scatter that satisfies the condition $\lim \phi \to 0\ \theta = 1$ when W_s is equal to the specific pore volume, v_p. Data are represented for 283.15 K (red circles), 303.15 K (blue triangles), and 323.15 K (green squares). Data obtained with $\alpha = 1$ are shown as empty symbols on the right-hand-side vertical axis, which is shifted upwards by 0.4 units for better visualization. Data obtained with a corrected value of α are shown as full symbols. 230

Figure 4.6.9 Determination of $\alpha(T)$ for F-gas adsorption on AC1 and AC2 carbons: R-32/AC1 (A), R-125/AC1 (B), R-134a/AC1 (C), R-125/AC2 pair (D), and R-134a/AC2 (E). The molar volume of the adsorbed phase, $v_a(T)$, is such that a plot of $W \equiv v_a q$ as a function of $\phi \equiv RT \ln(f_s/f)$ produces a single characteristic curve with minimum data scatter that satisfies the condition $\lim \phi \to 0\ \theta = 1$ when W_s is equal to the specific pore volume, v_p. Data are represented for 283.15 K (red circles), 303.15 K (blue triangles), and 323.15 K (green squares). Data obtained with $\alpha = 1$ are shown in empty symbols and the vertical axis (represented at the right side) was shifted 0.4 units upwards for better visualization. Data obtained with a corrected value of α are shown in full symbols. 231

Figure 4.6.10 Determination of $\alpha(T)$ for F-gas adsorption on BAC and Ecosorb carbons: R-32/BAC pair (A), R-125/BAC (B), R-134a/BAC (C), R-32/Ecosorb (D), R-125/Ecosorb (E), and R-134a/Ecosorb (F) The molar volume of the adsorbed phase, $v_a(T)$, is such that a plot of $W \equiv v_a q$ as a function of $\phi \equiv RT \ln(f_s/f)$ produces a single characteristic curve with minimum data scatter that satisfies the condition $\lim \phi \to 0\ \theta = 1$ when W_s is equal to the specific pore volume, v_p. Data are represented for 283.15 K (red circles), 303.15 K (blue triangles), and 323.15 K (green squares). Data obtained with $\alpha = 1$ are shown in empty symbols and the vertical axis (represented at the right side) was shifted 0.4 units upwards for better visualization. Data obtained with a corrected value of α are shown in full symbols..... 232

Figure 4.6.11 Fractional loading or pore volume filling, $\theta = W/W_s \equiv q v_a/v_p$, as a function of reduced pressure, $x = P/P_s$, for R-32 adsorption on AC1 at 283.15 K (red circles), 303.15 K (blue triangles), and 323.15 K (green squares)..... 234

Figure 4.6.12 Fractional loading or pore volume filling, $\theta = W/W_s \equiv q v_a/v_p$, as a function of reduced pressure, $x = P/P_s$, for R-32 adsorption on AC1 at 283.15 K (red circles), 303.15 K (blue triangles), and 323.15 K (green squares)..... 235

Figure 4.6.13 Fractional loading or pore volume filling, $\theta = W/W_s \equiv q v_a/v_p$, as a function of reduced pressure, $x = P/P_s$, for R-32 adsorption on AC1 at 283.15 K (red circles), 303.15 K (blue triangles), and 323.15 K (green squares)..... 236

Figure 4.6.14 Adsorption equilibrium isotherms of R-32 on AC1 (green triangles), AC2 (pink diamonds), BAC (blue circles), and Ecosorb (red squares), at 283.15 K (A), 303.15 K (B), and 323.15 K (C). The dashed lines represent the fittings with the dimensionless dual-site Langmuir isotherm model (eqn. 4.6.19)..... 241

Figure 4.6.15 Adsorption equilibrium isotherms of R-125 on AC1 (green triangles), AC2 (pink diamonds), BAC (blue circles), and Ecosorb (red squares), at 283.15 K (A), 303.15 K (B), and 323.15 K (C). The dashed lines represent the fittings with the dimensionless dual-site Langmuir isotherm model (eqn. 4.6.19). 241

Figure 4.6.16 Adsorption equilibrium isotherms of R-134a on AC1 (green triangles), AC2 (pink diamonds), BAC (blue circles), and Ecosorb (red squares), at 283.15 K (A), 303.15 K (B), and 323.15 K (C). The dashed lines represent the fittings with the dimensionless dual-site Langmuir isotherm model (eqn. 4.6.19). 242

Figure 4.6.17 Isosteric heats of F-gas adsorption on AC1 and AC2, determined experimentally (black dots) at 323.15 K and calculated by applying the Clausius-Clapeyron equation to the APT (long-dashed green line), dual-site Langmuir (short-dashed red line), and Toth (solid blue line) models, and the values. A, R-32/AC1; B, R-32/AC2; C, R-125/AC1; D, R-125/AC2; E, R-134a/AC1; F, R-134a/AC2. 246

Figure 4.6.18 Isosteric heats of F-gas adsorption of BAC and Ecosorb, determined experimentally (black dots) at 323.15 K and calculated by applying the Clausius-Clapeyron equation to the APT (long-dashed green line), dual-site Langmuir (short-dashed red line), and Toth (solid blue line) models. A, R-32/BAC; B, R-32/Ecosorb; C, R-125/BAC; D, R-125/Ecosorb; E, R-134a/BAC; F, R-134a/Ecosorb. 247

Figure 4.6.19 Isosteric heats of F-gas adsorption of BAC and Ecosorb, determined experimentally (black dots) at 323.15 K and calculated by applying the Clausius-Clapeyron equation to the APT (long-dashed green line), dual-site Langmuir (short-dashed red line), and Toth (solid blue line) models. A, R-32/BAC; B, R-32/Ecosorb; C, R-125/BAC; D, R-125/Ecosorb; E, R-134a/BAC; F, R-134a/Ecosorb. 248

Figure 4.6.20 Comparison of experimental R-134a adsorption data on AC1 (green triangles), AC2 (pink diamonds), BAC (blue circles), and Ecosorb (red squares) carbons at 323.15 K. Data are compared per unit (A) weight (mmol/g), (B) surface area (mmol/m^2), and (C) pore volume (mmol/cm^3) of adsorbent. 249

Figure 4.6.21 Characteristic curves obtained by superimposing the experimental adsorption data of R-32, R-125, and R-134a at 283.15 K, 303.15 K and 323.15 K on AC1 (A, B), AC2 (C, D), BAC (E, F), and Ecosorb (G, H) into a single temperature-independent curve. The characteristic curves were fitted to eqn. 23 (represented as dashed lines). The right-hand-side plots use a logarithmic scale of fractional volume filling. 250

Figure 4.6.22 IAST prediction of the adsorbed amounts of (A) R-410A and (B) R-407F as function of pressure at the equilibrium gas-phase mole fractions corresponding to the bulk composition of R-410A ($y_{R-32} = 0.7$ and $y_{R-125} = 0.3$) and R-407F ($y_{R-32} = 0.47$, $y_{R-125} = 0.21$, and $y_{R-134a} = 0.32$) and 303.15 K. 252

Figure 4.6.23 IAST prediction of the adsorbed amounts of (A) R-410A and (B) R-407F as function of pressure at the equilibrium gas-phase mole fractions corresponding to the bulk composition of R-410A ($y_{R-32} = 0.7$ and $y_{R-125} = 0.3$) and R-407F ($y_{R-32} = 0.47$, $y_{R-125} = 0.21$, and $y_{R-134a} = 0.32$) and 303.15 K. 253

Figure 4.6.24 IAST prediction of the adsorbed amount of R-410A (purple circles), and of each of its components, R-32 (red squares) and R-125 (blue circles), on AC2 as a function of *y*R-32, at 303.15 K and 0.05 MPa (A), 0.1 MPa (B), 0.3 MPa (C), and 0.5 MPa (D). 253

Figure 4.6.25 IAST prediction of the adsorbed amount of R-410A (purple circles), and of each of its components, R-32 (red squares) and R-125 (blue circles), on BAC as a function of *y*R-32, at 303.15 K and 0.05 MPa (A), 0.1 MPa (B), 0.3 MPa (C), and 0.5 MPa (D). 254

Figure 4.6.26 IAST prediction of the adsorbed amount of R-410A (purple circles), and of each of its components, R-32 (red squares) and R-125 (blue circles), on Ecosorb as a function of *y*R-32, at 303.15 K and 0.05 MPa (A), 0.1 MPa (B), 0.3 MPa (C), and 0.5 MPa (D). 254

Figure 4.6.27 Selectivities to R-125 over R-32 for AC1 (A), AC2 (B), BAC (C), and Ecosorb (D) activated carbons, for the commercial R-410A gas mixture, as a function of yR-32, at 0.05 MPa, 0.1 MPa, 0.3 MPa, and 0.5 MPa, and 303.15 K 256

Figure 4.6.28 Selectivity of AC1 (green triangles), AC2 (pink diamonds), BAC (blue circles), and Ecosorb (red squares) to R-125 over R-32 as function of pressure at 303.15 K, for the equilibrium gas phase composition of bulk the R-410A mixture ($y_{R-32} = 0.7$ and $y_{R-125} = 0.3$). 256

Figure 4.6.29 Selectivities to R-125 over R-32 (A), R-134a over R-32 (B), and R-134a over R-125 (C) for AC1 (green triangles), AC2 (pink diamonds), BAC (blue circles), and Ecosorb (red squares) carbons, for the commercial R-407F gas mixture ($y_{R-32} = 0.47$, $y_{R-125} = 0.21$, and $y_{R-134a} = 0.32$), as a function of pressure at 303.15 K. For a better visualization, the inset on each graph shows a zoomed-in view of the curves for the lowest values of the selectivity. 257

Figure 4.7.1 Pore size distribution of the biomaterials studied in this work: a) CC-1:3H_3PO_4 (red line), CC-1:1H_3PO_4 (blue line), CC-K_2CO_3 (pink line) and CC-CO_2 (green line); b) nitrogen adsorption (full symbols) and desorption (empty symbols) equilibrium isotherms at 77 K for CC-1:3H_3PO_4 (red up triangles), CC-1:1H_3PO_4 (blue circles), CC-K_2CO_3 (pink diamond) and CC-CO_2 (green square). 261

Figure 4.7.2 For the four biomaterials investigated in this work, XPS detailed regions C1s of: a) CC-1:3(H_3PO_4); b) CC-1:1(H_3PO_4); c) CC-K_2CO_3; d) CC-CO_2..... 264

Figure 4.7.3 For the four biomaterials investigated in this work, XPS detailed regions P2p of: a) CC-1:3(H_3PO_4); and b) CC-1:1(H_3PO_4)..... 264

Figure 4.7.4 For the four biomaterials investigated in this work, XPS detailed regions O1s of: a) CC-1:3(H_3PO_4); b) CC-1:1(H_3PO_4); c) CC-K_2CO_3; and d) CC-CO_2..... 265

Figure 4.7.5 FTIR spectra for the biomaterials studied in this work: a) CC-1:3H_3PO_4 (red line); b) CC-1:1H_3PO_4 (blue line); c) CC-K_2CO_3 (pink line) and CC-CO_2 (green line)..... 266

Figure 4.7.6 Thermogravimetric analysis (TGA) of the biomaterials studied in this work: a) CC-1:3H_3PO_4 (red line); b) CC-1:1H_3PO_4 (blue line); c) CC-K_2CO_3 (pink line) and CC-CO_2 (green line). 267

Figure 4.7.7 SEM images of the biomaterials studied in this work: a) CC-1:3H_3PO_4; b) CC-1:1H_3PO_4, c) CC-K_2CO_3; and d) CC-CO_2..... 268

Figure 4.7.8 Adsorption (full symbols) and desorption (empty symbols) equilibrium isotherms: a) R-32; b) R-125; c) R-134a; d) SF_6; e) N_2 on CC-1:3H_3PO_4 (red up triangles), CC-1:1H_3PO_4 (blue circles), CC-K_2CO_3 (pink diamond) and CC-CO_2 (green square) at 303.15 K..... 270

Figure 4.7.9 Adsorption (full symbols) and desorption (empty symbols) equilibrium isotherms of: a) R-32; b) R-125; c) R-134a; d) SF_6; and e) N_2 on CC-K_2CO_3..... 271

Figure 4.7.10 Adsorption (full symbols) and desorption (empty symbols) equilibrium isotherms of: a) R-32; b) R-125; c) R-134a; d) SF_6; and e) N_2 on CC-CO_2..... 272

Figure 4.7.11 Adsorption (full symbols) and desorption (empty symbols) equilibrium isotherms of: a) R-32; b) R-125; c) R-134a; d) SF_6; e) N_2 on CC-1:3H_3PO_4 (red up triangles), CC-1:1H_3PO_4 (blue circles), CC-K_2CO_3 (pink diamond) and CC-CO_2 (green square) at 303.15 K..... 273

Figure 4.7.12 Relationship of adsorption uptakes versus S_{BET} of: a) R-125; b) R-134a; c) SF_6 at 303.15 K and 0.1 MPa. 274

Figure 4.7.13 Relationship of adsorption uptakes versus S_{BET} of: a) R-125; b) R-134a; c) SF_6 at 303.15 K and 0.1 MPa. 276

Figure 4.7.14 The adsorption of R-32 on porous matrices at 0.1 MPa and 303.15 K. 276

Figure 4.7.15 The adsorption of R-32 on porous matrices at 0.1 MPa and 303.15 K 277

Figure 4.7.16 The adsorption of R-134a on porous matrices at 0.1 MPa and 303.15 K. 277

Figure 4.7.17 The adsorption of SF_6 on porous matrices at 0.1 MPa and 303.15 K. 278

Figure 4.7.18 Henry's law constants at 303.15 K for the biomaterials studied in this work. 285

Figure 4.7.19 Isosteric heat of adsorption: a) R-32; b) R-125; c) R-134a; d) SF_6; and e) N_2 on CC-K_2CO_3 and CC-CO_2. 287

Figure 4.7.20 Adsorption isosteres on CC-K_2CO_3 of: a) R-32; b) R-125; c) R-134a; d) SF_6; and e) N_2 in the temperature range 283.15-323.15 K 288

Figure 4.7.21 Adsorption isosteres on CC-CO_2 of: a) R-32; b) R-125; c) R-134a; d) SF_6 and E) N_2 in the 283.15-323.15 K temperature range. 289

Figure 4.7.22 Selectivity of CC-1:3H_3PO_4 (red up triangles), CC-1:1H_3PO_4 (blue circles), CC-K_2CO_3 (pink diamond) and CC-CO_2 (green square) to R-32 over R-125 as a function of pressure at 303.15 K for the equilibrium gas phase composition of the R-410A mixture (y_{R-32} = 0.7 and y_{R-125} = 0.3). 291

Figure 4.7.23 Selectivity of CC-1:3H_3PO_4 (red up triangles), CC-1:1H_3PO_4 (blue circles), CC-K_2CO_3 (pink diamond) and CC-CO_2 (green square) to SF_6 over N_2 as a function of pressure at 303.15 K, for the equilibrium gas phase composition of the SF_6/N_2 mixture (y_{SF_6}= 0.10 and y_{N_2} = 0.90). 291

Figure 4.7.24 Selectivity of CC-1:3H_3PO_4 (red up triangles), CC-1:1H_3PO_4 (blue circles), CC-K_2CO_3 (pink diamond) and CC-CO_2 (green square) to R-125 over R-32 as a function of pressure at 303.15 K, for the equilibrium gas phase composition of the R-410A mixture (y_{R-32} = 0.7 and y_{R-125} = 0.3). 292

Figure 4.7.25 Selectivity of CC-1:3H_3PO_4 (red up triangles), CC-1:1H_3PO_4 (blue circles), CC-K_2CO_3 (pink diamond) and CC-CO_2 (green square) to: a) R-134a over R-32; b) R-134a over R-125; and c) R-32 over R-125, for the commercial R-407C gas mixture (y_{R-32} = 0.38, y_{R-125} = 0.18, and y_{R-134a} = 0.44, as a function of pressure at 303.15 K. 293

Figure 4.7.26 Selectivity of CC-1:3H_3PO_4 (red up triangles), CC-1:1H_3PO_4 (blue circles), CC-K_2CO_3 (pink diamond) and CC-CO_2 (green square) to: a) R-134a over R-32; b) R-134a over R-125; and c) R-32 over R-125, for the commercial R-407F gas mixture (y_{R-32} = 0.47, y_{R-125} = 0.21, and y_{R-134a} = 0.32), as a function of pressure at 303.15 K..... 293

Figure 4.8.1 Pore size distribution of the adsorbents studied in this work of: (a) CS-CO_2 (red line), CS-$ZnCl_2$ (blue line), ACM (pink line) and Fe-BTC(green line); (b) nitrogen adsorption (full symbols) and desorption (empty symbols) equilibrium isotherms at 77 K for CS-CO_2 (red up triangles), CS-$ZnCl_2$ (blue circles), ACM (pink diamond) and Fe-BTC(green square). 298

Figure 4.8.2 Characterizations of (a) FTIR spectra and (b) thermogravimetric analysis (TGA) for the adsorbents studied in this work: CS-CO_2 (red line), CS-$ZnCl_2$ (blue line), ACM (pink line) and Fe-BTC (green line). 299

Figure 4.8.3 Characterizations of (a) FTIR spectra and (b) thermogravimetric analysis (TGA) for the adsorbents studied in this work: CS-CO_2 (red line), CS-$ZnCl_2$ (blue line), ACM (pink line) and Fe-BTC (green line). 302

Figure 4.8.4 Adsorption (full symbols) and desorption (empty symbols) equilibrium in the pressure range 0 – 0.1 MPa of: (a) R-32; (b) R-125; (c) R-134a; (d) R-143a; (e) CO_2 and (f) CH_4 at 303.15 K 303

Figure 4.8.5 Adsorption (full symbols) and desorption (empty symbols) equilibrium isotherms on CS-CO_2 of: (a) R-32; (b) R-125; (c) R-134a; (d) R-143a; (e) CO_2 and (f) CH_4. 304

Figure 4.8.6 Adsorption (full symbols) and desorption (empty symbols) equilibrium isotherms on CS-$ZnCl_2$ of: (a) R-32; (b) R-125; (c) R-134a; (d) R-143a; (e) CO_2; and (f) CH_4. 305

Figure 4.8.7 Adsorption (full symbols) and desorption (empty symbols) equilibrium isotherms on ACM of: (a) R-32; (b) R-125; (c) R-134a; (d) R-143a; (e) CO_2; and (f) CH_4..... 306

Figure 4.8.8 Adsorption (full symbols) and desorption (empty symbols) equilibrium isotherms on Fe-BTC of: (a) R-32; (b) R-125; (c) R-134a; (d) R-143a; (e) CO_2; and (f) CH_4. 307

Figure 4.8.9 Comparison of the fitting obtained for CS-$ZnCl_2$ with the adsorption models: (a) Dual site Langmuir; and (b) Toth. 308

Figure 4.8.10 Adsorption isosteres on CS-CO_2 of: (a) R-32; (b) R-125; (c) R-134a; (d) R-143a; (e) CO_2 and (f) CH_4 in the temperature range 283.15-323.15 K. 312

Figure 4.8.11 Adsorption isosteres on CS-$ZnCl_2$ of: (a) R-32; (b) R-125; (c) R-134a; (d) R-143a; (e) CO_2 and (f) CH_4 in the temperature range 283.15-323.15 K. 313

Figure 4.8.12 Adsorption isosteres on ACM of: (a) R-32; (b) R-125; (c) R-134a; (d) R-143a; (e) CO_2 and (f) CH_4 in the temperature range 283.15-323.15 K. 314

Figure 4.8.13 Adsorption isosteres on Fe-BTC of: (a) R-32; (b) R-125; (c) R-134a; (d) R-143a; (e) CO_2 and (f) CH_4 in the temperature range 283.15-323.15 K. 315

Figure 4.8.14 Isosteric heat of adsorption of: (a) R-32; (b) R-125; (c) R-134a; (d) R-143a; (e) CO_2; and (f) CH_4 at 303.15 K. 316

Figure 4.8.15 Selectivity of CS-CO_2 (red line), CS-$ZnCl_2$ (blue line), ACM (pink line) and Fe-BTC (green line) to R-32 over R-125 as a function of pressure at 303.15 K, for R-410A blend ($y_{R-32} = 0.7$ and $y_{R-125} = 0.3$). 318

Figure 4.8.16 Selectivity of CS-CO_2 (red line), CS-$ZnCl_2$ (blue line), ACM (pink line) and Fe-BTC (green line) to: (a) R-125 over R-32; (b) R-134a over R-125 and (c) R-134a over R-32, as a function of pressure at 303.15 K for the commercial R-407C blend ($y_{R-32} = 0.38$, $y_{R-125} = 0.18$, and $y_{R-134a} = 0.44$). 319

Figure 4.8.17 Selectivity of CS-CO_2 (red line), CS-$ZnCl_2$ (blue line), ACM (pink line) and Fe-BTC (green line) to: (a) R-134a over R-143a, (b) R-134a over R-125 and (c) R-143a over R-125, as a function of pressure at 303.15 K for the commercial R-404A blend ($y_{R-125} = 0.44$, $y_{R-143a} = 0.56$, and $y_{R-134a} = 0.04$). 320

Figure 4.8.18 Selectivity of CS-CO_2 (red line), CS-$ZnCl_2$ (blue line), ACM (pink line) and Fe-BTC (green line) to CO_2 over CH_4 as a function of pressure at 303.15 K, for the CO_2/CH_4 mixture ($y_{CO_2} = 0.4$ and y $y_{CH_4} = 0.6$). 320

Figure 4.9.1 Pore size distribution of the studied adsorbents, determined by deconvolution of the N_2 (77K) or Ar (87K) adsorption isotherms using standard methods based on the Non-Localized Density

Functional theory (NLDFT). Panel A: Cu-BTC (red up triangles), ZIF-8 (green down triangles), MOF-177 (yellow circles), and MIL-53 (Al) (blue squares). Panel B: Zeolite ZSM-5 (pink diamond). 324

Figure 4.9.2 Adsorption isotherms of nitrogen at 77 K for Cu-BTC, ZIF-8, MOF 177 and MIL 53 (Al) (panel A), and of argon at 87 K for zeolite ZSM5 (panel B). 325

Figure 4.9.3 Adsorption equilibrium isotherms of R-32 on Cu-BTC (red up triangles), ZIF-8 (green down triangles), MOF-177 (yellow circles), MIL-53(Al) (blue squares), and zeolite ZSM-5 (pink diamond), at 283.15 K (panel A), 303.15 K (panel B), and 323.15 K (panel C). The dashed lines represent the data fittings with the Toth's model for Cu-BTC, ZIF-8, ZSM-5, and MIL-53(Al) or the Virial model for MOF-177. 326

Figure 4.9.4 Adsorption equilibrium isotherms of R-125 on Cu-BTC (red up triangles), ZIF-8 (green down triangles), MOF-177 (yellow circles), MIL-53 (Al) (blue squares), and zeolite ZSM-5 (pink diamond), at 283.15 K (panel A), 303.15 K (panel B), and 323.15 K (panel C). The dashed lines represent the data fittings with the Toth's model for Cu-BTC, ZIF-8, ZSM-5, and MIL-53(Al) or the Virial model for MOF-177. 327

Figure 4.9.5 Adsorption equilibrium isotherms of R-134a on Cu-BTC (red up triangles), ZIF-8 (green down triangles), MOF-177 (yellow circles), MIL-53 (Al) (blue squares), and zeolite ZSM-5 (pink diamond), at 283.15 K (panel A), 303.15 K (panel B), and 323.15 K (panel C). The dashed lines represent the data fittings with the Toth's model for Cu-BTC, ZIF-8, ZSM-5, and MIL-53(Al) or the Virial model for MOF-177. 327

Figure 4.9.6 Adsorption equilibrium isotherms at 303.15 K of R-32 (panel A), R-125 (panel B), and R-134a (panel C) on Cu-BTC (red up triangles), ZIF-8 (green down triangles), MOF-177 (yellow circles), MIL-53 (Al) (blue squares), and zeolite ZSM-5 (pink diamond). The dashed lines represent the fittings with the Toth's or Virial models. 328

Figure 4.9.7 Comparison between the adsorption of R-32 (panel A) and R-125 (panel B) in Cu-BTC at 283.15, 303.15, and 323.15 K, studied in this work, and literature data available at 293.15 K [97]. . 329

Figure 4.9.8 Comparison of the Toth's and Virial models fitting to the adsorption of R-32 in MOF-177. 330

Figure 4.9.9 Adsorption equilibrium isotherms at 303.15 K of R-32 (squares), R-134a (diamond), and R-125 (hexagon) on Cu-BTC (panel A), ZIF-8 (panel B), MOF-177 (panel C), MIL-53(Al) (panel D),

and ZSM-5 (panel E). The dashed lines represent the fittings with the Toth's (panels A, B, D, and E) or the Virial models (panel C). 334

Figure 4.9.10 Differential heats of adsorption of R-32 (panel A), R-125 (panel B), and R-134a (panel C) at 323.15 K on Cu-BTC (red up triangles), ZIF-8 (green down triangles), MOF-177 (yellow circles), MIL-53 (Al) (blue squares), and Zeolite ZSM-5 (pink diamond). 335

Figure 4.9.11 IAST prediction of the adsorbed amounts of R-410A (panel A) and R-407F (panel B) as a function of pressure at the equilibrium gas-phase mole fractions corresponding to the bulk composition (R-410A: $y_{R-32} = 0.7$ and $y_{R-125} = 0.3$; and R-407F: $y_{R-32} = 0.47$, $y_{R-125} = 0.21$, and $y_{R-134a} = 0.32$) at 303.15 K. 337

Figure 4.9.12 Selectivity of Cu-BTC (red line), ZIF-8 (green line), MOF-177 (yellow line), MIL-53 (Al) (blue line), and zeolite ZSM-5 (pink line) to R-32 over R-125 as a function of pressure at 303.15 K, for the equilibrium gas phase composition of bulk the R-410A mixture ($y_{R-32} = 0.7$ and $y_{R-125} = 0.3$). 338

Figure 4.9.13 Selectivities of Cu-BTC, ZIF-8, MOF-177, MIL-53(Al), and ZSM-5 to: R-125 over R-32 (panel A); R-134a over R-32 (panel B); and R-134a over R-125 (panel C), for the commercial R-407F gas mixture ($y_{R-32} = 0.47$, $y_{R-125} = 0.21$, and $y_{R-134a} = 0.32$), as a function of pressure at 303.15 K. 339

Figure 4.10.1 Pore size distribution of the POPs studied in this work: a) RIO-55 (dark red line), b) RIO-20 (green line), c) RIO-23 (orange line) and RIO-12 (dark green line), and d) nitrogen adsorption (full symbols) and desorption (empty symbols) equilibrium isotherms at 77 K for RIO-55 (dark red), RIO-23 (orange), RIO-20 (green) and RIO-12 (dark green). 344

Figure 4.10.2 Equilibrium isotherms at 77 K for: a) RIO-55 (dark red) and RIO-12 (dark green). 345

Figure 4.10.3 FTIR spectra for the POPs studied in this work: RIO-55 (dark red line), RIO-23 (orange line), RIO-20 (green line), and RIO-12 (dark green line). 346

Figure 4.10.4 TGA of the POPs studied in this work: RIO-55 (dark red line), RIO-23 (orange line), RIO-20 (green line) and RIO-12 (dark green line). 347

Figure 4.10.5 SEM images of the POPs studied in this work: a) RIO-55, b) RIO-23, c) RIO-20, and d) RIO-12. 349

Figure 4.10.6 Adsorption (full symbols) and desorption (empty symbols) equilibrium isotherms of: a) R-32; b) R-125; and c) R-134a on RIO-55 (dark red), RIO-23 (orange), RIO-20 (green) and RIO-12 (dark green) at 303.15 K..... 352

Figure 4.10.7 Adsorption (full symbols) and desorption (empty symbols) equilibrium isotherms of: a) SF_6; b) N_2 on RIO-55 (dark red), RIO-23 (orange), RIO-20 (green) and RIO-12 (dark green) at 303.15 K..... 353

Figure 4.10.8 Henry's law constants at 303.15 K for the POPs studied in this work..... 353

Figure 4.10.9 Selectivity of RIO-55 (dark red), RIO-23 (orange), RIO-20 (green) and RIO-12 (dark green) to R-32 over R-125 as a function of pressure at 303.15 K, for the equilibrium gas phase composition of the R-32/R-125 mixture ($y_{R-32} = 0.7$ and $y_{R-125} = 0.3$). The dotted line represents the point where selectivity is equal to $y = 1$. 355

Figure 4.10.10 Selectivity of RIO-55 (dark red), RIO-23 (orange), RIO-20 (green) and RIO-12 (dark green) (green square) to SF_6 over N_2 as a function of pressure at 303.15 K, for the equilibrium gas phase composition of the SF_6/N_2 mixture ($y_{SF_6} = 0.10$ and $y_{N_2} = 0.90$). The dotted line represents the point where selectivity is equal to $y = 1$..... 356

Figure 4.10.11 Selectivity of RIO-55 (dark red circles), RIO-23 (orange triangles), RIO-20 (green diamonds) and RIO-12 (dark green squares) to: a) R-32 over R-125; b) R-134a over R-125; and c) R-134a over R-32 as a function of pressure at 303.15 K, for the commercial R-407C gas mixture ($y_{R-32} = 0.38$, $y_{R-125} = 0.18$ and $y_{R-134a} = 0.44$). The dotted line represents the point where selectivity is equal to $y = 1$. 357

Figure 4.10.12 Comparison of the adsorption capacity of R-32 and R-125, and the selectivity of the R-410A mixture ($y_{R-32} = 0.7$ and $y_{R-125} = 0.3$) for the materials studied in this work and those reported in the literature at a pressure of 0.1 MPa and 303.15 K [19,27,29,30,38,181–191]..... 358

Figure 4.10.13 Comparison of the adsorption capacity of SF_6 and N_2, and the selectivity of the SF_6/N_2 mixture ($y_{SF_6} = 0.10$ and $y_{N_2} = 0.90$) for the materials studied in this work and those reported in the literature at a pressure of 0.1 MPa and 303.15 K [107,120–122,195–200]..... 359

Figure 5.4.1 Adsorption (full symbols) and desorption (empty symbols) equilibrium isotherms on: (a) SF_6 and (b) N_2 at 303.15 K..... 389

Figure 5.4.2 Adsorption (full symbols) and desorption (empty symbols) equilibrium isotherms of SF_6 on: (a) CS-CO_2, (b) CS-$ZnCl_2$, (c) ACM and (d) Fe-BTC. 391

Figure 5.4.3 Adsorption (full symbols) and desorption (empty symbols) equilibrium isotherms of N_2 on: (a) CS-CO_2, (b) CS-$ZnCl_2$, (c) ACM and (d) Fe-BTC. 391

Figure 5.4.4 SF_6 working capacity (Δq_{SF_6}) as a function of desorption temperature T_H for isobaric operation at the pressure of 0.010 MPa and temperature of 303.15 K. 392

Figure 5.4.5 Contour plots of the working capacity (mmol/g) as a function of the degassing temperature, T_H, and the feed pressure, P on: (a) CS-CO_2, (b) CS-$ZnCl_2$, (c) ACM and (d) Fe-BTC..... 394

Figure 5.4.6 Isosteric heat of adsorption of: (a) SF_6 and (b) N_2. 396

Figure 5.4.7 Henry's Law constants at 303.15 K. 397

Figure 5.4.8 Selectivity of CS-CO_2, CS-$ZnCl_2$, ACM, Fe-BTC to SF_6 over N_2 as a function of pressure at 303.15 K for the equilibrium gas phase composition of the SF_6/N_2 mixture (y_{SF_6}= 0.02 and y_{N_2} = 0.98)..... 398

Figure 5.4.9 Comparison of materials studied in this work and literature, taking into account: (a) q_{SF_6} *versus* S_{BET}; (b) q_{SF_6} *versus* v_{total}; (c) SF_6/N_2 selectivity *versus* S_{BET}; and (d) SF_6/N_2 selectivity *versus* v_{total} at 303.15 K and 0.1 MPa for the equilibrium gas phase composition of y_{SF_6}= 0.02 and y_{N_2} = 0.98 [38,39,43–46,48,49,53,54,62–64]. 400

Figure 5.4.10 Selection criteria of porous solid matrices using Ackey's FOM, Yang's FOM, and regeneration capacity at an adsorption pressure of 0.1 MPa and 303.15 K, with desorption at 0.001 MPa and 303.15 K. 403

Figure 5.4.11 Selection criteria for porous solid matrices using Ackey's FOM, and Yang's FOM for: (a) condition 1 - feed pressure of 1 MPa at 303.15 K and desorption pressure of 0.1 MPa at 303.15 K, (b) Condition 2 - feed pressure of 1 MPa at 303.15 K and desorption pressure of 0.1 MPa at 313.15 K and (c) Condition 3 - feed pressure of 1 MPa at 303.15 K and desorption pressure of 0.001 MPa at 323.15 K. 405

Figure 5.5.1 Characterisation of the carbon samples studied in this work: a) pore size distribution (calculated using the DFT adsorption model) and b) the nitrogen adsorption (full symbols) and desorption (empty symbols) equilibrium isotherms at 77 K for AC1, AC2, AC3 and ACHM. 408

Figure 5.5.2 Adsorption (full symbols) and desorption (empty symbols) equilibrium isotherms of SF_6 on a) AC1 and b) AC2..... 409

Figure 5.5.3 Adsorption (full symbols) and desorption (empty symbols) equilibrium isotherms of N_2 on a) AC1, b) AC2, AC3 and c) ACHM. 410

Figure 5.5.4 SF_6 working capacity (Δq_{SF_6}) as a function of desorption temperature (T_H) for isobaric operation at 0.01 MPa and an adsorption temperature of 303 K. 412

Figure 5.5.5 Contour plots of the working capacity (mmol/g) as a function of the degassing temperature, T_H, and the feed pressure, P on: a) AC1, b) AC2, AC3 and c) ACH. 414

Figure 5.5.6 Isosteric heat of adsorption of: a) SF_6 and b) N_2 at 303 K. 416

Figure 5.5.7 Henry's law constants for all adsorbents at 303 K. 417

Figure 5.5.8 Selectivity of AC1, AC2, AC3, and ACHM to SF_6 over N_2 as a function of pressure at 303 K for the equilibrium gas phase composition of the SF_6/N_2 mixture (y_{SF_6} = 0.02 and y_{N_2} = 0.98)..... 419

Figure 5.5.9 Comparison of the SF_6 adsorption capacity (q, mmol·g^{-1}) and SF_6/N_2 selectivity of the materials in this work (AC1, AC2, AC3, and ACHM) with materials reported in the literature at 303.15 K [36–39,43–49]. 420

Figure 5.5.10 The selection criteria for the selection of materials at 303 K for: a) 0.1 MPa and b) 0.5 MPa. 421

LIST OF TABLES

Table 1.1.1 Greenhouse gases studied in this work. 4

Table 1.3.1 Adsorption models: scientific and mathematical comparison 16

Table 1.4.1 Overview of physical, chemical, and biomass-based activated carbons 25

Table 2.3.1 Chemical structures and acronyms of the ionic liquids used in this work. 51

Table 2.3.2 Values of dynamic viscosity (η), density (ρ), refractive index (n_D), molar volume (V_m), and molar refraction (R_m) of ionic liquids at 303.15 K. 57

Table 2.3.3 Determined parameters for the NRTL obtained from the binary system fluorinated gas (1) + ionic liquid (2). 62

Table 2.4.1 Chemical structures of the fluorinated ionic liquids, perfluorinated acids, and F-gases used in this work. 67

Table 2.4.2 Solid-solid transitions ($T_{s\text{-}s}$), melting temperatures (T_m), and glass transitions (T_g) of the FILs and binary mixtures studied in this work. 76

Table 2.4.3 Densities at different temperatures, fitting parameters for ln(ρ) as a function of temperature and standard deviations (σ) shown of the DES studied in this work. 78

Table 2.4.4 NRTL Parameters obtained for systems R-32 (*i*) + DES (*j*). 93

Table 2.4.5 NRTL Parameters obtained for systems R-125 (*i*) + DES (*j*). 93

Table 2.4.6 NRTL Parameters obtained for systems R-134a (*i*) + DES (*j*). 94

Table 2.4.7 NRTL Parameters obtained for systems R-134a (*i*) + DES (*j*). 94

Table 2.5.1 Chemical structures and acronyms of the ionic liquids used in this work. 101

Table 2.5.2 Calculated values used as input for pseudo component and property COSMOSAC specification in Aspen Plus v10 (1). 104

Table 2.5.3 Calculated values used as input for pseudo component and property COSMOSAC specification in Aspen Plus v10 (2). 107

Table 2.5.4 Operating and investment costs of the complete process using $[C_2C_1Im][CF_3SO_3]$ as absorbent at the optimized operating conditions. 123

Table 2.6.1 Chemical structures and acronyms of the ionic liquids used in this work. 127

Table 2.6.2 Physical properties of the ionic liquids under study. 128

Table 2.6.3 Degradation temperature of ionic liquids under study. 128

Table 2.6.4 Experimental and COSMO-RS Henry's law constants of solutes in ILs at near-ambient temperature and atmospheric pressure using experimental vapor pressures of pure compounds. 131

Table 2.6.5 Cations and anions of the ionic liquids of this work. 136

Table 2.6.6 NRTL Parameters obtained for systems R-32 (i) + ILs (j). 147

Table 2.6.7 NRTL Parameters obtained for systems R-134a (i) + ILs (j). 148

Table 2.6.8 Comparison of the molar (x) and mass (w) solubility and Henry constant for the F-gas in ILs of this work ($[P_{2444}][C_2C_2PO_4]$, $[P_{66614}][C_2NO_2]$ and $[P_{66614}][CNPyr]$) and with other ILs [29,30] at 303.15 K and pressures of 0.1, 0.2 and 0.4 MPa. 149

Table 3.2.1 Acronyms and chemical structures of the ILs and F-gases studied in this work. 172

Table 3.2.2 Affinity coefficient, β, for each sorbent/F-gas pair. 176

Table 3.2.3 BET surface area and pore volume of silica and of the silica/IL composites. 177

Table 3.2.4 Sips parameters obtained from the binary systems F-gas + SiO_2/IL composite. 182

Table 3.2.5 Henry's law constants (in MPa·g·mmol^{-1}) determined for the sorption of R-32, R-125, and R-134a on the composites studied in this work and for the pure ILs studied in previous work (Sosa et al. 2019) [29]. 190

Table 3.2.6 Dubinin–Astakhov (D–A) model parameters determined silica/ionic liquid composite. 195

Table 4.6.1 BET surface area, $\boldsymbol{S_{BET}}$ (m^2/g), and specific pore volume, $\boldsymbol{v_p}$ (cm^3/g), of the ACs. 223

Table 4.6.2 Molar volumes of the saturated liquid adsorptive and adsorbed phase, vm (cm^3/mol) and va (cm^3/mol), and molar volume ratio, $\alpha = v_a/vm$, for the twelve solid-fluid systems at each of the three studied temperatures, T (K). 233

Table 4.6.3 Best-fit parameter values of the dimensionless Toth model (eqn. 4.6.15) for each AC/F-gas pair. 240

Table 4.6.4 Best-fit parameter values of the dimensionless dual-site Langmuir model (eqn. 4.6.19) with adsorbate-dependent $\theta 1$ for each AC/F-gas pair. 240

Table 4.6.5 Best-fit parameter values of the APT model (eqn.4.6.21) for each AC/F-gas system. The γ_i's are expressed in J/mol. 242

Table 4.6.6 Best-fit parameter values of the dimensionless dual-site Langmuir model (eqn. 4.6.21) with adsorbate-independent $\theta 1$ for each AC/F-gas pair. 243

Table 4.7.1 Textural parameters of biomaterials studied in this work. 260

Table 4.7.2 Atomic concentrations (%) of relevant elements in carbon samples. 262

Table 4.7.3 Peak positions (eV), atomic concentrations (%) and assignments for the XPS detailed regions. 263

Table 4.7.4 Elemental analysis of the biomaterials studied in this work. 267

Table 4.7.5 The comparison between the literature data and experimental data of this work for F-gases (R-32, R-125, R-134a, and SF_6) on porous matrices. 279

Table 4.8.1 Textural parameters of the adsorbents studied in this work. 297

Table 4.8.2 Elemental analysis of the materials. 300

Table 4.8.3 DSL model parameters for sorption of R-32, R-125, R-134a, R-143a, CO_2 and CH_4 at 283.15 K, 303.15 K, and 323.15 K..... 309

Table 4.8.4 Viral model parameters obtained for R-32, R-125, R-134a, R-134a, CO_2 and CH_4..... 310

Table 4.9.1 BET surface area, $\boldsymbol{S_{BET}}$, and specific pore volume, $\boldsymbol{v_p}$, of the zeolite and MOFs. 323

Table 4.9.2 Best-fit parameter values of the Toth model for each adsorbent/F-gas pair..... 332

Table 4.9.3 Viral model parameters obtained for the system MOF-177 + F-gas. 332

Table 4.10.1 Textural parameters of POPs studied in this work obtained from N_2 adsorption isotherms. 344

Table 4.10.2 Elemental analysis of the POPs studied in this work..... 347

Table 4.10.3 Adsorption equilibrium model parameters for sorption of R-32, R-125, R-134a, SF_6 and N_2 on POPs at 303.15 K. 350

Table 5.4.1 Textural parameters of materials studied in this work obtained from N_2 adsorption-desorption isotherms..... 390

Table 5.4.2 Toth adsorption model parameters for sorption of SF_6 and N_2 at 283.15 K, 303.15 K, and 323.15 K. 390

Table 5.4.3 Toth adsorption model parameters for sorption of SF_6 and N_2 at 283.15 K, 303.15 K, and 323.15 K. 398

Table 5.5.1 Textural parameters of activated carbons obtained from N_2 adsorption at 77 K**.** 408

Table 5.5.2 Toth adsorption model parameters for adsorption of SF_6 and N_2 at 283, 303, and 323 K. 411

ACRONYMS AND ABBREVIATIONS

ACs	Activated carbon
ACM	Activated carbon monoliths
ARE	Average relative error
ATP	Adsorption potential theory
BET	Brunauer–emmett–teller
Bio-Acs	Biomaterials
CS	Coconut shell
EDS	Energy Dispersive X-ray Spectroscopy
exp	Experimental
DSC	Differential scanning calorimeter
DFT	Density functional theory
DES	Deep eutectic solvent
DSL	Dual–site langmuir
D–A	Dubinin–astakhov
DMSO	Dimethyl Sulfoxide
EA	Elemental analysis
EU	European union
EDS	Eenergy-dispersive X-ray spectroscopy
F-gases	Fluorinated gases
FILs	Fluorinated ionic liquids
FTIR	Fourier-transform infrared spectroscopy
fit	Adjusted
^{19}F NMR	Fluorine-19 nuclear magnetic resonance
ILs	Ionic liquids
IAST	Ideal adsorbed solution theory.
GHGs	Greenhouse gases
GWP	Global warming potential
^{1}H NMR	Resonancia Magnética Nuclear de Protón
HFCs	Hydrofluorocarbon
HB	Hydrogen bonding
H^E	Excess enthalpy

K_H	Henry's constant
MSB	Magnetic suspension microbalance
MOF	Metal-organic framework
MF	Electrostatic-misfit
NIST	National Institute of Standards and Technology
NRTL	Non-random two-liquid
PFCs	Perfluorocarbons
POPs	Porous Organic Polymers
Q_{st}	Isosteric heat
RMSD	Root mean square deviation
SEM	Scanning electron microscop
R_g	Ideal gas constant (J K^{-1} mol^{-1})
S_{BET}	Surface area (m^2 g^{-1})
TFA	Trifluoroacetic acid
TGA	Thermal gravimetric analysis
$T_{s\text{-}s}$	Solid-solid transitions
T_m	Melting temperatures
T_g	Glass transitions
VDW	van der waals
XPS	Photoelectron spectra
XRPD	Crystallographic analyses were conducted by X-ray powder diffraction

.

CHEMICAL FORMULAE

[Im]	1H-imidazolium
[C_1Im]	1-methylimidazolium
[C_2Im]	1-ethyl-imidazolium
[C_2C_1Im]	1-ethyl-3-methylimidazolium
[$C_2C_{1(OH)}$Im]	1-(2-hydroxyethyl)-3-methylimidazolium
[C_4C_1Im]	1-butyl-3-methylimidazolium
[C_4C_2Im]	1-butyl-3-ethylimidazolium
[C_6C_1Im]	1-hexyl-3-methylimidazolium
[C_9C_1Im]	1-nonyl-3-methylimidazolium
[C_8C_1Im]	1-octyl-3-methylimidazolium
[C_2C_3Im]	1-ethyl-3-propylimidazolium
[C_4C_4Im]	1,3-dibutyl-1H-imidazolium
[C_4C_9Im]	1-methyl-3-heptylimidazolium
[C_9C_9Im]	1,3-dinonyl-1H-imidazol-3-ium
[$C_{10}C_1$Im]	1-decyl-3-methylimidazolium
[$C_8H_4F_{13}$Im]	1-(3,3,4,4,5,5,6,6,7,7,8,8,8-tridecafluorooctyl)-3 methylimidazolium
[C_1py]	1-ethylpyridinium
[C_9py]	1-nonylpyridinium
[C_2C_1py]	1-ethyl-3-methylpyridinium
[C_1C_4py]	4-methyl-N-butylpyridinium
[C_4pyr]	1-butylpyrrolidinium
[C_8pyr]	1-octylpyrrolidinium
[C_1C_1pyr]	1,1-dimethylpyrrolidinium
[C_2C1pyr]	1-ethyl-1-methylpyrrolidinium
[C_4C_1pyr]	1-butyl-1-methylpyrrolidinium
[C_4C_2pyr]	1-butyl-1-ethylpyrrolidinium
[C_8C_1pyr]	1-octyl-1-methylpyrrolidinium
[C_9C_1pyr]	1-nonyl-1-methylpyrrolidinium
[C_4C_2pyr]	1-butyl-1-ethylpyrrolidinium
[$C_2C_2SO_4$]	Ethoxyethylsulfate

[S_{444}]	Tributylsulfonium
[P_{2222}]	Tetraethyl-phosphonium
[P_{2228}]	Triethyl-octylphosphonium
[P_{6661}]	Trihexyl-methylphosphonium
[P_{66614}]	Trihexyl-tetradecylphosphonium
[P_{8888}]	Tetraoctylphosphonium
[N_{2HHH}]	Ethylammonium
[N_{4444}]	Tetrabutylammonium
[$N_{1112(OH)}$]	(2-hydroxyethyl)-trimethyl ammonium
[C_1SO_4]	Methylsulfate
[C_2SO_4]	Ethylsulfate
[C_4SO_4]	Butylsulfate
[$C_2C_2SO_4$]	Ethoxyethylsulfate
[CF_3CO_2]	Trifluoroacetate
[CF_3SO_3]	Trifluoromethanesulfonate
[CF_4SO_3]	1,1,2,2-tetrafluoroethanesulfonate
[$C_4F_9SO_3$]	Perfluorobutanesulfonate
[$N(CF_3SO_2)_2$]	Bis(trifluoromethylsulfonyl)imide
[$N(C_2F_5SO_2)_2$]	Bis(pentafluoroethylsulfonyl)imide
[$N(C_4F_9SO_2)_2$]	Bis(nonafluorobutylsulfonyl)imide
[$(C_2F_5)_3PF_3$]	Tris(pentafluoroethyl)trifluorophosphate
[C_1CO_2]	Acetate
[CSO_3]	Methylsulphite
[C_2SO_3]	Tosylate; p-toluenesulfonate
[C_1CO_2]	Acetate
[C_2CO_2]	Propionate
[C_2NO_2]	Glycinate
[C_2PO_3]	Ethylphosphite
[C_1PO_3]	Methylphosphite
[BF_4]	Tetrafluoroborate
[PF_6]	Hexafluorophosphate
[C_4PO_4]	Butylphosphate
[$C_1C_1PO_4$]	Dimethylphosphate
[$C_2C_2PO_4$]	Diethylphosphate
[$C_4C_4PO_4$]	Dibutylphosphate
[C_4N_3]	Tricyanomethanide

[SCN]	Thiocyanate
[$N(CN)_2$)]	Dicyanamide
[CNpyr]	2-cyanopyrrolide
SF_6	Sulphur hexafluoride
R-32	Difluoromethane
R-125	Pentafluoroethane
R-134a	1,1,1,1-tetrafluoroethane
R-143a	1,1,1,1-trifluoroethane
SiO_2	Silica
H_2	Hydrogen
Ar	Argon
N_2	Nitrogen
S	Sulphur
CO_2	Carbon dioxide
O_2	Oxygen
CH_4	Methane
$C_4H_{10}O_2$	Monoethylene glycol dimethyl ether
$C_9H_6O_6$	Triformyl resorcinol
$C_{10}H_{22}O_5$	Etraethylene glycol dimethyl ether

SYMBOLS

A	Virial coefficient
B	Virial coefficient
b_{12}	Adsorption affinity
d_{ij}	Binary interaction difference
C	Virial coefficients
c_{ij}	*Energy parameters*
m_h	Mass of the measuring cell (g)
m_s	Mass of the porous solid matrix (g)
N_{exp}	Number of experimental points
n^{net}	Net moles adsorbed (mmol g^{-1})
n^{ex}	Excess moles adsorbed (mmol g^{-1})
n	Absolute moles adsorbed (mmol g^{-1})
ϕ_i	Fugacity
h	Dynamic Viscosity (mpa×s)
n_D	Refractive index
σ	Standard deviations
α_{ji}	Non-randomness parameters
γ	Surface tension of a liquid
P	Pressure (mpa)
P_i	Partial pressure
q	Absolute adsorbed amount (mmol g^{-1})
q_{ex}	Amount adsorbed in excess (mmol g^{-1})
q_{exp}	Experimental amount adsorbed (mmol g^{-1})
q_{fit}	Adjusted adsorbed quantity (mmol g^{-1})
$q_{m1,2}$	Maximum amount of adsorption (mmol g^{-1})
R_m	Refraction ($cm^3 \cdot mol^{-1}$)
S	Selectivity
T	Temperature (K)

t	Heterogeneity paramete
V_{h}	Volume of the measuring cell (cm^3)
V_{m}	Molar Volume ($cm^3 \cdot mol^{-1}$)
v_{meso}	Mesopore volume ($cm^3 g^{-1}$)
v_{micro}	Micropore volume ($cm^3 g^{-1}$)
V_P	Specific volume of the adsorbent ($cm^3 g^{-1}$)
v_{total}	Total pore volume ($cm^3 g^{-1}$)
w	Apparent mass (g)
x	Mole fraction adsorbed of the gas by the adsorbent
y	Mole fraction of gas in the gas phase
ΔH	Isosteric heat of adsorption ($J\ mol^{-1}$)
ρ_g	Density of the gas ($g\ cm^{-3}$)
f	Fugacity
f_i^{L}	Fugacity in the liquid phase
f_{s}	Saturation fugacity
g	Gas

CHAPTER 1

INTRODUCTION

1.1 Global Context

Climate change is one of the greatest challenges of the 21st century, primarily driven by the continuous increase in greenhouse gas (GHG) emissions, largely resulting from the need to meet the service demands of the global population [1]. GHGs are mainly composed of carbon dioxide (CO_2, 79.7 %), which is the most abundant and widely studied greenhouse gas, followed by methane (CH_4, 11.1 %), nitrous oxide (N_2O, 6.1 %), and fluorinated gases (F-gases, 3.1 %) [2], including hydrofluorocarbons (HFC), perfluorocarbons (PFCs), and sulphur hexafluoride (SF_6) (see Table 1.1.1). Emissions of SF_6 primarily result from improper handling and inadequate maintenance of equipment containing this gas, leading to significant leaks and its subsequent release into the atmosphere [3]. Approximately 80 % of SF_6 is used in the energy sector as a dielectric gas in electrical equipment, while about 4–8 % is employed in the magnesium industry and semiconductor manufacturing, where it protects molten magnesium and is used in etching and cleaning processes, leading to direct emissions into the atmosphere [4]. Therefore, SF_6 has been identified as one of the most potent GHG, with a global warming potential (GWP) of about 22 800 (see Figure 1.1.1), making it thousands of times more impactful than CO_2 [5].

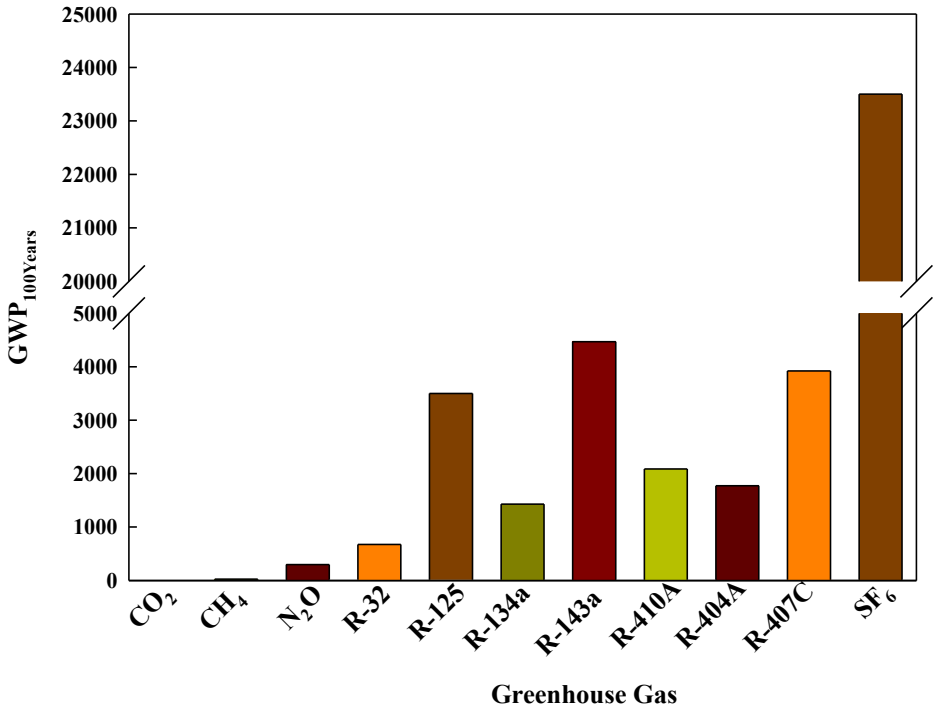
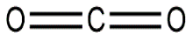
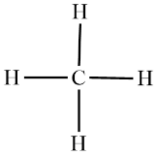
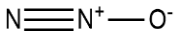
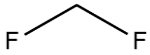
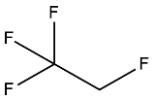
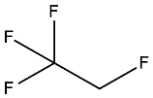
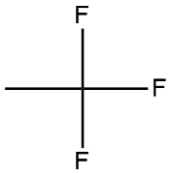
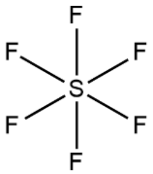


Figure 1.1.1 The global warming potential of greenhouse gases studied in this work [6].

Table 1.1.1 Greenhouse gases studied in this work.

Name	Formula	Chemical structure
Carbon dioxide	CO_2	
Methane	CH_4	
Nitrous oxide	N_2O	
Difluoromethane	R-32	
Pentafluoroethane	R-125	
1,1,1,2-Tetrafluoroethane	R-134a	
1,1,1-Trifluoroethane	R-143a	
Sulphur hexafluoride	SF_6	

Fluorinated gases also include HFCs selected for this work: R-32, R-134a, R-143a, and R-125 (see Table 1.1.1), which are used both individually and in commercial blends such as R-410A (R-32/R-125, 50/50 mol %), R-407C (R-32/R-125/R-134a, 23/25/52 mol %), R-407F (R-32/R-125/R-134a, 30/30/40 mol %), and R-404A (R-125/R-143a/R-134a, 44/52/4 mol %) [7]. These refrigerants belong to the third generation, developed as alternatives to CFCs and HCFCs due to their negligible ozone depletion potential [8]. However, they still have a high GWP (see Figure 1.1.1) and have been gradually replaced by fourth-generation refrigerants, which incorporate hydrofluoroolefins (HFOs) either as pure components or blended with small amounts of HFCs, resulting in mixtures with low GWP [9]. Examples of these newer blends include R-444A, R-447A, and R-448A, which combine HFOs with R-32, R-125, and R-134a for more sustainable refrigeration applications [10].

In this context, the separation and recovery of F-gases from third-generation refrigerants is crucial, not only to prevent their release into the atmosphere but also to enable their reuse in the production of low-GWP fourth-generation blends, supporting circular economy strategies [11]. Currently, only a few methods, such as cryogenic condensation or membrane separation, have been applied to recover these gases partially, and no fully commercialised, efficient technologies exist [12]. Therefore,

developing environmentally friendly processes for the capture, recovery, and recycling of F-gases is a priority for sustainable refrigeration [13]. Furthermore, the environmental impact of these F-gases is further amplified by their release during the operation, maintenance, and disposal of refrigeration and air conditioning systems, as well as during their manufacturing. Due to their long atmospheric lifetime and extremely high GWP, even small leaks can have a substantial effect on climate change (see Figure 1.1.1) [14]. This characteristic has led to F-gases being classified as "super greenhouse gases", with GWPs thousands of times higher than those of CO_2. Consequently, their capture, recovery, and recycling are critical steps in the mitigation of climate change, supporting sustainable management practices throughout the lifecycle of refrigeration equipment.

Beyond their environmental impact, these gases pose additional risks during atmospheric degradation or industrial use. The decomposition of F-gases can generate toxic byproducts such as hydrogen fluoride (HF), carbonyl fluoride (COF_2), and trifluoroacetic acid (TFA), which are corrosive and harmful to both human health and ecosystems [15]. TFA is highly soluble in water, precipitates in the soil, and bioaccumulates in water sources [16]. For instance, TFA is highly persistent, accumulates in aquatic systems, and has been classified as an emerging contaminant due to its potential ecological toxicity [17]. Human exposure to F-gases also carries significant health implications [18]. Although several F-gases are chemically inert under ambient conditions, prolonged or high-level exposure can cause adverse effects, including central nervous system depression, dizziness, cardiac sensitisation, and arrhythmias [19]. In confined spaces, high concentrations of SF_6 can displace oxygen and lead to hypoxia. Besides, electrical discharges in SF_6-insulated equipment produce decomposition products such as SOF_2, SO_2F_2, and HF, which are highly toxic, corrosive, and irritant to the eyes, lungs, and skin [20,21]. These environmental and health concerns underscore the urgency of reducing the use and emissions of F-gases.

To address this urgent issue, the international community has established several multilateral agreements. The Paris Agreement (2015) aims to limit the increase in global temperature to well below 2 °C, with efforts to reach 1.5 °C, through national commitments to reduce emissions across all sectors [22]. Complementing this, the Kigali Amendment to the Montreal Protocol (2016) specifically targets the gradual phasedown of HFCs, committing signatory countries to progressively reduce their production and consumption by more than 80 % over the coming decades [23]. Within the European Union, additional regulatory frameworks have been implemented, such as the EU F-Gas Regulation (No 2024/573) [10], which establishes strict quotas and promotes the adoption of alternative technologies with lower climate impact [24]. Collectively, these agreements have positioned the reduction of F-gases as a priority in global climate action due to their disproportionate effect on climate change and potential risks to human health.

Scientific advances are essential to support these regulatory objectives. Conventional approaches for GHG management, such as absorption with aqueous amines or cryogenic separation, often present drawbacks, including high energy consumption, corrosion, or limited selectivity [25,26]. This limitation has shifted attention to advanced materials and solvents capable of delivering more

sustainable performance. Among these, porous solid matrices such as zeolites, activated carbon (AC), porous organic polymers (POPs) and metal–organic frameworks (MOFs) have demonstrated high surface areas, tunable pore structures, and selective adsorption [27]. In parallel, liquid-based approaches, particularly ionic liquids (ILs) and deep eutectic solvents (DES) [28,29], have emerged as promising candidates for absorption processes due to their negligible vapour pressure, structural versatility, and tuneable physicochemical properties [29].

The integration of adsorption using porous solid matrices and absorption with ILs and DES, therefore, offers a complementary pathway to address the urgent challenge of GHG capture and separation. Such dual strategies not only broaden the scope of potential applications but also provide opportunities to design hybrid processes with enhanced efficiency, lower environmental impact, and industrial scalability [30]. Clearly, the development of innovative technologies for capturing and mitigating F-gases emissions directly supports the goals of the Paris Agreement, the Kigali Amendment, and related EU regulatory frameworks, reducing both environmental impacts and human health risks.

1.2 Absorption

Absorption is a unit operation widely used in chemical and environmental engineering, in which a gas mixture is brought into contact with a liquid to transfer one or more of its gas components into the liquid phase [31]. This process relies on the selective dissolution of gaseous species in the solvent, leading to the formation of a solution. The efficiency of absorption depends on factors such as the solubility of the gas in the liquid, the partial pressure of the gaseous component, the temperature, and the physicochemical nature of the solvent employed [31].

A classic example of this operation is found in the capture of gases generated as by-products in coke ovens, where compounds such as sulphur dioxide [32], ammonia [33], F-gases [34], or other volatile organic compounds, are absorbed into specific solutions for removal or recovery [35]. Such applications are essential not only for controlling pollutant emissions but also for valorising industrial by-products, representing a key tool in the development of clean and sustainable technologies. This process can be classified into two main categories:

- **Physical absorption:** primarily governed by solubility and molecular diffusion, occurs without the formation of new chemical bonds. A classic example is the dissolution of gases such as oxygen or carbon dioxide in water [95,96]. This process is driven by differences in concentration and partial pressure. This absorption is typically described by Henry's law, which relates the equilibrium concentration of the gas in the liquid to its partial pressure in the gas phase. Physical absorption is generally reversible and exhibits fast kinetics, making it suitable for the removal of gases with high solubility in the chosen solvent.
- **Chemical absorption:** in which the absorbate (gas, in this case) participates in a chemical reaction with the absorbent (liquid solvent, in this case), generating new products and generally increasing

the retention capacity. A representative case is the absorption of CO_2 in sodium hydroxide or amine solutions [97]. Chemical absorption offers higher selectivity and capacity compared to physical absorption, because the formation of stable chemical complexes enhances the efficiency of gas capture.

1.2.1 Absorption equilibrium

The concept of equilibrium is fundamental in thermodynamics and provides the basis for understanding absorption processes [31,38]. In a gas–liquid system, equilibrium is reached when the rates of mass transfer of a given component from the gas phase to the liquid phase and vice versa are equal, resulting in no net flux across the interface. At this point, the chemical potential of each component is the same in both phases, ensuring thermodynamic consistency [31,38].

The equilibrium state of a system is established when its temperature (T), pressure (P), and phase composition (x_i) are defined. However, these variables are interdependent: once equilibrium is reached, specifying a subset automatically determines the others. This relationship is formalised by the Gibbs phase rule, which links the degrees of freedom (F) of a non-reactive system to the number of coexisting phases (P) and the number of components (C) [38]:

$$F = C - P + 2 \qquad 1.2.1$$

In a gas mixture containing n components, at a P, T, and concentrations, the degrees of freedom are $F = n + 1$. Consequently, specifying P, T, and $\mathrm{n} + 1$ concentrations fully define the system. For example, when a solvent S absorbs a gas A from a binary mixture, fixing P, T, and the concentration y_A, all other variables can be determined. Then, the construction of phase equilibrium diagrams can be carried out, such as those shown in Figure 1.2.1 [38].

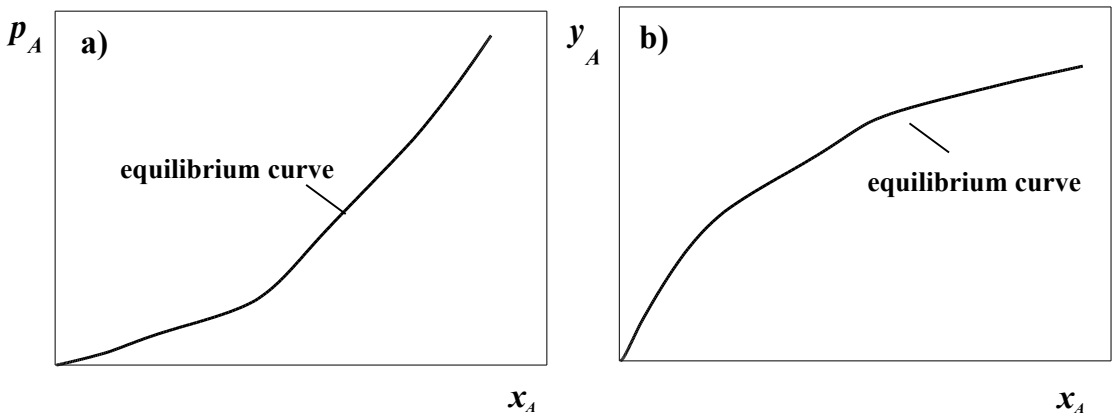


Figure 1.2.1 Gas-liquid phase equilibrium diagrams at constant P and T on: a) the equilibrium relationship between the partial pressure of component A in the vapour phase (P_A) and its mole fraction in the liquid phase (x_A); and b) the gas–liquid equilibrium curve that shows the mole fraction of component A in the vapour phase (y_A) as a function of its mole fraction in the liquid phase (x_A).

Figure 1.2.1 illustrates the behaviour of binary systems in gas–liquid equilibrium. Figure 1.2.1a is primarily used for thermodynamic analysis through Henry's and Raoult's laws, linking the gas solubility to its corresponding partial pressure [38]. In contrast, Figure 1.2.1b is more commonly employed in process engineering because it facilitates the design of mass transfer operations such as absorption, desorption, or distillation by directly showing the enrichment relationship between phases [38]. In this context, the determination of Henry's constant is essential for quantifying the solubility of a gas in a liquid under equilibrium conditions.

From an industrial and environmental perspective, the capture of greenhouse gases (GHGs) is of particular concern due to their high global warming potential and long atmospheric lifetimes. These gases are used in applications such as electrical insulation, refrigeration, and industrial processes where accidental releases or emissions contribute significantly to climate change. Therefore, the effective capture and separation of GHGs are crucial for environmental protection.

In the search for alternatives to traditional solvents, ionic liquids (ILs) and deep eutectic solvents (DESs) have emerged as highly promising candidates for gas separation. In this context, the solubility of greenhouse gases (GHGs) in a solvent can often be accurately described using Henry's law (K_{Hi}), elates the partial pressure of the gas to its concentration in the liquid for component i and is defined as follows [39]:

$$\mathrm{K_{Hi}} = \lim_{x_i \to 0} \frac{\phi_i(P,T)\, P}{x_i} \qquad 1.2.2$$

where, x_i is the mole fraction of gas dissolved in ILs or DES, P is the equilibrium pressure, and ϕ_i refers to the fugacity of GHG. Thus, Henry's law provides a fundamental basis for estimating gas solubility in these advanced solvents.

However, gas absorption in liquids depends not only on solubility, as defined by Henry's law, but also on the kinetics of mass transfer between the gas and liquid phases [40]. In fact, the efficiency

of an absorption process is determined by the combined resistance to mass transfer, which can be conceptualized in three main stages: resistance in the gas phase, resistance at the gas–liquid interface, and thermodynamic limitations. Initially, before a gas can dissolve into a liquid, it must first diffuse through the gas boundary layer surrounding the gas–liquid interface [40]. The molar flux of gas A toward the interface can be described using Fick's law [40]:

$$NA = -D_{AB}\frac{dC_A}{d_z} \quad 1.2.3$$

where D_{AB} is the diffusion coefficient of gas A in the mixture, and $\frac{dC_A}{d_z}$ is the concentration gradient perpendicular to the interface. This step is especially critical for gases with low solubility or low diffusivity, because resistance in the gas phase can significantly limit the overall absorption rate [41]. Then, at the gas–liquid interface, thermodynamic equilibrium governs the maximum amount of gas that can be absorbed [42]. The equilibrium condition is reached when the fugacity of the component in the gas phase equals its activity in the liquid phase:

$$f_A^g = f_A^l \rightarrow y_A P\varphi_A = \gamma_A x_A K_H \quad 1.2.4$$

where y_A is the mole fraction of *A* in the vapour phase, *P* is the total pressure, φ_A is the fugacity coefficient, x_A is the mole fraction in the liquid phase, γ_A is the activity coefficient, and K_H is Henry's law constant. This condition defines the thermodynamic driving force for absorption and establishes the upper limit of solubility under the given conditions. Finally, the overall absorption process results from the combination of mass transfer through the gas film and the thermodynamic partitioning at the interface. This behaviour can be quantitatively described by the two-film theory [43]:

$$N_A = K_L a(C_A^* - C_A) \quad 1.2.5$$

where K_L is the overall liquid-phase mass-transfer coefficient, a is the interfacial area per unit volume, and C_A^* is the equilibrium concentration in the liquid phase. This framework effectively links molecular transport phenomena with thermodynamic constraints, providing a solid foundation for the design and optimization of absorption processes in industrial applications.

1.2.2 Thermodynamic Modeling of Gas–Liquid Phase Equilibria

The study of gas–liquid phase equilibria is fundamental for understanding and optimising absorption processes, especially in systems involving complex solvents such as ILs and DES [44]. These solvents often exhibit strong molecular interactions, including hydrogen bonding, ion–dipole forces, and van der waals interactions, which result in significant non-ideality in the liquid phase [44]. Consequently, classical ideal thermodynamic models are insufficient to accurately describe their behaviour. Then, advanced thermodynamic approaches are required to capture these deviations and predict equilibrium properties with high consistency. The most widely employed approaches are NRTL (Non-Random Two-Liquid) and UNIQUAC (Universal Quasi-Chemical) [45]. These models enable the

quantitative description of activity coefficients, which are essential for predicting solubility, driving forces for mass transfer, and overall process performance [45].

The present section focuses on the theoretical framework for gas–liquid phase equilibrium and illustrates the application of the NRTL model for F-gas absorption in ILs and DES-based systems [45]. Absorption occurs when the chemical potential of the gas in the liquid phase equals its chemical potential in the gas phase. Mathematically, this condition can be expressed as [46]:

$$f_A = a_A \gamma_A x_A P_A^0 \quad 1.2.6$$

where f_A is the fugacity, a_A is the activity, γ_A is the activity coefficient, x_A is mole fraction, and P_A^0 is the standard reference pressure. This equilibrium relationship establishes the maximum solubility of the gas and ensures that the system follows fundamental thermodynamic principles.

In systems that contain ILs and/or DES, the liquid phase can exhibit significant non-ideality due to strong interactions, including hydrogen bonding, ion–dipole forces, and van der waals interactions. Under these conditions, activity coefficients (γ_A) accurately describe the behaviour of real solutions. The NRTL model provides a reliable framework to capture these effects, allowing the estimation of the equilibrium concentration, C_A^*, and offering insights into the mechanisms that control the solubility and mass transfer. In the NRTL model, the non-randomness parameter (α) and the binary interaction parameters (τ_{ij} and τ_{ji}) are optimised by minimising the root-mean-square deviation (RMSD) between experimental and predicted pressures. Finally, the parameters d_{ij} and d_{ji} were zero, resulting in $\alpha_{ij} = c_{ij}$ and $\alpha_{ji} = c_{ji}$. In the ILs and DES phase, the activity coefficient of component *i* is expressed as:

$$f_i = \gamma_i x_i f_i^0 \quad 1.2.7$$

and the fugacity of component *j* in the F-gas's vapour-phase fugacity, f_j, correlates with the molar fraction of the absorbed F-gas, x_i, by:

$$f_j = \gamma_j x_j f_j^0 \quad 1.2.8$$

where f_i^0 is the reference liquid-phase fugacity at the tested pressures and the corresponding temperature, and γ_i is the activity coefficient of the F-gas (*i*) in the IL phase (*j*), which can be determined as follows:

$$\ln \gamma_i = x_j^2 \left[\tau_{ji} \left(\frac{G_{ji}}{x_i + x_j G_{ji}} \right)^2 + \frac{\tau_{ij} G_{ij}}{\left(x_j + x_i G_{ij} \right)^2} \right] \quad 1.2.9$$

$$\ln \gamma_j = x_i^2 \left[\tau_{ij} \left(\frac{G_{ij}}{x_j + x_i G_{ij}} \right)^2 + \frac{\tau_{ji} G_{ji}}{\left(x_i + x_j G_{ji} \right)^2} \right] \quad 1.2.10$$

where:

$$\tau_{ij} = a_{ij} + \frac{b_{ij}}{T} + e_{ij} \ln T + f_{ij} T \,,\ \tau_{ii} = 0 \quad 1.2.11$$

$$\alpha_{ij} = c_{ij} + d_{ij}(T - T_0) \quad 1.2.13$$

$$G_{ij} = e^{-\alpha_{ij}\tau_{ij}} \quad 1.2.14$$

1.3 Adsorption

Adsorption is a surface phenomenon in which molecules, atoms, or ions from a liquid or gaseous phase accumulate and adhere to the surface of a solid [47]. This process is generally classified into two main types: i) physisorption, governed by weak and reversible van der waals forces; and ii) chemisorption, which involves strong and typically irreversible chemical bonds [47]. The species that attach to the surface are called adsorbates, while the solid material is known as the adsorbent [47]. To enhance adsorption capacity, porous solid matrices with high specific surface areas are commonly employed. These materials contain interconnected pores of small dimensions, which facilitate efficient contact between the adsorbate and the adsorbent surface [48]. Adsorption occurs predominantly on the internal surfaces of the pores, where interaction energies are maximized [47]. Among these porous solid matrices, activated carbons (ACs), zeolites, metal-organic frameworks (MOFs), and porous organic polymers (POPs) are outstanding as materials widely used in gas and liquid capture, purification, and separation processes. The efficiency of adsorption depends on multiple factors, including the chemical nature of the adsorbent and adsorbate, temperature, pressure, and the presence of competing species [48]. Figure 1.3.1 provides a schematic representation of the adsorption phenomenon. The grey area corresponds to the adsorbent surface with sites available for molecular interactions, while the dark blue circles represent adsorbate molecules that migrate from the gas phase toward the solid surface, which retain the gas in the active surface sites [49].

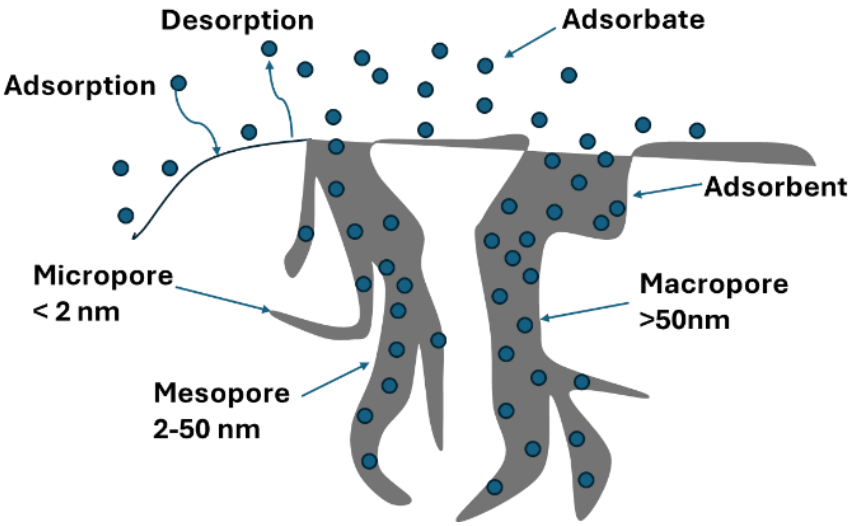


Figure 1.3.1 Schematic representation of the adsorption phenomenon on a porous solid [49].

1.3.1 Classification of Porous Materials and Adsorption Behaviour

Overall performance in gas capture and separation processes is conditioned by a complex interplay between the material's structural and thermodynamic parameters. This dependency makes the selection of adsorbents a critical parameter for the application at the industrial level. Then, GHGs mitigation and recovery processes must be designed and optimized with materials that have specific porous architectures to maximize process efficiency. In this context, the IUPAC has established specific recommendations for the characterization of porous solid materials, primarily based on the classification of porosity according to pore width [50]. This classification, generally determined through gas adsorption techniques as illustrated in Figure 1.3.2, distinguishes three fundamental categories: microporosity, mesoporosity, and macroporosity.

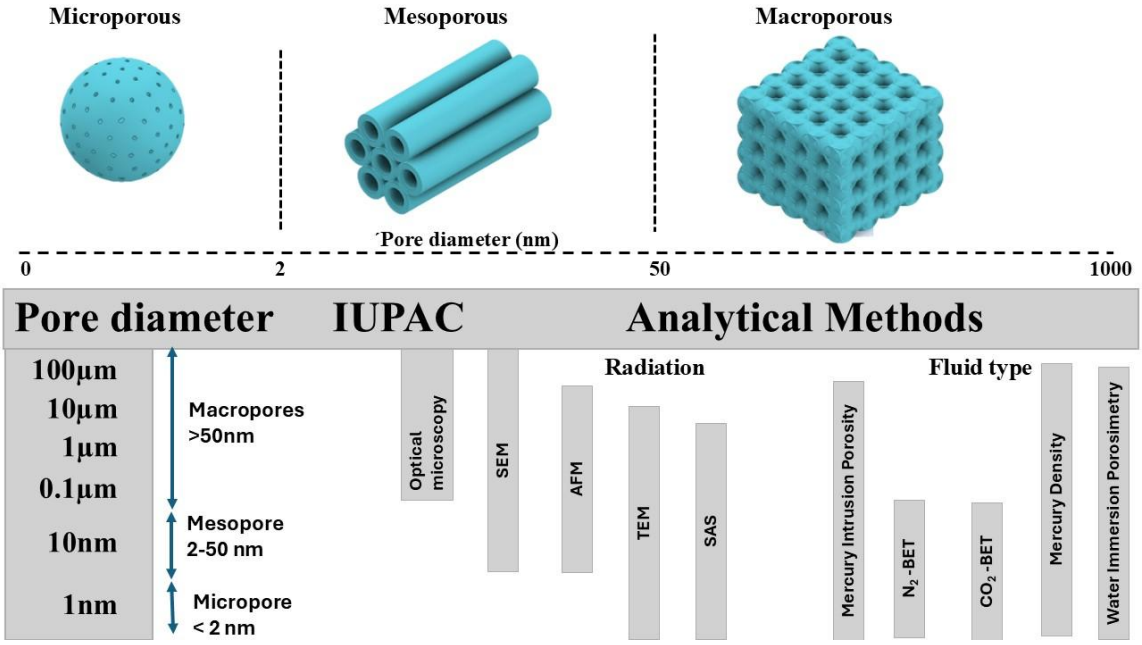


Figure 1.3.2 The classification of materials by their porosity, according to IUPAC terminology [51].

The significance of these recommendations lies in their ability to classify materials according to their pore size distribution (PSD). This classification not only facilitates the comparison of different adsorbents but also helps explain why experimental characterisation often yields adsorption isotherms with distinct shapes. Each type of isotherm corresponds to a particular porous structure and specific adsorption mechanism, as illustrated in Figure 1.3.3.

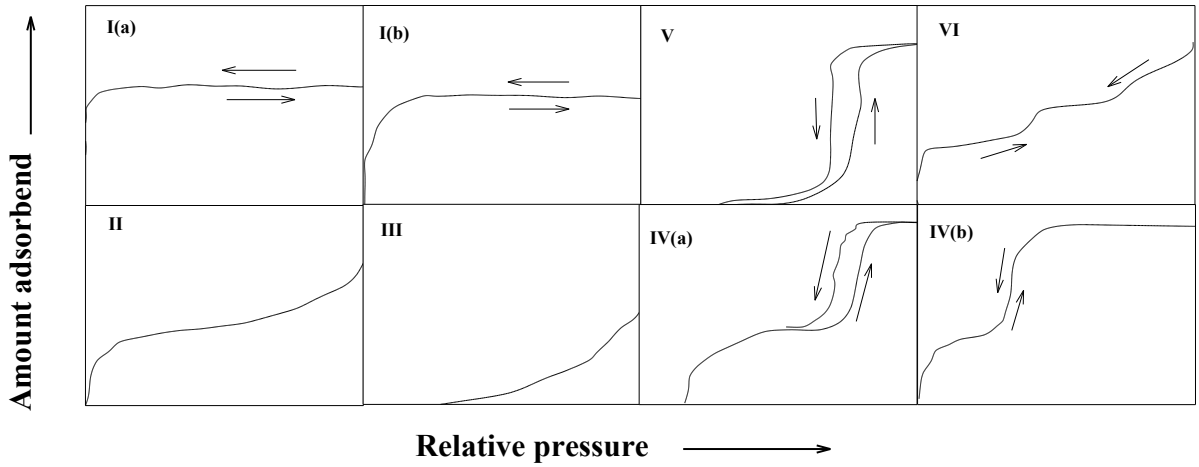


Figure 1.3.3 Classification of different types of adsorption isotherms [50].

As shown in Figure 1.3.3, the IUPAC defines six types of adsorption isotherms, each one representing the structural characteristics of different porous solid matrices. Type I isotherms (subtypes a and b) are typical for microporous materials. These isotherms are characterised by a rapid increase in adsorption at low relative pressures, followed by a concave behaviour when the pores become saturated [50]. Subtype I(a) corresponds to highly microporous solid matrices with narrow pores, whereas subtype I(b) is associated with matrices that have slightly larger micropores or micropores combined with mesopores. This behaviour is characteristic of materials such as activated carbons and zeolites, which are widely used in separation processes, gas capture, and as catalysts [50]. Type II adsorption isotherms are associated with nonporous or microporous materials [50]. They are characterised by reversible behaviour, showing an initial stage of monolayer adsorption at low pressures [50]. At higher pressures, multilayer adsorption takes place. This type of behaviour is typical of solids with smooth or microporous surfaces, such as glass or nonporous silica [50]. Type III isotherms reflect weak interactions between the adsorbate and the adsorbent surface. In this case, the curves exhibit an upward convex shape, indicating that significant adsorption occurs only at high pressures [50]. This behaviour is characteristic of materials such as non-activated carbons or nonpolar surfaces. Type IV isotherms are characteristic of mesoporous solids, displaying an initial adsorption pattern similar to Type II, corresponding to monolayer and subsequent multilayer adsorption [50]. At higher pressures, they exhibit a hysteresis loop, which arises from capillary condensation within the mesopores. Subtype IV(a) corresponds to materials with well-defined, uniform mesopores, whereas subtype IV(b) is associated with materials having pore networks with more complex connectivity. Typical examples include mesoporous silicas and MOFs. Type V isotherms are like Type III but occur in mesoporous materials. They are characterised by weak adsorbate–adsorbent interactions, resulting in minimal adsorption at low pressures, which increases significantly only at higher pressures [50]. These isotherms typically display a hysteresis loop, indicating capillary condensation within the mesopores. This behaviour is commonly observed in hydrophobic

mesoporous adsorbents. Type VI isotherms correspond to stepwise multilayer adsorption on uniform, non-porous surfaces. Each step represents the formation of an additional adsorbed layer [50]. Although this behaviour is rarely observed, it occurs on highly uniform and well-ordered surfaces, such as graphite.

The characterisation of adsorption isotherms plays a central role in the study of porous solid matrices, since it directly links the observed adsorption behaviour to the underlying pore structure and surface properties of the material [50]. This framework is especially valuable when analysing advanced porous materials such as MOFs, POPs, zeolites, ACs, and composite materials, which have emerged as key candidates in energy and environmental applications [52]. These materials exhibit a wide diversity of pore sizes, geometries, and surface chemistries, making their classification through isotherm analysis crucial for understanding their adsorption mechanisms. For example, zeolites and certain MOFs with narrow micropores often display Type I isotherms, reflecting strong uptake at low pressures, which is critical for CO_2 capture and gas separation [53]. In contrast, mesoporous MOFs, POPs, and composites typically show Type IV behaviour with hysteresis loops, indicative of capillary condensation and suitable for gas storage or catalytic applications [54]. ACs can exhibit a hybrid pore structure that combines micro- and mesoporosity, improving both storage capacity and adsorption kinetics [55].

1.3.2 Adsorption models

The study and classification of adsorption isotherms not only provide fundamental insight into the textural properties of these materials but also serve as a predictive tool to assess their suitability for targeted applications such as gas capture and storage, separation processes, catalysis, and environmental remediation [47]. In this way, isotherm-based characterisation becomes an indispensable step for the rational design and optimisation of porous adsorbents in both academic research and industrial development [47]. Then, it is important to highlight that each adsorption behaviour observed in these materials can be further analysed and quantitatively described through mathematical models. Mathematical adsorption models are fundamental tools for understanding the interaction between adsorbates and porous solid surfaces. They allow the interpretation of experimental isotherms, the determination of relevant physical parameters, and the prediction of adsorption performance under different conditions [56]. The most widely used models are the Langmuir, Sips, Toth, and Dual-Site Langmuir isotherms.

In this context of GHGs adsorption on solid porous adsorbents, the proper selection of the adsorption model becomes essential. Each model presents assumptions and limitations that must be considered, and the choice largely depends on the type of isotherm obtained experimentally. For instance, the Langmuir model assumes homogeneous adsorption sites and monolayer coverage [56]. The Sips model introduces a heterogeneity parameter, making it suitable for materials such as activated carbons and MOFs [57]. The Toth model corrects deviations at low and high pressures, providing accurate fits for microporous materials like zeolites [58]. Finally, the Dual-Site Langmuir model accounts for

materials with two distinct adsorption sites, exhibiting competitive adsorption in gas mixtures [47,58]. For this reason, Table 1.3.1 summarises the main adsorption models, highlighting both their scientific and mathematical importance, as well as their practical implications for the rational design of adsorbent materials.

Table 1.3.1 Adsorption models: scientific and mathematical comparison

Model	Main Assumptions	Scientific Importance	Mathematical Importance	Advantages	Limitations
Langmuir	-Monolayer adsorption. -Homogeneous surface with identical sites. -No adsorbate-adsorbate interactions.	Fundamental model of adsorption. Quantifies maximum capacity (q_m) and affinity b.	$q = \frac{q_m bP}{1+bP}$, Hyperbolic isotherm with saturation limit q_m	Simple (2 parameters).	Cannot describe heterogeneity. Overestimates adsorption at high pressures
Sips (Langmuir–Freundlich)	-Heterogeneous surface. -Monolayer adsorption. -Reduces to Langmuir when $n = 1$	Accounts for real heterogeneity in porous materials (e.g., ACs, MOFs). Interpolates between the Langmuir and the Freundlich models.	$q = \frac{q_m (bP)^n}{1+(bP)^n}$, n controls heterogeneity	Flexible (3 parameters). Better fit for non-uniform surfaces.	Less accurate at very high pressures. Requires more experimental data.
Toth	-Heterogeneous surface with continuous energy distribution. -Monomolecular adsorption.	Corrects Langmuir's overestimation at high pressures. Suitable for microporous materials (zeolites, MOFs).	$q = \frac{q_m bP}{(1 + (bP)^t)^{1/t}}$ t adjusts the curvature.	Accurate at both low and high pressures. Avoid overestimation of q_m.	Requires 3 fitted parameters. Does not account for multilayer adsorption.
Dual Site Langmuir (DSL)	-Two independent types of adsorption sites with different affinities.	Represents materials with multiple sites (MOFs, zeolites). Crucial for selectivity and competitive adsorption studies.	$q = \frac{q_m b_1 P}{1 + b_1 P} + q = \frac{q_m b_2 P}{1 + b_2 P}$	Captures bimodal systems (micro/meso-pores). Useful for gas mixtures.	4 parameters. Not suitable if more than two types of sites are present.

1.4 Green Absorbents and Porous Solid Adsorbents for Gas Capture and Separation

Green chemistry aims to design processes and products that minimise or eliminate the use and generation of substances hazardous to human health and the environment [59]. Within this context, green solvents, such as ionic liquids (ILs) and deep eutectic solvents (DES), have emerged as promising alternatives to conventional volatile organic compounds (VOCs) [59] which are associated with high toxicity, volatility, and significant emissions [60]. ILs and DES offer advantages such as negligible vapour pressure, enhanced thermal and chemical stability, potential biodegradability, and the ability to tune their physicochemical properties through rational molecular design or by adjusting the combination of their constituent ions or components [61]. These properties make them highly efficient absorbents, capable of selectively interacting with GHGs and other molecules, expanding their applications in GHG capture and storage, catalysis, selective extraction, and biotechnological processes, exemplifying the concept of "designer solvents" that bridges green chemistry theory with sustainable practice [62].

On the other hand, the performance of these absorbents is enhanced using porous solid matrices, whose structural diversity in terms of specific surface area, pore size distribution, pore volume, and surface chemistry decisively determines adsorption behaviour [48,63]. Adsorption capacity, storage, and kinetics depend on the structural development of the solid matrix rather than the adsorbate itself. Micropores favour high-energy adsorption of small molecules, whereas mesopores and macropores facilitate diffusion and transport, improving both total capacity and adsorption rate [63,64]. These characteristics define the suitability of each adsorbent for specific applications, such as catalysis, capture, separation, and purification of GHGs. Among the most studied and technologically relevant matrices are hybrid materials, activated carbons (ACs), zeolites, metal-organic frameworks (MOFs), and porous organic polymers (POPs). The combination of green absorbents and porous solid adsorbents provides an efficient and sustainable platform for gas capture, separation, and storage, integrating chemical solutions and advanced materials in environmentally friendly industrial processes.

1.4.1 Ionic liquids (ILs) and deep eutetic solvents (DES)

Ionic liquids have emerged as an ecological alternative to conventional organic solvents. These compounds have melting points close to 100 °C, remaining liquid even at room temperature [65]. They are composed of ions, which give them unique properties compared to traditional molecular solvents, as illustrated in Figure 1.4.1. They are called ILs because their physical and chemical properties can be tailored by adjusting their ionic components. This ability provides specific characteristics such as high solubility or selectivity that facilitate the optimisation of chemical reactions, separation processes, and other specialised applications. Then, ILs are often considered "designer solvents" or task-specific

solvents [65]. ILs are applied across various sectors, notably in gas capture (such as CO_2 and other GHGs), catalysis, the pharmaceutical industry, purification processes, the development of advanced materials, and energy storage systems. This wide range of applications highlights their relevance within the framework of green chemistry and sustainable technologies.

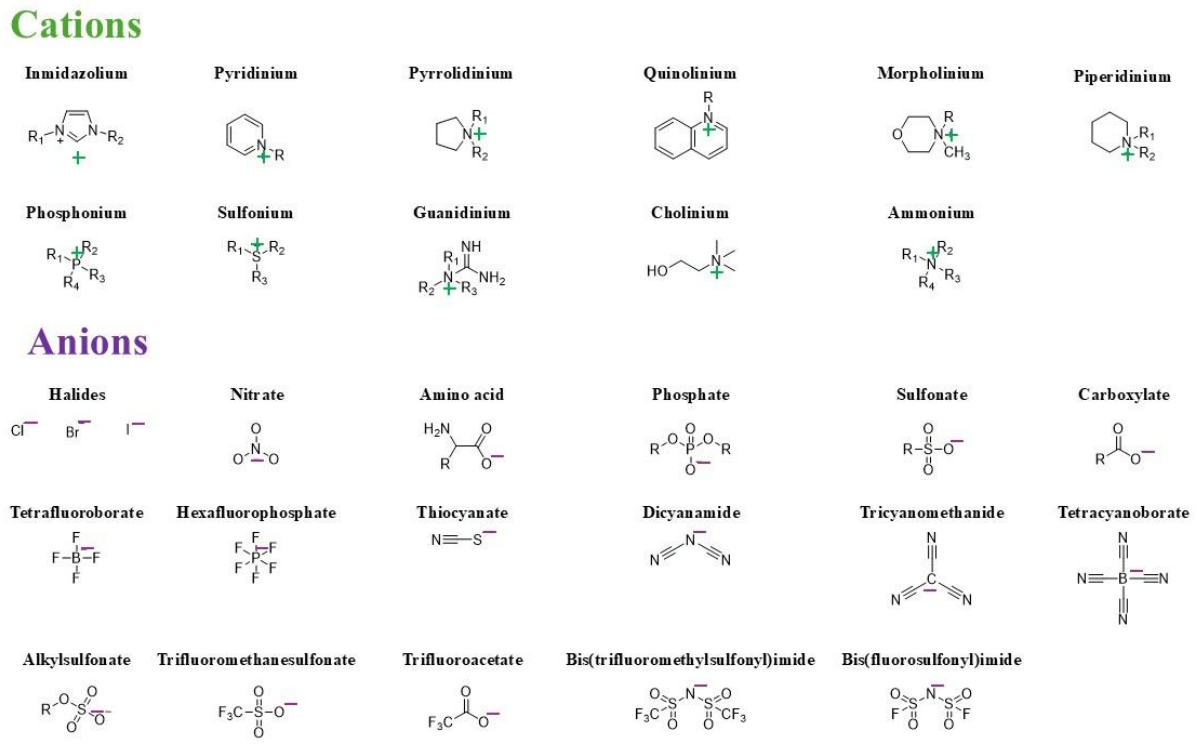


Figure 1.4.1 Some cations and anions commonly present in the structure of ionic liquids.

ILs constitute a family of compounds with unique properties (see Figure 1.4.2), such as low vapour pressure, high thermal stability, and the ability to dissolve and stabilise a wide variety of molecules, making them highly versatile in chemical, electrochemical, and biological processes. Within this diversity, distinct subcategories of ILs can be distinguished, each one tailored to specific design and functional needs.

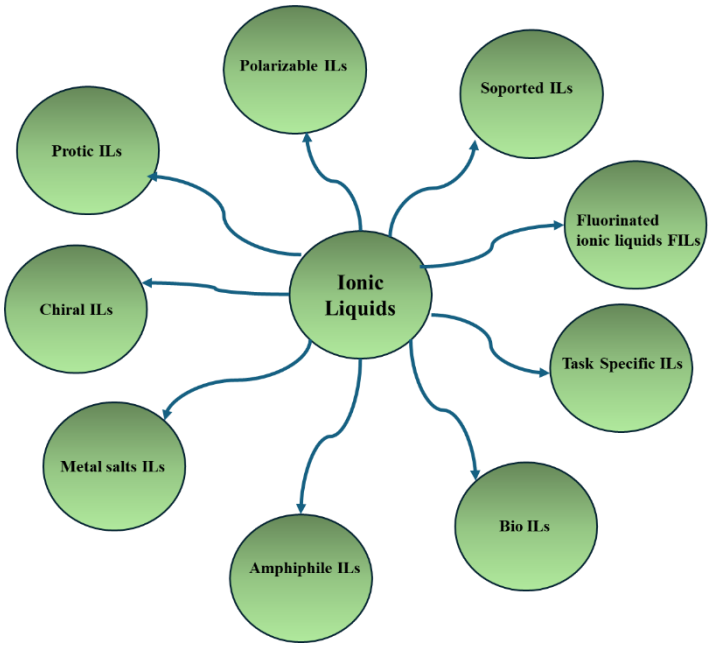


Figure 1.4.2 Classification of ionic liquids and their key applications [66].

Within this diversity, protic ILs can form hydrogen bonds, facilitating acid–base reactions and proton transfer processes, while chiral ILs enable chirality induction and enantiomeric separation, proving especially valuable in asymmetric catalysis [67]. Polarizable ILs, with deformable electronic distributions, are particularly effective at solvating polar molecules and performing advanced electrochemical operations. Amphiphilic ILs combine hydrophilic and hydrophobic domains, enabling micelle formation and nanoscale self-assembly. Bio ILs, derived from biomolecules or designed to be biocompatible, allow applications in biocatalysis, biomolecule extraction, and drug formulation with minimal toxicity. Task-specific ILs (TSILs) represent a targeted design approach, incorporating functional groups that confer high selectivity for specific applications, such as CO_2 capture, precious metal recovery, or selective catalysis. Supported ILs (SILs) merge the selectivity of ILs with the practical handling advantages of heterogeneous materials [68].

Fluorinated ionic liquids (FILs) constitute a specialized subset of ILs that incorporate fluorinated alkyl chains of at least four carbon atoms. FILs exhibit nanosegregated domains (polar, nonpolar, and fluorinated) that allow simultaneous interactions with diverse solutes, increasing solubilization capacity, tunability, and conformational diversity [69]. Short-chain FILs, such as those based on perfluorobutane sulfonate, are water-soluble, non-toxic, and retain oleophobic and hydrophobic properties [70], making them particularly suitable for F-gas absorption and other separation processes. The combination of fluorinated compound characteristics with the tunability inherent to ILs confers FILs with low surface tension, chemical inertness, and enhanced green potential [68]. This versatility allows the design of solvents optimised for the capture of fluorinated GHGs, and the presence of fluorine atoms increases their solubility [39]. Previous experimental studies have shown that FILs with four-carbon fluorinated

chains exhibit higher gas absorption capacities than simple fluoro-containing ILs under the same temperature and pressure conditions [39].

In recent years, a multiscale research strategy has been increasingly applied to the development of IL and FIL-based gas separation processes, integrating molecular modelling, experimental evaluation, and process-scale simulations [71]. The first stage employs COSMO-RS computational modelling to screen hundreds of IL combinations, identifying candidates with favourable thermodynamic and kinetic properties, including Henry's law constants, while reducing the need for time-consuming and costly laboratory trials [72]. COSMO-RS also provides insights into molecular interactions, including electrostatic, hydrogen-bonding, and van der waals contributions, guiding rational IL design to optimise solute–solvent affinity [73]. Selected ILs are then experimentally evaluated for gas–liquid equilibria, absorption isotherms, and diffusivities [72], followed by process-scale simulations using COSMO-based/Aspen methodologies to enable techno-economic assessment, optimise absorption and desorption operations, and compare performance with existing technologies [73]. FILs and ILs based on sulfonate and carboxylate anions have consistently demonstrated superior F-gas capture performance under realistic process conditions, confirming the importance of integrating molecular design with experimental and process-level evaluation.

Despite their promising properties, some ILs face limitations such as poor biodegradability, toxicity, elevated viscosity, and production costs. These challenges have encouraged the exploration of deep eutectic solvents (DES) as an alternative solvent. DES, formed by combining hydrogen-bond donors and acceptors, provide similar physicochemical behaviour to ILs, is straightforward to prepare, and its purity depends solely on the starting materials [74]. They have demonstrated efficacy in the absorption of CO_2, SO_2, and F-gases, as shown in both experimental and computational studies, offering a greener and more sustainable alternative to conventional ILs. DES overcome important ILs limitations that are listed as follows:

- High synthesis and purification costs: Many ILs require complex and expensive processes to achieve high purity.
- Low biodegradability: Certain ILs do not readily degrade in the environment, limiting their sustainability.
- Potential toxicity: Depending on the nature of their cations and anions, some ILs may be toxic to living organisms.
- Sensitivity to water and oxygen: Early generations of ILs can react with moisture or oxygen, affecting their stability.
- Limited liquid range: Some ILs remain liquid only within a relatively narrow temperature range, reducing their versatility in applications.

DES are recognized as green solvents that maintain many of the advantageous features of ILs, but with simpler preparation methods, no requirement for extensive purification, and reduced production cost. DES are typically composed of two or more components, a hydrogen bond donor (HBD) and a

hydrogen bond acceptor (HBA), which interact via strong hydrogen bonding networks. This interaction leads to a substantially reduced melting point compared to each individual component, allowing the formation of a stable liquid at or near room temperature (see Figure 1.4.3).

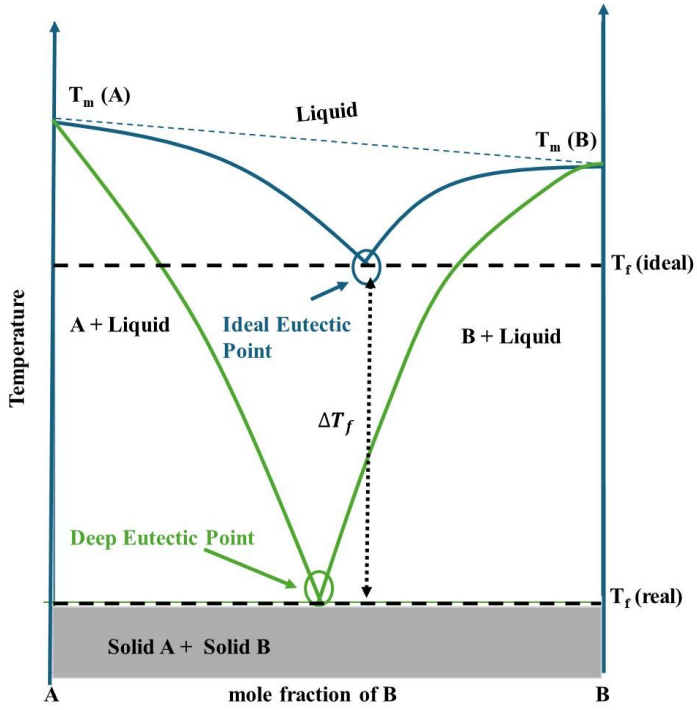


Figure 1.4.3 Comparison between the ideal solid-liquid behaviour of the mixtures of two solids (A+B) and the DES diagram [75].

Several studies have explored the solubility of gases in DES, using the soft-SAFT equation of state to model R-134a absorption in fluorinated ionic liquids and DES, revealing the pivotal role of molecular structure in governing solubilization mechanisms [76]. In parallel, the selective uptake of F-gases (such as R-32 and R-125) has been investigated, demonstrating remarkable selectivity in separating refrigerant mixtures [77]. The rational design of DES with tailored structural features has enabled the use of computational approaches to generate accurate thermodynamic models, providing essential tools to optimize and scale up separation processes [34]. Experimental investigations on common HFCs in choline chloride-based DES with perfluorinated acids further indicate that increased fluorination enhances gas absorption, confirming the link between DES chemical composition and solubilization performance [7]. In the context of CO_2 capture, DES-water systems combining tetrabutylphosphonium and ethanolamine have also shown high selectivity [78], while DES prepared from tetrapropylammonium bromide and formic acid improves CO_2 solubility under varying pressures and temperatures [78]. These studies underscore the versatility, efficiency, and sustainability of DES as advanced solvents for GHGs capture and recovery, positioning them as a promising alternative to conventional absorption technologies.

Overall, this comprehensive approach highlights the versatility of ILs, FILs, and DESs in gas separation and other applications, emphasising the critical interplay between molecular structure,

solvent selection, and process-scale considerations. By combining computational modelling, experimental characterisation, and industrially relevant process simulations, researchers can optimise absorption efficiency, reduce operational costs, and advance environmentally sustainable separation technologies, ultimately reinforcing the role of ILs and DES as cornerstone solvents in green chemistry, industrial processes, and biotechnology.

1.4.2 Hybrid materials

Hybrid materials consist of an IL or DES incorporated or immobilized on porous solid matrices, such as MOFs, zeolites, mesoporous silica, carbons, or ionic polymers. These hybrid materials aim to combine the chemical and functional properties of the IL or DES (such as selectivity, affinity for specific gases, and tuneable chemistry) with the structural advantages of the solid porous matrix, including high surface area, porosity, and mechanical stability. In these materials, ILs tend to reside within the pores of solid matrices, enhancing the selective adsorption of gas mixtures due to their specific chemical affinity with target gases [79]. Incorporating ILs or DES into porous solid matrices effectively combines their storage capacity and selectivity with the high surface area, porosity, and mechanical stability of the solid matrix, improving overall separation efficiency [79].

The method of IL impregnation is critical, and optimized immobilization strategies are essential to minimize partial pore blockage and surface area reduction [80]. Furthermore, the composition of the solid matrix can enhance ionic conductivity without compromising mechanical rigidity, further promoting gas storage efficiency [81]. Mesoporous silica provides precise control over pore diameters and distribution, yielding hybrid materials with improved selectivity toward specific gases [82]. Despite these advantages, compatibility issues may arise due to differences in polarity, hydrophobicity/hydrophilicity, and moisture stability, potentially affecting the structural integrity of the hybrid material [83]. Additionally, limitations in regeneration and reuse remain, because IL decomposition or material contamination can restrict the lifespan and long-term operational efficiency of these systems [83]. Overall, IL- and DES-based hybrid materials emerge as a promising alternative for the adsorption of GHGs, combining the chemical versatility of green solvents with the structural benefits of porous solids to enhance selectivity, storage capacity, and operational stability.

1.4.3 Activated Carbons (ACs)

Activated carbons can be produced from a wide range of precursors using different activation methods. The final characteristics of the material, such as surface area, pore distribution, performance, and suitability for specific applications, are strongly influenced by both the activation method (physical or chemical) and the nature of the precursor (residual biomass or commercial sources, see Figure 1.4.4). When residual biomass is used as a precursor, the main advantages are its low cost and sustainability, because this approach valorizes agricultural and wood residues while contributing to the circular

economy. However, the inherent variability in biomass composition can result in activated carbons with less homogeneous properties. In contrast, commercial activated carbons, derived from raw materials, offer more uniform, reproducible, and certified products [84]. This reliability is particularly important for demanding applications, including drinking water treatment, the pharmaceutical sector, and the food industry.

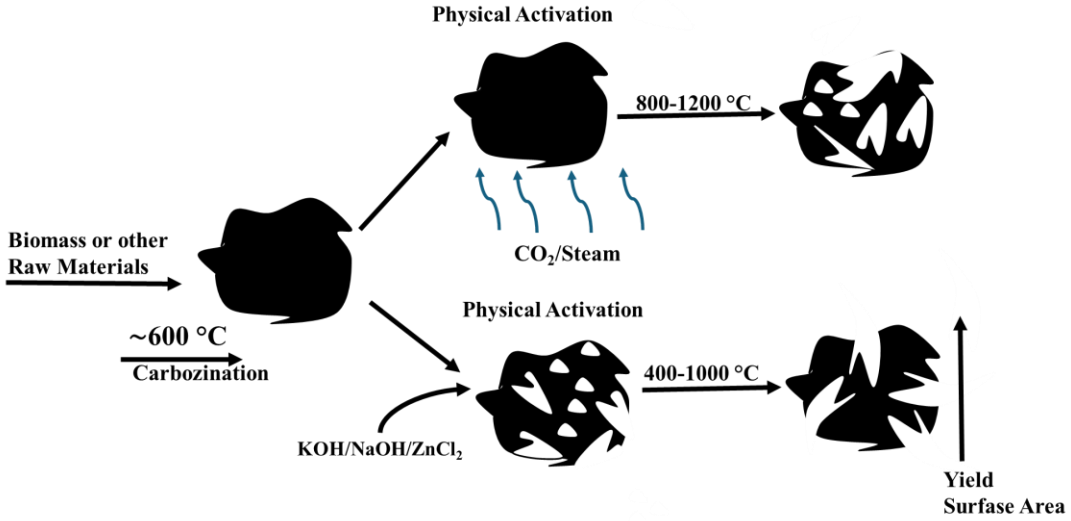


Figure 1.4.4 Activated carbon production: physical vs. chemical activation.

ACs have been extensively investigated for the adsorption of GHGs and refrigerants due to their low cost, large porosity, high surface area, and tuneable pore size distribution [85]. When residual biomass is used as a precursor, bio-derived activated carbons (Bio-ACs) can achieve high microporosity and mesoporosity, large surface areas, and excellent adsorption capacities, while also being cost-effective and easy to regenerate [86]. Specifically, ACs produced from palm waste have demonstrated high porosity, facilitating the adsorption of R-32 [87]. The presence of mesopores enhances gas diffusion and adsorption rates [88], while well-defined micropores, combined with functional groups such as imines and aromatics, promote the selective capture of larger molecules, such as SF_6, by creating a hydrophobic environment favourable for specific interactions [89]. In addition to the choice of precursors, the activation method, whether physical or chemical, plays a decisive role in determining the final properties of activated carbons and their performance in adsorption processes [90]. Physical activation, typically carried out with steam or carbon dioxide at high temperatures (see Table 1.4.1), favours the development of micropores, which are especially effective for the adsorption of small gas molecules [91]. On the other hand, chemical activation, usually performed with agents such as KOH, $ZnCl_2$, or H_3PO_4, allows for the creation of larger surface areas and a broader pore size distribution, including mesopores, at relatively lower temperatures (see Table 1.4.1). This duality enables tailoring the pore structure of ACs to target specific applications [92]. Binders, such as carboxymethylcellulose, have also been used to

improve the packing of activated carbon monoliths (ACM) [92], although they can reduce the overall adsorption capacity [92].

Overall, the combination of precursor selection, controlled pore structure, surface chemistry, and the method of chemical or physical activation makes activated carbons both commercial and bio-derived ACs, promising materials for the adsorption and separation of HFCs and other greenhouse gases. Their tuneable properties bridge the gap between fundamental studies and industrial applications, highlighting their potential for efficient gas capture and storage [93].

Table 1.4.1 Overview of physical, chemical, and biomass-based activated carbons

Aspect	Activating agent	Process temperature	Yield	Typical surface area	Pore distribution	Energy consumption	Waste handling	Environmental impact	Main advantage	Limitation	Ref
Physical Activation	Water vapour, CO_2	800-1200 °C	Low (20–35 %)	500–1500 m^2/g	Mostly micropores	High (due to high temperatures)	Gaseous, no washing required	Low liquid waste, high energy	Stable microporous structure	Low yield, high energy	[91]
Chemical Activation	KOH, H_3PO_4, $ZnCl_2$, NaOH.	400-1000 °C	High (40–60 %)	800–2500 m^2/g	Mixed: micro- and mesopores	Lower (lower temperatures)	Requires washing to remove chemicals	Requires effluent treatment	High surface area and versatility	Use of chemicals and environmental management	[94]
Residual Biomass	Agricultural residues, shells, bagasse, wood	Variable depending on biomass, usually compatible with chemical activation	Economic (uses waste) but variable	Depending on the residue and activation, more heterogeneous	Low energy cost if chemical activation is used	May generate leachates if chemicals are used	Very sustainable, utilises waste	Very sustainable, utilises waste	Low cost, circular economy, sustainable	Property variability depending on biomass	[91]
Commercial Carbons	Coal, lignite	Controlled and standardised according to the product	High and reproducible	Wide range (500–2000 m^2/g), standardised	More controlled, homogeneous, depending on the application	Industrial costs assumed, optimised	Industrial effluent control	Depends on precursor (some fossil, non-renewable	Reproducible, certified properties	Higher cost, dependent on global markets	[95]

1.4.4 Zeolites

Zeolites are a class of crystalline materials belonging to microporous aluminosilicates, whose three-dimensional structure is formed by SiO_4 and AlO_4 tetrahedra interconnected through oxygen atoms [96]. The partial substitution of silicon by aluminium in the crystalline framework generates a negative charge, which is compensated by exchangeable cations (Na^+, K^+, Ca^{2+}, among others) [97]. This feature endows zeolites with unique adsorption, ion-exchange, and molecular selectivity properties, further enhanced by their high surface area and remarkable thermal and chemical stability [97]. The crystalline topology of zeolites determines the size and dimensionality of their channels, typically ranging from 0.3 to 1 nm. Currently, more than 200 distinct structures have been identified and classified by the International Zeolite Association (IZA) [98]. The adsorption behaviour of zeolites is governed by a combined effect of steric exclusion, electrostatic interactions, and dispersion forces. Molecules with kinetic diameters larger than the pore openings are excluded, whereas smaller ones undergo differentiated adsorption depending on their polarity, quadrupole moment, or ability to interact with exchangeable cations [99]. The combination of molecular selectivity, regeneration capacity, and structural stability is essential for the production of efficient zeolites for adsorption and separation applications [99]. Their versatility enables the optimisation of industrial processes for purification, gas capture, and valorisation, making them a fundamental tool for the development of energy-efficient and sustainable technologies [99].

Due to these properties, zeolites have been extensively studied for gas adsorption. Depending on their structural features (pore volume), thermal stability, and polarity, they selectively favour CO_2 adsorption over CH_4 [100]. However, the high CO_2 adsorption capacity over CH_4 generates isotherms with steep slopes, leading to high energy requirements during regeneration [101]. Synthetic zeolites A, X, and Y are commonly employed due to their pore size and high purity [102]. In the separation of F-gas mixtures, zeolite 4A was used for selective separation due to its pore size, which favoured the adsorption of R-32 over R-125 [103]. However, the low adsorption capacity of R-32 represents a limiting factor for this process. In contrast, zeolite 13X has been studied for the separation of R-134a/R-143a/R-125 mixtures [104]. The separation of R-134a from R-125 and R-143a from R-125 was achieved due to the presence of acidic and basic active sites. F-gases are acidic molecules because of the high electronegativity of fluorine, which promotes interactions with Na^+ cations in the zeolite [104]. Moreover, the presence of fluorine atoms with high electronegativity on the same carbon as hydrogen atoms tends to increase acidity and may generate hydrogen bonds with oxygen atoms on the 13X zeolite surface [104]. Additionally, the adsorption equilibria of R-32 and R-125 in the LTA zeolite family (3A, 4A, and 5A) have been investigated, resulting in the separation of R-32 from R-125 using zeolite 3A [28]. However, this separation process faces kinetic limitations that make it unfeasible in practice. Furthermore, the adsorption of R-125 on zeolites 3A and 4A is negligible and irreversible [28]. Overall, although these materials are capable of separating mixtures of greenhouse gases, their low adsorption capacity and the

high energy consumption required for regeneration represent critical limitations that hinder their large-scale industrial application.

1.4.5 Metal–Organic Frameworks (MOFs)

MOFs are a class of highly porous crystalline materials formed by the coordination of metal ions or inorganic clusters with polydentate organic ligands [105]. This hybrid inorganic–organic architecture results in three-dimensional networks with extremely high surface areas (often exceeding 3000 m^2/g) and tuneable pore sizes, ranging from the microporous (< 2 nm) to the mesoporous domain (2–50 nm) [106]. The structure of MOFs is determined by the geometry of the metal nodes and the chemical nature of the organic linkers [105]. Representative examples include MOF-5 (Zn and terephthalic acid), HKUST-1 (Cu and benzene-1,3,5-tricarboxylic acid), and ZIF-8 (Zn^{2+} with imidazolates), all of which have been extensively studied for gas separation and catalysis [107]. Their synthetic versatility enables precise control over channel dimensions and surface functionalization, providing unprecedented tunability in adsorption selectivity and capacity [106]. The high crystallinity of MOFs also facilitates structural characterisation by X-ray diffraction, contributing to a detailed understanding of adsorption mechanisms [108].

In gas separation, MOFs exhibit remarkable performance in various processes: i) selective CO_2 capture over N_2 and CH_4 using materials such as Mg-MOF-74 and UiO-66-NH_2; ii) separation of light hydrocarbons, including xylene isomers and ethylene/ethane mixtures; iii) storage of gases such as H_2 and CH_4, benefiting from their high pore volumes and adsorption site densities; and iv) integration into hybrid membranes and dynamic adsorption systems [109]. MOFs have also attracted significant attention for the separation and storage of SF_6 due to their tuneable pore architectures and large surface areas. M-MOF-74 (M = Mg, Co, Zn) has shown strong affinity for SF_6, attributed to favourable host–guest interactions that enhance selective adsorption [110]. Pore size is a decisive factor: narrow-pore MOFs promote high selectivity, while large-pore structures are more suitable for high-capacity SF_6 storage [111]. Comparative studies reveal that UiO-67 exhibits superior selectivity over UiO-66, likely due to more optimal pore packing for SF_6 molecules [112]. Similarly, Sc-cage-MOF and YTU-30 enhance SF_6 uptake through specific host–guest interactions [113]. Other MOFs, such as SNNU-202, SNNU-203, and SNNU-204, incorporate binuclear metal sites and aromatic rings to improve SF_6 adsorption via synergistic effects [114]. BUT-53 has demonstrated the ability to recover high-purity SF_6 (>99.9%) even under humid conditions [115], while GNU-3, a cobalt-based MOF with molecular traps, effectively separates SF_6 from N_2 mixtures due to strong supramolecular interactions, achieving both high selectivity and excellent regeneration performance [116].

Despite these promising results, large-scale deployment of MOFs faces challenges related to the complexity and high cost of synthesis, which remain significant barriers to industrial application.

Nevertheless, their unique features, including high porosity, structural versatility, and functional tunability, position them as frontier materials for GHGs capture and purification [117].

1.4.6 Porous Organic Polymers (POPs)

Porous organic polymers are a versatile class of materials built entirely from organic building blocks connected by covalent bonds. Their intrinsic porosity, high surface area, and tuneable functionality include both crystalline and amorphous structures, such as covalent organic frameworks (COFs) [118]. POPs lack metal nodes, giving them a fully organic nature, low density, and high chemical stability [118]. By combining long-range crystalline order with the lightweight characteristics of organic polymers, POPs are highly attractive for applications in adsorption, catalysis, and storage [119]. POPs can also be designed in two- or three-dimensional architectures depending on the monomers used. Representative examples include COF-1 and COF-5, which are based on boron–oxygen linkages, and COF-LZU1, constructed from imine linkages [120]. The modularity of their synthesis allows fine-tuning of pore size, chemical functionality of the pore walls, and framework stability, achieving specific surface areas exceeding 1500 m^2/g. Moreover, the covalent linkages provide POPs with superior stability under harsh chemical environments, in some cases surpassing that of MOFs [121].

The absence of metal nodes prevents deactivation by reduction or oxidation, further expanding their applicability under extreme conditions. Additionally, functionalization of the organic building blocks enables modulation of surface interactions, which is critical for optimising selective adsorption behaviour [122]. Recently, POPs have been successfully synthesised using natural dyes and hydroxylated azines as sustainable precursors [123]. Natural dyes are cost-effective, widely available, and structurally diverse. Examples such as RIO-43, RIO-47, RIO-51, and RIO-55 exhibit high porosity, stacked laminar structures, ion exchange capacity, and water insolubility [124]. POPs derived from hydroxylated azines, such as RIO-13, RIO-12, RIO-11, and RIO-11m, display pronounced microporosity, elevated surface areas, and surface hydroxyl groups [123]. These functional groups facilitate Lewis acid–base interactions with GHGs, enhancing adsorption capacity [123]. Notably, RIO-12 and RIO-55 show particularly high porosity [125], a critical factor influencing selective gas separation performance. These combined properties make POPs highly promising candidates for use as adsorbents in GHGs capture and separation. Their tuneable porosity, structural stability, and surface functionality position them as next-generation materials for efficient and sustainable gas adsorption technologies.

1.5 Objectives of the Thesis

The main objective of this thesis is to develop advanced materials for the capture, separation, and recovery of fluorinated gases, focusing on both liquid absorbents and porous solid adsorbents. Ionic liquids (ILs) and deep eutectic solvents (DES) were investigated due to their high selectivity, low vapour pressure, and tuneable molecular design, making them promising candidates for targeted gas separation. Simultaneously, porous solid matrices including MOFs, POPs, ACs, and hybrid composites were studied for their structural stability, high surface area, and controlled porosity. Integrating these strategies provides a comprehensive approach to enhance efficiency and sustainability in GHGs management.

Different ILs were evaluated based on their absorption equilibria, selectivity, and molecular interactions with refrigerants. In a complementary study, the solubility and phase equilibrium behaviour of F-gases in various DES derived from FILs were determined to correlate their physicochemical properties with absorption efficiency and identify their potential application in industrial processes for the recovery and separation of F-gases. Furthermore, COSMO-RS simulations allowed a detailed understanding of thermodynamic behaviours and cation–anion interactions, guiding the proposal of a library of 600 potential ILs for improving refrigerant absorption and separation (Chapter 2). While some ILs exhibit high selectivity and strong gas interactions, high viscosity can limit mass transfer and process efficiency. To address these limitations, ILs were immobilised on mesoporous silica, combining the chemical affinity of ILs with the structural advantages of solid matrices, reducing viscosity, enhancing diffusion, and improving gas capture (Chapter 3).

Porous solid adsorbents, ACs, MOFs, POPs, and zeolites, were investigated for their selective adsorption and purification of fluorinated gases. High surface area, tuneable micropore-to-mesopore ratios, and functional groups enhance adsorption capacity, selectivity, and diffusion, while chemical and thermal stability ensure suitability for industrial applications (Chapter 4). Finally, the thesis addressed the selective capture of SF_6, analysing the influence of structural properties such as microporosity and surface area on adsorption and storage. Comparative studies with literature materials and evaluations under practical working conditions, which allow optimisation of SF_6 capture (Chapter 5).

Overall, this work demonstrates the potential of ionic liquids, deep eutectic solvents, hybrid composites, and porous solid matrices for efficient greenhouse gas capture, separation, and storage, providing a foundation for future applications in industrial and environmental contexts.

1.6 Scientific outputs

The work developed in this thesis has resulted in the following publications:

1- **J. E. Sosa**, R. P. P. L. Ribeiro, S. Kolakovic, J. P. B. Mota, J. M. M. Araújo, A. B. Pereiro, *Capture and separation of sulphur hexafluoride: the most powerful greenhouse gas*, J. Mol. Liq. (2025), (under revision).

2- **J.E. Sosa**, R.P.P.L. Ribeiro, S. Kolakovic, I. Matos, M. Bernardo, J. P. B. Mota, J. M. M. Araújo, Ana B. Pereiro, *Solid Porous Materials for Selective Capture and Separation of Sulfur Hexafluoride (SF_6)*, ChemPlusChem (2025). https://doi.org/10.1002/cplu.202500376.

3- **J.E. Sosa**, S.K.S. Freitas, L.R.C. Correa, R.P.P.L. Ribeiro, J.P.B. Mota, P. Mothé-Esteves, J.M.M. Araújo, L.C. Branco, A.B. Pereiro, *Porous Organic Polymers for the adsorption of fluorinated gases,* J. Mol. Liq. (2025), 128585. https://doi.org/10.1016/j.molliq.2025.128585.

4- **J.E. Sosa**, R.P.P.L. Ribeiro, I. Matos, M. Bernardo, I.M. Fonseca, J.P.B. Mota, J.M.M. Araújo, A.B. Pereiro, *Coconut shell derived activated carbon for effective separation of greenhouse gases*, Int. J. Refrig. 176 (2025) 66–78. https://doi.org/10.1016/j.ijrefrig.2025.04.022.

5- **J.E. Sosa**, R.P.P.L. Ribeiro, I. Matos, M. Bernardo, I.M. Fonseca, J.P.B. Mota, J.M.M. Araújo, A.B. Pereiro, *Exploring the potential of biomass-derived carbons for the separation of fluorinated gases with high global warming potential*, Biomass Bioenergy 188 (2024) 107323. https://doi.org/10.1016/j.biombioe.2024.107323.

6- **J.E. Sosa**, C. Malheiro, P.J. Castro, R.P.P.L. Ribeiro, M.M. Piñeiro, F. Plantier, J.P.B. Mota, J.M.M. Araújo, A.B. Pereiro, *Exploring the Potential of Metal–Organic Frameworks for the Separation of Blends of Fluorinated Gases with High Global Warming Potential*, Global Challenges 7 (2023) 2200107. https://doi.org/10.1002/gch2.202200107.

7- **J.E. Sosa**. R.P.P.L. Ribeiro, P.J. Castro, J.P.B. Mota, A.B. Pereiro, J.M.M. Araújo, *Sorption of fluorinated greenhouse gases in silica-supported fluorinated ionic liquids,* J. Environ. Chem. Eng. 10 (2022) 108580. https://doi.org/10.1016/j.jece.2022.108580.

8- **J.E. Sosa**, R. Santiago, A.E. Redondo, J. Avila, L.F. Lepre, M.C. Gomes, J.M.M. Araújo, J. Palomar, A.B. Pereiro, *Design of Ionic Liquids for Fluorinated Gas Absorption: COSMO-RS Selection and Solubility Experiments*, Environ. Sci. Technol. 56 (2022) 5898–5909. https://doi.org/10.1021/acs.est.2c00051.

9- **J.E. Sosa**, R. Santiago, D. Hospital-Benito, M. Costa Gomes, J.M.M. Araújo, A.B. Pereiro, J. Palomar, *Process Evaluation of Fluorinated Ionic Liquids as F-Gas Absorbents*, Environ. Sci. Technol. 54 (2020) 12784–12794. https://doi.org/10.1021/acs.est.0c05305.

10- **J.E. Sosa**, C. Malheiro, R.P.P.L. Ribeiro, P.J. Castro, M.M. Piñeiro, J.M.M. Araújo, F. Plantier, J.P.B. Mota, A.B. Pereiro, *Adsorption of fluorinated greenhouse gases on activated carbons: evaluation of their potential for gas separation*, J. Chem. Technol. Biotechnol. 95 (2020) 1892–1905. https://doi.org/https://doi.org/10.1002/jctb.637.

11- P.J. Castro, A.E. Redondo, **J.E. Sosa**, M.E. Zakrzewska, A.V.M. Nunes, J.M.M. Araújo, A.B. Pereiro, *Absorption of Fluorinated Greenhouse Gases in Deep Eutectic Solvents*, Ind. Eng. Chem. Res. 59 (2020) 13246–13259. https://doi.org/10.1021/acs.iecr.0c01893.

12- **J.E. Sosa**, R.P.P.L. Ribeiro, P.J. Castro, J.P.B. Mota, J.M.M. Araújo, A.B. Pereiro, *Absorption of Fluorinated Greenhouse Gases Using Fluorinated Ionic Liquids*, Ind. Eng. Chem. Res. 58 (2019) 20769–20778. https://doi.org/10.1021/acs.iecr.9b04648.

Another publication that was not included in this thesis but was published during the thesis project is

13- R.P.P.L. Ribeiro, **J.E. Sosa**, J.M.M. Araújo, A.B. Pereiro, J.P.B. Mota, *Vacuum swing adsorption for R-32 recovery from R-410A refrigerant blend*, International Journal of Refrigeration 150 (2023) 253–264. https://doi.org/10.1016/j.ijrefrig.2023.01.020.

The work developed in this thesis was also presented at several international conferences in the form of 8 oral communications and 14 poster communications.

1.7 References

[1] U.A. Bhatti, M.A. Bhatti, H. Tang, M.S. Syam, E.M. Awwad, M. Sharaf, Y.Y. Ghadi, Global production patterns: Understanding the relationship between greenhouse gas emissions, agriculture greening and climate variability, Environ Res 245 (2024) 118049. https://doi.org/https://doi.org/10.1016/j.envres.2023.118049.

[2] U.S. Environmental Protection Agency | US EPA, Overview of Greenhouse Gases., (n.d.). https://www.epa.gov/ghgemissions/overview-greenhouse-gases / (accessed on 21 June 2024) (accessed June 25, 2024).

[3] Z. Cui, Y. Li, S. Xiao, S. Tian, J. Tang, Y. Hao, X. Zhang, Recent progresses, challenges and proposals on SF6 emission reduction approaches, Science of The Total Environment 906 (2024) 167347. https://doi.org/https://doi.org/10.1016/j.scitotenv.2023.167347.

[4] S. Bartos, C. Laush, J. Scharfenberg, R. Kantamaneni, Reducing greenhouse gas emissions from magnesium die casting, J Clean Prod 15 (2007) 979–987. https://doi.org/https://doi.org/10.1016/j.jclepro.2006.01.008.

[5] P. Widger, A. (Manu) Haddad, Evaluation of SF6 Leakage from Gas Insulated Equipment on Electricity Networks in Great Britain, Energies (Basel) 11 (2018). https://doi.org/10.3390/en11082037.

[6] P.F.P.R.K.L. Abdelaziz O, Refrigeration, Air Conditioning and Heat Pumps Technical Options Committee (RTOC) 2022 Assessment Report (Montreal Protocol on Substances That Deplete the Ozone Layer), (2023). https://ozone.unep.org/system/files/documents/RTOC-assessment%20-report-2022.pdf (accessed December 17, 2024).

[7] V. Codera, D. Clijnk, J.O. Pou, J. Fernandez-Garcia, F. Llovell, R. Gonzalez-Olmos, Process design for the recovery of waste refrigerants using deep eutectic solvents, J Environ Chem Eng 11 (2023) 110255. https://doi.org/https://doi.org/10.1016/j.jece.2023.110255.

[8] C.G. Albà, I.I.I. Alkhatib, F. Llovell, L.F. Vega, Assessment of Low Global Warming Potential Refrigerants for Drop-In Replacement by Connecting their Molecular Features to Their Performance, ACS Sustain Chem Eng 9 (2021) 17034–17048. https://doi.org/10.1021/acssuschemeng.1c05985.

[9] A. Mota-Babiloni, P. Makhnatch, R. Khodabandeh, Recent investigations in HFCs substitution with lower GWP synthetic alternatives: Focus on energetic performance and environmental impact, International Journal of Refrigeration 82 (2017) 288–301. https://doi.org/https://doi.org/10.1016/j.ijrefrig.2017.06.026.

[10] A. Mota-Babiloni, J. Navarro-Esbrí, Á. Barragán-Cervera, F. Molés, B. Peris, Analysis based on EU Regulation No 517/2014 of new HFC/HFO mixtures as alternatives of high GWP refrigerants in refrigeration and HVAC systems, International Journal of Refrigeration 52 (2015) 21–31. https://doi.org/10.1016/j.ijrefrig.2014.12.021.

[11] P. Purohit, T. Chao, R. Cooke, H. Dhont, R. Kaur, R. Peixoto, H. Walter-Terrinoni, A. Woodcock, The Importance of Lifecycle Refrigerant Management in Climate and Ozone Protection, Sustainability 17 (2025). https://doi.org/10.3390/su17010053.

[12] R. Gonzalez-Olmos, F. Llovell, Life cycle assessment of fluorinated gas recovery from waste refrigerants through vacuum swing adsorption, Sustainable Materials and Technologies 39 (2024) e00811. https://doi.org/https://doi.org/10.1016/j.susmat.2023.e00811.

[13] D. Clijnk, V. Codera, J.O. Pou, J. Fernandez-Garcia, R. Gonzalez-Olmos, Enhancing circular economy of waste refrigerants management using deep eutectic solvents, Sustainable Materials and Technologies 41 (2024) e01062. https://doi.org/https://doi.org/10.1016/j.susmat.2024.e01062.

[14] B.K. Sovacool, S. Griffiths, J. Kim, M. Bazilian, Climate change and industrial F-gases: A critical and systematic review of developments, sociotechnical systems and policy options for reducing synthetic greenhouse gas emissions, Renewable and Sustainable Energy Reviews 141 (2021) 110759. https://doi.org/https://doi.org/10.1016/j.rser.2021.110759.

[15] A. Jordan, H. Frank, Trifluoroacetate in the environment. Evidence for sources other than HFC/HCFCs, Environ Sci Technol 33 (1999) 522–527. https://doi.org/10.1021/es980674y.

[16] K.R. Solomon, G.J.M. Velders, S.R. Wilson, S. Madronich, J. Longstreth, P.J. Aucamp, J.F. Bornman, Sources, fates, toxicity, and risks of trifluoroacetic acid and its salts: Relevance to substances regulated under the Montreal and Kyoto Protocols, J Toxicol Environ Health B Crit Rev 19 (2016) 289–304. https://doi.org/10.1080/10937404.2016.1175981.

[17] R. Holland, M.A.H. Khan, I. Driscoll, R. Chhantyal-Pun, R.G. Derwent, C.A. Taatjes, A.J. Orr-Ewing, C.J. Percival, D.E. Shallcross, Investigation of the Production of Trifluoroacetic Acid from Two Halocarbons, HFC-134a and HFO-1234yf and Its Fates Using a Global Three-Dimensional Chemical Transport Model, ACS Earth Space Chem 5 (2021) 849–857. https://doi.org/10.1021/acsearthspacechem.0c00355.

[18] N. Mathew, A. Somanathan, A. Tirpude, T. Arfin, The impact of short-lived climate pollutants on the human health, Environmental Pollution and Management 1 (2024) 1–14. https://doi.org/https://doi.org/10.1016/j.epm.2024.04.001.

[19] L.M.E. Sabik, R.A. Abbas, M.M. Ismail, S. El-Refaei, Cardiotoxicity of Freon among refrigeration services workers: comparative cross-sectional study, Environmental Health 8 (2009) 31. https://doi.org/10.1186/1476-069X-8-31.

[20] M.-B. Kim, K.-M. Kim, T.-H. Kim, Highly selective adsorption of SF6 over N2 in a bromine-functionalized zirconium-based metal-organic framework, Chem. Eng. J. 339 (2018) 223.

[21] E.K. Lee, J.D. Lee, H.J. Lee, B.R. Lee, Y.S. Lee, S.M. Kim, H.O. Park, Y.S. Kim, Y.-D. Park, Y. Do Kim, Pure SF6 and SF6−N2 Mixture Gas Hydrates Equilibrium and Kinetic Characteristics, Environ Sci Technol 43 (2009) 7723–7727. https://doi.org/10.1021/es901350v.

[22] E. Bevacqua, C.-F. Schleussner, J. Zscheischler, A year above 1.5 °C signals that Earth is most probably within the 20-year period that will reach the Paris Agreement limit, Nat Clim Chang 15 (2025) 262–265. https://doi.org/10.1038/s41558-025-02246-9.

[23] Z. Wu, X. Su, W. Zhu, T. Wang, Climate benefits from China's adherence to the Kigali Amendment, Cell Reports Sustainability 2 (2025) 100431. https://doi.org/https://doi.org/10.1016/j.crsus.2025.100431.

[24] M. Schulz, D. Kourkoulas, Regulation (EU) No 517/2014 of the European Parliament and of the Council of 16 April 2014 on fluorinated greenhouse gases and repealing Regulation (EC) No 842/2006, Official Journal of the European Union 2014 (2014) L150/195-230. http://eur-lex.europa.eu/eli/reg/2014/517/oj.

[25] W. Jiang, Y. Lin, C. Sun, Y. Sun, Y. Zhu, Comparative Review for Enhancing CO2 Capture Efficiency with Mixed Amine Systems and Catalysts, Molecules 29 (2024). https://doi.org/10.3390/molecules29194618.

[26] M.M. Mohd Pauzi, N. Azmi, K.K. Lau, Emerging Solvent Regeneration Technologies for CO2 Capture through Offshore Natural Gas Purification Processes, Sustainability 14 (2022). https://doi.org/10.3390/su14074350.

[27] A. Nuhnen, C. Janiak, A practical guide to calculate the isosteric heat/enthalpy of adsorption: Via adsorption isotherms in metal-organic frameworks, MOFs, Dalton Transactions 49 (2020) 10295–10307. https://doi.org/10.1039/d0dt01784a.

[28] A.D. Yancey, D.R. Corbin, M.B. Shiflett, Difluoromethane (HFC-32) and Pentafluoroethane (HFC-125) Sorption on Linde Type A (LTA) Zeolites for the Separation of Azeotropic Hydrofluorocarbon Refrigerant Mixtures, Langmuir 38 (2022) 1937–1953. https://doi.org/10.1021/acs.langmuir.1c02904.

[29] S. Asensio-Delgado, F. Pardo, G. Zarca, A. Urtiaga, Machine learning for predicting the solubility of high-GWP fluorinated refrigerants in ionic liquids, J Mol Liq 367 (2022) 120472. https://doi.org/10.1016/j.molliq.2022.120472.

[30] F.A. Philip, A. Henni, Incorporation of Amino Acid-Functionalized Ionic Liquids into Highly Porous MOF-177 to Improve the Post-Combustion CO2 Capture Capacity, Molecules 28 (2023). https://doi.org/10.3390/molecules28207185.

[31] R.E. Treybal, Mass Transfer Operations. 2nd Edition, McGraw Hill, New York., 1968.

[32] H.H. Park, B.R. Deshwal, I.W. Kim, H.K. Lee, Absorption of SO2 from flue gas using PVDF hollow fiber membranes in a gas–liquid contactor, J Memb Sci 319 (2008) 29–37. https://doi.org/https://doi.org/10.1016/j.memsci.2008.03.023.

[33] D. Shang, S. Zeng, X. Zhang, X. Zhang, L. Bai, H. Dong, Highly efficient and reversible absorption of NH3 by dual functionalised ionic liquids with protic and Lewis acidic sites, J Mol Liq 312 (2020) 113411. https://doi.org/https://doi.org/10.1016/j.molliq.2020.113411.

[34] M.G. Demirbek, S.B. Rodriguez Reartes, F. Llovell, Thermodynamic Analysis of the Absorption of Common Refrigerants in Fluorinated Deep Eutectic Solvents, Fluid Phase Equilib 581 (2024) 114077. https://doi.org/https://doi.org/10.1016/j.fluid.2024.114077.

[35] C. Gui, G. Li, R. Zhu, Z. Lei, Y. Dong, Capturing VOCs in the pharmaceutical industry with ionic liquids, Chem Eng Sci 252 (2022) 117504. https://doi.org/https://doi.org/10.1016/j.ces.2022.117504.

[36] I. Das, K. Rama Swami, R.L. Gardas, Chapter 12 - Ionic liquids: a tool for CO2 capture and reduced emission, in: J.A. Siddique, S.P. Ansari, A.A.P. Khan, A.M. Asiri (Eds.), Advanced Applications of Ionic Liquids, Elsevier, 2023: pp. 327–350. https://doi.org/https://doi.org/10.1016/B978-0-323-99921-2.00008-2.

[37] M. Fang, N. Yi, W. Di, T. Wang, Q. Wang, Emission and control of flue gas pollutants in CO2 chemical absorption system – A review, International Journal of Greenhouse Gas Control 93 (2020) 102904. https://doi.org/https://doi.org/10.1016/j.ijggc.2019.102904.

[38] J.M. Smith, Introduction to chemical engineering thermodynamics, J Chem Educ 27 (1950) 584. https://doi.org/10.1021/ed027p584.3.

[39] L.F. Lepre, D. Andre, S. Denis-Quanquin, A. Gautier, A.A.H. Pádua, M. Costa Gomes, Ionic Liquids Can Enable the Recycling of Fluorinated Greenhouse Gases, ACS Sustain Chem Eng 7 (2019). https://doi.org/10.1021/acssuschemeng.9b04214.

[40] S.B. Øyen, H.A. Jakobsen, T. Haug-Warberg, J. Solsvik, Interface Mass Transfer in Reactive Bubbly Flow: A Rigorous Phase Equilibrium-Based Approach, Ind Eng Chem Res 60 (2021) 17705–17732. https://doi.org/10.1021/acs.iecr.1c03131.

[41] T. Kataoka, Y. Orita, Y. Shimoyama, Analysis of CO2 Mass Transfer on Gas Absorption into Phase-Separated Gel, Ind Eng Chem Res 60 (2021) 8236–8243. https://doi.org/10.1021/acs.iecr.0c06353.

[42] A. Broderick, M.A. Rocha, Y. Khalifa, M.B. Shiflett, J.T. Newberg, Mass Transfer Thermodynamics through a Gas–Liquid Interface, J Phys Chem B 123 (2019) 2576–2584. https://doi.org/10.1021/acs.jpcb.9b00958.

[43] D.W. van Krevelen, P.J. Hoftijzer, Studies of gas absorption: V. Mass transfer in film reactors (wetted wall columns), Recueil Des Travaux Chimiques Des Pays-Bas 68 (1949) 221–233. https://doi.org/https://doi.org/10.1002/recl.19490680304.

[44] F.P. Pelaquim, A.M. Barbosa Neto, I.A.L. Dalmolin, M.C. da Costa, Gas Solubility Using Deep Eutectic Solvents: Review and Analysis, Ind Eng Chem Res 60 (2021) 8607–8620. https://doi.org/10.1021/acs.iecr.1c00947.

[45] A. Zarei, R. Haghbakhsh, S. Raeissi, Overview and thermodynamic modelling of deep eutectic solvents as co-solvents to enhance drug solubilities in water, European Journal of Pharmaceutics and Biopharmaceutics 193 (2023) 1–15. https://doi.org/https://doi.org/10.1016/j.ejpb.2023.10.007.

[46] J.H. Vera, Molecular thermodynamics of fluid-phase equilibria by John M. Prausnitz, Rüdiger N. Lichtenthaler and Edmundo Comes de Azevedo, Third Edition, 1999, Can J Chem Eng 78 (2000) 429–430. https://doi.org/https://doi.org/10.1002/cjce.5450780222.

[47] E. Smolková-Keulemansová, L. Feltl, eds., Chapter 10 - Gas chromatography, in: Analysis of Substances in the Gaseous Phase, Elsevier, 1991: pp. 223–462. https://doi.org/https://doi.org/10.1016/S0166-526X(05)80100-X.

[48] H. Alkhaldi, S. Alharthi, S. Alharthi, H.A. AlGhamdi, Y.M. AlZahrani, S.A. Mahmoud, L.G. Amin, N.H. Al-Shaalan, W.E. Boraie, M.S. Attia, S.A. Al-Gahtany, N. Aldaleeli, M.M. Ghobashy, A.I. Sharshir, M. Madani, R. Darwesh, S.F. Abaza, Sustainable polymeric adsorbents for adsorption-based water remediation and pathogen deactivation: a review, RSC Adv. 14 (2024) 33143–33190. https://doi.org/10.1039/D4RA05269B.

[49] F. Shabir, M. Sultan, T. Miyazaki, B.B. Saha, A. Askalany, I. Ali, Y. Zhou, R. Ahmad, R.R. Shamshiri, Recent updates on the adsorption capacities of adsorbent-adsorbate pairs for heat transformation applications, Renewable and Sustainable Energy Reviews 119 (2020) 109630. https://doi.org/https://doi.org/10.1016/j.rser.2019.109630.

[50] M. Thommes, K. Kaneko, A. V. Neimark, J.P. Olivier, F. Rodriguez-Reinoso, J. Rouquerol, K.S.W. Sing, Physisorption of gases, with special reference to the evaluation of surface area and pore size distribution (IUPAC Technical Report), Pure and Applied Chemistry 87 (2015) 1051–1069. https://doi.org/10.1515/pac-2014-1117.

[51] P. V Mane, R.M. Rego, P.L. Yap, D. Losic, M.D. Kurkuri, Unveiling cutting-edge advances in high surface area porous materials for the efficient removal of toxic metal ions from water, Prog Mater Sci 146 (2024) 101314. https://doi.org/https://doi.org/10.1016/j.pmatsci.2024.101314.

[52] X. Wang, H. Cheng, G. Ye, J. Fan, F. Yao, Y. Wang, Y. Jiao, W. Zhu, H. Huang, D. Ye, Key factors and primary modification methods of activated carbon and their application in adsorption of carbon-based gases: A review, Chemosphere 287 (2022) 131995. https://doi.org/https://doi.org/10.1016/j.chemosphere.2021.131995.

[53] H. Ma, H. Fu, Y. Tong, A. Umar, Y.M. Hung, X. Wang, Advances in CO2 capture and separation materials: Emerging trends, challenges, and prospects for sustainable applications, Carbon Capture Science & Technology 15 (2025) 100441. https://doi.org/https://doi.org/10.1016/j.ccst.2025.100441.

[54] K. Cychosz Struckhoff, M. Thommes, L. Sarkisov, On the Universality of Capillary Condensation and Adsorption Hysteresis Phenomena in Ordered and Crystalline Mesoporous Materials, Adv Mater Interfaces 7 (2020) 2000184. https://doi.org/https://doi.org/10.1002/admi.202000184.

[55] N. Yalçın, V. Sevinç, Studies of the surface area and porosity of activated carbons prepared from rice husks, Carbon N Y 38 (2000) 1943–1945. https://doi.org/https://doi.org/10.1016/S0008-6223(00)00029-4.

[56] M.M. Dubinin, The Potential Theory of Adsorption of Gases and Vapors for Adsorbents with Energetically Nonuniform Surfaces., Chem Rev 60 (1960) 235–241. https://doi.org/10.1021/cr60204a006.

[57] S. Ozawa, S. Kusumi, Y. Ogino, Physical adsorption of gases at high pressure. IV. An improvement of the Dubinin—Astakhov adsorption equation, J Colloid Interface Sci 56 (1976) 83–91. https://doi.org/https://doi.org/10.1016/0021-9797(76)90149-1.

[58] M.M. DUBININ, V.A. ASTAKHOV, Description of Adsorption Equilibria of Vapors on Zeolites over Wide Ranges of Temperature and Pressure, in: Molecular Sieve Zeolites-II, AMERICAN CHEMICAL SOCIETY, 1971: pp. 69–85. https://doi.org/doi:10.1021/ba-1971-0102.ch044.

[59] J.C. Slootweg, Sustainable chemistry: Green, circular, and safe-by-design, One Earth 7 (2024) 754–758. https://doi.org/https://doi.org/10.1016/j.oneear.2024.04.006.

[60] L. Zhu, X. Guan, J. Li, Y. Peng, X. Zhang, A. Gong, M. Li, H. Xie, S. Chen, J. Li, H. Wang, Q. Zhang, W. Wang, Characterization of VOCs emissions and associated health risks inherent to the packaging and printing industries in Shandong Province, China, Science of The Total Environment 946 (2024) 174108. https://doi.org/https://doi.org/10.1016/j.scitotenv.2024.174108.

[61] M. Bystrzanowska, M. Tobiszewski, Assessment and design of greener deep eutectic solvents – A multicriteria decision analysis, J Mol Liq 321 (2021) 114878. https://doi.org/https://doi.org/10.1016/j.molliq.2020.114878.

[62] P. Verdía Barbará, H. Choudhary, P.S. Nakasu, A. Al-Ghatta, Y. Han, C. Hopson, R.I. Aravena, D.K. Mishra, A. Ovejero-Pérez, B.A. Simmons, J.P. Hallett, Recent Advances in the Use of Ionic Liquids and Deep Eutectic Solvents for Lignocellulosic Biorefineries and Biobased Chemical and Material Production, Chem Rev 125 (2025) 5461–5583. https://doi.org/10.1021/acs.chemrev.4c00754.

[63] Y. Artioli, Adsorption, in: S.E. Jørgensen, B.D. Fath (Eds.), Encyclopedia of Ecology, Academic Press, Oxford, 2008: pp. 60–65. https://doi.org/https://doi.org/10.1016/B978-008045405-4.00252-4.

[64] S. Wang, L. Lu, D. Wu, X. Lu, W. Cao, T. Yang, Y. Zhu, Molecular Simulation Study of the Adsorption and Diffusion of a Mixture of CO2/CH4 in Activated Carbon: Effect of Textural Properties and Surface Chemistry, J Chem Eng Data 61 (2016) 4139–4147. https://doi.org/10.1021/acs.jced.6b00554.

[65] N. Nasirpour, M. Mohammadpourfard, S. Zeinali Heris, Ionic liquids: Promising compounds for sustainable chemical processes and applications, Chemical Engineering Research and Design 160 (2020) 264–300. https://doi.org/https://doi.org/10.1016/j.cherd.2020.06.006.

[66] R.L. Vekariya, A review of ionic liquids: Applications towards catalytic organic transformations, J Mol Liq 227 (2017) 44–60. https://doi.org/https://doi.org/10.1016/j.molliq.2016.11.123.

[67] D. Peng, D.P. Horvat, F. Picchioni, Computer-Aided Ionic Liquid Design and Experimental Validation for Benzene–Cyclohexane Separation, Ind Eng Chem Res 60 (2021) 4951–4961. https://doi.org/10.1021/acs.iecr.0c05935.

[68] A.B. Pereiro, J.M.M. Araújo, S. Martinho, F. Alves, S. Nunes, A. Matias, C.M.M. Duarte, L.P.N. Rebelo, I.M. Marrucho, Fluorinated Ionic Liquids: Properties and Applications, ACS Sustain Chem Eng 1 (2013) 427–439. https://doi.org/10.1021/sc300163n.

[69] M.L. Ferreira, M.J. Pastoriza-Gallego, J.M.M. Araújo, J.N. Canongia Lopes, L.P.N. Rebelo, M. M Piñeiro, K. Shimizu, A.B. Pereiro, Influence of Nanosegregation on the Phase Behavior of Fluorinated Ionic Liquids, Journal of Physical Chemistry C 121 (2017) 5415–5427. https://doi.org/10.1021/acs.jpcc.7b00516.

[70] B.J. Konwick, G.T. Tomy, N. Ismail, J.T. Peterson, R.J. Fauver, D. Higginbotham, A.T. Fisk, Concentrations and patterns of perfluoroalkyl acids in Georgia, USA surface waters near and distant to a major use source, Environ Toxicol Chem 27 (2008) 2011–2018. https://doi.org/10.1897/07-659.1.

[71] V.R. Ferro, C. Moya, D. Moreno, R. Santiago, J. de Riva, G. Pedrosa, M. Larriba, I. Diaz, J. Palomar, J. De Riva, G. Pedrosa, M. Larriba, I. Diaz, J. Palomar, Enterprise Ionic Liquids Database (ILUAM) for Use in Aspen ONE Programs Suite with COSMO-Based Property Methods, Ind Eng Chem Res 57 (2018) 980–989. https://doi.org/10.1021/acs.iecr.7b04031.

[72] J. Palomar, M. Gonzalez-Miquel, J. Bedia, F. Rodriguez, J.J. Rodriguez, Task-specific ionic liquids for efficient ammonia absorption, Sep Purif Technol 82 (2011) 43–52. https://doi.org/10.1016/j.seppur.2011.08.014.

[73] J. Palomar, M. Gonzalez-Miquel, A. Polo, F. Rodriguez, Understanding the physical absorption of CO2 in ionic liquids using the COSMO-RS method, Ind Eng Chem Res 50 (2011) 3452–3463. https://doi.org/10.1021/ie101572m.

[74] G. García, S. Aparicio, R. Ullah, M. Atilhan, Deep eutectic solvents: physicochemical properties and gas separation applications, Energy Fuels 29 (2015) 2616.

[75] F. Oyoun, A. Toncheva, L.C. Henríquez, R. Grougnet, F. Laoutid, N. Mignet, K. Alhareth, Y. Corvis, Deep Eutectic Solvents: An Eco-friendly Design for Drug Engineering, ChemSusChem 16 (2023) e202300669. https://doi.org/https://doi.org/10.1002/cssc.202300669.

[76] D. Jovell, S. B. Gómez, M.E. Zakrzewska, A.V.M. Nunes, J.M.M. Araújo, A.B. Pereiro, F. Llovell, Insight on the Solubility of R134a in Fluorinated Ionic Liquids and Deep Eutectic Solvents, J Chem Eng Data 65 (2020) 4956–4969. https://doi.org/10.1021/acs.jced.0c00588.

[77] Z. Zuo, M. Cao, W. Mu, I.B. Jovein, C. Held, B. Chen, G. Yu, Selective absorption of fluorinated gases by deep eutectic solvents: Thermodynamics and molecular insights, Sep Purif Technol 364 (2025) 132342. https://doi.org/https://doi.org/10.1016/j.seppur.2025.132342.

[78] A.A. Manafpour, F. Feyzi, M. Rezaee, An environmentally friendly deep eutectic solvent for CO2 capture, Sci Rep 14 (2024) 19744. https://doi.org/10.1038/s41598-024-70761-4.

[79] F.P. Kinik, A. Uzun, S. Keskin, Ionic Liquid/Metal–Organic Framework Composites: From Synthesis to Applications, ChemSusChem 10 (2017) 2842–2863. https://doi.org/https://doi.org/10.1002/cssc.201700716.

[80] S. Zheng, S. Zeng, G. Li, B. Li, L. Bai, H. Jiang, Q. Yang, X. Zhang, Novel Fluid Ionic Liquid Composites with Self-Assembled Porosity and Chemical Sites for Facilitating CO2 Separation, ACS Sustain Chem Eng 11 (2023) 11635–11644. https://doi.org/10.1021/acssuschemeng.3c02618.

[81] S.-Y. Zhang, Q. Zhuang, M. Zhang, H. Wang, Z. Gao, J.-K. Sun, J. Yuan, Poly(ionic liquid) composites, Chem. Soc. Rev. 49 (2020) 1726–1755. https://doi.org/10.1039/C8CS00938D.

[82] A.-M. Putz, A. Len, C. Ianăşi, C. Savii, L. Almásy, Ultrasonic preparation of mesoporous silica using pyridinium ionic liquid, Korean Journal of Chemical Engineering 33 (2016) 749–754. https://doi.org/10.1007/s11814-016-0021-x.

[83] A.H. Ab Rahim, N.M. Yunus, M.A. Bustam, Ionic Liquids Hybridization for Carbon Dioxide Capture: A Review, Molecules 28 (2023). https://doi.org/10.3390/molecules28207091.

[84] X. Su, Z. Ren, P. Li, Review on physical and chemical activation strategies for ultra-high performance concrete (UHPC), Cem Concr Compos 149 (2024) 105519. https://doi.org/https://doi.org/10.1016/j.cemconcomp.2024.105519.

[85] J. Shen, X. Wang, Y. Chen, Adsorbents for adsorption separation of CO2 and CH4: A literature review, Can J Chem Eng 101 (2023) 7115–7133. https://doi.org/https://doi.org/10.1002/cjce.24942.

[86] R. Maniarasu, S.K. Rathore, S. Murugan, Biomass-based activated carbon for CO2 adsorption–A review, Energy & Environment 34 (2023) 1674–1721. https://doi.org/10.1177/0958305X221093465.

[87] Md.A. Islam, B.B. Saha, Harnessing waste palm-based activated carbon/difluoromethane pair for sustainable low-emission cooling systems, J Environ Chem Eng 12 (2024) 114869. https://doi.org/https://doi.org/10.1016/j.jece.2024.114869.

[88] J. Serafin, B. Dziejarski, Activated carbons—preparation, characterization and their application in CO2 capture: A review, Environmental Science and Pollution Research 31 (2024) 40008–40062. https://doi.org/10.1007/s11356-023-28023-9.

[89] T. Hasell, M. Miklitz, A. Stephenson, M.A. Little, S.Y. Chong, R. Clowes, L.J. Chen, D. Holden, G.A. Tribello, K.E. Jelfs, A.I. Cooper, Porous Organic Cages for Sulfur Hexafluoride Separation, J. Am. Chem. Soc. 138 (2016) 1653.

[90] R.T. Yang, Gas Separation by Adsorption Processes, 1997.

[91] R. Kumar Mishra, B. Singh, B. Acharya, A comprehensive review on activated carbon from pyrolysis of lignocellulosic biomass: An application for energy and the environment, Carbon Resources Conversion 7 (2024) 100228. https://doi.org/https://doi.org/10.1016/j.crcon.2024.100228.

[92] S. Reljic, C. Cuadrado-Collados, J. Farrando-Perez, E.O. Jardim, M. Martinez-Escandell, J. Silvestre-Albero, Carbon-based monoliths with improved thermal and mechanical properties for methane storage, Fuel 324 (2022) 124753. https://doi.org/https://doi.org/10.1016/j.fuel.2022.124753.

[93] D.P. Vargas, L. Giraldo, J.C. Moreno-Piraján, CO2 Adsorption on Activated Carbon Honeycomb-Monoliths: A Comparison of Langmuir and Tóth Models, Int J Mol Sci 13 (2012) 8388–8397. https://doi.org/10.3390/ijms13078388.

[94] W. Spencer, G. Senanayake, M. Altarawneh, D. Ibana, A.N. Nikoloski, Review of the effects of coal properties and activation parameters on activated carbon production and quality, Miner Eng 212 (2024) 108712. https://doi.org/https://doi.org/10.1016/j.mineng.2024.108712.

[95] J. Serafin, B. Dziejarski, Activated carbons—preparation, characterization and their application in CO2 capture: A review, Environmental Science and Pollution Research 31 (2024) 40008–40062. https://doi.org/10.1007/s11356-023-28023-9.

[96] N. Kordala, M. Wyszkowski, Zeolite Properties, Methods of Synthesis, and Selected Applications, Molecules 29 (2024). https://doi.org/10.3390/molecules29051069.

[97] J. Li, M. Gao, W. Yan, J. Yu, Regulation of the Si/Al ratios and Al distributions of zeolites and their impact on properties, Chem. Sci. 14 (2023) 1935–1959. https://doi.org/10.1039/D2SC06010H.

[98] J.T. Crum, J.R. Crum, C. Taylor, W.F. Schneider, Characterization and analysis of ring topology of zeolite frameworks, Microporous and Mesoporous Materials 351 (2023) 112466. https://doi.org/https://doi.org/10.1016/j.micromeso.2023.112466.

[99] D.G. Boer, J. Langerak, P.P. Pescarmona, Zeolites as Selective Adsorbents for CO2 Separation, ACS Appl Energy Mater 6 (2023) 2634–2656. https://doi.org/10.1021/acsaem.2c03605.

[100] A. Sayari, Y. Belmabkhout, R. Serna-Guerrero, Flue gas treatment via CO2 adsorption, Chemical Engineering Journal 171 (2011) 760–774. https://doi.org/https://doi.org/10.1016/j.cej.2011.02.007.

[101] C. Belviso, F. Cavalcante, A. Lettino, S. Fiore, A and X-type zeolites synthesised from kaolinite at low temperature, Appl Clay Sci 80–81 (2013) 162–168. https://doi.org/https://doi.org/10.1016/j.clay.2013.02.003.

[102] M. Gougazeh, J.-Ch. Buhl, Synthesis and characterization of zeolite A by hydrothermal transformation of natural Jordanian kaolin, Journal of the Association of Arab Universities for Basic and Applied Sciences 15 (2014) 35–42. https://doi.org/https://doi.org/10.1016/j.jaubas.2013.03.007.

[103] D.K.J.A. Wanigarathna, J. Gao, B. Liu, Fluorocarbon Separation in a Thermally Robust Zirconium Carboxylate Metal–Organic Framework, Chem Asian J 13 (2018) 977–981. https://doi.org/10.1002/asia.201800337.

[104] D.K.J.A. Wanigarathna, B. Liu, J. Gao, Adsorption separation of R134a, R125, and R143a fluorocarbon mixtures using 13X and surface modified 5A zeolites, AIChE Journal 64 (2018) 640–648. https://doi.org/10.1002/aic.15955.

[105] K. Leus, I. Muylaert, V. Van Speybroeck, G.B. Marin, P. Van Der Voort, A coordinative saturated vanadium containing metal organic framework that shows a remarkable catalytic activity, in: E.M. Gaigneaux, M. Devillers, S. Hermans, P.A. Jacobs, J.A. Martens, P. Ruiz (Eds.), Scientific Bases for the Preparation of Heterogeneous Catalysts, Elsevier, 2010: pp. 329–332. https://doi.org/https://doi.org/10.1016/S0167-2991(10)75053-9.

[106] V.C. Anadebe, A. Thakur, C. Verma, B.B. Mamba, A. Alfantazi, E.E. Ebenso, R.C. Barik, Unveiling cutting-edge progress in coordination chemistry of the metal-organic frameworks (MOFs) and their composites: Fundamentals, synthesis strategies, electrochemical and environmental applications,

Journal of Industrial and Engineering Chemistry 148 (2025) 247–299. https://doi.org/https://doi.org/10.1016/j.jiec.2025.01.033.

[107] A. Subhadarshini, B. Nanda, Zeolitic imidazolium framework (ZIF-8) and their derivative-based material for antibacterial study: a comprehensive review, Discov Mater 5 (2025) 50. https://doi.org/10.1007/s43939-025-00229-3.

[108] B. Liu, J. Jiao, Y. Du, Y. Jiang, Z. Zhang, D. Cai, H. Shan, T. Jiao, From imperfection to innovation: Exploring defect engineering in metal-organic frameworks, J Colloid Interface Sci 700 (2025) 138433. https://doi.org/https://doi.org/10.1016/j.jcis.2025.138433.

[109] Q.-W. Zeng, L. Hu, Y. Niu, D. Wang, Y. Kang, H. Jia, W.-T. Dou, L. Xu, Metal–organic cages for gas adsorption and separation, Chem. Commun. 60 (2024) 3469–3483. https://doi.org/10.1039/D3CC05935A.

[110] M.-B. Kim, S.-J. Lee, C.Y. Lee, Y.-S. Bae, High SF6 selectivities and capacities in isostructural metal-organic frameworks with proper pore sizes and highly dense unsaturated metal sites, Microporous and Mesoporous Materials 190 (2014) 356–361. https://doi.org/https://doi.org/10.1016/j.micromeso.2014.02.028.

[111] I. Senkovska, E. Barea, J.A.R. Navarro, S. Kaskel, Adsorptive capturing and storing greenhouse gases such as sulfur hexafluoride and carbon tetrafluoride using metal–organic frameworks, Microporous and Mesoporous Materials 156 (2012) 115–120. https://doi.org/https://doi.org/10.1016/j.micromeso.2012.02.021.

[112] M.-B. Kim, T.-H. Kim, T.-U. Yoon, J.H. Kang, J.-H. Kim, Y.-S. Bae, Efficient SF6/N2 separation at high pressures using a zirconium-based mesoporous metal–organic framework, Journal of Industrial and Engineering Chemistry 84 (2020) 179–184. https://doi.org/https://doi.org/10.1016/j.jiec.2019.12.032.

[113] Y.-P. Li, X.-J. Zhang, J.-J. Ni, W.-J. Ji, S. Li, Y.-L. Li, W. Wen, J. Wang, Z.-Y. Sui, X.-F. Xu, Design of a highly-stable cobalt (II) porous framework based on aromatic stacking strategy for efficient SF6 capture and SF6/N2 mixture separation, Sep Purif Technol 343 (2024) 126995. https://doi.org/https://doi.org/10.1016/j.seppur.2024.126995.

[114] Y.-P. Li, J.-J. Ni, S. Li, J. Wang, Z.-Y. Sui, X.-F. Xu, Rational pore-window size control in three Cu-MOFs with different pore environments for efficient capture of the greenhouse gas SF6, J Solid State Chem 329 (2024) 124443. https://doi.org/https://doi.org/10.1016/j.jssc.2023.124443.

[115] X. Zhang, Y.-L. Zhao, X.-Y. Li, X. Bai, Q. Chen, J.-R. Li, Recovery of High-Purity SF6 from Humid SF6/N2 Mixture within a Co(II)-Pyrazolate Framework, J Am Chem Soc 146 (2024) 19303–19309. https://doi.org/10.1021/jacs.4c05075.

[116] S.-M. Li, Q. Zhang, H.-C. Jiang, Q.-L. Ni, L.-C. Gui, X.-J. Wang, T.-L. Hu, Constructing local nanomolecular trap in a scalable, low-cost, and ultramicroporous metal–organic framework for efficient capture of greenhouse gases SF6 and CO2, Chemical Engineering Journal 496 (2024) 154026. https://doi.org/https://doi.org/10.1016/j.cej.2024.154026.

[117] C.C. Obi, J.T. Nwabanne, P.K. Igbokwe, C.I. Idumah, V.U. Okpechi, H.C. Oyeoka, Novel advances in synthesis and catalytic applications of metal-organic frameworks - based nanocatalysts for CO2 capture and transformation, J Environ Chem Eng 12 (2024) 112835. https://doi.org/https://doi.org/10.1016/j.jece.2024.112835.

[118] H.H. Hegazy, S.S. Sana, T. Ramachandran, Y.A. Kumar, D.K. Kulurumotlakatla, H.S.M. Abd-Rabboh, S.C. Kim, Covalent organic frameworks in supercapacitors: Unraveling the pros and cons for energy storage, J Energy Storage 74 (2023) 109405. https://doi.org/https://doi.org/10.1016/j.est.2023.109405.

[119] Y. Song, S. Ma, Pore engineering in metal–organic frameworks and covalent organic frameworks: strategies and applications, Chem. Sci. 16 (2025) 11740–11767. https://doi.org/10.1039/D5SC01635E.

[120] H. Fan, A. Mundstock, A. Feldhoff, A. Knebel, J. Gu, H. Meng, J. Caro, Covalent Organic Framework–Covalent Organic Framework Bilayer Membranes for Highly Selective Gas Separation, J Am Chem Soc 140 (2018) 10094–10098. https://doi.org/10.1021/jacs.8b05136.

[121] T. Huang, W. Zhang, S. Yang, L. Wang, G. Yu, Imine-linked covalent organic frameworks: Recent advances in design, synthesis, and application, SmartMat 5 (2024) e1309. https://doi.org/https://doi.org/10.1002/smm2.1309.

[122] J. Lin, J. Ouyang, T. Liu, F. Li, H.H.-Y. Sung, I. Williams, Y. Quan, Metal-organic framework boosts heterogeneous electron donor–acceptor catalysis, Nat Commun 14 (2023) 7757. https://doi.org/10.1038/s41467-023-43577-5.

[123] R.A. Maia, F. Lopes Oliveira, V. Ritleng, Q. Wang, B. Louis, P. Mothé Esteves, CO2 Capture by Hydroxylated Azine-Based Covalent Organic Frameworks, Chemistry – A European Journal 27 (2021) 8048–8055. https://doi.org/https://doi.org/10.1002/chem.202100478.

[124] S.K.S. Freitas, F.L. Oliveira, C. Merlini, E.P.S. Justo, A. Gioda, P.M. Esteves, Dye-based covalent organic networks, Journal of Physics: Materials 3 (2020) 025011. https://doi.org/10.1088/2515-7639/ab854b.

[125] A. Carvalho, L.C. Branco, L.R.C. Corrêa, A.B. Paninho, P.M. Esteves, H. Cruz, S.K.S. Freitas, Impregnation of different lanthanides in a covalent organic framework (RIO-55) to a chemical determination of dopants substances, Heliyon 10 (2024) e36181. https://doi.org/https://doi.org/10.1016/j.heliyon.2024.e36181.

CHAPTER 2

F-GASES ABSORPTION WITH IONIC LIQUIDS AND DEEP EUTECTIC SOLVENTS: DESIGN AND PROCESS SIMULATION USING COSMO-RS

2.1 Introduction

Global temperature is rising every year, mostly due to the increasing concentrations of atmospheric greenhouse gases (GHG) [1]. Although carbon dioxide (CO_2) accounts for at least two-thirds of the global GHG emissions [2], fluorinated gases (F-gases), such as the families of hydrofluorocarbons and perfluorocarbons, as well as sulfur hexafluoride (SF_6), are also major contributors to global warming [3]. The emissions of these gases have increased 60% since 1990 [4] and HFCs emissions are projected to grow by nearly 140% between 2005 and 2020 [5]. In order to accomplish the EU commitments related to Kyoto's Protocol, the use of F-gases has been controlled since 2006. The different legislations aim to combat the effect of these compounds on global warming. A new EU regulation was applied on 1 January 2015 (no. 517/2014) with the aim to cut F-gas emissions by two-thirds compared to 2014 levels, until 2030 [5]. This represents a decisive contribution to the EU's objective of cutting its overall GHG emissions by 80–95%, compared to 1990 levels, by 2050 [5].

Although there are technologies under development aiming to avoid the increase in F-gas emissions, they may not be successful for specific applications [6–16]. In some cases, a partial recovery is achieved by adsorption on activated carbons [9–12], by cryo-condensation, or by membrane separation processes [13–15]. Therefore, there is a great interest in the development of innovative technologies based on circular economy that are able to recover F-gases at the end of the equipment's life cycle.

In the past decades, ILs emerged as an environmentally friendly alternative to conventional organic solvents [13,17]. These compounds present exceptional properties, such as nonvolatility, null flammability, low melting point, high ionic conductivity, thermal and electrochemical stability, and a remarkable recyclability [18]. Moreover, ILs can be fine-tuned through suitable anion–cation combinations and can be developed for specific applications, such as gas solubilization [18,19]. Fluorinated ionic liquids (FILs) are a specific IL family containing fluorinated alkyl chains with at least four carbon atoms. FILs can form three different nanosegregated domains (polar, nonpolar, and fluorinated) [20] with completely different behaviors and a unique ability to solubilize and interact with three totally different moieties at the same time. This nanosegregation increases the number of different conformations of these solvents, thereby facilitating interactions with different solutes and increasing their solubilization capacity and tunability [19,21].

The FILs enables us to combine some characteristics of highly fluorinated compounds and those of ionic liquids, such as exceptional low surface tension; chemical and biological inertness, vanishingly low vapor pressure, and greener potential [18]. However, FILs with long perfluorinated alkyl chains based on perfluorooctane sulfonate anions are the conjugate bases of perfluorooctane sulfonic acid (PFOS), which is a known persistent organic pollutant that is bioaccumulative and being phased out [22,23]. For this reason, perfluorobutane sulfonate has been commercialized as an alternative in a variety of applications. Perfluorooctane sulfonate presents a C8 perfluorinated chain with a terminal sulfonyl functional group imparting both oleophobic and hydrophobic properties. Conversely, perfluorobutane

sulfonate shares some of the oleophobic and hydrophobic properties but it is not considered to be bio-accumulative or toxic [22,24–26]. Then, FILs with short perfluorinated alkyl chains are demonstrated to be nontoxic [22,27] and are fully water-soluble [28]. These numerous intrinsic properties make FILs very attractive for several separation processes. The vast range of possible variations in the size of the fluorinated domain and the different types of interactions could allow the design of a suitable solvent for the separation of fluorinated GHG-containing mixtures. This information has propelled us to study the utilization of ILs with perfluorinated alkyl chains in the anion to increase the absorption of F-gases [29]. Moreover, the presence of fluorine atoms on the cation alkyl chains of FILs has been demonstrated to increase HFC solubility in molar terms [30]. These two works demonstrated that ILs that contain a fluorinated alkyl side chain with four carbon atoms (FILs) present a higher gas absorption capacity in molar terms compared to mere fluoro-containing ILs under the same conditions of temperature and pressure. However, to date, works involving HFCs' capture with FILs were focused on obtaining gas–liquid equilibria data at lab scale [29,30].

Although ILs are promising for technological applications such as gas separation, their drawbacks are high melting point, toxicity, low biodegradability, high viscosity, and high production cost have motivated the search for alternatives. Deep eutectic solvents (DESs) have emerged as a viable option due to their IL-like physicochemical properties. DESs are formed by a hydrogen-bond acceptor and donor, exhibit lower melting points than their individual components, are easy to prepare, and have been reported as effective solvents for CO_2 and SO_2 capture. [31]. Moreover, the absorption of F-gases in DESs has also been evaluated in the literature using computational tools [32].

In the last years, a successful multiscale research strategy was validated for the development of new gas separation processes based on ILs, integrating molecular modeling, experimental essays, and process simulation [33,34]. COSMO-RS calculations enable the selection of the most promising ILs [34–36]. A wide IL database (more than 600 cation/anion combinations) is used to perform a preliminary screening of favorable thermodynamic and kinetic properties for the solute–solvent mixtures [37], instead of time-consuming and costly experimental tests. Specifically, Henry's law constant (K_H) has been widely used as the main thermodynamic parameter for the IL absorbent selection [38,39], due to its main role in solvent consumption, energy duty, and operating and investment costs of industrial operation [40,41]. Moreover, COSMO-RS provides insights into gas absorption phenomena in ILs from a molecular perspective, showing that solubility is often governed by absorption enthalpy [34,42,43]. The COSMO-RS method provides the intermolecular interaction (electrostatic, hydrogen bond, and van der waals) contribution to the excess enthalpy of the solute + solvent mixture, allowing for the rational design of the IL structure to promote the chemical affinity between the components in absorption media [44–46]. In addition, this program allows the generation of ILs with different combinations of anions and cations, thus offering a wide range of possibilities for selecting the most promising candidates. Based on these predictions, selected ILs are tested experimentally by measuring gas–liquid equilibrium data under different temperature and pressure conditions [35,47,48]. From these experiments, key

parameters for the design of industrial absorption processes are obtained, such as absorption isotherms and diffusivities [49,50].

Subsequently, the performance of ILs at the process scale is analyzed by modeling absorption and desorption operations using the COSMO-based/Aspen methodology [33], which enables techno-economic analysis and comparison with existing technologies. This methodology has been widely applied to various gas capture processes using ILs, including acetylene [39], CO_2 [51], and H_2S [40], More recently, it has been applied to fluorinated gases, demonstrating that FILs/ILs based on sulfonate and carboxylate anions exhibit the best process performance for F-gas capture [52].

This chapter contributes to advancing the assessment of FILs and DES for F-gas capture using gravimetric and volumetric adsorption methods. Furthermore, the COSMO-RS-based tool was integrated into a multiscale research strategy to analyze the thermodynamic effects governing adsorption processes and to design new ILs with improved properties for F-gas absorption. Based on this computational approach, the behavior of FILs/ILs was examined in absorption columns under realistic process conditions. Finally, the relevance of evaluating gas capture applications at the process scale was underscored, particularly with respect to absorbent consumption and operational costs.

This chapter is adapted from the following publications:

Section 2.3

J.E. Sosa, R.P.P.L. Ribeiro, P.J. Castro, J.P.B. Mota, J.M.M. Araújo, A.B. Pereiro, *Absorption of Fluorinated Greenhouse Gases Using Fluorinated Ionic Liquids*, Ind. Eng. Chem. Res. 58 (2019) 20769–20778. https://doi.org/10.1021/acs.iecr.9b04648.

Section 2.4

P.J. Castro, A.E. Redondo, **J.E. Sosa**, M.E. Zakrzewska, A.V.M. Nunes, J.M.M. Araújo, A.B. Pereiro, *Absorption of Fluorinated Greenhouse Gases in Deep Eutectic Solvents*, Ind. Eng. Chem. Res. 59 (2020) 13246–13259. https://doi.org/10.1021/acs.iecr.0c01893.

Section 2.5

J.E. Sosa, R. Santiago, D. Hospital-Benito, M. Costa Gomes, J.M.M. Araújo, A.B. Pereiro, J. Palomar, *Process Evaluation of Fluorinated Ionic Liquids as F-Gas Absorbents*, Environ. Sci. Technol. 54 (2020) 12784–12794. https://doi.org/10.1021/acs.est.0c05305.

The author of this thesis contributed to this section by writing part of the original manuscript, specifically the sections related to the COSMO-RS validations of pure FILs and solvents reported in the literature, the determination of the L/G ratio with the separation column in Aspen Plus, and the recovery of their mixtures with HFCs. The author also collaborated in the preparation of the graphical contents of the section, such as figures.

Section 2.6

J.E. Sosa, R. Santiago, A.E. Redondo, J. Avila, L.F. Lepre, M.C. Gomes, J.M.M. Araújo, J. Palomar, A.B. Pereiro, *Design of Ionic Liquids for Fluorinated Gas Absorption: COSMO-RS Selection and Solubility Experiments*, Environ. Sci. Technol. 56 (2022) 5898–5909. https://doi.org/10.1021/acs.est.2c00051.

2.2 Non-Random Two-Liquid (NRTL) thermodynamic model

The NRTL thermodynamic model is a widely applied activity coefficient model for representing phase equilibria in liquid–liquid and vapor–liquid systems, particularly in highly non-ideal mixtures [29,53–55]. Its capacity to account for non-randomness in molecular interactions makes it especially suitable for complex solvents such as ILs, FILs, and DES. These solvents exhibit strong specific interactions, including hydrogen bonding and electrostatic forces, which the NRTL model can effectively correlate through adjustable interaction parameters. As a result, this model provides reliable predictions of phase equilibria, excess properties, and thermodynamic behaviors for mixtures containing ILs, FILs, and DES [56–60]. In the context of gas capture processes, integrating the NRTL model into process simulation tools allows the optimization of separation and absorption operations, aiding in the design of more efficient and sustainable industrial systems [56–60].

In this study, the general condition for thermodynamic equilibrium between a pure F-gas *i* in the vapor phase and its absorption in an IL, FILs, and DES is expressed as:

$$f_i = \gamma_i x_i f_i^{\mathrm{o}} \qquad 2.2.1$$

where f_i is the F-gas's vapor-phase fugacity, which is well approximated by the pressure p for the conditions of this study, x_i and γ_i are its mole fraction and activity coefficient in the IL phase, respectively, and f_i^{o} is its liquid-phase reference fugacity, which at the pressures under study is nearly the pure-component vapor pressure, p_i^*, at the same temperature as the mixture. In the NRTL model the activity coefficients for a binary mixture of F-gas (1) dissolved in an IL (2) phase are calculated as follows:

$$\ln\gamma_1 = x_2^2\left[\tau_{21}\left(\frac{G_{21}}{x_1+x_2G_{21}}\right)^2 + \frac{\tau_{12}G_{12}}{(x_2+x_1G_{12})^2}\right] \qquad 2.2.2$$

$$\ln\gamma_2 = x_1^2\left[\tau_{12}\left(\frac{G_{12}}{x_2+x_1G_{12}}\right)^2 + \frac{\tau_{21}G_{21}}{(x_1+x_2G_{21})^2}\right] \qquad 2.2.3$$

$$G_{ij} = e^{-\alpha\tau_{ij}} \text{ and } \tau_{ij} = \frac{g_{ij}-g_{jj}}{RT} \qquad 2.2.4$$

where g_{ij} is the energy parameter between molecular surfaces i and j, R is the gas constant, and T is the absolute temperature. The non-random parameter α was optimized and the dimensionless interaction parameters, τ_{12} and τ_{21}, were used to correlate the experimental data for each binary mixture by least-squares minimization of the root mean standard deviation (RMSD) between the predicted and measured pressure values, where the RMSD is given by the following equation:

$$RMSD = \left(\frac{1}{N}\sum_{i=1}^{N}(x_i^{exp}-x_i^{calc})^2\right)^{1/2} \qquad 2.2.5$$

where *N* is the number of experimental data points, x_i^{calc} is the calculated or fitted value, and x_i^{exp} is the experimental value.

2.3 Absorption of fluorinated greenhouse gases using fluorinated ionic liquids

The increasing awareness of the environmental impact of fluorinated gases (F-gases) used in refrigeration is instigating the development of technologies to recover and recycle them. With this goal in mind, single-component absorption equilibrium isotherms at 303.15 K of F-gases in different ionic liquids (ILs) were determined using a gravimetric method. The selected F-gases are the most used in domestic refrigeration (R-32: difluoromethane, R-125: pentafluoroethane, and R-134a: 1,1,1,2-tetrafluoroethane). The results show that ILs containing a fluorinated alkyl side chain with four carbon atoms, i.e., fluorinated ionic liquids (FILs), have higher gas absorption capacity than conventional fluoro-containing ILs. All studied ILs showed ideal selectivity towards R-134a. Conventional fluoro-containing ILs showed better selectivities for the separation of the binary mixtures R-134a/R-125 and R-32/R-125 and FILs showed better selectivities for the R-134a/R-32 mixture. These results provide fundamental knowledge of the behavior of these new alternative solvents and key information for their application in the separation of F-gases mixtures of commercial refrigerants.

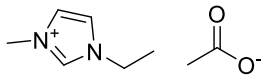
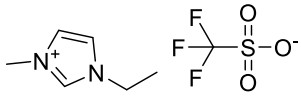
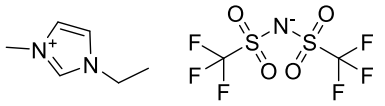
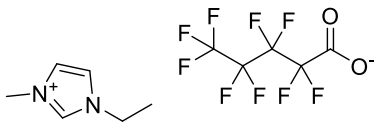
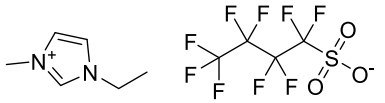
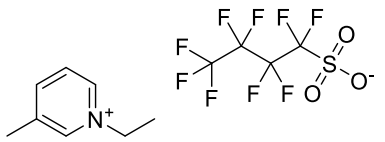
2.3.1 Experimental section

2.3.1.1 Materials

1-Ethyl-3-methylimidazolium acetate ($[C_2C_1Im][C_1CO_2]$, > 90 % mass fraction purity), 1-ethyl-3-methylimidazolium perfluoromethanesulfonate ($[C_2C_1Im][CF_3SO_3]$, > 99 % mass fraction purity), 1-ethyl-3-methylimidazolium bis(trifluoromethylsulfonyl)imide ($[C_2C_1Im][N(CF_3SO_2)_2]$, 99.5 % mass fraction purity), 1-ethyl-3-methylimidazolium perfluorobutanesulfonate ($[C_2C_1Im][C_4F_9SO_3]$, > 97 % mass fraction purity), and 1-ethyl-3-methylpyridinium perfluorobutanesulfonate ($[C_2C_1py][C_4F_9SO_3]$, >97% mass fraction purity) were supplied by IoLiTec GmbH. 1-Ethyl-3-methylimidazolium perfluoropentanoate ($[C_2C_1Im][C_4F_9CO_2]$, >99 % mass fraction purity) was previously synthesized, through an ion-exchange resin method, and characterized in our laboratory [61,62]. Detailed structure and nomenclature of FILs is shown in Table 2.3.1. Purity of all ionic liquids was checked by ^{1}H and ^{19}F NMR as well as by Elemental Analysis. To ensure the absence of water and volatiles all FILs were dried under vacuum (4 Pa) and vigorously stirred at 323.15 K for at least 48 hours, immediately prior to their use. After drying, water content was verified to be less than 100 ppm by volumetric Karl-Fischer titration technique (Metrohm Ion analysis, 831 KF Coulometer). Each sample was taken from the respective Schlenk flask with a syringe under nitrogen flow to avoid humidity and immediately placed in the measuring devices.

F-gases R32 (difluoromethane, ≥ 99.8 % mass fraction purity), R125 (pentafluoroethane, ≥ 99.8 % mass fraction purity), and R134a (1,1,1,2- tetrafluoroethane, ≥ 99.8 % mass fraction purity) (Table 2.3.2) were acquired from Polo Zero.

Table 2.3.1 Chemical structures and acronyms of the ionic liquids used in this work.

Ionic Liquid Designation	Chemical Structure
1-Ethyl-3-methylimidazolium acetate **$[C_2C_1Im][C_1CO_2]$**	
1-Ethyl-3-methylimidazolium triflate **$[C_2C_1Im][CF_3SO_3]$**	
1-Ethyl-3-methylimidazolium bis(trifluoromethylsulfonyl)imide **$[C_2C_1Im][N(CF_3SO_2)_2]$**	
1-Ethyl-3-methylimidazolium perfluoropentanoate **$[C_2C_1Im][C_4F_9CO_2]$**	
1-Ethyl-3-methylimidazolium perfluorobutanesulfonate **$[C_2C_1Im][C_4F_9SO_3]$**	
1-Ethyl-3-methylpyridinium perfluorobutanesulfonate **$[C_2C_1py][C_4F_9SO_3]$**	

2.3.1.2 Methods and procedures

Single-component absorption equilibrium isotherms for the aforementioned R-32, R-125, and R-134a gases in FILs were determined at 303.15 K and pressures ranging from 0.02 to 0.5 MPa. Data were acquired using a standard gravimetric method, which consists in the stepwise supply of the pure fluorinated gas to the measurement cell containing the pure IL sample (approximately 0.3 g). To ensure the absence of water and volatile substances' contents all FILs were dried in-situ under vacuum at 323.15 K for at least 12 hours, immediately prior to their use. The whole system was kept isothermal at 303.15 K throughout the stepwise equilibrium steps generated along the absorption/desorption cycles. Mass and pressure variations were monitored until equilibrium was achieved in the cell.

Figure 2.3.1 shows a schematic diagram of the equipment used for these experiments [63–65]. It consists in a high-accuracy ISOSORP 2000 high-pressure magnetic-suspension balance (Rubotherm GmbH, Germany) with a 10^{-5} g resolution, uncertainty ≤ 0.002 % and reproducibility ≤ $3 \cdot 10^{-5}$ g for a maximum load of 25 g. Isothermal conditions are ensured by using a thermostatic bath F32 HL (± 0.1 K) from Julabo GmbH (Germany). Pressure is measured with a couple of pressure transducers that guarantee good measurement accuracy over all pressure ranges of operation: firstly, one Baratron model 627D (MKS Instruments GmbH, Germany) for 0–0.1 MPa, accuracy of 0.12 % of the reading; and secondly an Omegadyne Inc. (Sunbury, OH, USA) model PX01C1-150A5T for 0–1 MPa (accuracy of 0.05 % of Full Scale, FS). Further details about the experimental apparatus can be found elsewhere [63–65].

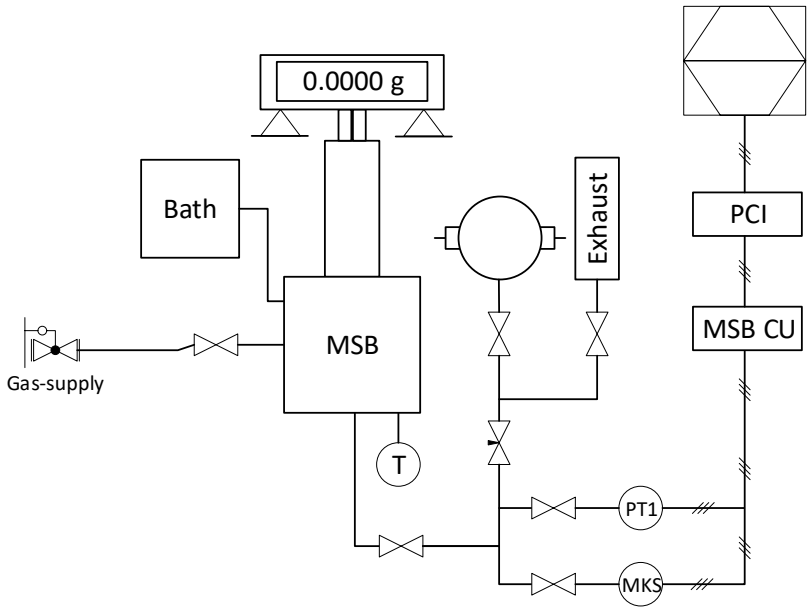


Figure 2.3.1 Schematic diagram of the experimental set up (MSB: magnetic suspension microbalance where PCI is the PC interface for data acquisition, T is the Pt100 temperature sensor, PT represents the Omegadyne pressure transducer and MKS is the MKS Baratron pressure transducer).

The apparent mass of sorbed gas, w, i.e., the recorded weight at a given applied gas pressure p minus the initial recorded weight at 0 bar, measured by the balance under isothermal conditions, is related to the absolute gas solubility, n (mass of dissolved gas per unit mass of sorbent), as follows:

$$w = m_s n - [V_c + m_s \tilde{v}_s(T, p, x)]\rho_g \quad 2.3.1$$

where m_s is the mass or sorbent sample (i.e., pure IL), V_c is the skeletal volume of the holding basket ($V_c = m_c \rho_c$, where m_c and ρ_c are the mass and density of the material of which the basket is made of), $\rho_g(T, p)$ is the density of the gas at pressure p and temperature T, and $\tilde{v}_s(T, p, x)$ is the specific volume of the IL/gas system on a solute-free basis (mixture volume per unit mass of IL) at the p, T conditions of the experiment and mass fraction of dissolved gas $y = n/(1 + n)$.

However, the quantity that is directly extracted from a gravimetric or volumetric experiment is the net gas solubility, n^{net}, defined as:

$$w = m_s n^{net} - V_c \rho_g \quad 2.3.2$$

whose calculation does not require any information about the IL/gas system besides the initial mass of the sample; n^{net} is a particularly important volume-basis metric for gas storage but much less so for gas separation.

A more useful and well-defined thermodynamic quantity, whose calculation does not depend upon any knowledge or assumption about how the dissolved gas changes the volume of the IL/gas system, is the excess gas solubility, n^{ex}, defined as:

$$n^{ex} = n^{net} + \tilde{v}_s(T, p, 0)\rho_g \quad 2.3.3$$

where $\tilde{v}_s(T, p, 0)$ is the specific volume of the pure IL ($y = 0$) at system temperature and imposed gas pressure p.

Invariably, $\tilde{v}_s(T, p, y)$ must be known or estimated in order to calculate the absolute gas solubility whether directly from eq. (1), or from n^{ex} via:

$$n = n^{ex} + [\tilde{v}_s(T, p, y) - \tilde{v}_s(T, p, 0)] = n^{ex} + \Delta\tilde{v}_s(T, p, y)\rho_g \quad 2.3.4$$

where $\Delta\tilde{v}_s(T, p, y)$ is the specific volume change due to the dissolved gas. If the IL/gas mixture is an ideal fluid mixture, which is assumed to hold in the present work,

$$\Delta\tilde{v}_s(T, p, y) = v_g^l(T)n = v_g^l(T)\frac{1}{1 - y} \quad 2.3.5$$

where $v_g^l(T)$ is the specific volume of the liquified gas under saturation conditions at the system temperature T.

Gas solubility is commonly reported in terms of molar fraction of dissolved gas, x, and the conversion from n to x is straightforward:

$$x = \frac{n/M_g}{1/M_{IL} + n/M_g} \quad (2.3.6)$$

where M_g and M_{IL} are the molecular weights of the gas and IL, respectively.

2.3.2 Results and discussion

2.3.2.1 Gas solubility in fluorinated ionic liquids

This experimental procedure was validated using the pure IL $[C_2C_1Im][N(CF_3SO_2)_2]$ for CO_2 absorption. The results obtained were compared with published data [66] and are plotted in Figure 2.3.2.

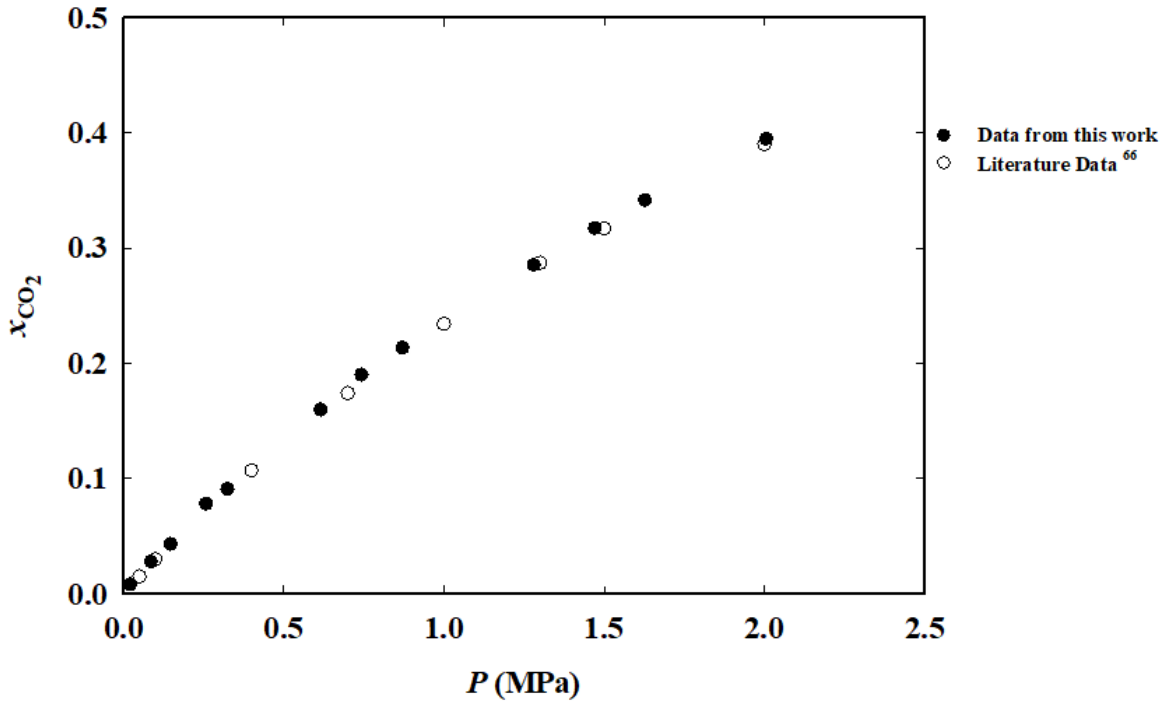


Figure 2.3.2 Comparison of data of CO_2 absorption in $[C_2C_1Im][N(CF_3SO_2)_2]$ obtained in this work and obtained by other authors [66].

The ionic liquids studied in this work have improved capacity of solubilization of F-gases in relation to most conventional organic absorbents [67–70]. In Figure 2.3.3, the moles of adsorbed F-gas per unit of absorbent mass (ILs or conventional organic solvents) determined is illustrated at 303.15 K and equilibrium pressures (0.1 MPa for R-32 and 0.3 MPa for R-134a). In the case of R-32, all studied ILs show better solubilization performance relatively to organic solvents and for R-134a only two solvents, monoethylene glycol dimethyl ether and tetraethylene glycol dimethyl ether [67,69], showed better performance than ILs. No data were found in the literature regarding to the R-125 absorption in organic solvents.

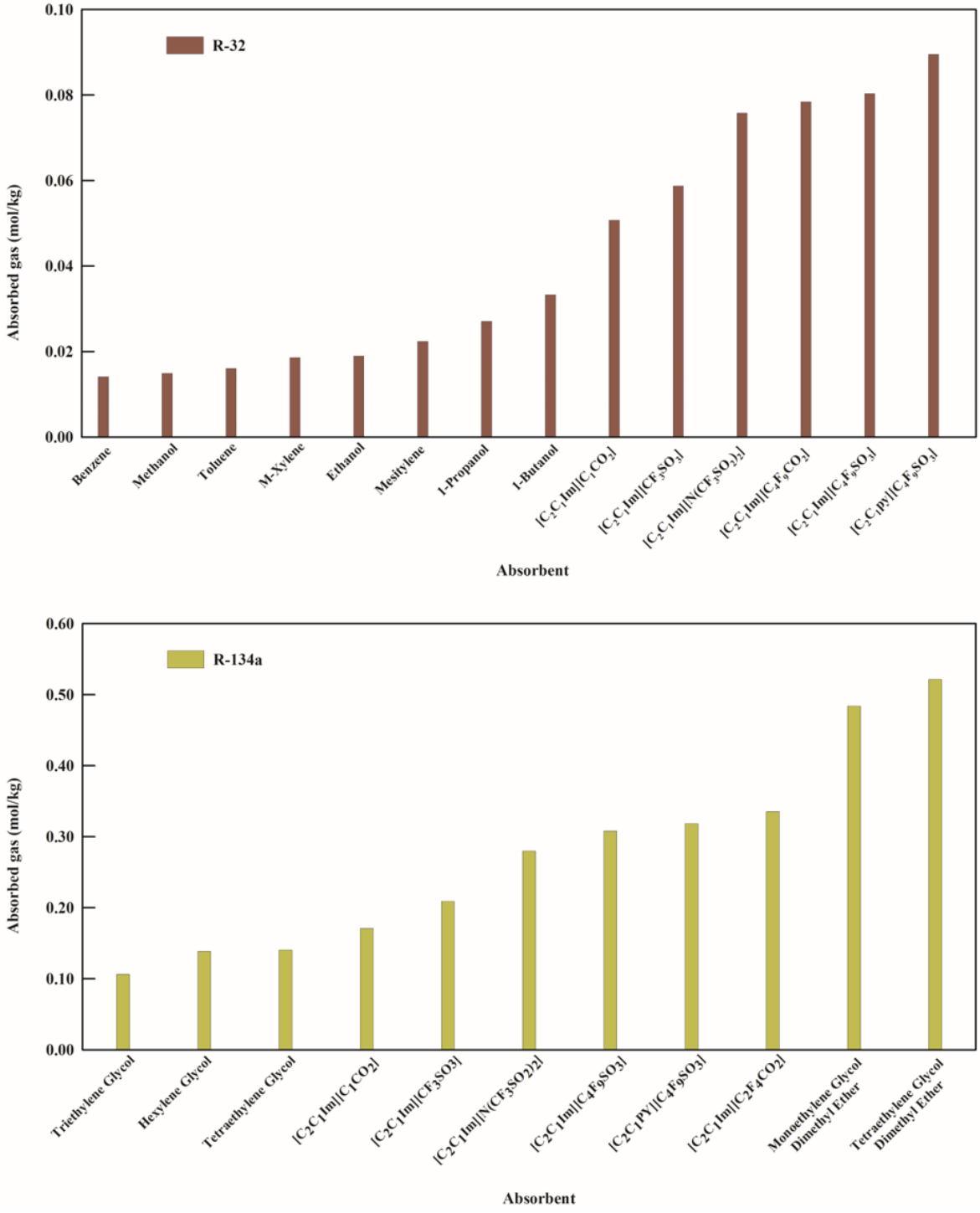


Figure 2.3.3 Comparison of the absorption of R-32 and R-134a in the ILs studied in this work and in conventional organic solvents [67–70]. Absorption was determined at 303.15 K and equilibrium pressures of 0.1 MPa (for R-32) or 0.3 MPa (for R-134a).

The experimental solubility data, expressed as mole fraction of dissolved gas (x_i), of each F-gas, i ,in the six ILs are presented in Figure 2.3.4 as a function of the applied equilibrium gas pressure (0.02 to 0.5 MPa) at 303.15 K (see also Table 2.3.3). The absorption equilibrium isotherms were studied up to 0.5 MPa in order to not exceed the lowest saturation pressure of the F-gases studied in this work (0.77 MPa for R-134a, 1.57 MPa for R-125 and 1.92 MPa for R-32). The absorption and desorption isotherms shown in Figure 2.3.4 are superimposable, indicating the inexistence of hysteresis between the absorption and desorption branches.

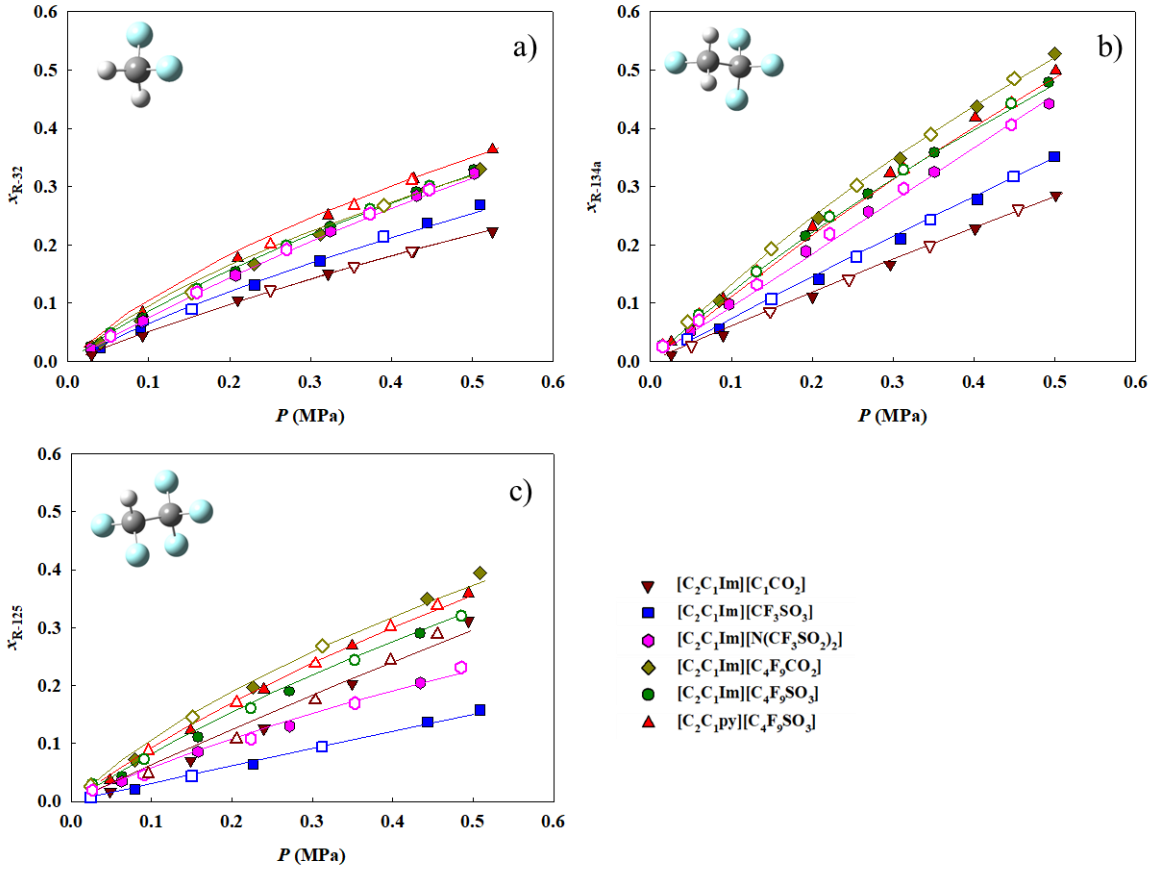


Figure 2.3.4 Absorption (full symbols) and desorption (empty symbols) isotherms of : a) R-32, b) R-134a, and c) R-125, refrigerants in different ILs, determined at 303.15 K and equilibrium pressures ranging from 0.02 to 0.5 MPa. Solid lines are the NRTL model calculations.

One of the most remarkable characteristics of ILs is their high tuneability. Therefore, absorption capacity and selectivity for a specific gas can be improved by combining different cations and anions. We studied six different ILs based on two cations ($[C_2C_1Im]^+$ and $[C_2C_1py]^+$) and on five anions ($[C_1CO_2]^-$, $[CF_3SO_3]^-$, $[N(CF_3SO_2)_2]^-$, $[C_4F_9SO_3]^-$ and $[C_4F_9CO_2]^-$). In this way, it is possible to study how gas solubility is affected by: (i) cation nature (presence of either an imidazolium- or pyridinium-based cation); (ii) presence of fluorine atoms or alkyl fluorinated chains in the anion; and (iii) anion nature (presence of either a sulfonate or a carboxylate group in the alkyl fluorinated chain of the anion).

Gas absorption in ILs can be intrinsically related to the physicochemical and transport properties of the ILs studied in this work, which are summarized in Table 2.3.2 [18,61,71,72].

Table 2.3.2 Values of dynamic viscosity (η), density (ρ), refractive index (n_D), molar volume (V_m), and molar refraction (R_m) of ionic liquids at 303.15 K.

Ionic Liquid	η (mPa·s)	ρ (g·cm^{-3})	n_D	V_m (cm^3·mol^{-1})	R_m (cm^3·mol^{-1})
[C_2C_1Im][C_1CO_2] [72]	105.3	1.0962	1.4950	155.27	45.62
[C_2C_1Im][CF_3SO_3] [61]	35.72	1.3805	1.4315	189.06	48.85
[C_2C_1Im][$N(CF_3SO_2)_2$] [71]	27.10	1.5134	1.4216	258.56	65.65
[C_2C_1Im][$C_4F_9CO_2$] [61]	83.32	1.4815	1.4405	252.56	60.68
[C_2C_1Im][$C_4F_9SO_3$] [61]	124.7	1.5412	1.3969	266.16	64.09
[C_2C_1py][$C_4F_9SO_3$] [18]	150.3	1.5098	1.4185	279.01	70.39

Figure 2.3.4 shows that R-134a is the most soluble gas in all studied ILs, except in [C_2C_1Im][C_1CO_2] which has better absorption capacity for R-125. The absorption of the three gases (specially of R-125 and R-134a, which contain a higher number of fluorine atoms) is enhanced in FILs with respect to conventional ILs. These results highlight the key role of the fluorinated alkyl side chain (fluorinated nanosegregated domain) in the solubility of fluorinated gases. The gas solubility in the studied ILs is related to three types of phenomena: (i) a physical one, resulting from intermolecular interactions between solute and solvent (such as hydrogen bonding or electrostatic interactions, among others) which determine the enthalpic contribution to the physical absorption; (ii) a entropic one, that can also contribute to the gas solubility, and the free volume of the IL, that can create cavities where the gas molecules can accommodate; and (iii) a chemical one, meanly controlling the enthalpic contribution due to the formation of new intramolecular bonds between the F-gases and the IL.

The study of the cation nature for FILs containing the $[C_4F_9SO_3]^-$ anion showed that the substitution of an imidazolium-based cation by a pyridinium-based cation does not change the gas absorption significatively (see Figure 2.3.4). Moreover, the study of the influence of the anion functional group shows that the solubility of the R-32 and R-134a is not affected by the substitution of a sulfonate group to a carboxylate group for imidazolium-based FILs. However, the presence of a carboxylate group slightly enhances the solubility of R-125 (see Figure 2.3.4). These results suggest a relevant role of the carboxylate group in the solubility of R-125 where a chemical solubility process may be significative. This fact may also explain the good solubility of this gas in [C_2C_1Im][C_1CO_2].

Figure 2.3.5 compares the sorption isotherms determined in this work for [C_2C_1Im][$C_4F_9SO_3$] and [C_2C_1Im][$N(CF_3SO_2)_2$] with those obtained with a conventional fluoro-containing IL, [C_6C_1Im][$N(CF_3SO_2)_2$] [73,74]. Taking these results into account, it is concluded that two main factors increase gas solubility at higher pressures in imidazolium-based ILs: the presence of a fluorinated

domain (at least up to a four-carbon fluorinated alkyl chain) for R-134a and R-125; and the increment of the hydrogenated chain in the cation (at least up to a six-carbon chain) for F-gases. However, it has been widely reported in the literature that an increase in the hydrogenated or fluorinated alkyl chains is associated with increased toxicity [75]. On the other hand, we have already demonstrated[18] that FILs with up to four carbon atoms in the alkyl fluorinated chain have negligible toxicity. In this way, the presence of a fluorinated alkyl chain represents a less toxic approach to increase the solubility of fluorinated gases, specially R-134a and R-125. It is important to refer that our solubility data was obtained at 303.15 K, the same temperature at which the solubility of R-32 and R-125 in $[C_6C_1Im][N(CF_3SO_2)_2]$ was reported [74]. However, the solubility data for R-134a in $[C_6C_1Im][N(CF_3SO_2)_2]$ was obtained at 298.15 K [73].

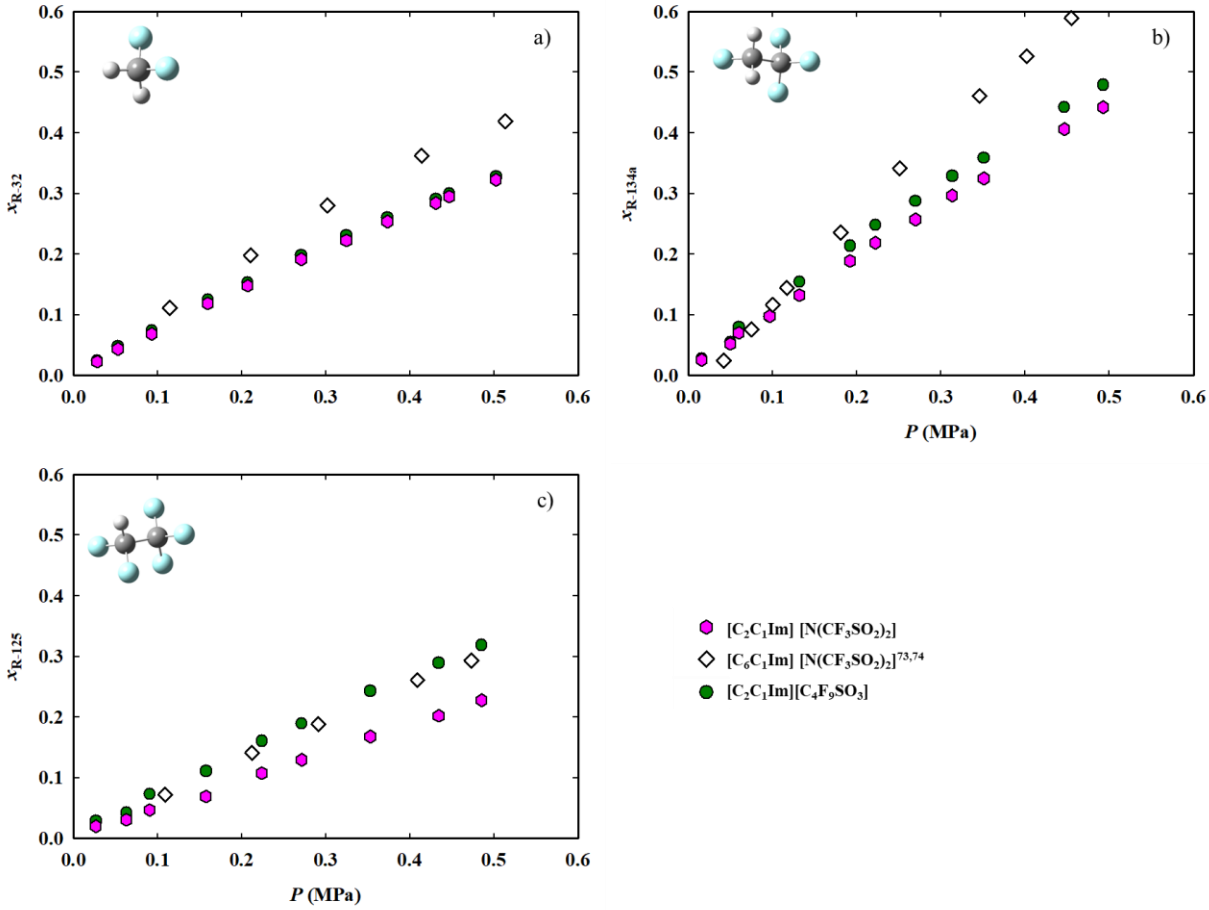


Figure 2.3.5 Sorption isotherms of : a) R-32, b) R-134a and c) R-125 refrigerants in ILs studied in this work and by other authors [73,74] with different number of fluorine atoms in the anion and with different lengths of the hydrogenated chain in the cation. Isotherms were determined at 303.15 K (except for R-134a in $[C_6C_1Im][N(CF_3SO_2)_2]$, which was determined at 298.15 K) and equilibrium pressures ranging from 0.02 to 0.5 MPa.

This paper also provides a critical review of the solubility data of the F-gases studied in this work in other ILs reported in the literature [56,59,73,74,76–78]. The nomenclature and abbreviations of the ILs reported in the literature are shown in Table 2.3.4. Figure 2.3.6. compares the experimental data determined in this work with those reported in the literature (see also Table 2.3.4) in terms of the Henry's constant, H, which for component i is defined as:

$$H_i(T,p) = \lim_{x_i \to 0} f_i^{\mathrm{L}}/x_i \qquad 2.3.7$$

where f_i^{L} is the fugacity of the gas dissolved in the ionic liquid. Considering that under thermodynamic equilibrium the fugacity of the F-gas in the IL phase is equal to its fugacity in the gas phase, the fugacity is taken as the gas pressure and the Henry's law equation rewritten as:

$$p_i = H_i(T)x_i \qquad 2.3.8$$

where p_i is the partial pressure of the F-gas. Strictly speaking, Henry's law relates the partial pressure of the F-gas to its solubility in IL phase under infinitely dilute conditions. The reported Henry's constants for the ILs studied in this work are the values extrapolated to zero pressure of second-order polynomial fittings of the experimental (p, x) data. It is helpful to remember that a smaller value of the Henry's constant is related to a higher F-gas solubility.

Of the three F-gases studied in this work, R-32 is the most studied in the literature using ILs as solvents. The best solubility for this F-gas is obtained with $[P_{66614}][PO_2(C_8)_2]$ IL, which has long hydrogenated alkyl chains. These chains can create cavities (higher free volume) where this F-gas can be accommodated. Conventional fluoro-containing imidazolium-based ILs with longer hydrogenated alkyl chains in the cation also present small Henry's constants for R-32, supporting the claim that the solubility of this gas is largely governed by entropic effects. In these imidazolium-based ILs, absorption is also improved with the increment of the number of carbon and fluorine atoms in the anion that also increases the molar volume and the free volume of these ILs (see Table 2.3.2). These results indicate that R-32 absorption is controlled by an entropic contribution where the free volume is of vital importance.

The ILs with the lowest Henry's constants for R-134a are the literature-reported $[C_2C_1Im][N(C_2F_5SO_2)_2]$, $[C_4C_1Im][C_2F_5OC_2HF_3SO_3]$ and $[C_6C_1Im][N(CF_3SO_2)_2]$ [73,76]. These Henry's constants are of the same order of magnitude as those for the three FILs studied in this work. A decrease in the Henry's constant is observed when the $[CF_3SO_3]^-$ anion is substituted to $[N(CF_3SO_2)_2]^-$ or to $[N(C_2F_5SO_2)_2]^-$ in $[C_2C_1Im]$-based ILs and when the $[C_2C_1Im]^+$ cation is substituted to $[C_6C_1Im]^+$ in $[N(CF_3SO_2)_2]$-based ILs. These two cases are related to an increment in the free volume of the IL and to an increase in the number of potential C-F- - - H-C or C-F- - - F-C bonds between the IL and the F-gas. Moreover, we observed that the utilization of FILs, such as $[C_2C_1Im][C_4F_9SO_3]$ and $[C_2C_1Im][C_4F_9CO_2]$, improves gas sorption with respect to the corresponding fluoro-containing ILs ($[C_2C_1Im][CF_3SO_3]$ and $[C_2C_1Im][C_1CO_2]$). This suggests that the absorption of R-134a is improved in ILs with higher free volumes and with the presence of the fluorinated

nanosegregated domains. These nanosegregated domains contribute to an absorption controlled by physical effects, i.e. higher molar volume (see Table 2.3.2) and interactions F - - - F and H - - - F [79,80].

Solubility of R-125 in fluoro-containing ILs and FILs is lower than the one of R-134a. These two gases are very similar but in the case of R-125 one hydrogen atom is substituted by one fluorine atom. The decrease in the solubility of R-125 may be associated with the loss of one C-H (F-gas) - - - F-C (IL) interaction, or to a reduced flexibility of the gas molecule, which hampers its physical absorption. The lowest Henry's constants of R-125 were obtained for FILs and the highest values were obtained for fluoro-containing ILs. Therefore, in this case the utilization of FILs, which form three nanosegregated domains, improves gas.

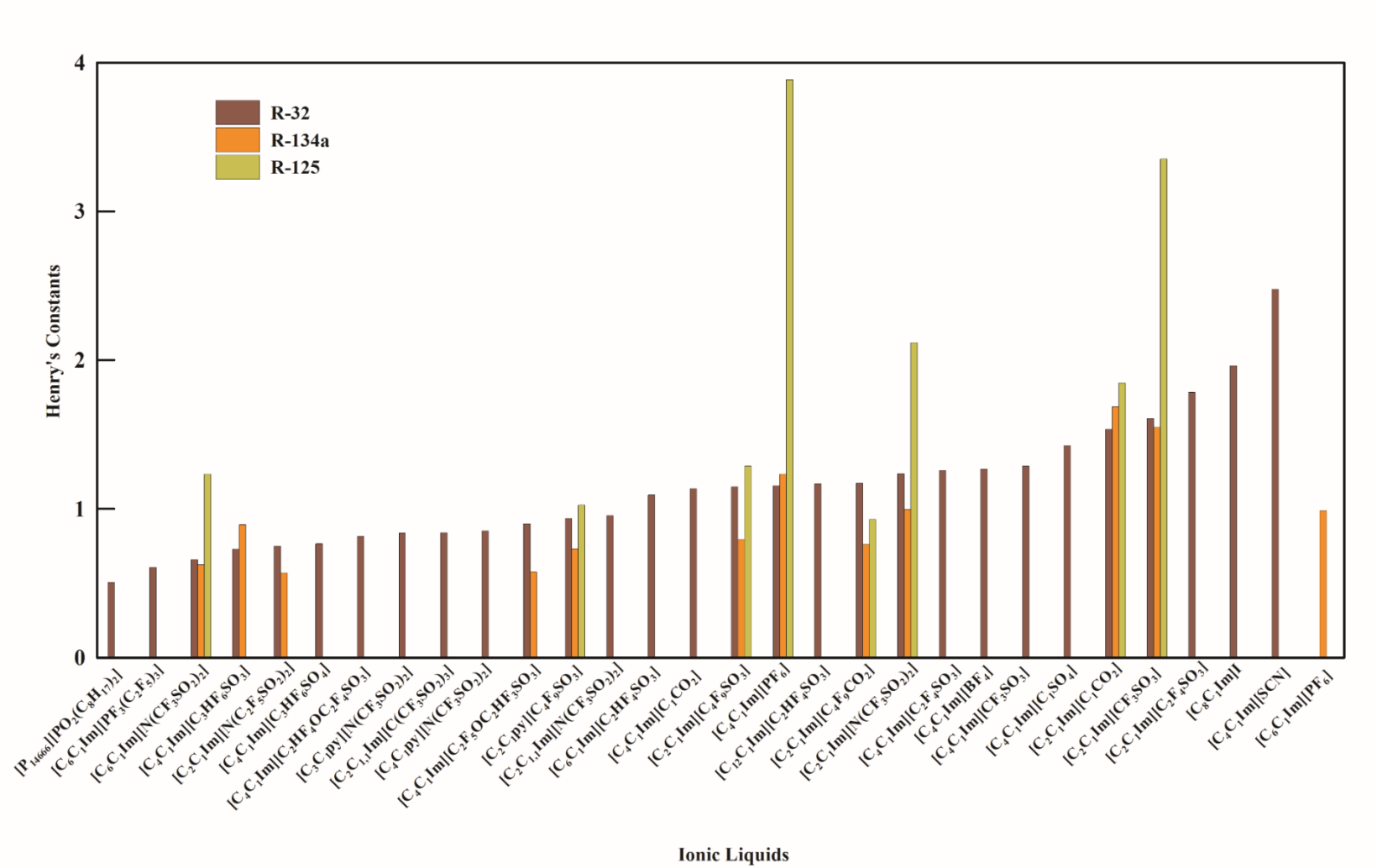


Figure 2.3.6 Henrry's law constants (in MPa) determined for the absorption of R-32, R-125, and R-134a in the ILs studied in this work and in others reported in the literature [56,57,59,73,74,76–78], at 298.15 K or 303.15K .

2.3.2.2 Correlation using NRTL model

The correct design of a separation process requires careful control and accurate knowledge of the thermodynamic properties and the phase behavior of the F-gases mixtures. The experimental data of this work were fitted by the NRTL (Non-Random Two-Liquid) model, which has been able to correlate satisfactorily the activity coefficients of different solutes in ILs [57–60]. For further details on the calculation procedure, see Section 2.2.

The values of the non-randomness parameter α are listed in Table 2.3.3 together with the values of the NRTL binary parameters. The RMSD values given in Table 2.3.3 are lower than 0.03 for the binary F-gas+IL systems studied in this work. The solid lines in Figure 2.3.4 represent the mole fraction of F-gas for each F-gas+IL system calculated by the NRTL equation as a function of the applied F-gas pressure. The good agreement between experimental and calculated data shows that the NRTL model describes well the phase behavior of the studied mixtures.

Table 2.3.3 Determined parameters for the NRTL obtained from the binary system fluorinated gas (1) + ionic liquid (2).

System (1) + (2)	Δg_{ij} / J mol^{-1}	Δg_{ji} / J mol^{-1}	α	RMSD
R-32 + [C_2C_1Im][C_1CO_2]	-617.50	3788.6	0.30	0.0049
R-32 + [C_2C_1Im][CF_3SO_3]	742.15	3993.9	0.30	0.0147
R-32 + [C_2C_1Im][$N(CF_3SO_2)_2$]	-325.63	1078.1	0.30	0.0088
R-32 + [C_2C_1Im][$C_4F_9CO_2$]	-1050.3	3914.7	0.29	0.0186
R-32 + [C_2C_1Im][$C_4F_9SO_3$]	4181.6	-1023.6	0.28	0.0102
R-32 + [C_2C_1py][$C_4F_9SO_3$]	-1023.6	4181.6	0.28	0.0144
R-125 + [C_2C_1Im][C_1CO_2]	1456.3	-1178.3	0.15	0.0271
R-125 + [C_2C_1Im][CF_3SO_3]	-423.63	2497.9	0.30	0.0134
R-125 +[C_2C_1Im][$N(CF_3SO_2)_2$]	-978.36	4760.6	0.22	0.0279
R-125 + [C_2C_1Im][$C_4F_9CO_2$]	-2365.3	3000.7	0.10	0.0231
R-125 + [C_2C_1Im][$C_4F_9SO_3$]	-2115.2	2556.2	0.10	0.0117
R-125 + [C_2C_1py][$C_4F_9SO_3$]	-1523.6	1894.1	0.17	0.0110
R-134a + [C_2C_1Im][C_1CO_2]	-415.89	4738.9	0.22	0.0089
R-134a + [C_2C_1Im][CF_3SO_3]	-125.36	9758.4	0.19	0.0094
R-134a + [C_2C_1Im][$N(CF_3SO_2)_2$]	-1245.3	2748.8	0.15	0.0177
R-134a + [C_2C_1Im][$C_4F_9CO_2$]	-295.36	2160.4	0.13	0.0064
R-134a + [C_2C_1Im][$C_4F_9SO_3$]	-350.23	6738.8	0.27	0.0094
R-134a + [C_2C_1py][$C_4F_9SO_3$]	-2150.6	4017.1	0.10	0.0163

2.3.2.4 Ideal selectivities

Different F-gases mixtures are used industrially and the selective separation of different pure F-gases from these gas mixtures is valuable. R-134a + R-32 and R-134a + R-125 mixtures have not azeotrope and thus these mixtures can be separated through distillation. However, the most important constraint is related to the energy costs required in this separation process. The separation of R-32+R-125 mixture is not possible using distillation due to the existence of an azeotrope. Then, we investigated the separation of these F-gases mixtures through the selective absorption of pure F-gas in ILs. The ability of a pure IL to selectively absorb a gas from a mixture of gases is the most important characteristic in order to evaluate if a material or solvent is suitable for a specific gas separation process. We have determined the ideal selectivity for the binary mixtures of F-gases studied in this work in each pure IL over the full pressure range spanned experimentally. The ideal selectivity for a binary pair of gases i and j at a given pressure P and temperature T is expressed as the ratio of pure-gas solubilities in the IL:

$$S_{ij}=\left(\frac{x_i}{x_j}\right)_{P,T} \qquad 2.3.9$$

where x_i and x_j are the mole fraction of the dissolved gases i and j, respectively, in the IL in equilibrium with its pure-vapor phase at pressure P and temperature T.

The selectivities of the ILs studied in this work have been compared with those of ILs available in the literature in Figure 2.3.7 [57,59,73,74,76]**.** The highest selectivities were obtained for the separation of R-134a + R-125 and R-32 + R-125, using the literature-reported IL $[C_2C_1Im][PF_6]$. However, it has been shown that PF_6 based ILs decompose in aqueous media, at high temperatures or low pH, originating corrosive fluoride compounds, such as HF [81]. This may restrict the utilization of $[C_2C_1Im][PF_6]$ in separation processes, unless efficient processes, in which all water is removed from the system and where high temperatures are not used, are applied. Thus, the utilization of other ILs that do not present those problems may be a good alternative to avoid pre-treatment processes.

The two fluoro-containing ILs studied in this work, ($[C_2C_1Im][CF_3SO_3]$ and $[C_2C_1Im][N(CF_3SO_2)_2]$), also present high selectivities for the separation of R-134a + R-125 and R-32 + R-125. In general, all FILs and conventional fluoro-containing ILs are selective for the separation of R-125 of the mixtures with R-134a and with R-32. However, the non-fluorinated IL, $[C_2C_1Im][C_1CO_2]$, shows low selectivity for the separations of these refrigerants. The lowest selectivities were obtained for the separation of R-134a + R-32, where FILs and two literature-reported ILs ($[C_4C_1Im][C_2F_5OC_2HF_3SO_3]$ and $[C_2C_1Im]$ $[N(C_2F_5SO_2)_2]$) present the best results. Thus, the increase in the number of fluorine atoms seems to favor the selectivity of ILs for the separation of R-134a + R-32 (the two refrigerants with the most different sizes). The opposite behavior is observed for the separation of R-134a + R-125, which have similar sizes, where fluoro-containing ILs yield the best results. On the other hand, the mixture R-32 + R-125 obtained the highest ideal selectivities with literature-reported IL $[C_4C_1Im][PF_6]$ and for the two fluoro-containing ILs ($[C_2C_1Im][CF_3SO_3]$ and

$[C_2C_1Im][N(CF_3SO_2)_2]$). For this separation, $[C_2C_1Im][C_4F_9SO_3]$ and $[C_2C_1py][C_4F_9SO_3]$ presented selectivities close to 1 and $[C_2C_1Im][C_4F_9CO_2]$ was more selective towards R-125 over R-32.

The ideal selectivity can also be defined as the ratio of the Henry's law constants of the gases at a specific temperature:

$$S_{ij}=\left(\frac{H_i}{H_j}\right)_T \qquad 2.3.10$$

where H_i and H_j are the Henry's law constants for the gases i and j, respectively. The results obtained with this equation, as expected, are similar to those obtained with Equation (2.3.8), with the same trends.

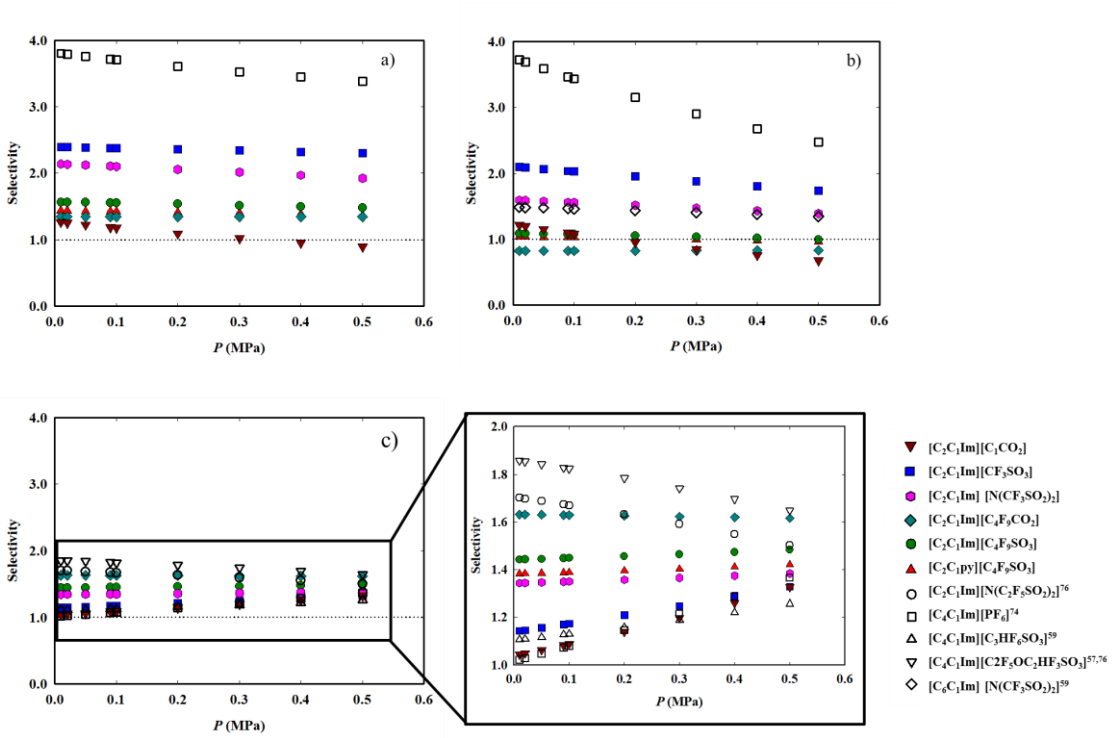


Figure 2.3.7 Ideal selectivities of ILs studied in this work and ILs available in the literature [57,59,74,76] for the separation of the refrigerants mixtures: a) R-134a + R-125, b) R-32 + R-125 and c) R-134a + R-32 (where an ampliation of the selectivities range of 1 - 2 was incorporated for a better visualization) at 303.15 K and equilibrium pressures ranging from 0.01 to 0.5 MPa.

2.3.3 Conclusions

In the present work we studied the absorption of the three most used F-gases, R-32, R-125, and R-134, in various ILs with different cations and anions. The NRTL model was used to correlate the experimental data because the use of thermodynamic models allows the implementation of simulation studies for the design of extraction processes. The experimental results show that the absorption of these gases is considerably increased in ILs with alkyl fluorinated chains up to four carbons (FILs). Therefore, FILs may be an alternative to conventional ILs with longer hydrogenated chains, which are more toxic. The results obtained with the different ILs used in this work were compared with the ones available in the literature in order to evaluate the F-gas solubility capacity. This comparison was carried out using

Henry's constants. The results demonstrated that the solubility of F-gases in ILs directly depends on the structure and the size of each F-gas.

Since those F-gases are utilized not only as pure gases, but also in gas mixtures, the utilization of ILs with selectivity towards specific F-gas is valuable. Ideal selectivity for the binary mixtures R-134a + R-125 and R-32 + R-125 was improved using fluoro-containing ILs, lacking an alkyl fluorinated chain. However, the selectivity for the mixture R-134a + R-32 was improved by utilizing FILs. This work delivers both fundamental understanding of the behavior of these new alternative solvents and the skills to manipulate their performance towards the design of separation processes of F-gases mixtures, such as R-410A (mixture of R-32 and R-125) and R-407F or R-407C (mixture of R32, R125 and R-134a).

2.4 Absorption of fluorinated greenhouse gases in deep eutectic solvents

The environmental impact resulting from the release of fluorinated gases (F-gases), commonly used in refrigeration, is prompting the development of technologies to recover and recycle them. Fluorinated Ionic Liquids (FILs) have been investigated as promising candidates for the absorption and selective separation of F-gases. In this work, we prepared Deep Eutectic Solvents (DES) composed of FILs and perfluorinated acids, which allowed to explore the excellent gas solubilization properties of FILs with high melting points in a wider liquidous range. A screening of DES prepared from 5 different FILs was performed for the solubilization of 1,1,1,2-tetrafluoroethane (R-134a) at 303.15 K, using a stainless steel volumetric system. $[N_{4444}][C_4F_9SO_3]$:$C_4F_9CO_2H$ and $[C_2C_1Im][C_8F_{17}SO_3]$:$C_4F_9CO_2H$ were selected as the systems with the best absorption capacities and were studied in three different FIL:perfluorinated acid ratios, for the absorption of difluoromethane (R-32), pentafluoroethane (R-125), and R-134a at 303.15 K, 313.15 K, and 323.15 K. All studied DES have ideal selectivity towards R-134a in mixtures with the other two F-gases. The results presented here provide knowledge of the behavior of these new alternative solvents for the separation of F-gases mixtures of commercial refrigerants, at three different temperatures and in a wide range of operating pressures.

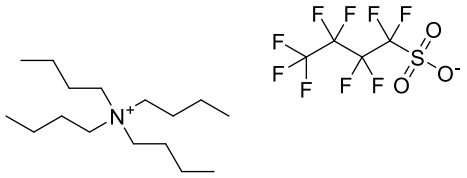
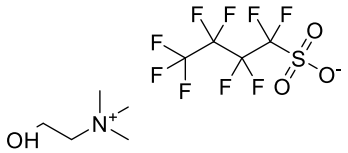
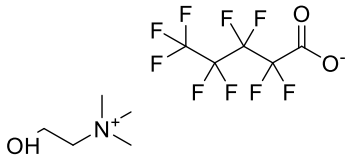
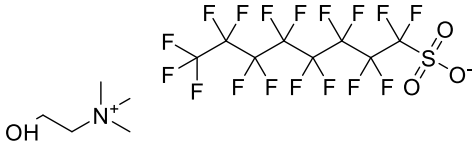
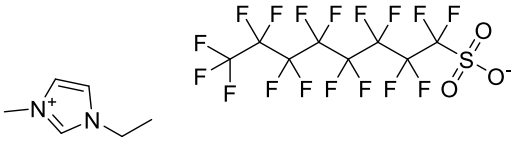
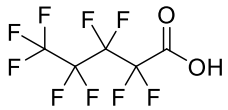
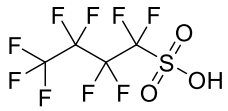
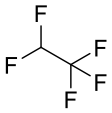
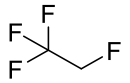
2.4.1 Experimental section

2.4.1.1 Materials

1-Ethyl-3-methylimidazolium perfluorooctanesulfonate ($[C_2C_1Im][C_8F_{17}SO_3]$, 98 % mass fraction purity), tetrabutylammonium perfluorobutanesulfonate ($[N_{4444}][C_4F_9SO_3]$, 97 % mass fraction purity), and (2-hydroxyethyl)trimethylammonium perfluorobutanesulfonate ($[N_{1112(OH)}][C_4F_9SO_3]$, 97 % mass fraction purity) were supplied by IoLiTec GmbH. (2-Hydroxyethyl)trimethylammonium

perfluoropentanoate ($[N_{1112(OH)}][C_4F_9CO_2]$, 98 % mass fraction purity) and (2-hydroxyethyl)trimethylammonium perfluorooctanesulfonate ($[N_{1112(OH)}][C_8F_{17}SO_3]$, 98 % mass fraction purity) were previously synthesized, through an ion-exchange resin method [82], and characterized in our laboratory [22,61]. ^{1}H and ^{19}F NMR and elemental analysis techniques were used to evaluate FILs purity. All FILs were dried under vacuum (4 Pa) and vigorously stirred at 323.15 K for at least 48 hours, immediately before use. A water content below 100 ppm was verified by volumetric Karl-Fischer titration technique (Metrohm Ion analysis, 831 KF Coulometer) for all FILs. Nonafluoro-1-butanesulfonic acid (≥ 98 % mass fraction purity) was supplied by TCI (Tokyo, Japan) and n-perfluoropentanoic acid (≥ 97 % mass fraction purity) was supplied by Fluorochem (Hadfield, UK). Difluoromethane (R-32, ≥ 99.8 % mass fraction purity), pentafluoroethane (R-125 , ≥ 99.8 % mass fraction purity), and 1,1,1,2- tetrafluoroethane (R-134a, ≥ 99.8 % mass fraction purity) were acquired from Polo Zero. Detailed structures and nomenclature of the compounds used in this work are presented in Table 2.4.1.

Table 2.4.1 Chemical structures of the fluorinated ionic liquids, perfluorinated acids, and F-gases used in this work.

	Chemical Structure
Tetrabutylammonium perfluorobutanesulfonate **[N_{4444}][$C_4F_9SO_3$]**	
(2-Hydroxyethyl)trimethylammonium perfluorobutanesulfonate **[$N_{1112(OH)}$][$C_4F_9SO_3$]**	
(2-Hydroxyethyl)trimethylammonium perfluoropentanoate **[$N_{1112(OH)}$][$C_4F_9CO_2$]**	
(2-Hydroxyethyl)trimethylammonium perfluorooctanesulfonate **[$N_{1112(OH)}$][$C_8F_{17}SO_3$]**	
1-Ethyl-3-methylimidazolium perfluorooctanesulfonate **[C_2C_1Im][$C_8F_{17}SO_3$]**	
n-Perfluoropentanoic acid **$C_4F_9CO_2H$**	
Nonafluoro-1-butanesulfonic acid **$C_4F_9SO_3H$**	
Difluoromethane **R-32**	
Pentafluoroethane **R-125**	
1,1,1,2-Tetrafluoroethane **R-134a**	

2.4.1.2 Preparation DES

The systems were prepared by mixing n-perfluoropentanoic acid with [N_{4444}][$C_4F_9SO_3$], [$N_{1112(OH)}$][$C_4F_9SO_3$], [$N_{1112(OH)}$][$C_8F_{17}SO_3$], and [C_2C_1Im][$C_8F_{17}SO_3$] or by mixing nonafluoro-1-butanesulfonic acid with [$N_{1112(OH)}$][$C_4F_9CO_2$] and [$N_{1112(OH)}$][$C_4F_9SO_3$] in a 1:1 molar ratio (see Figure 2.4.1). In the case of the mixtures [N_{4444}][$C_4F_9SO_3$]:$C_4F_9CO_2H$ and [C_2C_1Im][$C_8F_{17}SO_3$]:$C_4F_9CO_2H$,

ratios of 1:2 and 2:1 were also prepared (see Figure 2.4.1). The mixtures were prepared in glass vials using an analytical high precision balance (Sartorius, Germany) with 0.01 mg resolution and were sealed under nitrogen atmosphere. Three cycles of heating (up to 373.15 K) / cooling (down to 273.15 K) were performed under agitation. ^{1}H and ^{19}F NMR techniques were employed to verify that the IL and the perfluorinated acid have not reacted.

A dynamic visual method was carried out to determine the solid−liquid transitions of the mixtures, i.e. the temperatures at which a liquid phase appears, and the last crystal disappears. First, the mixtures were cooled down to 233.15 K, maintained at that temperature for at least 30 minutes, and examined for the presence of crystals. If the mixtures remained in the liquid state, their melting temperature was considered as lower than 233.15 K. If crystals were detected, the mixtures were heated up to achieve a complete liquid phase. Then, the mixtures were cooled down and checked again for the presence of crystals. This procedure was carried out with a successive increment of 5 K in the heating / cooling runs until the solid−liquid transition was determined.

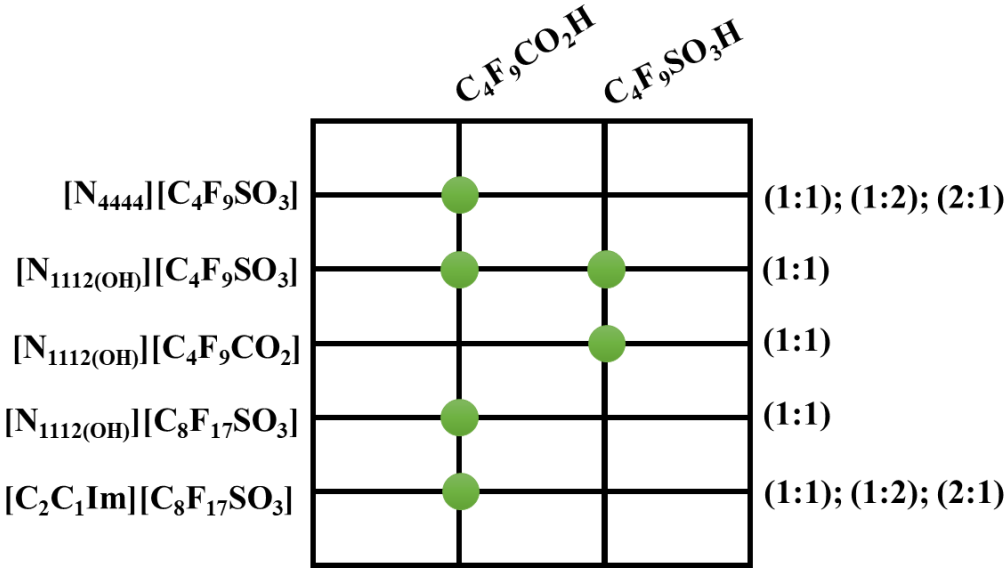


Figure 2.4.1 Matrix of the DESs studied in this work, resulting from the mixture of a FIL with a perfluorinated acid at molar ratios 1:1, 1:2 or 2:1.

2.4.1.3 Characterization DES

The densities of the DESs were determined in an automated SVM 3000 Anton Paar rotational Stabinger viscometer−densimeter, at atmospheric pressure and in the temperature range of 293.15−323.15 K. The temperature uncertainty of the equipment is 0.02 K. For each sample, duplicates were measured, with estimated uncertainties of 0.0002 $g \cdot cm^{-3}$.

The solid−solid phase transitions (T_{s-s}), glass transitions (T_g), and melting temperature (T_m) of each DES, were determined in a Differential Scanning Calorimeter (DSC) Q200 (TA Instrument) with a refrigerated cooling system, using about 5-10 mg of each DES in a sealed aluminum sample pan. The DSC cell was purged with dry N_2 at a flow rate of 50 $cm^3 \cdot min^{-1}$. Samples were cooled from room temperature down to 183.15 K and kept at isothermal for 30 min, and then were heated back to 293.15 K. The first cooling-heating cycle was performed at a rate of 10 $K \cdot min^{-1}$ and the subsequent cycles were performed at different rates, 10 $K \cdot min^{-1}$, 5 $K \cdot min^{-1}$, and 1 $K \cdot min^{-1}$. The optimal rate for each sample was selected to achieve the best characterization of the several solid-fluid phase transitions and melting points. The standard uncertainty was estimated as ± 1 K. Universal Analysis 2000 v. 4.5A software (TA instruments) was used to integrate the peaks and to determine the different transitions and melting points.

2.4.1.4 Determination of gas absorption

An initial screening of all DESs with a FIL: acid ratio of 1:1 was performed for the absorption of R-134a at 303.15 K and pressures up to 0.6 MPa. The DESs that presented the best absorption capacities towards R-134a were selected. Then, ratios of 1:2 and 2:1 were also prepared for the selected DESs and further studied for the absorption of R-32, R-125, and R-134a. Then, single-component absorption equilibrium isotherms were determined at 303.15 K, 313.15 K, and 323.15 K, and pressures up to 1 MPa.

Absorption experiments were performed through an isochoric saturation method based on contacting a known amount of gas with a degassed precise quantity of sample, in a closed equilibrium cell, at constant temperature (see Figure 2.4.2). The apparatus consisted in two different subsystems, well calibrated and connected by a needle valve. The first subsystem comprises a stainless-steel cylinder (gas reservoir) and the second subsystem a visual stainless-steel cell (equilibrium cell) with a magnetic stirrer to accelerate equilibrium. Pressure in subsystem 1 was measured through a pressure transducer LEX 1 (KELLER AG, Winterthur, Switzerland) with an accuracy of 0.05 % Full Scale (FS) in a 0.01-2 MPa range. Pressure in subsystem 2 was measured through a LEO 2 manometer (KELLER AG, Winterthur, Switzerland) with an accuracy of 0.1% FS in a 0.01-1 MPa range. Isothermal conditions of both subsystems were ensured by using a CORIO CD Heating Immersion Circulator (± 0.03 K) from Julabo GmbH (Germany). Temperature was measured using a Pt100 probe within ±0.02 K coupled to a

Yokogawa 7561 digital multimeter (Ohm accuracy of ±0.009 % of reading). Figure 2 shows the experimental setup assembled for these measurements.

In a typical run a certain amount of sample (0.5-0.8 g) was weighted in an analytical balance (Sartorius, Germany, with 0.01 mg resolution), introduced into the equilibrium cell and the whole system evacuated under stirring for 2 hours by means of a vacuum pump (Edwards, model RV5). Pure gas was fed into gas reservoir (subsystem 1) at a determined pressure (P_1). The experiment starts by opening the needle valve to introduce the gas into the equilibrium cell (subsystem 2). This leads to a drop of pressure, and subsequently of gas density, in subsystem 1 from $P_{1,i}$ ($\rho_{1,i}$) to $P_{1,f}$ ($\rho_{1,f}$), at isothermal conditions (T_1). On the other hand, the pressure in the equilibrium cell (subsystem 2) first increases, then starts to decrease due to the absorption of gas into the liquid sample. Subsystem 2 is left for equilibrating for approximately 1 hour while stirring, until pressure remains stable (P_2) for at least 30 minutes meaning equilibrium is reached.

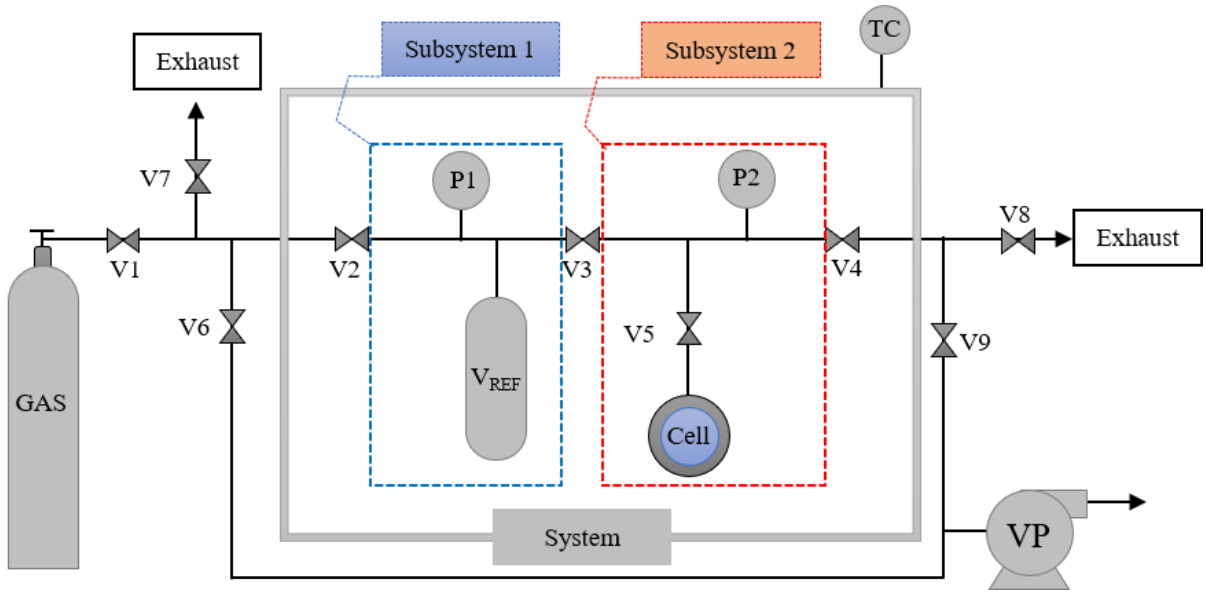


Figure 2.4.2 Schematic diagram of the experimental setup used in this work. TC: temperature controller, VREF: gas cylinder of subsystem 1, P1: manometer of subsystem 1, P2: manometer of subsystem 2, Cell: high-pressure absorption cell, and VP: vacuum pump.

The quantification of gas absorption in the absorbent phase was performed based on the Gibbsian surface model [29,83–85]. Thus, mass of gas absorbed in the absorbent phase (m_{abs}) was calculated as:

$$m_{abs}=V_1\left(\rho_{1,i}-\rho_{1,f}\right)-(V_{gas})\rho_{gas} \qquad 2.4.1$$

where: V_1 is the volume of subsystem 1 to which the gas is first loaded; $\rho_{1,i}$ and $\rho_{1,f}$ are the gas densities in subsystem 1 before and after gas expansion into the subsystem 2, respectively. ρ_{gas} is the gas density at subsystem 2, when equilibrium is achieved at P_2; and V_{gas} is the volume of gas in subsystem 2, calculated as:

$$V_{gas}=V_2-V_{liq} \qquad 2.4.2$$

where V_2 is the volume of subsystem 2 and V_{liq} is the volume of the absorbent located in the absorption cell.

Gas densities were obtained from the website of the National Institute of Standards and Technology (NIST) [86]. The amount of gas absorbed in excess per unit mass of absorbent was calculated as:

$$n_{ex} = \frac{m_{abs}}{m_{liq}} \quad 2.4.3$$

where m_{liq} is the mass of absorbent. As consequence of gas absorption, the volume of the absorbent phase change:

$$y = \frac{n^{ex}}{1\text{-}v_g^l(T) r_g(T, P) + n^{ex}} \quad 2.4.4$$

where $v_g^l(T)$ is the specific volume of the liquified gas at temperature T at equilibrium, $r_g(T, P)$ is the gas density at subsystem 2 at temperature T and pressure P when equilibrium is achieved, and n^{ex} is the value of the excess amount of absorbed gas per unit mass of the absorbent, determined using equation 2.3.3. The total amount of absorbed gas per mass unit of the absorbent (n) is determined as follow:

$$n = n^{ex} + v_g^l(T) r_{gas}(T, P) \frac{y}{1\text{-}y} \quad 2.4.5$$

Then, equation 2.3.4 can be rewritten in terms of molar fraction (x):

$$x = \frac{n/M_g}{1/M_{IL} + n/M_g} \quad 2.4.6$$

where M_{IL} and M_g are the molecular weights of the absorbent and of the gas, respectively.

2.4.2 Results and discussion

2.4.2.1 Characterization of DES

The utilization of FILs for the absorption and selective separation of F-gases has been studied and reported in the literature, with promising results [29]. However, an increase in the number of fluorine atoms of FILs is associated with an increment of melting temperature, resulting in a decrease of the range of temperature where they can be operated at liquid state [87]. In this work, we selected 5 FILs with high melting temperatures, and mixed them with perfluorinated acids to produce eutectic mixtures with a significant decrease of the melting point, compared to the neat FIL. This allowed us to take advantage of the properties of FILs in a wider liquidus range for the solubilization of F-gases.

The selected FILs contain three different cations (cholinium, imidazolium or tetrabutylammonium), with anions with different functional group (sulfonate or carboxylate) and different size of the fluorinated alkyl chain (4-carbon or 8-carbon). While $[C_4F_9SO_3]^-$ and $[C_8F_{17}SO_3]^-$ - based FILs were mixed with n-perfluoropentanoic acid, the $[C_4F_9CO_2]^-$ - based FIL was mixed with nonafluoro-1-

butanesufonic acid. By mixing two components with different functional groups, the asymmetry of the mixture increases, leading to a greater decrease of the melting temperature of the system, compared to the neat FIL. The mixture of two components with the same functional group was also tested by preparing a $[N_{1112(OH)}][C_4F_9SO_3]$:$C_4F_9SO_3H$ mixture in a 1:1 molar ratio. However, this binary mixture was solid at room temperature and therefore was not selected for further studies. Since the mixtures $[N_{4444}][C_4F_9SO_3]$:$C_4F_9CO_2H$ (1:1) and $[C_2C_1Im][C_8F_{17}SO_3]$:$C_4F_9CO_2H$ (1:1) have the highest adsorption capacity towards R-134a at 303.15 K, as shown in the next section, they were also prepared in the ratios of 1:2 and 2:1. These new mixtures (1:2 and 2:1 ratios) were liquid down to 233.15 K and therefore were also considered as DESs.

^{1}H and ^{19}F NMR techniques were employed to verify that the FIL and the perfluorinated acid have not reacted. The NMR spectra for the neat ILs, perfluorinated acids, and prepared mixtures were compared for all mixtures studied in this work. Figure 2.4.3 to Figure 2.4.6 show the ^{1}H and ^{19}F NMR spectra for the $[N_{4444}][C_4F_9SO_3]$:$C_4F_9CO_2H$ and $[C_2C_1Im][C_8F_{17}SO_3]$:$C_4F_9CO_2H$ mixtures at the three different ratios. The chemical shift of the proton of the perfluorinated acid moves upfield in the mixtures relatively to the pure perfluorinated acid and this change is more noticeable when the proportion of IL relatively to the acid is higher.

By visual determination (at naked eye), we validated that the 1:1 molar ratio mixtures $[N_{4444}][C_4F_9SO_3]$:$C_4F_9CO_2H$, $[N_{1112(OH)}][C_4F_9SO_3]$:$C_4F_9CO_2H$, $[N_{1112(OH)}][C_4F_9CO_2]$:$C_4F_9SO_3H$, and $[N_{1112(OH)}][C_8F_{17}SO_3]$:$C_4F_9CO_2H$ have a melting point below 233.15 K and therefore were considered as DESs. In the case of $[C_2C_1Im][C_8F_{17}SO_3]$:$C_4F_9CO_2H$ (1:1), crystals were observed at 248.15 K and the mixture was totally liquid at 253.15 K, when a gradual increment of temperature was applied. This temperature is much lower than the melting point of neat FIL (see Table 2.3.2), so it was also considered DES.

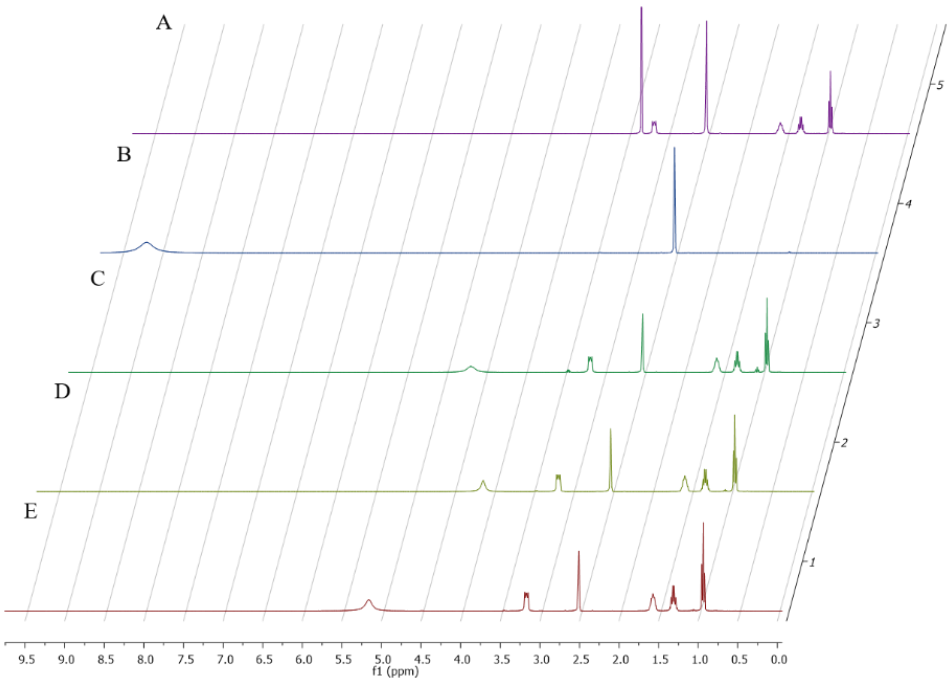


Figure 2.4.3 ^{1}H NMR of : a) $[N_{4444}][C_4F_9SO_3]$, b) n-perfluoropentanoic acid and c) $[N_{4444}][C_4F_9SO_3]$:$C_4F_9CO_2H$ at molar ratios of 1:1, d) 2:1 , and e) 1:2.

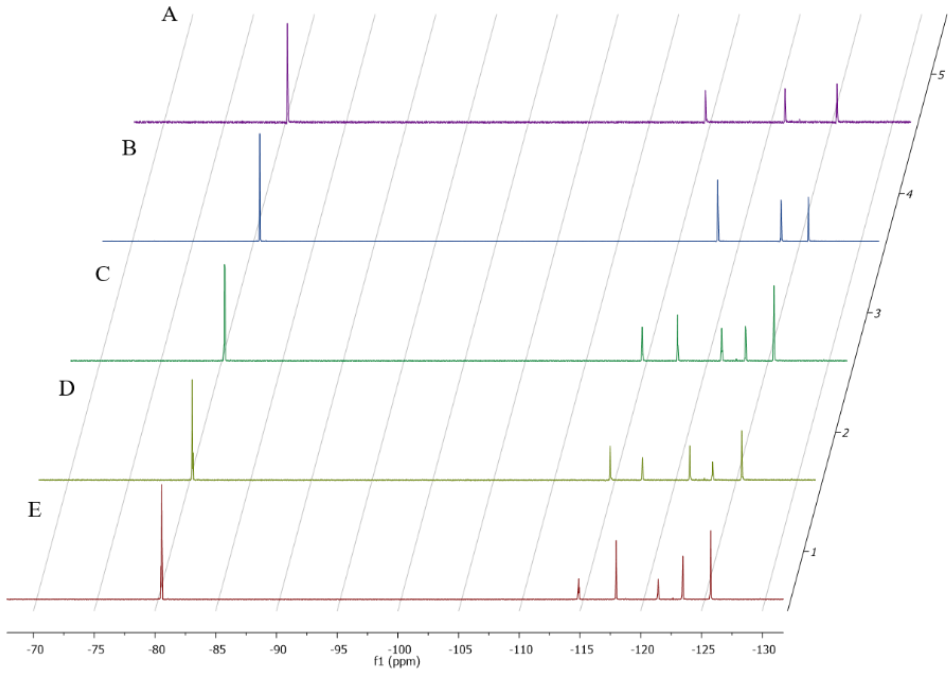


Figure 2.4.4 ^{19}F NMR of: a) $[N_{4444}][C_4F_9SO_3]$, b) n-perfluoropentanoic acid, c) $[N_{4444}][C_4F_9SO_3]$:$C_4F_9CO_2H$ at molar ratio of 1:1, d) 2:1, and e) 1:2.

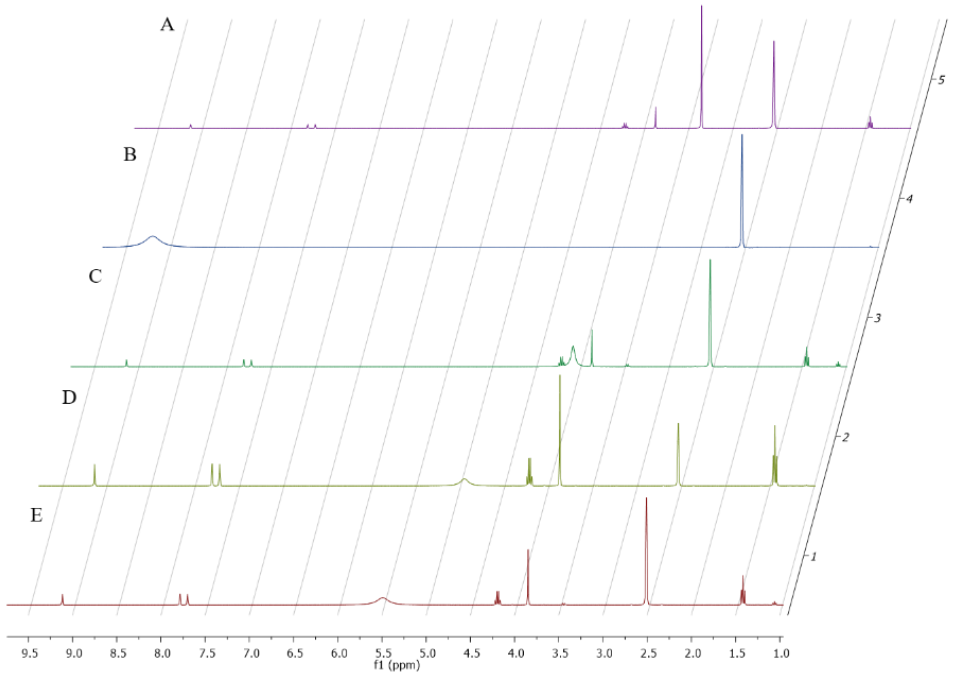


Figure 2.4.5 ^{1}H NMR of : a) $[C_2C_1Im][C_8F_{17}SO_3]$, b) n-perfluoropentanoic acid, c) $[C_2C_1Im][C_8F_{17}SO_3]$:$C_4F_9CO_2H$ at molar ratio of 1:1, d) 2:1 and e) 1:2.

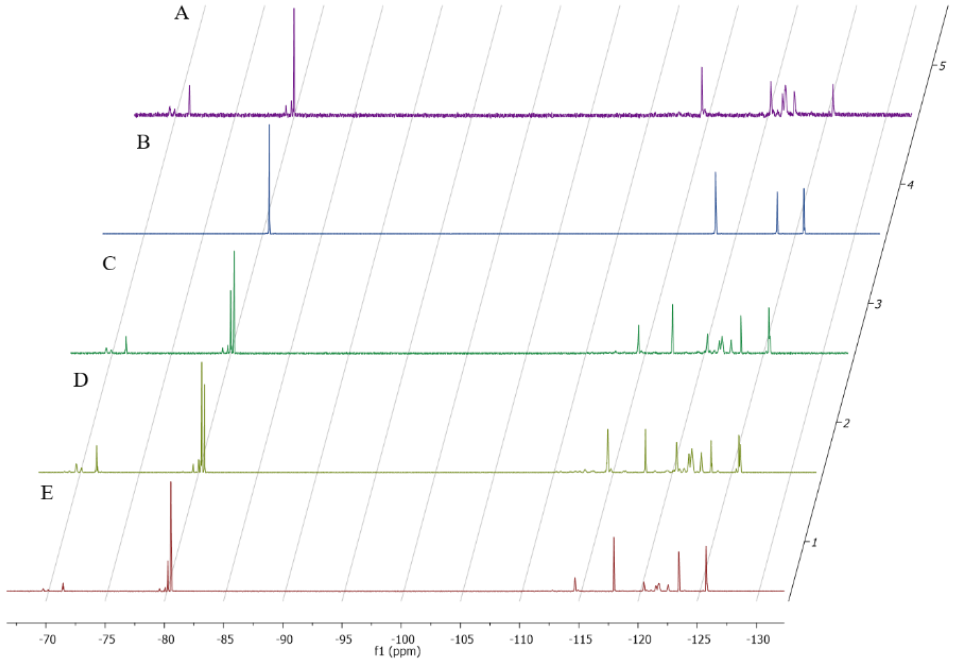


Figure 2.4.6 ^{19}F NMR of : a) $[C_2C_1Im][C_8F_{17}SO_3]$, b) n-perfluoropentanoic acid, c) $[C_2C_1Im][C_8F_{17}SO_3]$:$C_4F_9CO_2H$ at molar ratio of 1:1, d) 2:1, and e) 1:2.

Table 2.4.2 presents the solid-solid transitions (T_{s-s}), melting temperatures (T_m), and glass transitions (T_g) of the FILs and DESs studied in this work. The T_m of the perfluorinated acids was not determined due to incompatibilities with the employed technique. From the 5 FILs selected in this work, 3 of them have been thermally characterized before [20,61,62], with the lowest T_m being 327.15K for $[N_{4444}][C_4F_9SO_3]$ [20]. The thermal characterization of pure $[N_{1112(OH)}][C_4F_9CO_2]$ and $[N_{1112(OH)}][C_8F_{17}SO_3]$ was also performed in this work. No T_m was determined for these two FILs since the process of decomposition started before melting point (temperatures higher than 373.15K). These two FILs present two solid-solid transitions, above 290 K in the case of $[N_{1112(OH)}][C_4F_9CO_2]$ and above 364K in the case of $[N_{1112(OH)}][C_8F_{17}SO_3]$.

All the prepared DESs were thermally characterized and only for $[N_{1112(OH)}][C_4F_9CO_2]$:$C_4F_9SO_3H$ and $[C_2C_1Im][C_8F_{17}SO_3]$:$C_4F_9CO_2H$ (1:1) was possible to determine melting points (T_m = 273 K and T_m = 268 K, respectively) in the range of temperatures tested by DSC (see Figure 2.4.7). In these two cases, cold crystallizations were visualized in the DSC heating curves, at 239 K for $[N_{1112(OH)}][C_4F_9CO_2]$:$C_4F_9SO_3H$ (1:1) and at 238 K for $[C_2C_1Im][C_8F_{17}SO_3]$:$C_4F_9CO_2H$ (1:1) (see Figure 2.4.7). However, these two mixtures were considered for the purpose of this work since they are liquid at room temperature and in the range of temperatures tested for the solubilization of F-gases. All DESs show only a glass transition Figure 2.4.7 shows an example for $[C_2C_1Im][C_8F_{17}SO_3]$:$C_4F_9CO_2H$ (2:1)), except $[C_2C_1Im][C_8F_{17}SO_3]$:$C_4F_9CO_2H$ (1:2), which do not present transitions.

Table 2.4.2 Solid-solid transitions (T_{s-s}), melting temperatures (T_m), and glass transitions (T_g) of the FILs and binary mixtures studied in this work.

	T_{s-s} (K)	T_m (K)	T_g (K)
$[N_{4444}][C_4F_9SO_3]$ [20]	-	327	234
$[N_{1112(OH)}][C_4F_9SO_3]$ [62]	-	436	-
$[N_{1112(OH)}][C_4F_9CO_2]$	274 290	*	-
$[N_{1112(OH)}][C_8F_{17}SO_3]$	222 364	*	-
$[C_2C_1Im][C_8F_{17}SO_3]$[61]	-	368	-
$[N_{4444}][C_4F_9SO_3]$:$C_4F_9CO_2H$ (1:1)	-	-	212
$[N_{4444}][C_4F_9SO_3]$:$C_4F_9CO_2H$ (2:1)	-	-	222
$[N_{4444}][C_4F_9SO_3]$:$C_4F_9CO_2H$ (1:2)	-	-	191
$[N_{1112(OH)}][C_4F_9SO_3]$:$C_4F_9CO_2H$ (1:1)	-	-	194
$[N_{1112(OH)}][C_4F_9CO_2]$: $C_4F_9SO_3H$ (1:1)	-	273	198
$[N_{1112(OH)}][C_8F_{17}SO_3]$:$C_4F_9CO_2H$ (1:1)	-	-	186
$[C_2C_1Im][C_8F_{17}SO_3]$:$C_4F_9CO_2H$ (1:1)	-	269	189
$[C_2C_1Im][C_8F_{17}SO_3]$:$C_4F_9CO_2H$ (2:1)	-	-	193
$[C_2C_1Im][C_8F_{17}SO_3]$:$C_4F_9CO_2H$ (1:2)	-	-	-

*These FILs begin the process of decomposition before melting.

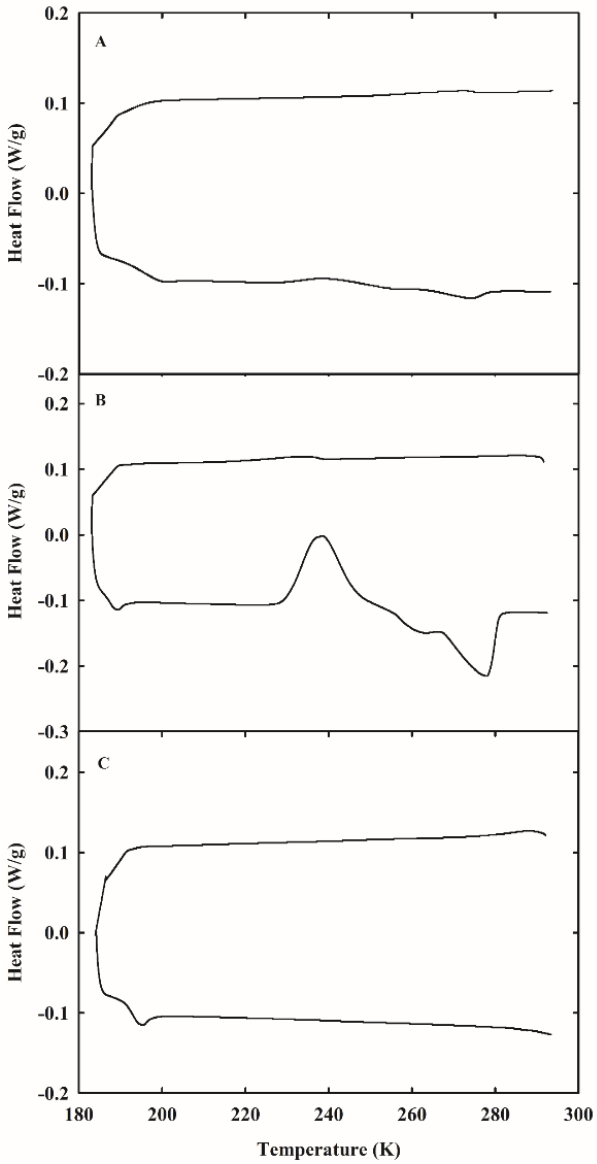


Figure 2.4.7 DSC curves at 5 K/min of: a) $[N_{1112(OH)}][C_4F_9CO_2]$:$C_4F_9SO_3H$ (1:1), b) $[C_2C_1Im][C_8F_{17}SO_3]$:$C_4F_9CO_2H$ (1:1) and c) $[C_2C_1Im][C_8F_{17}SO_3]$:$C_4F_9CO_2H$ (2:1).

The densities of all tested DESs were determined in the temperatures range of 293.15 K – 323.15 K (see Table 2.4.3). For all tested DES, density decreases linearly with the increase of temperature (see Figure 2.4.8). The temperature dependence of the density was studied applying the following expression:

$$\ln\rho = A_0 + A_1 T \qquad 2.4.7$$

where ρ is the density of each DES, and A_0 and A_1 are the fitting parameters (see Table 2.4.3).

Table 2.4.3 Densities at different temperatures, fitting parameters for ln(ρ) as a function of temperature and standard deviations (σ) shown of the DES studied in this work.

DES	ρ (g.cm^{-3})				Fitting parameters		
	293.15 K	303.15 K	313.15 K	323.15 K	A_0	A_1	σ
$[N_{4444}][C_4F_9SO_3]$: $C_4F_9CO_2H$ (1:1)	1.3517	1.3414	1.3311	1.3208	0.5269	$-8\cdot10^{-4}$	$1\cdot10^{-4}$
$[N_{4444}][C_4F_9SO_3]$: $C_4F_9CO_2H$ (2:1)	1.3066	1.2985	1.2893	1.2795	0.4607	$-7\cdot10^{-4}$	$6\cdot10^{-4}$
$[N_{4444}][C_4F_9SO_3]$: $C_4F_9CO_2H$ (1:2)	1.4191	1.4063	1.3946	1.3836	0.5949	$-8\cdot10^{-4}$	$3\cdot10^{-4}$
$[N_{1112(OH)}][C_4F_9SO_3]$: $C_4F_9CO_2H$ (1:1)	1.6336	1.6210	1.6087	1.5964	0.7178	$-8\cdot10^{-4}$	$1\cdot10^{-4}$
$[N_{1112(OH)}][C_4F_9CO_2]$: $C_4F_9SO_3H$ (1:1)	1.6291	1.6167	1.6044	1.5922	0.7142	$-8\cdot10^{-4}$	$1\cdot10^{-4}$
$[N_{1112(OH)}][C_8F_{17}SO_3]$: $C_4F_9CO_2H$ (1:1)	1.6841	1.6710	1.6578	1.6448	0.7522	$-8\cdot10^{-4}$	$1\cdot10^{-4}$
$[C_2C_1Im][C_8F_{17}SO_3]$: $C_4F_9CO_2H$ (1:1)	1.6721	1.6620	1.6490	1.6351	0.7212	$-7\cdot10^{-4}$	$8\cdot10^{-4}$
$[C_2C_1Im][C_8F_{17}SO_3]$: $C_4F_9CO_2H$ (2:1)	1.6875	1.6732	1.6608	1.6477	0.7523	$-8\cdot10^{-4}$	$3\cdot10^{-4}$
$[C_2C_1Im][C_8F_{17}SO_3]$: $C_4F_9CO_2H$ (1:2)	1.6893	1.6739	1.6564	1.6428	0.7816	$-9\cdot10^{-4}$	$1\cdot10^{-3}$

Uncertainties of density data were determined to be less than ± 0.0002 g·cm^{-3}
The temperature dependence of the density was studied applying the equation $\ln\rho = A_0 + A_1 T$

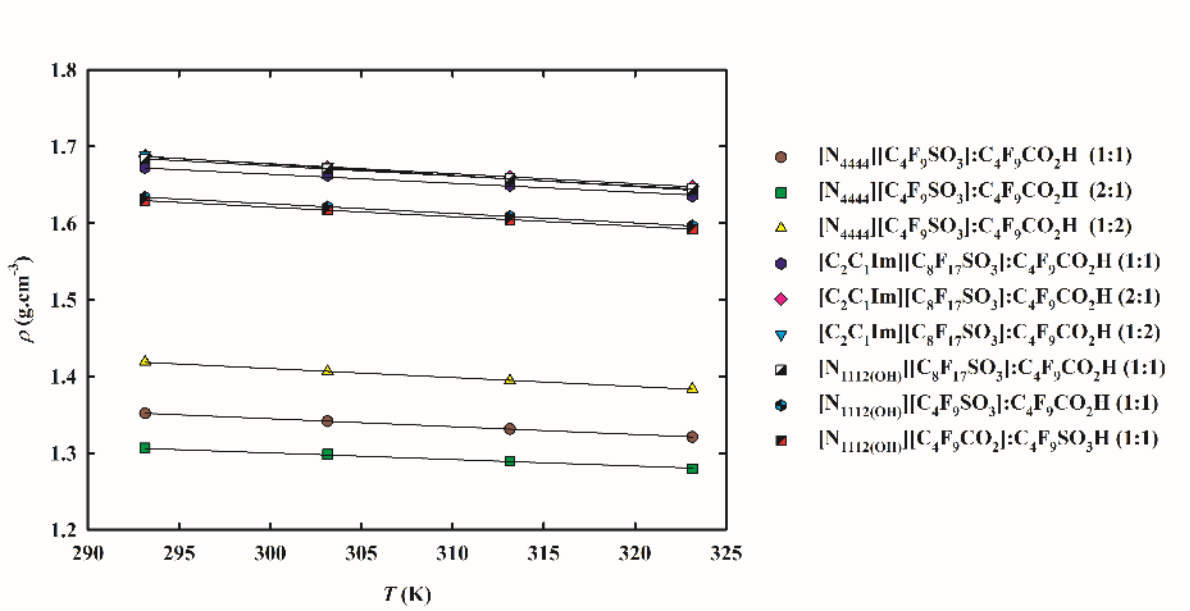


Figure 2.4.8 Density of each DES as a function of temperature.

The highest densities for the mixtures of 1:1 molar ratio were obtained for the ones prepared with $[C_8F_{17}SO_3]^-$- based FILs, probably related to a higher number of fluorine atoms. $[C_2C_1Im][C_8F_{17}SO_3]$:$C_4F_9CO_2H$ (2:1) and (1:2) have higher density than the respective (1:1) mixture, probably due to an increment of the interactions in these two ratios, which may also explain their much lower T_m relatively to the (1:1) mixture. In the case of $[N_{4444}][C_4F_9SO_3]$:$C_4F_9CO_2H$, an increase of density is observed when the proportion of perfluorinated acid increases, while a decrease of density is observed when the proportion of FIL increases.

At room temperature, the mixtures with higher proportion of IL relatively to the perfluorinated acid have higher viscosity. Moreover, $[N_{4444}][C_4F_9SO_3]$:$C_4F_9CO_2H$ mixtures are more viscous than the $[C_2C_1Im][C_8F_{17}SO_3]$:$C_4F_9CO_2H$ mixtures, when the same ratios are compared.

2.4.2.2 Gas solubilization

This experimental procedure was validated using the pure IL $[C_2C_1Im][N(CF_3SO_2)_2]$ for the absorption of R-134a at 303.15 K and the results were compared with the literature data obtained at 303.15 K and 298.2 K (see Figure 2.4.9) [29,30]. The reproducibility of the measurements was attested by repeating the experiments several times at the same experimental conditions. The overall experimental uncertainty was determined to be less than 3 %.

From the three F-gases tested in this work, R-134a is the one that showed higher solubility in pure ILs, as previously reported [29]. Therefore, we evaluated the solubility of R-134a in the 5 DESs prepared in the 1:1 molar ratio. The experimental solubility data, expressed as molar fraction of dissolved gas (x_i), of the F-gas *i* in the each DES are presented in Figure 2.4.10 as a function of the applied

equilibrium gas pressure at 303.15 K. The absorption equilibrium isotherms were studied up to 0.6 MPa in order to not exceed the saturation pressure of R-134a (0.77 MPa at 303.15 K) [86].

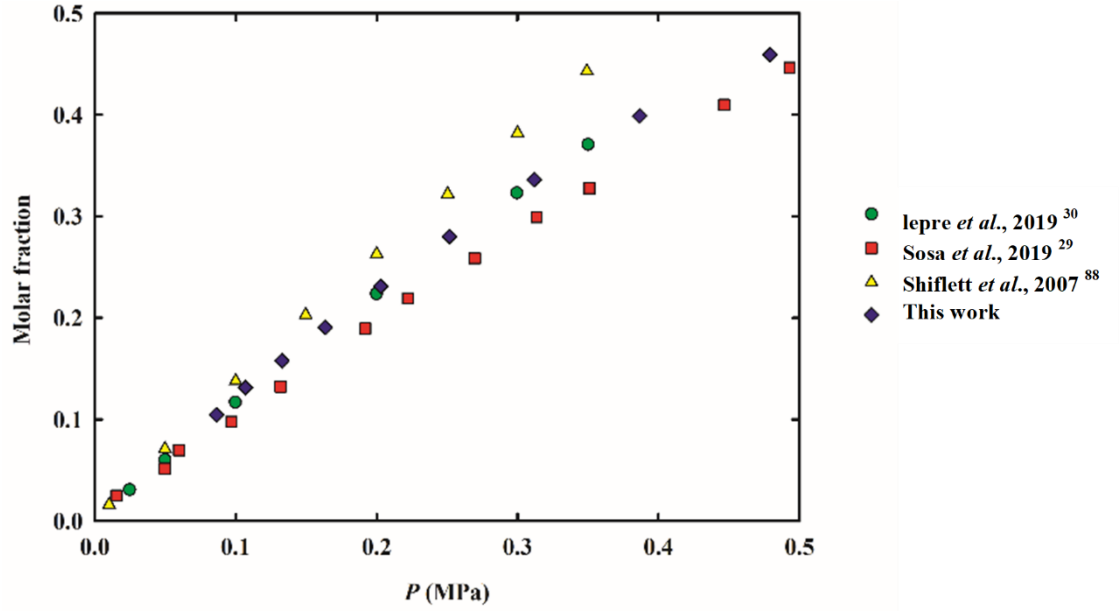


Figure 2.4.9 Comparison of experimental data of R-134a absorption in $[C_2C_1Im][N(CF_3SO_2)_2]$ obtained in this work at 303.15 K and obtained by other authors. Data from Lepre *et al.*, 2019 [30] and Sosa *et al.*, [29] was obtained at 303.15 K and data from Shiflett *et al.*, 2007 [88] was obtained at 298.2 K.

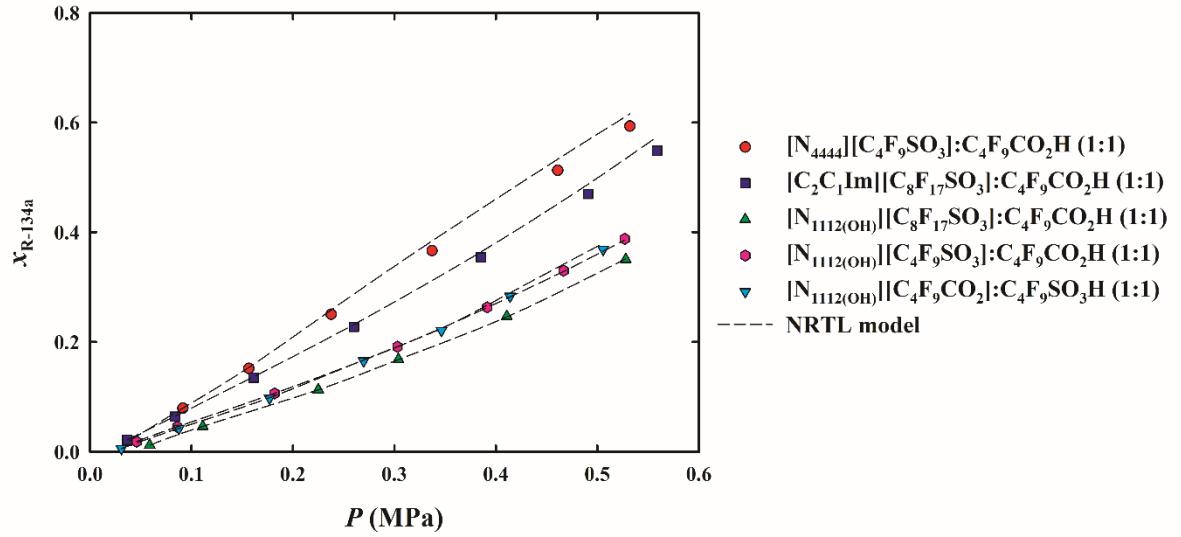


Figure 2.4.10 Absorption isotherms of R-134a in all tested DESs prepared in a molar fraction 1:1, determined at 303.15 K and equilibrium pressures up to 0.6 MPa.

As it has been previously shown [18,19,29], the high tuneability of FILs make them excellent candidates for the design of systems for the absorption of specific gases. In this work, we studied three $[N_{1112(OH)}]^+$-based FILs, with different size of the perfluorinated chain ($[C_4F_9SO_3]^-$ or $[C_8F_{17}SO_3]^-$) and with different functional groups ($[C_4F_9SO_3]^-$ or $[C_4F_9CO_2]^-$). Changes in the nature of the FIL cation were also evaluated by comparing the solubilization capacities of $[N_{4444}][C_4F_9SO_3]$ and $[C_2C_1Im][C_8F_{17}SO_3]$ with the ones of their $[N_{1112(OH)}]^+$-based counterparts.

All the DESs prepared from $[N_{1112(OH)}]^+$-based FILs have very similar absorption capacities, with the $[N_{1112(OH)}][C_8F_{17}SO_3]$:$C_4F_9SO_3H$ presenting the lowest absorption capacity. This indicates that the major factor affecting gas absorption was the nature of FIL cation. In fact, the substitution of $[N_{1112(OH)}]^+$ to $[C_2C_1Im]^+$ in $[C_8F_{17}SO_3]^-$ - based FILs leads to a drastic increment in gas solubility. The same trend was observed when $[N_{1112(OH)}]^+$ was substituted to $[N_{4444}]^+$ in $[C_4F_9SO_3]^-$ - based FILs. Since the absorption isotherms of $[N_{1112(OH)}][C_4F_9SO_3]$:$C_4F_9CO_2H$ and $[N_{1112(OH)}][C_4F_9CO_2]$:$C_4F_9SO_3H$ are almost superimposable in all range of pressures, it can be concluded that in this case, the location of the carboxylate and sulfonate groups in either the FIL anion or in the perfluorinated acid did not affect gas absorption.

Then, the DESs prepared from $[N_{4444}][C_4F_9SO_3]$ and $[C_2C_1Im][C_8F_{17}SO_3]$ showed higher absorption capacity towards R-134a, and therefore were chosen to study the absorption of R-32, R-125, and R-134a at 303.15 K, 313.15 K, and 323.15 K. Moreover, these mixtures were also prepared in the molar ratios 1:2 and 2:1.

Figure 2.4.10 shows the isotherms of $[N_{4444}][C_4F_9SO_3]$:$C_4F_9CO_2H$ and $[C_2C_1Im][C_8F_{17}SO_3]$:$C_4F_9CO_2H$ at the 1:1, 2:1, and 1:2 ratios, for each F-gas, at 303.15 K. The isotherms determined at 313.15 K and 323.15 K are presented at Figures 2.4.11 and 2.4.13, respectively . The absorption and desorption isotherms are superimposable, indicating the inexistence of hysteresis between the absorption and desorption branches. As example, the absorption and desorption isotherms of R-32, R-125, and R-134a in $[N_{4444}][C_4F_9SO_3]$:$C_4F_9CO_2H$ (2:1) at 323.15 K are shown in Figure 2.4.14.

For R-32, $[N_{4444}][C_4F_9SO_3]$:$C_4F_9CO_2H$ at 1:1 and 2:1 molar ratios showed the highest absorption capacity at the 3 tested temperatures, and $[C_2C_1Im][C_8F_{17}SO_3]$:$C_4F_9CO_2H$ (1:2) showed the lowest absorption capacity. For R-125, the highest absorption capacities were obtained with the same DESs, $[N_{4444}][C_4F_9SO_3]$:$C_4F_9CO_2H$ at 1:1 and 2:1 molar ratios, and also with $[C_2C_1Im][C_8F_{17}SO_3]$:$C_4F_9CO_2H$ (2:1) at 303.15K and 313.15K. At 323.15K, $[N_{4444}][C_4F_9SO_3]$:$C_4F_9CO_2H$ (2:1) presents the best results. $[C_2C_1Im][C_8F_{17}SO_3]$:$C_4F_9CO_2H$ (1:2) has again the lowest absorption capacity at all tested temperatures. For R-134a, $[N_{4444}][C_4F_9SO_3]$:$C_4F_9CO_2H$ (2:1) presents the highest absorption capacity while the lowest absorption capacities were obtained for $[C_2C_1Im][C_8F_{17}SO_3]$:$C_4F_9CO_2H$ (1:1) at 303.15 K and for $[C_2C_1Im][C_8F_{17}SO_3]$:$C_4F_9CO_2H$ (1:2) at 313.15 K and 323.15 K.

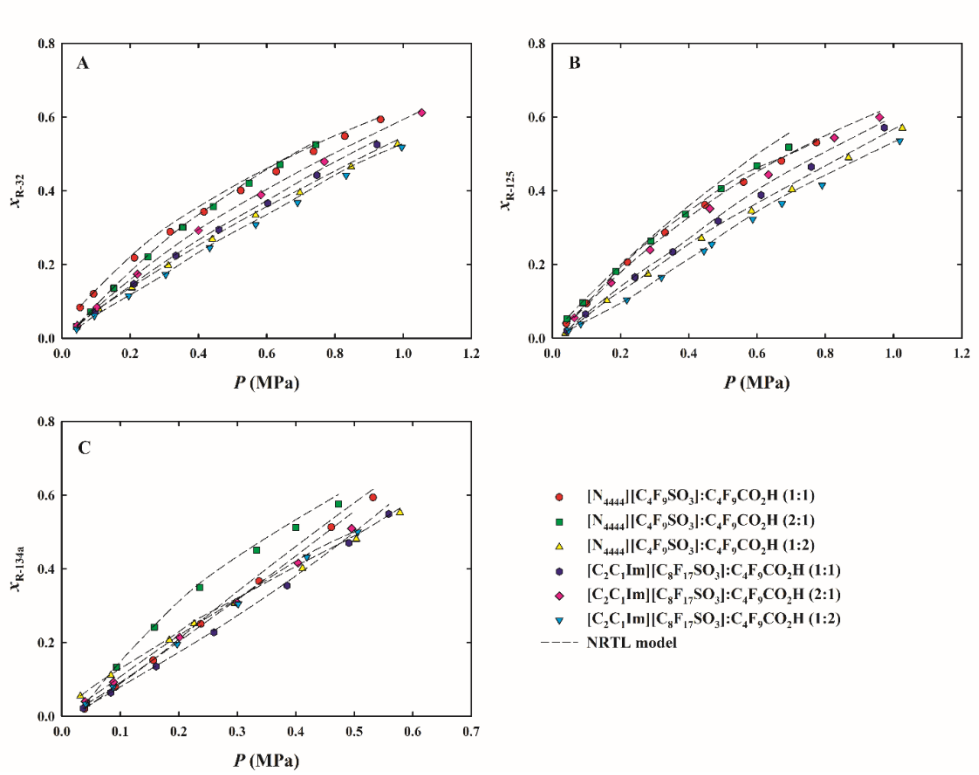


Figure 2.4.11 Absorption equilibrium isotherms: a) R-32, b) R-125 and c) R-134a on $[N_{4444}][C_4F_9SO_3]$:$C_4F_9CO_2H$ and $[C_2C_1Im][C_8F_{17}SO_3]$:$C_4F_9CO_2H$ at molar ratios of 1:1, 2:1, and 1:2, at 303.15 K. The dashed lines represent the isotherms fitting with the NRTL model.

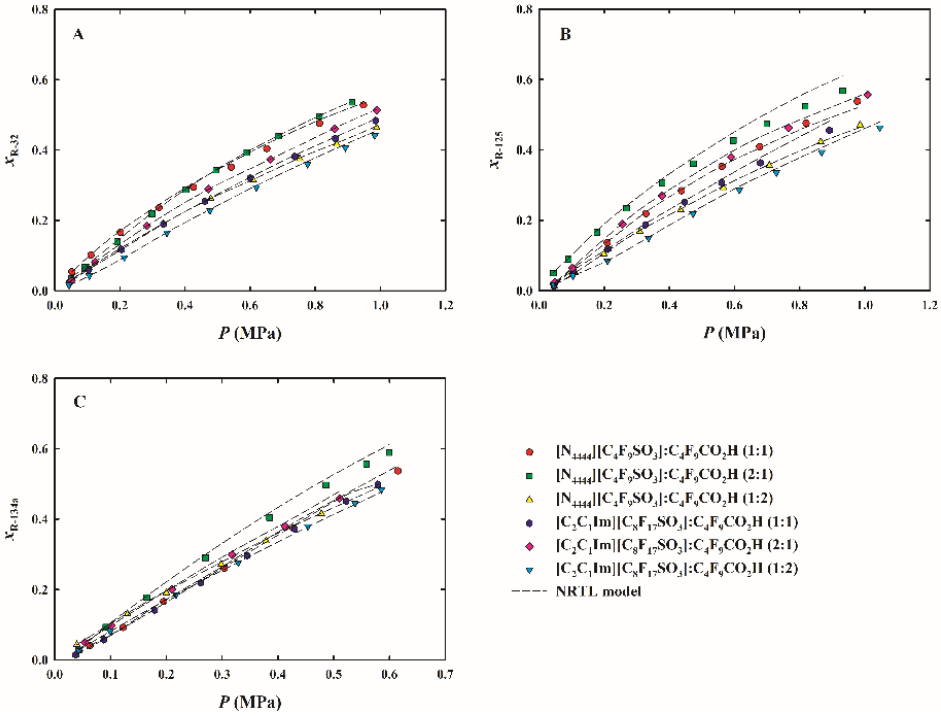


Figure 2.4.12 Absorption equilibrium isotherms of : a) R-32, b) R-125 and c) R-134a on $[N_{4444}][C_4F_9SO_3]$:$C_4F_9CO_2H$ and $[C_2C_1Im][C_8F_{17}SO_3]$:$C_4F_9CO_2H$ at molar ratios of 1:1, 2:1, and 1:2, at 313.15 K. The dashed lines represent the isotherms fitting with the NRTL model.

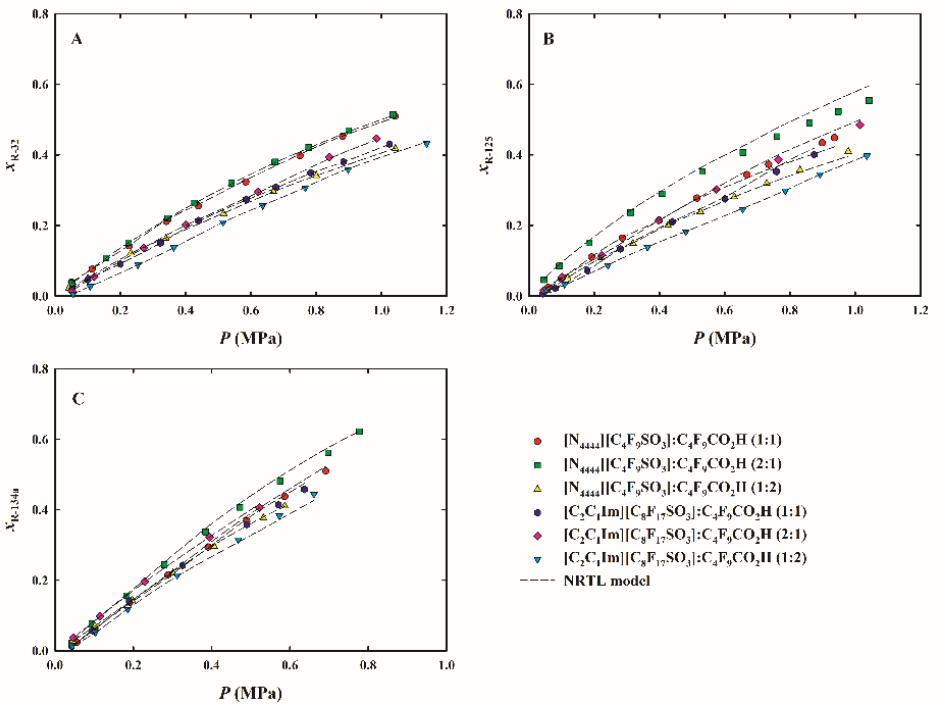


Figure 2.4.13 Absorption equilibrium isotherms of: a) R-32, b) R-125 and c) R-134a on $[N_{4444}][C_4F_9SO_3]$:$C_4F_9CO_2H$ and $[C_2C_1Im][C_8F_{17}SO_3]$:$C_4F_9CO_2H$ at molar ratios of 1:1, 2:1, and 1:2, at 323.15 K. The dashed lines represent the isotherms fitting with the NRTL model.

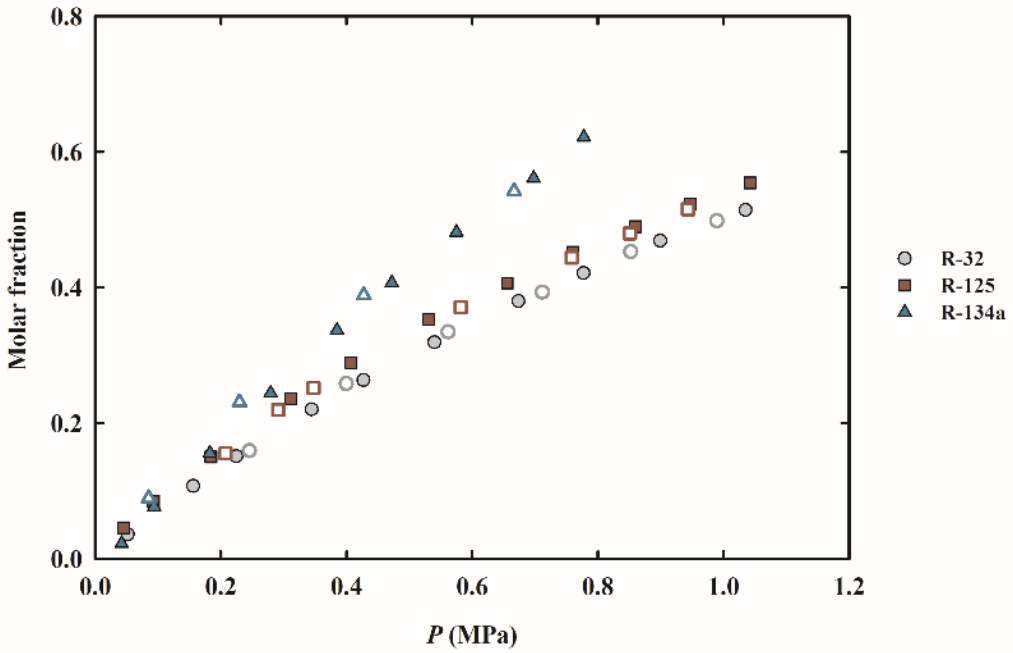


Figure 2.4.14 Absorption (full symbols) and desorption (open symbols) equilibrium isotherms of R-32, R-125, and R-134a on $[N_{4444}][C_4F_9SO_3]$:$C_4F_9CO_2H$ (2:1) at 323.15 K.

In Figure 2.4.15 the absorption isotherms of the three gas in the six selected DESs: $[N_{4444}][C_4F_9SO_3]$:$C_4F_9CO_2H$ and $[C_2C_1Im][C_8F_{17}SO_3]$:$C_4F_9CO_2H$ at 1:1, 2:1, and 1:2 ratios, at 303.15 K are presented. The isotherms determined at 313.15 K and 323.15 K are presented at Figures 2.4.15 and 2.4.16, respectively. All DESs have higher absorption capacity towards R-134a, as expected, while the absorption capacity towards the other two gases is very similar, with almost superimposable isotherms in most cases.

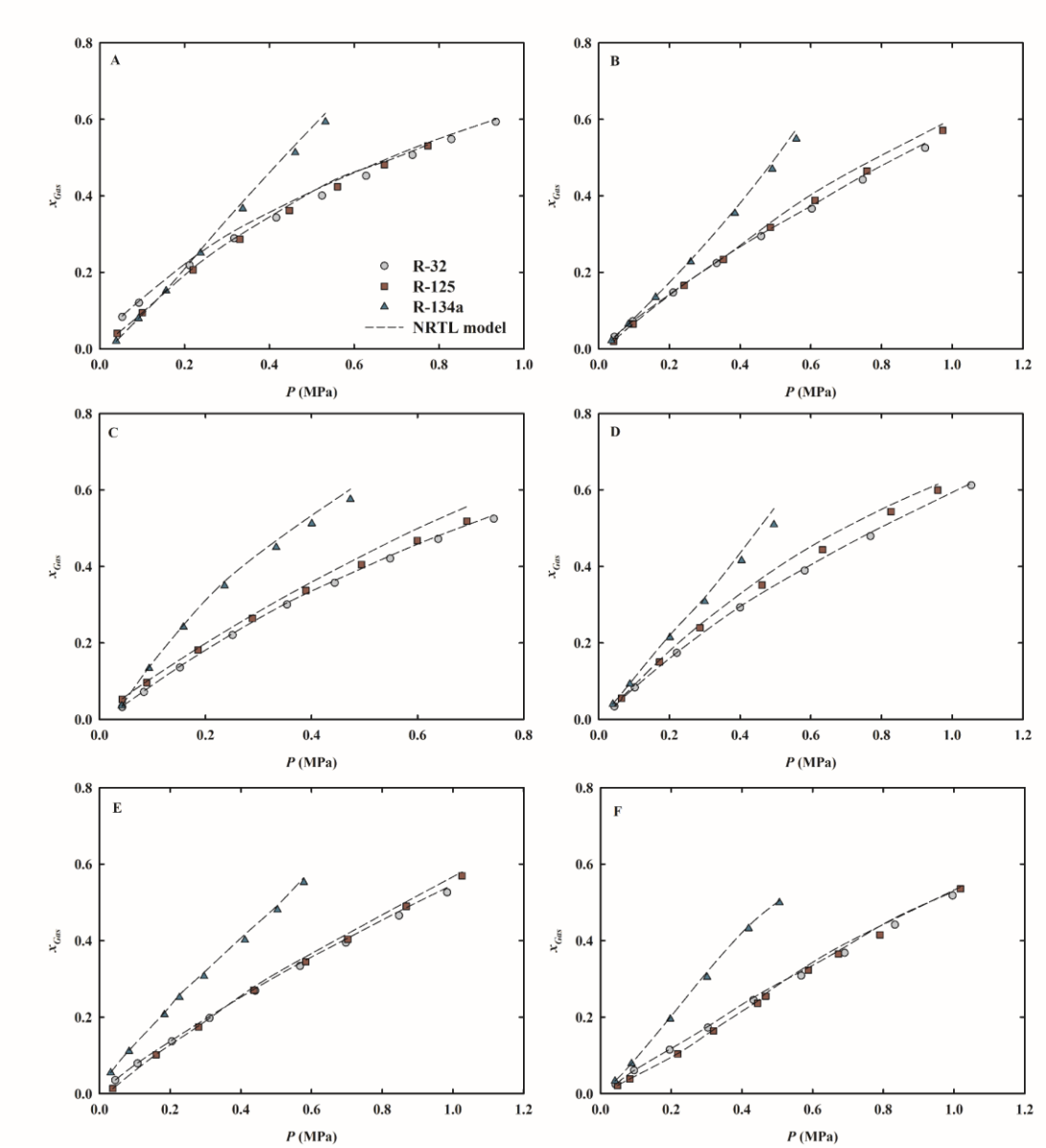


Figure 2.4.15 Absorption equilibrium isotherms of : a) R-32, R-125, and R-134a in $[N_{4444}][C_4F_9SO_3]$:$C_4F_9CO_2H$ (1:1), b) $[C_2C_1Im][C_8F_{17}SO_3]$:$C_4F_9CO_2H$ (1:1), c) $[N_{4444}][C_4F_9SO_3]$:$C_4F_9CO_2H$ (2:1), d) $[C_2C_1Im][C_8F_{17}SO_3]$:$C_4F_9CO_2H$ (2:1), e) $[N_{4444}][C_4F_9SO_3]$:$C_4F_9CO_2H$ (1:2) and f) $[C_2C_1Im][C_8F_{17}SO_3]$:$C_4F_9CO_2H$ (1:2), at 303.15 K. The dashed lines represent the isotherms fitting with the NRTL model.

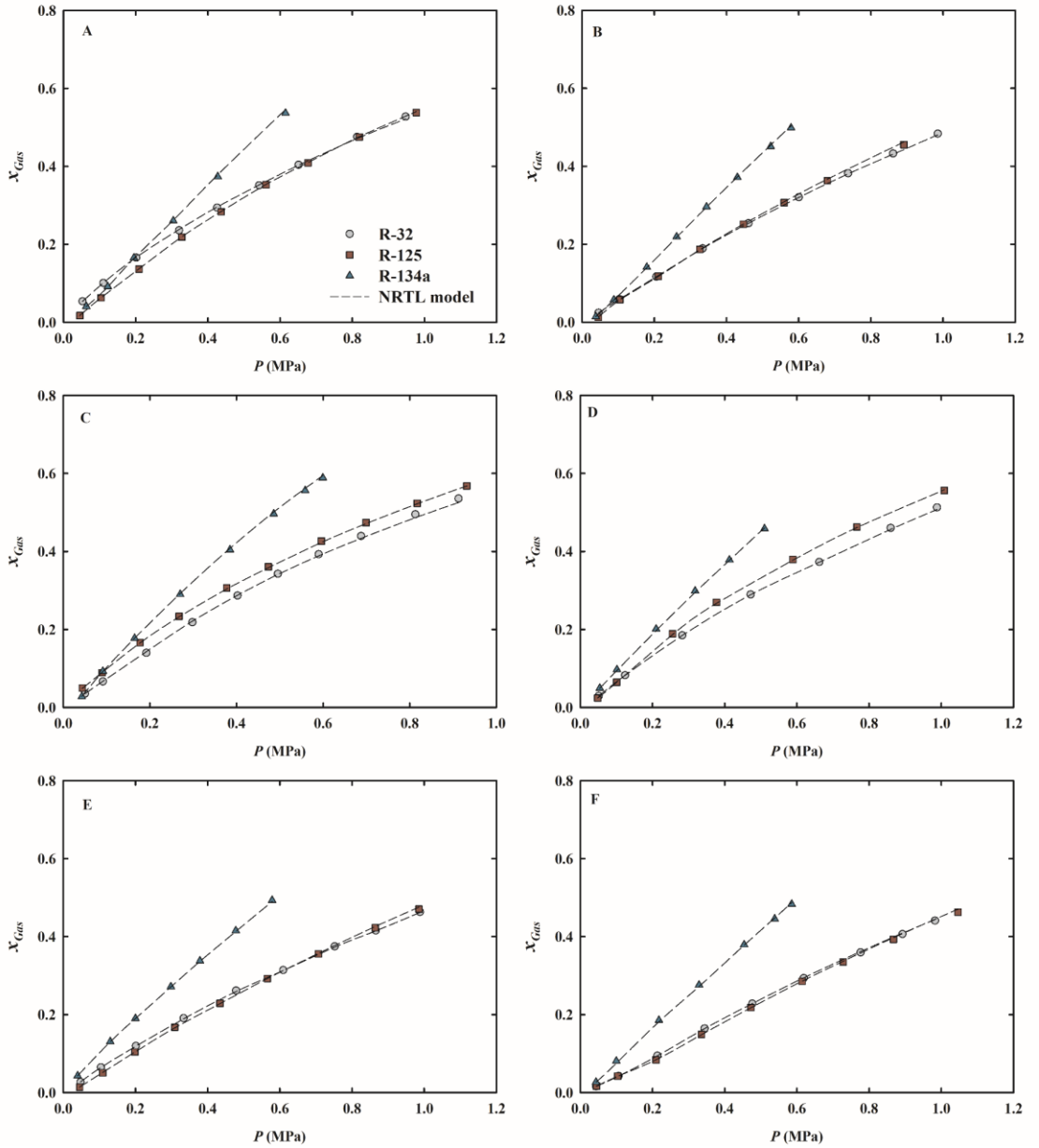


Figure 2.4.16 Absorption equilibrium isotherms of a) R-32, R-125, and R-134a in $[N_{4444}][C_4F_9SO_3]/C_4F_9CO_2H$ (1:1), b) $[C_2C_1Im][C_8F_{17}SO_3]/C_4F_9CO_2H$ (1:1), c) $[N_{4444}][C_4F_9SO_3]/C_4F_9CO_2H$ (2:1), d) $[C_2C_1Im][C_8F_{17}SO_3]/C_4F_9CO_2H$ (2:1), e) $[N_{4444}][C_4F_9SO_3]/C_4F_9CO_2H$ (1:2) and f) $[C_2C_1Im][C_8F_{17}SO_3]/C_4F_9CO_2H$ (1:2) (Panel F), at 313.15 K. The dashed lines represent the isotherms fitting with the NRTL model.

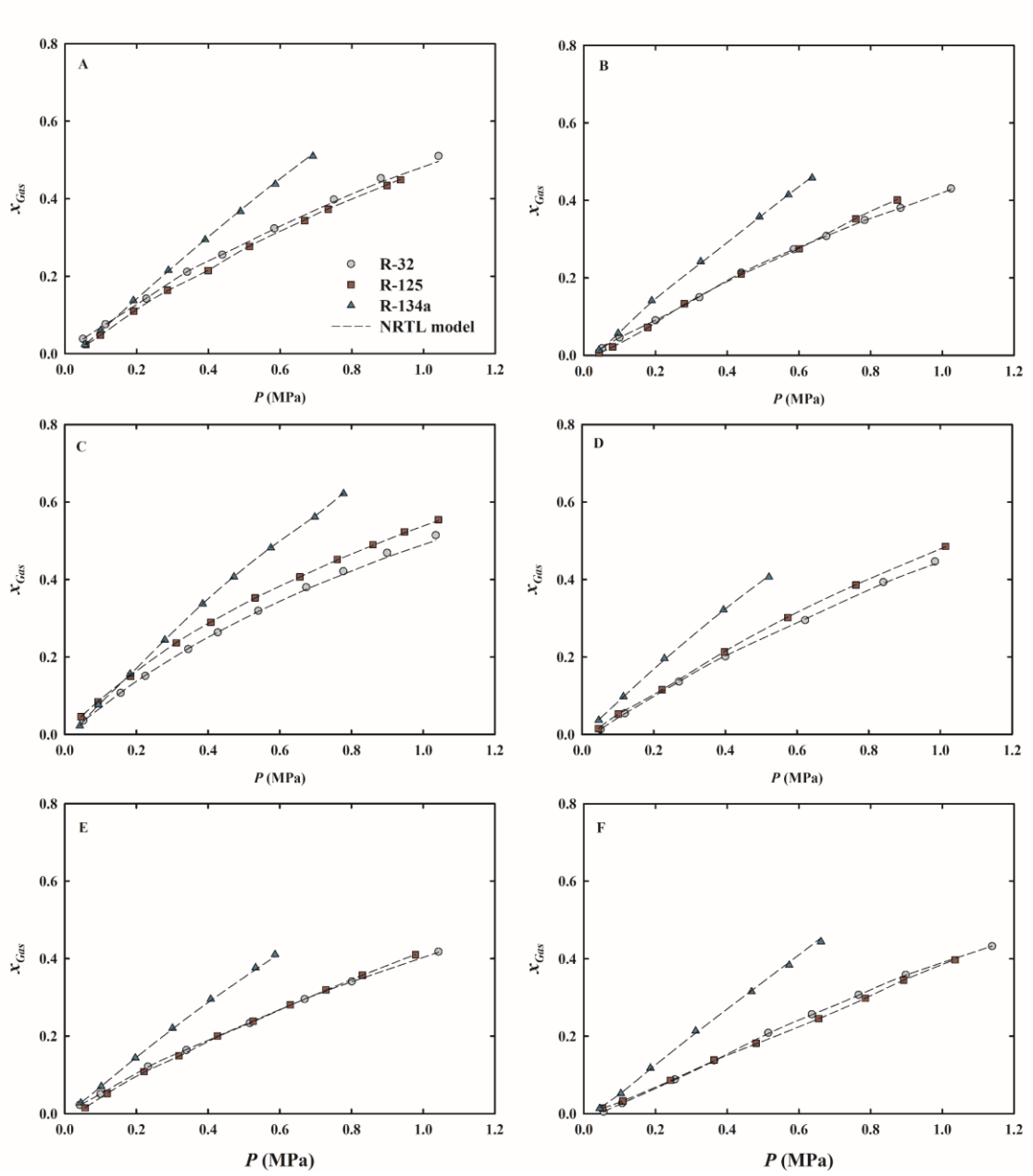


Figure 2.4.17 Absorption equilibrium isotherms of: a) R-32, R-125, and R-134a in $[N_{4444}][C_4F_9SO_3]/C_4F_9CO_2H$ (1:1), b) $[C_2C_1Im][C_8F_{17}SO_3]/C_4F_9CO_2H$ (1:1), c) $[N_{4444}][C_4F_9SO_3]/C_4F_9CO_2H$ (2:1), d) $[C_2C_1Im][C_8F_{17}SO_3]/C_4F_9CO_2H$ (2:1), e) $[N_{4444}][C_4F_9SO_3]/C_4F_9CO_2H$ (1:2) and f) $[C_2C_1Im][C_8F_{17}SO_3]/C_4F_9CO_2H$ (1:2) at 323.15 K. The dashed lines represent the isotherms fitting with the NRTL model.

For the design of separation processes, gas solubility in mass fraction must be considered. When comparing the solubility data at 303.15 K in mol fraction (see Figure 2.4.15 and Figure 2.4.17) and in mass fraction, w, (see Figure 2.4.18 and 2.4.9) a relative decrease of performance of $[C_2C_1Im][C_8F_{17}SO_3]$:$C_4F_9CO_2H$ (2:1) and a relative increase of performance of $[N_{4444}][C_4F_9SO_3]$:$C_4F_9CO_2H$ (1:2) are evident. Moreover, a decrease in the solubility of R-32 relatively to the other two gases occurs for all DES when mass fraction is considered (see Figure 2.4.18 and Figure 2.4.19).

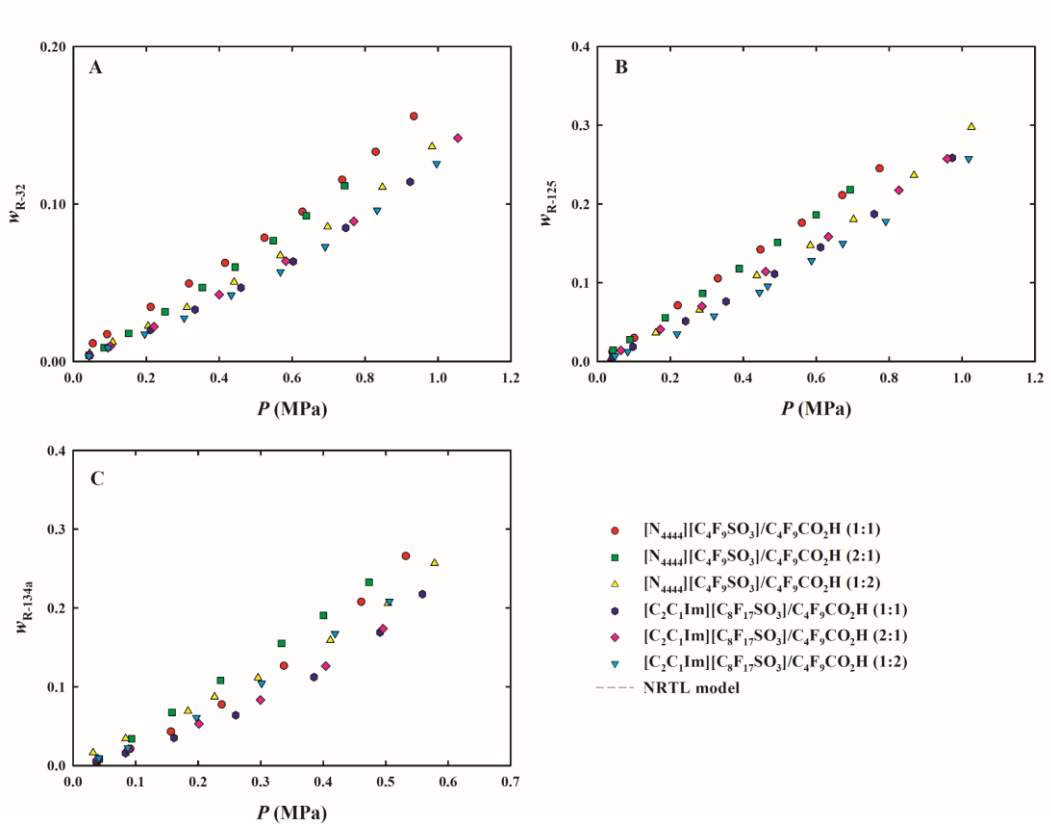


Figure 2.4.18 Absorption equilibrium isotherms in mass fraction (*w*) of : a) R-32, b) R-125 and R-134a (Panel C) on $[N_{4444}][C_4F_9SO_3]/C_4F_9CO_2H$ and $[C_2C_1Im][C_8F_{17}SO_3]/C_4F_9CO_2H$ at molar ratios of 1:1, 2:1, and 1:2 at 303.15 K.

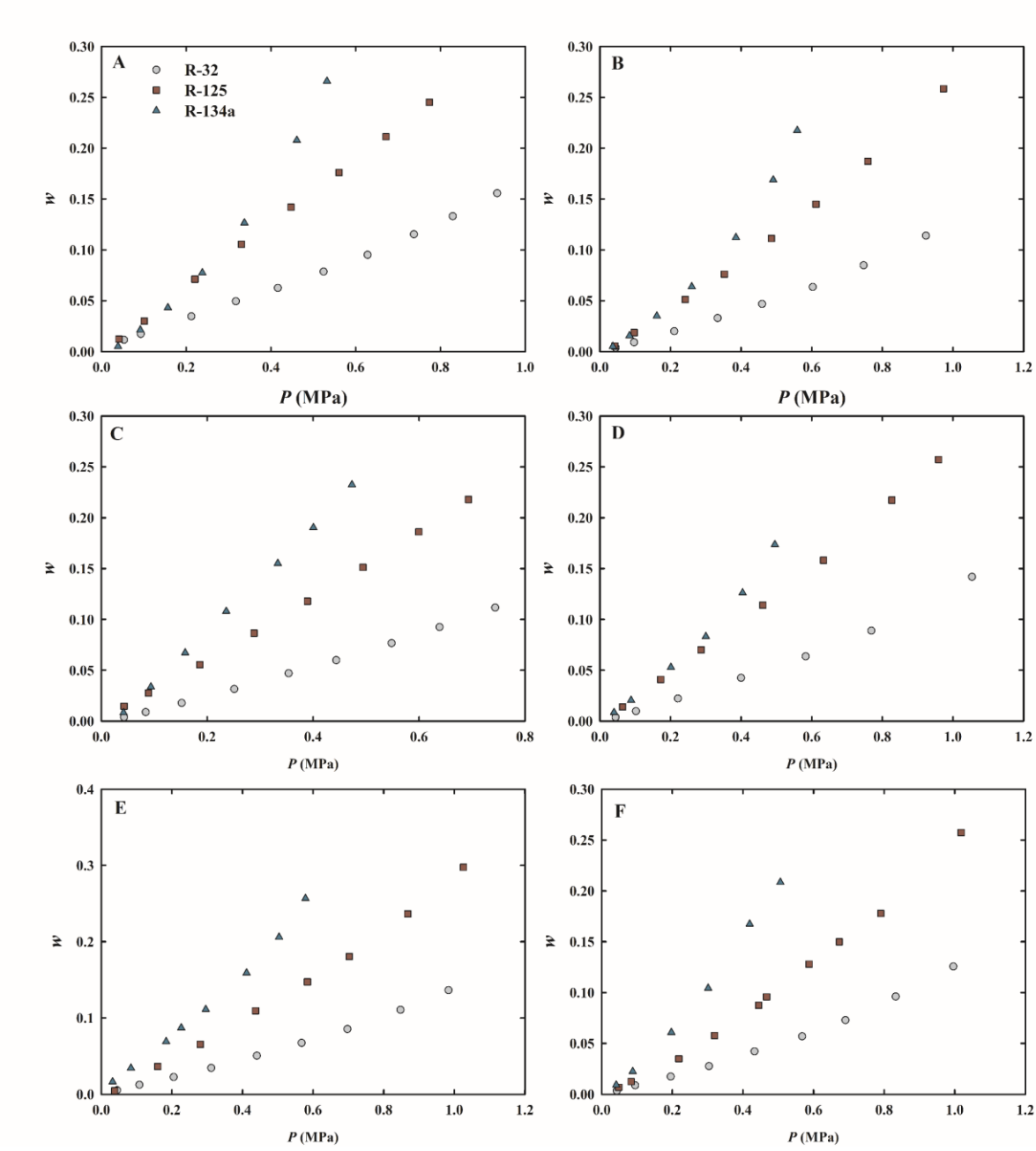


Figure 2.4.19 Absorption equilibrium isotherms in mass fraction (*w*) of : a) R-32, R-125, and R-134a in $[N_{4444}][C_4F_9SO_3]/C_4F_9CO_2H$ (1:1), b) $[C_2C_1Im][C_8F_{17}SO_3]/C_4F_9CO_2H$ (1:1), c) $[N_{4444}][C_4F_9SO_3]/C_4F_9CO_2H$ (2:1), d) $[C_2C_1Im][C_8F_{17}SO_3]/C_4F_9CO_2H$ (2:1), e) $[N_{4444}][C_4F_9SO_3]/C_4F_9CO_2H$ (1:2) and f) $[C_2C_1Im][C_8F_{17}SO_3]/C_4F_9CO_2H$ (1:2) at 303.15 K.

The absorption of each F-gas in the absorbent phase was also evaluated based on the Henry's law constant (H_i), defined as:

$$H_i(T) = \lim_{x_i \to 0} \frac{f^L_{i(T,P)}}{x_i} \quad 2.4.8$$

where f_i^L is the fugacity of the gas i dissolved in the absorbent and x_i is the gas molar fraction in the absorbent phase, considering infinite dilution conditions. Since in thermodynamic equilibrium the fugacity of the F-gas in the absorbent phase is equal to the fugacity in the gas phase, Henry's law can be rewritten as follow:

$$P_i = H_i(T)\, x_i \quad 2.4.9$$

where P_i is the partial pressure of F-gas in the gas phase. Therefore, Henry's law is a proportionality constant between the partial pressure of F-gas in the gas phase and its solubility in the absorbent phase, at infinitely dilute conditions. The slope of the tangent at P=0 of the experimental (x,P) data corresponds to the Henry's law constants. Therefore, at infinite dilution conditions, lower values of this constant correspond to higher gas solubility. However, this is not indicative of the behavior of the system at high pressures. Figure 2.4.20 compares the DESs studied in this work in terms of the Henry's law constants.

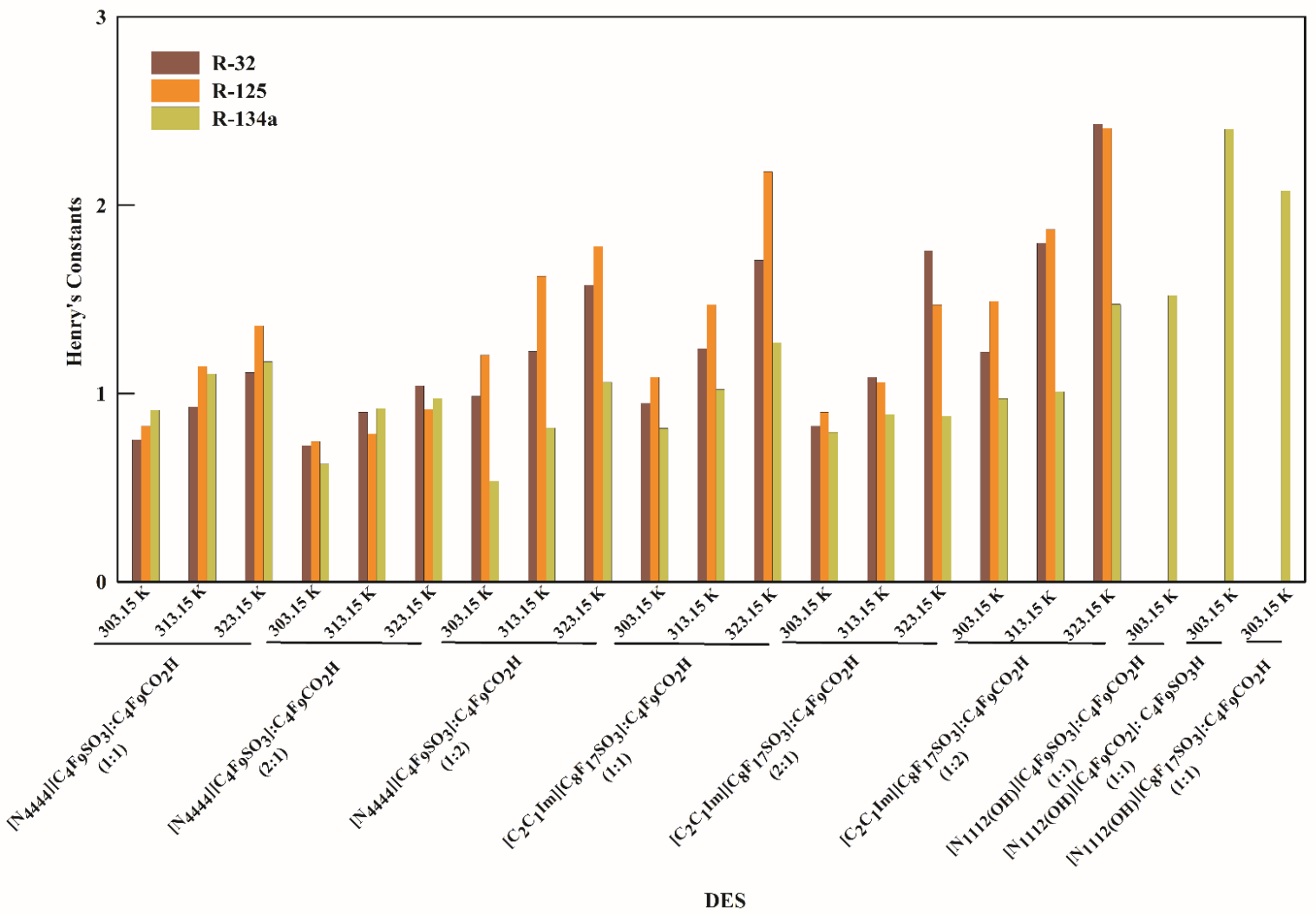


Figure 2.4.20 Henry's law constants (in MPa) determined for the absorption of R-32, R-125 and R-134a at 303.15 K, 313.15 K, and 323.15 K.

The conclusions taken from the analysis of the results presented in Figure 2.4.20 are in clear agreement with the conclusions taken from the analysis of the absorption isotherms (Figures 2.4.12 – 2.4.17). As expected, an increase of the Henry's constants is observed with the increasing of temperature, showing that gas absorption decreases with the increment of the temperature. The DES prepared from $[N_{1112(OH)}]^+$-based FILs have the greatest Henry´s constants for the systems with R-134a at 303.15 K, confirming that these DES have lowest capacities to absorb this F-gas. Moreover, the systems with R-134a have in all cases similar or smaller Henry's constants than the ones with R-32 and R-125, indicating that the DESs tested in this work are selective towards R-134a.

In a previous work the solubilization of R-32, R-125, and R-134a was determined in one IL lacking fluorine atoms, in two conventional fluoro-containing ILs, and in three different FILs [29]. Moreover, that data was compared with the data available in the literature for other FILs [29]. In the present work we compare the Henry's constants obtained for the solubilization of F-gases in DES at 303.15 K with the Henry's constants obtained for the solubilization of F-gases at 303.15 K in $[C_2C_1Im][C_1CO_2]$, ($[C_2C_1Im][CF_3SO_3]$, $[C_2C_1Im][N(CF_3SO_2)_2]$, $[C_2C_1Im][C_4F_9CO_2]$, $[C_2C_1Im][C_4F_9SO_3]$, and $[C_2C_1py]$ $[C_4F_9SO_3]$ (Figure 2.4.21) [29].

For R-32, $[N_{4444}][C_4F_9SO_3]$:$C_4F_9CO_2H$ (1:1), $[N_{4444}][C_4F_9SO_3]$:$C_4F_9CO_2H$ (2:1), and $[C_2C_1Im][C_8F_{17}SO_3]$:$C_4F_9CO_2H$ (2:1) present lower Henry's constants (higher solubility) that the ones obtained for the FILs, while the Henry's constants determined for the other DES are similar to the ones determined for FILs. For R-125, the lowest Henry's constants were obtained for $[N_{4444}][C_4F_9SO_3]$:$C_4F_9CO_2H$ (1:1), $[N_{4444}][C_4F_9SO_3]$:$C_4F_9CO_2H$ (2:1). For R-134a, $[N_{4444}][C_4F_9SO_3]$:$C_4F_9CO_2H$ (1:2) presents lower Henry's constants than the one obtained for the FILs, while the other DES present Henry's constants similar to the ones of FILs.

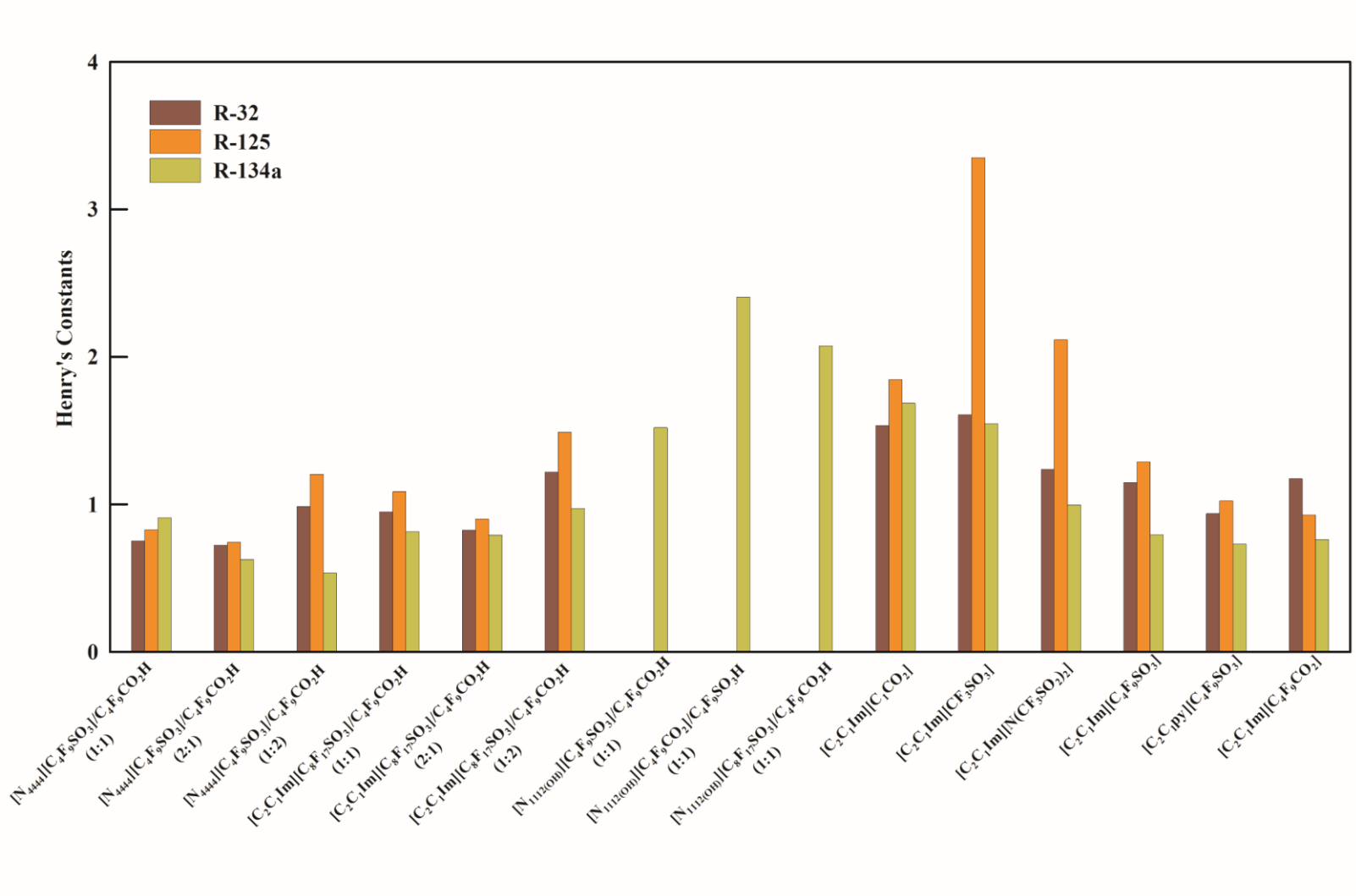


Figure 2.4.21 Henry's law constants (in MPa) determined for the absorption of R-32, R-125 and R-134a in the systems studied in this work, and in selected ILs reported in the literature [29], at 303.15 K.

2.4.2.3 Correlation Using NRTL Model

The experimental solubilization data of a F-gas, i, in an absorbent phase, j, was successfully correlated by the NRTL model [62,89–91]. The results at 303.15 K, 313.15 and 323.15 are plotted in Figures 2.4.10 - 2.4.12 and 2.4.14 - 2.4.17. This thermodynamic model has been shown to adequately correlate systems containing ILs or DESs [29,58–60,92,93]. For further details on the calculation procedure, see Section 2.2. Tables 2.4.4-2.4.7 contain the NRTL parameters and the RMSD values. Since for all systems the obtained dij and dji parameters were zero, $\alpha_{ij} = c_{ij}$ and $\alpha_{ji} = c_{ji}$. Figures 2.4.10 - 2.4.12 and 2.4.14 - 2.4.17 show a good fitting between calculated and experimental data, demonstrating that NRTL correlates satisfactorily the experimental data of F-gas solubility in the studied DESs.

Table 2.4.4 NRTL Parameters obtained for systems R-32 (*i*) + DES (*j*).

	$[N_{4444}][C_4F_9SO_3]/C_4F_9CO_2H$			$[C_2C_1Im][C_8F_{17}SO_3]/C_4F_9CO_2H$		
	(1:1)	**(2:1)**	**(1:2)**	**(1:1)**	**(2:1)**	**(1:2)**
a_{ij}	-7.5951	-7.5494	-8.3474	-7.4190	-3.4371	-3.3949
a_{ji}	20.000	7.4807	16.838	20.000	18.066	20.000
b_{ij} **(K)**	1018.7	937.87	2124.3	1701.5	462.09	566.58
b_{ji} **(K)**	-4451.8	-231.62	-4619.7	-5314.0	-4594.5	-5368.6
c_{ij}	0.10	0.10	0.30	0.25	0.29	0.30
c_{ji}	0.10	0.10	0.30	0.25	0.29	0.30
T_0	0	0	0	0	0	0
RMSD	0.0039	0.0049	0.0016	0.0012	0.0023	0.0027

For all systems, the parameters d_{ij} , d_{ji} , e_{ij} , e_{ji} , f_{ij} ,and f_{ji} were zero, and therefore, $\alpha_{ij}=c_{ij}$ and $\alpha_{ji}=c_{ji}$.

Table 2.4.5 NRTL Parameters obtained for systems R-125 (*i*) + DES (*j*).

	$[N_{4444}][C_4F_9SO_3]/C_4F_9CO_2H$			$[C_2C_1Im][C_8F_{17}SO_3]/C_4F_9CO_2H$		
	(1:1)	**(2:1)**	**(1:2)**	**(1:1)**	**(2:1)**	**(1:2)**
a_{ij}	-4.0047	4.8115	-4.3617	20.000	15.979	20.000
a_{ji}	19.135	-10.065	6.2875	-4.1381	-3.8453	-11.750
b_{ij} **(K)**	711.91	-1496.0	1342.3	-5412.5	-4100.5	-5900.2
b_{ji} **(K)**	-5107.5	2883.5	4105.3	826.86	659.87	3457.0
c_{ij}	0.30	0.30	0.30	0.30	0.30	0.30
c_{ji}	0.30	0.30	0.30	0.30	0.30	0.30
T_0	0	0	0	0	0	0
RMSD	0.0013	0.0018	0.0030	0.0039	0.0030	0.0030

For all systems, the parameters d_{ij} , d_{ji} , e_{ij} , e_{ji} , f_{ij} ,and f_{ji} were zero, and therefore, $\alpha_{ij}=c_{ij}$ and $\alpha_{ji}=c_{ji}$.

Table 2.4.6 NRTL Parameters obtained for systems R-134a (*i*) + DES (*j*).

	$[N_{4444}][C_4F_9SO_3]/C_4F_9CO_2H$			$[C_2C_1Im][C_8F_{17}SO_3]/C_4F_9CO_2H$		
	(1:1)	**(2:1)**	**(1:2)**	**(1:1)**	**(2:1)**	**(1:2)**
a_{ij}	-7.9654	-1.3078	20.000	20.000	-7.0374	19.895
a_{ji}	14.981	0.9599	1.5965	-8.4305	-3.1104	-20.000
b_{ij} **(K)**	2173.2	-72.818	9653.9	-5729.5	1869.6	-5961.8
b_{ji} **(K)**	-4058.0	618.71	-620.12	2392.3	1548.2	6180.9
c_{ij}	0.30	0.30	0.10	0.30	0.30	0.30
c_{ji}	0.30	0.30	0.10	0.30	0.30	0.30
T_0	0	0	0	0	0	0
RMSD	0.0039	0.0035	0.0033	0.0043	0.0026	0.0040

For all systems, the parameters d_{ij} , d_{ji} , e_{ij} , e_{ji} , f_{ij} ,and f_{ji} were zero, and therefore, $\alpha_{ij}=c_{ij}$ and $\alpha_{ji}=c_{ji}$.

Table 2.4.7 NRTL Parameters obtained for systems R-134a (*i*) + DES (*j*).

	$[N_{1112(OH)}][C_4F_9SO_3]$/ $C_4F_9CO_2H$ **(1:1)**	$[N_{1112(OH)}][C_4F_9CO_2]$/ $C_4F_9SO_3H$ **(1:1)**	$[N_{1112(OH)}][C_8F_{17}SO_3]$/ $C_4F_9CO_2H$ **(1:1)**
a_{ij}	20.000	20.000	20.000
a_{ji}	20.000	20.000	20.000
b_{ij} **(K)**	-6366.9	-5296.5	-5443.3
b_{ji} **(K)**	-5259.4	-6355.4	-6207.7
α_{ij}	0.10	0.10	0.10
α_{ji}	0.10	0.10	0.10
T_0	0	0	0
RMSD	0.0001	0.0001	0.0001

For all systems, the parameters d_{ij} , d_{ji} , e_{ij} , e_{ji} , f_{ij} ,and f_{ji} were zero, and therefore, $\alpha_{ij}=c_{ij}$ and $\alpha_{ji}=c_{ji}$.

2.4.2.5 Ideal selectivity

The capacity of an absorbent to selectively absorb a F-gas from a gas mixture is of vital importance for the design of specific gas separation processes. Considering the absorption isotherms determined for each F-gas in $[N_{4444}][C_4F_9SO_3]$:$C_4F_9CO_2H$ and $[C_2C_1Im][C_8F_{17}SO_3]$:$C_4F_9CO_2H$ at the molar ratios of 1:1, 2:1, and 1:2, we determined the ideal selectivity of each DES for each component of binary F-gas mixtures, over the full pressure range spanned experimentally. The ideal selectivity for a binary pair of gases i and j at a given pressure P and temperature T is expressed as the ratio of pure-gas solubilities in the DES:

$$S_{ij}=\left(\frac{x_i}{x_j}\right)_{P,T} \qquad 2.4.10$$

where x_i is the molar fraction of the absorbed gas i in the DES in equilibrium with its pure-vapor phase at pressure P and temperature T.

Figures 2.4.22 to 2.4.24 show the selectivities R-32/R-125, R-134a/R-125, and R-134a/R-32 at 303.15 K, 313.15 K, and 323.15 K, respectively (see also Tables 2.4.18 to 2.4.20).

R-32/R-125 selectivities (Panel A of Figures 2.4.22 to 2.4.24) are close to 1 at pressures above 0.2 MPa at the 3 tested temperatures. At pressures below 0.2 MPa, $[N_{4444}][C_4F_9SO_3]$:$C_4F_9CO_2H$ (1:1), $[N_{4444}][C_4F_9SO_3]$:$C_4F_9CO_2H$ (1:2), $[C_2C_1Im][C_8F_{17}SO_3]$:$C_4F_9CO_2H$ (1:1) (at 313.15 K and 323.15 K), and $[C_2C_1Im][C_8F_{17}SO_3]$:$C_4F_9CO_2H$ (1:2) (at 303.15 K) are selective towards R-32. Meanwhile, $[N_{4444}][C_4F_9SO_3]$:$C_4F_9CO_2H$ (2:1), $[C_2C_1Im][C_8F_{17}SO_3]$:$C_4F_9CO_2H$ (2:1), and $[C_2C_1Im][C_8F_{17}SO_3]$:$C_4F_9CO_2H$ (1:2) (only at 323.15 K) are selective toward R-125.

At pressures above 0.2 MPa, all DES are selective towards R-134a over R-32 and R-125, with selectivity values close to 2, at all tested temperatures. At pressures bellow 0.2 MPa, higher R-134a/R-125 selectivities (Panel B of Figures 2.4.22 to 2.4.24) were obtained for $[N_{4444}][C_4F_9SO_3]$:$C_4F_9CO_2H$ (1:2) and $[C_2C_1Im][C_8F_{17}SO_3]$:$C_4F_9CO_2H$ (1:2) at 303.15 K and 313.15 K, and for $[C_2C_1Im][C_8F_{17}SO_3]$:$C_4F_9CO_2H$ (1:1) at 323.15 K. Higher R-134a/R-32 selectivities (Panel C of Figures 2.4.22 to 2.4.24) were obtained at low pressures for $[C_2C_1Im][C_8F_{17}SO_3]$:$C_4F_9CO_2H$ (1:2) (at 313.15 K and 323.15 K) and $[C_2C_1Im][C_8F_{17}SO_3]$:$C_4F_9CO_2H$ (2:1) (at 323.15 K), while higher selectivity towards R-32 was obtained for $[N_{4444}][C_4F_9SO_3]$:$C_4F_9CO_2H$ (1:1).

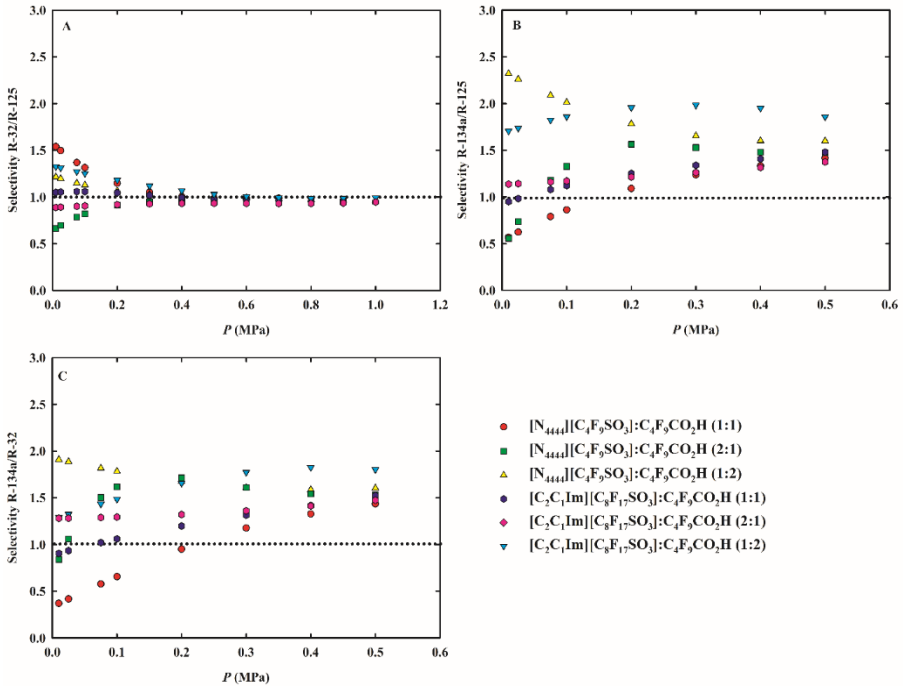


Figure 2.4.22 Ideal selectivities of the systems studied in this work towards: a) R-32 over R-125, b) R-134a over R-125 and c) R-134a over R-32 at 303.15 K.

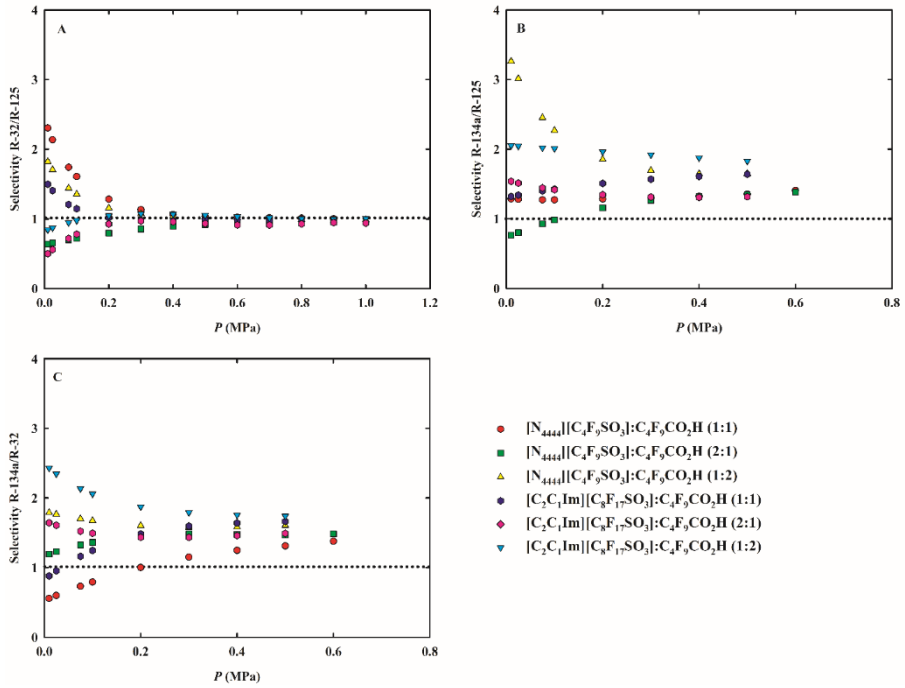


Figure 2.4.23 Ideal selectivities of the systems studied in this work towards: a) R-32 over R-125, b) R-134a over R-125, and c) R-134a over R-32 at 313.15 K.

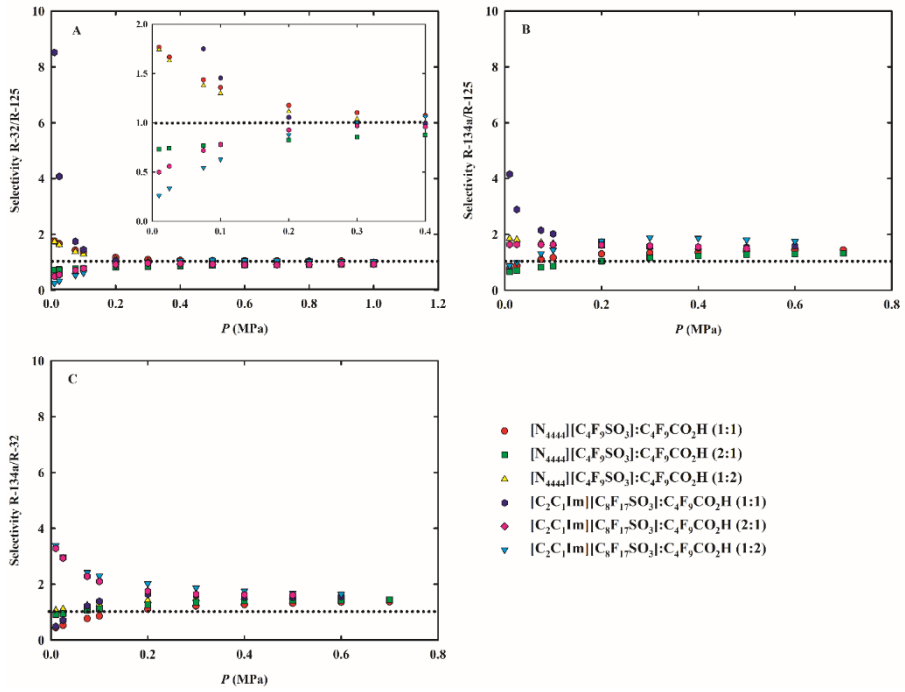


Figure 2.4.24 Ideal selectivities of the systems studied in this work towards: a) R-32 over R-125, b) where an amplification of the selectivities range of 0−2 and pressures range of 0-0.4 was incorporated for better visualization), R-134a over R-125 and c) R-134a over R-32 (panel C) at 323.15 K.

The ideal selectivity for each binary pair of gases *i* and *j* was also determined considering the Henry's constants of each gas *i* and *j* in the same absorbent at a specific temperature (*H*i and *H*j) as:

$$S_{ij} = \frac{H_j}{H_i} \qquad 2.4.11$$

The results, presented in Figure 2.4.25, are in clear agreement with the conclusions taken at lower pressures when selectivity was determined through the molar fractions of absorbed gas (Figures 2.4.22 to 2.4.25).

In the present work we also compared the selectivities obtained from the Henry's constants for the studied DES with the ones obtained for the ILs studied in a previous work (Figure 2.4.26) [29]. While highest selectivities for the components of the R-32 + R-125 mixture were obtained for two fluoro-containing ILs and one FIL, the highest selectivities towards R-134a in mixtures with either R-32 or R-125 were obtained for $[N_{4444}][C_4F_9SO_3]$:$C_4F_9CO_2H$ (1:2).

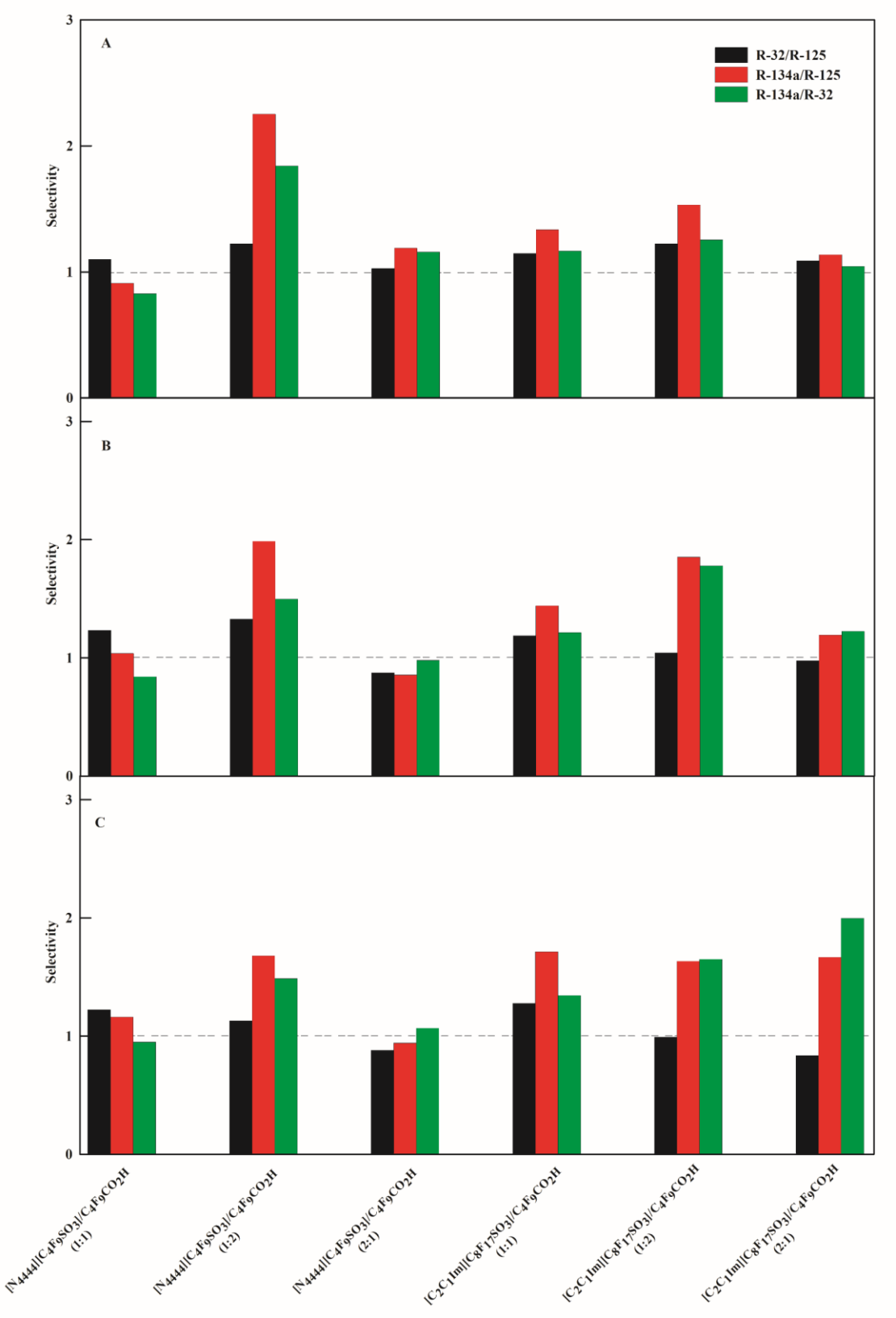


Figure 2.4.25 Ideal selectivities, determined from the Henry's constants, of the systems studied in this work at: a) 303.15 K, b) 313.15 K, and c) 323.15 K.

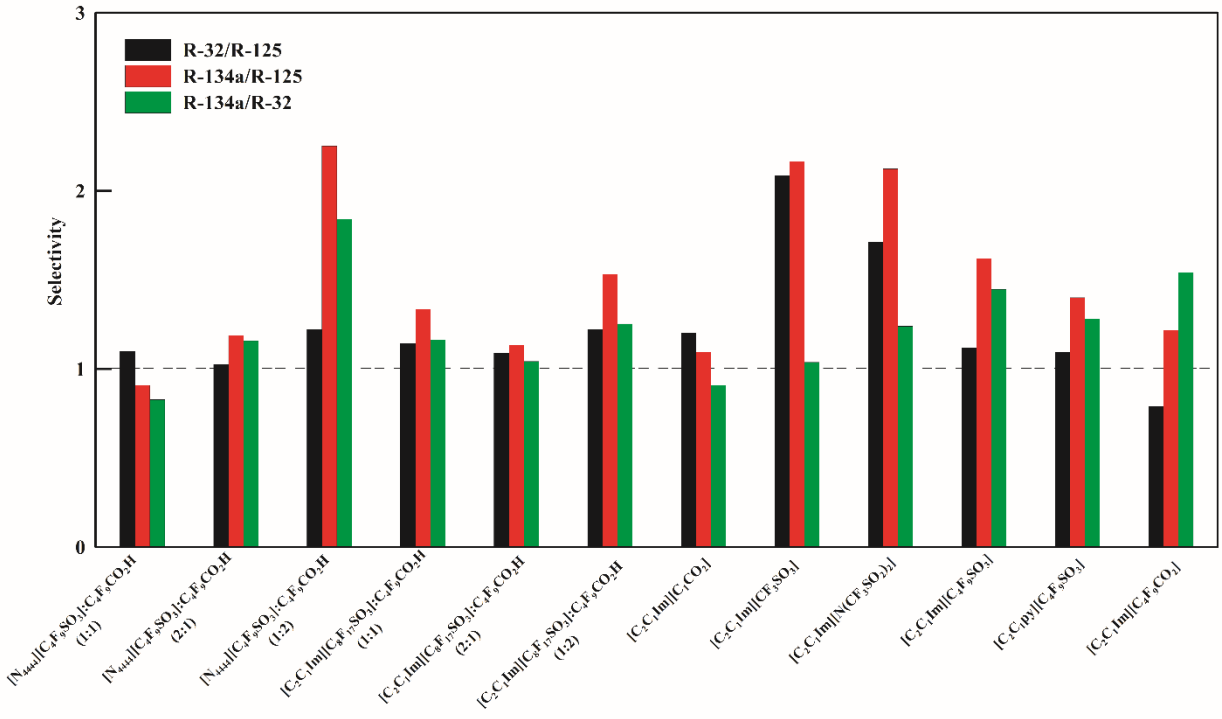


Figure 2.4.26 Ideal selectivities, determined from the Henry's constants, of the systems studied in this work, and of selected ILs reported in the literature, at 303.15 K [29].

2.4.3 Conclusions

In this work, the preparation of eutectic mixtures of FILs with perfluorinated acids allowed us to take advantage of the properties of FILs for the absorption of F-gases, in a wider range of temperatures at which they can be used at liquid state. The initial screening of mixtures prepared with 5 different FILs for the absorption of R-134a showed that the nature of the FIL cation was the major factor impacting in the gas solubilization. Therefore, we selected mixtures of $[N_{4444}][C_4F_9SO_3]$ or $[C_2C_1Im][C_8F_{17}SO_3]$ and n-perfluoropentanoic acid, at different molar ratios, for the absorption of R-32, R-125, and R-134a at 303.15 K, 313.15 K and 323.15 K. The solubilization data were compared using Henry's constants and successfully correlated with the NRTL model for each DES/F-gas system.

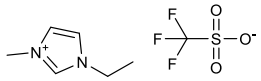
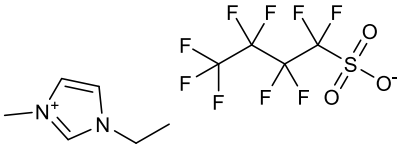
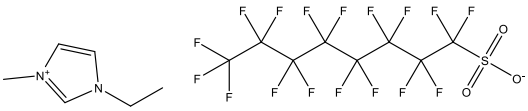
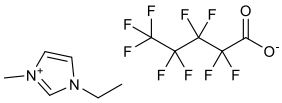
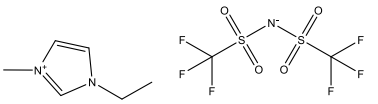
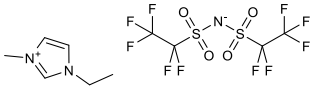
From the three tested gases, R-134a showed the highest solubility in all tested DES, in a wide range of operating pressures. In fact, all studied DES showed ideal selectivity towards R-134a in binary gas mixtures with the other two F-gases, at pressures above 0.2 MPa. At lower pressures, selectivity towards each F-gas could be tuned by selecting the appropriate component ratio of each DES and the temperature of operation.

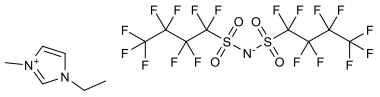
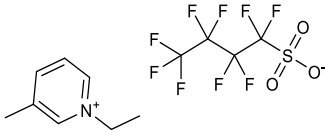
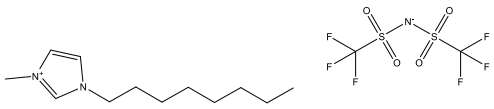
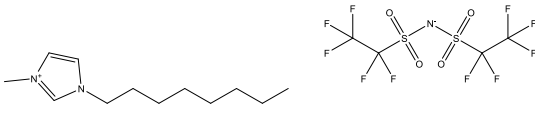
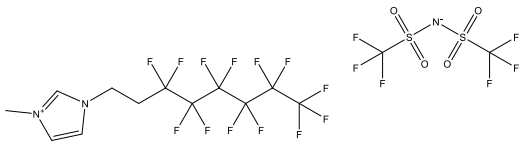
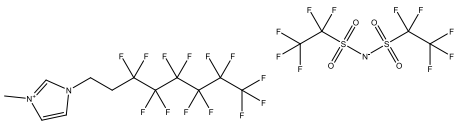
Therefore, this works represents a step forward in the study of alternative solvents, such as FILs and DES, for the selective separation of commercial refrigerants (F-gases mixtures). Furthermore, this study provides tools for the selection and performance enhancement of absorbents for the development and scale-up of specific gas separation processes.

2.5 Process evaluation of fluorinated ionic liquids as F-gas absorbents

The environmental impact generated by fluorinated gases (F-gases) makes essential the development of green technologies to mitigate them. Fluorinated ionic liquids (FILs) emerged as an alternative absorbent due to their unique and exceptional properties. In this work, a COSMO-based/Aspen Plus methodology was applied to evaluate the performance of 12 FILs (see Table 2.5.1) as absorbents in process scale of two F-gases: 1,1,1,2-tetrafluoroethane (R-134a) and difluoromethane (R-32). Results of the absorption column in equilibrium mode revealed that the behavior of FILs is similar in the same conditions, reaching higher efficiencies in the case of absorbing R-134a at high F-gas partial pressure. Rate-based calculations in packing column demonstrated a kinetic control with high viscous FILs, revealing higher performance differences between FIL absorbents. The regeneration stage was also evaluated in near industrial conditions. Operating conditions of the absorption column were optimized with a column of 10 m tall and diameter ranging 1.1-1.2 m at 10 bar of total pressure reaching a 90 % of F gas recovery with L/G ranges between 6-10. Last, preliminary economic analysis revealed an operating cost to recover the 90 % of F-gas of 70 $/ton (R-134a) and 130 $/ton (R-32) with the FIL that revealed the best behavior, 1-ethyl-3-methylimidazolium triflate.

Table 2.5.1 Chemical structures and acronyms of the ionic liquids used in this work.

Ionic Liquid Designation	Molecular Weight	Chemical Structure
1-Ethyl-3-methylimidazolium triflate **[C_2C_1Im][CF_3SO_3]**	264.26	
1-Ethyl-3-methylimidazolium perfluorobutanesulfonate **[C_2C_1Im][$C_4F_9SO_3$]**	410.25	
1-Ethyl-3-methylimidazolium perfluorooctanesulfonate **[C_2C_1Im][$C_8F_{17}SO_3$]**	610.29	
1-Ethyl-3-methylimidazolium perfluoropentanoate **[C_2C_1Im][$C_4F_9CO_2$]**	374.21	
1-Ethyl-3-methylimidazolium bis(trifluoromethylsulfonyl)imide **[C_2C_1Im][$N(CF_3SO_2)_2$]**	391.32	
1-Ethyl-3-methylimidazolium bis(pentafluoroethylsulfonyl)imide **[C_2C_1Im] [$N(C_2F_5SO_2)_2$]**	491.33	

1-Ethyl-3-methylimidazolium bis(nonafluorobutylsulfonyl)imide **[C_2C_1Im][N($C_4F_9SO_2$)$_2$]**	691.362	
1-Ethyl-3-methylpyridinium perfluorobutanesulfonate **[C_2C_1py][$C_4F_9SO_3$]**	421.28	
1-Octyl-3-methylimidazolium bis[trifluoromethylsulfonyl]amide **[C_8C_1Im][N(CF_3SO_2)$_2$]**	475.48	
1-octyl-3-methylimidazolium bis(pentafluoroethylsulfonyl)imide **[C_8C_1Im][N($C_2F_5SO_2$)$_2$]**	856.64	
1-(3,3,4,4,5,5,6,6,7,7,8,8,8-tridecafluorooctyl)-3 methylimidazolium bis(pentafluoroethylsulfonyl)imide **[$C_8H_4F_{13}$Im][N(CF_3SO_2)$_2$]**	709.35	
1-(3,3,4,4,5,5,6,6,7,7,8,8,8-tridecafluorooctyl)-3-methylimidazolium bis(trifluoromethylsulfonyl)imide **[$C_8H_4F_{13}$Im][N($C_2F_5SO_2$)$_2$]**	809.36	

2.5.1 Computational details

2.5.1.1 Component definition and property model specification in Aspen

Aspen Plus v10 was used to model the absorption-regeneration processes. COSMOSAC property model was selected to estimate the activity coefficients of the mixtures involved in the study. First, R-32 and R-134a refrigerant gases were employed as default on the simulation since all the required information is already present on Aspen's databanks. Second, FILs are incorporated to the simulator as pseudo-components using the independent ions model (C+A). Therefore, the files that contain all the FILs information (*.cosmo) were generated using Turbomole v4.5 at BP86/TZVP computational level. Some molecular information is needed to define the IL such as molecular weight, normal boiling point and density as detailed elsewhere [33]. All these properties were estimated using COSMO-RS methodology (COSMOtherm v19) using the *.cosmo files previously created. The complete definition of FILs requires more information for COSMOSAC property model, molecular volume (COSMO volume) and σ-profile were also calculated using COSMO-RS method. Last, experimental viscosity-to-temperature dependence was also included to the simulator in order to perform mass transfer calculations on the column. The complete description of this methodology can be found on our previous publication [33]. The calculated values incorporated to the property system are included on Table 2.5.2 and 2.5.3.

Table 2.5.2 Calculated values used as input for pseudo component and property COSMOSAC specification in Aspen Plus v10 (1).

Property		**$[C_2C_1Im][C_4F_9CO_2]$**	**$[C_2C_1Im][C_4F_9SO_3]$**	**$[C_2C_1Im][C_8F_{17}SO_3]$**	**$[C_2C_1Im][CF_3SO]$**	**$[C_2C_1Im][N(C_2F_5SO_2)_2]$**	**$[C_2C_1Im][N(C_4F_9SO_2)_2]$**
MW		374.20	410.26	610.29	260.24	491.33	691.36
Density, g/mL		1.41	1.45	1.55	1.35	1.48	1.56
CSACVL		374.75	399.96	547.60	282.13	463.18	607.95
NBP, K		1152.38	1315.23	1294.89	1201.73	1271.44	1225.59
Viscos-ity	**1 (A)**	-8.62	-8.94	-	-5.83	-	-
MU-LAND	**2 (B)**	3954.74	4174.95	-	2852.84	-	-
Reference		[61]	[61]		[61]		
SGPRF1-1	1	0.00	0.00	0.00	0.00	0.00	0.00
	2	0.00	0.00	0.00	0.00	0.00	0.00
	3	0.00	0.00	0.00	0.00	0.00	0.00
	4	0.00	0.00	0.00	0.00	0.00	0.00
	5	0.00	0.00	0.00	0.00	0.00	0.00
	6	0.00	0.00	0.00	0.00	0.00	0.00
	7	0.00	0.00	0.00	0.00	0.00	0.00
	8	0.00	0.00	0.00	0.00	0.00	0.00
	9	0.00	0.00	0.00	0.00	0.00	0.00
	10	0.00	0.00	0.00	0.00	0.00	0.00
	11	0.00	0.00	0.01	0.01	0.03	0.03
	12	0.48	0.58	0.59	0.52	0.61	0.73
SGPRF2-1	1	1.93	2.25	2.30	2.03	2.43	2.48
	2	3.73	3.93	4.08	3.75	4.24	3.93
	3	4.47	4.35	4.54	4.22	4.60	4.38
	4	5.76	6.15	6.41	5.66	6.31	6.82
	5	9.73	10.77	11.03	9.80	10.23	10.78
	6	12.16	13.00	13.08	11.88	11.98	11.69
	7	12.14	13.42	13.45	11.89	13.29	13.05

	8	13.79	16.87	16.57	14.50	17.30	17.62
	9	16.98	20.12	19.89	17.94	20.61	20.40
	10	18.11	17.75	19.86	17.57	18.38	18.07
	11	14.90	12.13	16.78	13.35	12.76	14.65
	12	12.10	11.01	17.08	9.63	12.26	18.09
SGPRF3-1	1	15.59	16.64	30.75	9.36	19.57	33.43
	2	24.78	28.28	58.27	11.95	33.57	64.07
	3	34.06	39.51	68.68	14.69	46.98	81.94
	4	33.00	34.87	43.84	16.93	41.48	56.00
	5	21.32	17.25	16.60	16.19	20.57	20.07
	6	12.22	6.15	6.64	9.83	8.32	6.91
	7	7.68	4.14	4.41	3.95	5.23	4.12
	8	3.80	3.22	3.09	1.88	3.35	2.79
	9	2.12	1.68	1.52	1.63	3.64	3.21
	10	1.76	1.08	1.28	2.35	5.09	4.56
	11	1.58	1.60	1.98	3.25	8.52	8.93
	12	1.89	2.11	2.77	4.11	12.70	13.85
SGPRF4-1	1	2.21	3.25	5.02	5.30	12.87	13.10
	2	1.98	6.17	8.36	6.83	8.52	7.91
	3	1.95	9.57	10.41	8.15	3.52	2.98
	4	2.46	10.58	9.89	8.56	0.94	0.50
	5	3.60	7.61	6.20	6.17	0.28	0.00
	6	4.82	3.08	1.84	2.16	0.05	0.00
	7	4.67	0.54	0.09	0.19	0.00	0.00
	8	3.50	0.01	0.00	0.00	0.00	0.00
	9	2.08	0.00	0.00	0.00	0.00	0.00
	10	0.84	0.00	0.00	0.00	0.00	0.00
	11	0.19	0.00	0.00	0.00	0.00	0.00

	12	0.00	0.00	0.00	0.00	0.00	0.00
SGPRF5-1	1	0.00	0.00	0.00	0.00	0.00	0.00
	2	0.00	0.00	0.00	0.00	0.00	0.00
	3	0.00	0.00	0.00	0.00	0.00	0.00
	4	0.00	0.00	0.00	0.00	0.00	0.00
	5	0.00	0.00	0.00	0.00	0.00	0.00
	6	0.00	0.00	0.00	0.00	0.00	0.00
	7	0.00	0.00	0.00	0.00	0.00	0.00
	8	0.00	0.00	0.00	0.00	0.00	0.00
	9	0.00	0.00	0.00	0.00	0.00	0.00
	10	0.00	0.00	0.00	0.00	0.00	0.00
	11	0.00	0.00	0.00	0.00	0.00	0.00
	12	0.00	0.00	0.00	0.00	0.00	0.00

Table 2.5.3 Calculated values used as input for pseudo component and property COSMOSAC specification in Aspen Plus v10 (2).

Property		**[C_2C1Im] [N(CF3SO2)2]**	**[C_2C_1py] [$C_4F_9SO_3$]**	**[$C_8H_4F1_3$Im] [$N(CF_3SO_2)_2$]**	**[$C_8H_4F_{13}$Im] [$(CF_3SO_2)_2$]**	**[$C_8H_4F_{13}$Im] [$N(C_2F_5SO_2)_2$]**
MW		391.31	421.28	575.49	809.36	709.35
Density, g/mL		1.42	1.46	1.33	1.58	1.61
CSACVL		385.34	411.70	588.23	703.87	616.63
NBP, K		1084.43	1357.40	1126.13	1354.67	1241.86
Viscosity	**1 (A)**	-7.33	-12.79	-9.42	-12.15	-12.36
MULAND	**2 (B)**	3238.71	5408.33	4340.85	5861.66	5782.39
Reference		[71]	[18]	[30]	[30]	[30]
SGPRF1-1	1	0.00	0.00	0.00	0.00	0.00
	2	0.00	0.00	0.00	0.00	0.00
	3	0.00	0.00	0.00	0.00	0.00
	4	0.00	0.00	0.00	0.00	0.00
	5	0.00	0.00	0.00	0.00	0.00
	6	0.00	0.00	0.00	0.00	0.00
	7	0.00	0.00	0.00	0.00	0.00
	8	0.00	0.00	0.00	0.00	0.00
	9	0.00	0.00	0.00	0.00	0.07
	10	0.00	0.00	0.00	0.16	0.35
	11	0.02	0.11	0.02	0.70	1.01
	12	0.56	0.76	0.57	2.00	2.38
SGPRF2-1	1	2.22	1.63	2.20	4.94	4.85
	2	4.04	2.73	3.91	7.98	6.72
	3	4.31	5.29	4.31	9.17	7.41
	4	5.39	7.71	5.37	10.05	9.39
	5	8.86	8.21	8.34	10.82	10.81
	6	10.07	10.45	9.13	11.50	9.91
	7	10.30	14.71	8.83	12.36	10.33
	8	14.40	16.89	12.30	12.30	12.94

	9	18.89	17.81	18.69	11.99	14.02
	10	18.69	18.16	25.17	11.78	13.12
	11	15.41	17.30	30.51	13.55	14.88
	12	13.83	17.93	34.83	20.26	20.17
SGPRF3-1	1	16.85	22.37	38.41	37.22	33.74
	2	24.33	30.89	46.34	72.16	61.88
	3	33.13	38.92	58.66	97.29	81.76
	4	31.19	33.58	54.37	74.83	63.93
	5	15.81	16.65	30.69	31.83	27.50
	6	5.79	6.02	12.69	9.80	7.90
	7	4.58	4.09	5.49	5.24	3.84
	8	4.48	3.62	3.44	4.66	3.87
	9	5.47	2.59	4.44	4.77	5.62
	10	6.27	1.71	5.45	5.03	6.83
	11	7.95	1.97	8.72	7.63	9.27
	12	11.56	2.89	12.48	11.46	12.90
SGPRF4-1	1	12.40	4.89	11.38	11.87	12.67
	2	8.09	8.06	6.33	8.10	7.83
	3	2.79	9.93	1.81	3.31	2.56
	4	0.30	9.31	0.08	0.79	0.21
	5	0.00	6.07	0.00	0.19	0.00
	6	0.00	1.95	0.00	0.02	0.00
	7	0.00	0.12	0.00	0.00	0.00
	8	0.00	0.00	0.00	0.00	0.00
	9	0.00	0.00	0.00	0.00	0.00
	10	0.00	0.00	0.00	0.00	0.00
	11	0.00	0.00	0.00	0.00	0.00
	12	0.00	0.00	0.00	0.00	0.00

SGPRF5-1	1	0.00	0.00	0.00	0.00	0.00
	2	0.00	0.00	0.00	0.00	0.00
	3	0.00	0.00	0.00	0.00	0.00
	4	0.00	0.00	0.00	0.00	0.00
	5	0.00	0.00	0.00	0.00	0.00
	6	0.00	0.00	0.00	0.00	0.00
	7	0.00	0.00	0.00	0.00	0.00
	8	0.00	0.00	0.00	0.00	0.00
	9	0.00	0.00	0.00	0.00	0.00
	10	0.00	0.00	0.00	0.00	0.00
	11	0.00	0.00	0.00	0.00	0.00
	12	0.00	0.00	0.00	0.00	0.00

2.5.1.2 Fluorinated gas absorption

The absorption column was simulated with the RADFRAC model implemented in Aspen Plus v10. It allows us to use two operating modes: Equilibrium (only thermodynamic equilibrium is considered) and Rate-Based (mass transfer kinetics is also included on calculations). The fluorinated gas inlet consists of an inert gas (Ar) and the refrigerant in each case (R-32 or R-134a). They were considered two HFC partial pressures (0.02 and 1 bar) in order to compare different conditions. The gas flow was maintained at 10 kg/h (100 L/min) as reference of pilot plant to compare all the cases in good agreement with that used in previous work [34,39]. The base case operates at 298.15 K of temperature and 1 bar of total pressure. Then, different scenarios were considered. First, RADFRAC in equilibrium mode was simulated at two different refrigerant partial pressures and changing the absorbent/gas ratio that is fed to the column, using a column with 5 stages. Second, using Rate-Based mode, the operating temperature was changed from 278.15 to 323.15 K and HFC recoveries were compared with those obtained in equilibrium mode. KOCH metal packing (700Y) was selected with a column height of 1 m as reference and 5 stages for calculations. The diameter of the column was calculated using the "Packing Sizing" utility ensuring a fractional approach to maximum capacity of 80 %.

2.5.1.3 Complete process

The complete process was modeled using RADFRAC in Rate-Based mode for both absorption and desorption operations (see Figure 2.5.1). The gas flow was increased to 10 ton/h in order to simulate

near industrial conditions and the HFC concentration was maintained at 2% balanced with Argon. The gas flow matches typical industrial flue gas streams [41,94,95], and low concentrations are evaluated since we consider F-gases as contaminants at low partial pressures. Consequently, absorption column height was risen to 10 meters with the FLEXIPAC KOCH metal packing (700Y) and five stages. As before, rating calculations were applied to calculate the column diameter needed to ensure a fractional approach to maximum capacity of 80 % in each case.

In all cases, the absorption column operates at 298.15 K. First, the total pressure of the absorption column was changed to optimize the operating conditions of the unit. As a result, HFC recoveries and diameters were obtained. Then, the desorption column was also modeled using RADFRAC in rate-based mode with the specification of no condenser with a kettle-type reboiler. The dimensions of the column are 10 m height with five equilibrium stages and FLEXIPAC KOCH metal packing (700Y). The diameter was calculated to ensure an 80% of fractional approach to the maximum capacity. The reboiler duty was calculated to ensure a temperature at the bottom of the column of 423.15 K for each case, to ensure the thermal stability of the FIL/ILs. The pressure of the desorption column was varied from 0.1 to 1 bar. Final simulations for the economic analysis used 0.1 bar of pressure on the regeneration column because higher recoveries were obtained.

Regarding the preliminary economic analysis of the process, operating costs were detailed as: pump (recycle the FIL/IL to the absorption column); compressor (estimate the consumption of vacuum on the regenerator); and heat exchangers (reboiler of the column and cooler prior to absorption column). The power consumptions of the pump and compressor were calculated with a pumping/compression efficiency of 65 % and an electric motor efficiency of 85 %. Their operating cost was then calculated using the electricity utility. MP steam was used in the reboiler of the desorption column, and water was used as cooler. All computations used the utility costs as default on Aspen Plus. The investment cost was estimated based on the equipment installation cost. We have decided to neglect the ionic liquid's cost since it is not easy to estimate FIL/ILs cost when produced in largescale.

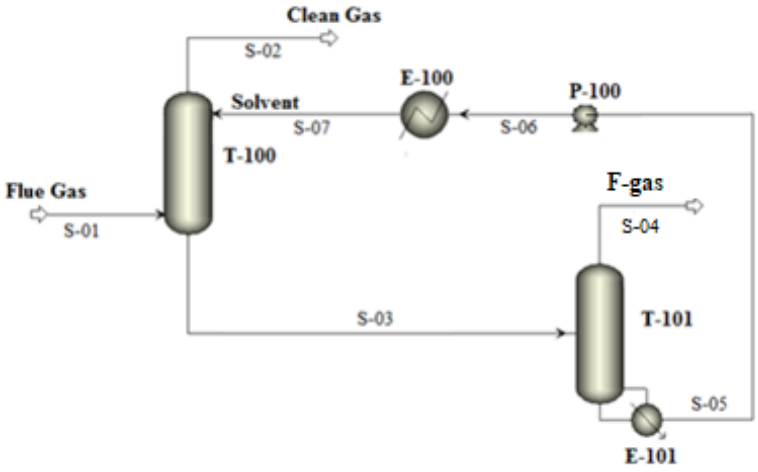


Figure 2.5.1 Complete process scheme used in Aspen Plus v10.

2.5.2 Results and discussion

2.5.2.1 Gas−Liquid equilibria validation

The COSMO-based/Aspen methodology was validated by comparing experimental gas-liquid equilibria data with those calculated by Aspen Plus. At this point, COSMOSAC property model implemented in Aspen Plus allows the use of three different equations for the calculation of mixtures activity coefficients: (i) the original COSMO-SAC model proposed by Lin and Sandler [95]; (ii) the original COSMO-RS model proposed by Klamt [96]; and (iii) the modification to the Lin and Sandler model developed by Mathias *et al* [97]. In this work, we used COSMOSAC property model 2 (original COSMO-RS method). This model presented the lowest deviations from experimental data compared to the other two.

Figure 2.5.2 shows the Henry's law constants validation not only for HFCs but also for other solutes of interest [39,40]. This validation includes those FILs of Table 2.5.1 with available experimental data that present HFC physical absorption.

As can be seen, fluorinated gases follow the expected general trend, giving reasonably good results (slope = 0.98, $R^2 > 0.97$, $\sigma = 0.88$). This figure let us not only validate COSMO-RS predictions but also give an idea of F-gas absorption by ILs in the context of different solutes, such as aromatics, acid gases, or inert gases, among others.

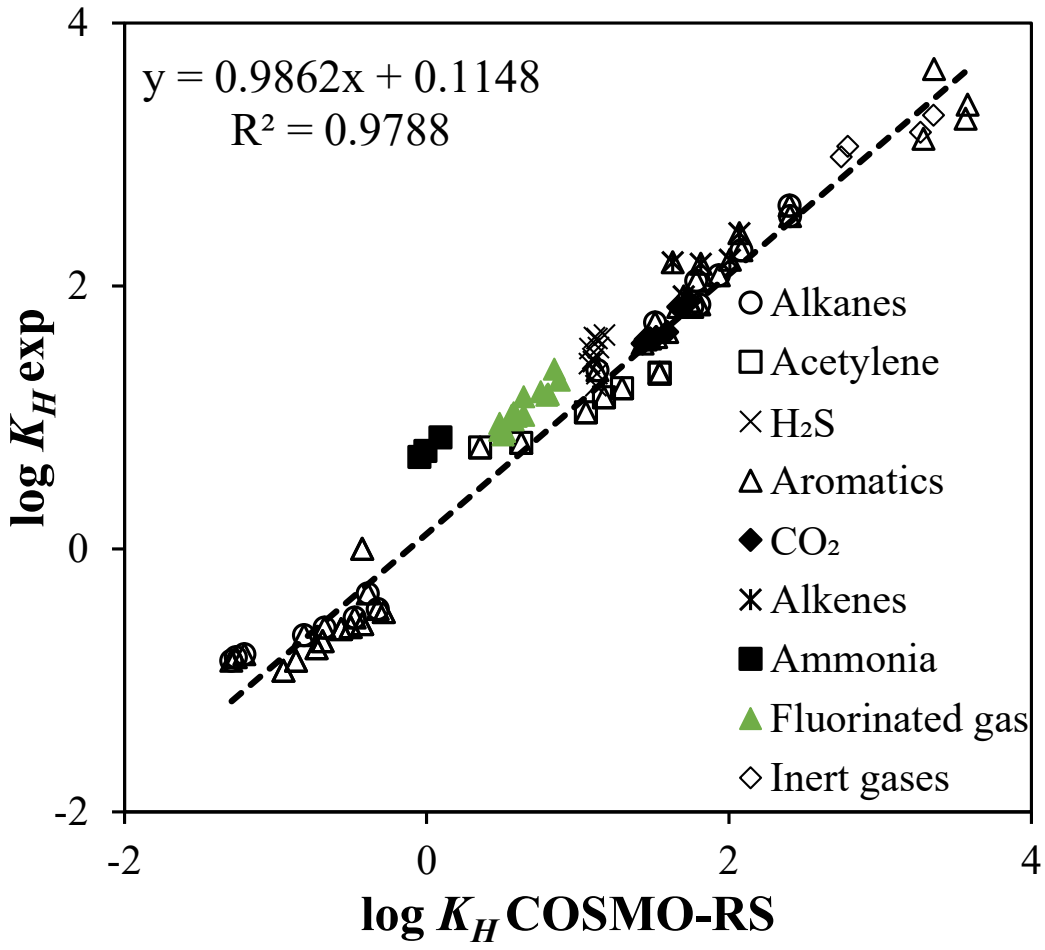


Figure 2.5.2 Validation of Henry's law constant prediction: [C+A] model using COSMO-based/Aspen calculations at T = 298 K using COSMO-RS model [96].

Moreover, Figure 2.5.3 shows the experimental molar solubility of the two HFCs in the selected FIL/ILs against the calculated ones at two different partial pressures. As can be seen, COSMO-based/Aspen methodology predicts reasonably well (mean relative deviation ≈ 30 %) the experimental gas solubility behavior under the operating conditions and HFC-FIL/IL systems of interest. The obtained prediction of gas–liquid equilibrium thermodynamics of HFC-FIL/IL mixtures is good enough to proceed to first stages of the conceptual design of new separation processes [26]. Validation tests carried out with both Henry's law constants and solubilities at two different partial pressures obtaining MRD lower than 30 % compared to available literature experimental data are considered enough for the objectives of this work. Solubility validation covers the whole range tested on the different analyses carried out, from low partial pressures (0.02 bar) to moderate partial pressures (1 bar).

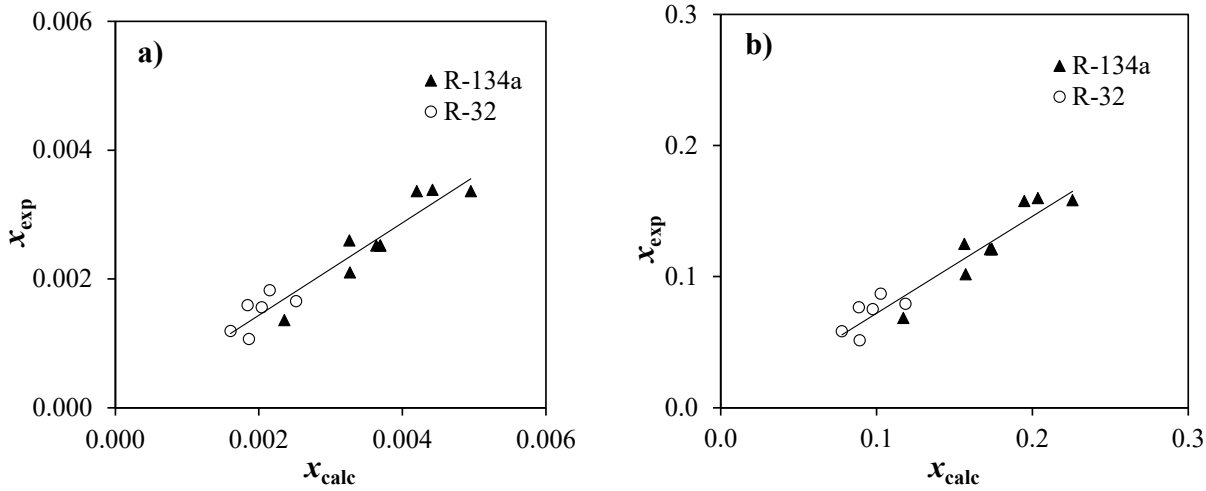


Figure 2.5.3 Experimental molar solubility of HFC in FILs and comparison with the values predicted in COSMO-based/Aspen Plus approach at T = 298 K at HFC partial pressure of: a) 0.02 bar; and b) 1 bar.

2.5.2.2 HFC absorption operation

Once the COSMO-based/Aspen approach was validated, different process simulations were carried out to systematically evaluate the performance of the selected FIL/ILs in HFC capture from gas streams with different concentrations of solute, using a packed absorption column. First, the performance of the selected FIL/ILs was evaluated by modeling the RADFRAC absorption column in equilibrium mode (only absorption thermodynamics is considered) at a given number of stages (5) and operating temperature (298.15 K). Figure 2.5.4 shows the HFC recovery at the given 0.02 bar of HFC partial pressure for the two systems containing R-134a (a) and R-32 (b) at different L/G ratios (in mass units) for the evaluated FIL/ILs. The mass units were selected to evaluate FIL/IL consumption since it is one of the industrial criteria for this kind of operations. Higher relative HFC recoveries were found on mixtures containing R-134a (30–75 %) compared to the ones including R-32 (20–25 %), a result in good agreement with experimental gas solubilities reported in previous publications [29,30].

It is observed that an increase in IL mass flow leads to higher HFC recoveries. In fact, the calculated HFC recoveries are relatively low (with values up to 75 % in the case of R-134a and 25 % in the case of R-32), compared to other solutes (CO_2, H_2S) under similar operating conditions [40,41]. In this sense, the presence of more atoms of fluorine seems to imply higher absorption capacities by FIL/ILs, as we analyzed in more detail below. It is important to consider that the low HFC recoveries obtained are due to the combinations of low gas solubility of the HFC in FIL/ILs and the low HFC partial pressures in absorption columns. For this reason, we have also evaluated the HFC recoveries by absorption with FIL/IL in the same column using an HFC partial pressure of 1 bar and different L/G ratios (in mass units) for (a) R-134a and (b) R-32 systems Figure 2.5.5. As expected, more efficient HFC capture was achieved, reaching relative HFC recoveries of 60–90 % for mixtures containing R-134a and 25–50 % for the ones including R-32.

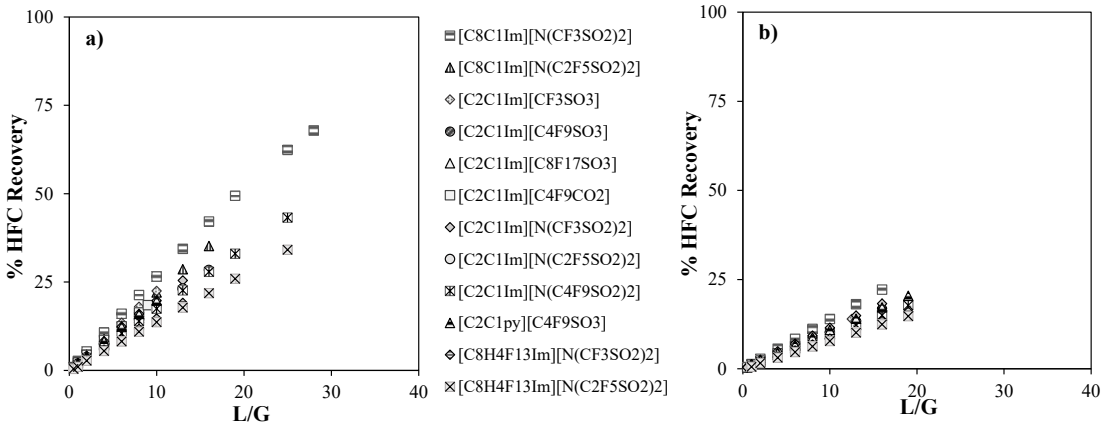


Figure 2.5.4 HFC recovery as a function of L/G ratio (in mass unit) at T = 298 K and HFC partial pressure of 0.02 bar for systems: a) R-134a and b) R-32 for a RADFRAC column in equilibrium mode.

To facilitate the comparison between the performances of different absorbents, Figure 2.5.5. shows relative HFC recoveries by the studied FIL/ILs at a given L/G of 6 (common value in industrial absorption operations [98]) and at two different partial pressures for R-134a (a) and R-32 (b). First, relative HFC recoveries are found to be higher in the case of R-134a compared to R-32, in good agreement with the conclusions extracted above and in previous works [9,29,30].

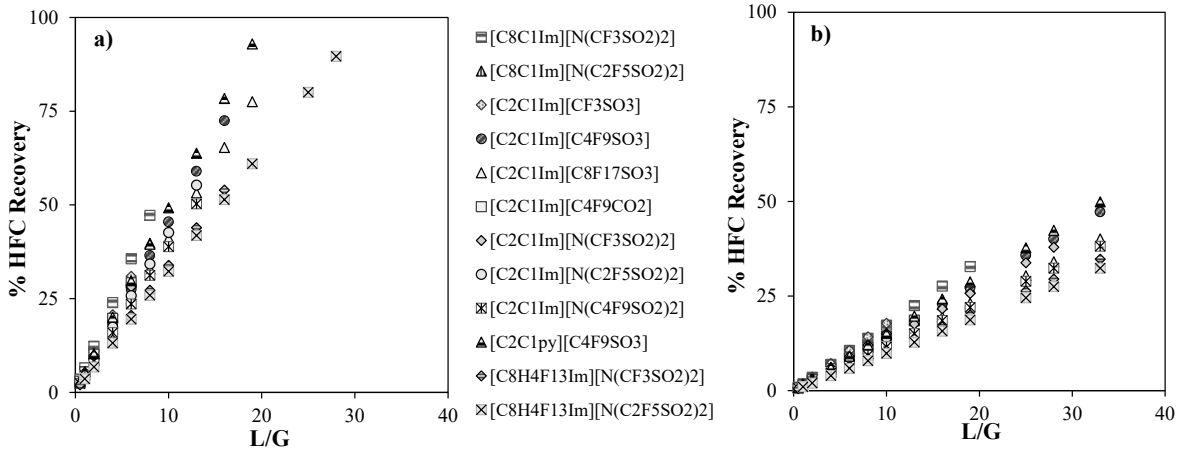


Figure 2.5.5 HFC recovery as a function of L/G ratio at T = 298 K and HFC partial pressure of 1 bar for systems: a) R-134a and b) R-32 for a RADFRAC column in equilibrium mode.

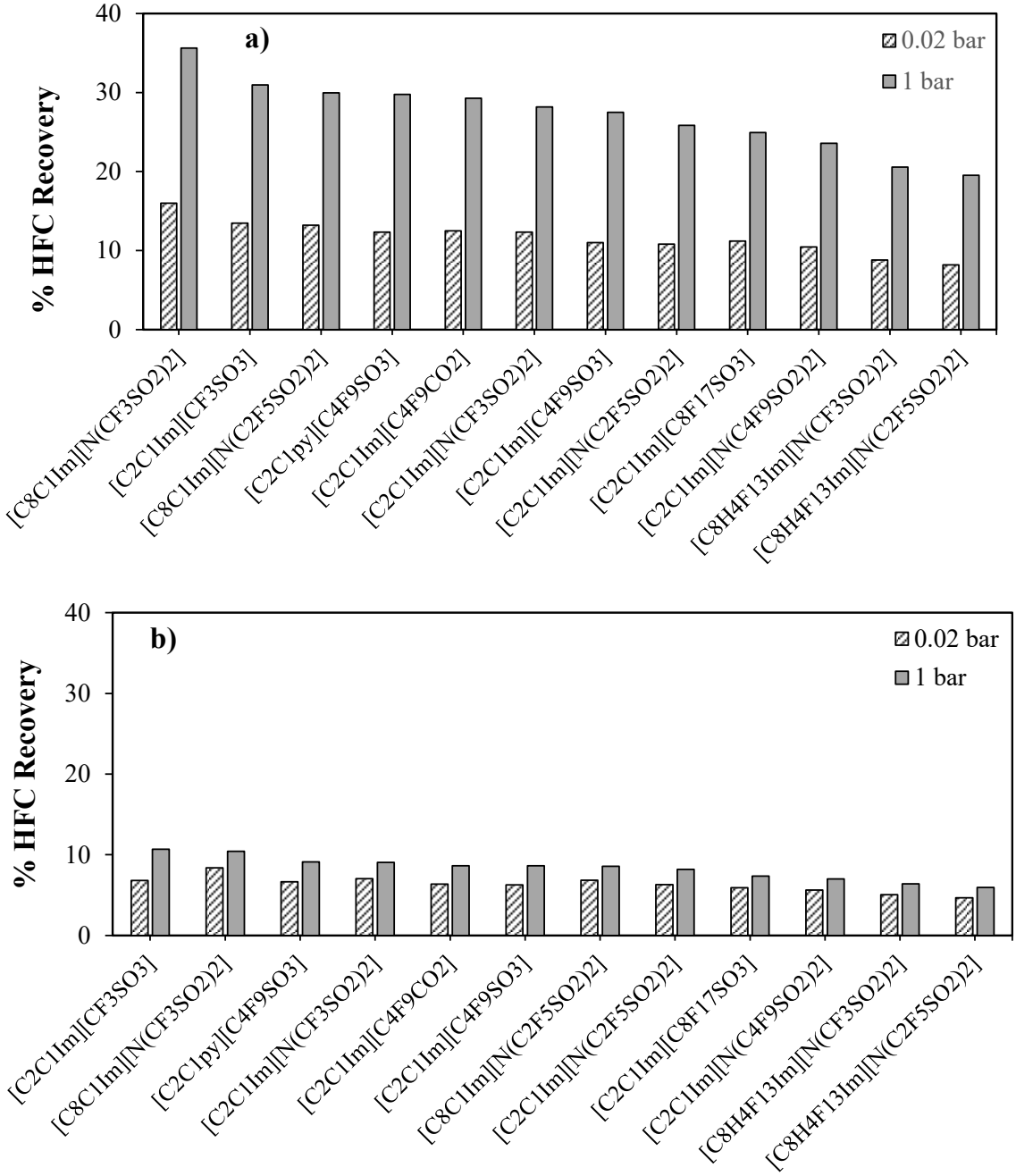


Figure 2.5.6 HFC recovery for different FIL/ILs tested on this work at $T = 298$ K, L/G=6 and HFC partial pressure of 0.02 and 1 bar for systems: a) R-134a and b) R-32 for a RADFRAC column in equilibrium mode.

The effect of changing the cation, the anion, or the presence of fluorinated chains on both the cation and anion and of the functional groups of the anion (carboxylate or sulfonate) can be identified from the observation of Figure 2.5.6. Even if the relative HFC recoveries are low and similar for all FIL/ILs used, in the case of R-134a, we can observe higher differences (20–35 %) between the used FIL/ILs, with $[C_8C_1im][N(CF_3SO_2)_2]$ being the IL showing the best performance. For R-125, $[C_2C_1im][CF_3SO_3]$ is the IL that exhibits the highest recoveries. As far as the different cations are concerned, no significant differences are found in the absorption of the different HFCs that reach almost the same recoveries for the two systems ($[C_2C_1py][C_4F_9SO_3]$) and ($[C_2C_1Im][C_4F_9SO_3]$), in good

agreement with previous work [29]. This is related to almost the same thermodynamic behavior (mole fraction solubilities of 0.17 in both cases for R-134a system at p_{HFC} = 1 bar) and close molecular weights. Since we have fixed the mass absorbent flow, the presence of fluorine atoms on the cation appears to negatively affect the HFC absorption, due to the increase of the IL molar weight. Regarding the alkyl chain of the cation, higher recoveries were found for IL with longer alkyl side chains on the imidazolium cation using the same anion, which is in good agreement with mole fraction solubilities previously studied [29] (0.22 for $[C_8C_1Im][N(CF_3SO_2)_2]$ and 0.15 for $[C_2C_1Im][N(CF_3SO_2)_2]$ in R-134a systems at p_{HFC} = 1 bar).

HFC recoveries can also be compared by changing the partial pressure of the gas. In the case of R-134a (Figure 2.5.6a), significantly higher recoveries were found when increasing the partial pressure. On the contrary, in the case of R-32, the HFC recoveries reached are almost the same. This may be explained by the differences found on R-134a absorption isotherms compared to R-32 ones.

In sum, current thermodynamic simulation analysis describes the HFC capture by absorption with FIL/ILs as a challenging issue, where both the absorbent nature and the operating conditions should be carefully selected to obtain the higher possible efficiency.

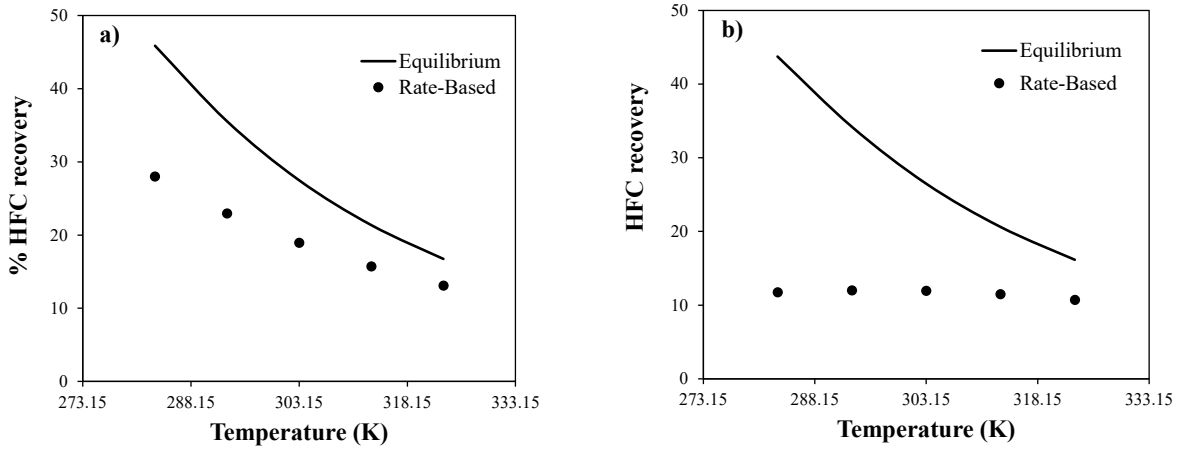


Figure 2.5.7 HFC recovery as a function of the temperature using equilibrium and rate-based mode of RADFRAC column at L/G=6 and 1 bar of partial pressure for the systems: (a) R-134a-$[C_2C_1Im][CF_3SO_3]$; and (b) R-134a-$[C_2C_1py][C_4F_9SO_3]$.

Subsequently, the HFC absorption by FIL/ILs was evaluated in the RADFRAC column in rate-based mode. This allows us to evaluate if mass transfer kinetics is controlling the operation, as previously observed with CO_2 physical absorption in other ILs [41]. Figure 2.5.7 compares R-134a recoveries as a function of temperature obtained by equilibrium- and rate-based calculations under the same conditions for two FIL/ILs with remarkably different transport properties: $[C_2C_1Im][CF_3SO_3]$ (Figure 2.5.7a) presents the lowest viscosity (41.9 cP at 298.15 K [61]), and $[C_2C_1py][C_4F_9SO_3]$ (Figure 2.5.7b) the highest viscosity (209.8 cP at 298.15 K [18]). As can be seen, a lower HFC capture is obtained with the more rigorous rate-based mode (mass transfer kinetics is also considered) compared to the equilibrium mode (only thermodynamic equilibrium is implemented in calculations). However, for the case of

the lowest-viscosity IL (Figure 2.5.7a), kinetic control is not very significant, and the recovery trends are governed by thermodynamics. At low temperatures, mass transfer kinetics has a greater influence on the process, decreasing HFC recovery due to the higher viscosity of IL media. In contrast, relevant differences are found in rate-based mode when using the highest-viscosity IL (Figure 2.5.7b), with a lower HFC recovery at near-room temperatures. It means that mass transfer kinetics is the controlling stage on HFC absorption in packed columns employing FIL/ILs with high viscosity values. Similar conclusions were achieved when analyzing the absorption of R-32 by FIL/IL/IL using RADFRAC rate-based simulations (see Figure 2.5.8).

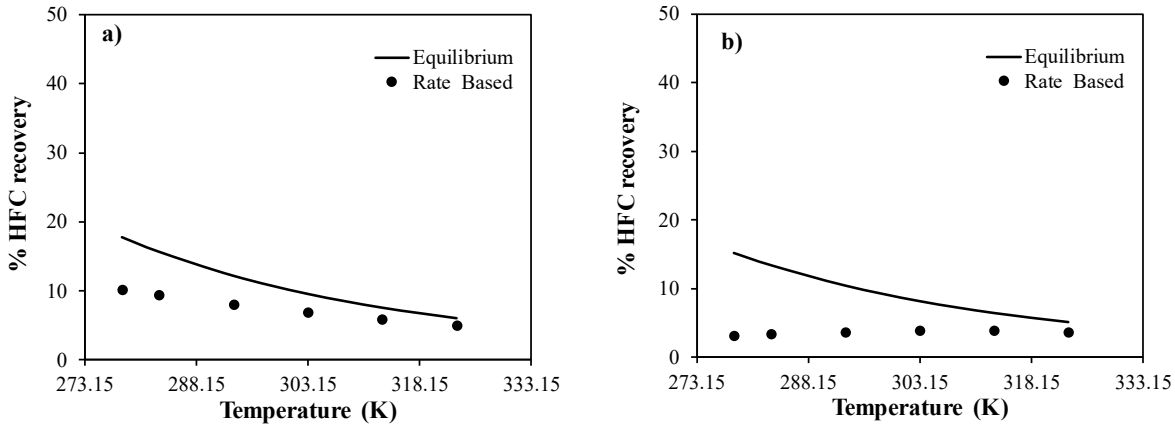


Figure 2.5.8 HFC recovery as a function of the temperature using equilibrium and rate-based mode of RADFRAC column at L/G=6 and 1 bar of partial pressure for the systems: (a) R-32-[C_2C_1Im][CF_3SO_3]; and (b) R-32-[C_2C_1py][$C_4F_9SO_3$].

The current results indicate the need of considering viscosity as a key property in the selection of FIL/ILs for practical applications in HFC capture. Figure 2.5.9 represents HFC recoveries in rate-based mode as a function of viscosity for different systems. As can be seen, recoveries seem to be directly related to the viscosity of the IL, with higher recoveries being calculated for FIL/ILs with lower viscosity.

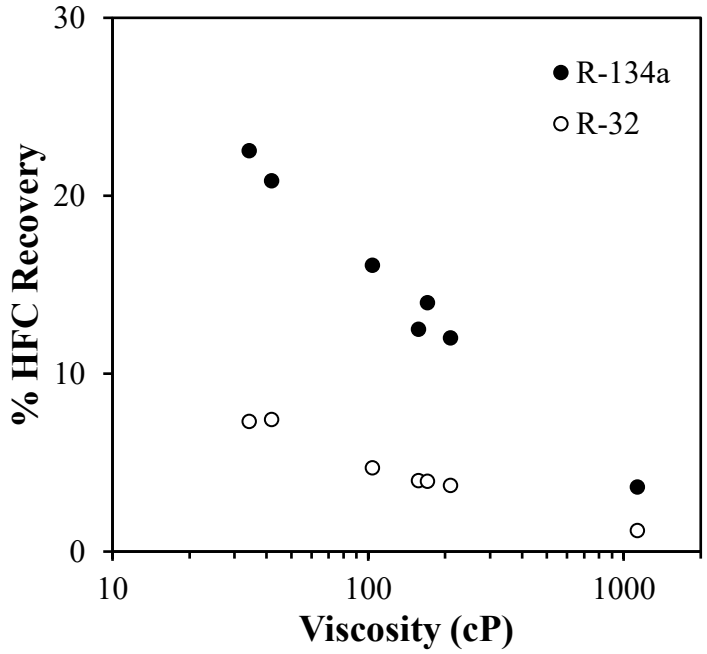


Figure 2.5.9 HFC recoveries in rate-based mode as a function of the viscosity (T=298.15 K) for the FIL/ILs tested on this work at L/G=6 and 1 bar of partial pressure.

To complete the analysis, Figure 2.5.10 shows HFC recoveries in rate-based mode against recoveries in equilibrium mode for all of the studied HFC/FIL/ILs systems. In general, it is observed that HFC recovery achieved with the most rigorous rate-based calculations follows the trend obtained when only considering gas–liquid equilibrium. It should be noted that FIL/ILs with lower molecular weight lead to more favorable HFC absorption thermodynamics (higher mass gas solubility) and kinetics (lower viscosity), which generally explains the results of Figure 2.5.9 and 2.5.10. The best performance in R-134a absorption is obtained with $[C_2C_1Im][N(CF_3SO_2)_2]$, an absorbent with relatively high molar gas solubility, low molar weight, and low viscosity. Other FIL/ILs with higher molar gas solubilities [29] are less suitable due to their higher viscosity (as $[C_8C_1Im][N(CF_3SO_2)_2]$) or higher molar weight (as $[C_8H_4F_{13}Im][N(CF_3SO_2)_2]$). As expected, higher HFC partial pressures imply higher efficiency in HFC capture column, an additional evidence of the thermodynamic influence under the operating conditions. The capture of R-134a shows a higher efficiency but with relevant kinetic control, which means that both gas solubility and viscosity must be considered for the adequate selection of absorbents for this HFC. In addition, the operating pressure must be considered to optimize the HFC absorption efficiency.

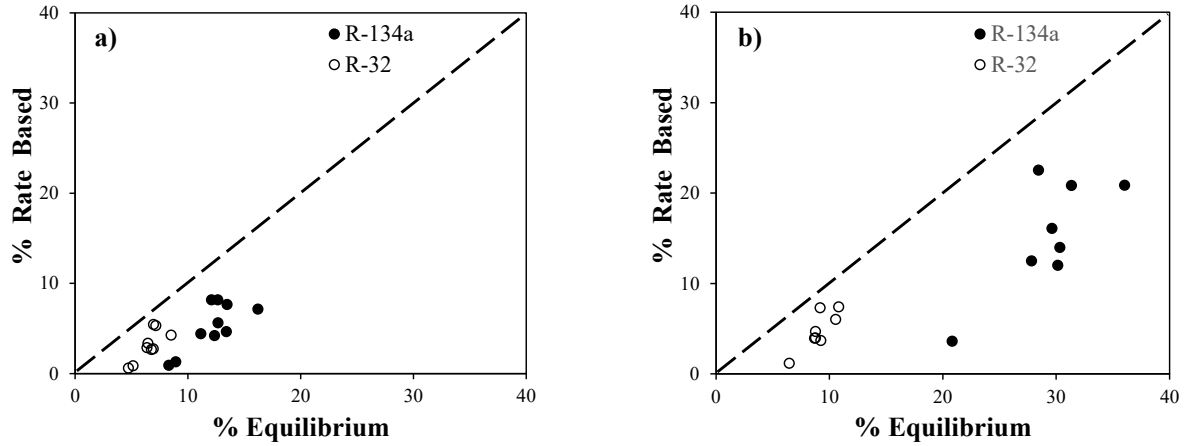


Figure 2.5.10 HFC recoveries in rate-based mode vs recoveries in equilibrium mode for all the systems studied in this work at 298.15 K, L/G=6 and HFC partial pressures of: (a) 0.02 bar; and (b) 1 bar.

2.5.2.3 Complete process

The last study aims to compare the behavior of FIL/ILs that exhibited the best performance ($[C_2C_1Im][CF_3SO_3]$, $[C_2C_1Im][N(CF_3SO_3)_2]$ and $[C_8C_1Im][N(CF_3SO_3)_2]$) in near-industrial conditions by modeling the complete HFC separation process, including both absorption operation and solvent regeneration stage. For this reason, the gas flow to be treated was increased to 10 ton/h. In all cases, the HFC inlet concentration was maintained at 2 %. Moreover, the absorption height is 10 m simulating industrial conditions for this kind of processes. From the conclusions drawn from previous studies, it was decided to increase the total pressure on the absorption column to reach higher HFC recoveries.

The first analysis tries to find the best operating conditions for the absorption column. Thus, Figure 2.5.11 shows HFC recoveries changing the IL flow fed to the column and the total pressure for R-134a and R-32 using $[C_2C_1Im][CF_3SO_3]$ as absorbent. As can be seen, an increase in the total pressure leads to higher HFC recoveries. A better performance is observed for R-134a compared to R-32, in good agreement with the conclusions drawn from previous sections. It is clearly seen that recoveries above 90 % are obtained with a total pressure exceeding 10 bar (0.2 bar of HFC partial pressure).

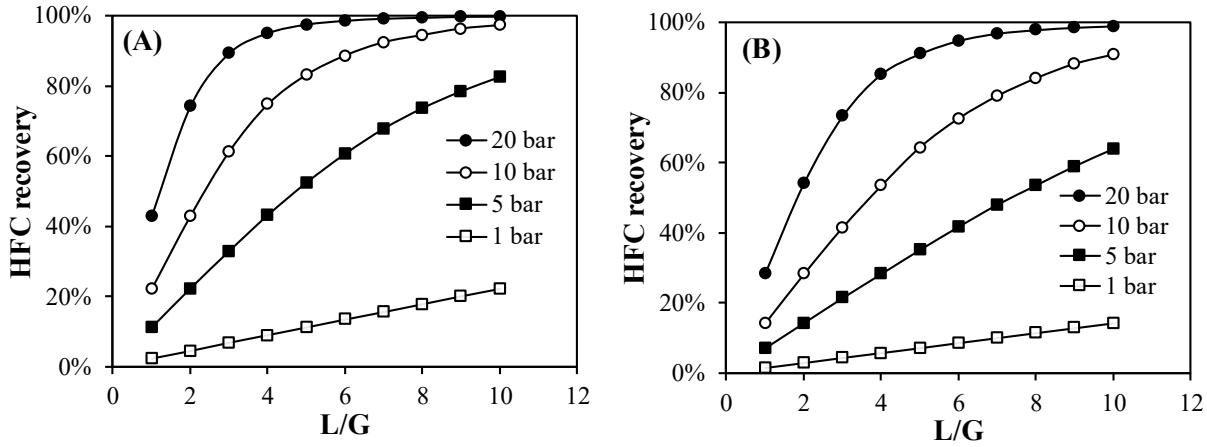


Figure 2.5.11 HFC recoveries in rate-based mode as a function of L/G ratio (in mass units) at different total pressures on the absorption column in the complete process (see Figure 2.5.1) using $[C_2C_1Im][CF_3SO_3]$ as absorbent for the systems: (a) R-134a; and (b) R-32.

Then, we decided to operate at 10 bar total pressure at L/G ratios that allow us to reach 90% HFC recovery on the column. Therefore, the R-134a system needs an L/G of 6.2 (Figure 2.5.11a), whereas for R-32, the L/G ratio must be increased to 9.8 (Figure 2.5.11b). These ratios are in the common industrial range [99] and will be used for the following studies of the complete process. The results of the two other FIL/ILs are similar and can be found in Figures 2.5.12 and 2.5.13.

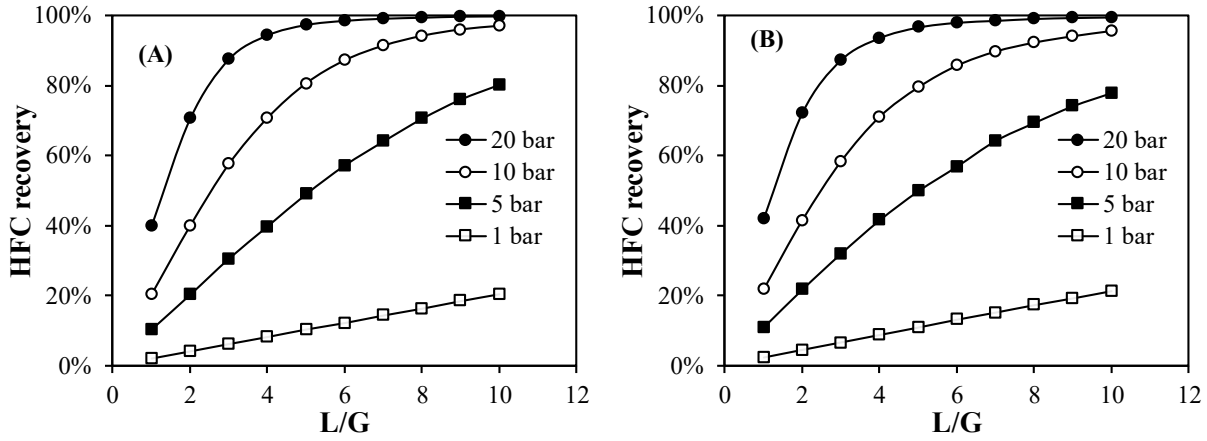


Figure 2.5.12 HFC recoveries in rate-based mode as a function of L/G ratio (in mass units) at different total pressures on the absorption column in the complete process using R-134 as solute for the systems: (a) $[C_2C_1Im][N(CF_3SO_3)_2]$; and (b) $[C_8C_1Im][N(CF_3SO_3)_2]$.

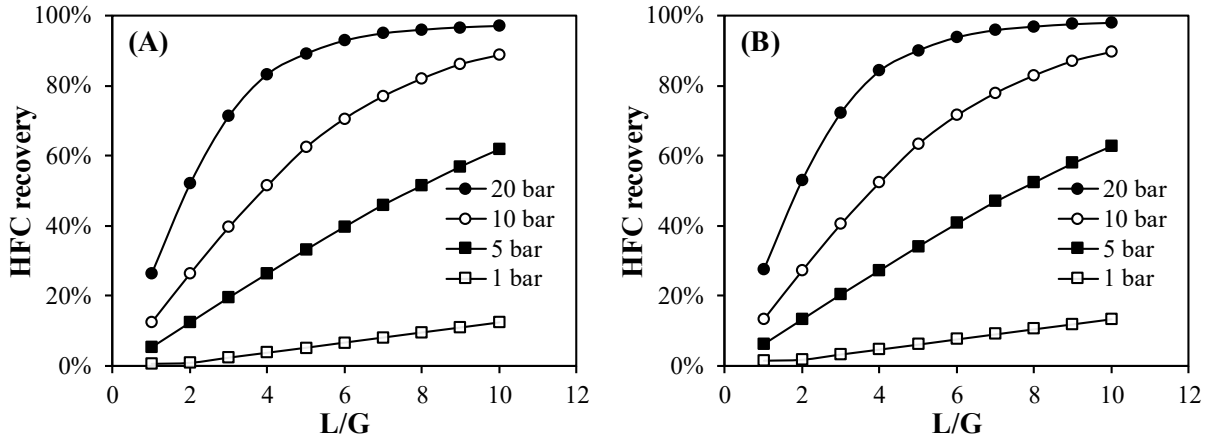


Figure 2.5.13 HFC recoveries in Rate-Based mode as a function of L/G ratio (in mass units) at different total pressures on the absorption column in the complete process using R-32 as solute for the systems: (a) $[C_2C_1Im][N(CF_3SO_3)_2]$; and (b) $[C_8C_1Im][N(CF_3SO_3)_2]$.

Figure 2.5.14 shows the calculated diameters of the absorption column for the different cases studied and are represented in Figure 2.5.11. The obtained column height/diameter ratios are in the suggested range for industrial applications [99]. It is observed that an increase in the L/G ratio leads to larger column diameters since more liquid is present on the absorption column. Wider diameters are also calculated with lower total pressures on the column due to the higher gas volumetric flow. It is important to remark that in all cases, H/D ratios are inside the heuristic range (5–30) [99]. All of the other studied FIL/IL–HFC systems presents similar results that can be found in Figure 2.5.15 of the Supporting Information.

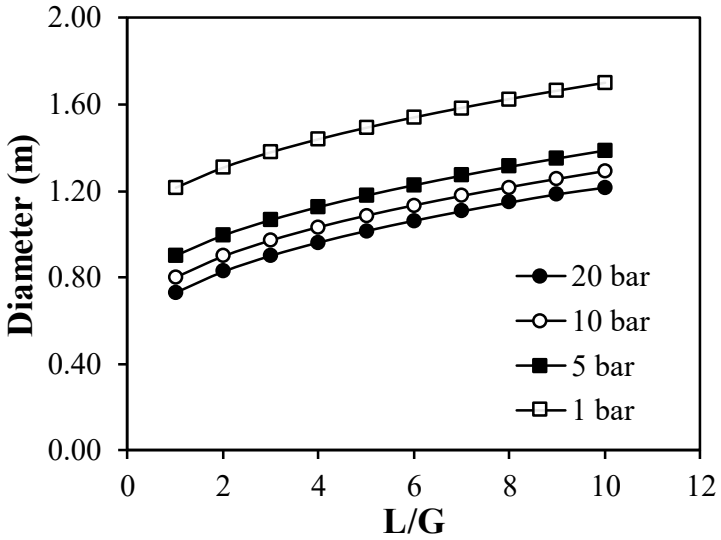


Figure 2.5.14 Absorption column diameters as a function of L/G ratio (in mass units) and total pressure for R-134a-$[C_2C_1Im][CF_3SO_3]$ system.

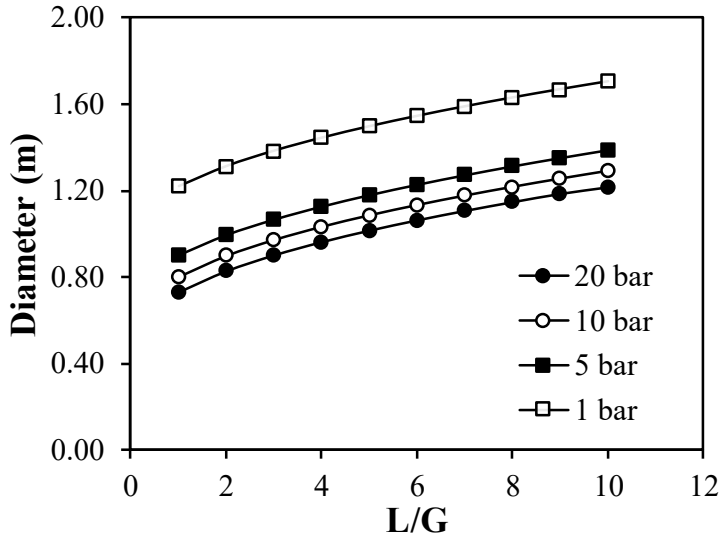


Figure 2.5.15 Absorption column diameters as a function of L/G ratio (in mass units) and total pressure for R-32-$[C_2C_1Im][CF_3SO_3]$ system.

Figure 2.5.16 shows the HFC recovery reached operating the desorption column at 423.15 K as a function of pressure. It is clearly seen that a decrease in pressure leads to higher relative recoveries. In all cases, the pressure needed to reach the reference relative recovery of 95% was 0.1 bar. The same trend was found for all of the FIL/ILs studied herein.

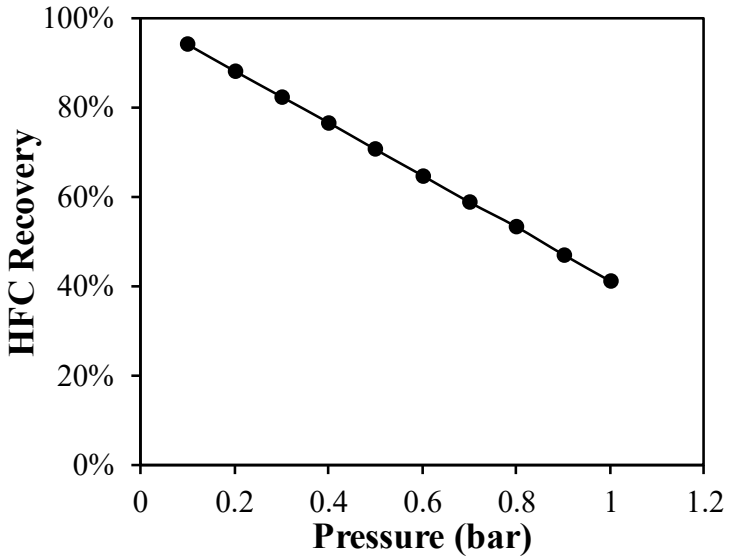


Figure 2.5.16 HFC recovery on the desorption column as a function of the pressure on it for R-134a-$[C_2C_1Im][CF_3SO_3]$ system at 423.15 K of temperature in the reboiler.

Finally, it was decided to perform a preliminary economic analysis of the process with the FIL/IL $[C_2C_1Im][CF_3SO_3]$ using the optimized operating conditions of absorption and desorption columns. The pressure in the desorption column was maintained at 0.1 bar to ensure the maximum HFC recovery. The F-gas purities reached are higher than 99 % independent of the pressure of the system since argon is used as the diluting gas. Table 2.4.4 shows the operating and investment costs found for

this case. It can be seen that both operating and investment costs are higher in the case of R-32, in good agreement with the flow needed to recover 90 % of HFC (62 ton/h in the case of R-134a and 98 ton/h in the case of R-32). The operating costs were estimated at 70 $/ton$_{R-134a}$ and 130 $/ton$_{R-32}$, which are close to those obtained for postcombustion CO_2 physical capture by ILs [41] or by CO_2 chemical absorption with aqueous amine solutions [100]. As seen in Table 2.4.4, the cost of the medium-pressure stream on the reboiler of the desorption column accounts for 90 % of the operating costs pointing toward the importance of selecting the softest possible conditions on the regeneration column. As far as the investment costs are concerned, the vacuum pump on the desorption column corresponds to 55 % of the total costs, which means that it is important to avoid vacuum conditions as much as possible. The estimated investment costs for HFC capture from diluted gas streams are in the range of those calculated for post-combustion CO_2 capture by physical absorption with ILs [41].

Table 2.5.4 Operating and investment costs of the complete process using $[C_2C_1Im][CF_3SO_3]$ as absorbent at the optimized operating conditions.

			Operating Costs				**Cost per-ton of HFC**
HFC	**Pump**	**Compressor**	**Electricity**	**MP steam**	**Cooling Water**	**OPEX**	
	k$/year	k$/year	k$/year	k$/year	k$/year	k$/year	$/ton$_{HFC}$
R-32	26.97	16.70	43.67	383.18	0.06	426.91	130
R-134a	17.07	12.60	29.68	243.11	0.10	272.89	70
			Investment Cost				
HFC	**Absorber**	**Desorber**	**Pump**	**Compressor**	**Reboiler**	**Cooler**	**CAPEX**
	k$	k$	k$	k$	k$	k$	k$
R-32	221.5	197.6	38.9	948.4	119.2	60.7	1586.3
R-134a	221.5	170.3	32.6	634.0	96.2	61.0	1215.6

In this work, a COSMO-based/Aspen Plus methodology was used to evaluate the performance of fluorinated ionic liquids (FIL/ILs) as hydrofluorocarbon (HFC) absorbents in commercial packing column at process scale. Two different fluorinated gases (R-32 and R-134a) were evaluated at two different partial pressures under different conditions. First, our calculation procedures were validated by appropriate comparisons with experimental Henry's law constants and solubilities. We have confirmed that our methodology allows predictions accurate enough for the initial stages of the conceptual design of new absorption processes. Then, absorption columns in equilibrium mode revealed the possibility of a wide range of different recoveries in the case of R-134a, while the range is narrower when absorbing R-32. In both cases, the efficiency of the operation is improved when the HFC partial pressure is increased.

This study demonstrates that FIL/ILs based on sulfonate and carboxylate anions present the best thermodynamic performance for HFC capture. Rigorous calculations of the absorption column using rate-based model showed remarkable differences on HFC recoveries depending on the viscosity of the

FIL/IL evaluated. The performance of low-viscosity FIL/ILs follows the trend of the thermodynamic equilibrium. On the contrary, high-viscosity FIL/ILs get lower efficiencies since mass transfer kinetics is controlling the operation. From this study, three FIL/ILs ($[C_2C_1Im][CF_3SO_3]$, $[C_2C_1Im][N(CF_3SO_3)_2]$, and $[C_8C_1Im][N(CF_3SO_3)_2]$) stand out as the most promising absorbents. These FIL/ILs were evaluated in a complete HFC capture process from a dilute gas stream, including the regeneration stage in near-industrial conditions. First, operating conditions of the absorption column were optimized to reach 90 % HFC recovery, obtaining an L/G ratio of 6–10 depending on the system and a total pressure of 10 bar for a 10 m high absorption column with diameter between 1.1 and 1.2 m.

The current study demonstrates the technical viability of HFC absorption process based on ILs. The preliminary estimations of operating and investment costs for a complete process reveal that those of HFC capture process are close to the ones required for post-combustion CO_2 capture using IL physical absorbents. Future studies should be focused on enhancing the thermodynamic and kinetic properties of selected ILs for HFC absorption and on the process optimization to minimize energy and solvent consumptions.

2.5.3 Conclusions

FILs demonstrates significant potential as absorbents for the capture of F-gases due to their unique thermophysical properties. Using a COSMO-based/Aspen Plus methodology, the absorption performance of 12 FILs was evaluated for R-134a and R-32. Simulations revealed that R-134a is generally absorbed more efficiently than R-32, particularly at higher partial pressures, and that FIL viscosity is a critical factor influencing mass transfer and overall HFC recovery. Lower-viscosity FILs with moderate molar weights, such as $[C_2C_1Im][CF_3SO_3]$ and $[C_2C_1Im][N(CF_3SO_2)_2]$, showed superior performance, achieving recoveries above 90 % under optimized industrial-like conditions. Regeneration studies indicated that low-pressure operation enhances HFC recovery, and preliminary economic analysis showed operating costs of 70 $/ton for R-134a and 130 $/ton for R-32, comparable to CO_2 capture technologies. Overall, the study highlights the importance of selecting FILs with appropriate viscosity, molecular weight, and operating conditions to maximize F-gas absorption efficiency while maintaining economic feasibility.

2.6 Design of ionic liquids for fluorinated gas absorption: COSMO-RS selection and solubility experiments

In recent years, the fight against climate change and the mitigation of the impact of fluorinated gases (F-gases) on the atmosphere is a global concern. Development of technologies that help to efficiently separate and recycle hydrofluorocarbons (HFCs) at the end of the refrigeration and air conditioning equipment life is a priority. The technological development is important to stimulate the F-gas capture, specifically difluoromethane (R-32) and 1,1,1,2-tetrafluoroethane (R-134a), due to their high global warming potential. In this work, the COSMO-RS method is used to analyze the solute–solvent interactions and to determine Henry's constants of R-32 and R-134a in more than 600 ionic liquids. The three most performant ionic liquids were selected on the basis of COSMO-RS calculations, and F-gas absorption equilibrium isotherms were measured using gravimetric and volumetric methods. Experimental results are in good agreement with COSMO-RS predictions, with the ionic liquid tributyl(ethyl)phosphonium diethyl phosphate, $[P_{2444}][C_2C_2PO_4]$, being the salt presenting the highest absorption capacities in molar and mass units compared to salts previously tested. The other two ionic liquids selected, trihexyltetradecylphosphonium glycinate, $[P_{66614}][C_2NO_2]$, and trihexyl(tetradecyl)phosphonium 2-cyano-pyrrole, $[P_{66614}][CNPyr]$, may be competitive as far as their absorption capacities are concerned. Future works will be guided on evaluating the performance of these ionic liquids at an industrial scale by means of process simulations, in order to elucidate the role in process efficiency of other relevant absorbent properties such as viscosity, molar weight, or specific heat.

2.6.1 Materials and methods

2.6.1.1 Cosmos-RS Calculations

First, the geometries of all the ILs included in this work were calculated to their minimum energy structure (optimized) using Turbomole v.7.4 and its graphical interface TmoleX. In all cases, calculations were made at the BP86/TZVP computational level using the solvent effect (COSMO continuum solvation method). In all cases, the independent counter ion (C + A) model was used to describe the ILs. Once the molecules are completely optimized, a single point calculation was carried out in order to ensure that no negative vibrational frequencies are found. Then, all the information required for COSMO-RS calculations is stored in a *.cosmo file, obtained by a single point calculation. COSMOtherm program package (version 19) with its implicit parametrization BP_TZVP_19 was used for COSMO-RS calculations. Henry's law constant and excess property (enthalpy with contributions, entropy, and Gibbs energy) calculations were made for all the systems including the two F-gases and all the IL database. Henry's law constants were calculated by the following equation.

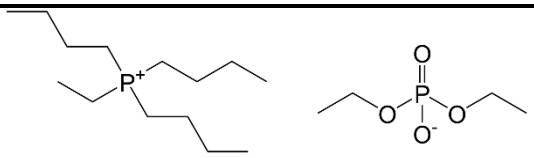
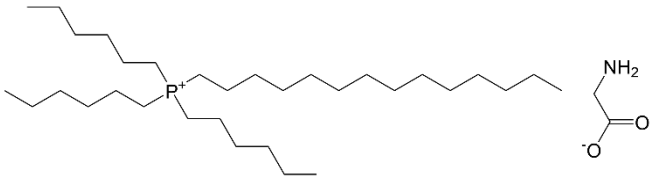
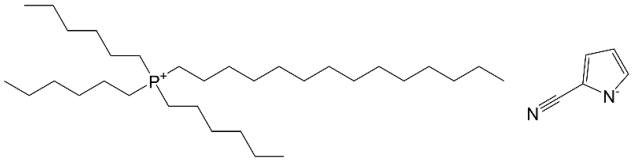
$$K_H = \gamma_i^{\infty} \cdot P_0^{vap} \quad 2.6.1$$

where K_H is the Henry's law constant, γ_i^{∞} is the activity coefficient of the solute at infinite dilution in the IL (calculated by COSMOtherm) and P_0^{vap} is the solute vapor pressure estimated by using the Antoine equation (R-134a and R-32 data from literature [101,102]).

2.6.1.2 Materials

The ionic liquids and gases used in this work are listed in Table 2.6.1. The ionic liquid tributyl(ethyl)phosphonium diethyl phosphate, ($[P_{2444}][C_2C_2PO_4]$, > 95 % mass fraction purity) was supplied by Solvay (Lyon, France), and the ionic liquid trihexyl(tetradecyl)phosphonium glycinate, ($[P_{66614}][C_2NO_2]$, > 95 % mass fraction purity) was supplied by Iolitec (Heilbronn, Germany). The ionic liquid trihexyl(tetradecyl)phosphonium 2-cyano-pyrrolide ($[P_{66614}]$[CNPyr], > 95 % mass fraction purity) was synthetized in our laboratory following the methodology described elsewhere [103,104]. Two solutions of trihexyl(tetradecyl)phosphonium bromide (1.1 g, 2 mmol) in ethanol (200 mL) and Amberlite IRN78 (10 g) were mixed for 2 days using two 500 mL containers. $AgNO_3$ was used to ensure that no residual halide was still present in the mixture, confirming the formation of trihexyl(tetradecyl)phosphonium hydroxide. Then, the solutions were filtered and mixed with pyrrole-2-carbonitrile (0.34 mL, 4 mmol) for 2 days. The volatile compounds were completely removed at 343 K and vacuum pressure (48 Pa). The compounds and materials used for synthesis were supplied by Sigma-Aldrich (Darmstadt, Germany): trihexyl(tetradecyl)phosphonium bromide (>95 % mass fraction purity), ethanol (>99 % mass fraction purity), Amberlite IRN78 (> 95 % mass fraction purity), $AgNO_3$ (> 99 % mass fraction purity), and pyrrole-2-carbonitrile (> 95 % mass fraction purity). ^{1}H nuclear magnetic resonance (NMR) spectroscopy was employed to verify the structure of the IL synthesized by using a Bruker Varian Unity 500.

Table 2.6.1 Chemical structures and acronyms of the ionic liquids used in this work.

Ionic Liquid Designation	**Molecular Weight**	**Chemical Structure**
Tributyl(ethyl)phosphonium diethyphosphate **[P_{2444}][$C_2C_2PO_4$]**	384.50	
Trihexyl(tetradecyl)phosphonium glycinate **[P_{66614}][C_2NO_2]**	557.95	
Trihexyl(tetradecyl)phosphonium 2-cyano-pyrrolide **[P_{66614}][CNPyr]**	574.96	

All ILs were dried under vacuum (4 Pa) and vigorously stirred at 323.15 K for at least 48 h, immediately before their use. Difluoromethane (R-32, ≥99.8 % mass fraction purity) and 1,1,1,2-tetrafluoroethane (R-134a, ≥ 99.8 % mass fraction purity) were acquired from Polo Zero (Lisbon, Portugal) for volumetric measurements and from Euro Refrigerant for gravimetric measurements. Tables 2.6.2 and 2.6.3 show the physical properties and degradation temperatures, respectively, of the ILs used in this work. The physical properties were compared and are plotted in Figure 2.6.1. The thermal stability of ionic liquids is a very important parameter for the application of these compounds. Phosphonium ILs are reported to exhibit higher chemical stability than imidazolium-based ILs [105,106]. Furthermore, the thermal stabilities of [P_{2444}][$C_2C_2PO_4$], [P_{66614}][C_2NO_2], and [P_{66614}][CNPyr] are reported to be above 580 K (see Table 2.6.3), showing high degradation temperatures.

Table 2.6.2 Physical properties of the ionic liquids under study.

ILs	ρ/g·cm^{-3}			μ/mPa·s			Reference
	303.15 K	313.15 K	323.15 K	303.15 K	313.15 K	323.15 K	
[P_{2444}] [$C_2C_2PO_4$]	1.008 [107,108]	1.001 [107,108]	0.994 [107,108]	227 [107]	125 [107]	73 [107]	Bhattacharjee et al. [107] Ficke *et al*.[108]
[P_{66614}] [CNPyr]	0.898 [109]	0.892 [109]	0.886 [109]	297 [110]	170 [110]	106 [110]	Seo *et al*.[109] Fillion *et al*.[110]
[P_{66614}] [C_2NO_2]	0.901 [111]	0.895 [111]	0.889 [111]	280 [111]	170 [111]	100 [111]	Goodrich *et al*.[111]

Table 2.6.3 Degradation temperature of ionic liquids under study.

ILs	T_d (K)	Reference
[P_{2444}][$C_2C_2PO_4$]	673	Nguyen *et al.* [112]
[P_{66614}][CNPyr]	589	Seo *et al*. [109]
[P_{66614}][C_2NO_2]	592	Goodrich *et al*. [111]

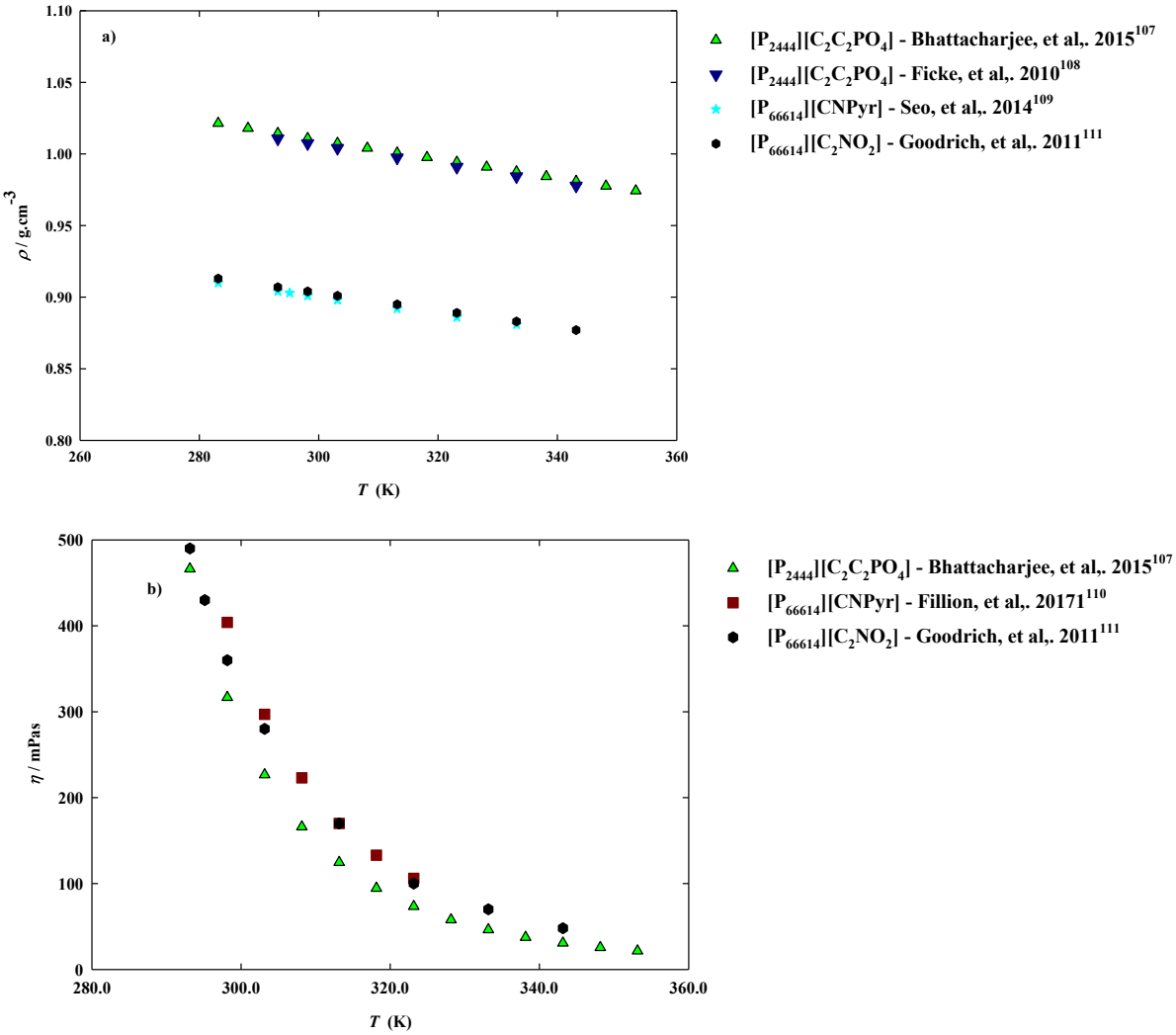


Figure 2.6.1 Physical properties obtained in the literature [107,108,109,110,111] for $[P_{2444}][C_2C_2PO_4]$, $[P_{66614}][CNPyr]$ and $[P_{66614}][C_2NO_2]$ where: a) density (ρ) and b) viscosity (η).

2.6.1.3 Absorption of F-Gas measurements

2.6.1.3.1 Absorption of F-gas Measurements using volumetric method

The R-32 and R-134a absorption isotherms in the chosen ILs were determined using an isochoric saturation method at different temperatures (303.15, 313.15, and 323.15 K) and a pressure range of 0.05–0.5 MPa. A certain known amount of gas was put in contact with a precisely quantity of degassed ILs in a completely closed cell, at constant temperature. The detailed methodology of the experimental setup, as well as the models used for quantification, are presented in Section 2.4.1.4, Determination of Gas Absorption.

2.6.1.3.2 Absorption of F-gas Measurements using gravimetric method

The mass of gas absorbed by the ionic liquid, m_g, at a given temperature and pressure, is obtained from the raw weight data, $m_{reading}$, using the following main equation:

$$m_{reading} = m_0 + m_s + m_g + m_g^{EP} - \sum_i \frac{m_i}{\rho_i}\rho_g(T_i,p) + \sum_j \frac{m_j}{\rho_j}\rho_g(T_j,p) - \frac{m_s}{\rho_s}\rho_g(T_s,p) \quad 2.6.2$$

where m_0 is a small residual mass that may be present after the tare performed by the IGA balance with the empty pan at zero pressure, m_s is the mass of degassed sample, and m_g^{EP} is the mass effect resulting from adsorbed gas on the balance components (determined by performing a blank measurement with the empty pan, equation 2.6.3). The sums over the i and j components account for the buoyancy effects due to the surrounding gas on the sample and counterweight sides, respectively. The last term in equation 2.6.3 is the buoyancy effect on the sample. Additional buoyancy differences associated with changes in sample volume due to the (small) amount of dissolved gas are negligible. Finally, $\rho_g(T_i,p)$ is the gas density at the measurement temperature and pressure.

The raw weight data of the blank measurement, $m_{reading}^{EP}$ observed to be linear with pressure along isotherms, allows determination of the third, fourth and fifth terms on the right-hand side of equation 2.6.3 from which m_g, the mass of gas absorbed, is calculated as follow:

$$m_{reading}^{EP} = m_0 + m_g^{EP} - \sum_i \frac{m_i}{\rho_i}\rho_g(T_i,p) + \sum_j \frac{m_j}{\rho_j}\rho_g(T_j,p) = m_0 + Ap \quad 2.6.3$$

2.6.2 Results and discussion

2.6.2.1 Henry's law constant validation

The first step when applying the multiscale research strategy is to validate the predictions made with the COSMO-RS method. In this work, the absorption of F-gases in ILs is evaluated, using Henry's law constant (K_H) as a key parameter of reference for solvent selection. Figure 2.6.2 (data reported also in Table 2.6.4) compares the experimental K_H as a function of calculated K_H for a wide collection of solutes and ILs, including those of very different natures such as inert gases, CO_2, hydrocarbons, among others.

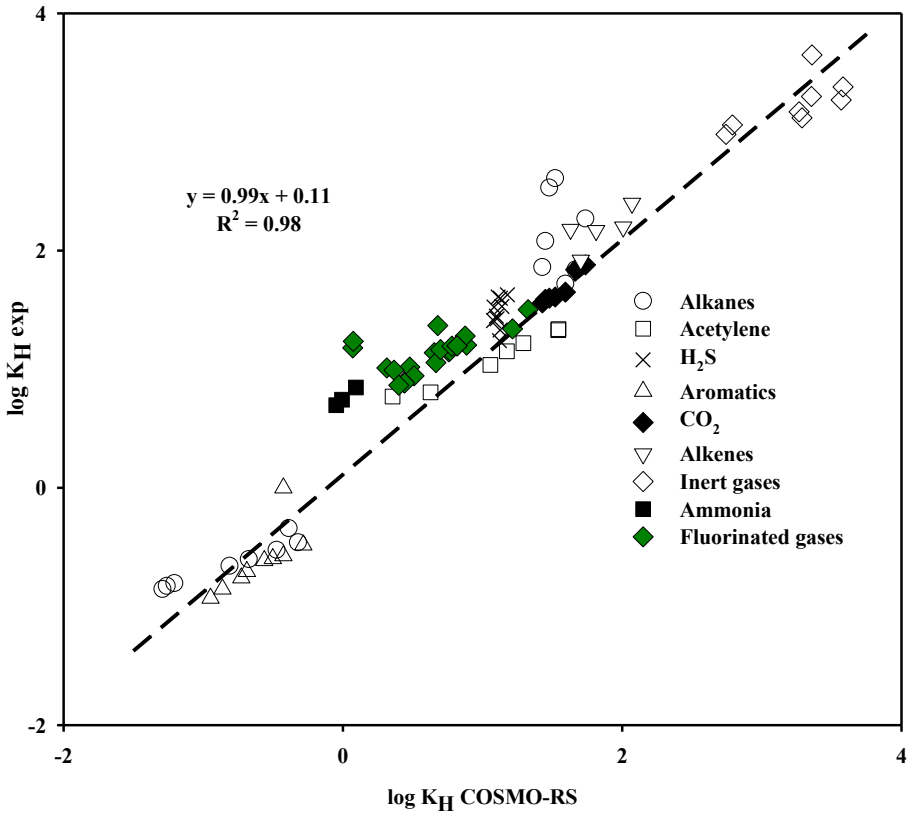


Figure 2.6.2 Validation of Henry's law constants (bar) of solutes in ILs, calculated by COSMO-RS determined using experimental vapor pressure of the different solutes at room temperature with C+A model.

Table 2.6.4 Experimental and COSMO-RS Henry's law constants of solutes in ILs at near-ambient temperature and atmospheric pressure using experimental vapor pressures of pure compounds.

Solute	ILs	log (K_H exp) (MPa)	log (K_H COSMO-RS) (bar)	Reference
Acetone	**[C_2C_1Im][BF_4]**	-0.03	-0.04	[113]
Acetone	**[C_4C_1Im][BF_4]**	-0.05	-0.03	[113]
Acetone	**[C_6C_1Im][BF_4]**	-0.05	-0.05	[113]
Acetone	**[C_4C_1Im][PF_6]**	-0.06	-0.07	[113]
Acetone	**[C_6C_1Im][PF_6]**	-0.07	-0.08	[113]
Acetone	**[C_2C_1Im][$N(CF_3SO_2)_2$]**	-0.08	-0.12	[113]
Acetone	**[C_4C_1Im][$N(CF_3SO_2)_2$]**	-0.08	-0.13	[113]
Acetone	**[C_6C_1Im][$N(CF_3SO_2)_2$]**	-0.09	-0.13	[113]
Benzene	**[C_4C_1Im][BF_4]**	0.00	-0.04	[113]
Benzene	**[C_2C_1Im][BF_4]**	-0.05	-0.03	[113]
Benzene	**[C_4C_1Im][BF_4]**	-0.06	-0.04	[113]
Benzene	**[C_6C_1Im][BF_4]**	-0.06	-0.06	[113]
Benzene	**[C_4C_1Im][PF_6]**	-0.06	-0.05	[113]
Benzene	**[C_6C_1Im][PF_6]**	-0.07	-0.07	[113]
Benzene	**[C_2C_1Im][$N(CF_3SO_2)_2$]**	-0.08	-0.07	[113]

Benzene	**$[C_4C_1Im][N(CF_3SO_2)_2]$**	-0.09	-0.09	[113]
Benzene	**$[C_6C_1Im][N(CF_3SO_2)_2]$**	-0.09	-0.10	[113]
C_2H_4	**$[C_4C_1Im][N(CF_3SO_2)_2]$**	0.19	0.17	[114]
C_2H_4	**$[C_2C_1Im][N(CF_3SO_2)_2]$**	0.22	0.18	[114]
C_2H_4	**$[C_6C_1Im][N(CF_3SO_2)_2]$**	0.22	0.16	[114]
C_2H_4	**$[C_4C_1Im][PF_6]$**	0.22	0.20	[114]
C_2H_4	**$[C_4C_1Im][BF_4]$**	0.24	0.21	[114]
C_2H_6	**$[C_6C_1Im][N(CF_3SO_2)_2]$**	0.19	0.18	[115]
C_2H_6	**$[C_4C_1Im][N(CF_3SO_2)_2]$**	0.21	0.19	[115]
C_2H_6	**$[C_4C_1Im][PF_6]$**	0.25	0.24	[116]
C_2H_6	**$[C_4C_1Im][BF_4]$**	0.26	0.24	[117]
C_3H_8	**$[C_2C_1Im][N(CF_3SO_2)_2]$**	0.18	0.18	[114]
C_3H_8	**$[C_4C_1Im][PF_6]$**	0.23	0.21	[114]
C_4H_{10}	**$[C_4C_1Im][N(CF_3SO_2)_2]$**	0.14	0.11	[114]
C_4H_{10}	**$[C_4C_1Im][BF_4]$**	0.20	0.18	[114]
C_2H_2	**$[C_4C_1Im][BF_4]$**	0.12	0.13	[118]
C_2H_2	**$[C_4C_1Im][C_1CO_2]$**	0.08	0.06	[118]
C_2H_2	**$[C_4C_1Im][CF_3CO_2]$**	0.12	0.12	[118]
C_2H_2	**$[C_4C_1Im][N(CF_3SO_2)_2]$**	0.13	0.15	[118]
C_2H_2	**$[C_4C_1pyr][N(CF_3SO_2)_2]$**	0.13	0.15	[118]
C_2H_2	**$[C_4C_1Im][C_1SO_4]$**	0.10	0.11	[118]
C_2H_2	**$[C_4C_1pyr][C_1CO_2]$**	0.08	0.04	[118]
CO_2	**$[C_{10}C_1Im][N(CF_3SO_2)_2]$**	0.16	0.14	[115]
CO_2	**$[C_8C_1Im][N(CF_3SO_2)_2]$**	0.16	0.15	[119]
CO_2	**$[C_6C_1Im][N(CF_3SO_2)_2]$**	0.16	0.15	[116]
CO_2	**$[C_4C_1Im][N(CF_3SO_2)_2]$**	0.16	0.15	[116]
CO_2	**$[C_2C_1Im][N(CF_3SO_2)_2]$**	0.17	0.16	[116]
CO_2	**$[C_4C_1Im][PF_6]$**	0.18	0.17	[116]
CO_2	**$[C_4C_1Im][BF_4]$**	0.19	0.17	[116]
H_2	**$[C_6C_1Im][N(CF_3SO_2)_2]$**	0.31	0.33	[120]
H_2	**$[C_4C_1Im][PF_6]$**	0.33	0.36	[117]
H_2	**$[C_4C_1Im][BF_4]$**	0.34	0.36	[117]
H_2	**$[C_4C_1Im][N(CF_3SO_2)_2]$**	0.37	0.34	[117]
N_2	**$[C_4C_1Im][N(CF_3SO_2)_2]$**	0.30	0.27	[121]
N_2	**$[C_2C_1Im][N(CF_3SO_2)_2]$**	0.31	0.28	[121]
N_2	**$[C_4C_1Im][PF_6]$**	0.32	0.33	[121]
N_2	**$[C_4C_1Im][BF_4]$**	0.33	0.34	[121]

NH_3	**$[C_2C_1Im][BF_4]$**	0.09	0.01	[35]
NH_3	**$[C_6C_1Im][BF_4]$**	0.07	-0.01	[35]
NH_3	**$[C_4C_1Im][BF_4]$**	0.07	0.00	[35]
H_2S	**$[C_6C_1Im][BF_4]$**	0.14	0.11	[122]
H_2S	**$[C_6C_1Im][N(CF_3SO_2)_2]$**	0.16	0.11	[123]
H_2S	**$[C_6C_1Im][PF_6]$**	0.16	0.11	[122]
H_2S	**$[C_8C_1Im][PF_6]$**	0.13	0.11	[122]
H_2S	**$[C_8C_1Im][N(CF_3SO_2)_2]$**	0.12	0.11	[123]
H_2S	**$[C_4C_1Im][BF_4]$**	0.15	0.11	[122]
H_2S	**$[C_4C_1Im][N(CF_3SO_2)_2]$**	0.14	0.11	[124]
H_2S	**$[C_4C_1Im][PF_6]$**	0.15	0.11	[122]
H_2S	**$[C_2C_1Im][BF_4]$**	0.16	0.12	[122]
H_2S	**$[C_2C_1Im][N(CF_3SO_2)_2]$**	0.15	0.11	[124]
R-134a	**$[C_2C_1Im][C_1CO_2]$**	0.12	0.01	[29]
R-134a	**$[C_2C_1Im][CF_3SO_3]$**	0.12	0.08	[29]
R-134a	**$[C_2C_1Im][N(CF_3SO_2)_2]$**	0.11	0.07	[29]
R-134a	**$[C_2C_1Im][C_4F_9SO_3]$**	0.10	0.05	[29]
R-134a	**$[C_2C_1py][C_4F_9SO_3]$**	0.10	0.03	[29]
R-134a	**$[C_2C_1Im][N(C_4F_9SO_2)_2]$**	0.10	0.04	[29]
R-134a	**$[C_8C_1Im][N(CF_3SO_2)_2]$**	0.10	0.05	[30]
R-134a	**$[C_8C_1Im][N(C_2F_5SO_2)_2]$**	0.09	0.04	[30]
R-134a	**$[C_8H_4F_{13}Im][N(CF_3SO_2)_2]$**	0.09	0.04	[30]
R-134a	**$[C_8H_4F_{13}Im][N(C_2F_5SO_2)_2]$**	0.09	0.04	[30]
R-32	**$[C_2C_1Im][C_1CO_2]$**	0.14	0.07	[29]
R-32	**$[C_2C_1Im][CF_3SO_3]$**	0.13	0.09	[29]
R-32	**$[C_2C_1Im][N(CF_3SO_2)_2]$**	0.12	0.08	[29]
R-32	**$[C_2C_1Im][C_4F_9CO_2]$**	0.12	0.08	[29]
R-32	**$[C_2C_1Im][C_4F_9SO_3]$**	0.12	0.08	[29]
R-32	**$[C_2C_1py][C_4F_9SO_3]$**	0.12	0.07	[29]

It can be seen that the experimental–computational data follow a general linear trend for all the solutes. Specifically, F-gases (marked in green) are placed in the middle of the trend (in general, higher solubility than CO_2 but lower than NH_3) and following the same linear behavior compared to the rest of the solute's data. Therefore, we can conclude that COSMO-RS predicts reasonably well the experimental K_H trends for a diversity of solutes and ILs with remarkably different chemical natures, including the F-gases of interest in this study. Once COSMO-RS is validated, the next stage is to perform a K_H screening among a representative database of cations and anions (including those that were

previously experimentally studied) trying to find some combinations that may improve the performance of those previously presented in the literature. Figure 2.6.3a - b presents the results of K_H screening (more than 600 cation/anion combinations) for R-134a and R-32 gases at 298 K, with the cations and anions experimentally studied previously in the literature represented in red and those studied in this work represented in blue. Detailed nomenclature of ILs studied in this work is shown in Table 2.6.5.

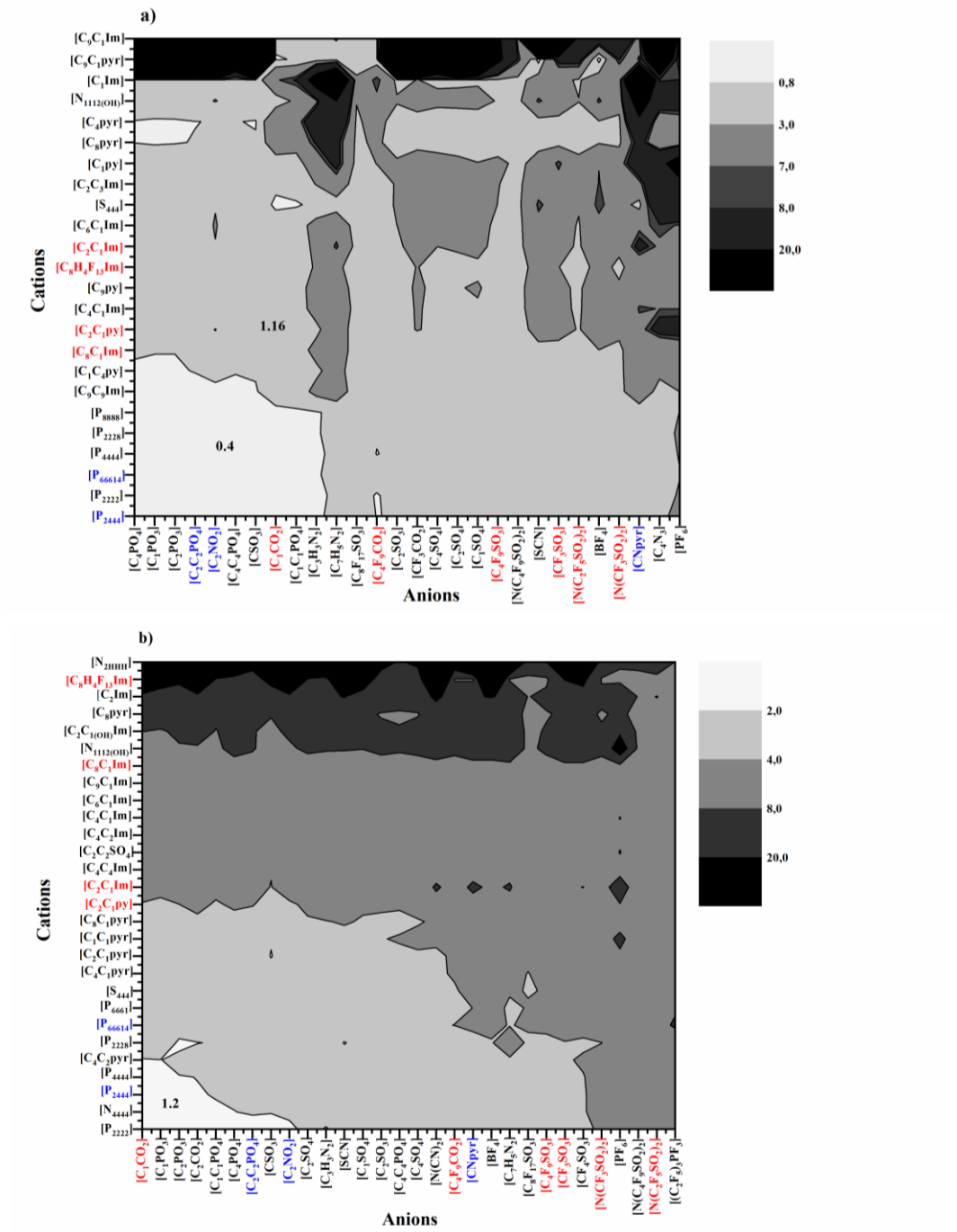


Figure 2.6.3 Henry's law constants (bar) screening of: a) R-134a and b) R-32 in >600 different ILs at T = 298 K calculated by COSMO-RS method. The blue color highlights the cations and anions studied in this work and the red color highlights the ILs studied in our previous works [29,30].

Table 2.6.5 Cations and anions of the ionic liquids of this work.

Cation		Anion	
[Im]	1H-imidazolium	**[$N_{1112(OH)}$]**	(2-hydroxyethyl)-trimethyl ammonium
[C_1Im]	1-methylimidazolium	**[C_1SO_4]**	methylsulfate
[C_2Im]	1-ethyl-imidazolium	**[C_2SO_4]**	ethylsulfate
[C_2C_1Im]	1-ethyl-3-methylimidazolium	**[C_4SO_4]**	butylsulfate
[$C_2C_{1(OH)}$Im]	1-(2-hydroxyethyl)-3-methylimidazolium	**[$C_2C_2SO_4$]**	ethoxyethylsulfate
[C_4C_1Im]	1-butyl-3-methylimidazolium	**[CF_3CO_2]**	trifluoroacetate
[C_4C_2Im]	1-butyl-3-ethylimidazolium	**[CF_3SO_3]**	trifluoromethanesulfonate
[C_6C_1Im]	1-hexyl-3-methylimidazolium	**[CF_4SO_3]**	1,1,2,2-tetrafluoroethanesulfonate
[C_9C_1Im]	1-nonyl-3-methylimidazolium	**[$C_4F_9SO_3$]**	perfluorobutanesulfonate
[C_8C_1Im]	1-octyl-3-methylimidazolium	**[$N(CF_3SO_2)_2$]**	bis(trifluoromethylsulfonyl)imide
[C_2C_3Im]	1-ethyl-3-propylimidazolium	**[$N(C_2F_5SO_2)_2$]**	bis(pentafluoroethylsulfonyl)imide
[C_4C_4Im]	1,3-dibutyl-1H-imidazolium	**[$N(C_4F_9SO_2)_2$]**	bis(nonafluorobutylsulfonyl)imide
[C_4C_9Im]	1-methyl-3-heptylimidazolium	**[$(C_2F_5)_3PF_3$]**	tris(pentafluoroethyl)trifluorophosphate
[C_9C_9Im]	1,3-dinonyl-1H-imidazol-3-ium	**[C_1CO_2]**	acetate
[$C_{10}C_1$Im]	1-decyl-3-methylimidazolium	**[CSO_3]**	Methylsulphite
[$C_8H_4F_{13}$Im]	1-(3,3,4,4,5,5,6,6,7,7,8,8,8-tridecafluorooctyl)-3 methylimidazolium	**[C_2SO_3]**	tosylate; p-toluenesulfonate
[C_1py]	1-ethylpyridinium	**[C_1CO_2]**	acetate
[C_9py]	1-nonylpyridinium	**[C_2CO_2]**	propionate
[C_2C_1py]	1-ethyl-3-methylpyridinium	**[C_2NO_2]**	glycinate
[C_1C_4py]	4-methyl-N-butylpyridinium	**[C_2PO_3]**	ethylphosphite
[C_4pyr]	1-butylpyrrolidinium	**[C_1PO_3]**	Methylphosphite
[C_8pyr]	1-octylpyrrolidinium	**[BF_4]**	tetrafluoroborate
[C_1C_1pyr]	1,1-dimethylpyrrolidinium	**[PF_6]**	hexafluorophosphate
[C_2C1pyr]	1-ethyl-1-methylpyrrolidinium	**[C_4PO_4]**	butylphosphate
[C_4C_1pyr]	1-butyl-1-methylpyrrolidinium	**[$C_1C_1PO_4$]**	dimethylphosphate
[C_4C_2pyr]	1-butyl-1-ethylpyrrolidinium	**[$C_2C_2PO_4$]**	diethylphosphate
[C_8C_1pyr]	1-octyl-1-methylpyrrolidinium	**[$C_4C_4PO_4$]**	Dibutylphosphate
[C_9C_1pyr]	1-nonyl-1-methylpyrrolidinium	**[C_4N_3]**	tricyanomethanide
[C_4C_2pyr]	1-butyl-1-ethylpyrrolidinium	**[SCN]**	thiocyanate
[$C_2C_2SO_4$]	ethoxyethylsulfate	**[$N(CN)_2$)]**	dicyanamide
[S_{444}]	tributylsulfonium	**[CNpyr]**	2-cyanopyrrolide
[P_{2222}]	tetraethyl-phosphonium		

[P_{2228}]	triethyl-octylphosphonium
[P_{2444}]	tributyl(ethyl)phosphonium
[P_{6661}]	Trihexyl-methylphosphonium
[P_{66614}]	trihexyl-tetradecylphosphonium
[P_{8888}]	tetraoctylphosphonium
[N_{2HHH}]	ethylammonium
[N_{4444}]	tetrabutylammonium

As can be seen in Figure 2.6.3a, the K_H values for R-134a solute in ILs present a wide range of values. This means that the proper selection of the IL is important because the gas solubility of R-134a may increase 2 orders of magnitude by choosing adequate cation/anion combination. It can be observed that the selection of both the anion and the cation is important to obtain a low K_H value (high absorption capacity). Analyzing the anions previously studied in the literature (marked in red), we conclude that ILs based on fluorinated carboxylate and sulfonate anions promote intermediate/high R-134a solubility. However, there will appear some anions containing phosphate ([$C_2C_2PO_4$]) or amino acid ([C_2NO_2]) groups (marked in blue in Figure 2.6.3a) that form ILs with remarkable lower K_H than those previously studied. On the other hand, [CNPyr] anion may be interesting for practical applications in GHG capture because [CNPyr]-based ILs simultaneously behave as the CO_2 chemical absorbent and present high F-gas solubility [98]. Regarding the cation role, it is again found that those cations, previously evaluated (marked in red in Figure 2.6.3a), as imidazolium and pyridinium, constitute ILs with intermediate K_H values. Therefore, the correct selection of the cation may significantly improve the solubility of R-134a in the IL. Specifically, it is found that those cations using phosphonium as the head group, as [P_{66614}] and [P_{2444}] (marked in blue in Figure 2.6.3a), seem to be the best for the task. Based on the abovementioned results, we select three available ILs ([P_{2444}][$C_2C_2PO_4$], [P_{66614}][C_2NO_2], and [P_{66614}][CNPyr])─previously synthesized in our laboratory [103,104] as promising new R-134a absorbents in F-gas capture for next stages of this work. Figure 2.6.3b shows the same COSMO-RS screening of K_H for R-32 solute in >600 ILs. In general, K_H values of R-32 in ILs are slightly higher than that of R-134a, in good agreement with the slightly lower experimental gas solubility reported previously [29,52]. Again, both the cation and the anion are important for the proper selection of the IL. Most of the ILs previously studied (marked in red in Figure 2.6.3b) are in the range of intermediate/high K_H, implying that some other ILs may offer higher R-32 solubility. It is observed that the selected ILs ([P_{2444}][$C_2C_2PO_4$], [P_{66614}][C_2NO_2], and [P_{66614}][CNPyr]) that are mentioned above seem to be also potential good candidates for R-32 absorption in F-gas treatment. Of course, there are also other interesting combinations (as those including phosphonium cation and [C_1CO_2] anion), but these ILs are not currently available. Therefore, we propose to carry out the subsequent absorption measurements with the available ILs [P_{2444}][$C_2C_2PO_4$], [P_{66614}][C_2NO_2], and [P_{66614}][CNPyr], as alternative candidates for R-134a and R-32 capture.

COSMO-RS analysis is now used to gain a better fundamental understanding of the thermodynamic of F-gas absorption phenomena in ILs. To do so, the excess properties of the solute–solvent equimolar mixtures were observed. Figure 2.6.4 and 2.6.5 show the excess enthalpy, entropy, and Gibbs energy of a representative sample of F-gases + IL mixtures (Figure 2.6.4: results for R-134a; Figure 2.6.5: results for R-32), involving previously studied ILs (marked in red) and selected ILs (marked in blue). The two figures show that mixtures with previously studied ILs and F-gases promote excess Gibbs energy close to zero, indicating that the absorption of R-134a or R-32 in ILs is not particularly favored thermodynamically. This is directly attributed to the unfavorable entropic contribution to the mixture, despite their exothermic behavior. In contrast, mixtures with the selected ILs and R-134a or R-32 compounds present remarkably more negative excess Gibbs energies, suggesting a more spontaneous absorption process. In these cases, the exothermic enthalpy contribution determines the thermodynamics of the mixture, with the entropy playing a minor role. Clearly, ILs constituted by phosphonium-based cations and anions with phosphate or amino acid-based groups are among those presenting the most spontaneous mixtures with the R-134a refrigerant, in good agreement with the low K_H values found in the abovementioned COSMO-RS screening. Regarding the R-32 compound, the selected ILs are also expected to behave as good absorbents due to the favorable solute–solvent mixture, probably with lower selectivity than R-134a according to the obtained excess properties (less negative G^E values, due to more positive $-T S^E$ term).

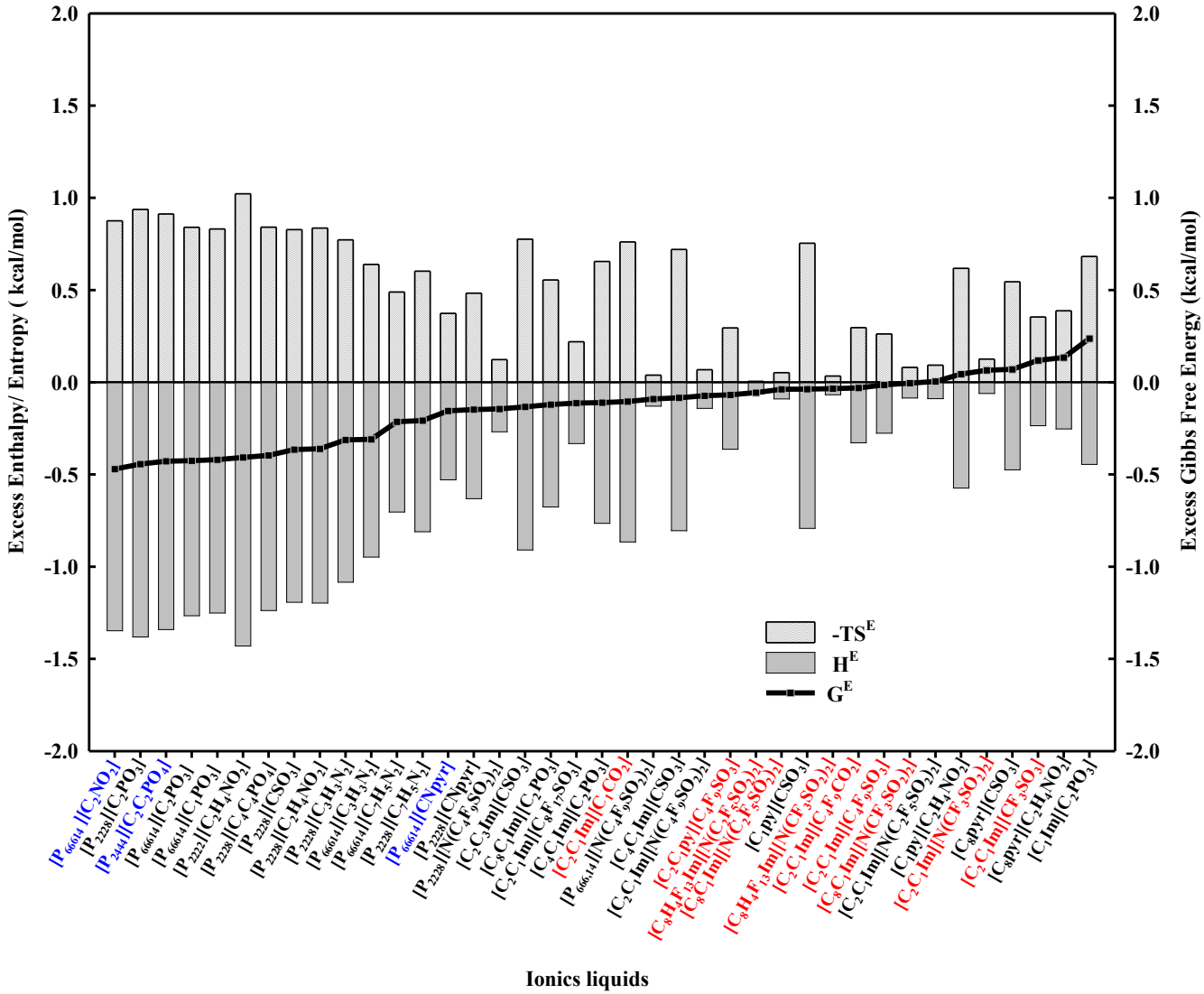


Figure 2.6.4 Effect of cation on the excess enthalpy, entropy, and Gibbs free energy of R-134a + IL equimolar mixture calculated using COSMO-RS at T = 298 K. The blue color highlights the cations and anions studied in this work, the red color highlights the ILs studied in our previous work [29,30].

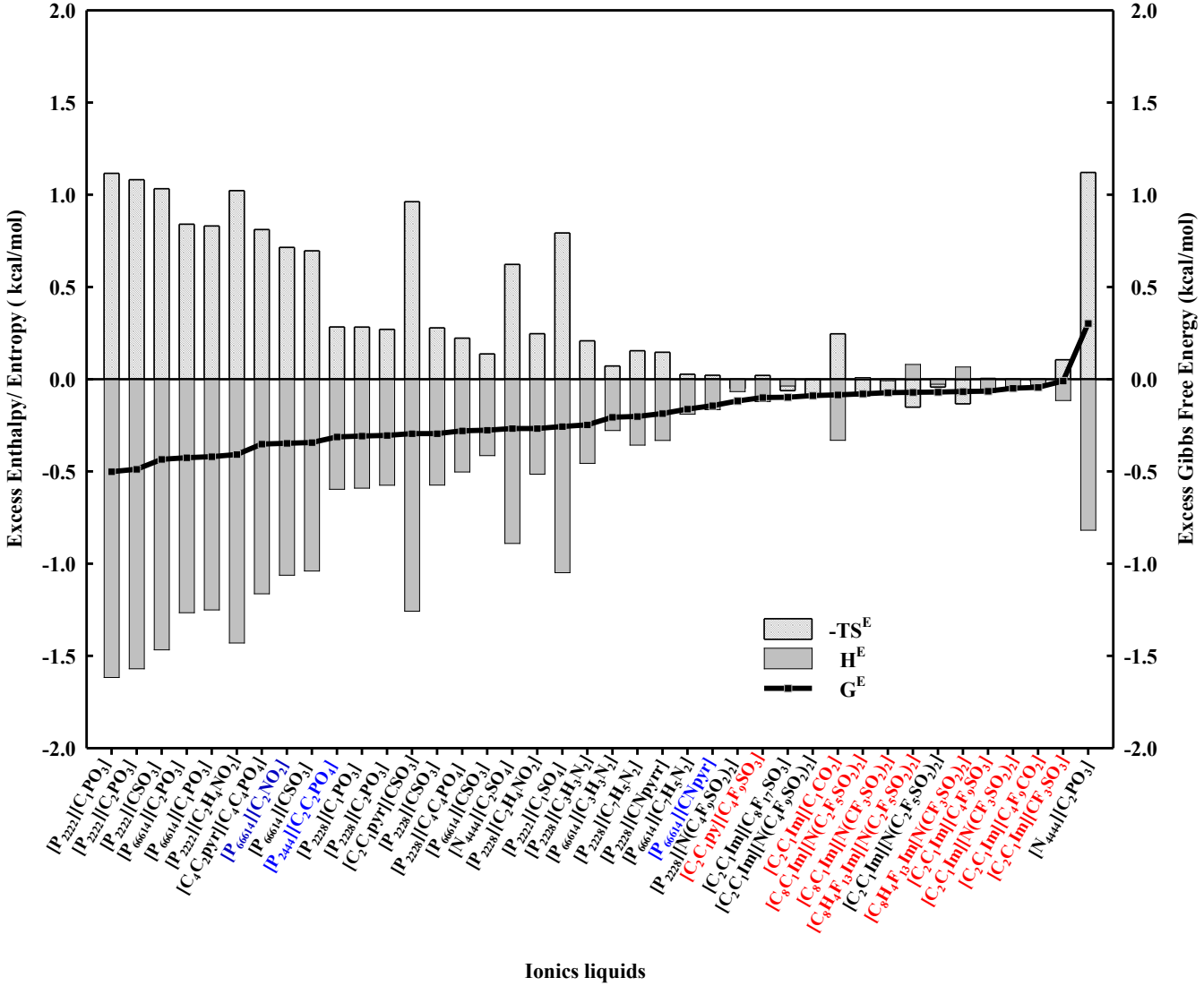


Figure 2.6.5 Effect of cation on the excess enthalpy, entropy, and Gibbs free energy of R-32 + IL equimolar mixture calculated using COSMO-RS at T = 298 K. The blue color highlights the cations and anions studied in this work, the red color highlights the ILs studied in our previous work [29].

We demonstrated that the enthalpic contribution governs the F-gases/IL mixtures in those ILs presenting the most thermodynamically favored absorption process, and Figures 2.6.6 and 2.6.7 show the detailed contributions of the intermolecular interactions to the excess enthalpy in the equimolar mixtures of F-gases/ILs where Figure 2.6.6 shows the results for R-134a and Figure 2.6.7 for R-32. The intermolecular interactions in the liquid are calculated following the equation

$$H^E = H^E(HB) + H^E(MF) + H^E(vdW) \quad 2.6.4$$

where H^E is the excess enthalpy, and it is obtained by the sum of hydrogen bonding (HB), electrostatic-misfit (MF) and van der waals (vdW) contributions.

Figures 2.6.6 and 2.6.7 show that attractive hydrogen bonding and electrostatic intermolecular interactions between R-134a and R-32 and IL components are responsible of the exothermic enthalpy of these mixtures. On the contrary, van der waals contributions are unfavorable to the mixing phenomena. Paying special attention to the differences between the ILs previously studied (marked in red) and the new proposed ILs (marked in blue), one main difference is the anion nature. The most promising anions are those presenting remarkable polar structures with oxygenated or nitrogenated functional groups, able to behave as hydrogen bond acceptor groups. This promotes attractive electrostatic interactions and hydrogen bonds with R-134a and R-32 molecules, which present a weak acidic character [125]. Regarding the cation, ILs marked in red are based on the imidazolium cation, whereas ILs marked in blue include phosphonium-based cations. Imidazolium are polar structures presenting hydrogen bond donor groups, promoting strong anion–cation interactions. In contrast, phosphonium-based cations are nearly nonpolar structures due to their long alkyl chains, with low capacity to form hydrogen bonds. As a consequence, designing ILs based on the phosphonium cation and basic anion promote effective F-gas solute-IL solvent interaction, avoiding competitive effects due to cation–anion interaction. Summarizing that COSMO-RS computational analysis indicates that the three selected IL should have a better performance (in the order of $[P_{2444}][C_2C_2PO_4]$ > $[P_{66614}][C_2NO_2]$ > $[P_{66614}][CNPyr]$) for R-134a and R-32 absorption than other previously studied ILs.

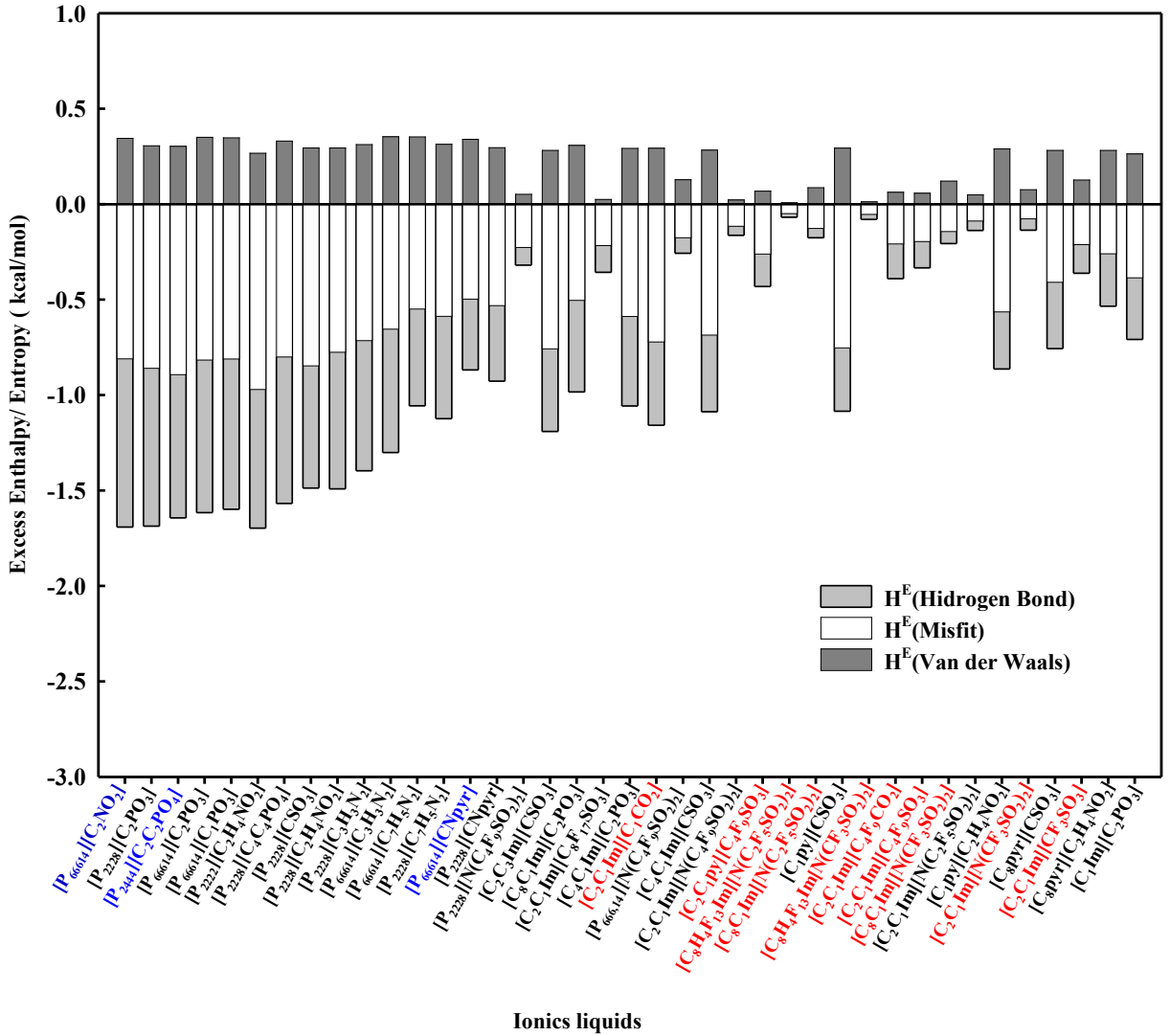


Figure 2.6.6 The intermolecular interaction (misfit-electrostatic, van der waals and hydrogen-bonding) contributions to excess molar enthalpies of R-134a + IL equimolar mixtures calculated using COSMO-RS (C+ A model). The blue color highlights the cations and anions studied in this work, the red color highlights the ILs studied in our previous work [29,30].

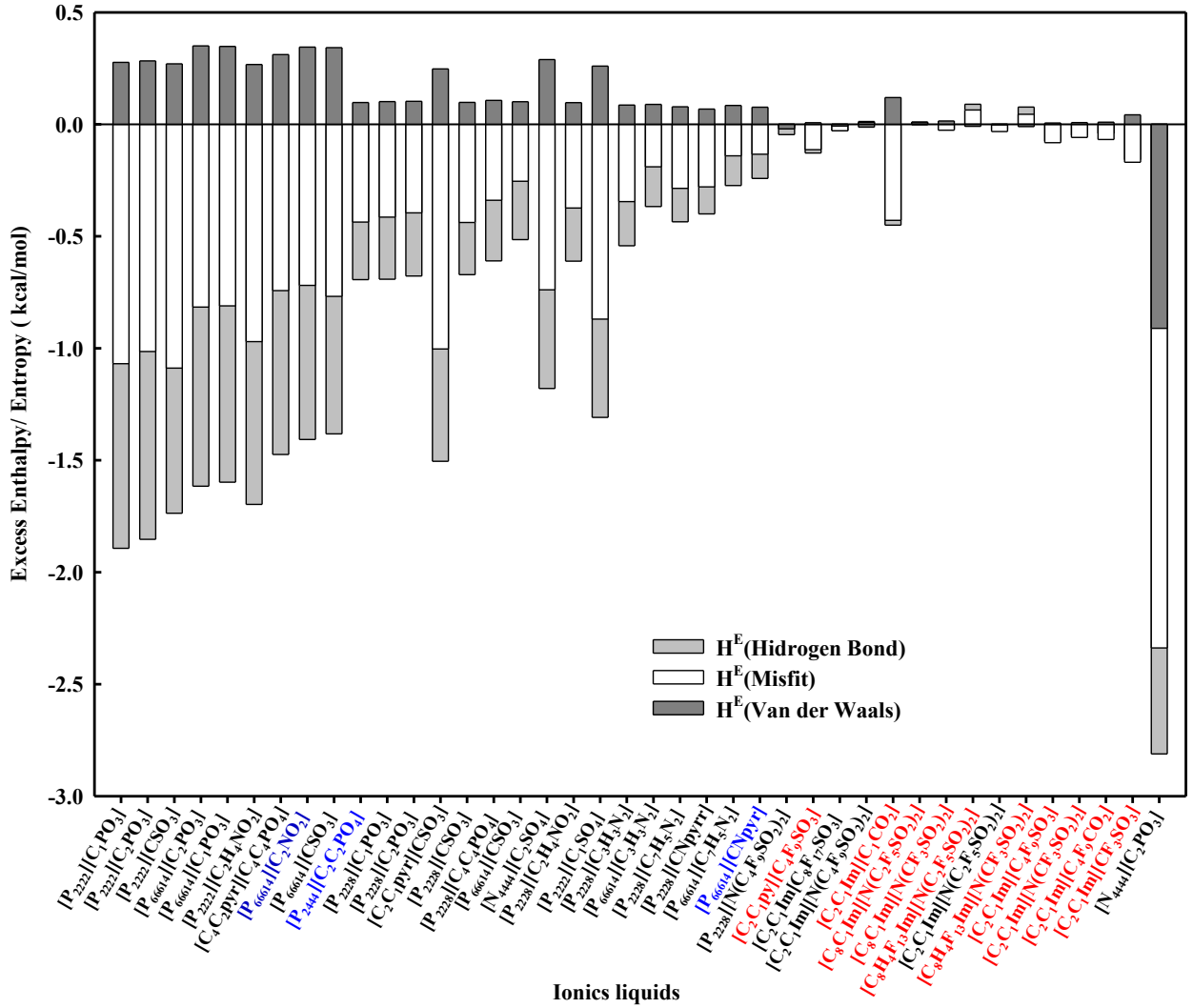


Figure 2.6.7 The intermolecular interaction (misfit-electrostatic, van der waals and hydrogen-bonding) contributions to excess molar enthalpies of R-32 + IL equimolar mixtures calculated using COSMO-RS (C+ A model). The blue color highlights the cations and anions studied in this work, the red color highlights the ILs studied in our previous work [29].

2.6.2.2 Determination of gas absorption

The validation of this experimental method was carried out with the pure IL $[P_{2444}][C_2C_2PO_4]$ for the absorption of R-134a at 303.15 and 323.15 K. Then, the results obtained using the volumetric method were compared with the data measured using the gravimetric method (see Figure 2.6.8 of and Tables 2.6.6 and 2.6.11), which were measured as a function of pressure and temperature using an Intelligent Gravimetric Analyzer (IGA001) from Hidden Analytical following a procedure previously described [126,127]. In the gravimetric measurements, the pure IL was loaded into the IGA001 sample holder, approximately 70 mg, degassed, and dried during 24 h by a turbo pump (Edwards, EXT75DX) at 303 K before starting the absorption/desorption cycles at each temperature. The detailed measurement setup and data treatment are described in the Adsorption of F-Gas Measurements section and in our previous work [55,127]. The experimental measurements were repeated several times under the same conditions to verify the reproducibility of the data. The overall experimental uncertainty was found to be less than 3 %.

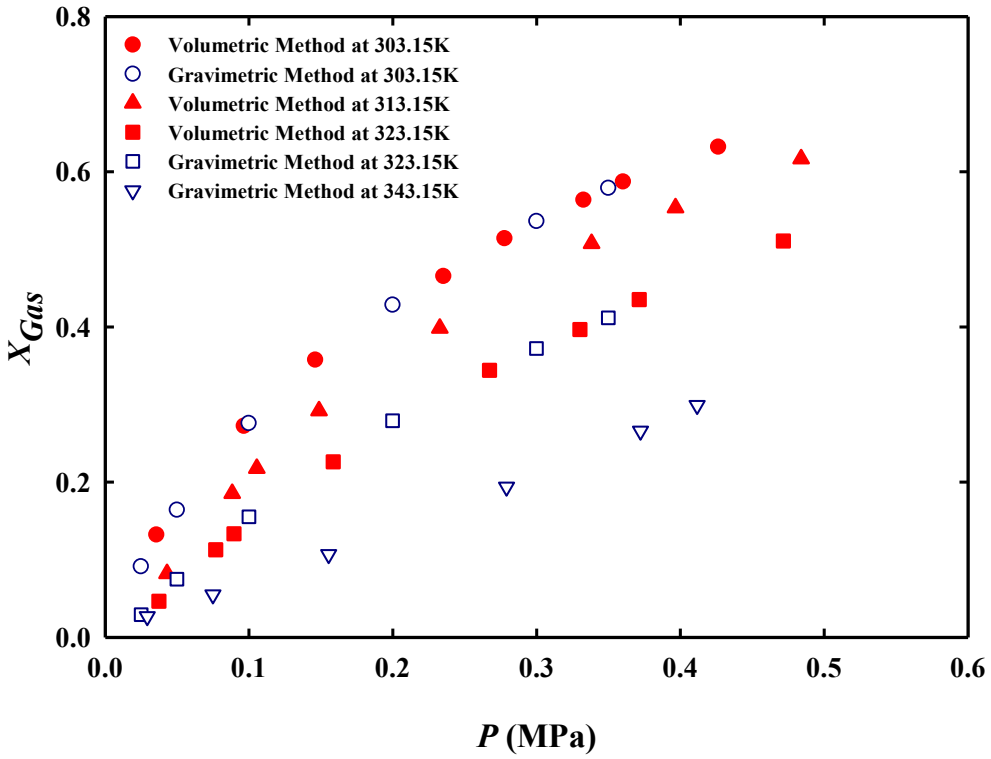


Figure 2.6.8 Comparison of experimental absorption data for R-134a in $[P_{2444}][C_2C_2PO_4]$ as a function of pressure, using the volumetric and the gravimetric methods at different working temperatures.

Previous works showed that the solubility of F-gas in F-ILs is determined by the affinity between the fluorinated moieties of the solutes and the solvents [67,68,70,128]. The nature of the C–F bonds in the FILs are marked by the high electronegativity of fluorine, enhancing the absorption of F-gases [21,129]. All these properties motivated us to evaluate FILs in process simulation [52], where we demonstrated the practical limitations of these compounds due to their high viscosities and high molar weights [52].

In this work, a COSMO-RS mapping was performed using the Henry's constants between F-gas with approximately 600 ILs in order to understand the thermodynamic behavior and interactions that improve and enhance the solute/solvent interactions in the F-gas + IL systems. Then, three ILs were selected to improve the physical absorption of F-gas, taking into account different criteria such as Henry's constant and molecular interactions like hydrogen-bonding, electrostatic, and van der Waals [45]. We, thus, provide an alternative route to FILs or conventional solvents for F-gas capture. The three selected ILs were evaluated using gravimetric and volumetric methods.

The experimental solubility data are shown in Figures 2.6.9 – 2.6.11, expressed as mole fraction of the solubilized F-gas in the three ILs. The isotherms were measured at temperatures from 303.15 to 323.15 K and in a range of equilibrium pressures from 0.5 to 5.5 MPa for the F-gases under study. The maximum equilibrium pressures are selected 80 % below the saturation pressure of F-gas in order to be uniform in all experimental data. The experimental isotherms were correlated using the NRTL thermodynamic model (The binary interaction parameters are shown in the results from 303.15 K to 343.15K are plotted in Figures 2.6.9 – 2.6.11 and Table 2.3.6-2.6.7). For further details on the calculation procedure, see Section 2.2.

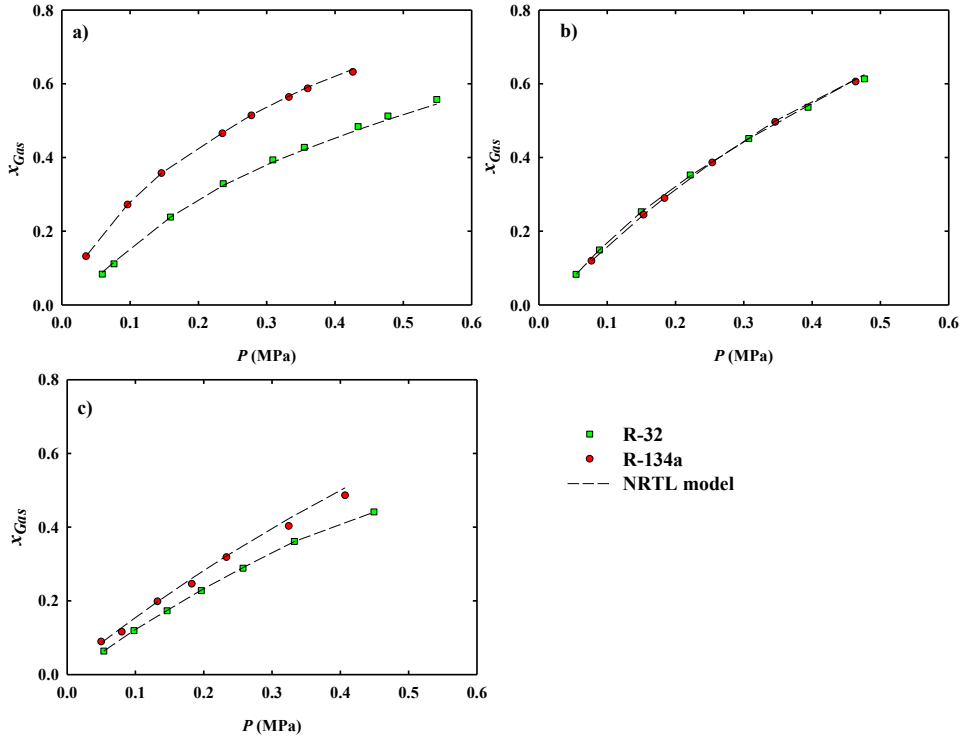


Figure 2.6.9 Absorption equilibrium isotherms of F-gas in: a) $[P_{2444}][C_2C_2PO_4]$; b) $[P_{66614}][C_2NO_2]$; and c) $[P_{66614}][CNPyr]$ at 303.15 K. The dashed lines represent the fitting using the NRTL model.

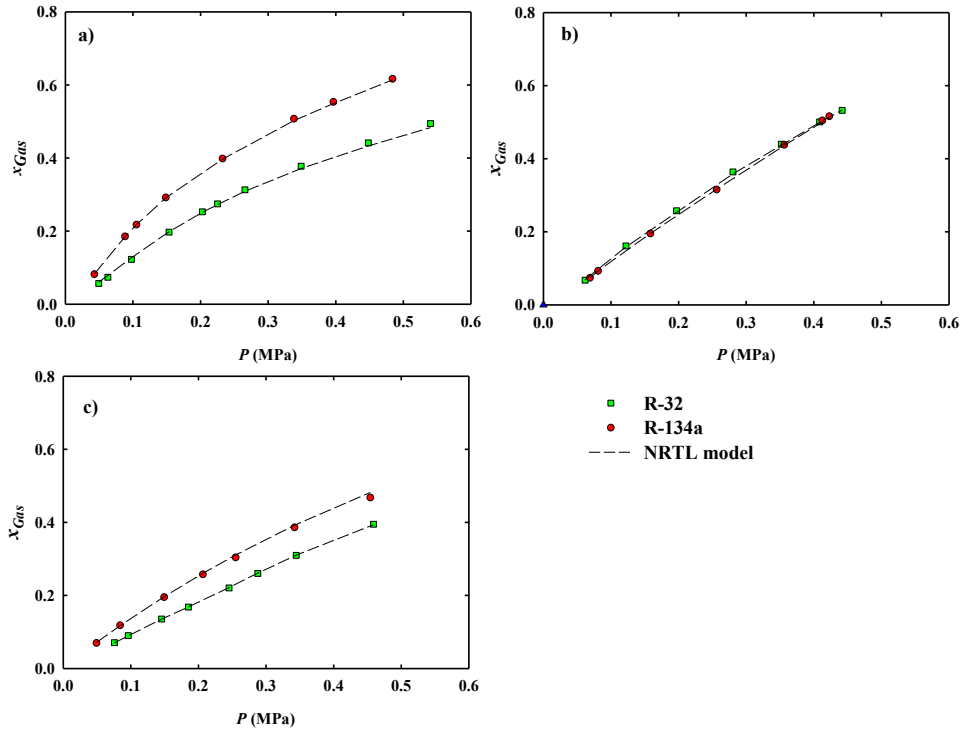


Figure 2.6.10 Absorption equilibrium isotherms of F-gas in: a) $[P_{2444}][C_2C_2PO_4]$; b) $[P_{66614}][C_2NO_2]$; and c) $[P_{66614}][CNPyr]$ at 313.15 K. The dashed lines represent the fitting using the NRTL model.

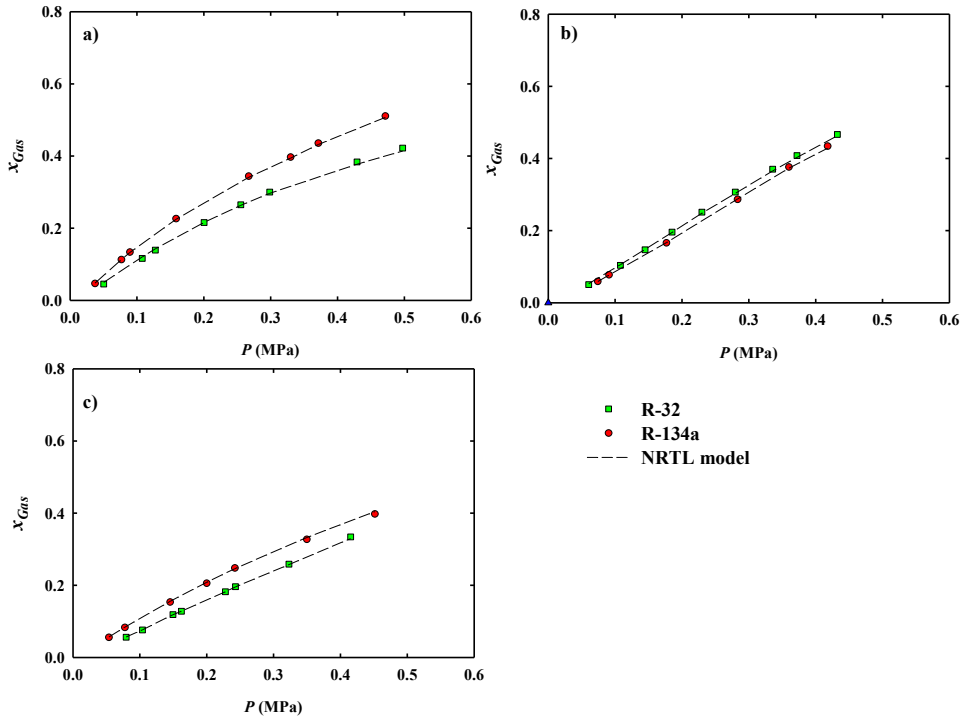


Figure 2.6.11 Absorption equilibrium isotherms of F-gas in: a) $[P_{2444}][C_2C_2PO_4]$; b) $[P_{66614}][C_2NO_2]$; and c) $[P_{66614}]$[CNPyr] at 323.15 K. The dashed lines represent the fitting using the NRTL model.

Table 2.6.6 NRTL Parameters obtained for systems R-32 (i) + ILs (j).

	$[P_{2444}][C_2C_2PO_4]$	**$[P_{66614}]$[CNPyr]**	**$[P_{66614}][C_2NO_2]$**
a_{ij}	4.0168	-27.697	-33.424
a_{ji}	-5.7550	-10.072	-3.835
b_{ij} (K)	-716.37	7314.7	9999.2
b_{ji} (K)	1024.3	2448.7	856.0
c_{ij}	0.28	0.30	0.30
c_{ji}	0.28	0.30	0.30
T_0	0	0	0
RMSD	0.0060	0.0013	0.0038

For all systems, the parameters d_{ij} , d_{ji} , e_{ij} , e_{ji} , f_{ij} ,and f_{ji} were zero, and therefore, $c_{ij}=\alpha_{ij}$, and $c_{ij}=\alpha_{ij}$.

Table 2.6.7 NRTL Parameters obtained for systems R-134a (i) + ILs (j).

	$[P_{2444}]$ $[C_2C_2PO_4]$	**$[P_{66614}][CNPyr]$**	**$[P_{66614}][C_2NO_2]$**
a_{ij}	23.866	-7.2544	-12.5206
a_{ji}	-11.396	7.8529	26.762
b_{ij} (K)	-7394.8	1800.6	2748.2
b_{ji} (K)	3198.3	-2026.0	-6646.9
c_{ij}	0.30	0.12	0.10
c_{ji}	0.30	0.12	0.10
T_0	0	0	0
RMSD	0.0026	0.0082	0.0026

For all systems, the parameters d_{ij} , d_{ji} , e_{ij} , e_{ji} , f_{ij} ,and f_{ji} were zero, and therefore, $c_{ij}=\alpha_{ij}$, and $c_{ij}=\alpha_{ij}$.

For quantitative comparison, Table 2.6.8 collects the F-gas solubility in currently and previously studied ILs at 303.15 K and 0.1, 0.2 and 0.4 MPa, using molar (x) and mass (w) units. The experimental absorption isotherms show that the mole fraction solubility increases in the order $[P_{66614}][CNPyr] < [P_{66614}][C_2NO_2] \leq [P_{2444}][C_2C_2PO_4]$ for R-134a and R-32, in good agreement with COSMO-RS predictions, being the absorption higher at lower temperatures, as expected. R-32 has one less fluorine atom and lower hydrogen bonding capacity, directly affecting the solubility in all ILs studied in this work except to $[P_{66614}][C_2NO_2]$ where similar values are obtained for R-32 and R-134a. Figure 2.6.12 compares the experimental F-gas solubility data in mass fraction of the ILs studied in this work with those reported in the literature [29,30], since mass unit is more commonly used in industrial process [37,130]. As can be seen, the selected IL $[P_{2444}][C_2C_2PO_4]$ presents remarkably enhanced R-134a and R-32 absorption mass capacity than previously studied ILs and FILs, a fact that could be attributed to more favorable solute-solvent interactions as well as to the molar weight of $[P_{2444}][C_2C_2PO_4]$. $[P_{66614}][C_2NO_2]$ also presents a relatively high mass solubility, better or similar the values reported for FILs or other ILs in the literature, demonstrating that F-gas solubility can be enhanced by hydrogen bond acceptor ILs as the ones selected in this work or by hydrogen bond donor ILs as the FILs studied previously. As expected from COSMO-RS calculations, the CO_2 chemical absorbent $[P_{66614}][CNPyr]$ presents a reasonably high mass uptake of R-134a and R-32 gases, close to those previously reported for FILs, making this IL an interesting absorbent for combined greenhouse gases treatments.

Table 2.6.8 Comparison of the molar (*x*) and mass (*w*) solubility and Henry constant for the F-gas in ILs of this work ($[P_{2444}][C_2C_2PO_4]$, $[P_{66614}][C_2NO_2]$ and $[P_{66614}][CNPyr]$) and with other ILs [29,30] at 303.15 K and pressures of 0.1, 0.2 and 0.4 MPa.

Gas	ILs	Pressure (MPa)	w	x	K_H (MPa)
		0.1	0.088	0.277	
	$[P_{2444}][C_2C_2PO_4]$	0.2	0.167	0.438	0.471
		0.35	0.268	0.571	
		0.1	0.035	0.165	
	$[P_{66614}][C_2NO_2]$	0.2	0.077	0.312	0.641
		0.35	0.153	0.496	
		0.1	0.037	0.125	
	$[C_2C_1Im][C_4F_9CO_2]$	0.2	0.079	0.240	0.810
		0.35	0.151	0.394	
		0.1	0.038	0.101	
	$[C_2C_1Im][N(CF_3SO_2)_2]$	0.2	0.079	0.197	0.944
		0.35	0.146	0.328	
		0.1	0.034	0.056	
	$[C_2C_1Im][C_1CO_2]$	0.2	0.071	0.113	1.760
		0.35	0.130	0.199	
		0.1	0.031	0.147	
R-134a	**$[C_8C_1Im][N(C_2F_5SO_2)_2]$**	0.2	0.067	0.274	0.654
		0.35	0.128	0.463	
		0.1	0.032	0.121	
	$[C_2C_1py][C_4F_9SO_3]$	0.2	0.068	0.231	0.845
		0.35	0.127	0.376	
		0.1	0.031	0.126	
	$[C_8C_1Im][N(CF_3SO_2)_2]$	0.2	0.065	0.237	0.766
		0.35	0.124	0.404	
		0.1	0.032	0.115	
	$[C_2C_1Im][C_4F_9SO_3]$	0.2	0.066	0.220	0.862
		0.35	0.123	0.362	
		0.1	0.031	0.123	
	$[P_{66614}][CNPyr]$	0.2	0.063	0.232	0.691
		0.35	0.119	0.370	
		0.1	0.028	0.069	
	$[C_2C_1Im][CF_3SO_3]$	0.2	0.059	0.138	1.354
		0.35	0.113	0.244	

		0.1	0.026	0.152	
	$[C_8H_4F_{13}Im][N(CF_3SO_2)_2]$	0.2	0.056	0.286	0.639
		0.35	0.109	0.487	
		0.1	0.023	0.151	
	$[C_8H_4F_{13}Im][N(C_2F_5SO_2)_2]$	0.2	0.051	0.278	0.638
		0.35	0.103	0.469	
		0.1	0.025	0.151	
	$[P_{2444}][C_2C_2PO_4]$	0.2	0.051	0.280	0.771
		0.35	0.091	0.430	
		0.1	0.019	0.170	
	$[P_{66614}][C_2NO_2]$	0.2	0.042	0.318	0.647
		0.35	0.084	0.498	
		0.1	0.017	0.052	
	$[C_2C_1Im][C_1CO_2]$	0.2	0.033	0.099	2.127
		0.35	0.056	0.162	
		0.1	0.014	0.075	
	$[C_2C_1Im][N(CF_3SO_2)_2]$	0.2	0.029	0.145	1.365
		0.35	0.053	0.239	
		0.1	0.013	0.123	
R-32	**$[P_{66614}][CNPyr]$**	0.2	0.027	0.232	0.863
		0.35	0.050	0.370	
		0.1	0.012	0.058	
	$[C_2C_1Im][CF_3SO_3]$	0.2	0.025	0.114	1.739
		0.35	0.045	0.192	
		0.1	0.012	0.087	
	$[C_2C_1py][C_4F_9SO_3]$	0.2	0.024	0.166	1.237
		0.35	0.043	0.268	
		0.1	0.012	0.077	
	$[C_2C_1Im][C_4F_9CO_2]$	0.2	0.024	0.148	1.354
		0.35	0.043	0.243	
		0.1	0.011	0.079	
	$[C_2C_1Im][C_4F_9SO_3]$	0.2	0.022	0.151	1.310
		0.35	0.040	0.247	

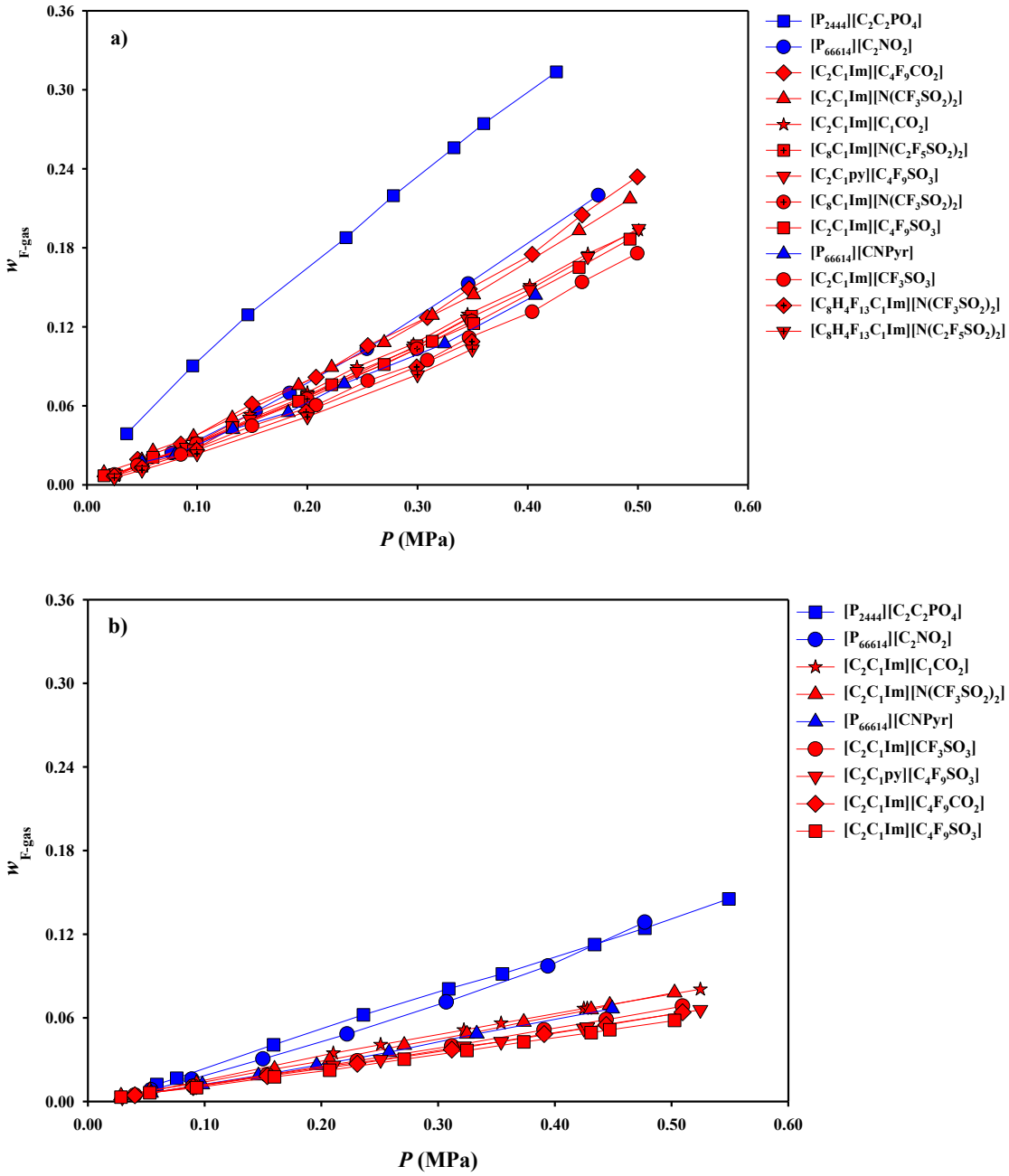


Figure 2.6.12 Comparison of the absorption equilibrium isotherms, in mass fraction unit, for the F-gas in ILs of this work ([P_{2444}][$C_2C_2PO_4$], [P_{66614}][C_2NO_2] and [P_{66614}][CNPyr]) and ILs studied in our previous work [29,30] at 303.15 K where: a) R-134a and b) R-32.

In addition, Henry's constants were determined from the experimental gas absorption data in order to complete current computational-experimental analysis. Henry's constant, K_H [56,76,103], for component *i* is defined as:

$$K_{Hi} = \lim_{x_i \to 0} \frac{\phi_i(P,T)\, P}{x_i} \qquad 2.6.5$$

where, x_i the mole fraction of F-gas dissolved in ILs, P is the equilibrium pressure and ϕ_i refers to the fugacity of F-gas. The Henry's constants were determined for experimental and literature data [29,30] and collected in Table 2.6.8. Figure 2.6.13 compares the experimentally obtained Henry's constant with the molar fraction of R-134a and R-32 in selected ILs (this work) and previously studied FILs or ILs. Figure 2.6.13 clearly shows the excellent thermodynamic behavior of $[P_{2444}][C_2C_2PO_4]$, particularly for R-134a absorption; whereas the other two selected ILs, $[P_{66614}][CNPyr]$ and $[P_{66614}][C_2NO_2]$ also present favorable absorption capacities. It should be remarked the high R-32/ R-134a selectivity (see Figure 2.6.14) of proposed ILs what could be taken advantage for potential separation of F-gas based refrigerants.

The selected ILs compare favorably as F-gas absorbents but, because their viscosity (see Table 2.6.2) is higher than that of the FILs previously proposed [52], more research has to be conducted to evaluate the process performance of $[P_{2444}][C_2C_2PO_4]$, $[P_{66614}][C_2NO_2]$ and $[P_{66614}][CNPyr]$ in commercial industrial equipment. Furthermore, toxicity studies are very important for the industrial application of these compounds and will also have to be carried out to complete the characterization of these compounds.

In this work, a thermodynamic analysis of the solubility of the F-gases (R-134a and R-32) in ILs was performed by means of COSMO-RS method. This study allows us to explore different cations and anions, combined in approximately 600 ILs, and to select three with a significantly improved solubility with respect to those reported in the literature. Henry's constant was the descriptor used to select the ILs, because this thermodynamic benchmark quantity probes solute-solvent interactions. The selected ILs present significantly more negative excess Gibbs free energy when mixed with the F-gases and contribute to a more spontaneous absorption process. The hydrogen bond acceptor character of the ILs anions plays an important role in favorable solute-solvent interactions. Experimental measurements confirmed COSMO-RS predictions with $[P_{2444}][C_2C_2PO_4]$ presenting a higher R-134a and R-32 absorption capacity than any other IL previously studied, whereas selected $[P_{66614}][C_2NO_2]$ and $[P_{66614}][CNPyr]$ may be just competitive solvent alternatives in F-gas absorption process.

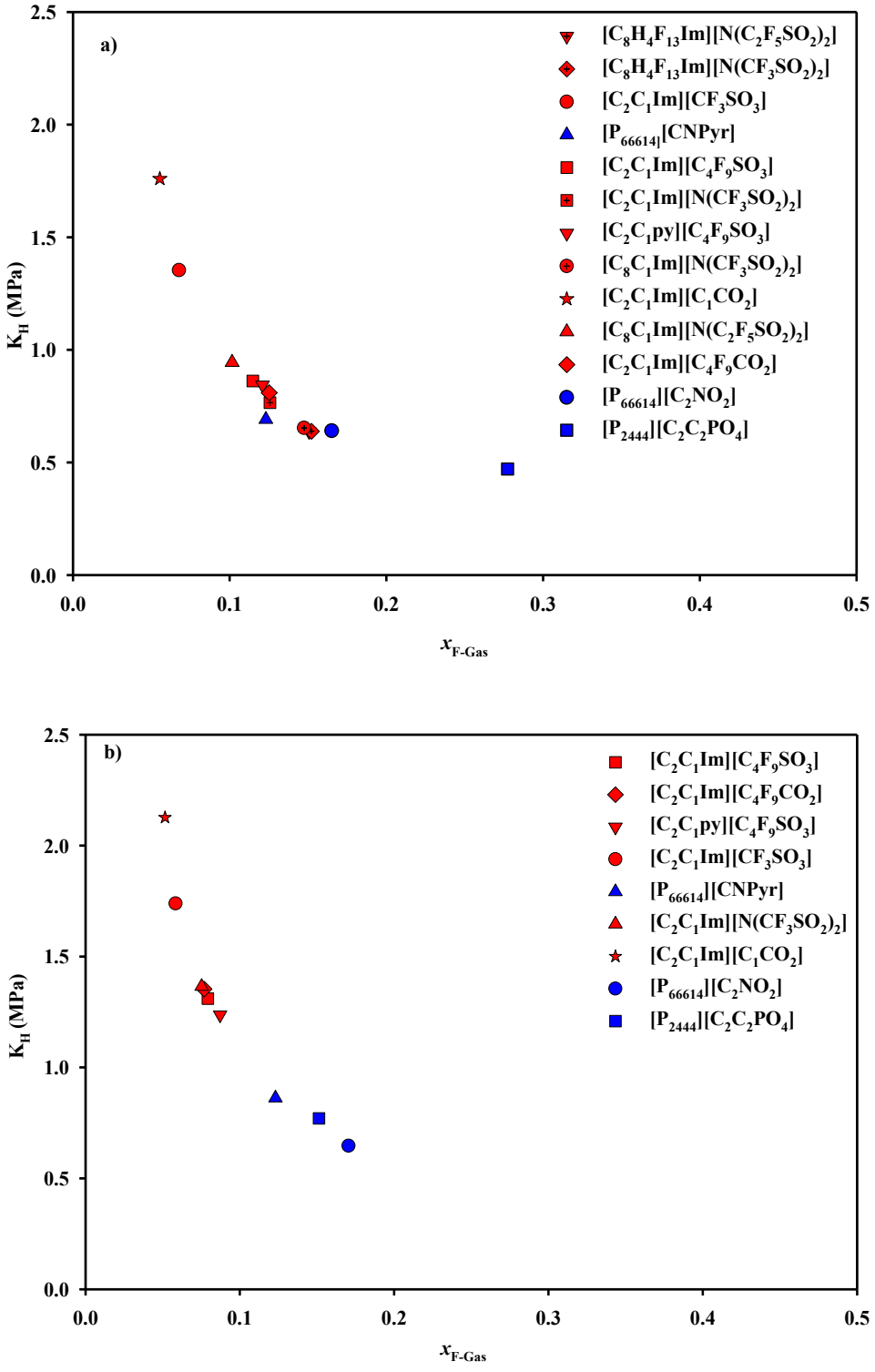


Figure 2.6.13 Comparison of Henry constants versus mass solubility the F-gas in ILs studied in this work ([P2444][C2C2PO4], [P66614][C2NO2] and [P66614][CNPyr]) and ILs studied in our previous work [29,30] at 303.15 K and 0.1 MPa where: a) R-134a and b) R-32.

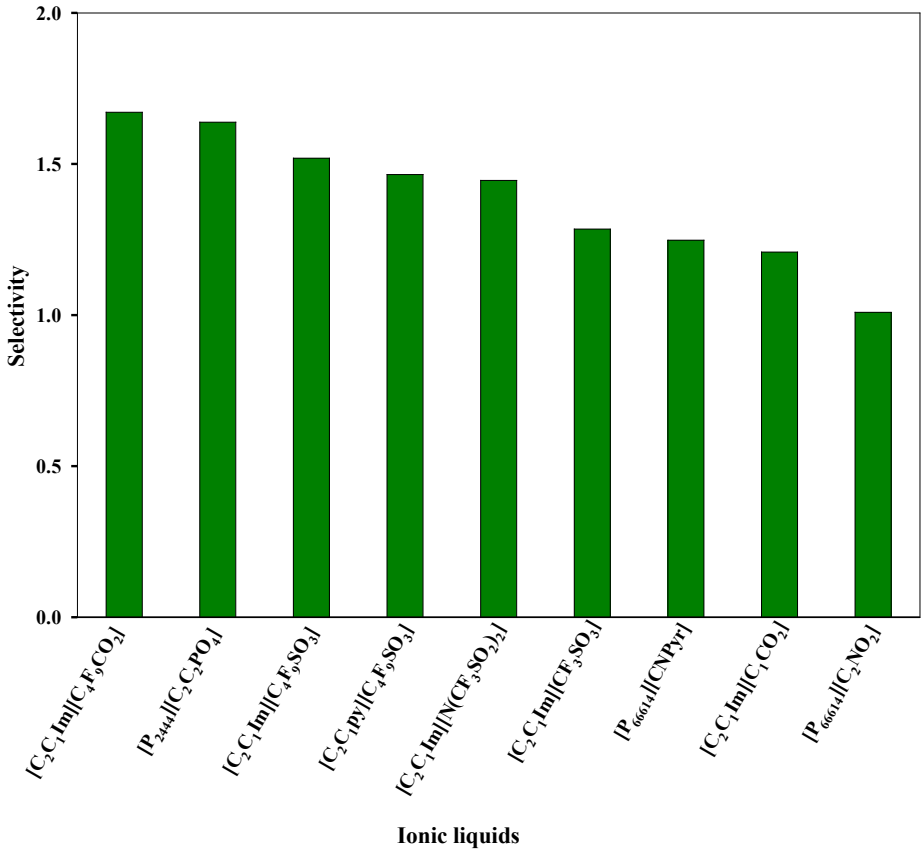


Figure 2.6.14 Ideal selectivity at 303.15 K, determined from the Henry's constants, for the ILs studied in this work and ILs available in the literature [29,30] for the separation of the refrigerant mixtures R-32/R-134a.

2.6.3 Conclusions

The study demonstrates that designing ILs based on phosphonium cations and anions functionalized with phosphate or amino acid groups constitutes an effective approach for the capture of F-gases such as R-134a and R-32. The absorption process is dominated by specific solute–solvent interactions, with hydrogen bonding and electrostatic forces playing a key role in stabilizing the gases within the IL matrix. Favorable entropic contributions indicate that the structural organization of the IL facilitates the accommodation of F-gases, while negative enthalpies reflect the formation of strong attractive interactions. The variation in gas affinity among different ILs is closely linked to the polarity and solvation capacity of their cations and anions, highlighting $[P_{2444}][C_2C_2PO_4]$, $[P_{66614}][C_2NO_2]$, and $[P_{66614}][CNPyr]$ as particularly promising candidates. Importantly, the consistency between COSMO-RS predictions and experimental measurements validates the computational approach as a reliable tool for large-scale screening of ILs. Overall, this research provides a viable alternative to traditional fluorinated ionic liquids, offering an optimized pathway for industrial F-gas capture, separation, and recycling processes.

2.7 References

[1] United States Environmental Protection Agency, Overview of Greenhouse Gases, (n.d.). https://www.epa.gov/ghgemissions/overview-greenhouse-gases (accessed July 31, 2019).

[2] M. Filonchyk, M.P. Peterson, L. Zhang, V. Hurynovich, Y. He, Greenhouse gases emissions and global climate change: Examining the influence of CO2, CH4, and N2O, Science of The Total Environment 935 (2024) 173359. https://doi.org/https://doi.org/10.1016/j.scitotenv.2024.173359.

[3] European Environment Agency (EEA)., Emissions and supply of fluorinated greenhouse gases in Europe, (n.d.). https://www.eea.europa.eu/data-and-maps/indicators/emissions-and-consumption-of-fluorinated-2 (accessed October 28, 2024).

[4] S.M.S.U.S.U. Eskander, S. Fankhauser, Reduction in greenhouse gas emissions from national climate legislation, Nat Clim Chang 10 (2020) 750–756. https://doi.org/10.1038/s41558-020-0831-z.

[5] M. Schulz, D. Kourkoulas, Regulation (EU) No 517/2014 of the European Parliament and of the Council of 16 April 2014 on fluorinated greenhouse gases and repealing Regulation (EC) No 842/2006, Official Journal of the European Union 2014 (2014) L150/195-230. http://eur-lex.europa.eu/eli/reg/2014/517/oj.

[6] Q. Fu, Y. Zhou, Y. Shen, H. Yan, D. Li, Y. Qin, D. Zhang, R23/R22 Separation and Recovery Using the DIST-PSA Hybrid System, Ind Eng Chem Res 56 (2017) 331–341. https://doi.org/10.1021/acs.iecr.6b03701.

[7] C. Genta, C. Marotta, F. Migliardini, Study and Development of a Complete System for Recovery, Recycle, and Disposal of Refrigerant Gas from Existent Plants, Journal of Engineering 2017 (2017) 9202185. https://doi.org/https://doi.org/10.1155/2017/9202185.

[8] X. Ruan, Y. Dai, L. Du, X. Yan, G. He, B. Li, Further separation of HFC-23 and HCFC-22 by coupling multi-stage PDMS membrane unit to cryogenic distillation, Sep Purif Technol 156 (2015) 673–682. https://doi.org/https://doi.org/10.1016/j.seppur.2015.10.064.

[9] J.E. Sosa, C. Malheiro, R.P.P.L. Ribeiro, P.J. Castro, M.M. Piñeiro, J.M.M. Araújo, F. Plantier, J.P.B. Mota, A.B. Pereiro, Adsorption of fluorinated greenhouse gases on activated carbons: evaluation of their potential for gas separation, Journal of Chemical Technology & Biotechnology 95 (2020) 1892–1905. https://doi.org/https://doi.org/10.1002/jctb.6371.

[10] B.S. Akkimaradi, M. Prasad, P. Dutta, K. Srinivasan, Adsorption of 1,1,1,2-Tetrafluoroethane on Activated Charcoal, J Chem Eng Data 46 (2001) 417–422. https://doi.org/10.1021/je000277e.

[11] M. Ghazy, K. Harby, A.A. Askalany, B.B. Saha, Adsorption isotherms and kinetics of activated carbon/Difluoroethane adsorption pair: Theory and experiments, International Journal of Refrigeration 70 (2016) 196–205. https://doi.org/https://doi.org/10.1016/j.ijrefrig.2016.01.012.

[12] B.B. Saha, I.I. El-Sharkawy, R. Thorpe, R.E. Critoph, Accurate adsorption isotherms of R134a onto activated carbons for cooling and freezing applications, International Journal of Refrigeration 35 (2012) 499–505. https://doi.org/https://doi.org/10.1016/j.ijrefrig.2011.05.002.

[13] K. Bélafi-Bakó, N. Nemestóthy, P. Bakonyi, Chapter 8 - Separation of Gases Using Membranes Containing Ionic Liquids, in: A. Pérez De Los Ríos, F.J. Hernández Fernández (Eds.), Ionic Liquids in Separation Technology, Elsevier, Amsterdam, 2014: pp. 261–273. https://doi.org/https://doi.org/10.1016/B978-0-444-63257-9.00008-0.

[14] W.T. Tsai, H.P. Chen, W.Y. Hsien, A review of uses, environmental hazards and recovery/recycle technologies of perfluorocarbons (PFCs) emissions from the semiconductor manufacturing processes, J. Loss Prev. Process Ind. 15 (2002) 65.

[15] K. Shiojiri, Y. Yanagisawa, A. Yamasaki, F. Kiyono, Separation of F-gases (HFC-134a and SF6) from gaseous mixtures with nitrogen by surface diffusion through a porous Vycor glass membrane, J Memb Sci 282 (2006) 442–449. https://doi.org/https://doi.org/10.1016/j.memsci.2006.06.003.

[16] T. Okano, K. Shiojiri, M. Fujii, A. Yamasaki, F. Kiyono, Y. Yanagisawa, - Separation Process of Hydrofluorocarbons (HFCs) by Clathrate Hydrate Formation, in: J. Gale, Y. Kaya (Eds.), Greenhouse Gas Control Technologies - 6th International Conference, Pergamon, Oxford, 2003: pp. 1799–1802. https://doi.org/https://doi.org/10.1016/B978-008044276-1/50301-9.

[17] M. Regel-Rosocka, K. Materna, Chapter 4 - Ionic Liquids for Separation of Metal Ions and Organic Compounds from Aqueous Solutions, in: A. Pérez De Los Ríos, F.J. Hernández Fernández (Eds.), Ionic Liquids in Separation Technology, Elsevier, Amsterdam, 2014: pp. 153–188. https://doi.org/https://doi.org/10.1016/B978-0-444-63257-9.00004-3.

[18] A.B. Pereiro, J.M.M. Araújo, S. Martinho, F. Alves, S. Nunes, A. Matias, C.M.M. Duarte, L.P.N. Rebelo, I.M. Marrucho, Fluorinated Ionic Liquids: Properties and Applications, ACS Sustain Chem Eng 1 (2013) 427–439. https://doi.org/10.1021/sc300163n.

[19] A.B. Pereiro, L.C. Tomé, S. Martinho, L.P.N. Rebelo, I.M. Marrucho, Gas permeation properties of fluorinated ionic liquids, Ind Eng Chem Res 52 (2013) 4994–5001. https://doi.org/10.1021/ie4002469.

[20] A.B. Pereiro, M.J. Pastoriza-Gallego, K. Shimizu, I.M. Marrucho, J.N.C. Lopes, M.M. Piñeiro, L.P.N. Rebelo, On the formation of a third, nanostructured domain in ionic liquids, Journal of Physical Chemistry B 117 (2013) 10826–10833. https://doi.org/10.1021/jp402300c.

[21] M.L. Ferreira, M.J. Pastoriza-Gallego, J.M.M. Araújo, J.N. Canongia Lopes, L.P.N. Rebelo, M. M Piñeiro, K. Shimizu, A.B. Pereiro, Influence of Nanosegregation on the Phase Behavior of Fluorinated Ionic Liquids, Journal of Physical Chemistry C 121 (2017) 5415–5427. https://doi.org/10.1021/acs.jpcc.7b00516.

[22] N.S.M. Vieira, S. Stolte, J.M.M. Araújo, L.P.N. Rebelo, A.B. Pereiro, M. Markiewicz, Acute Aquatic Toxicity and Biodegradability of Fluorinated Ionic Liquids, ACS Sustain Chem Eng 7 (2019) 3733–3741. https://doi.org/10.1021/acssuschemeng.8b03653.

[23] A.B. Lindstrom, M.J. Strynar, E.L. Libelo, J.A. Field, Guest Comment: Perfluoroalkyl Acid Focus Issue, Environ Sci Technol 45 (2011) 7951–7953. https://doi.org/10.1021/es202963p.

[24] B.J. Konwick, G.T. Tomy, N. Ismail, J.T. Peterson, R.J. Fauver, D. Higginbotham, A.T. Fisk, Concentrations and patterns of perfluoroalkyl acids in Georgia, USA surface waters near and distant to a major use source, Environ Toxicol Chem 27 (2008) 2011–2018. https://doi.org/10.1897/07-659.1.

[25] A.A. Jensen, Short-chain Polyfluoroalkyl Substances (PFAS). A literature review of information on human health effects and environmental fate and effect aspects of short-chain PFAS, n.d. www.mst.dk/english.

[26] J.L. Newsted, S.A. Beach, S.P. Gallagher, J.P. Giesy, Acute and Chronic Effects of Perfluorobutane Sulfonate (PFBS) on the Mallard and Northern Bobwhite Quail, Arch Environ Contam Toxicol 54 (2008) 535–545. https://doi.org/10.1007/s00244-007-9039-8.

[27] N.S.M. Vieira, J.C. Bastos, L.P.N. Rebelo, A. Matias, J.M.M. Araújo, A.B. Pereiro, Human cytotoxicity and octanol/water partition coefficients of fluorinated ionic liquids, Chemosphere 216 (2019) 576–586. https://doi.org/https://doi.org/10.1016/j.chemosphere.2018.10.159.

[28] A.B. Pereiro, J.M.M. Araújo, F.S. Teixeira, I.M. Marrucho, M.M. Piñeiro, L.P.N. Rebelo, Aggregation Behavior and Total Miscibility of Fluorinated Ionic Liquids in Water, Langmuir 31 (2015) 1283–1295. https://doi.org/10.1021/la503961h.

[29] J.E.J.E. Sosa, R.P.P.L.R.P.P.L. Ribeiro, P.J.P.J. Castro, J.P.B.J.P.B. Mota, J.M.M.J.M.M. Araújo, A.B.A.B. Pereiro, Absorption of Fluorinated Greenhouse Gases Using Fluorinated Ionic Liquids, Ind Eng Chem Res 58 (2019) 20769–20778. https://doi.org/10.1021/acs.iecr.9b04648.

[30] L.F. Lepre, D. Andre, S. Denis-Quanquin, A. Gautier, A.A.H. Pádua, M. Costa Gomes, Ionic Liquids Can Enable the Recycling of Fluorinated Greenhouse Gases, ACS Sustain Chem Eng 7 (2019). https://doi.org/10.1021/acssuschemeng.9b04214.

[31] G. García, S. Aparicio, R. Ullah, M. Atilhan, Deep eutectic solvents: physicochemical properties and gas separation applications, Energy Fuels 29 (2015) 2616.

[32] R. Abedin, S. Heidarian, J.C. Flake, F.R. Hung, Computational Evaluation of Mixtures of Hydrofluorocarbons and Deep Eutectic Solvents for Absorption Refrigeration Systems, Langmuir 33 (2017) 11611–11625. https://doi.org/10.1021/acs.langmuir.7b02003.

[33] V.R. Ferro, C. Moya, D. Moreno, R. Santiago, J. de Riva, G. Pedrosa, M. Larriba, I. Diaz, J. Palomar, J. De Riva, G. Pedrosa, M. Larriba, I. Diaz, J. Palomar, Enterprise Ionic Liquids Database (ILUAM) for Use in Aspen ONE Programs Suite with COSMO-Based Property Methods, Ind Eng Chem Res 57 (2018) 980–989. https://doi.org/10.1021/acs.iecr.7b04031.

[34] J. Bedia, E. Ruiz, J. de Riva, V.R. Ferro, J. Palomar, J.J. Rodriguez, J. de Riva, V.R. Ferro, J. Palomar, J.J. Rodriguez, Optimized Ionic Liquids for Toluene Absorption, Aiche Journal 59 (2013) 1648. https://doi.org/10.1002/AIC.13926.

[35] J. Palomar, M. Gonzalez-Miquel, J. Bedia, F. Rodriguez, J.J. Rodriguez, Task-specific ionic liquids for efficient ammonia absorption, Sep Purif Technol 82 (2011) 43–52. https://doi.org/10.1016/j.seppur.2011.08.014.

[36] A. Klamt, COSMO-RS: From Quantum Chemistry to Fluid Phase Thermodynamics, Computer Aided Chemical Engineering 43 (2018) 9. https://doi.org/10.1016/B978-0-444-64235-6.50003-6.

[37] J. Palomar, M. Larriba, J. Lemus, D. Moreno, R. Santiago, C. Moya, J. de Riva, G. Pedrosa, J. De Riva, G. Pedrosa, J. de Riva, G. Pedrosa, Demonstrating the key role of kinetics over thermodynamics in the selection of ionic liquids for CO2 physical absorption, Sep Purif Technol 213 (2019) 578–586. https://doi.org/10.1016/j.seppur.2018.12.059.

[38] R. Santiago, C. Moya, J. Palomar, Siloxanes capture by ionic liquids: Solvent selection and process evaluation, Chemical Engineering Journal 401 (2020) 126078. https://doi.org/10.1016/j.cej.2020.126078.

[39] R. Santiago, J. Bedia, D. Moreno, C. Moya, J. de Riva, M. Larriba, J. Palomar, Acetylene absorption by ionic liquids: A multiscale analysis based on molecular and process simulation, Sep Purif Technol 204 (2018) 38–48. https://doi.org/10.1016/j.seppur.2018.04.060.

[40] R. Santiago, J. Lemus, A.X. Outomuro, J. Bedia, J. Palomar, Assessment of ionic liquids as H2S physical absorbents by thermodynamic and kinetic analysis based on process simulation, Sep Purif Technol 233 (2020) 116050. https://doi.org/10.1016/j.seppur.2019.116050.

[41] J. de Riva, J. Suarez-Reyes, D. Moreno, I. Díaz, V. Ferro, J. Palomar, Ionic liquids for post-combustion CO2 capture by physical absorption: Thermodynamic, kinetic and process analysis, International Journal of Greenhouse Gas Control 61 (2017) 61–70. https://doi.org/10.1016/j.ijggc.2017.03.019.

[42] L. Tan, J. Zhu, M. Zhou, X. He, S. Zhang, The effect of imidazolium and phosphonium ionic liquids on toluene absorption studied by a molecular simulation, J Mol Liq 298 (2020) 112054. https://doi.org/10.1016/j.molliq.2019.112054.

[43] C. Moya, R. Santiago, D. Hospital-Benito, J. Lemus, J. Palomar, Design of biogas upgrading processes based on ionic liquids, Chemical Engineering Journal 428 (2022). https://doi.org/10.1016/j.cej.2021.132103.

[44] E. Ruiz, V.R. Ferro, J. Palomar, J. Ortega, J.J. Rodriguez, Interactions of ionic liquids and acetone: Thermodynamic properties, quantum-chemical calculations, and NMR analysis, Journal of Physical Chemistry B 117 (2013) 7388–7398. https://doi.org/10.1021/jp402331y.

[45] J. Palomar, M. Gonzalez-Miquel, A. Polo, F. Rodriguez, Understanding the physical absorption of CO2 in ionic liquids using the COSMO-RS method, Ind Eng Chem Res 50 (2011) 3452–3463. https://doi.org/10.1021/ie101572m.

[46] M. Gonzalez-Miquel, J. Palomar, F. Rodriguez, Selection of ionic liquids for enhancing the gas solubility of volatile organic compounds, Journal of Physical Chemistry B 117 (2013) 296–306. https://doi.org/10.1021/jp310499p.

[47] M. Gonzalez-Miquel, M. Talreja, A.L. Ethier, K. Flack, J.R. Switzer, E.J. Biddinger, P. Pollet, J. Palomar, F. Rodriguez, C.A. Eckert, C.L. Liotta, COSMO-RS Studies: Structure-property

relationships for CO2 capture by reversible ionic liquids, Ind Eng Chem Res 51 (2012) 16066–16073. https://doi.org/10.1021/ie302449c.

[48] M. Gonzalez-Miquel, J. Bedia, C. Abrusci, J. Palomar, F. Rodriguez, Anion Effects on Kinetics and Thermodynamics of CO2 Absorption in Ionic Liquids, Journal of Physical Chemistry B 117 (2013) 3398–3406. https://doi.org/10.1021/jp4007679.

[49] M. Gonzalez-Miquel, J. Bedia, J. Palomar, F. Rodriguez, Solubility and Diffusivity of CO2 in [hxmim][NTf2], [omim][NTf2], and [dcmim][NTf2] at T = (298.15, 308.15, and 323.15) K and Pressures up to 20 bar, J Chem Eng Data 59 (2014) 212–217. https://doi.org/10.1021/JE4001944.

[50] C. Moya, J. Palomar, M. Gonzalez-Miquel, J. Bedia, F. Rodriguez, Diffusion Coefficients of CO2 in Ionic Liquids Estimated by Gravimetry, Ind Eng Chem Res 53 (2014) 13782–13789. https://doi.org/10.1021/ie501925d.

[51] D. Hospital-Benito, J. Lemus, C. Moya, R. Santiago, V.R. Ferro, J. Palomar, Techno-economic feasibility of ionic liquids-based CO2 chemical capture processes, Chemical Engineering Journal 407 (2021) 127196. https://doi.org/10.1016/j.cej.2020.127196.

[52] J.E. Sosa, R. Santiago, D. Hospital-Benito, M. Costa Gomes, J.M.M.M. Araújo, A.B. Pereiro, J. Palomar, M.C. Gomes, J.M.M.M. Araújo, A.B. Pereiro, J. Palomar, Process Evaluation of Fluorinated Ionic Liquids as F-Gas Absorbents, Environ Sci Technol 54 (2020) 12784–12794. https://doi.org/10.1021/acs.est.0c05305.

[53] J.H. Vera, Molecular thermodynamics of fluid-phase equilibria by John M. Prausnitz, Rüdiger N. Lichtenthaler and Edmundo Comes de Azevedo, Third Edition, 1999; Prentice Hall PTR, Upper-Saddle River, New Jersey 07458, xxiii + 860 pages; price $131.95 CND; ISBN 0-13-977745-8, Can J Chem Eng 78 (2000) 429–430. https://doi.org/https://doi.org/10.1002/cjce.5450780222.

[54] S. Gebreyohannes, B.J. Neely, K.A.M. Gasem, Generalized Nonrandom Two-Liquid (NRTL) Interaction Model Parameters for Predicting Liquid–Liquid Equilibrium Behavior, Ind Eng Chem Res 53 (2014) 12445–12454. https://doi.org/10.1021/ie501699a.

[55] P.J. Castro, A.E. Redondo, J.E. Sosa, M.E. Zakrzewska, A.V.M. Nunes, J.M.M. Araújo, A.B. Pereiro, Absorption of Fluorinated Greenhouse Gases in Deep Eutectic Solvents, Ind Eng Chem Res 59 (2020) 13246–13259. https://doi.org/10.1021/acs.iecr.0c01893.

[56] L. Dong, D. Zheng, G. Sun, X. Wu, Vapor-liquid equilibrium measurements of difluoromethane + [Emim]OTf, difluoromethane + [Bmim]OTf, difluoroethane + [Emim]OTf, and difluoroethane + [Bmim]OTf systems, J Chem Eng Data 56 (2011) 3663–3668. https://doi.org/10.1021/je2005566.

[57] M.B. Shiflett, M.A. Harmer, C.P. Junk, A. Yokozeki, Solubility and Diffusivity of Difluoromethane in Room-Temperature Ionic Liquids, J Chem Eng Data 51 (2006) 483–495. https://doi.org/10.1021/je050386z.

[58] M.A. Rocha, M.B. Shiflett, Water Sorption and Diffusivity in [C2C1im][BF4], [C4C1im][OAc], and [C4C1im][Cl], Ind Eng Chem Res 58 (2019) 1743–1753. https://doi.org/10.1021/acs.iecr.8b05689.

[59] M.B. Shiflett, A. Yokozeki, Solubility and diffusivity of hydrofluorocarbons in room-temperature ionic liquids, AIChE Journal 52 (2006) 1205–1219. https://doi.org/10.1002/aic.10685.

[60] M. Zoubeik, M. Mohamedali, A. Henni, Experimental solubility and thermodynamic modeling of CO2 in four new imidazolium and pyridinium-based ionic liquids, Fluid Phase Equilib 419 (2016) 67–74. https://doi.org/https://doi.org/10.1016/j.fluid.2016.03.009.

[61] N.S.M. Vieira, P.M. Reis, K. Shimizu, O.A. Cortes, I.M. Marrucho, J.M.M. Araújo, J.M.S.S. Esperança, J.N.C. Lopes, A.B. Pereiro, L.P.N. Rebelo, A thermophysical and structural characterization of ionic liquids with alkyl and perfluoroalkyl side chains, RSC Adv. 5 (2015) 65337–65350. https://doi.org/10.1039/C5RA13869H.

[62] N.S.M. Vieira, A. Luís, P.M. Reis, P.J. Carvalho, J.A. Lopes-da-Silva, J.M.S.S. Esperança, J.M.M. Araújo, L.P.N. Rebelo, M.G. Freire, A.B. Pereiro, Fluorination effects on the thermodynamic, thermophysical and surface properties of ionic liquids, J Chem Thermodyn 97 (2016) 354–361. https://doi.org/https://doi.org/10.1016/j.jct.2016.02.013.

[63] R.P.P.L. Ribeiro, C.L. Antunes, A.U. Garate, A.F. Portela, M.G. Plaza, J.P.B. Mota, I.A.A.C. Esteves, Binderless shaped metal-organic framework particles: Impact on carbon dioxide adsorption, Microporous and Mesoporous Materials 275 (2019) 111–121. https://doi.org/https://doi.org/10.1016/j.micromeso.2018.08.002.

[64] B.C.R. Camacho, R.P.P.L. Ribeiro, I.A.A.C. Esteves, J.P.B. Mota, Adsorption equilibrium of carbon dioxide and nitrogen on the MIL-53(Al) metal organic framework, Sep Purif Technol 141 (2015) 150–159. https://doi.org/10.1016/j.seppur.2014.11.040.

[65] A.R. Nabais, R.P.P.L. Ribeiro, J.P.B. Mota, V.D. Alves, I.A.A.C. Esteves, L.A. Neves, CO2/N2 gas separation using Fe(BTC)-based mixed matrix membranes: A view on the adsorptive and filler properties of metal-organic frameworks, Sep Purif Technol 202 (2018) 174–184. https://doi.org/https://doi.org/10.1016/j.seppur.2018.03.028.

[66] M.B. Shiflett, A.D. Shiflett, A. Yokozeki, Separation of tetrafluoroethylene and carbon dioxide using ionic liquids, Sep Purif Technol 79 (2011) 357–364. https://doi.org/https://doi.org/10.1016/j.seppur.2011.03.023.

[67] S.I. Tseregounis, M.J. Riley, Solubility of HFC-134a refrigerant in glycol-type compounds: Effects of glycol structure, AIChE Journal 40 (1994) 726–737. https://doi.org/https://doi.org/10.1002/aic.690400415.

[68] J.M.M.V. Sousa, J.P.B. Almeida, A.G.M. Ferreira, H.C. Fachada, I.M.A. Fonseca, Solubility of HFCs in lower alcohols, Fluid Phase Equilib 303 (2011) 115–119. https://doi.org/https://doi.org/10.1016/j.fluid.2011.01.003.

[69] S.K. Chaudhari, D. Salavera, X. Esteve, A. Coronas, Vapour–liquid equilibria of the system 1,1,1,2-tetrafluoroethane+monoethylene-glycol dimethylether from 283.15 to 353.15K: New modified UNIFAC parameters, Fluid Phase Equilib 271 (2008) 28–33. https://doi.org/https://doi.org/10.1016/j.fluid.2008.07.003.

[70] J.M.M.V. Sousa, A.J. Queimada, E.A. Macedo, I.M.A. Fonseca, Solubility of hydrofluorocarbons in aromatic solvents and alcohols: Experimental data and modeling with CPA EoS, Fluid Phase Equilib 337 (2013) 60–66. https://doi.org/https://doi.org/10.1016/j.fluid.2012.09.013.

[71] A.P. Fröba, H. Kremer, A. Leipertz, Density, Refractive Index, Interfacial Tension, and Viscosity of Ionic Liquids [EMIM][EtSO4], [EMIM][NTf2], [EMIM][N(CN)2], and [OMA][NTf2] in Dependence on Temperature at Atmospheric Pressure, J Phys Chem B 112 (2008) 12420–12430. https://doi.org/10.1021/jp804319a.

[72] M.G. Freire, A.R.R. Teles, M.A.A. Rocha, B. Schröder, C.M.S.S. Neves, P.J. Carvalho, D. V Evtuguin, L.M.N.B.F. Santos, J.A.P. Coutinho, Thermophysical Characterization of Ionic Liquids Able To Dissolve Biomass, J Chem Eng Data 56 (2011) 4813–4822. https://doi.org/10.1021/je200790q.

[73] W. Ren, A.M. Scurto, Phase equilibria of imidazolium ionic liquids and the refrigerant gas, 1,1,1,2-tetrafluoroethane (R-134a), Fluid Phase Equilib 286 (2009) 1–7. https://doi.org/10.1016/j.fluid.2009.07.007.

[74] X. Liu, M. He, N. Lv, X. Qi, C. Su, Vapor–Liquid Equilibrium of Three Hydrofluorocarbons with [HMIM][Tf2N], J Chem Eng Data 60 (2015) 1354–1361. https://doi.org/10.1021/je501069b.

[75] K.S. Egorova, V.P. Ananikov, Toxicity of Ionic Liquids: Eco(cyto)activity as Complicated, but Unavoidable Parameter for Task-Specific Optimization, ChemSusChem 7 (2014) 336–360. https://doi.org/https://doi.org/10.1002/cssc.201300459.

[76] M.B. Shiflett, A. Yokozeki, Absorption cycle utilizing ionic liquid as working Fluid, EP1846535A1, 2005. https://patentimages.storage.googleapis.com/84/61/36/3d826a03e6af7f/EP1846535B1.pdf (accessed May 7, 2025).

[77] X. Liu, P. Pan, M. He, Vapor-liquid equilibrium and diffusion coefficients of R32 + [HMIM][FEP], R152a + [HMIM][FEP] and R161 + [HMIM][FEP], J Mol Liq 253 (2018) 28–35. https://doi.org/https://doi.org/10.1016/j.molliq.2018.01.032.

[78] X. Liu, N. Lv, C. Su, M. He, Solubilities of R32, R245fa, R227ea and R236fa in a phosphonium-based ionic liquid, J Mol Liq 218 (2016) 525–530. https://doi.org/10.1016/j.molliq.2016.02.041.

[79] G. Cavallo, P. Metrangolo, R. Milani, T. Pilati, A. Priimagi, G. Resnati, G. Terraneo, The Halogen Bond, Chem Rev 116 (2016) 2478–2601. https://doi.org/10.1021/acs.chemrev.5b00484.

[80] P. Panini, D. Chopra, Understanding of Noncovalent Interactions Involving Organic Fluorine, in: Z.-T. Li, L.-Z. Wu (Eds.), Hydrogen Bonded Supramolecular Structures, Springer Berlin Heidelberg, Berlin, Heidelberg, 2015: pp. 37–67. https://doi.org/10.1007/978-3-662-45756-6_2.

[81] M.G. Freire, C.M.S.S. Neves, I.M. Marrucho, J.A.P. Coutinho, A.M. Fernandes, Hydrolysis of Tetrafluoroborate and Hexafluorophosphate Counter Ions in Imidazolium-Based Ionic Liquids, J Phys Chem A 114 (2010) 3744–3749. https://doi.org/10.1021/jp903292n.

[82] K. Fukumoto, M. Yoshizawa, H. Ohno, Room temperature ionic liquids from 20 natural amino acids, J Am Chem Soc 127 (2005) 2398–2399. https://doi.org/10.1021/ja043451i.

[83] S. Sircar, Gibbsian surface excess for gas adsorption - Revisited, Ind Eng Chem Res 38 (1999) 3670–3682. https://doi.org/10.1021/ie9900871.

[84] R.P.P.L. Ribeiro, R.J.S. Silva, I.A.A.C. Esteves, J.P.B. Mota, Development, construction, and operation of a multisample volumetric apparatus for the study of gas adsorption equilibrium, J Chem Educ 92 (2015) 757–761. https://doi.org/10.1021/ed500633h.

[85] S. Sircar, Excess properties and thermodynamics of multicomponent gas adsorption, Journal of the Chemical Society, Faraday Transactions 1: Physical Chemistry in Condensed Phases 81 (1985) 1527–1540. https://doi.org/10.1039/F19858101527.

[86] National Institute of Standards and Technology (NIST), NIST, (2025). https://www.nist.gov/ (accessed on 21 June 2024). (accessed June 25, 2024).

[87] A.R.R. Teles, H. Correia, G.J. Maximo, L.P.N. Rebelo, M.G. Freire, A.B. Pereiro, J.A.P. Coutinho, Solid-liquid equilibria of binary mixtures of fluorinated ionic liquids, Physical Chemistry Chemical Physics 18 (2016) 25741–25750. https://doi.org/10.1039/c6cp05372f.

[88] M.B. Shiflett, A. Yokozeki, Solubility differences of halocarbon isomers in ionic liquid [emim][Tf 2N], J Chem Eng Data 52 (2007) 2007–2015. https://doi.org/10.1021/je700295e.

[89] Y. Hu, E.G. Azevedo, J.M. Prausnitz, Lawrence Berkeley National Laboratory Recent Work Title THE MOLECULAR BASIS FOR LOCAL COMPOSITIONS IN LIQUID MIXTURE MODELS Permalink https://escholarship.org/uc/item/3x693561 Publication Date, 1983.

[90] B.E. Reid, R. C.; Prausnitz, J. M.; Poling, The Properties of Gases & Liquids, 1988.

[91] H. Renon, J.M. Prausnitz, Local compositions in thermodynamic excess functions for liquid mixtures, AIChE Journal 14 (1968) 135–144. https://doi.org/https://doi.org/10.1002/aic.690140124.

[92] M.B. Haider, D. Jha, B. Marriyappan Sivagnanam, R. Kumar, Thermodynamic and Kinetic Studies of CO2 Capture by Glycol and Amine-Based Deep Eutectic Solvents, J Chem Eng Data 63 (2018) 2671–2680. https://doi.org/10.1021/acs.jced.8b00015.

[93] A. Kamgar, S. Mohsenpour, F. Esmaeilzadeh, Solubility prediction of CO2, CH4, H2, CO and N2 in Choline Chloride/Urea as a eutectic solvent using NRTL and COSMO-RS models, J Mol Liq 247 (2017) 70–74. https://doi.org/10.1016/j.molliq.2017.09.101.

[94] J. de Riva, V. Ferro, C. Moya, M.A. Stadtherr, J.F. Brennecke, J. Palomar, Aspen Plus supported analysis of the post-combustion CO2 capture by chemical absorption using the [P2228][CNPyr] and [P66614][CNPyr]AHA Ionic Liquids, International Journal of Greenhouse Gas Control 78 (2018) 94–102. https://doi.org/https://doi.org/10.1016/j.ijggc.2018.07.016.

[95] S.-T. Lin, S.I. Sandler, A Priori Phase Equilibrium Prediction from a Segment Contribution Solvation Model, Ind Eng Chem Res 41 (2002) 899–913. https://doi.org/10.1021/ie001047w.

[96] A. Klamt, Conductor-like Screening Model for Real Solvents: A New Approach to the Quantitative Calculation of Solvation Phenomena, J Phys Chem 99 (1995) 2224–2235. https://doi.org/10.1021/j100007a062.

[97] S.-T. Lin, P.M. Mathias, Y. Song, C.C. Chen, S.I. Sandler, Improvements of Phase-Equilibrium Predictions for Hydrogen-Bonding Systems from a New Expression for COSMO Solvation Models, in: In AIChE Annual Meeting. 2002: Indianapolis, 2002.

[98] D. Hospital-Benito, J. Lemus, C. Moya, R. Santiago, J. Palomar, Process analysis overview of ionic liquids on CO2 chemical capture, Chemical Engineering Journal 390 (2020) 124509. https://doi.org/10.1016/j.cej.2020.124509.

[99] G. Towler, R. Sinnott, A.• Boston, • Heidelberg, • London, P.• San, D. San, F.• Singapore, S.• Tokyo, Chemical Engineering Design Principles, Practice and Economics of Plant and Process Design, 2008. http://elsevier.com.

[100] M.B. Shiflett, D.W. Drew, R.A. Cantini, A. Yokozeki, Carbon Dioxide Capture Using Ionic Liquid 1-Butyl-3-methylimidazolium Acetate, Energy & Fuels 24 (2010) 5781–5789. https://doi.org/10.1021/ef100868a.

[101] K. Fujiwara, S. Nakamura, M. Noguchi, K. Fujiwara, and S. Nakamura, M. Noguchi, Critical parameters and vapor pressure measurements for 1,1,1-trifluoroethane (R-143a), J Chem Eng Data 43 (1998) 55–59. https://doi.org/10.1021/je970177h.

[102] Y.D. Fu, L.Z. Han, M.S. Zhu, PVT properties, vapor pressures and critical parameters of HFC-32, Fluid Phase Equilib 111 (1995) 273–286. https://doi.org/10.1016/0378-3812(95)02776-B.

[103] C. Moya, V. Sabater, G. Yagüe, M. Larriba, J. Palomar, CO2 conversion to cyclic carbonates catalyzed by ionic liquids with aprotic heterocyclic anions: DFT calculations and operando FTIR analysis, Journal of CO2 Utilization 28 (2018) 66–72. https://doi.org/10.1016/j.jcou.2018.09.012.

[104] R. Santiago, E. Hernández, C. Moya, S. Vela, P. Navarro, J. Palomar, Fatty alcohol/water reaction-separation platform to produce propylene carbonate from captured CO2 using a hydrophobic ionic liquid, Sep Purif Technol 275 (2021). https://doi.org/10.1016/j.seppur.2021.119143.

[105] Z. Xue, L. Qin, J. Jiang, T. Mu, G. Gao, Thermal, electrochemical and radiolytic stabilities of ionic liquids, Physical Chemistry Chemical Physics 20 (2018) 8382–8402. https://doi.org/10.1039/c7cp07483b.

[106] B. Wang, L. Qin, T. Mu, Z. Xue, G. Gao, Are Ionic Liquids Chemically Stable?, Chem Rev 117 (2017) 7113–7131. https://doi.org/10.1021/acs.chemrev.6b00594.

[107] A. Bhattacharjee, J.A. Lopes-da-Silva, M.G. Freire, J.A.P. Coutinho, P.J. Carvalho, Thermophysical properties of phosphonium-based ionic liquids, Fluid Phase Equilib 400 (2015) 103–113. https://doi.org/10.1016/j.fluid.2015.05.009.

[108] L.E. Ficke, R.R. Novak, J.F. Brennecke, Thermodynamic and thermophysical properties of ionic liquid + water systems, J Chem Eng Data 55 (2010) 4946–4950. https://doi.org/10.1021/je100522z.

[109] S. Seo, M. Quiroz-Guzman, M.A. Desilva, T.B. Lee, Y. Huang, B.F. Goodrich, W.F. Schneider, J.F. Brennecke, Chemically tunable ionic liquids with aprotic heterocyclic anion (AHA) for CO2 capture, Journal of Physical Chemistry B 118 (2014) 5740–5751. https://doi.org/10.1021/jp502279w.

[110] J.J. Fillion, J.F. Brennecke, Viscosity of Ionic Liquid-Ionic Liquid Mixtures, J Chem Eng Data 62 (2017) 1884–1901. https://doi.org/10.1021/acs.jced.7b00221.

[111] B.F. Goodrich, J.C. De La Fuente, B.E. Gurkan, D.J. Zadigian, E.A. Price, Y. Huang, J.F. Brennecke, Experimental measurements of amine-functionalized anion-tethered ionic liquids with carbon dioxide, Ind Eng Chem Res 50 (2011) 111–118. https://doi.org/10.1021/ie101688a.

[112] T.K.L. Nguyen, B.G. Soares, J. Duchet-Rumeau, S. Livi, Dual functions of ILs in the core-shell particle reinforced epoxy networks: Curing agent vs dispersion aids, Compos Sci Technol 140 (2017) 30–38. https://doi.org/10.1016/j.compscitech.2016.12.021.

[113] C.-H. Li, K.-X. Gao, Y.-N. Meng, X.-K. Wu, F. Zhang, Z.-X. Wang, Solution Thermodynamics of Imidazolium-Based Ionic Liquids and Volatile Organic Compounds: Benzene and Acetone, J Chem Eng Data 60 (2015) 1600–1607. https://doi.org/10.1021/je500986b.

[114] D. Camper, C. Becker, C. Koval, R. Noble, Low Pressure Hydrocarbon Solubility in Room Temperature Ionic Liquids Containing Imidazolium Rings Interpreted Using Regular Solution Theory, Ind Eng Chem Res 44 (2005) 1928–1933. https://doi.org/10.1021/ie049312r.

[115] P.K. Kilaru, P. Scovazzo, Correlations of Low-Pressure Carbon Dioxide and Hydrocarbon Solubilities in Imidazolium-, Phosphonium-, and Ammonium-Based Room-Temperature Ionic Liquids. Part 2. Using Activation Energy of Viscosity, Ind Eng Chem Res 47 (2008) 910–919. https://doi.org/10.1021/ie070836b.

[116] J.L. Anderson, J.K. Dixon, J.F. Brennecke, Solubility of CO2, CH4, C2H6, C2H4, O2, and N2 in 1-Hexyl-3-methylpyridinium Bis(trifluoromethylsulfonyl)imide: Comparison to Other Ionic Liquids, Acc Chem Res 40 (2007) 1208–1216. https://doi.org/10.1021/ar7001649.

[117] J. Jacquemin, M.F. Costa Gomes, P. Husson, V. Majer, Solubility of carbon dioxide, ethane, methane, oxygen, nitrogen, hydrogen, argon, and carbon monoxide in 1-butyl-3-methylimidazolium tetrafluoroborate between temperatures 283K and 343K and at pressures close to atmospheric, J Chem Thermodyn 38 (2006) 490–502. https://doi.org/https://doi.org/10.1016/j.jct.2005.07.002.

[118] J. Palgunadi, H.S. Kim, J.M. Lee, S. Jung, Ionic liquids for acetylene and ethylene separation: Material selection and solubility investigation, Chemical Engineering and Processing: Process Intensification 49 (2010) 192–198. https://doi.org/https://doi.org/10.1016/j.cep.2009.12.009.

[119] D. Almantariotis, T. Gefflaut, A.A.H. Pádua, J.-Y. Coxam, M.F. Costa Gomes, Effect of Fluorination and Size of the Alkyl Side-Chain on the Solubility of Carbon Dioxide in 1-Alkyl-3-methylimidazolium Bis(trifluoromethylsulfonyl)amide Ionic Liquids, J Phys Chem B 114 (2010) 3608–3617. https://doi.org/10.1021/jp912176n.

[120] M.F. Costa Gomes, Low-Pressure Solubility and Thermodynamics of Solvation of Carbon Dioxide, Ethane, and Hydrogen in 1-Hexyl-3-methylimidazolium Bis(trifluoromethylsulfonyl)amide between Temperatures of 283 K and 343 K, J Chem Eng Data 52 (2007) 472–475. https://doi.org/10.1021/je0604129.

[121] D. Camper, J. Bara, C. Koval, R. Noble, Bulk-Fluid Solubility and Membrane Feasibility of Rmim-Based Room-Temperature Ionic Liquids, Ind Eng Chem Res 45 (2006) 6279–6283. https://doi.org/10.1021/ie060177n.

[122] M. Safavi, C. Ghotbi, V. Taghikhani, A.H. Jalili, A. Mehdizadeh, Study of the solubility of CO2, H2S and their mixture in the ionic liquid 1-octyl-3-methylimidazolium hexafluorophosphate: Experimental and modelling, J Chem Thermodyn 65 (2013) 220–232. https://doi.org/https://doi.org/10.1016/j.jct.2013.05.038.

[123] A.H. Jalili, M. Safavi, C. Ghotbi, A. Mehdizadeh, M. Hosseini-Jenab, V. Taghikhani, Solubility of CO2, H2S, and Their Mixture in the Ionic Liquid 1-Octyl-3-methylimidazolium Bis(trifluoromethyl)sulfonylimide, J Phys Chem B 116 (2012) 2758–2774. https://doi.org/10.1021/jp2075572.

[124] H. Sakhaeinia, A.H. Jalili, V. Taghikhani, A.A. Safekordi, Solubility of H2S in Ionic Liquids 1-Ethyl-3-methylimidazolium Hexafluorophosphate ([emim][PF6]) and 1-Ethyl-3-methylimidazolium Bis(trifluoromethyl)sulfonylimide ([emim][Tf2N]), J Chem Eng Data 55 (2010) 5839–5845. https://doi.org/10.1021/je100794k.

[125] D. Moreno, V.R. Ferro, J. de Riva, R. Santiago, C. Moya, M. Larriba, J. Palomar, Absorption refrigeration cycles based on ionic liquids: Refrigerant/absorbent selection by thermodynamic and process analysis, Appl Energy 213 (2018) 179–194. https://doi.org/10.1016/j.apenergy.2018.01.034.

[126] L.F. Lepre, J. Szala-Bilnik, L. Pison, M. Traïkia, A.A.H. Pádua, R.A. Ando, M.F. Costa Gomes, Can the tricyanomethanide anion improve CO2 absorption by acetate-based ionic liquids?, Physical Chemistry Chemical Physics 19 (2017) 12431–12440. https://doi.org/10.1039/c7cp01559c.

[127] J. Avila, C. Červinka, P.Y. Dugas, A.A.H. Pádua, M. Costa Gomes, Porous Ionic Liquids: Structure, Stability, and Gas Absorption Mechanisms, Adv Mater Interfaces 8 (2021) 1–15. https://doi.org/10.1002/admi.202001982.

[128] S.K. Chaudhari, D. Salavera, X. Esteve, A. Coronas, Vapour-liquid equilibria of the system 1,1,1,2-tetrafluoroethane + monoethylene-glycol dimethylether from 283.15 to 353.15 K: New modified UNIFAC parameters, Fluid Phase Equilib 271 (2008) 28–33. https://doi.org/10.1016/j.fluid.2008.07.003.

[129] Y. Liu, L. Jiang, H. Wang, H. Wang, W. Jiao, G. Chen, P. Zhang, D. Hui, X. Jian, A brief review for fluorinated carbon: Synthesis, properties and applications, Nanotechnol Rev 8 (2019) 573–586. https://doi.org/10.1515/ntrev-2019-0051.

[130] P.J. Carvalho, K.A. Kurnia, J.A.P. Coutinho, Dispelling some myths about the CO2 solubility in ionic liquids, Physical Chemistry Chemical Physics 18 (2016) 14757–14771. https://doi.org/10.1039/c6cp01896c.

CHAPTER 3

HYBRID MATERIALS FOR THE SORPTION OF F-GASES

3.1 Introduction

In 1987, the Montreal Protocol determined the phasing-out of second-generation refrigerants based on chlorofluorocarbons, which cause ozone depletion [1]. As consequence, the utilization of man-made fluorinated greenhouse gases (F-gases) based on hydrofluorocarbons (HFCs) has increased drastically for refrigeration and air conditioning applications [2]. These third-generation refrigerants are energetically efficient, non-toxic, have low flammability, and are not harmful to the ozone layer. However, they are potent greenhouse gases (GHGs) with a global warming potential up to 23,000 times greater than that of carbon dioxide and an extensive atmospheric lifetime. While the emissions of all other GHGs in the EU have decreased, the emissions of HFCs have increased by 60% since 1990 [2]. Besides, to accomplish the goals of the United Nations Framework Convention on Climate Change, the Kigali Amendment (entered into force in 2019) regulates the phase-down of HFCs at a global level [3]. In the EU, Regulation Nº 517/2014 imposes restrictions for placing on the market equipment and substances with high GWP.

Because of the commitments to the international agreements and the EU F-gases Regulation, a rapid development of the research on more environment-friendly refrigerant alternatives, including HFCs with lower GWP, hydrofluoroolefins (HFOs), HFC-HFO blends, hydrocarbons, and others natural refrigerant, was observed. Nevertheless, the challenge has been to find alternative refrigerants that ensure a lower GWP and are simultaneously: (i) safe (low flammability and low toxicity); (ii) energy efficient; and (iii) easily recycled and reused. Nowadays, most F-gases recovered from end-of-life equipment are incinerated, contributing to global warming and creating pressure in the refrigeration supply chain. Therefore, there is a clear need to develop technologies to recover and recycle those F-gases from refrigeration and cooling equipment to be recycled into new blends with lower GWP, applying circular economy (an EU priority), avoiding the costs associated with incineration processes, and reducing the GHGs emissions. In most developed countries, and especially in Europe, increasing attention is being paid to the need to separate and recycle the HFCs at the end of life of refrigeration and air conditioning equipment. In fact, in the last years, different projects, such as KET4F-Gas and LIFE-4-Fgases [4,5], have been put forward at the European level, aiming at developing technologies to separate HFC blends with high GWP into their pure components.

The capture of pure F-gases and the separation of blends have been extensively investigated using solvents, advanced materials, and membrane technology. A variety of studies have dealt with the use of ionic liquids (ILs) and other alternative solvents for the selective uptake of the most commonly used pure F-gases in the EU market (for example, R-134a (1,1,1,2-tetrafluoroethane), R-32 (difluoromethane), and R-125 (pentafluoroethane)) [6–20]. Fluorinated ionic liquids (FILs), defined as ILs containing fluorinated alkyl chains with at least four carbon atoms, form polar, nonpolar, and fluorinated domains with the ability to solubilize and interact simultaneously with three totally different moieties

[21–23]. Moreover, FILs are highly tunable, with a vast range of possible variations in the size of the three different domains, which allows different types of interactions. Additionally, FILs containing short perfluorinated or hydrogenated alkyl chains are not toxic for different human cell lines and aquatic species [21,24,25]. Finally, the fluorination of ILs is a key process to decrease the viscosity and therefore to increase mass transfer [21,26]. Previous work has shown that ILs have high F-gas absorption capacity and that the properties of the absorbed F-gas play a key role in its effective absorption [19]. Moreover, the combination of FILs and membrane technology has been demonstrated to be relevant for the separation of refrigerants mixtures, as addressed by Pardo et al. [27–30] and Hermida-Merino et al.[27].

The adsorption of pure F-gases has also been studied on various adsorbent types [31], such as silica and activated carbons [32–39], zeolites [40,41], and metal-organic frameworks (MOFs) [26,42]. The investigation of porous materials for separation processes has advanced greatly in the last decades, as the selection of materials with different properties, such as surface area and pore volume and dimensions, and functionalization allows to direct the selectivity toward a specific species of a gas blend, allowing to separate it from the other components of the mixture.

The support of ILs in solid porous materials represents an advantage to increase the contact area between the gaseous sorbate and the solubilization media, increasing the mass transfer. Some authors have already studied the preparation of mesoporous silica with impregnated ILs for CO_2 sorption [43–45], CO_2 conversion [46], and desalination . In this work, we are stepping forward in the study of FILs and other fluoro-containing ILs (with a variety of functional groups and sizes of the perfluorinated chain) supported in silica, aiming at increasing the contact area to increase the sorption capacity. While a variety of new materials, such as MOFs, have been developed in the last years for the adsorption of F-gases with very high adsorption capacity [47], these materials are still difficult to produce in high amounts and have high costs. Therefore, in this study, we have selected silica, a cheap, well-studied and widely available porous material for the support of ILs.

We report the measurement and comparison of the sorption properties of R-32, R-125 and R-134a on silica and nine different silica/IL composites at room temperature. The experimental data are successfully correlated with the Sips adsorption isotherm model and an analogy model with the adsorption potential theory (APT). Since various fluorinated refrigerants composed of different F-gases are used industrially, the study of the selective separation of different F-gases from mixtures is crucial. To this end, we predict the sorption equilibria of two commercial refrigerants, R-410A (a binary blend of R-32 and R-125) and R-407 F (a ternary blend of R-32, R-125, and R-134a), in the studied composites, assuming the IL/F-gas system in the silica/IL composites behaves as an ideal mixture. Moreover, the selectivity is evaluated at different equilibrium pressures. This work presents a step forward in the study of single- and multi-component F-gas sorption in ILs supported on porous materials and in the still poorly explored area of F-gas capture and separation from commercial refrigerants.

This chapter is adapted from the following publications:

Section 3.2

J.E. Sosa, R.P.P.L. Ribeiro, P.J. Castro, J.P.B. Mota, A.B. Pereiro, J.M.M. Araújo, *Sorption of fluorinated greenhouse gases in silica-supported fluorinated ionic liquids*, J. Environ. Chem. Eng. 10 (2022) 108580. https://doi.org/10.1016/j.jece.2022.108580.

3.2 Sorption of fluorinated greenhouse gases in silica-supported fluorinated ionic liquids

The Kigali Amendment to the Montreal Protocol limits the global use of fluorinated greenhouse gases (F-gases) and encourages the development of a new generation of refrigerants with lower global warming potential. Therefore, there is a need to develop efficient and sustainable technologies to selectively capture and recycle the F-gases as new environmentally sustainable refrigerants. Here, ionic liquids (ILs) with high F-gas uptake capacity and selectivity were supported on silica and their potential as media for selective F-gas sorption was studied. For this purpose single-component sorption equilibria of difluoromethane (R-32), pentafluoroethane (R-125), and 1,1,1,2-tetrafluoroethane (R-134a) were measured at 303.15 K by gravimetry. The sorption data were successfully correlated using classical models of sorption thermodynamics. The results show that the IL supported in the porous volume and on the external surface of the porous silica controls the F-gas uptake in the composites and that changing the IL's cations and anions allows fine-tuning the selectivity of the sorption process. This work brings crucial knowledge for the development of new materials based on ILs for the selective sorption of F-gases.

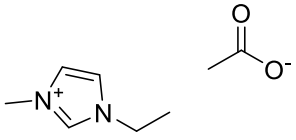
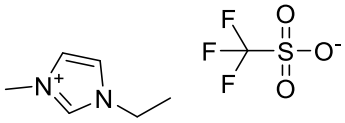
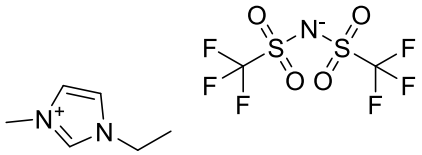
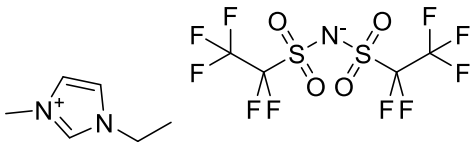
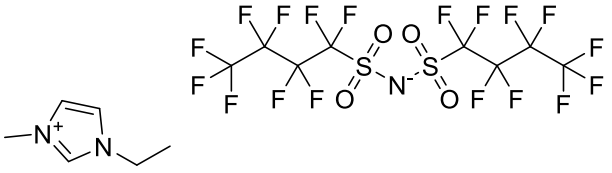
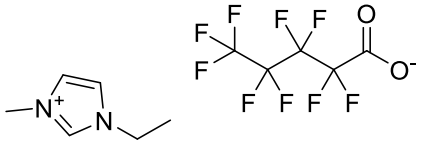
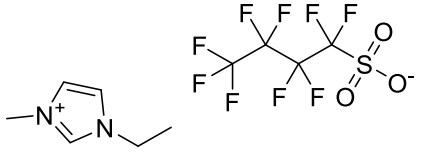
3.2.1 Experimental section

3.2.1.1 Materials

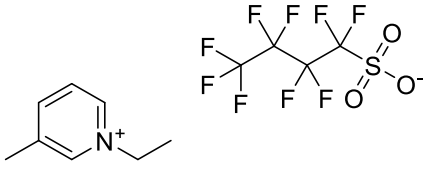
1-Ethyl-3-methylimidazolium acetate ($[C_2C_1Im][C_1CO_2]$, ≥ 90 % mass fraction purity), 1-ethyl-3-methylimidazolium perfluoromethanesulfonate ($[C_2C_1Im][CF_3SO_3]$, ≥ 99 % mass fraction purity), 1-ethyl-3-methylimidazolium bis(trifluoromethylsulfonyl)imide ($[C_2C_1Im]$ $[N(CF_3SO_2)_2]$, ≥ 99.5 % mass fraction purity), 1-ethyl-3-methylimidazolium perfluorobutanesulfonate ($[C_2C_1Im][C_4F_9SO_3]$, ≥ 97 % mass fraction purity), 1-ethyl-3-methylpyridinium perfluorobutanesulfonate ($[C_2C_1py][C_4F_9SO_3]$, ≥ 97 % mass fraction purity), and 1-ethyl-3-methylimidazolium bis(pentafluoroethylsulfonyl)imide $[C_2C_1Im][N(C_2F_5SO_2)_2]$, ≥ 98 % mass fraction purity) were supplied by IoLiTec GmbH. 1-Ethyl-3-methylimidazolium perfluoropentanoate ($[C_2C_1Im][C_4F_9CO_2]$, ≥ 99 % mass fraction purity), 1-ethyl-3-methyl-imidazolium bis(nonafluorobutylsulfonyl)imide ($[C_2C_1Im][N(C_4F_9SO_2)_2]$, ≥ 99 % mass fraction

purity), and 1-ethyl-3-methylimidazolium perfluorooctanesulfonate ([C_2C_1Im][$C_8F_{17}SO_3$], ≥ 99 % mass fraction purity) were previously synthesized, through an ion-exchange resin method [48], and characterized in our laboratory [24,25] Fumed silica (powder, 0.2–0.3 μm average particle size; 200 ± 25 m^2/g surface area) was purchased from Sigma-Aldrich. Detailed structures and nomenclatures of the studied ILs are shown in Table 3.2.1. The purity of all ILs was checked by ^1H, ^{19}F NMR, and elemental analysis. All ILs were dried under vacuum (4 Pa) and vigorously stirred at 323.15 K for at least 48 hours, immediately prior to their use. By volumetric Karl-Fischer titration technique (Metrohm Ion analysis, 831 KF Coulometer), the water content of the ILs was quantified as less than 100 ppm. R-32 (difluoromethane, ≥ 99.8 % mass fraction purity), R-125 (pentafluoroethane, ≥ 99.8 % mass fraction purity), and R-134a (1,1,1,2- tetrafluoroethane, ≥ 99.8 % mass fraction purity) (Table 1.1.1) were acquired from Polo Zero.

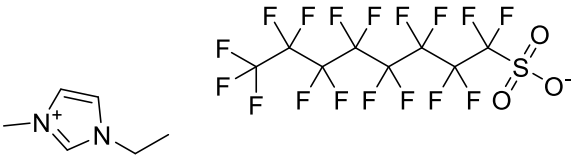
Table 3.2.1 Acronyms and chemical structures of the ILs and F-gases studied in this work.

Ionic Liquid	Chemical Structure
1-Ethyl-3-methylimidazolium acetate **[C_2C_1Im][C_1CO_2]**	
1-Ethyl-3-methylimidazolium triflate **[C_2C_1Im][CF_3SO_3]**	
1-Ethyl-3-methylimidazolium bis(trifluoromethylsulfonyl)imide **[C_2C_1Im][$N(CF_3SO_2)_2$]**	
1-Ethyl-3-methylimidazolium bis(pentafluoroethylsulfonyl)imide **[C_2C_1Im] [$N(C_2F_5SO_2)_2$]**	
1-Ethyl-3-methylimidazolium bis(nonafluorobutylsulfonyl)imide **[C_2C_1Im] [$N(C_4F_9SO_2)_2$]**	
1-Ethyl-3-methylimidazolium perfluoropentanoate **[C_2C_1Im][$C_4F_9CO_2$]**	
1-Ethyl-3-methylimidazolium perfluorobutanesulfonate **[C_2C_1Im][$C_4F_9SO_3$]**	

1-Ethyl-3-methylpyridinium perfluorobutanesulfonate
[C_2C_1py][$C_4F_9SO_3$]



1-Ethyl-3-methylimidazolium perfluorooctanesulfonate
[C_2C_1Im][$C_8F_{17}SO_3$]



3.2.1.2 Experimental Methods and characteristics

The silica/IL composites were prepared by mixing 40 % of the IL with 60 % of fumed silica (% weight) in the presence of pure ethanol in excess, which was further removed under vacuum for 24h. After this procedure, a white powder composite, with larger particles than the ones of fumed silica, was obtained (see Figure 3.2.1).



Figure 3.2.1 Fumed silica (A) and ionic liquid (B) used to prepare the IL/silica composites (C).

The BET superficial area and pore volume of the prepared composites and fumed silica were determined by nitrogen porosimetry, at 77 K on a Micromeritics ASAP 2010 apparatus, after a pre-treatment at 343.15 K for 4h, under vacuum. Scanning electron microscopy (SEM) analyses were performed in an ultra-resolution field-emission scanning electron microscope JEOL JSM-6700f with elements energy-dispersive X-ray spectroscopy (EDS) detector at a working voltage of 15 kV.

3.2.1.3 Sorption of F-Gas measurements

The single-component sorption equilibrium isotherms for R-32, R-125, and R-134a on the IL/silica composites were measured using a standard gravimetric method at 303.15 K [39,49–51], and at pressures up to 0.54 MPa (the maximum ratio applied for pressure/saturation pressure was of 0.28 for R-32, 0.38 for R-125, and 0.69 for R-134a). This method consists of the stepwise supply of pure F-gas to a temperature-controlled measurement cell containing the sorbent (ca. 0.3–0.4 g), while the mass and

pressure variations are monitored until equilibrium is reached. sorption/desorption cycles were performed to check for the presence of hysteresis.

Sorption measurements were performed in a high-accuracy IsoSORP high-pressure magnetic-suspension balance (MSB) (Rubotherm GmbH, Germany, maximum load of 25 g, resolution of 10 μg, uncertainty less than 0.002 %, and reproducibility smaller than 3×10^{-5} g), schematized in Figure 2.3.1. The temperature was kept constant by using a thermostatic bath (uncertainty of ± 0.1 K) and the pressure was measured with transducers working with accuracy over the full range of operating pressures: a Baratron model 627D (MKS Instruments GmbH, Germany) for 0–0.1 MPa, the accuracy of 0.12 %; one Omegadyne Inc. (Sunbury, OH, USA) model PX01C1-150A5T for 0–1 MPa (with an accuracy of 0.05 % of the full scale). The equilibrium was considered when pressure and mass changes in the system were no longer observed. Before the measurements, the sorbent samples were degassed for at least 12 hours under vacuum at 333.15 K.

The sorption loading under equilibrium conditions, expressed as excess sorption, q_{ex}, is defined as:

$$q_{ex} = \frac{w - m_s + V_h\rho_g}{m_s} + v_s\rho_g \qquad 3.2.1$$

where w is the apparent mass weighed by the balance, m_s is the degassed mass of sorbent sample in the measurement cell, V_h is the cumulative volume of all physical parts in the measuring cell contributing to buoyancy effects, ρ_g is the density of the gas at the equilibrium pressure and temperature of the experiment, and v_s is the specific volume of the sorption medium impenetrable to the sorbate ($v_s = 1/\rho_s$, where ρ_s is the density of the solid matrix). The density ρ_s was determined experimentally by helium (He) picnometry.

Excess sorption can be converted to total sorption, q, via

$$q = \frac{q_{ex}}{1 - v_a\rho_g} \qquad 3.2.2$$

where v_a (cm^3/mol) is the molar volume of the sorbed phase, which we approximate by the specific (or molar) volume, v_m, of the saturated liquid sorptive at the sorption temperature, assuming a subcritical sorption from the vapor phase [52]. The gas density, $\rho_g(T, P)$, was extracted from the NIST Chemistry Webbook [53,54]. The uncertainty of the calculated sorbed mass is around 1% over the full range of temperature and pressure [55].

All the sorption isotherms were fitted with the Sips model, given by [56]:

$$q = q_s\frac{(aP)^{1/n}}{1 + (aP)^{1/n}} \qquad 3.2.3$$

where q is the sorbed amount of gas at equilibrium per unit mass of sorption medium (mmol/g), q_s the saturated amount, a an affinity constant (MPa^{-1}), and n a heterogeneity parameter (dimensionless).

3.2.1.4 An analogy with the Adsorption Potential Theory (APT).

A formulation similar to the adsorption Potential Theory (APT) was applied to the sorption equilibrium data in the composites and silica [57–59]. In the APT, the sorbed amount of gas, q, measured as an equivalent volume of condensed gas, W, is expressed as

$$W = qV_{\mathrm{m}} = W(\Phi) \qquad 3.2.4$$

where V_{m} is the molar volume of the gas if it were condensed into a liquid phase,

$$\Phi = RT\ln(f_{\mathrm{s}}/f) \qquad 3.2.5$$

is usually referred to as the sorption potential, R is the ideal gas constant, T the system temperature, f the fugacity, and f_{s} the saturation fugacity (considering the non-ideal gas behavior at high pressure). However, we prefer to identify Φ as the difference in free energy (or chemical potential) when a gas molecule is moved from the gas phase to its condensed state. Since we are analyzing the sorption data at a single temperature, this formulation is perfectly valid because of eqs. 3.2.4 and 3.2.5 are equivalent to simply stating that $q = q(P)_{\text{fixed } T}$. The fugacity values were determined using Aspen Plus v10 database and V_{m} obtained from the NIST Chemistry Webbook (assuming the sorbate is in the liquid state)[54].

But one can go a step further and test whether introducing an affinity coefficient β, as a scaling factor of Φ, collapses the curves $W_i(\Phi_i)$ of the different gases in the same composite into a single characteristic curve $W(\Phi_i/\beta_i)$, as in the APT. Thus, eq. 3.2.4 is replaced by

$$W_i = q_i V_{i,\mathrm{m}} = W\left(\widetilde{\Phi}_i\right), \qquad \widetilde{\Phi}_i = \frac{\Phi_i}{\beta_i} \qquad 3.2.6$$

In the literature β has often been correlated to the molecular parachor of the sorbate, $P_{\mathrm{M}} = \gamma^{1/4}V_{\mathrm{m}}$, an empirical constant that relates the surface tension of a liquid, γ, to its molecular volume V_{m}. P_{M} was originally used for comparing molecular volumes under conditions such that the liquids have the same surface tension and for determining the partial structure of compounds by adding values obtained for constituent atoms and structural features. In the absence of knowledge of γ, the value of can be approximated as $P_{\mathrm{M}} = 8 + 0.707V_{\mathrm{c}}$, where V_{c} is the critical volume of the gas. In the present V_{c} was obtained by the NIST Chemistry Webbook [54]. For sorption of organic vapors in activated carbon the following correlation has been proposed [60,61]:

$$\beta = 8.27 \times 10^{-3} P_{\mathrm{M}} \qquad 3.2.7$$

which arbitrarily gives $\beta = 1$ for benzene (reference compound).

Table 3.2.2. lists the values of β that collapse the curves $W_i(\Phi_i)$ of the three different F-gases in the same composite into a single characteristic curve. For reference, we also include the values obtained for silica and those given by eq. 3.2.7. Interestingly, it is not only possible to collapse the sorption

data for the three F-gases on the same composite into a single characteristic curve by use of an affinity coefficient, but also the obtained values of β are nearly independent of the type of composite.

The experimental characteristic curve for each composite can be fitted by a Dubinin–Astakhov (D–A) type equation [57–59,62].

$$W = W_s \exp\left(-\gamma \tilde{\Phi}^n\right) \qquad 3.2.8$$

where γ and n are fitting parameters related to the characteristic energy for the given sorbent medium and W_s is the saturation capacity of the medium expressed as the volume of liquid sorbate. These parameters were obtained from the linear fitting:

$$\ln[\ln(W_s/W)] = \ln\gamma + n \ln\tilde{\Phi} \qquad 3.2.9$$

Table 3.2.2 Affinity coefficient, β, for each sorbent/F-gas pair.

	R-32	**R-125**	**R-134a**
SiO_2/[C_2C_1Im] [N($C_2F_5SO_2$)]	0.62	0.74	0.56
SiO_2/[C_2C_1Im] [CF_3SO_3]	0.62	0.74	0.56
SiO_2/[C_2C_1Im] [$C_4F_9CO_2$]	0.62	0.86	0.56
SiO_2/[C_2C_1Im] [$C_8F_{17}SO_3$]	0.62	0.80	0.56
SiO_2/[C_2C_1Im] [N($C_4F_9SO_2$)$_2$]	0.62	0.74	0.56
SiO_2/[C_2C_1Im] [C1CO_2]	0.64	0.74	0.56
SiO_2/[C_2C_1Im] [$C_4F_9SO_3$]	0.64	0.74	0.56
SiO_2/[C_2C_1py] [$C_4F_9SO_3$]	0.60	0.80	0.56
Silica	0.62	0.82	0.69
Eq. 3.2.7	0.49	0.78	0.75

3.2.2 Results and discussion

3.2.2.1 Characterization of the composites

Each composite was prepared by mixing 40 wt % IL with 60 wt % fumed silica, according to the experimental procedure detailed in section 3.2.1.2. Given that the specific volumes of the tested ILs are in the range 0.65–0.91 cm^3/g, 40-wt % IL is 30–85 % in excess of the amount required to completely fill the 0.33×0.6=0.20 cm^3/g porous volume of the composite with bulk liquid IL. The composites were characterized in terms of BET surface area (S_{BET}) and pore volume (V_p) (SI shows the experimental procedure). The surface area and porous volume of silica are significantly decreased when it is impregnated with 40-wt % IL (see Table 3.2.3 and Figure 3.2.2). The S_{BET} and V_p values decreased between ~60 % for the SiO_2/[C_2C_1Im][$C_8F_{17}SO_3$] composite and ~80 % (S_{BET}) and ~90 % (V_p) for SiO_2/[C_2C_1Im][C_1CO_2]. These results indicate that the IL not only penetrated into the pore volume of

the silica but also covered the external surface of the silica particles, rather than existing as droplets surrounded by a silica envelope, as observed in other studies [45].

Table 3.2.3 BET surface area and pore volume of silica and of the silica/IL composites.

	S_{BET} (m^2/g)	Pore volume (cm^3/g)
$SiO_2/[C_2C_1Im][C_1CO_2]$	028.4	0.06
$SiO_2/[C_2C_1Im][CF_3SO_3]$	068.4	0.09
$SiO_2/[C_2C_1Im][N(CF_3SO_2)_2]$	052.7	0.12
$SiO_2/[C_2C_1Im][N(C_2F_5SO_2)_2]$	061.2	0.11
$SiO_2/[C_2C_1Im][N(C_4F_9SO_2)_2]$	048.2	0.13
$SiO_2/[C_2C_1Im][C_4F_9CO_2]$	065.4	0.12
$SiO_2/[C_2C_1Im][C_4F_9SO_3]$	062.3	0.11
$SiO_2/[C_2C_1py][C_4F_9SO_3]$	068.4	0.13
$SiO_2/[C_2C_1Im][C_8F_{17}SO_3]$	082.0	0.15
SiO_2	212.4	0.33

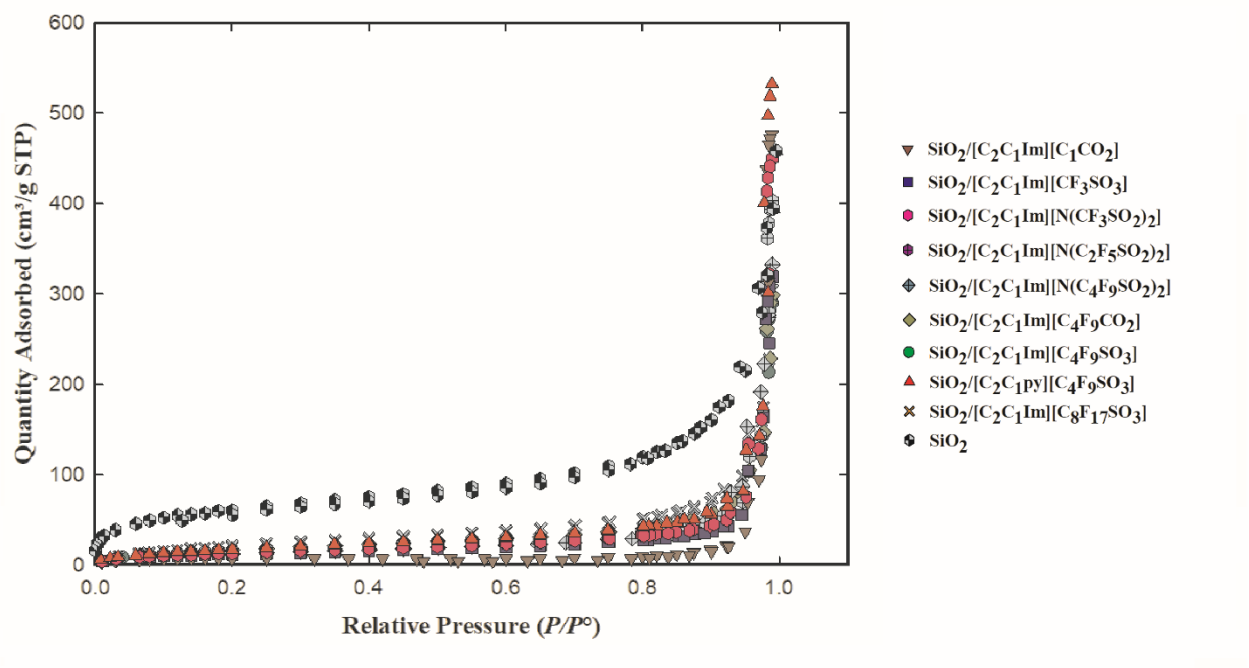


Figure 3.2.2 Nitrogen sorption isotherms at 77 K for the silica/IL composites.

The morphology of the composites was evaluated and compared with those of pure IL and fumed silica by scanning electron microscopy (SEM). Figure 3.2.3 – 3.2.5 compare the SEM images

of: (i) fumed silica; (ii) three pure ILs, ([C_2C_1Im][C_1CO_2] as reference IL, [C_2C_1Im][$N(CF_3SO_2)_2$], and [C_2C_1Im][$C_4F_9SO_3$]); and (iii) the composites prepared with these ILs. The morphology of the composites is very similar to that of pure silica and has notable differences from that of pure ILs. Moreover, the energy-dispersive X-ray spectroscopy (EDS) analysis of each sample (see Figure 3.2.3 – 3.2.5) detected fluorine atoms on the surface of the composites prepared with ILs containing fluorine atoms but not on the silica samples. These results indicate that some of the ILs are located on the external surface of the silica particles and the rest inside of their porous volume, reinforcing the previous conclusions from ASAP results.

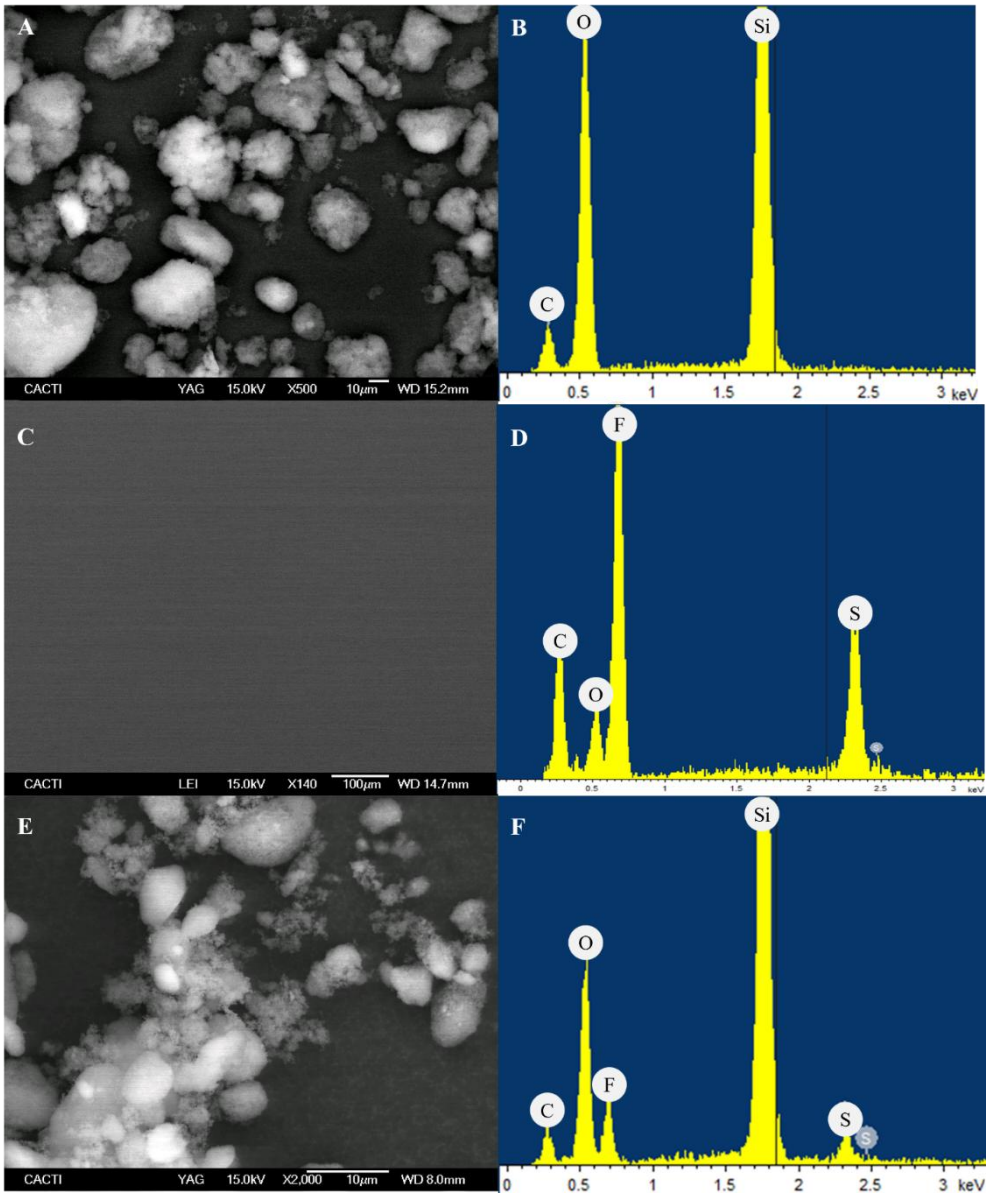


Figure 3.2.3 Electron scanning microscopy image and energy-dispersive X-ray spectroscopy spectrum of SiO_2 (panels A and B), [C_2C_1Im][$C_4F_9SO_3$] (panels C and D), and SiO_2/[C_2C_1Im][$C_4F_9SO_3$] (panel E and F).

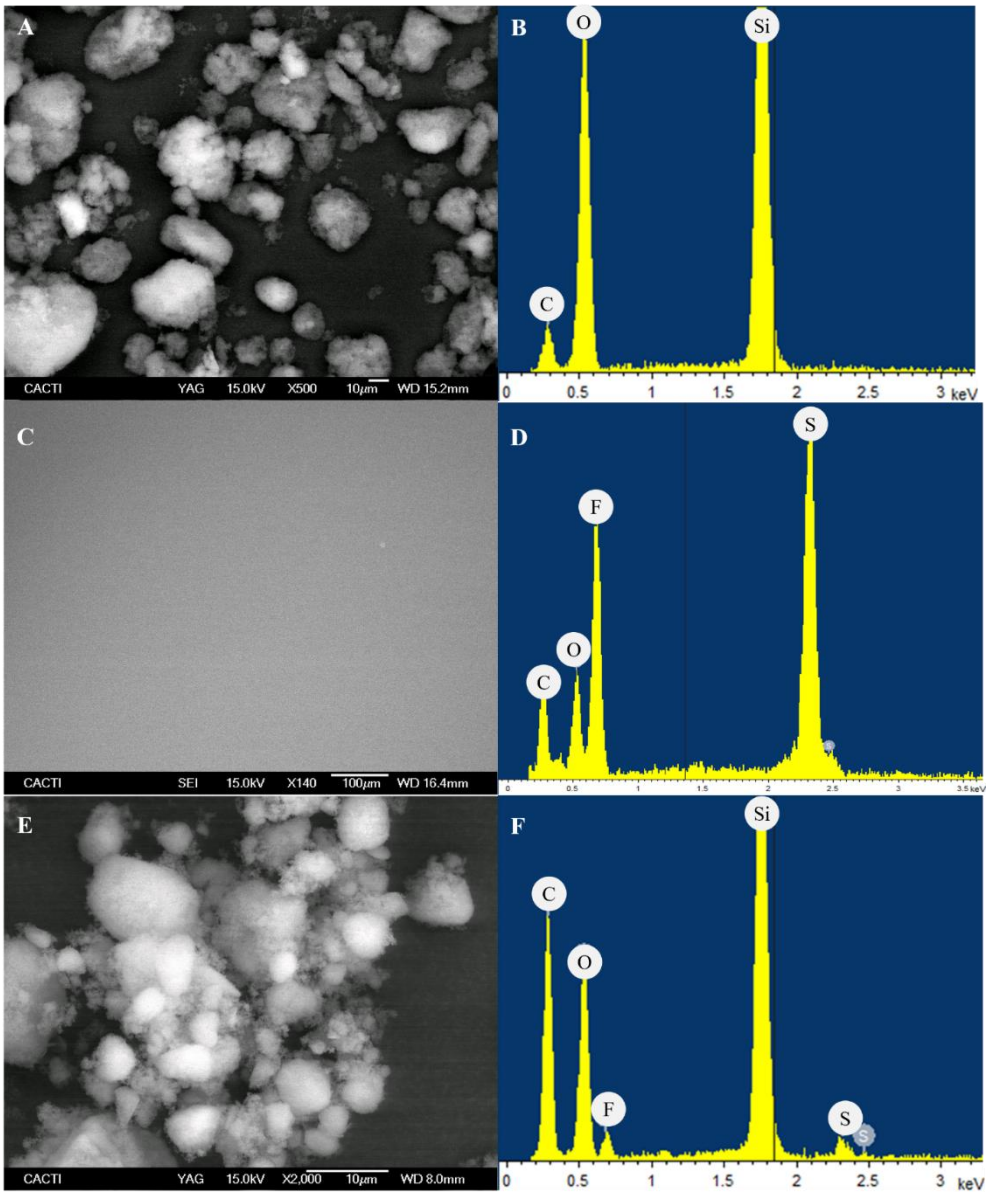


Figure 3.2.4 Electron scanning microscopy image and energy-dispersive X-ray spectroscopy spectrum of SiO_2 (panels A and B), $[C_2C_1Im][N(CF_3SO_2)_2]$ (panels C and D), and $SiO_2/[C_2C_1Im][N(CF_3SO_2)_2]$ (panels E and F).

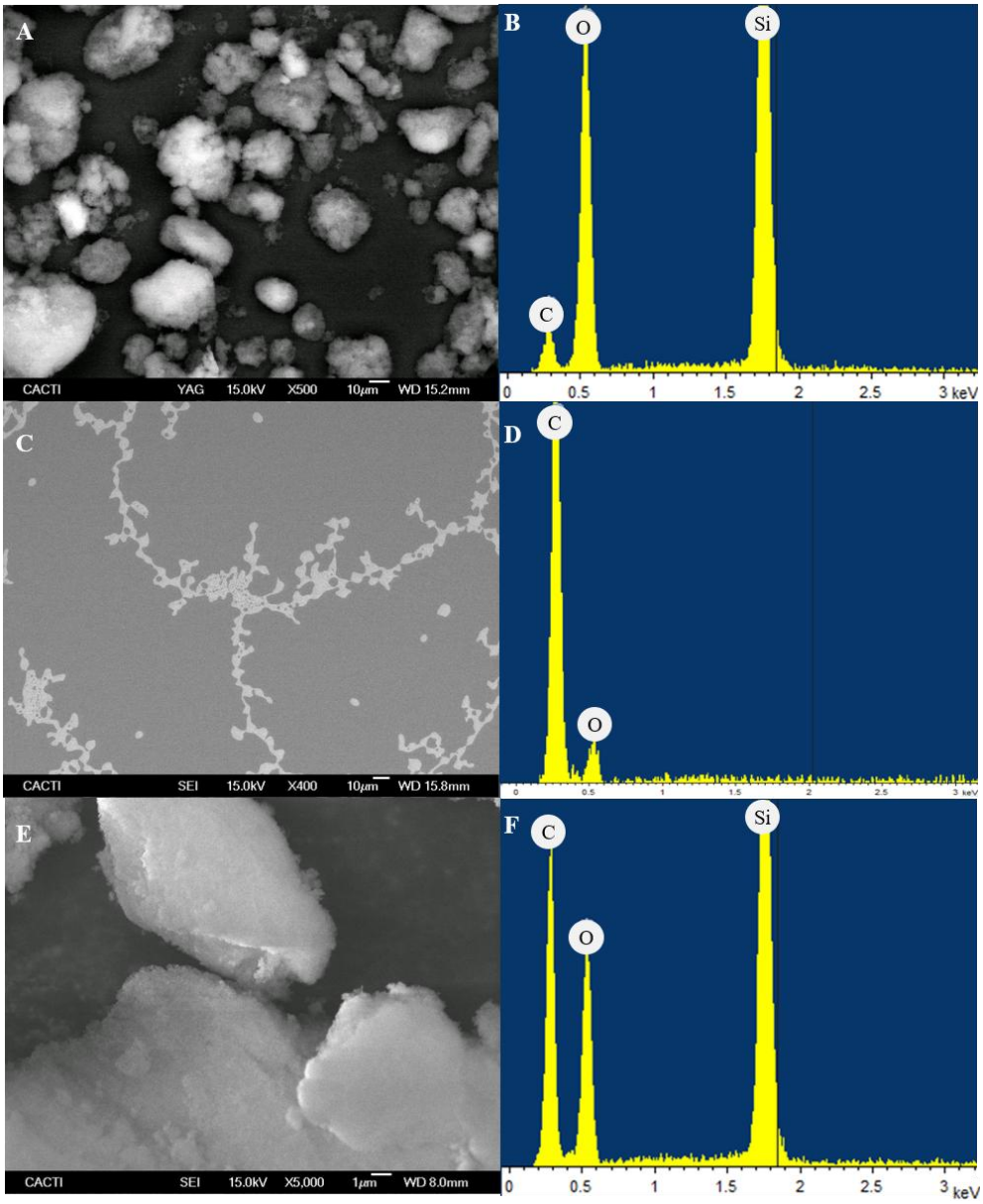


Figure 3.2.5 Electron scanning microscopy image and energy-dispersive X-ray spectroscopy spectrum of SiO_2 (panels A and B), $[C_2C_1Im][C_1CO_2]$ (panels C and D), and $SiO_2/[C_2C_1Im][C_1CO_2]$ (panels E and F).

3.2.2.2 Gas sorption in the silica/IL composite

The procedure for determining the F-gas sorption on the composites is detailed in section 3.2.1.3. The equilibration time required for measuring each experimental data point was about 40 min. Sorption data of each F-gas on silica and the composites are presented as excess sorption, q_{ex}, in Figure 3.2.6 and total sorption, q, in Figure 3.2.7, as a function of equilibrium gas pressure. The sorption and desorption branches of the isotherm are superimposable, indicating the inexistence of hysteresis between the sorption and desorption processes (see Figure 3.2.8). Figure 3.2.6 shows that for gas pressures below ca. 0.18 MPa the porous silica adsorbs more F-gas than the pure ILs and the composites; however, above $P = 0.18$ MPa, the F-gas uptake by the pure ILs is higher than by the porous silica and the composites.

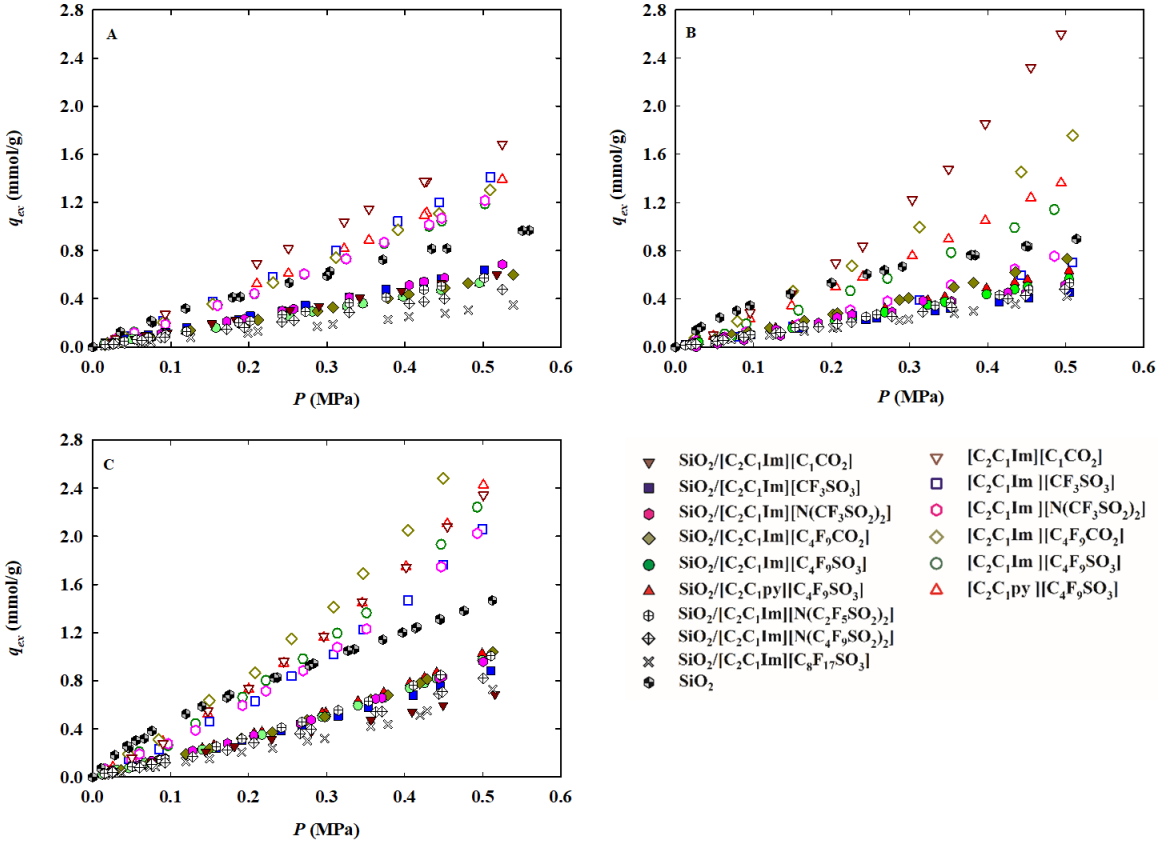


Figure 3.2.6 Sorption equilibrium isotherms, at 303.15 K, of R-32 (panel A), R-125 (panel B), and R-134a (panel C) on the fumed silica, composites studied in this work, and on pure ILs studied previously [19].

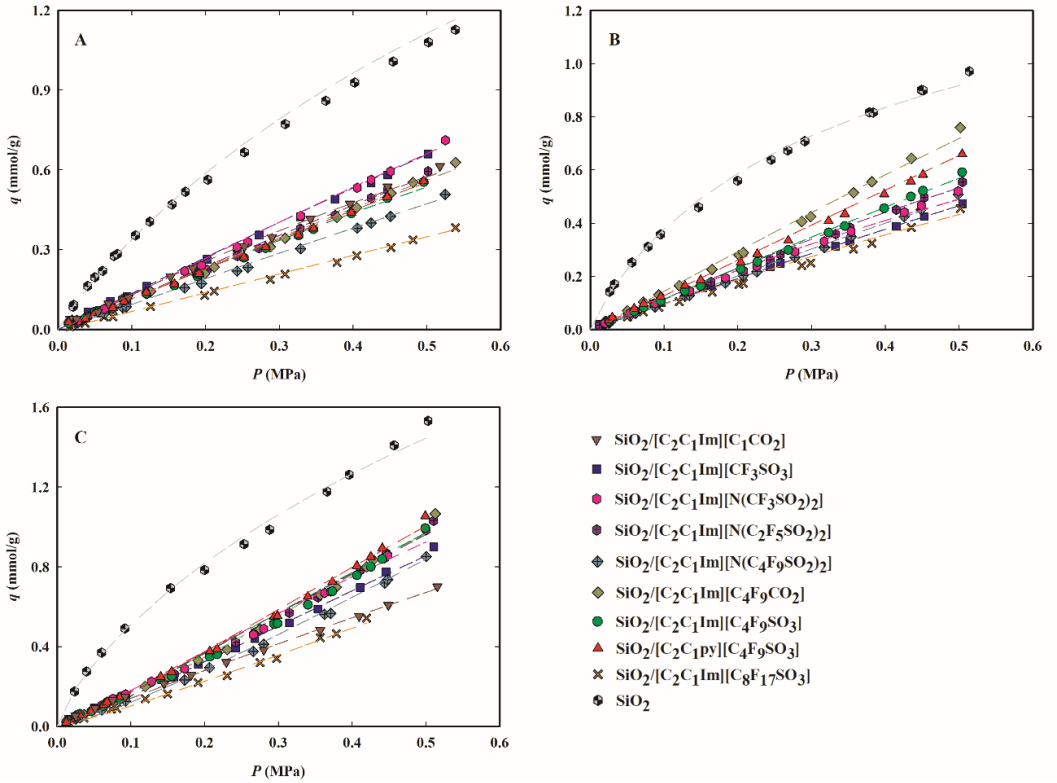


Figure 3.2.7 Sorption equilibrium isotherms, at 303.15 K, of R-32 (panel A), R-125 (panel B), and R-134a (panel C) on SiO_2 and SiO_2/IL composites studied in this work. The dashed lines represent the data fitting to the Sips equation.

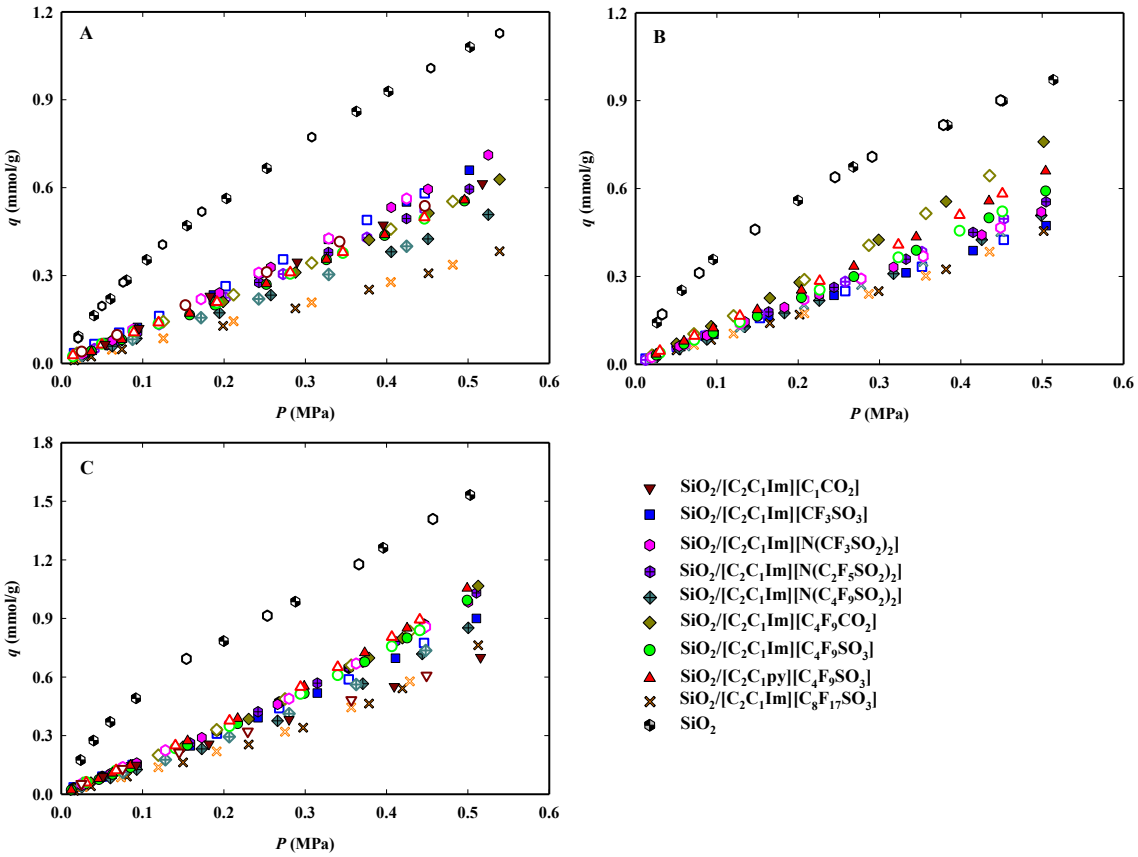


Figure 3.2.8 Sorption (full symbols) and desorption (empty symbols) of R-32 (panel A), R-125 (panel B), and R-134a (panel C) on SiO_2 and SiO_2/IL composites at 303.15 K.

Since to predict binary adsorption and calculate selectivity's it is necessary to manipulate analytical expressions of loading as a function of pressure, the sorption data were fitted by a Sips isotherm model [56], as detailed in section 3.2.1.3, with good agreement between calculated and experimental data. The Sips parameters determined for each composite/F-gas pair are listed in Table 3.2.4 and the fittings are illustrated in Figure 3.2.7. Although the Sips model was originally developed as a combined form of Langmuir and Freundlich models for predicting the adsorption in heterogeneous systems and circumventing the limitation of the rising adsorbate concentration associated with the Freundlich isotherm, we use it here as a general three-parameter model with enough flexibility to adequately fit our experimental sorption data.

Table 3.2.4 Sips parameters obtained from the binary systems F-gas + SiO_2/IL composite.

	F-gas	q_s (mmol/g)	a (MPa^{-1})	n
	R-32	2.746	0.546	0.975
SiO_2/[C_2C_1Im] [C_1CO_2]	R-125	-	-	-
	R-134a	7.628	0.200	0.984
SiO_2/[C_2C_1Im] [CF_3SO_3]	R-32	8.641	0.173	0.980

	R-125	4.938	0.223	0.970
	R-134a	8.545	0.288	0.883
	R-32	4.406	0.413	0.911
SiO_2/[C_2C_1Im] [$N(CF_3SO_2)_2$]	R-125	1.641	0.910	0.921
	R-134a	5.091	0.521	0.893
	R-32	4.020	0.377	0.932
SiO_2/[C_2C_1Im] [$N(C_2F_5SO_2)_2$]	R-125	2.201	0.704	0.915
	R-134a	9.304	0.292	0.890
	R-32	5.454	0.211	0.955
SiO_2/[C_2C_1Im] [$N(C_4F_9SO_2)_2$]	R-125	2.739	0.506	0.905
	R-134a	9.545	0.310	0.796
	R-32	7.323	0.174	0.982
SiO_2/[C_2C_1Im] [$C_4F_9CO_2$]	R-125	5.471	0.344	0.932
	R-134a	7.943	0.392	0.825
	R-32	4.001	0.326	0.972
SiO_2/[C_2C_1Im] [$C_4F_9SO_3$]	R-125	5.571	0.252	0.952
	R-134a	7.155	0.412	0.854
	R-32	7.801	0.159	0.985
SiO_2/[C_2C_1py] [$C_4F_9SO_3$]	R-125	10.953	0.144	0.955
	R-134a	6.865	0.455	0.840
	R-32	7.171	0.116	0.957
SiO_2/[C_2C_1Im] [$C_8F_{17}SO_3$]	R-125	2.316	0.492	0.954
	R-134a	7.532	0.260	0.850
	R-32	3.545	0.8491	1.098
SiO_2	R-125	1.653	2.566	1.118
	R-134a	5.872	0.4623	1.308

The purpose of supporting the ILs on silica, a material with a relatively high porous volume, is to enhance the mass transfer and increase the contact area with the F-gas. The sorption capacity and selectivity of the prepared composites towards R-32, R-125, and R-134a were evaluated. Due to the high tuneability of the ILs, the appropriate combination of cation and anion allows the sorption and selectivity of a given gas to be optimized. The absorption of R-32, R-125, and R-134a into different ILs

containing fluorine atoms was previously studied [19]. Here, six different ILs based on two cations ($[C_2C_1Im]^+$ and $[C_2C_1py]^+$) and on five different anions ($[C_1CO_2]^-$, $[CF_3SO_3]^-$, $[N(CF_3SO_2)_2]^-$, $[C_4F_9SO_3]^-$, $[C_4F_9CO_2]^-$) were examined [19]. Additionally, three other ILs, $[C_2C_1Im][N(C_2F_5SO_2)_2]^-$, $[C_2C_1Im][C_8F_{17}SO_3]^-$, and $[C_2C_1Im][N(C_4F_9SO_2)_2]^-$, are supported on silica to prepare composites used to study the effect of increasing the size of the perfluorinated chain of the IL anion on gas sorption and selectivity.

Figure 3.2.6 compares our experimental results with previously published absorption data of pure ILs [19] over the entire pressure range studied in this work. F-gas absorption in pure IL shows improved performance relative to the SiO_2/IL composite and fumed silica. However, when a correction factor of 0.4 is applied to the IL sorption data on the composite (to account for 40 % weight of IL in the composite), the uptake values for both pure IL and its composite are similar, in most cases with slightly better results for the composite (See Figure 3.2.9), due to the effect of the force field exerted by the internal surface of the silica on the confined IL which improves its absorption capacity. These results show that F-gas sorption in the composites is controlled by the IL. Moreover, F-gas solubility in the pure ILs is higher than the F-gas sorption in the porous silica.

As noted earlier for pure ILs [19], the use of ILs with different cations and anions, and especially with different numbers of fluorine atoms in the anion, strongly influences the solubility and selectivity of the gas. In this work, it was observed that the ILs play a major role in F-gas sorption in the composites. Moreover, the preparation of composites using different ILs led to significant differences in F-gas sorption, with trends similar to the ones observed for gas solubility in pure ILs (see Figure 3.2.6 and Figure 3.2.7). All composites have a higher sorption capacity to R-134a than to the other two F-gases (see Figure 3.2.10).

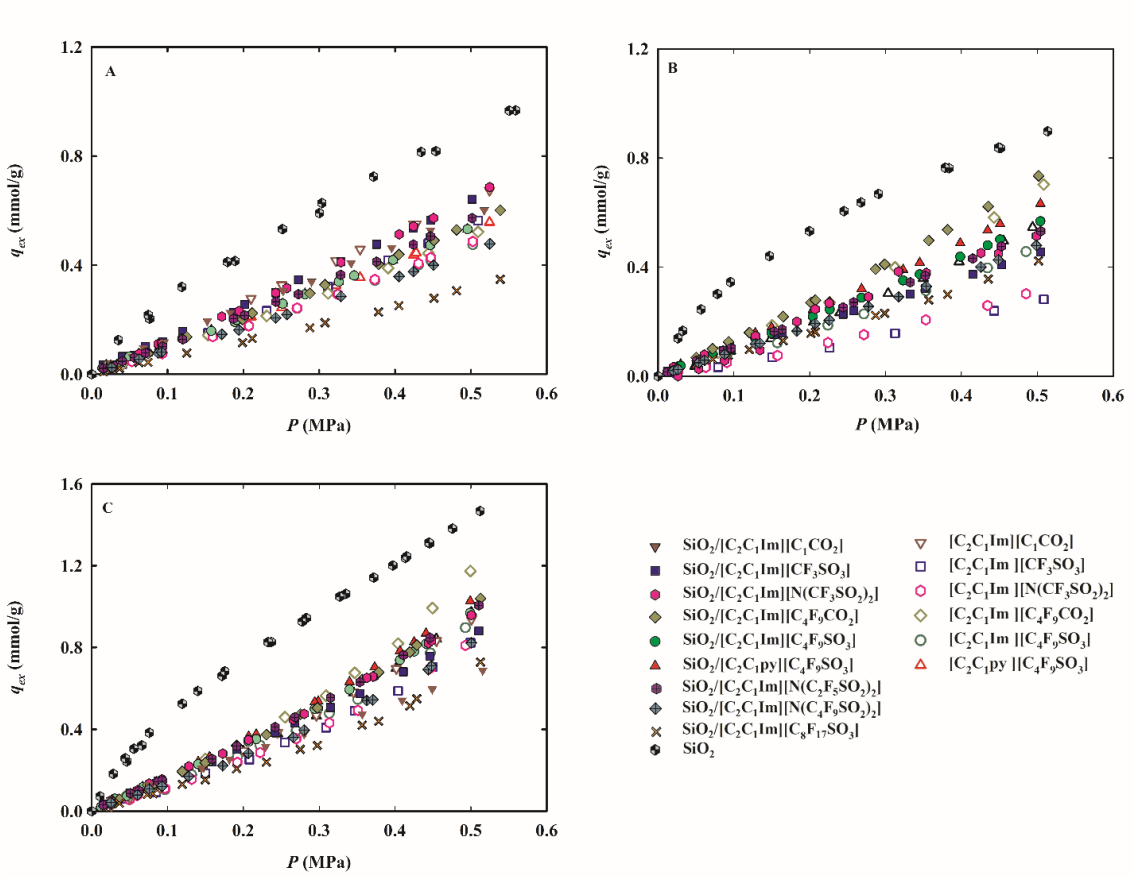


Figure 3.2.9 Sorption equilibrium isotherms, at 303.15 K, of R-32 (panel A), R-125 (panel B), and R-134a (panel C) on silica and silica/IL composites studied in this work, and on pure ILs studied previously (with a correction factor of 0.4 to account to the percentage of ILs in the composites, 40% weight) [19].

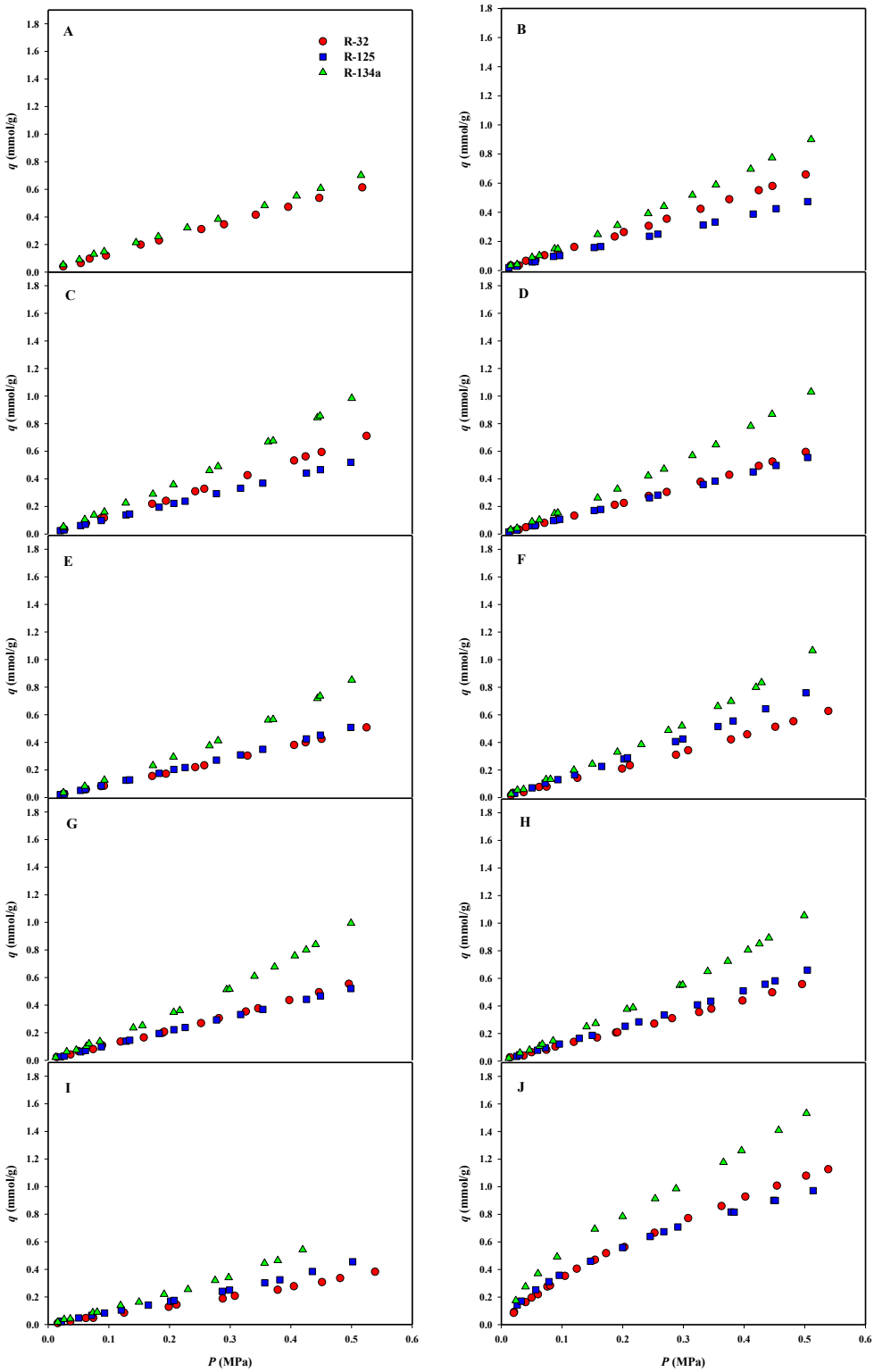


Figure 3.2.10 Sorption of R-32, R-125, and R-134a at 303.15 K on SiO_2/[C_2C_1Im][C_1CO_2] (panel A), SiO_2/[C_2C_1Im][CF_3SO_3] (panel B), SiO_2/[C_2C_1Im][$N(CF_3SO_2)_2$] (panel C), SiO_2/[C_2C_1Im][$N(C_2F_5SO_2)_2$] (panel D), SiO_2/[C_2C_1Im][$N(C_4F_9SO_2)_2$] (panel E), SiO_2/[C_2C_1Im][$C_4F_9CO_2$] (panel F), SiO_2/[C_2C_1Im] [$C_4F_9SO_3$] (panel G), SiO_2/[C_2C_1py] [$C_4F_9SO_3$] (panel H), SiO_2/[C_2C_1Im][$C_8F_{17}SO_3$] (panel I), and SiO_2 (panel J).

The presence of a carboxylate group, instead of a sulfonyl group, in the IL anion slightly enhances the sorption of R-125 but not of R-32 and R-134a (see Figure 3.2.11.). The same tendency is observed for the pure ILs studied in the work of [19] (see Figure 3.2.6.). Interestingly, R-125 has also good solubility in the pure $[C_2C_1Im][C_1CO_2]$, suggesting that polar interactions with the carboxylate group may play an important role in the solubility of R-125 [19]. Similar conclusions were obtained by Asensio-Delgado et al [63], where the sorption of R-125 in carboxylate-based ILs was observed to deviate from the Regular Solution Theory [63].

While the presence of either an imidazolium or a pyridinium group in the IL cation does not significantly affect F-gas sorption (see Figure 3.2.12), the size of the perfluorinated chain plays a key role in the sorption capacity of the studied ILs (see Figure 3.2.13-3.2.14). The increment from $[CF_3SO_3]^-$ to $[C_4F_9SO_3]^-$ has no significant effect on F-gas sorption but the composites prepared from ILs with the highest number of carbons in the perfluorinated chain ($[C_2C_1Im][C_8F_{17}SO_3]$ and $[C_2C_1Im][N(C_4F_9SO_2)_2]$) have the poorest sorption capacity for the three F-gases. However, the influence of the increment of the fluorinated alkyl chain length is higher for the sorption of R-32 and R-134a than for the adsorption of R-125, demonstrating specific interactions with this F-gas.

On the other hand, the composites containing the two studied conventional fluoro-containing ILs ($[C_2C_1Im][CF_3SO_3]$ and $[C_2C_1Im][N(CF_3SO_2)_2]$) presented the best sorption capacities for R-32. On the other hand, composites containing ILs with up to 4 carbons in the perfluorinated chain present the best results for R-134a and R-125 (see Figure 3.2.13-3.2.14). The presence of ramified perfluorinated chains in the anion of the ILs does not significantly affect the uptake of R-125 and R-134a (see Figure 3.2.14). However, the increase in the anion size and the change of linear to ramified chains in the ILs anion leads to a decrease in gas uptake in the case of R-32 (see Figure 3.2.14).

These effects in gas uptake are in accordance with those previously observed for pure ILs [19], revealing that the properties of the ILs are commanding the sorption of the F-gases in the composites. In this way, the sorption of the F-gases containing a higher number of fluorine atoms (R-125 and R-134a) is enhanced in composites prepared with FILs (fluorinated ILs with fluorinated chain lengths equal to or greater than 4 carbon atoms), relatively to conventional fluoro-containing ILs (with perfluorinated chains shorter than 4 carbon atoms). These results highlight the key role of the fluorinated alkyl side chain (fluorinated nanosegregated domain) of the IL, either pure or as a composite, in the solubility of the studied F-gases.

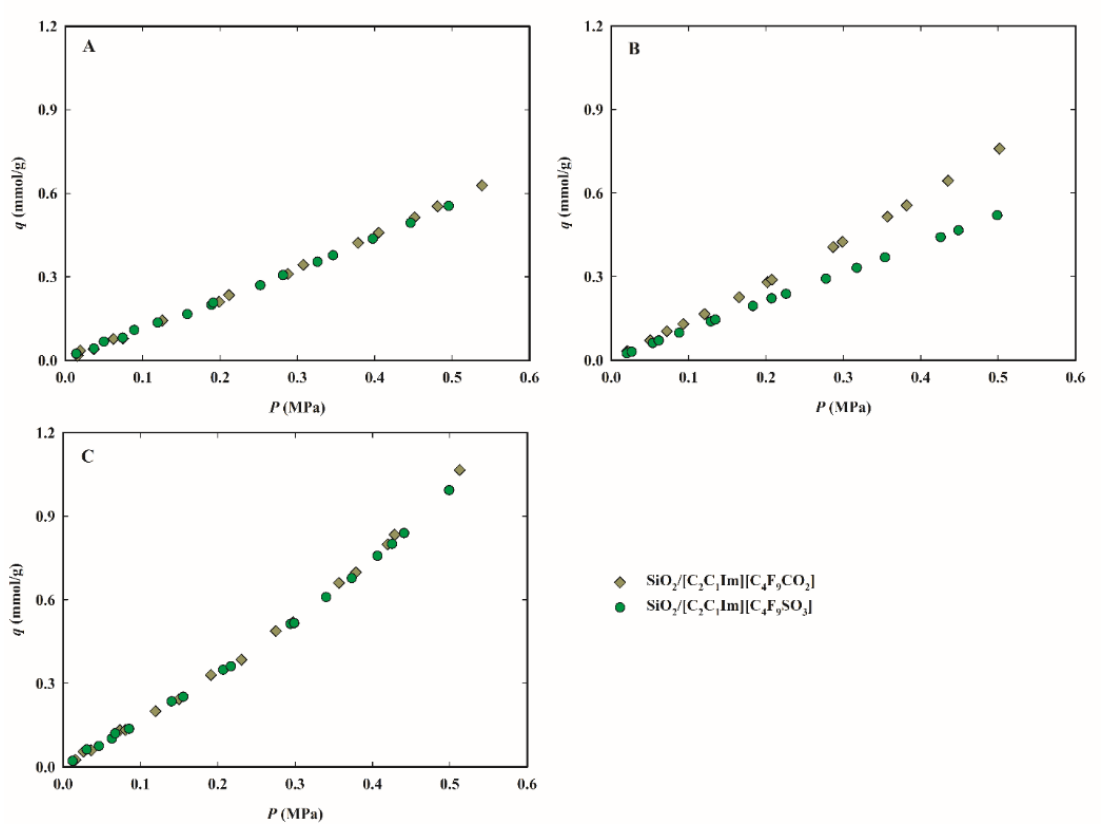


Figure 3.2.11 Comparison of the sorption of R-32 (panel A), R-125 (panel B), and R-134a (panel C) at 303.15 K on SiO_2/IL composites prepared with ILs with different functional groups in the anion.

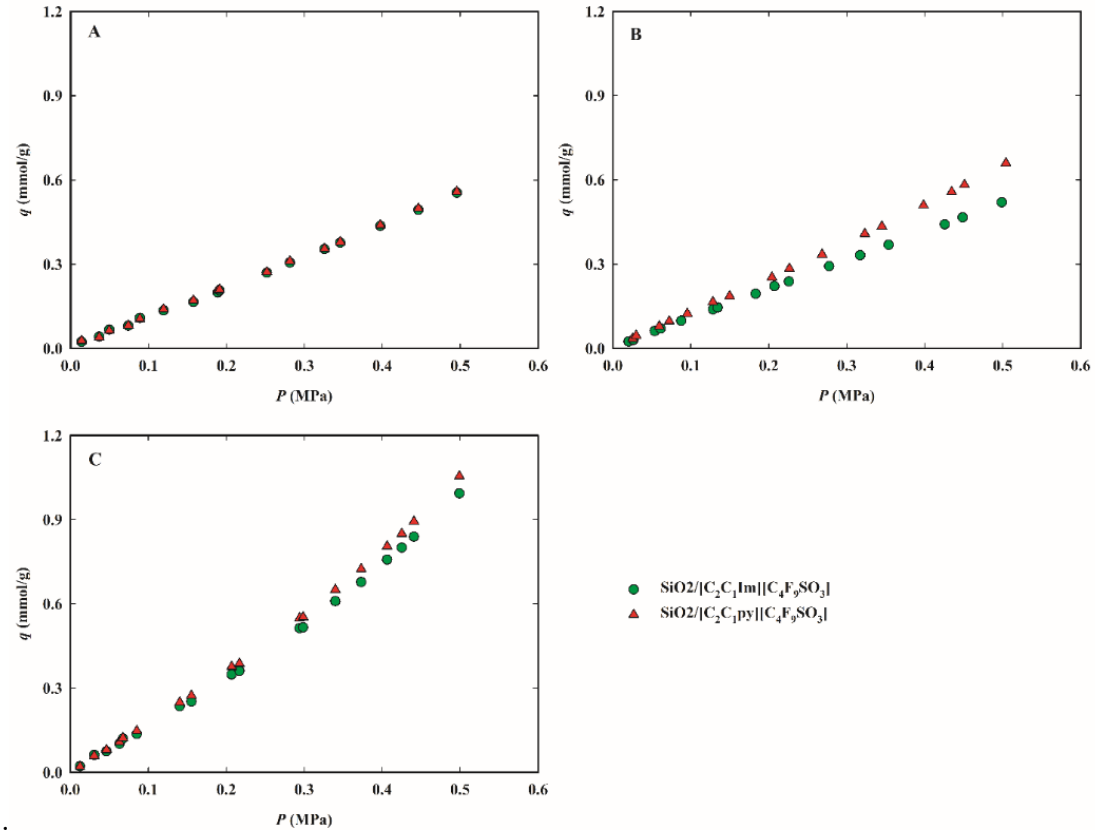


Figure 3.2.12 Comparison of the sorption of R-32 (panel A), R-125 (panel B), and R-134a (panel C) at 303.15 K on SiO_2/IL composites prepared with ILs with different functional groups in the cation.

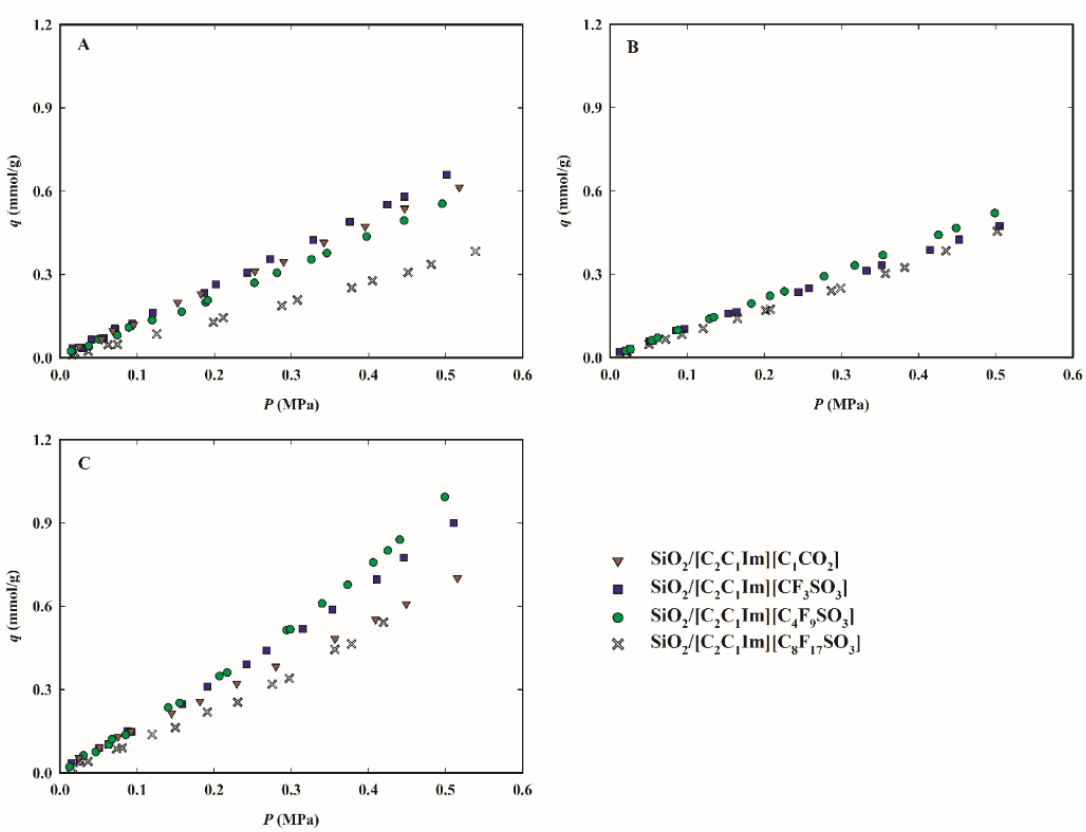


Figure 3.2.13 Comparison of the sorption of R-32 (panel A), R-125 (panel B), and R-134a (panel C) at 303.15 K on SiO_2/IL composites prepared with ILs with different sizes (or absence) of the perfluorinated chain in the anion.

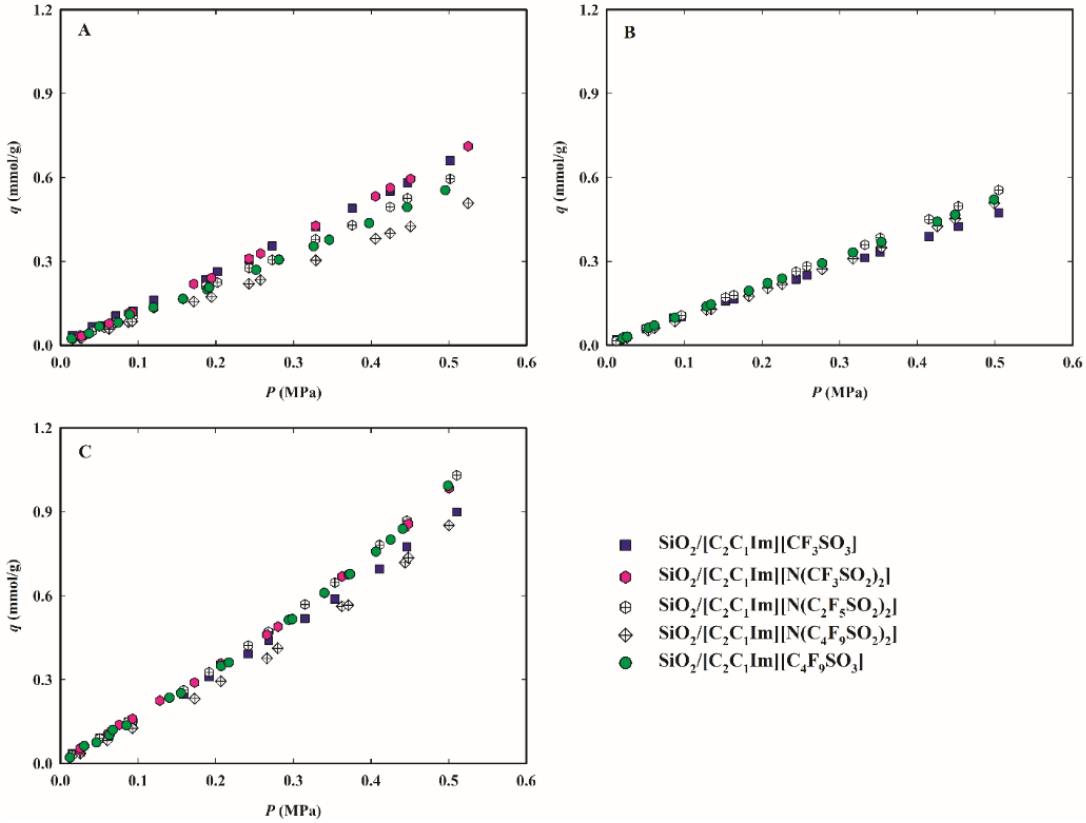


Figure 3.2.14 Comparison of the sorption of R-32 (panel A), R-125 (panel B), and R-134a (panel C) at 303.15 K on SiO_2/IL composites prepared with ILs with linear or ramified perfluorinated chain in the anion.

3.2.2.3 Henry's Law Constant

The sorption of each F-gas was also evaluated based on the Henry's law constant, H_i [64], defined as

$$H_i(T, P) = \lim_{x_i \to 0} \frac{f_i^{\mathrm{L}}}{q_i} \qquad 3.2.10$$

where f_i^{L} is the fugacity of gas i and q_i the uptake of gas by the sorption medium expressed as total or excess sorption (mmol/g), under infinite dilution conditions ($\lim_{f_i \to 0} q_i = \lim_{f_i \to 0} q_i^{\mathrm{ex}}$). Since under thermodynamic equilibrium the fugacity of the F-gas in the sorbent phase is equal to the fugacity in the gas phase, the Henry's law (Prausnitz et al., 1999) can be rewritten as follows:

$$H_i(T) = \lim_{P_i \to 0} \frac{P_i}{q_i} \qquad 3.2.11$$

where P_i is the partial pressure of F-gas in the gas phase. Therefore, the Henry constant is the proportionality value between the partial pressure of F-gas in the gas phase and its solubility in the sorbent phase, under infinitely dilute conditions. The slope of the tangent at $P = 0$ of the experimental (q, P) data is the Henry's law constant and consequently, a smaller value of this parameter corresponds to a higher gas solubility.

The comparison with the pure ILs was also made through the Henry's law constants (see Figure 3.2.15 and Table 3.2.5) [19], which confirmed that gas sorption into the composites is lower than into the pure ILs. Moreover, these results clearly show that the tendencies of gas sorption in the composites are identical to those in pure ILs. Finally, it is observed that under infinite dilution (low pressure) conditions, silica has the best gas adsorption capacity, contrary to what is observed at higher pressures, where the pure ILs have higher absorption capacity (see Figure 3.2.6).

Table 3.2.5 Henry's law constants (in MPa·g·mmol^{-1}) determined for the sorption of R-32, R-125, and R-134a on the composites studied in this work and for the pure ILs studied in previous work (Sosa et al. 2019) [29].

	R-32	**R-125**	**R-134a**
SiO_2/[C_2C_1Im] [C_1CO_2]	0.707	-	0.511
[C_2C_1Im] [C_1CO_2]	0.393	0.526	0.355
SiO_2/[C_2C_1Im] [CF_3SO_3]	0.650	0.806	0.568
[C_2C_1Im] [CF_3SO_3]	0.469	0.970	0.390
SiO_2/[C_2C_1Im] [$N(CF_3SO_2)_2$]	0.819	0.905	0.571
[C_2C_1Im] [$N(CF_3SO_3)_2$]	0.491	0.667	0.304
SiO_2/[C_2C_1Im] [$N(C_2F_5SO_2)_2$]	0.862	0.889	0.594
SiO_2/[C_2C_1Im] [$N(C_4F_9SO_2)_2$]	1.098	1.076	0.732

SiO_2/[C_2C_1Im] [$C_4F_9CO_2$]	0.840	0.724	0.602
[C_2C_1Im] [$C_4F_9CO_2$]	0.490	0.485	0.307
SiO_2/[C_2C_1Im] [$C_4F_9SO_3$]	0.788	0.847	0.604
[C_2C_1Im] [$C_4F_9SO_3$]	0.473	0.647	0.296
SiO_2/[C_2C_1py] [$C_4F_9SO_3$]	0.768	0.765	0.595
[C_2C_1py] [$C_4F_9SO_3$]	0.467	0.549	0.316
SiO_2/[C_2C_1Im] [$C_8F_{17}SO_3$]	1.505	1.102	0.899
SiO_2	0.234	0.148	0.109

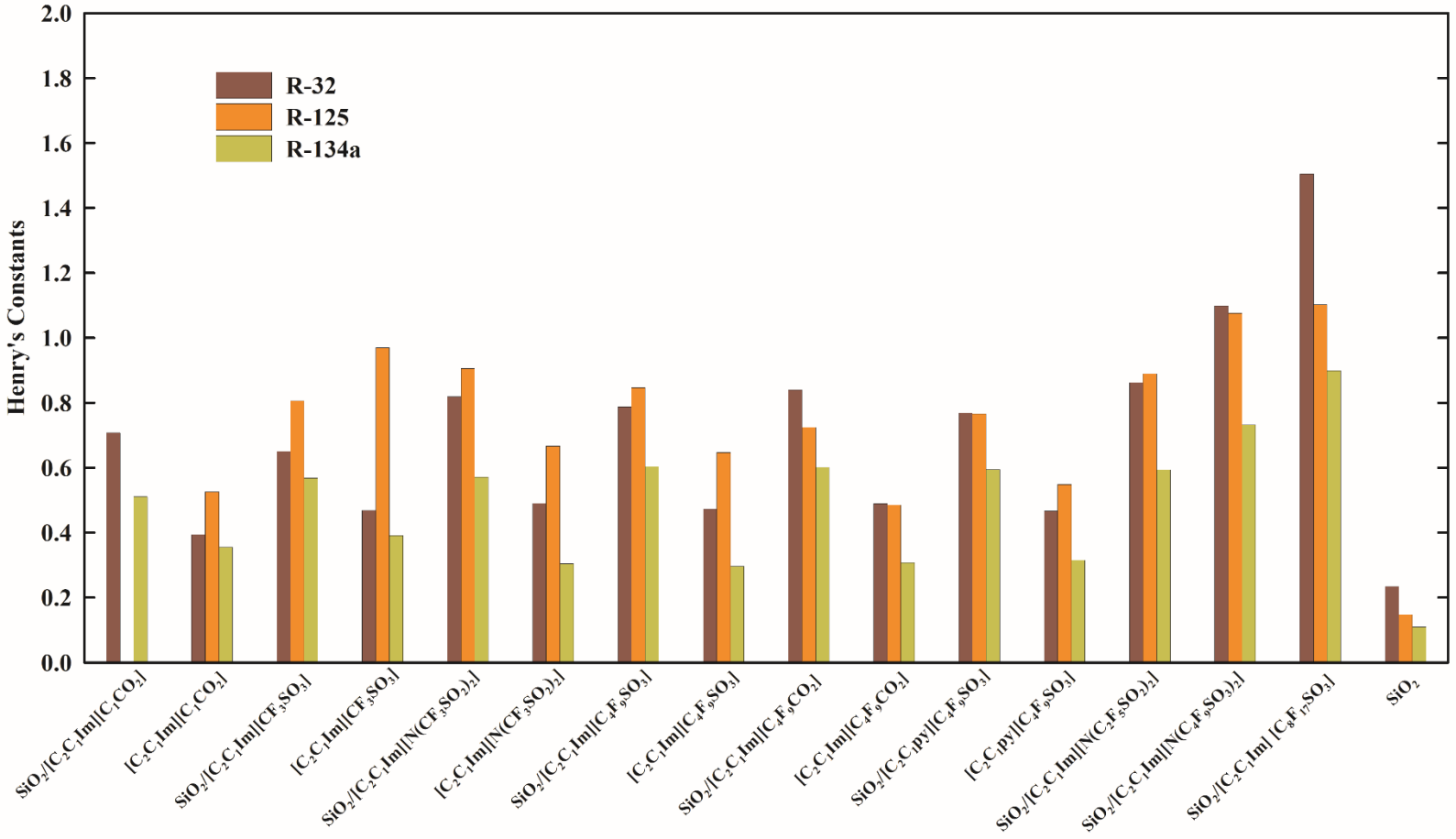


Figure 3.2.15 Henry's law constants (in MPa·g·mmol^{-1}) determined for the sorption of R-32, R-125, and R-134a, at 303.15 K, in the SiO_2/ILs composites studied in this work and pure ILs studied previously [19].

3.2.2.4 Adsorption Potential Theory (APT).

A formulation similar to the Adsorption Potential Theory (APT) was applied to the sorption equilibrium data in the composites and silica, as detailed in the SI. As in the APT [49,65], the sorbed amount of gas, q, measured as an equivalent volume of condensed gas, W, is expressed as

$$W = qV_{\mathrm{m}} = W(\Phi) \qquad 3.2.12$$

where V_{m} is the molar volume of the gas if it were condensed into a liquid phase,

$$\Phi = RT\ln(f_{\mathrm{s}}/f) \qquad 3.2.13$$

is usually referred to as the sorption potential [49,65], R is the ideal gas constant, T the system temperature, f the fugacity, and f_{s} the saturation fugacity (to account for non-ideal gas behaviour at high pressure). However, we prefer to identify Φ as the difference in free energy (or chemical potential) when a gas molecule is moved from the gas phase to its condensed state. Since in this work the sorption data were measured at a single temperature, the formulation above is perfectly valid because equations 3.2.12 and 3.2.13 are equivalent to simply stating that $q = q(P)_{\text{fixed } T}$. But, inspired by the APT, one can go a step further and test whether introducing an affinity coefficient β, as a scaling factor of Φ, collapses the curves $W_i(\Phi_i)$ of the different gases in the same composite into a single characteristic curve $W(\Phi_i/\beta_i)$ [49,65]. Thus, eq. 3.2.12 is replaced by

$$W_i = q_i V_{i,\mathrm{m}} = W\left(\widetilde{\Phi}_i\right), \qquad \widetilde{\Phi}_i = \frac{\Phi_i}{\beta_i} \qquad 3.2.14$$

where $\widetilde{\Phi}_i$ is the sorption potential scaled by β_i. In the literature, β is often correlated to the molecular parachor of the adsorbate.

Table 3.2.2. lists the values of β that collapse the curves $W_i(\widetilde{\Phi}_i)$ of the three different F-gases in the same composite into a single characteristic curve. For reference, we also include the values obtained for silica and those given by a correlation often used for adsorption in carbon materials (see the section 3.2.1.4). These characteristic curves are plotted in Figure 3.2.16 and fitted to an equation similar to the Dubinin–Astakhov (D–A) model. The D–A isotherm parameters obtained from the curve fitting are indicated in Table 3.2.6 and the comparison between the experimental sorption isotherms and the D-A model fitting is presented in Figure 3.2.17.

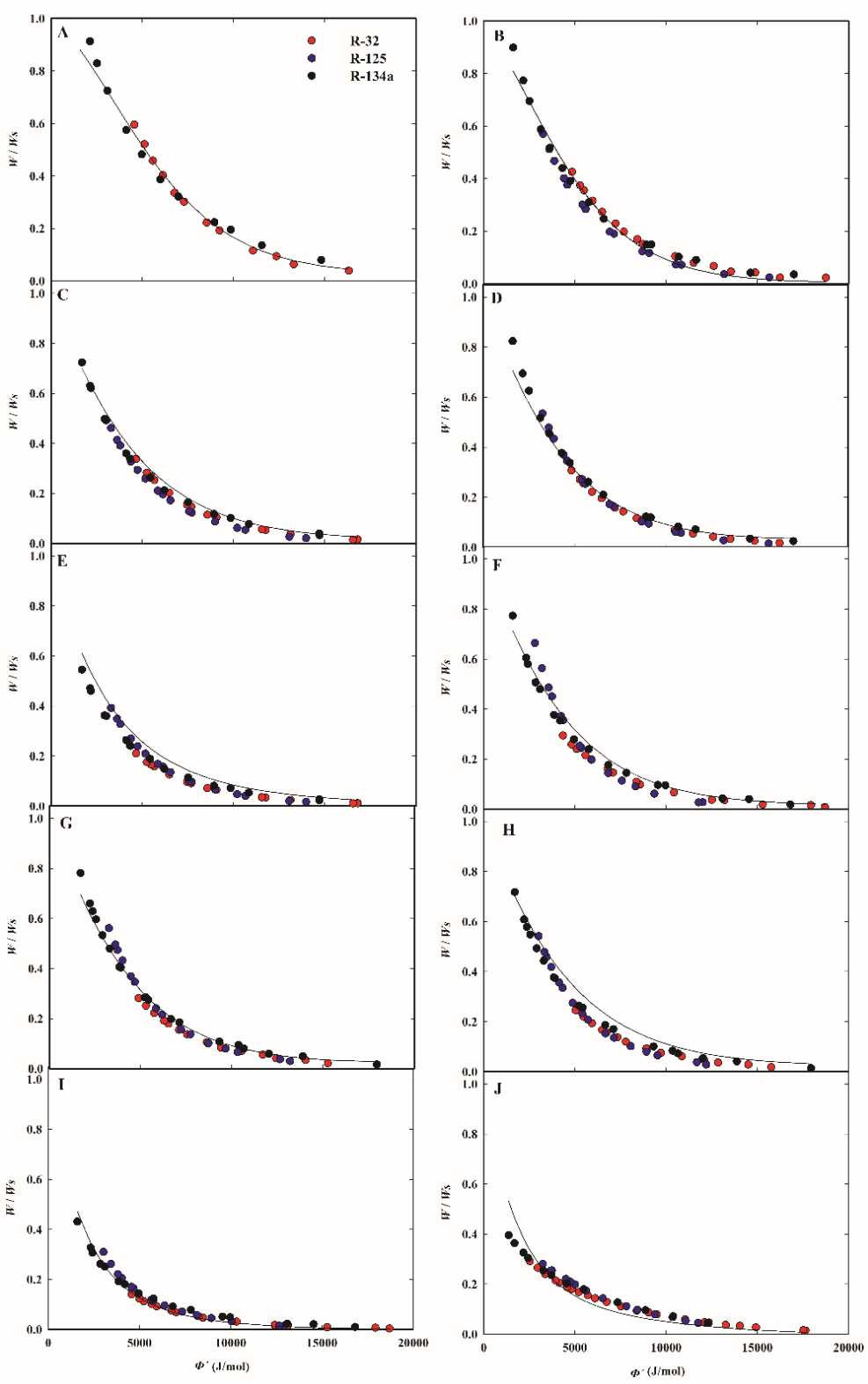


Figure 3.2.16 Characteristic curves obtained by adsorption potential theory (APT) using the experimental sorption data of R-32, R-125, and R-134a at 303.15 K on $SiO_2/[C_2C_1Im][C_1CO_2]$ (panel A), $SiO_2/[C_2C_1Im][CF_3SO_3]$ (panel B), $SiO_2/[C_2C_1Im][N(CF_3SO_2)_2]$ (panel C), $SiO_2/[C_2C_1Im][N(C_2F_5SO_2)_2]$ (panel D), $SiO_2/[C_2C_1Im][N(C_4F_9SO_2)_2]$ (panel E), $SiO_2/[C_2C_1Im][C_4F_9CO_2]$ (panel F), $SiO_2/[C_2C_1Im]$ $[C_4F_9SO_3]$.

Table 3.2.6 Dubinin–Astakhov (D–A) model parameters determined silica/ionic liquid composite.

Ionic liquid	γ (J/mol)^n	n
$[C_2C_1Im]$ $[C_1CO_2]$	9.886×10^{-7}	1.56
$[C_2C_1Im]$ $[CF_3SO_3]$	1.919×10^{-5}	1.27
$[C_2C_1Im]$ $[N(CF_3SO_2)_2]$	1.432×10^{-4}	1.06
$[C_2C_1Im]$ $[N(C_2F_5SO_2)_2]$	4.698×10^{-5}	1.18
$[C_2C_1Im]$ $[N(C_4F_9SO_2)_2]$	8.661×10^{-4}	0.88
$[C_2C_1Im]$ $[C_4F_9CO_2]$	1.665×10^{-4}	1.05
$[C_2C_1Im]$ $[C_4F_9SO_3]$	6.663×10^{-5}	1.15
$[C_2C_1py]$ $[C_4F_9SO_3]$	1.707×10^{-4}	1.05
$[C_2C_1Im]$ $[C_8F_{17}SO_3]$	3.183×10^{-3}	0.75
SiO_2	9.787×10^{-3}	0.61

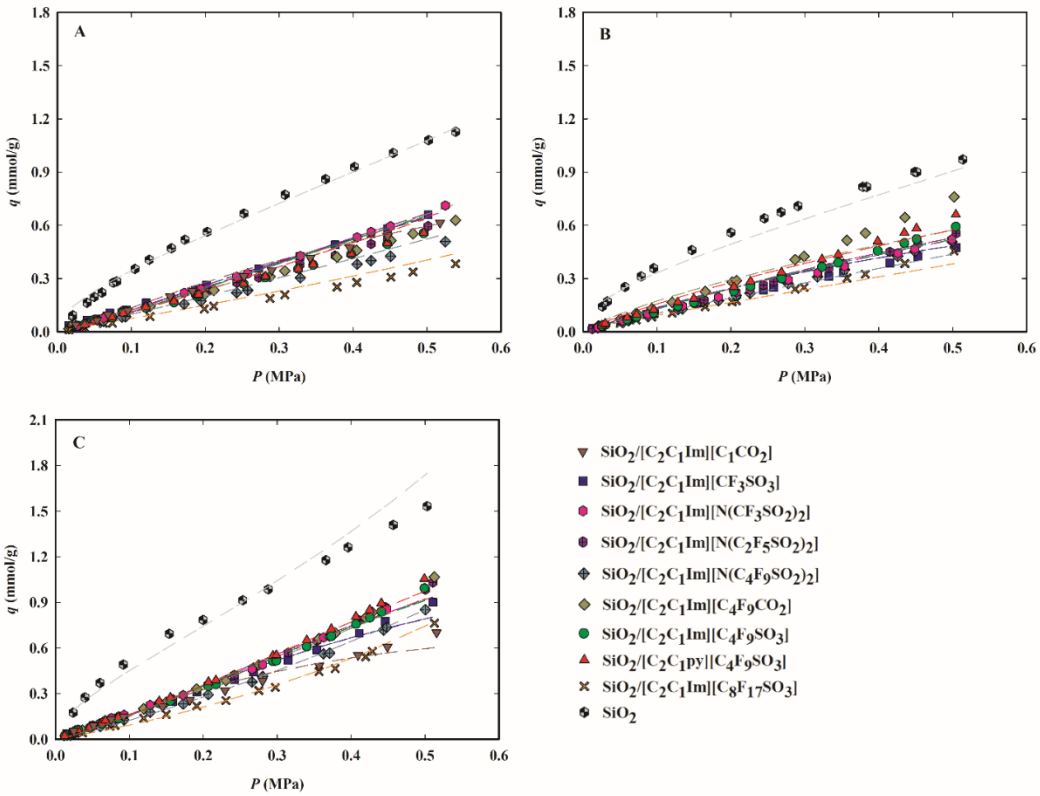


Figure 3.2.17 Sorption equilibrium isotherms of R-32 (panel A), R-125 (panel B), and R-134a (panel C) at 303.15 K on the studied SiO_2/IL composites. The dashed lines represent the fittings with the Dubinin–Astakhov (D–A) equation.

Surprisingly, not only is it possible to collapse the sorption data of the three F-gases on the same composite into a single characteristic curve by using an affinity coefficient but also the obtained values of β are almost independent of the type of composite but different from those for pure silica. These results are another indication that the IL supported in the porous volume and on the external surface of the porous silica controls the F-gas uptake in the composites.

3.2.2.5 Prediction of multicomponent sorption using the ideal adsorption solution theory (IAST)

In this work, the sorption equilibria of R-410A (R-32/R-125, 50/50 wt %), R-407F (R-32/R-125/R-134a, 30/30/40 wt %), and of each component of these systems, were predicted using the Ideal Adsorption Solution Theory (IAST) [66]. These predictions were based on the experimentally determined isotherms of the pure F-gases R-32, R-125, and R-134a, fitted with the Sips model. The study was applied to all composites over the pressure range 0.01–0.6 MPa (see Figure 3.2.18). The equilibrium mole fractions of the gas phase (y) are those of the commercial F-gases blends: $y^0_{\text{R-32}} = 0.70$ and $y^0_{\text{R-125}}$ = 0.30 for R-410A, and $y^0_{\text{R-32}}$ = 0.47, $y^0_{\text{R-125}}$ = 0.21, and $y^0_{\text{R-134a}}$ =0.32 for R-407F. The uptake of both gas mixtures increases with increasing pressure. Silica and the composites prepared with FILs with up to ten fluorine atoms in the anion have the highest R-410A and R-407F sorption capacities, while the composites prepared from fluoro-containing ILs (with fluorinated chains shorter than 4 carbon atoms) and FILs with 17 or 18 fluorine atoms in the anion have the lowest sorption capacities at the highest pressures.

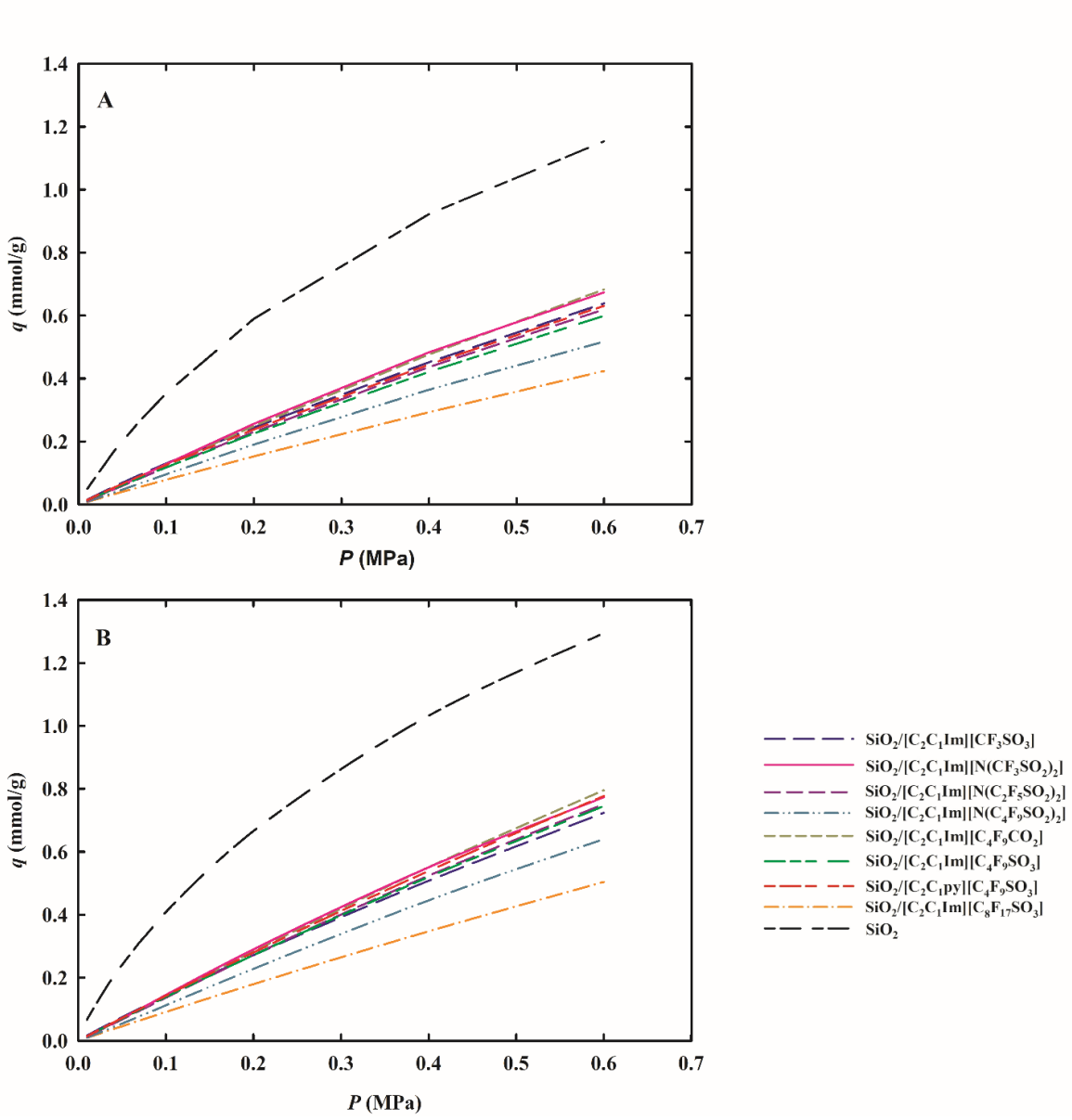


Figure 3.2.18 IAST predictions for the sorption of R-404A (panel A) and R-407F (panel B).

3.2.2.6 Selectivity for the separation of F-gases from commercial refrigerants

The capacity of the composites studied in this work for the separation of R-410A and R-407F refrigerants in their components (R-32, R-125, and R-134a) was analyzed using the predictions determined by IAST. The gas selectivity (S) at 303.15 K of each composite and silica for the separation of a gas i from the mixture with a gas j was determined as follows [67]:

$$S_{ij} = \frac{x_i / x_j}{y_i / y_j} \qquad 3.2.15$$

where x_i and x_j are the sorbed molar fractions of gas i and of gas j, respectively, and y_i and y_j are the molar fractions of gas i and of gas j in the gas phase at equilibrium, respectively.

The capacity of each composite and silica for the separation of the commercial refrigerant R-410A into its components (R-32 and R-125) was evaluated by determining the R-32/R-125 selectivity, using the IAST results. If the selectivity values are greater than 1, R-32 is preferentially sorbed, and if these values are less than 1, R-125 is preferentially sorbed. The value of the selectivity was determined as a function of pressure for the equilibrium gas-phase composition corresponding to that of bulk R-410A and the results are plotted in Figure 3.2.19. At low pressures, most composites are selective towards R-32 (with $SiO_2/[C_2C_1Im][C_4F_9SO_3]$ presenting the highest selectivity), while silica, $SiO_2/[C_2C_1Im]$ $[C_4F_9CO_2]$, and $SiO_2/[C_2C_1Im][C_8F_{17}SO_3]$ are selective towards R-125. At higher pressures, the R-32/R-125 selectivity is higher for $SiO_2/[C_2C_1Im][CF_3SO_3]$ and $SiO_2/[C_2C_1Im][N(CF_3SO_3)_2]$, and the R-125/R-32 selectivity is higher for $SiO_2/[C_2C_1Im][C_4F_9CO_2]$, $SiO_2/[C_2C_1py][C_4F_9SO_3]$, and $SiO_2/[C_2C_1Im][C_8F_{17}SO_3]$. In this same pressures range, the selectivity of silica approaches 1 and the selectivity of $SiO_2/[C_2C_1py][C_4F_9SO_3]$ is shifted towards R-125.

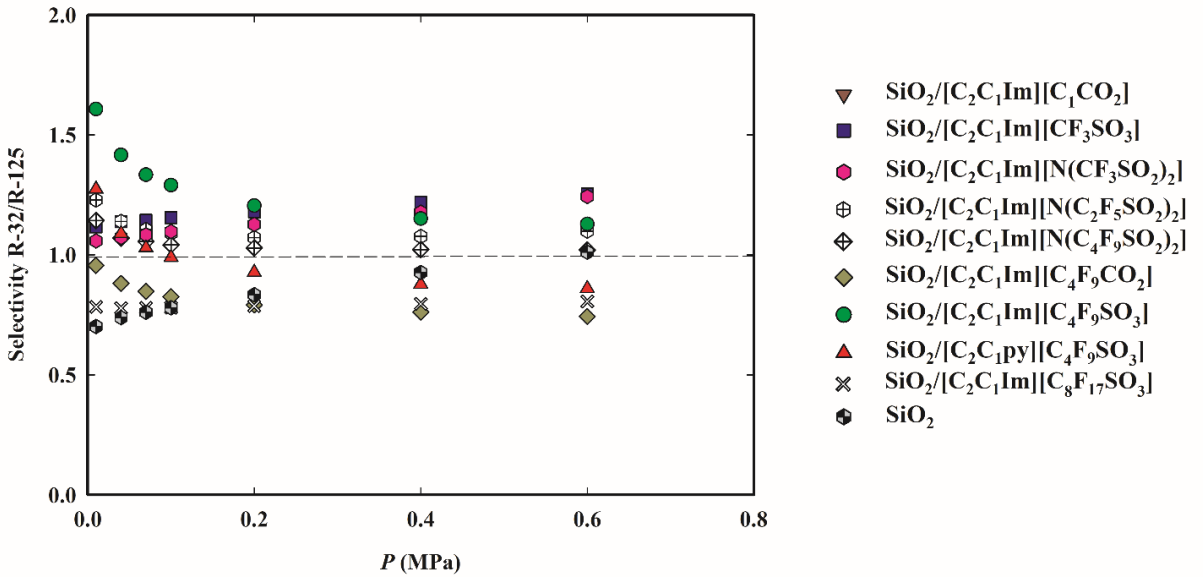


Figure 3.2.19 Selectivity of SiO_2 and the SiO_2/composites to the separation of the mixture R-32 / R-125 as a function of pressure at 303.15 K from the commercial R-410A refrigerant ($y_{R\text{-}32} = 0.7$ and $y_{R\text{-}125} = 0.3$).

In the case of the R-407F blend, a ternary mixture of R-32, R-125, and R-134a, the selectivities for the separations of R-32/R-125, R-134a/R-32, and R-134a/R-125 were determined as a function of pressure at 303.15 K for the equilibrium gas-phase composition of the bulk R-407F. The results are shown in Figure 3.2.21. All composites are selective for the separation of R-134a from their mixtures with the other two gases (panels B and C of Figure 3.2.20), with silica presenting the highest selectivities. Higher R-32/R-125 selectivities were obtained for the composites prepared with the conventional fluoro-containing ILs ($SiO_2/[C_2C_1Im][CF_3SO_3]$ and $SiO_2/[C_2C_1Im][N(CF_3SO_3)_2]$) at all range of pressures and to the composite prepared with $SiO_2/[C_2C_1Im][C_4F_9SO_3]$ at low pressures. Higher R-125/R-32 selectivities were obtained for silica and for the composite prepared from $SiO_2/[C_2C_1Im][C_8F_{17}SO_3]$ at low pressures, and for the composites prepared from $SiO_2/[C_2C_1Im][C_8F_{17}SO_3]$, $SiO_2/[C_2C_1py][C_4F_9SO_3]$, and $SiO_2/[C_2C_1Im][C_4F_9CO_2]$ at higher pressures.

In order to determine if the support of ILs into fumed silica has effects on the gas selectivity, the ideal selectivity for each binary pair of gases *i* and *j* was also determined using the Henry's constants of each gas *i* and *j* (H_i and H_j) in the same sorbent as follows [67]:

$$S_{ij}=\frac{H_j}{H_i} \qquad 3.2.16$$

The comparison of the ideal selectivities of fumed silica, composites, and pure ILs is represented in Figure 3.2.21. The results clearly show that, when compared to the composites, the pure ILs have a greater capacity to separate these F-gas mixtures, with the best performance being achieved for the separation of the R-134a + R-125 mixture. Pure fumed silica has the highest capacity for the separation of the R-134a + R-32 mixture. The results show that the selectivities of the composites and ILs follow the same trends, with composites presenting similar or lower values in most cases. The exceptions are SiO_2/[C_2C_1Im][$C_4F_9CO_2$], which is more selective towards R-125 over R-32, and SiO_2/[C_2C_1Im][C_1CO_2], which is more selective towards R-134a over R-32. All composites are selective towards R-134a over R-32 and R-125. As reported before for pure ILs, an increase in the number of fluorine atoms favours the selectivity for the separation of the two F-gases with the most different sizes, R-134a and R-32. The composite with the highest selectivity for the R-134/R-32 separation is SiO_2/[C_2C_1Im][$C_8F_{17}SO_3$]. The results presented here also show that an increase in the number of fluorine atoms moves the selectivity towards R-125 for the R-32 + R-125 mixture. The same behaviour is observed when the functional group in the IL anion is changed from a sulfonyl to a carboxylate group. SiO_2/[C_2C_1Im][CF_3SO_3] presents the highest selectivity towards R-32 over R-125 while SiO_2/[C_2C_1Im][$C_8F_{17}SO_3$] and fumed silica present the best selectivity toward R-125 over R-32. Moreover, the separation of mixtures of R-134a and R-125, which have similar sizes, is favoured in composites prepared with ILs with ramified perfluorinated chains in the anion.

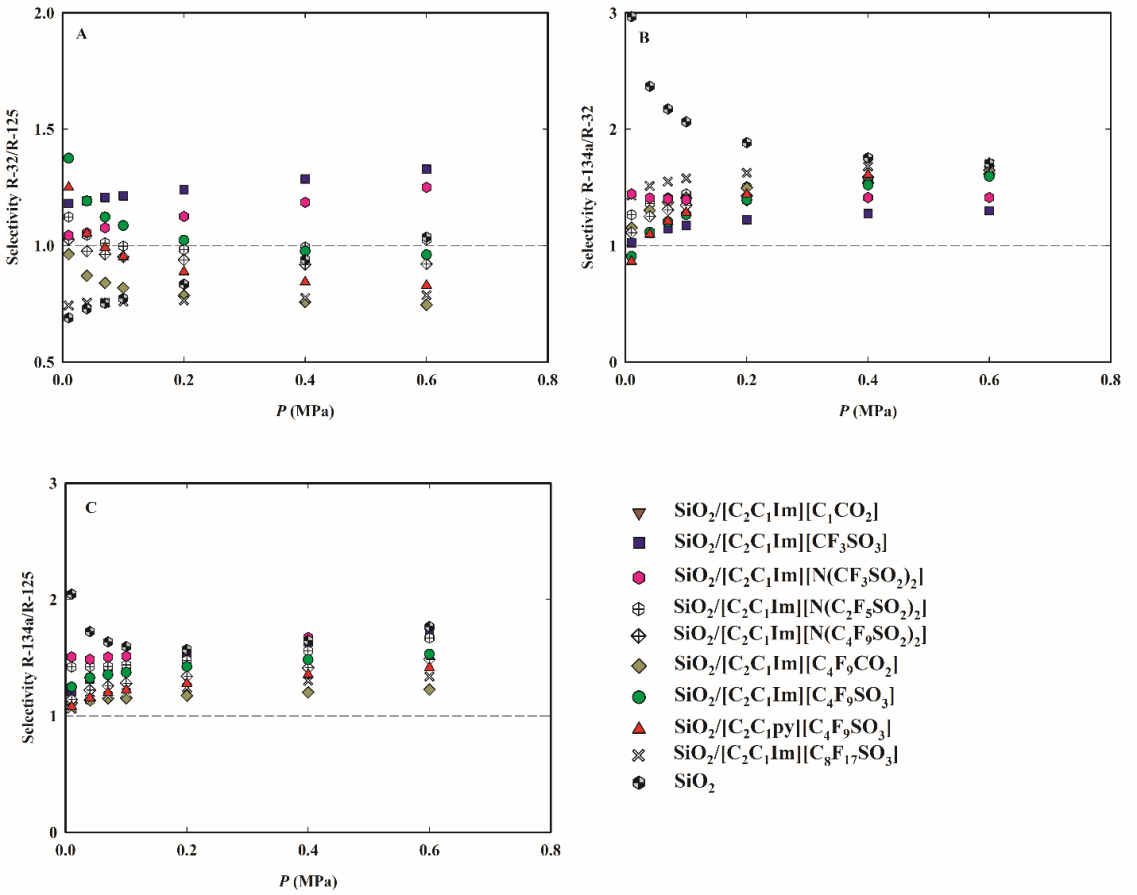


Figure 3.2.20 Selectivity of SiO_2 and the SiO_2/composites to the separations of: R-32/R-125 (panel A); R-134a/R-32 (panel B); and R-134a/R-125 (panel C), as a function of pressure at 303.15 K from the commercial refrigerant R-407F ($y_{\text{R-32}} = 0.47$, $y_{\text{R-125}} = 0.21$, and $y_{\text{R-134a}} = 0.32$).

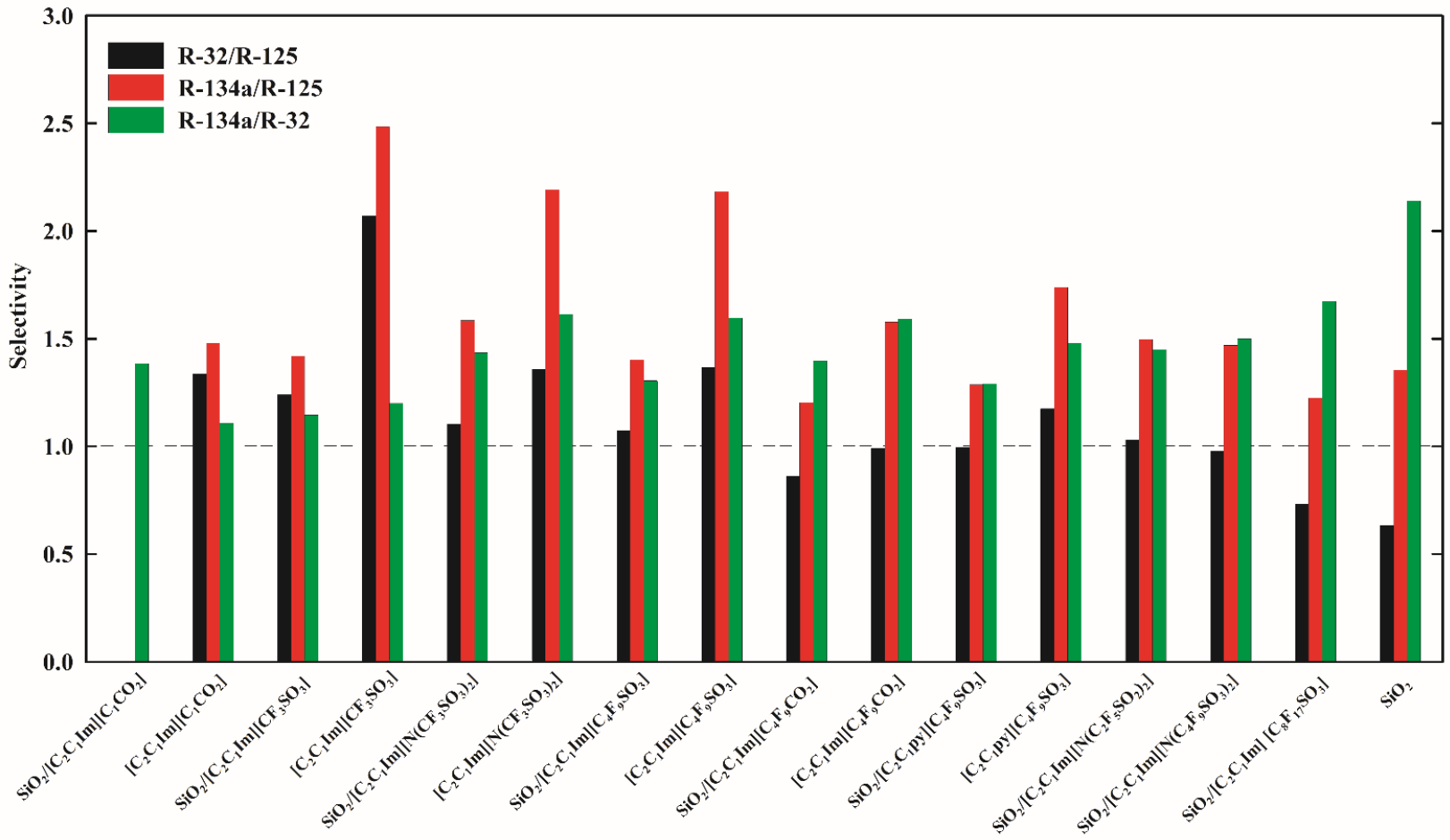


Figure 3.2.21 Selectivities, determined from the Henry's constants, of SiO_2 and composites studied in this work, and of ILs previously studied [19] at 303.15 K.

3.3 Conclusions

Fluorinated ionic liquids have optimal properties for the selective absorption of F-gases. In this work, we supported different FILs and other fluoro-containing ILs in silica with the aim to increase the contact area and mass transfer between the F-gas and the ILs. The results from BET superficial area, pore volume analysis, SEM, and EDS suggest that the ILs are located at the surface and inside the pores of silica. These composites and pure fumed silica were evaluated for their capacity to sorb the three most used pure F-gases used in refrigeration and air conditioning equipment (R-32, R-125, and R-134) at 303.15 K and pressures up to 0.54 MPa. The sorption data were successfully correlated with the Sips equation and by an analogy to the Adsorption Potential Theory. The sorption data of these three gases in each composite were successfully collapsed into a single characteristic curve, which was well fitted by the D–A model.

The capacity of the composites and silica to sorb the three F-gases was compared to the previously published results for the pure ILs 29. Moreover, the Henry's Law constants were also calculated to obtain valuable information on gas solubility at diluted conditions. At high pressures, the pure ILs present higher gas solubility capacity than silica, evidencing the advantages of using ILs for F-gases sorption. From these comparisons, it became clear that similar effects on gas solubilization occur when the same modifications were performed in the cation or anion of the pure IL or the corresponding composites. Therefore, it is evident that the properties of the ILs are commanding the sorption of the F-gases.

Using the Ideal Adsorption Solution Theory (IAST), the sorption of two commercial refrigerants, R-410A and R-407F, in each composite and silica was calculated at different pressures. Then, the selectivity of the composites and silica to each component of the F-gas blends was determined. The results show that the composites are selective towards R-134a in relation to either R-32 or R-125. Moreover, better separations are obtained for the R-407F refrigerant than for the R-410A blend. Pure ILs presented higher R-134a/R-125 selectivities, compared to fumed silica, which confirms that ILs are advantageous systems for the separation of R-134a and R-125.

The results presented in this work show that ILs have good sorption capacities for the selective separation of F-gas from gas blends and that ILs present in the composites control not only gas solubility but also gas selectivity. By supporting the ILs into a porous material, it was possible to obtain a new material, maintaining the selective sorption capacities of the ILs. Thus, this work obtains key information to the fundamental understanding of the behaviour of these alternative materials and opens the road for the development and manipulation of new materials based on ILs for the selective uptake of F-gases

3.4 References

[1] Handbook for the Montreal Protocol on Substances that Deplete the Ozone Layer. Fourteenth edition (2020), n.d.

[2] W. Schwarz, B. Gschrey, A. Leisewitz, A. Herold, S. Gores, I. Papst, J. Usinger, M. Kauffeld, K. Kaar, A. Lindborg, Preparatory study for a review of Regulation (EC) No 842/2006 on certain fluorinated greenhouse gases Final Report Prepared for the European Commission in the context of, 2011.

[3] E.A. Heath, Amendment to the Montreal Protocol on Substances that Deplete the Ozone Layer (Kigali Amendment), International Legal Materials 56 (2017) 193–205. https://doi.org/DOI: 10.1017/ilm.2016.2.

[4] KET4F-Gas, Reducción del impacto ambiental de los gases fluorados en el espacio Sudoe mediante tecnologías facilitadoras clave, 2023 (2021). http://www.ket4f-gas.eu/?page_id=350 (accessed January 14, 2025).

[5] LIFE-4-Fgases, LIFE-4-Fgases, (2024). https://www.life4fgases.eu/ (accessed January 14, 2025).

[6] S. Asensio-Delgado, F. Pardo, G. Zarca, A. Urtiaga, Vapor–Liquid Equilibria and Diffusion Coefficients of Difluoromethane, 1,1,1,2-Tetrafluoroethane, and 2,3,3,3-Tetrafluoropropene in Low-Viscosity Ionic Liquids, J Chem Eng Data 65 (2020) 4242–4251. https://doi.org/10.1021/acs.jced.0c00224.

[7] P.J. Castro, A.E. Redondo, J.E. Sosa, M.E. Zakrzewska, A.V.M. Nunes, J.M.M. Araújo, A.B. Pereiro, Absorption of Fluorinated Greenhouse Gases in Deep Eutectic Solvents, Ind Eng Chem Res 59 (2020) 13246–13259. https://doi.org/10.1021/acs.iecr.0c01893.

[8] L. Dong, D. Zheng, G. Sun, X. Wu, Vapor-liquid equilibrium measurements of difluoromethane + [Emim]OTf, difluoromethane + [Bmim]OTf, difluoroethane + [Emim]OTf, and difluoroethane + [Bmim]OTf systems, J Chem Eng Data 56 (2011) 3663–3668. https://doi.org/10.1021/je2005566.

[9] X. Liu, M. He, N. Lv, X. Qi, C. Su, Solubilities of R-161 and R-143a in 1-Hexyl-3-methylimidazolium bis(trifluoromethylsulfonyl)imide, Fluid Phase Equilib 388 (2015) 37–42. https://doi.org/https://doi.org/10.1016/j.fluid.2014.12.026.

[10] X. Liu, M. He, N. Lv, X. Qi, C. Su, Vapor-liquid equilibrium of three hydrofluorocarbons with [HMIM][Tf2N], J Chem Eng Data 60 (2015) 1354–1361. https://doi.org/10.1021/je501069b.

[11] X. Liu, N. Lv, C. Su, M. He, Solubilities of R32, R245fa, R227ea and R236fa in a phosphonium-based ionic liquid, J Mol Liq 218 (2016) 525–530. https://doi.org/10.1016/j.molliq.2016.02.041.

[12] X. Liu, P. Pan, M. He, Vapor-liquid equilibrium and diffusion coefficients of R32 + [HMIM][FEP], R152a + [HMIM][FEP] and R161 + [HMIM][FEP], J Mol Liq 253 (2018) 28–35. https://doi.org/https://doi.org/10.1016/j.molliq.2018.01.032.

[13] A. Mota-Babiloni, P. Makhnatch, R. Khodabandeh, Recent investigations in HFCs substitution with lower GWP synthetic alternatives: Focus on energetic performance and environmental impact,

International Journal of Refrigeration 82 (2017) 288–301. https://doi.org/https://doi.org/10.1016/j.ijrefrig.2017.06.026.

[14] W. Ren, A.M. Scurto, Phase equilibria of imidazolium ionic liquids and the refrigerant gas, 1,1,1,2-tetrafluoroethane (R-134a), Fluid Phase Equilib 286 (2009) 1–7. https://doi.org/10.1016/j.fluid.2009.07.007.

[15] M.B. Shiflett, A. Yokozeki, Solubility and diffusivity of hydrofluorocarbons in room-temperature ionic liquids, AIChE Journal 52 (2006) 1205–1219. https://doi.org/10.1002/aic.10685.

[16] M.B. Shiflett, A. Yokozeki, Absorption cycle utilizing ionic liquid as working Fluid, EP1846535A1, 2005. https://patentimages.storage.googleapis.com/84/61/36/3d826a03e6af7f/EP1846535B1.pdf (accessed May 7, 2025).

[17] M.B. Shiflett, A. Yokozeki, Solubility differences of halocarbon isomers in ionic liquid [emim][Tf 2N], J Chem Eng Data 52 (2007) 2007–2015. https://doi.org/10.1021/je700295e.

[18] M.B. Shiflett, A. Yokozeki, Binary Vapor–Liquid and Vapor–Liquid–Liquid Equilibria of Hydrofluorocarbons (HFC-125 and HFC-143a) and Hydrofluoroethers (HFE-125 and HFE-143a) with Ionic Liquid [emim][Tf2N], J Chem Eng Data 53 (2008) 492–497. https://doi.org/10.1021/je700588d.

[19] J.E.J.E. Sosa, R.P.P.L.R.P.P.L. Ribeiro, P.J.P.J. Castro, J.P.B.J.P.B. Mota, J.M.M.J.M.M. Araújo, A.B.A.B. Pereiro, Absorption of Fluorinated Greenhouse Gases Using Fluorinated Ionic Liquids, Ind Eng Chem Res 58 (2019) 20769–20778. https://doi.org/10.1021/acs.iecr.9b04648.

[20] J.E. Sosa, A.E. Redondo, J. Avila, L.F. Lepre, M.C. Gomes, J. Palomar, A.B. Pereiro, M.M. Arau, Design of Ionic Liquids for Fluorinated Gas Absorption : COSMO-RS Selection and Solubility Experiments, (2022). https://doi.org/10.1021/acs.est.2c00051.

[21] A.B. Pereiro, J.M.M. Araújo, S. Martinho, F. Alves, S. Nunes, A. Matias, C.M.M. Duarte, L.P.N. Rebelo, I.M. Marrucho, Fluorinated Ionic Liquids: Properties and Applications, ACS Sustain Chem Eng 1 (2013) 427–439. https://doi.org/10.1021/sc300163n.

[22] A.B. Pereiro, L.C. Tomé, S. Martinho, L.P.N. Rebelo, I.M. Marrucho, Gas permeation properties of fluorinated ionic liquids, Ind Eng Chem Res 52 (2013) 4994–5001. https://doi.org/10.1021/ie4002469.

[23] A.B. Pereiro, M.J. Pastoriza-Gallego, K. Shimizu, I.M. Marrucho, J.N.C. Lopes, M.M. Piñeiro, L.P.N. Rebelo, On the formation of a third, nanostructured domain in ionic liquids, Journal of Physical Chemistry B 117 (2013) 10826–10833. https://doi.org/10.1021/jp402300c.

[24] N.S.M. Vieira, J.C. Bastos, L.P.N. Rebelo, A. Matias, J.M.M. Araújo, A.B. Pereiro, Human cytotoxicity and octanol/water partition coefficients of fluorinated ionic liquids, Chemosphere 216 (2019) 576–586. https://doi.org/https://doi.org/10.1016/j.chemosphere.2018.10.159.

[25] N.S.M. Vieira, S. Stolte, J.M.M. Araújo, L.P.N. Rebelo, A.B. Pereiro, M. Markiewicz, Acute Aquatic Toxicity and Biodegradability of Fluorinated Ionic Liquids, ACS Sustain Chem Eng 7 (2019) 3733–3741. https://doi.org/10.1021/acssuschemeng.8b03653.

[26] M. Sattari, A. Kamari, H. Hashemi, A.H. Mohammadi, D. Ramjugernath, A group contribution model for prediction of the viscosity with temperature dependency for fluorine-containing ionic liquids, J Fluor Chem 186 (2016) 19–27. https://doi.org/10.1016/j.jfluchem.2016.04.001.

[27] F. Pardo, S. V Gutiérrez-Hernández, C. Hermida-Merino, J.M.M. Araújo, M.M. Piñeiro, A.B. Pereiro, G. Zarca, A. Urtiaga, Integration of Stable Ionic Liquid-Based Nanofluids into Polymer Membranes. Part II: Gas Separation Properties toward Fluorinated Greenhouse Gases, Nanomaterials 11 (2021). https://doi.org/10.3390/nano11030582.

[28] F. Pardo, G. Zarca, A. Urtiaga, Effect of feed pressure and long-term separation performance of Pebax-ionic liquid membranes for the recovery of difluoromethane (R32) from refrigerant mixture R410A, J Memb Sci 618 (2021) 118744. https://doi.org/https://doi.org/10.1016/j.memsci.2020.118744.

[29] F. Pardo, S. V Gutiérrez-Hernández, G. Zarca, A. Urtiaga, Toward the Recycling of Low-GWP Hydrofluorocarbon/Hydrofluoroolefin Refrigerant Mixtures Using Composite Ionic Liquid–Polymer Membranes, ACS Sustain Chem Eng 9 (2021) 7012–7021. https://doi.org/10.1021/acssuschemeng.1c00668.

[30] F. Pardo, G. Zarca, A. Urtiaga, Separation of Refrigerant Gas Mixtures Containing R32, R134a, and R1234yf through Poly(ether-block-amide) Membranes, ACS Sustainable Chemistry & Engineering 8 (2020) 2548–2556. https://doi.org/10.1021/acssuschemeng.9b07195.

[31] A.D. Yancey, S.J. Terian, B.J. Shaw, T.M. Bish, D.R. Corbin, M.B. Shiflett, A review of fluorocarbon sorption on porous materials, Microporous and Mesoporous Materials 331 (2022) 111654. https://doi.org/10.1016/j.micromeso.2021.111654.

[32] B.S. Akkimaradi, M. Prasad, P. Dutta, K. Srinivasan, Adsorption of 1,1,1,2-Tetrafluoroethane on Activated Charcoal, J Chem Eng Data 46 (2001) 417–422. https://doi.org/10.1021/je000277e.

[33] W.S. Loh, M. Kumja, K.A. Rahman, K.C. Ng, B.B. Saha, S. Koyama, I.I. El-Sharkawy, Adsorption Parameter and Heat of Adsorption of Activated Carbon/HFC-134a Pair, Heat Transfer Engineering 31 (2010) 910–916. https://doi.org/10.1080/01457631003603949.

[34] W.S. Loh, A. Bin Ismail, B. Xi, K.C. Ng, W.G. Chun, Adsorption Isotherms and Isosteric Enthalpy of Adsorption for Assorted Refrigerants on Activated Carbons, J Chem Eng Data 57 (2012) 2766–2773. https://doi.org/10.1021/je3008099.

[35] B.B. Saha, K. Habib, I.I. El-Sharkawy, S. Koyama, Adsorption characteristics and heat of adsorption measurements of R-134a on activated carbon, International Journal of Refrigeration 32 (2009) 1563–1569. https://doi.org/https://doi.org/10.1016/j.ijrefrig.2009.03.010.

[36] A.A. Askalany, M. Salem, I.M. Ismail, A.H.H. Ali, M.G. Morsy, Experimental study on adsorption–desorption characteristics of granular activated carbon/R134a pair, International Journal of Refrigeration 35 (2012) 494–498. https://doi.org/https://doi.org/10.1016/j.ijrefrig.2011.04.002.

[37] A.A. Askalany, B.B. Saha, K. Uddin, T. Miyzaki, S. Koyama, K. Srinivasan, I.M. Ismail, Adsorption Isotherms and Heat of Adsorption of Difluoromethane on Activated Carbons, J Chem Eng Data 58 (2013) 2828–2834. https://doi.org/10.1021/je4005678.

[38] M. Attalla, S. Sadek, Experimental Investigation of Granular Activated Carbon/R-134a Pair for Adsorption Cooling System Applications, Journal of Power and Energy Engineering 02 (2014) 11–20. https://doi.org/10.4236/jpee.2014.22002.

[39] J.E. Sosa, C. Malheiro, R.P.P.L. Ribeiro, P.J. Castro, M.M. Piñeiro, J.M.M. Araújo, F. Plantier, J.P.B. Mota, A.B. Pereiro, Adsorption of fluorinated greenhouse gases on activated carbons: evaluation of their potential for gas separation, Journal of Chemical Technology & Biotechnology 95 (2020) 1892–1905. https://doi.org/https://doi.org/10.1002/jctb.6371.

[40] DarshikaK.K.J.A.J.A. Wanigarathna, J. Gao, T. Takanami, Q. Zhang, B. Liu, A.D. Yancey, D.R. Corbin, M.B. Shiflett, DarshikaK.K.J.A.J.A. Wanigarathna, B. Liu, J. Gao, M.B. Shiflett, D.R. Corbin, B.A. Elliott, A. Yokozeki, S. Savitz, F.R. Siperstein, R. Huber, S.M. Tieri, R.J. Gorte, A.L. Myers, C.P. Grey, D.R. Corbin, A.D. Yancey, S.J. Terian, B.J. Shaw, T.M. Bish, D.R. Corbin, M.B. Shiflett, Q. Fu, Y. Qin, D. Zhang, Y. Han, Adsorption of Hydrofluorocarbons HFC-134 and HFC-134A on X and Y Zeolites: Effect of Ion-Exchange on Selectivity and Heat of Adsorption, Adsorption Science and Technology 64 (2013) 640–648. https://doi.org/10.1016/j.jct.2013.04.018.

[41] D.K.J.A. Wanigarathna, J. Gao, T. Takanami, Q. Zhang, B. Liu, Adsorption Separation of R-22, R-32 and R-125 Fluorocarbons using 4A Molecular Sieve Zeolite, ChemistrySelect 1 (2016) 3718–3722. https://doi.org/10.1002/slct.201600689.

[42] R.K. Motkuri, H.V.R. Annapureddy, M. Vijaykumar, Fluorocarbon adsorption in hierarchical porous frameworks, Nat. Commun. 5 (2014) 4368.

[43] K. Kumar, A. Kumar, Enhanced CO2 Adsorption and Separation in Ionic-Liquid-Impregnated Mesoporous Silica MCM-41: A Molecular Simulation Study, The Journal of Physical Chemistry C 122 (2018) 8216–8227. https://doi.org/10.1021/acs.jpcc.7b11529.

[44] M. Mohamedali, H. Ibrahim, A. Henni, Imidazolium based ionic liquids confined into mesoporous silica MCM-41 and SBA-15 for carbon dioxide capture, Microporous and Mesoporous Materials 294 (2020). https://doi.org/10.1016/j.micromeso.2019.109916.

[45] G.Em. Romanos, P.S. Schulz, M. Bahlmann, P. Wasserscheid, A. Sapalidis, F.K. Katsaros, C.P. Athanasekou, K. Beltsios, N.K. Kanellopoulos, CO2 Capture by Novel Supported Ionic Liquid Phase Systems Consisting of Silica Nanoparticles Encapsulating Amine-Functionalized Ionic Liquids, The Journal of Physical Chemistry C 118 (2014) 24437–24451. https://doi.org/10.1021/jp5062946.

[46] Q. Su, Y. Qi, X. Yao, W. Cheng, L. Dong, S. Chen, S. Zhang, Ionic liquids tailored and confined by one-step assembly with mesoporous silica for boosting the catalytic conversion of CO2 into cyclic carbonates, Green Chem. 20 (2018) 3232–3241. https://doi.org/10.1039/C8GC01038B.

[47] D.K.J.A. Wanigarathna, J. Gao, B. Liu, Metal Organic Frameworks for Adsorption-Based Separation of Fluorocompounds: a review, Mater. Adv. 1 (2020) 310.

[48] K. Fukumoto, M. Yoshizawa, H. Ohno, Room Temperature Ionic Liquids from 20 Natural Amino Acids, J Am Chem Soc 127 (2005) 2398–2399. https://doi.org/10.1021/ja043451i.

[49] B.C.R. Camacho, R.P.P.L. Ribeiro, I.A.A.C. Esteves, J.P.B. Mota, Adsorption equilibrium of carbon dioxide and nitrogen on the MIL-53(Al) metal organic framework, Sep Purif Technol 141 (2015) 150–159. https://doi.org/10.1016/j.seppur.2014.11.040.

[50] R. Coupan, F. Plantier, J.P. Torré, C. Dicharry, P. Sénéchal, F. Guerton, P. Moonen, A. Khoukh, S.A. Kessas, M. Hemati, Creating innovative composite materials to enhance the kinetics of CO2 capture by hydroquinone clathrates, Chemical Engineering Journal 325 (2017) 35–48. https://doi.org/10.1016/j.cej.2017.05.038.

[51] R.P.P.L. Ribeiro, C.L. Antunes, A.U. Garate, A.F. Portela, M.G. Plaza, J.P.B. Mota, I.A.A.C. Esteves, Binderless shaped metal-organic framework particles: Impact on carbon dioxide adsorption, Microporous and Mesoporous Materials 275 (2019) 111–121. https://doi.org/https://doi.org/10.1016/j.micromeso.2018.08.002.

[52] D.D. Do, Adsorption Analysis: Equilibria and Kinetics, 1998.

[53] National Institute of Standards and Technology (NIST), NIST, (2025). https://www.nist.gov/ (accessed on 21 June 2024). (accessed June 25, 2024).

[54] P.J. Linstrom, W.G. Mallard, The NIST Chemistry WebBook: A Chemical Data Resource on the Internet, J Chem Eng Data 46 (2001) 1059–1063. https://doi.org/10.1021/je000236i.

[55] A. Mouahid, D. Bessieres, F. Plantier, G. Pijaudier-Cabot, A thermostated coupled apparatus for the simultaneous determination of adsorption isotherms and differential enthalpies of adsorption at high pressure and high temperature, J Therm Anal Calorim 109 (2012) 1077–1087. https://doi.org/10.1007/s10973-011-1820-2.

[56] R. Sips, On the structure of a catalyst surface, J Chem Phys 16 (1948) 490–495. https://doi.org/10.1063/1.1746922.

[57] M.M. DUBININ, Physical Adsorption of Gases and Vapors in Micropores, in: D.A. CADENHEAD, J.F. DANIELLI, M.D. ROSENBERG (Eds.), Elsevier, 1975: pp. 1–70. https://doi.org/https://doi.org/10.1016/B978-0-12-571809-7.50006-1.

[58] M.M. Dubinin, Adsorption in micropores, J Colloid Interface Sci 23 (1967) 487–499. https://doi.org/https://doi.org/10.1016/0021-9797(67)90195-6.

[59] M.M. DUBININ, V.A. ASTAKHOV, Description of Adsorption Equilibria of Vapors on Zeolites over Wide Ranges of Temperature and Pressure, in: Molecular Sieve Zeolites-II, AMERICAN CHEMICAL SOCIETY, 1971: pp. 69–85. https://doi.org/doi:10.1021/ba-1971-0102.ch044.

[60] G.O. Wood, Affinity coefficients of the Polanyi/Dubinin adsorption isotherm equations: A review with compilations and correlations, Carbon N Y 39 (2001) 343–356. https://doi.org/https://doi.org/10.1016/S0008-6223(00)00128-7.

[61] G. Odell Wood, Activated carbon adsorption capacities for vapors, Carbon N Y 30 (1992) 593–599. https://doi.org/https://doi.org/10.1016/0008-6223(92)90177-X.

[62] S. Ozawa, S. Kusumi, Y. Ogino, Physical adsorption of gases at high pressure. IV. An improvement of the Dubinin—Astakhov adsorption equation, J Colloid Interface Sci 56 (1976) 83–91. https://doi.org/https://doi.org/10.1016/0021-9797(76)90149-1.

[63] S. Asensio-Delgado, F. Pardo, G. Zarca, A. Urtiaga, Absorption separation of fluorinated refrigerant gases with ionic liquids: Equilibrium, mass transport, and process design, Sep Purif Technol 276 (2021) 119363. https://doi.org/10.1016/j.seppur.2021.119363.

[64] J.H. Vera, Molecular thermodynamics of fluid-phase equilibria by John M. Prausnitz, Rüdiger N. Lichtenthaler and Edmundo Comes de Azevedo, Third Edition, 1999; Prentice Hall PTR, Upper-Saddle River, New Jersey 07458, xxiii + 860 pages; price $131.95 CND; ISBN 0-13-977745-8, Can J Chem Eng 78 (2000) 429–430. https://doi.org/https://doi.org/10.1002/cjce.5450780222.

[65] M.M. Dubinin, The potential theory of adsorption of gasAL THEORY OF ADSORPTION OF GASES AND VAP, Chem Rev 60 (1969) 235–241.

[66] A.L. Myers, J.M. Prausnitz, Thermodynamics of Mixed-Gas Adsorption, AIChE J. 11 (1965) 121.

[67] A.R.C. Morais, A.N. Harders, K.R. Baca, G.M. Olsen, B.J. Befort, A.W. Dowling, E.J. Maginn, M.B. Shiflett, Phase Equilibria, Diffusivities, and Equation of State Modeling of HFC-32 and HFC-125 in Imidazolium-Based Ionic Liquids for the Separation of R-410A, Ind Eng Chem Res 59 (2020) 18222–18235. https://doi.org/10.1021/acs.iecr.0c02820.

CHAPTER 4

POROUS SOLID MATRICES FOR ADSORPTION AND SEPARATION OF GHGS

4.1 Introduction

One of the main priorities of the European Union (EU) is the development of alternative and innovative technologies that provide solutions to mitigate the effects of greenhouse gases, such as fluorinated gases (F-gases). These gases, which are one of the major contributors to global change, comprise the families of hydrofluorocarbons (HFCs), sulphur hexafluoride (SF_6), and perfluorocarbons (PFCs). F-gases have a global warming potential (GWP) up to 23000 times higher than carbon dioxide. F-gases are currently used in the refrigeration, meat, fish, food distribution, and milk industries and are also present in approximately 80 % of the air conditioners in public and private transport vehicles [1–4]. In order to minimize F-gases emissions, the EU has imposed restrictions on 74 % of the F-gases used in the above-mentioned industries [4]. The commercial blends most used in the EU are R-410A, R-407F and R-407C because they have a high cooling capacity and a high performance coefficient [4–6]. These commercial blends contain the following pure F-gases: R-32, R-125, and R-134a, among others. However, their utilization is limited by their high GWP: 2088 for R410A, 1825 for R407F and 1774 for R407C [4–7].

According to EU restrictions, refrigerants with a GWP greater than 1500 (normally in refrigerants of the third generation) must be substituted by refrigerants with lower GWP (the new refrigerants of the fourth generation). In addition, poor maintenance of the equipment containing F-gases leads to leakage of these gases which end up being released into the atmosphere [8]. In the atmosphere, F-gases have a lifetime of up to 50000 years and their degradation can contribute to the formation of trifluoroacetic acid (TFA) which can pollute soils and water through acid rain [1,2,9–12]. TFA is a strong organic acid, highly soluble in water, which makes it easy to return to the soil by precipitation, directly contaminating water sources. High TFA concentrations tend to increase the acidity of water sources, irritate the nasal passages of mammals, and have a high eco-toxicity and an important accumulation in the different ecosystems [13–15]. All these problems explained above demonstrate the importance of: (i) the development of new refrigerants with low global warming potential; (ii) the mitigation of F-gases emissions to the atmosphere; (iii) the avoidance of the generation of TFA derived from F-gases emissions.

The capture and separation of F-gases have been studied using different solid porous matrices [16–21]. The use of porous solid matrices, such as Porous organic Polymers (POPs), including Covalent Organic Frameworks (COFs), activated carbons, and zeolites, have emerged as promising materials for the separation and purification of F-gases [17,22–30] because they possess high surface area, thermal stability and structural characteristics (microporosity and mesoporosity) that facilitate selective adsorption and separation of these compounds.

POPs have emerged as a promising class of porous solid materials in the search for advanced adsorbents. These POPs are entirely organic, highly porous, and exhibit long-range order due to their self-assembling nature. Recent studies have demonstrated the successful synthesis of POPs using

naturally derived dyes and hydroxylated azines [31–33]. Natural dyes, characterised by their low cost, structural diversity, and large-scale availability, represent a sustainable source of precursors. In previous works, POPs RIO-43, RIO-47, RIO-51, and RIO-55 have been synthesised from various dyes to investigate their influence on material characteristics [31–33]. These materials exhibit high porosity, stacked laminar structures, ion exchange capacity, and water insolubility [31]. On the other hand, the synthesis of RIO-13, RIO-12, RIO-11, and RIO-11m from hydroxylated azines has also been explored [33]. These materials display pronounced microporosity, elevated surface areas, and surface hydroxyl groups derived from their precursors [34–36]. The presence of these functional groups facilitates Lewis's acid-base interactions with GHGs, enhancing adsorption capacity [33]. Besides, RIO-12 and RIO-55 exhibit particularly high porosity [31,32,37], a critical parameter influencing selective gas separation performance [27,38].

A comprehensive review of the literature data related to F-gases shows that the zeolite 4A successfully separated the F-gas mixture (R-32 and R-125) through molecular sieving, although the low adsorption capacity of R-32 poses a limiting factor [39]. However, zeolite 5A enables enhanced adsorption capability for R-32, with negligible adsorption capacity for R-125, owing to the larger pore size [20]. The adsorption and separation processes containing R-125 with R-134A have been also investigated using zeolite 13X [19]. Separation occurs for R-134A over R-125 because zeolite 13X has both acidic and basic active sites. However, it is important to note that F-gases contain fluorine, which is highly electronegative, increasing the acidity of the molecule. This feature enables the formation of hydrogen bonds with the acidic adsorption sites present in the zeolite 13X [19]. In addition, the adsorption potential of R-32 and R-125 on LTA zeolites (3A, 4A and 5A) have been also investigated [18]. Kinetic limitations in the adsorption equilibria for R-32 with zeolite 3A was observed. Furthermore, the adsorption equilibria of R-125 on zeolites 3A and 4A are negligible and irreversible [18]. These materials enable the separation of F-gases mixtures. Nonetheless, their low adsorption capacity and high energy consumption during the degassing process have resulted in extra costs, rendering industrial-scale implementation challenging.

Recently, organometallic frameworks (MOFs) have emerged in this field. The MOFs provide diverse structural characteristics, including adjustments in surface area and pore size, that may enhance the adsorption of F-gases. The UiO-66(Zr) has been utilized to investigate the adsorption equilibria and separation processes of mixtures containing R-32/R-125 and R-32/R-125/R-134a [39]. This MOF selectively achieved the separation of mixtures containing R-134a over R-32/R-125. The selectivity and separation of R-134a can be attributed to strong interactions because this gas possesses the highest boiling point and dipole moment, which directly favours its selectivity over other gases [39]. On the other hand, adsorption equilibria of R-32, R-134a, and R-125 on Cu-BTC, ZIF-8, MIL-53, and MOF-177 have been also studied. At low pressures, selectivity is preferential towards R-125 and R-134a. Nonetheless, selectivities decrease with the increment of the pressure [29]. Finally, the industrial application of MOFs is limited by the high price.

In addition to the above-mentioned porous solids, activated carbons were also investigated. Adsorption kinetics and equilibria of R-32 on Maxsorb III (ACP) and activated carbon fibre type A-20 (ACF) were determined [40]. The material with the highest adsorption capacity was ACP. In addition, the adsorption and separation equilibria of R-125/R-115 with VRU-f activated carbon were also studied [41]. This activated carbon has a higher adsorption capacity of R-125 compared to R-115. In this case, the molecular differences significantly favour an effective packing of R-125 in the pores of the activated carbons. The R-134a adsorption study was also carried out using Maxsorb III activated carbon (ACP) [42]. The ACP is highly porous and has micropores of different widths, which favours the adsorption. This gas is rapidly adsorbed on high-energy sites in the narrower pores. On the other hand, Chemviron Charcoal was also studied for R-134a adsorption [43]. In this case, the adsorption capacity is influenced by structural characteristics, such as surface area and pore size distribution.

Nowadays, there is currently no standardised technology for the recovery of F-gases. However, there have been studies of processes for the separation and recovery of R-32 by using commercial carbons [28]. Life cycle studies have been carried out to validate the complex separation of R-32 using the VSA separation process [44]. On the other hand, a semi-continuous separation process (adsorption prototype) has been optimized in the European project KET4F-Gas [45] using only commercial activated carbons. Among carbon porous materials, biomass-derived ones appear as an appealing alternative since they can represent the valorisation of a residue or a by-product. Furthermore, these biomaterials can be tuned using chemical or physical treatment, resulting in a material with a high surface area, different structural properties and a lower carbon footprint [46–48].

Various types of residual biomass can be used as sustainable precursors for the preparation of porous activated carbons, offering a valuable route for waste valorizations. Among them, one notable source is the residual coconut shells generated by Brazilian industries, for which identifying scalable industrial applications is particularly important. Likewise, corn cobs represent another abundant lignocellulosic by-product, as corn is the most produced cereal globally. After harvesting the grain, large quantities of cobs are typically left in the fields as soil conditioners, generating approximately 150 g of cobs for every 1 kg of dry corn grain [46,49], rendering these an abundant raw material. This Corn Cob (CC) is a lignocellulosic waste material and can be considered a suitable raw material to obtain porous carbons with good adsorption properties. Additionally, CC waste is characterised by high carbon content (around 45% w/w) and a low percentage of ashes (about 2% w/w) [46,49,50], which turns this agricultural waste into a high-potential precursor for porous carbon production [46,48,51]. Thus, the production of biocarbons from this biomass has aroused great interest in the scientific community. Depending on the chemical and physical treatment, they can generate attractive characteristics for specific processes. For example, the increase in the proportion of the chemical agent H_3PO_4 generates corn cob-derived carbons with an increased pore volume, widening the pores [52]. In addition, the activation with KOH has been studied for the production of biocarbons from CC for CO_2 adsorption [53]. The obtained biocarbons show a high microporosity and C-O, O-H and -NH- functional groups, which favour CO_2

adsorption [53]. Furthermore, the effects of carbonisation time and the ratio of KOH were also investigated [54]. An extended carbonisation period resulted in a notable reduction in particle size and the increase in the structural characteristics of the materials [54]. The potential for microwave activation to reduce the production time of biocarbons from CC was also investigated, utilising KOH and $(NH_4)_2SO_4$ as chemical agents. This study indicated that biocarbons produced with KOH exhibited enhanced surface area and adsorption capacity [55]. On the other hand, a comparison has been made between the preparation of biocarbons from CC using the methods of chemical activation with KOH and steam physical activation [56]. The comparison of the two methods reveals that chemical activation has the effect of improving the development of structural characteristics, generating an increase in CO_2 adsorption capacity [56]. Finally, the preparation of biomaterials by physical activation with CO_2 has been studied, resulting in the production of highly microporous and highly CO_2-selective materials [57]. Then, the reuse of corn cob residues offers the potential for the preparation of cost-effective and highly selective materials for the capture of pollutants.

The aim of this work is to reuse the CC to prepare four different porous biocarbons through two different chemical activation processes (acidic and basic) and a physical activation process with carbon dioxide. The selected chemical agents were chosen to promote the porosity and increase the surface area of the biomaterials. H_3PO_4 generates exothermic reactions that wear down the pore walls of the material, creating micro and mesopores and increasing surface area [41, 52]. On the other hand, the chemical treatment with K_2CO_3 was carried out to promote the microporosity and surface area in the materials [59]. In contrast, the physical treatment with CO_2, promotes micro- and ultramicro-porosity [46]. The influence of these properties was evaluated by measuring and comparing the adsorption equilibria of R-32, R-134a, R-125, SF_6 and N_2 at 303.15 K in the 4 different biocarbons. The two best carbon materials were also evaluated at 283.15 and 323.15 K for a complete characterization. The experimental adsorption data were fitted with the dual-site Langmuir adsorption model. The Ideal Adsorption Solution Theory (IAST) was also used to determine the selectivity in the separation of R-410A (mixture of R-32 and R-125), R-407C (mixture of R-32, R-125 and R-134a), R407F (mixture of R-32, R-125 and R-134a) and SF_6/N_2 mixtures. This work takes a step forward in the knowledge of the development of biomaterials, from CC, which are highly selective for the separation and capture of the most potent greenhouse gases used massively in many industrial applications and household equipment.

In this chapter, five families of adsorbent materials were evaluated for the capture and separation of F-gases, selected for their structural properties (porosity and surface area) and for the interaction of functional groups present on the surface with the studied gases, thereby facilitating the adsorption process. The selection included commercial ACs (AC1, AC2, BAC, Ecosorb, and ACM) with different porosities and surface areas to analyze their behavior in competitive adsorption. Additionally, biocarbons were prepared from residual biomass of corn cob and coconut shell (CC-1:3H_3PO_4, CC-1:1H_3PO_4, CC-K_2CO_3, CC-CO_2, CS-CO_2, and CS-$ZnCl_2$), activated through chemical and physical treatments, aiming to valorize agro-industrial residues, obtain low-cost adsorbents, and improve their structural

properties to enhance selective adsorption. These treatments optimize micropore development and the incorporation of surface functional groups, increasing the capture capacity for fluorinated gases. Furthermore, MOFs (Fe-BTC, MOF-177, MIL-53(Al), ZIF-8, and Cu-BTC), POPs (RIO-55, RIO-23, RIO-20, and RIO-12), and ZSM-5 zeolite were studied, materials widely recognized for their adjustable structural properties and selective affinity. This comprehensive selection allowed comparison of the performance of commercial, synthetic, and sustainable materials in capturing refrigerants and industrial gases with high environmental impact.

This chapter is adapted from the following publications:

Section 4.6

J.E. Sosa, C. Malheiro, R.P.P.L. Ribeiro, P.J. Castro, M.M. Piñeiro, J.M.M. Araújo, F. Plantier, J.P.B. Mota, A.B. Pereiro, *Adsorption of fluorinated greenhouse gases on activated carbons: evaluation of their potential for gas separation*, Journal of Chemical Technology & Biotechnology 95 (2020) 1892–1905. https://doi.org/https://doi.org/10.1002/jctb.637.

The author of this thesis contributed to this section through the drafting of the original manuscript and the preparation of tables and figures. In particular, the author's contributions encompassed equilibrium determination, the development of mathematical models, and material characterizations, with the exception of the subsection concerning the differential heat of adsorption.

Section 4.7

J.E. Sosa, R.P.P.L. Ribeiro, I. Matos, M. Bernardo, I.M. Fonseca, J.P.B. Mota, J.M.M. Araújo, A.B. Pereiro, *Exploring the potential of biomass-derived carbons for the separation of fluorinated gases with high global warming potential*, Biomass Bioenergy 188 (2024) 107323. https://doi.org/10.1016/j.biombioe.2024.107323.

Section 4.8

J.E. Sosa, R.P.P.L. Ribeiro, I. Matos, M. Bernardo, I.M. Fonseca, J.P.B. Mota, J.M.M. Araújo, A.B. Pereiro, *Coconut shell derived activated carbon for effective separation of greenhouse gases*, International Journal of Refrigeration 176 (2025) 66–78. https://doi.org/10.1016/j.ijrefrig.2025.04.022.

Section 4.9

J.E. Sosa, C. Malheiro, P.J. Castro, R.P.P.L. Ribeiro, M.M. Piñeiro, F. Plantier, J.P.B. Mota, J.M.M. Araújo, A.B. Pereiro, *Exploring the Potential of Metal–Organic Frameworks for the Separation of Blends of Fluorinated Gases with High Global Warming Potential*, Global Challenges 7 (2023) 2200107. https://doi.org/10.1002/gch2.202200107.

The author of this thesis contributed to this section by drafting the original manuscript and preparing the tables and figures. Specifically, the author's involvement included the determination of selected adsorption equilibria, the development of mathematical models, and material characterizations.

Section 4.10

J.E. Sosa, S.K.S. Freitas, L.R.C. Correa, R.P.P.L. Ribeiro, J.P.B. Mota, P. Mothé-Esteves, J.M.M. Araújo, L.C. Branco, A.B. Pereiro, *Porous Organic Polymers for the adsorption of fluorinated gases*, J. Mol. Liq. (2025), 128585. https://doi.org/10.1016/j.molliq.2025.128585.

4.2 Materials Characteristics

4.2.1 Textural properties

The porous solid matrices were degassed overnight at 423.15 K to determine the materials' structural characteristics. The nitrogen adsorption-desorption isotherms at 77 K (ASAP 2010 Micromeritics) were determined for each of the porous solid matrices. The surface area was obtained using the Brunauer-Emmett-Teller equation (S_{BET}). Besides, the total pore volume (v_{total}) for each of the porous solid matrices was determined with the isotherms of N_2 at a relative pressure P/P^0 of 0.95. Then, the volume of the micropores (v_{micro}) was determined by the t-plot method. Finally, the determination of the volume of the mesopores (v_{meso}) was calculated by the difference of v_{total} with v_{micro}. Finally, the pore size distribution for the porous solid matrices was determined by the density functional theory (DFT) adsorption model.

4.2.2 Fourier-transform infrared spectroscopy (FTIR)

FTIR with KBr disk method (Perkin-Elmer Spectrum 1000 Spectrometer, Waltham, MA, USA) was used in the range of 400 – 4000 cm^{-1} (with a resolution of 1 cm^{-1}) to determine the functional groups present on the surface of the porous solid matrices.

4.2.3 Thermal gravimetric analysis (TGA)

The determination of decomposition temperature of the materials was determined using the TGA analysis. This analysis was performed between the temperature range of 303.15 – 1173 K with a heating rate of 5 K·min-1 and under an argon atmosphere.

4.2.4 Elemental analysis (EA)

The Thermo Finnigan-CE Instruments Flash EA 1112 CHNS was used to quantify the relative amounts of carbon (C), hydrogen (H), nitrogen (N), and sulphur (S) in the porous solid matrices.

4.2.5 Photoelectron spectra (XPS)

The spectra were acquired using a Thermo fisher Nexsa spectrometer equipped with a Hemispherical electron analyser and micro-focused monochromatic Aluminium Al Kα x-ray source (1486.6 eV). The samples were prepared fixing the pieces to the holder by a copper clamp. The biggest x-ray spot of 400 μm was chosen. The residual vacuum in the analysis chamber was maintained at around 3 x 10^{-10} mbar. Intensities were estimated by calculating the area under peaks, after the subtraction of the (Shirley) S-shaped background. The experimental curve was fitted using a mix of Lorentzian-Gaussian lines in variable proportions. A Flood gun (e- and Argon ions) was used to electron flood gun to minimize surface charging. The accurate binding energies (BE) were determined by reference to the adventitious C1s peak at 284.8 eV. Atomic ratios were computed from peak intensity ratios and reported the Scofield atomic sensitivity factors. Data analysis and quantification were performed using the Advantage software version 5.47 from the manufacturer Thermo-Scientific. The chemical composition and chemical environment of the sample were examined ex-situ by XPS surface measurements acquiring C1s, O1s, and survey spectra. Pass energy for survey spectra was adjusted to 100 eV and for high-resolution spectra Pass energy was adjusted to 20 eV. The survey scan number was 5 for the Carbon high-resolution spectra and 7 scans for Oxygen.

4.2.6 Scanning Electron Microscopy with Energy Dispersive Spectroscopy (SEM-EDS)

This technique was used to observe the impact of physical and chemical treatments, as well as to analyze the morphology and elemental composition of the samples. A JEOL JSM-6700F microscope equipped with an Oxford Ultimax 40 EDS detector was employed. The samples were previously coated with gold.

4.2.7 Crystallographic analyses were conducted by X-ray powder diffraction (XRPD)

XRPD analysis was performed using an XPert Pro (PANalytical) diffractometer to evaluate the pure phase and the crystalline composition of the materials in the 2θ angle from 2° to 70° through a Cu Kα radiation source (λ = 0.15418 nm). Version 3.0d (c) PANalytical B.V. software was used to semi-quantify the crystalline phases. Finally, the morphological features of the materials were analysed using

Scanning Electron Microscopy (SEM). A Jeol JSM6F microscope was used for the measurements. Before analysis, the samples were coated with a thin layer of gold.

4.3 Adsorption equilibrium of GHGs

The gravimetric method was employed to measure the adsorption and desorption of GHGs in the porous solid matrices in the pressure range 0.01-1.5 MPa and at 283.15, 298.15 and 323.15 K. (the maximum ratio applied for pressure/saturation pressure was of 0.78 for R-32, 0.88 for R-125, and 0.79 for R-134a). This method consists of the stepwise supply of GHGs to a temperature-controlled measurement cell containing the adsorbent (0.5–0.7 g), while the mass and pressure variations are monitored until equilibrium is reached. Adsorption/desorption cycles were performed to check for the presence of hysteresis.

Adsorption measurements were performed, as described elsewhere [60–62], in a high-accuracy ISOSORP high-pressure magnetic-suspension balance (MSB) (Rubotherm GmbH, Germany, maximum load of 25 g, resolution of 10 μg, uncertainty less than 0.002 %, and reproducibility smaller than 3×10^{-5} g). The experimental setup is schematized in Figure 2.3.1. This type of balance uses a measurement method based on the mechanical equilibrium between a magnetic force, sample weight, and buoyancy effect [62,63]. The temperature was kept constant by using a thermostatic bath (uncertainty of ± 0.1 K). The pressure was measured with transducers working with accuracy over the full range of operation pressures: a Baratron model 627D (MKS Instruments GmbH, Germany) for 0–0.1 MPa, accuracy of 0.12 %; two Omegadyne Inc. (Sunbury, OH, USA) models PX01C1-150A5T and PX01C1-500A5T, respectively for 0–1 MPa and 0–3.5 MPa (both with accuracy of 0.05 % of the full scale). The equilibrium was considered to have been attained when pressure and mass changes in the system were no longer observed. Before the measurements, the porous solid matrix samples were degassed for at least 12 hours under vacuum at a minimum of 373.15 K.

The adsorption equilibria data are reported in terms of excess adsorption, q_{ex}, defined as

$$q_{ex} = \frac{w - m_s + V_h \rho_g}{m_s} + v_s \rho_g \qquad 4.3.1$$

where w is the apparent mass weighed by the balance, m_s the degassed mass of porous solid matrix sample in the measurement cell, V_h the cumulative volume of all physical parts in the measuring cell contributing to buoyancy effects, ρ_g the density of the gas at the equilibrium pressure and temperature of the experiment, and v_s the specific volume of the adsorbent impenetrable to the adsorbate ($v_s = 1/\rho_s$, where ρ_s is the density of the solid matrix of the adsorbent). The solid density ρ_s was determined experimentally by helium (He) picnometry (assuming He behaves as a non-adsorbing probe molecule).

Excess adsorption can be converted to total adsorption, q, via

$$q = \frac{q_{ex}}{1 - v_a \rho_g} \qquad 4.3.2$$

where v_a (cm^3/mol) is the specific (or molar) volume of the adsorbed phase. It is usually assumed that for (subcritical) adsorption from the vapor phase v_a can be approximated by the specific (or molar) volume, v_m, of the saturated liquid adsorptive at the adsorption temperature [64]. In this work, however, v_a has been determined more accurately from the temperature-dependent saturation capacity of the adsorbent estimated in the framework of the Adsorption Potential theory. This procedure is detailed below.

The gas density, $\rho_g(T,P)$, can be determined experimentally with the MSB by measuring the buoyancy effect exerted by the gas on a calibrated volume with known mass and density, but it can also be calculated with an appropriate equation of state, or even extracted from the NIST Chemistry Webbook [65]. In the present work the latter method was adopted. The uncertainty of the calculated adsorbed mass is around 1 % over the full range of temperature and pressure [63].

4.4 Isosteric Heat of Adsorption and Henry's Constant

In the design of separation processes, it is important to consider the isosteric heat of adsorption (Q_{st}) because the separation can present temperature peaks that affect the capacity of the materials. Therefore, the theoretical Q_{st} was calculated from the experimental adsorption equilibria. Firstly, the experimental data were fitted to the virial equation, which is defined as follows:

$$P = \frac{q}{K_H} exp\left(2Aq + \frac{3}{2}Bq^2 + \frac{4}{3}Cq^3\right) \quad 4.4.1$$

$$A = \sum_m^{\infty} \frac{A_m}{T^m} \quad 4.4.2$$

$$B = \sum_m^{\infty} \frac{B_m}{T^m} \quad 4.4.3$$

$$C = \sum_m^{\infty} \frac{C_m}{T^m} \quad 4.4.4$$

where P is the partial pressure of the gas, q is the adsorbed capacity in equilibrium (absolute adsorption), K_H is Henry's constant, and A, B and C are the virial coefficients. These parameters are contingent upon temperature and are truncated after the second term.

Then, the value Q_{st} was determined using the Clausius-Clapeyron equation in an integrated manner [66–68]:

$$(\log_e P)_q = constant - \frac{Q_{st}}{RT} \quad 4.4.5$$

In this second step, linear isosteric plots were converted to $(\log_e P)_{q=const}\ vs\ 1/T$ for different adsorbed quantities, enabling the determination of the Q_{st}.

4.5 Prediction of the Adsorption and Selectivity of GHGs Using Ideal Adsorption Solution Theory (IAST)

The Ideal Adsorption Solution Theory (IAST) was employed to predict the adsorbed phase composition of multicomponent GHG systems [27,69–71]. However, it is important to note that the fugacity of a single component within a multicomponent mixture is given by $f_i^0(\pi')$, where component *i* of the mixture provides the same dispersion pressure and the adsorbent surface area π' of the other components should be calculated as [27,69–73]:

$$\frac{\pi'}{RT} = \begin{cases} \int_0^{f_i^0} q_i^0(P_i,T) d\ln f_i & if\ f_i^0 < f_i^s \\ \int_0^{f_i^0} q_i^0(P_i,T) d\ln f_i + q_i^s \ln \frac{f_i^s}{f_i^0}, & if\ f_i^0 > f_i^s \end{cases} \quad 4.5.1$$

where q_i^s is the saturation capacity, $q_i^0(P_i,T)$ is obtained from the single-component adsorption isotherm, and p_i^s is the vapour pressure of the pure component at the same temperature. However, if the single-component pressure P_i^0 exceeds P_i^s, or if the pure-component fugacity f_i^0 exceeds f_i^s, the amount adsorbed must remain equal to the corresponding q_i^s or f_i^s [27].

The equilibria of the GHGs multicomponent mixture on the four porous solid matrices at 303.15 K, within the pressure range of 0.01-1 MPa. Based on the results obtained from the multicomponent equilibria, the selectivity of the mixture was determined, considering that the amount of free gas not adsorbed on the four porous solid matrices is negligible compared to the amount adsorbed. Thus, the selectivity for the solid-fluid system is defined as:

$$S_{ij} = \frac{x_i/x_j}{y_i/y_j} \quad 4.5.2$$

where x_i and x_j are the adsorbed mole fractions of gas *i* and *j*, respectively, and y_i and y_j are the mole fractions of gas *i* and *j,* respectively, in the gas phase at equilibrium.

4.6 Adsorption of fluorinated greenhouse gases on activated carbons: evaluation of their potential for gas separation

The estimation of the density of the adsorbed phase as a function of temperature allows the experimental fractional loading of each F-gas on any of the ACs to be correlated as a temperature-independent function of its reduced pressure, which is described by Toth or dual-site Langmuir equations or as an exponential function of the adsorption potential under the Adsorption Potential theory (APT). It is shown that the APT can be generalized with excellent accuracy to the systems studied if an

adsorbate-dependent affinity coefficient is used as a shifting factor to bring the characteristic curves of F-gases on the same AC. R-32 is the F-gas more adsorbed by all adsorbents, followed by R-134a, and by R-125. All ACs are selective for R-125 in R-410A commercial refrigerants, specially at lower pressures. Additionally, all ACs are selective for R-125 and R-134a over R-32 in R407-F commercial refrigerant.

4.6.1 Experimental section

4.6.1.1 Materials

Difluoromethane, R-32 (wt % purity ≥ 99.9), and 1,1,1,2-tetrafluoroethane, R-134a (wt % purity ≥ 99.8), were supplied by Linde, and pentafluoroethane, R-125 (wt % purity ≥ 99.8, was supplied by Sepim. The designation and chemical structure of these F-gases are shown in Table 1. Helium (wt % purity ≥ 99.999) was supplied by Praxair.

The two noncommercial ACs, referred here to as AC1 and AC2 were developed and produced by Sutcliffe Speakman Carbons Ltd. (UK). AC1 is a granular coconut shell carbon and AC2 is an extruded carbon coal based (2 mm diameter pellets). Ecosorb activated carbon, in form of pellets (4 mm diameter), was supplied by Jacobi, and BAC bead-shaped activated carbon (0.70 mm average diameter) was supplied by Kureha.

4.6.1.2 Differential heat of adsorption

The differential heat of adsorption, Q_{st}, of each AC was determined using a homemade apparatus coupling manometric and calorimetric techniques, whose scheme is shown in Figure 4.6.1. This apparatus allows the simultaneous measurement of Q_{st} and the equilibrium amount of gas adsorbed at a given temperature and pressure [74]. Briefly, gas is injected into a dosing cell, which is connected to an adsorption cell containing the adsorbent. As the gas is adsorbed it releases heat, which is recorded. A material balance before and after the connection of the dosing and adsorption cells gives the amount of adsorbed gas. At the same time, the recorded heat peak gives information about the total heat flow (Q), which is the sum of the integral heat of adsorption, Q_a, and of the heat of compression (Q_c) due to the gas injection into the adsorption cell. Q_a is then calculated from

$$Q_a = Q - Q_c \qquad 4.6.1$$

where Q is directly estimated by integration of the heat peak and Q_c given by [74]

$$Q_c = -V_e T\left(\alpha_p - \alpha_{ss}\right)\Delta P \qquad 4.6.2$$

where V_e is the volume considered by the thermopiles and is calculated from helium calibration, α_p the isobaric expansion coefficient, α_{ss} the isobaric coefficient of the stainless steel of the calorimeter, and

ΔP the difference between the equilibrium pressure of the measured point and the previous one. The differential heat of adsorption is then approximated by

$$Q_{st} = \frac{Q_a}{\Delta q} \qquad 4.6.3$$

where Δq is the amount of gas adsorbed between the two consecutive pressure steps. The overall uncertainty in the measurement of Q_{st} is less than 5 % [74].

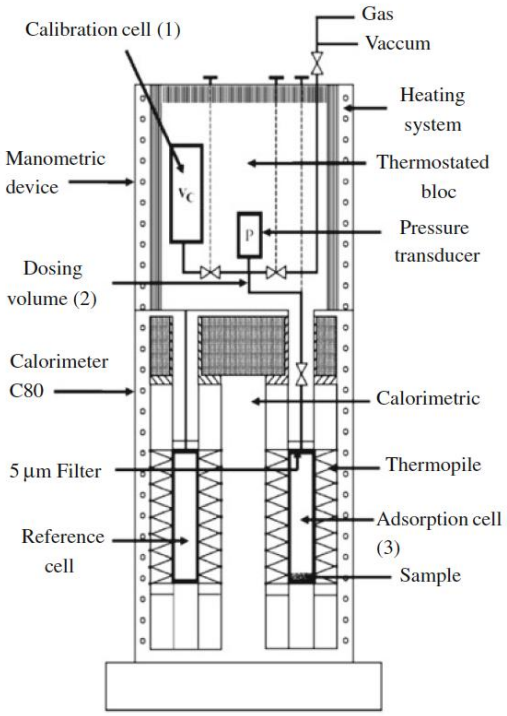


Figure 4.6.1 Schematic diagram of the manometric/calorimetric device.

4.6.2 Results and discussion

4.6.2.1 Materials Characterization

The methodology utilized in this work is detailed in Section 4.2, based on which the F-gas adsorption was studied on four ACs with different textural characteristics. The specific BET surface area, $S_{BET,}$ and specific pore volume, v_p, of each AC are listed in Table 4.6.1 and the PSDs depicted in Figure 4.6.2. The S_{BET} value determined AC1 (1695 m^2/g) is in reasonable agreement with the previously reported data (1669 m^2/g) [75], while the value of AC2 (1280 m^2/g) is slightly lower than previously reported (1342 m^2/g) [75,76] (see Figure 4.6.3).

Table 4.6.1 BET surface area, S_{BET} (m^2/g), and specific pore volume, v_p (cm^3/g), of the ACs.

	EcoSorb	BAC	AC1	AC2
S_{BET}	1100	1250	1695	1280
v_p	0.52	0.49	0.76	0.68

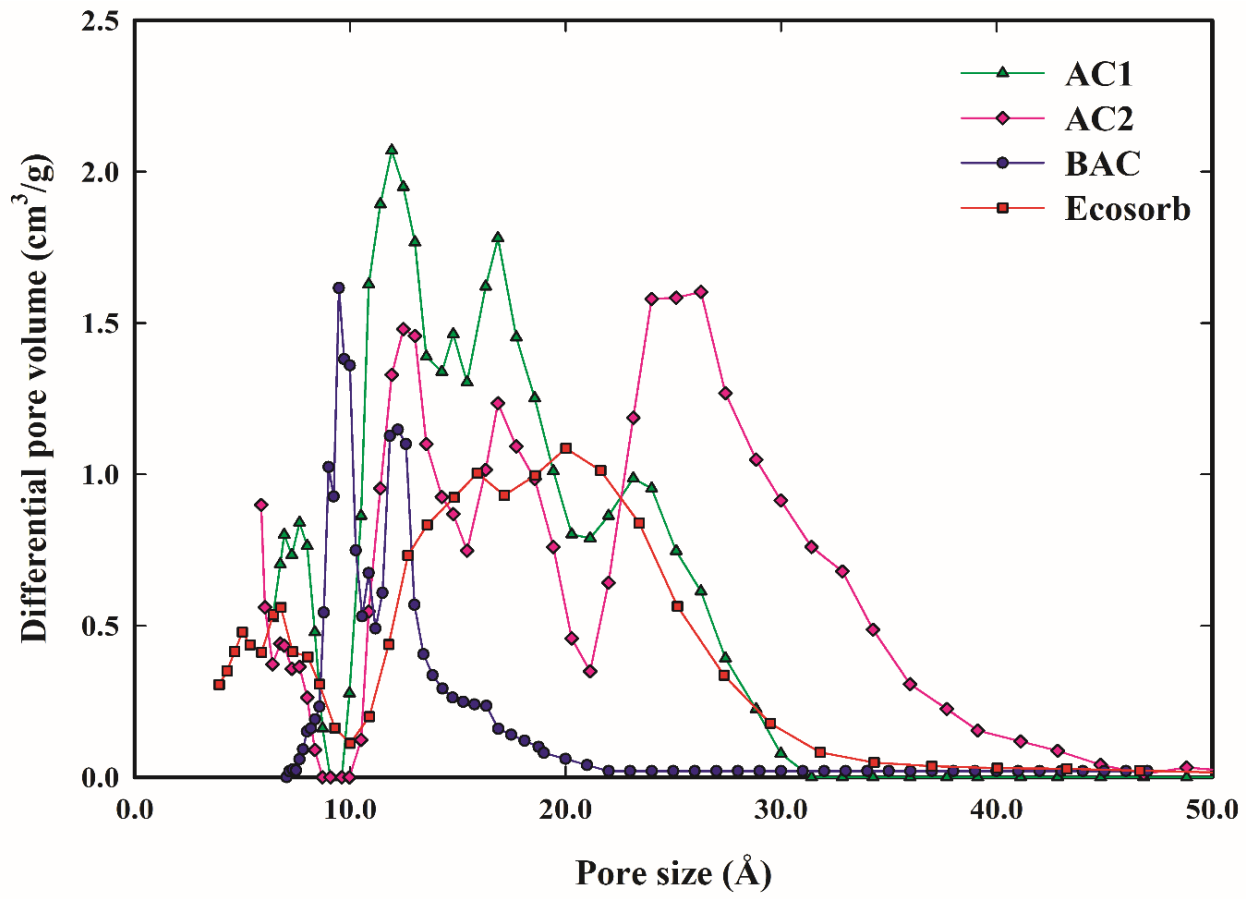


Figure 4.6.2 Pore size distribution of AC1 (green triangles), AC2 (pink diamonds), BAC (blue circles), and Eco-sorb (red squares), determined by deconvolution of the N_2 adsorption isotherm at 77 K using standard methods based on the Non-Localized Density Functional Theory (NLDFT).

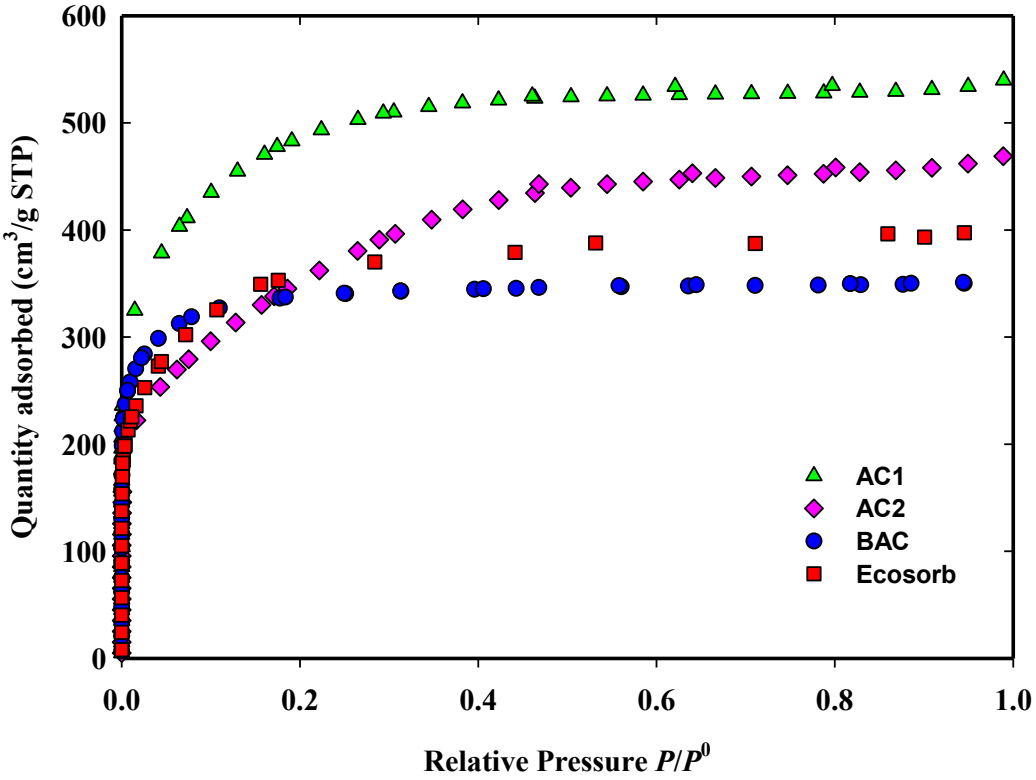


Figure 4.6.3 Nitrogen adsorption isotherm at 77 K for AC1 (green triangles), AC2 (pink diamonds), BAC (blue circles), and Ecosorb (red squares) carbons.

Despite the similar values of S_{BET} and v_p for the two commercial ACs (Ecosorb and BAC), their different PSDs (see Figure 4.6.2) influence the capture of F-gases. While Ecosorb has a polydisperse PSD in the micropore (pores smaller than 20 Å) and mesopore (pore diameters between 20 Å and 500 Å) regions, BAC has a narrower pore size distribution lying in the micropore region with a peak around 10 Å (see Figure 4.6.2). The two non-commercial ACs have larger values of S_{BET} and v_p (see Table 4.6.1) than BAC and Ecosorb, which favor gas adsorption. While AC1 has a polydisperse PSD in the micropore and ultra-micropore (pore size smaller than 10 Å) regions, the PSD of AC2 also extends into the mesopore regions (see Figure 4.6.2).

4.6.2.2 Adsorption Equilibrium of F-gases on ACs

The details of the adsorption equilibrium determination are provided in Section 4.3. Based on this methodology, experimental adsorption equilibrium data at 283.15 K, 303.15 K, and 323.15 K, expressed as milimoles of adsorbed gas per gram of adsorbent (mmol/g), are plotted in Figure 4.6.4 – 4.6.6 as a function of the applied equilibrium gas pressure. The maximum adsorption pressures for each studied F-gas was around 15 % lower than its vapor pressure at 283.15K (0.77 MPa for R-134a, 1.57 MPa for R-125, and 1.93 MPa for R-32). The isosteric heat of adsorption for each AC/F-gas pair was measured at 323.15 K (Figure 4.6.7).

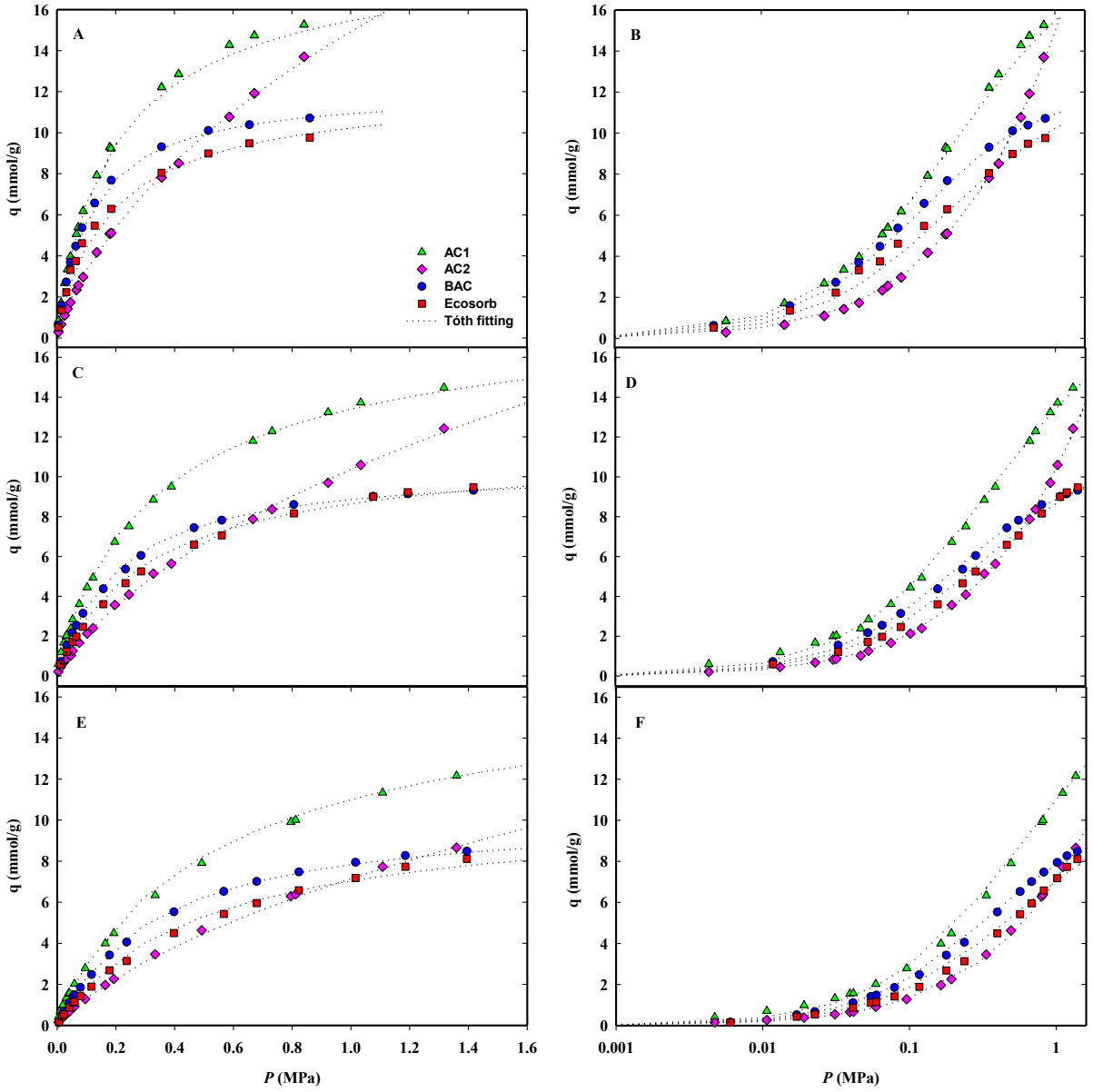


Figure 4.6.4 Adsorption equilibrium isotherms of R-32 on AC1 (green triangles), AC2 (pink diamonds), BAC (blue circles), and Ecosorb (red squares), at 283.15 K (A, B), 303.15 K (C, D), and 323.15 K (E, F). The dashed lines represent the data fittings with the dimensionless form of Toth's model (eqn. 4.6.15). The right-hand-side plots use a logarithmic pressure scale.

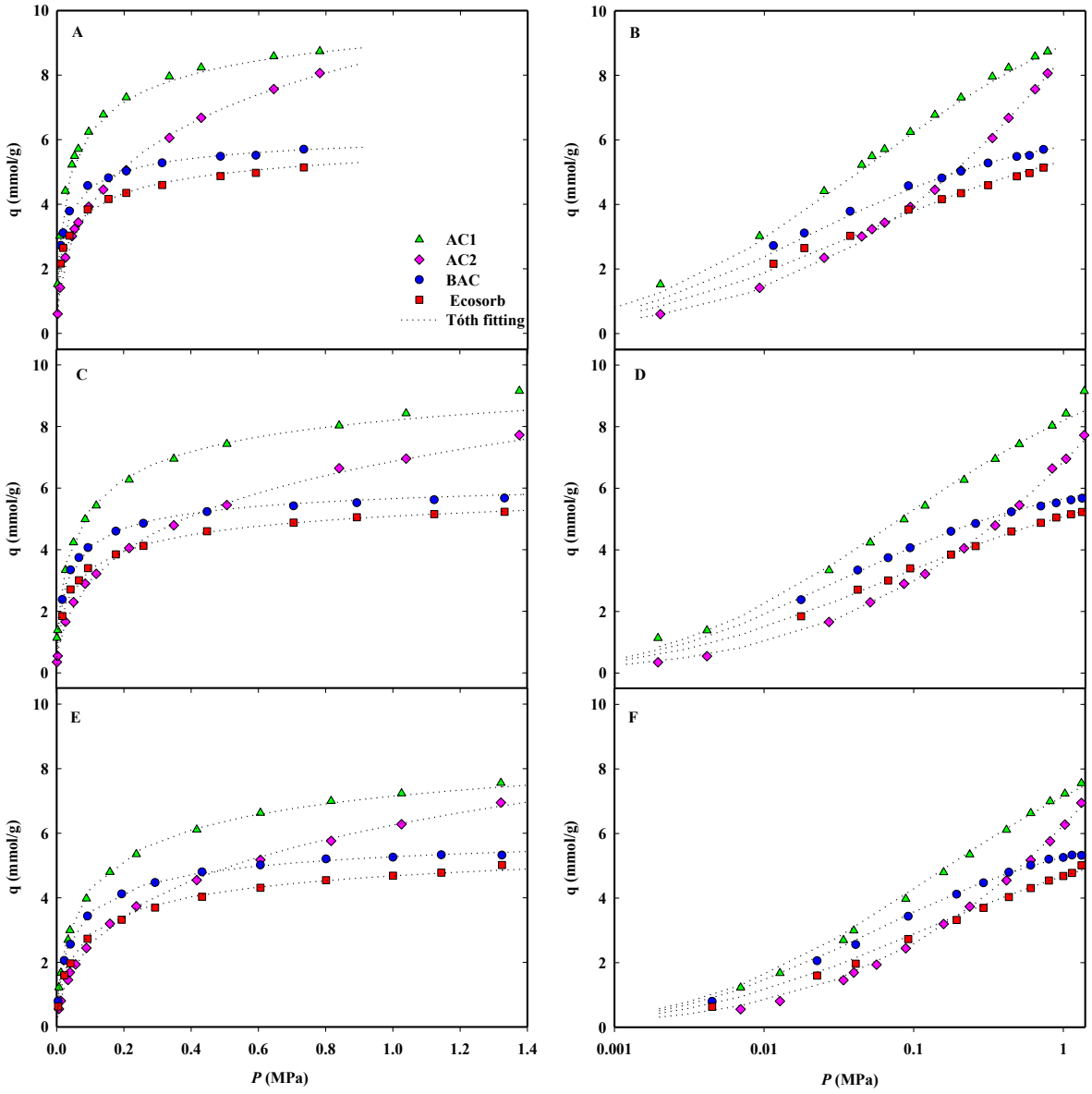


Figure 4.6.5 Adsorption equilibrium isotherms of R-125 on AC1 (green triangles), AC2 (pink diamonds), BAC (blue circles), and Ecosorb (red squares), at 283.15 K (A, B), 303.15 K (C, D), and 323.15 K (E, F). The dashed lines represent the fittings with the dimensionless form of Toth's model (eqn. 4.6.15). The right-hand-side plots use a logarithmic pressure scale.

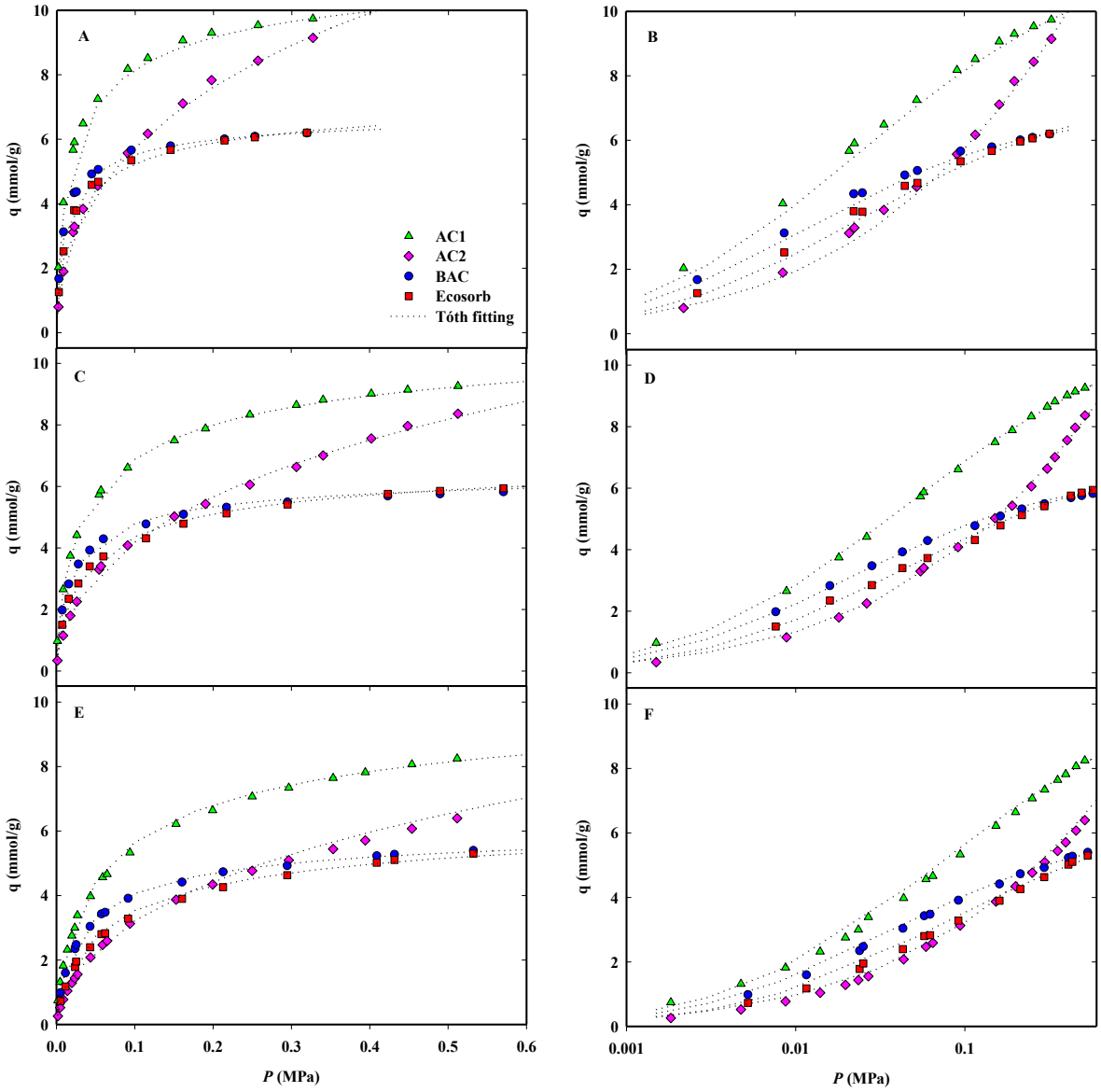


Figure 4.6.6 Adsorption equilibrium isotherms of R-134a on AC1 (green triangles), AC2 (pink diamonds), BAC (blue circles), and Ecosorb (red squares), at 283.15 K (A, B), 303.15 K (C, D), and 323.15 K (E, F). The dashed lines represent the fittings with the dimensionless form of Toth's model (eqn. 4.6.15). The right-hand-side plots use a logarithmic pressure scale.

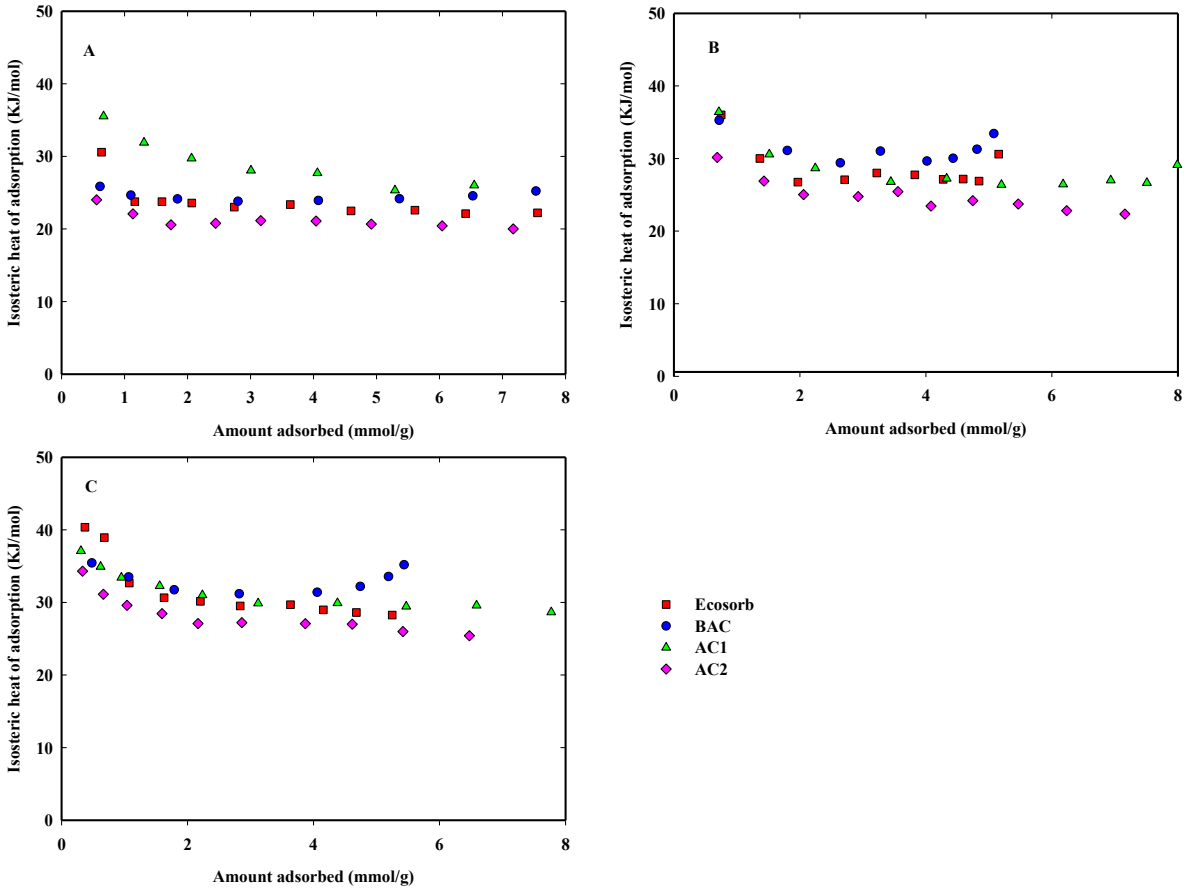


Figure 4.6.7 Isosteric heats of adsorption of R-32 (A), R-125 (B), and R-134a (C) at 323.15 K on AC1 (green triangles), AC2 (pink diamonds), BAC (blue circles), and Ecosorb (red squares).

The adsorption data were analyzed in the framework of the Adsorption Potential theory (APT), for it is assumed that the main mechanism governing subcritical F-gas adsorption in essentially microporous ACs is pore filling [77–80]. According to this theory the specific volume of adsorbed phase, W (cm3 of adsorbed phase per gram of AC), is a function solely of the adsorption potential, ϕ:

$$W \equiv q v_{\mathrm{a}} = W(\phi) \qquad 4.6.4$$

where $W(\phi)$ is a temperature-independent characteristic curve for each solid–fluid system. The adsorption potential is defined as

$$\phi = \mu_{\mathrm{s}} - \mu = RT \ln\left(\frac{f_{\mathrm{s}}}{f}\right) \quad f \leq f_{\mathrm{s}} \qquad 4.6.5$$

where R is the ideal gas constant, T the system temperature, f the fugacity of the gas at the equilibrium pressure and temperature, f_{s} its saturation fugacity at the same temperature, and μ and μ_{s} are the corresponding chemical potentials. All fugacity values were determined using the Aspen Plus v.10 database.

The characteristic curve, $W(\phi)$, should be a positive monotonic decreasing function of ϕ satisfying the two limits

$$\lim_{\phi \to 0} \theta = 1, \quad \lim_{\phi \to \infty} \theta = 0 \qquad 4.6.6$$

where $\theta \equiv W/W_s$ is the fractional loading or pore volume filling and W_s is the specific pore volume of the adsorbent accessible to the adsorbate, taken to be equal to the corresponding value of v_p listed in Table 4.6.1.

Although v_a is usually approximated by v_m, it is known that the force field exerted by a micropore compresses the adsorbed phase beyond that of a saturated liquid. Although this effect is small at temperatures well below the critical value, T_c, of the adsorbate, it should be more pronounced as the temperature approaches T_c, i.e.,

$$\alpha(T) = \frac{v_a}{v_m} \qquad 4.6.7$$

should be a monotonic decreasing function of T as the latter is increased up to the critical value. In this work a more accurate estimate of v_a is obtained by calculating it in such a way that the expression

$$v_a(T) = \lim_{P \to P_s(T)} v_p/q(T) \equiv v_p/q_s(T) \qquad 4.6.8$$

where $q_s(T)$ is the saturation capacity of the adsorbent, results in a temperature-independent $W(\phi)$ curve. This procedure, an example of which is shown in Figure 4.6.8 for R-32 adsorption on AC2 (similar graphs for the other AC/F-gas combinations are included in Figure 4.6.9-4.6.9), serves two purposes: (i) it produces a single, temperature-independent characteristic curve with minimum data scatter and (ii) corrects the limiting behavior of $W(\phi)$ so that it satisfies the condition $\lim_{\phi \to 0} \theta = 1$ when W_s is equal to the specific pore volume, v_p. In Figure 4.6.9 - 4.6.10, which include similar graphs for the other AC/F-gas combinations, there are several cases where the effectiveness of the proposed procedure is striking.

It was found that for all studied solid-fluid systems $\alpha(T)$ is very well approximated by a linear function

$$\alpha = (\alpha_1 - \alpha_2 T) \qquad 4.6.9$$

where α_1 and α_2 are constants specific of each AC/F-gas pair, or, alternatively, $v_a(T)$ can be fitted directly to an expression of the type

$$\ln v_a = a - \frac{b}{T} \qquad 4.6.10$$

where a and b are fitting parameters. The values of α, v_a, and v_m (the latter obtained as a function of T from the NIST Chemistry Webbook [65]) are listed in Table 4.6.2. The average value of α over all studied solid-fluid systems and temperatures is 0.89 with standard deviation of 0.08, which indicates that the adsorbed phases are slightly more compressed than the saturated, liquefied F-gases.

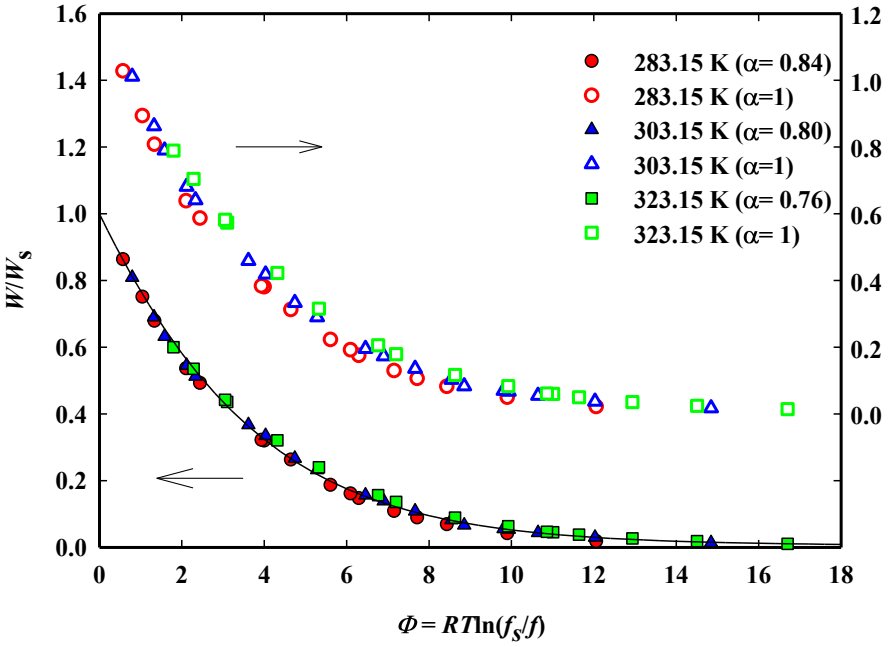


Figure 4.6.8 Determination of $\alpha(T)$ for R-32 adsorption on AC2. The molar volume of the adsorbed phase, $v_a(T)$, is such that a plot of $W \equiv v_a q$ as a function of $\phi \equiv RT \ln(f_s/f)$ produces a single characteristic curve with minimum data scatter that satisfies the condition $\lim_{\phi \to 0} \theta = 1$ when W_s is equal to the specific pore volume, v_p. Data are represented for 283.15 K (red circles), 303.15 K (blue triangles), and 323.15 K (green squares). Data obtained with $\alpha = 1$ are shown as empty symbols on the right-hand-side vertical axis, which is shifted upwards by 0.4 units for better visualization. Data obtained with a corrected value of α are shown as full symbols.

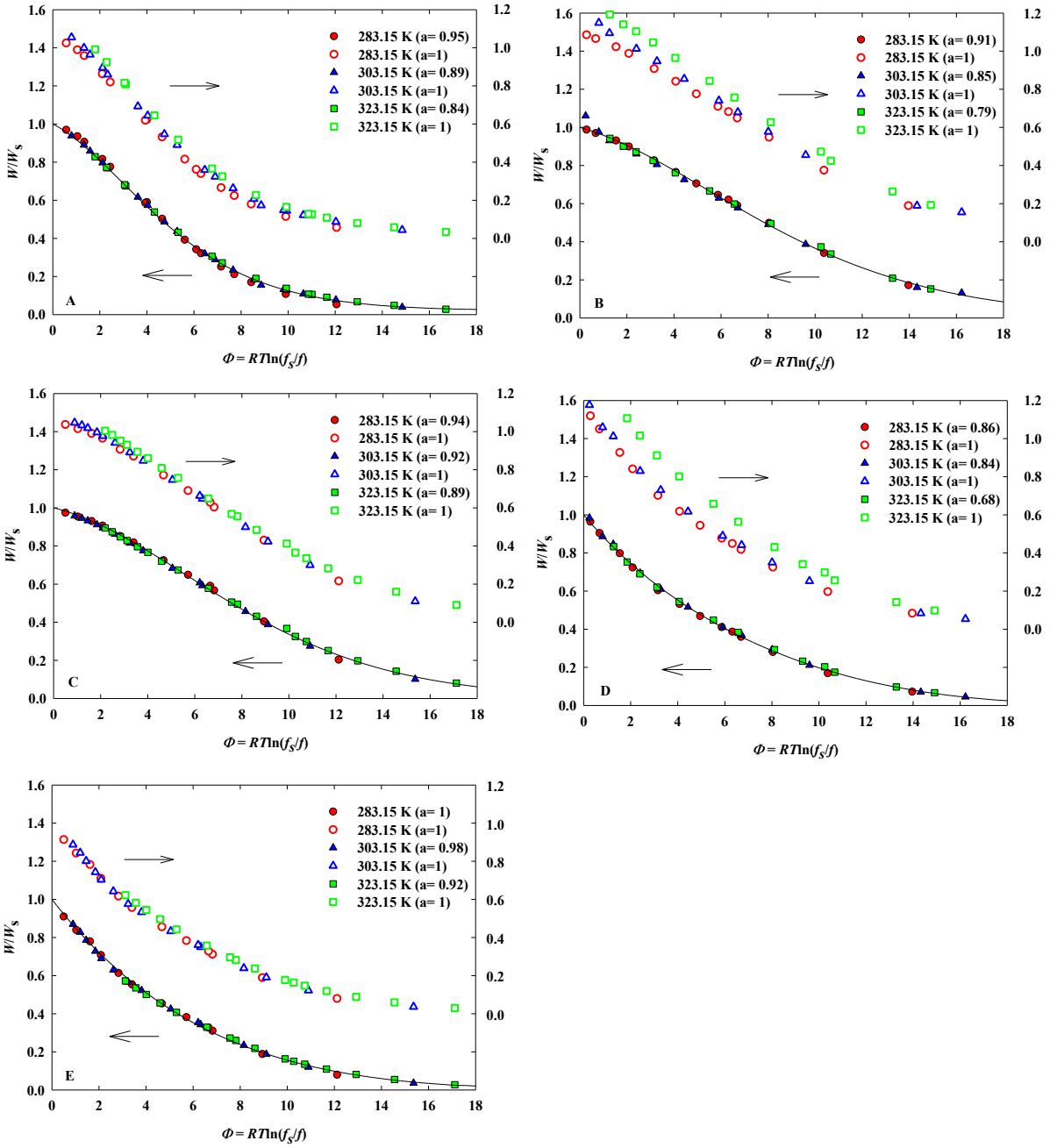


Figure 4.6.9 Determination of $\alpha(T)$ for F-gas adsorption on AC1 and AC2 carbons: R-32/AC1 (A), R-125/AC1 (B), R-134a/AC1 (C), R-125/AC2 pair (D), and R-134a/AC2 (E). The molar volume of the adsorbed phase, $v_a(T)$, is such that a plot of $W \equiv v_a q$ as a function of $\phi \equiv RT\ \ln(f_s/f)$ produces a single characteristic curve with minimum data scatter that satisfies the condition $\lim_{\phi \to 0} \theta = 1$ when W_s is equal to the specific pore volume, v_p. Data are represented for 283.15 K (red circles), 303.15 K (blue triangles), and 323.15 K (green squares). Data obtained with $\alpha = 1$ are shown in empty symbols and the vertical axis (represented at the right side) was shifted 0.4 units upwards for better visualization. Data obtained with a corrected value of α are shown in full symbols.

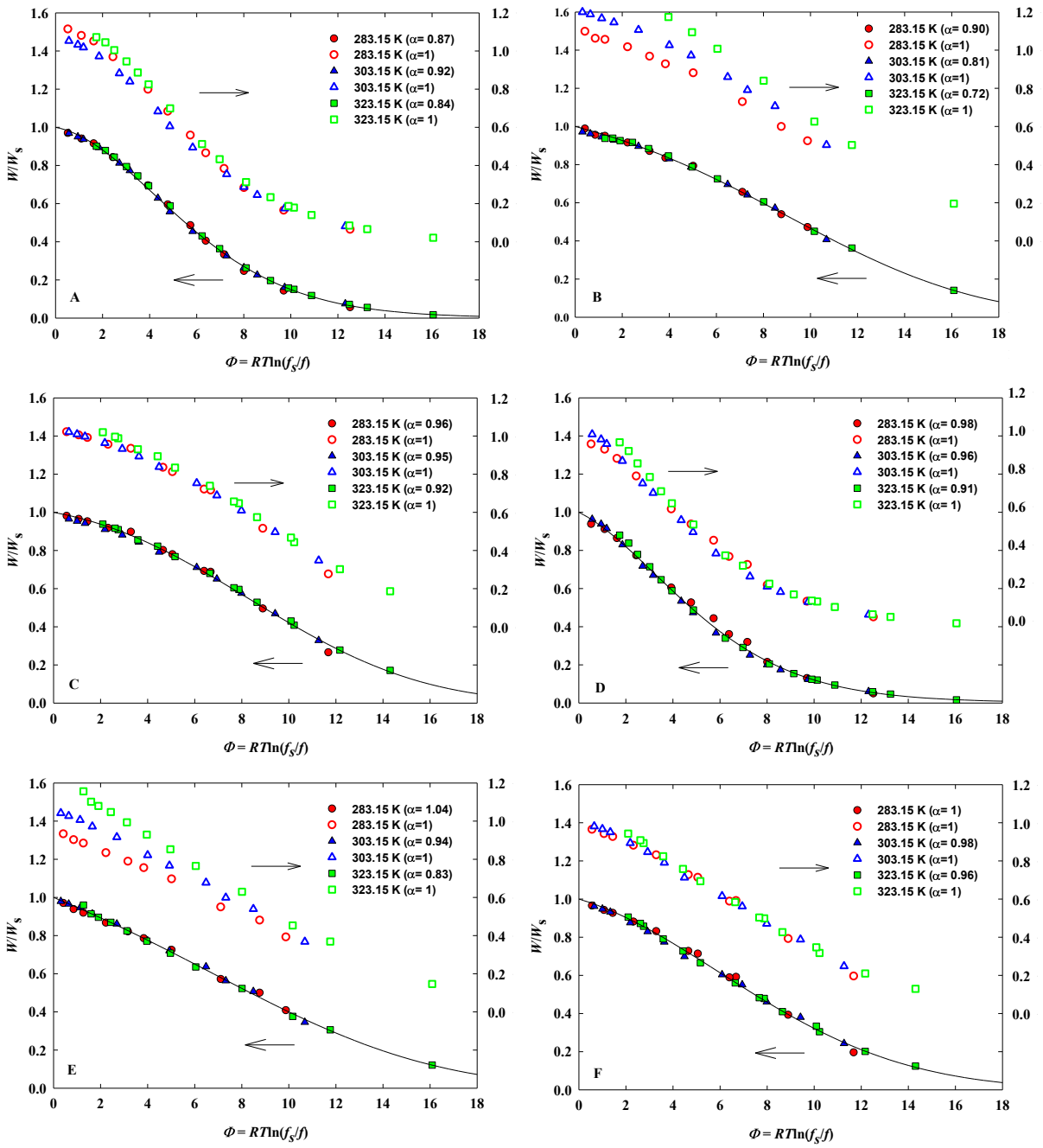


Figure 4.6.10 Determination of $\alpha(T)$ for F-gas adsorption on BAC and Ecosorb carbons: R-32/BAC pair (A), R-125/BAC (B), R-134a/BAC (C), R-32/Ecosorb (D), R-125/Ecosorb (E), and R-134a/Ecosorb (F) The molar volume of the adsorbed phase, $v_a(T)$, is such that a plot of $W \equiv v_a q$ as a function of $\phi \equiv RT\ \ln(f_s/f)$ produces a single characteristic curve with minimum data scatter that satisfies the condition $\lim_{\phi \to 0} \theta = 1$ when W_s is equal to the specific pore volume, v_p. Data are represented for 283.15 K (red circles), 303.15 K (blue triangles), and 323.15 K (green squares). Data obtained with $\alpha = 1$ are shown in empty symbols and the vertical axis (represented at the right side) was shifted 0.4 units upwards for better visualization. Data obtained with a corrected value of α are shown in full symbols.

Table 4.6.2 Molar volumes of the saturated liquid adsorptive and adsorbed phase, v_m (cm^3/mol) and v_a (cm^3/mol), and molar volume ratio, $\alpha = v_a/v_m$, for the twelve solid-fluid systems at each of the three studied temperatures, T (K).

		R-32		**R-125**		**R-134a**	
	T	$\boldsymbol{v_m}$		$\boldsymbol{v_m}$		$\boldsymbol{v_m}$	
	283.15	51.0		094.4		80.9	
	303.15	55.4		103.6		85.9	
	323.15	62.0		119.9		92.6	
	T	$\boldsymbol{v_a}$	$\boldsymbol{\alpha}$	$\boldsymbol{v_a}$	$\boldsymbol{\alpha}$	$\boldsymbol{v_a}$	$\boldsymbol{\alpha}$
	283.15	44.4	0.87	85.0	0.90	77.7	0.96
BAC	303.15	50.9	0.92	83.9	0.81	81.2	0.95
	323.15	52.1	0.84	86.3	0.72	85.2	0.92
	283.15	50.0	0.98	98.2	1.04	80.9	1.00
Ecosorb	303.15	52.9	0.96	97.4	0.94	84.2	0.98
	323.15	56.4	0.91	99.5	0.83	88.9	0.96
	283.15	48.2	0.95	85.9	0.91	76.0	0.94
AC1	303.15	49.3	0.89	88.1	0.85	78.6	0.92
	323.15	51.8	0.84	94.7	0.79	82.4	0.89
	283.15	42.9	0.84	81.3	0.86	80.6	1.00
AC2	303.15	44.3	0.80	86.6	0.84	84.2	0.98
	323.15	47.1	0.76	81.5	0.68	85.2	0.92

Interestingly, it turns out that a graph of θ as a function of the reduced pressure $x = P/P_s$, obtained using the estimated values of v_a, merges quite nicely in a single master curve the three experimental adsorption isotherms for each of the twelve AC/F-gas systems studied. Figure 4.6.11 shows a representative example of such plot for R-32 adsorption on AC1 (similar graphs for the other AC/F-gas combinations are included in Figure 4.6.12 - 4.6.13.

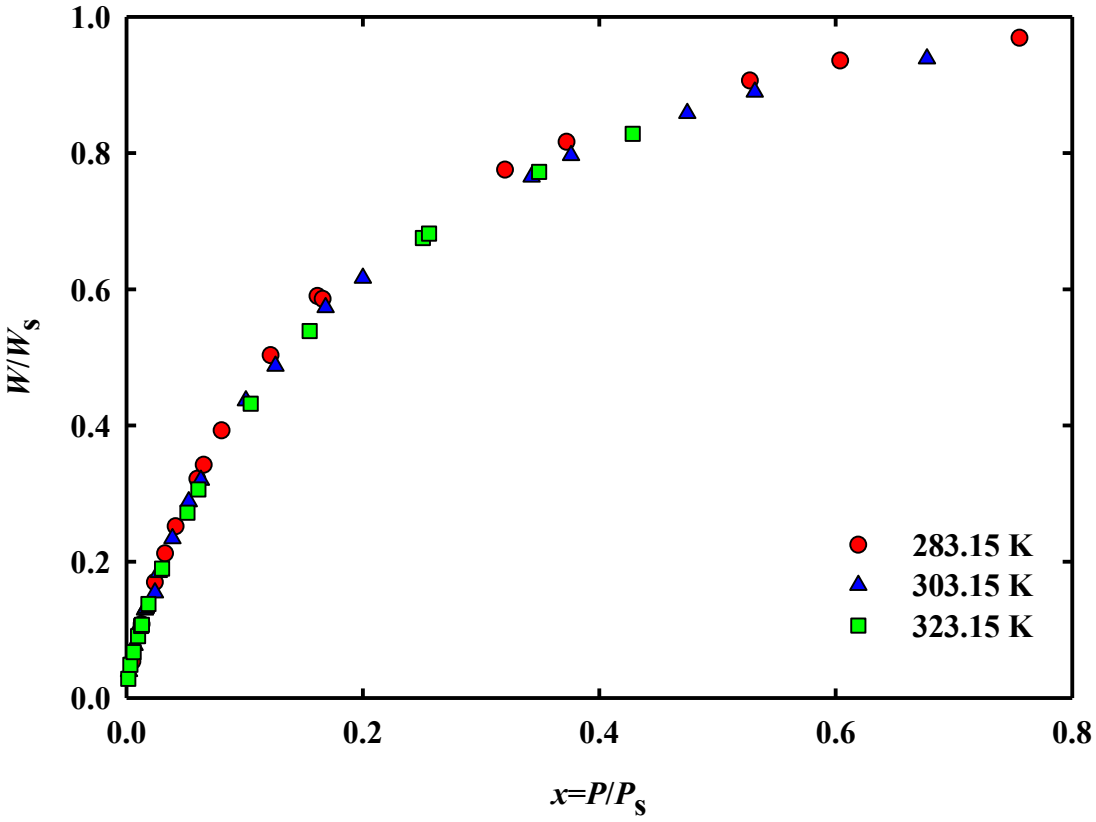


Figure 4.6.11 Fractional loading or pore volume filling, $\theta = W/W_s \equiv q v_a/v_p$, as a function of reduced pressure, $x = P/P_s$, for R-32 adsorption on AC1 at 283.15 K (red circles), 303.15 K (blue triangles), and 323.15 K (green squares).

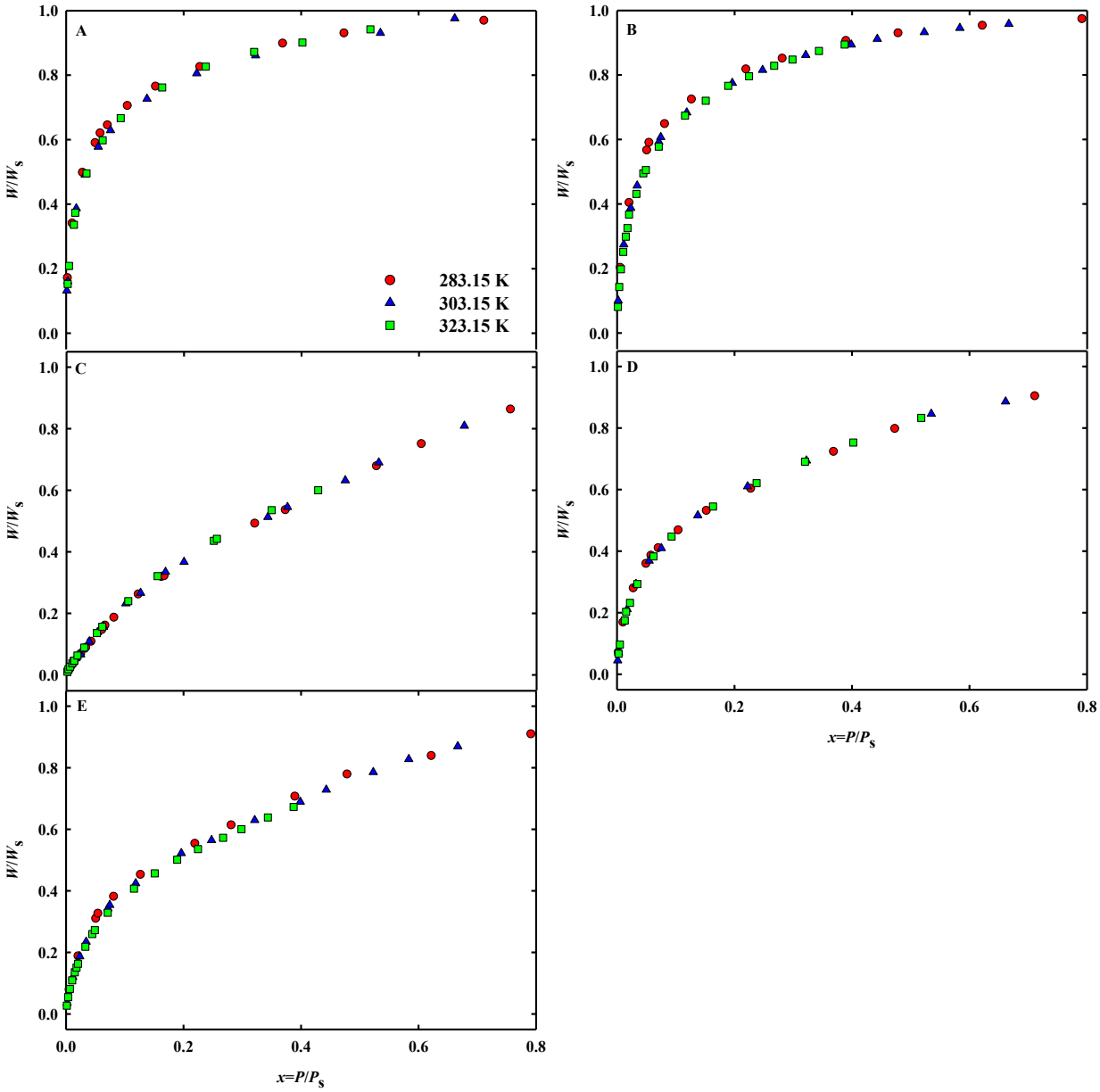


Figure 4.6.12 Fractional loading or pore volume filling, $\theta = W/W_s \equiv qv_a/v_p$, as a function of reduced pressure, $x = P/P_s$, for R-32 adsorption on AC1 at 283.15 K (red circles), 303.15 K (blue triangles), and 323.15 K (green squares).

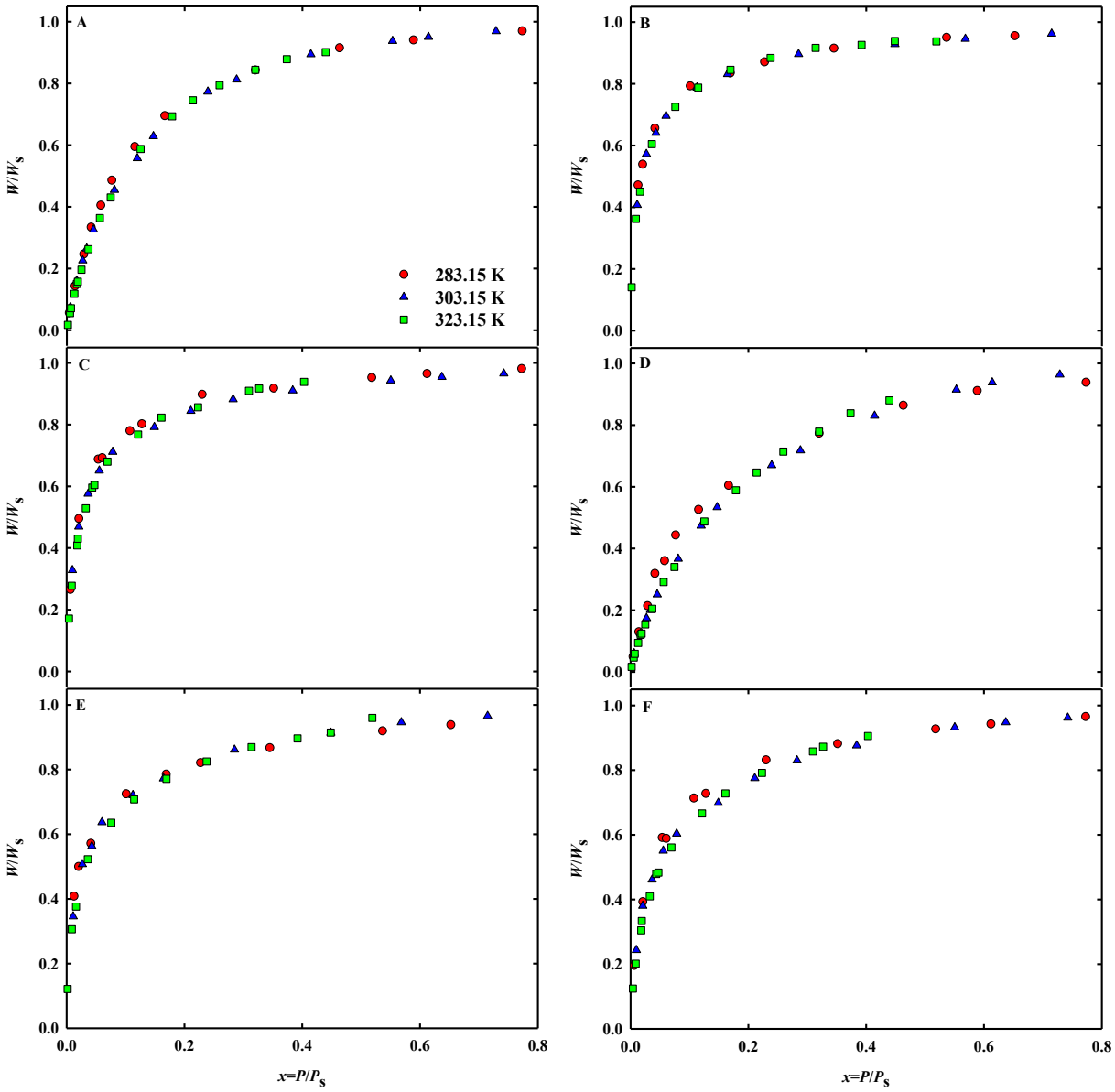


Figure 4.6.13 Fractional loading or pore volume filling, $\theta = W/W_s \equiv qv_a/v_p$, as a function of reduced pressure, $x = P/P_s$, for R-32 adsorption on AC1 at 283.15 K (red circles), 303.15 K (blue triangles), and 323.15 K (green squares).

Single-component adsorption equilibrium data are commonly fitted to classical thermodynamic models for predicting multicomponent, competitive adsorption equilibria and for applying in model-based process design [77]. One of the most often used models is that of Tóth [81], which is described by

$$q = \frac{q_\infty bP}{[1 + (bP)^t]^{1/t}} \qquad 4.6.11$$

where $q_\infty = \log_{P\to\infty} q$, $b = H/q_\infty$ an affinity constant (bar^{-1}), H (mmol g^{-1} bar^{-1}) the Henry constant, and t a dimensionless heterogeneity parameter. The temperature dependencies of the parameters b and t are usually defined as

$$b = b_0 \exp\left(\frac{Q}{RT}\right) \quad 4.6.12$$

$$t = t_0 + B\left(1 - \frac{T_0}{T}\right) \quad 4.6.13$$

where b_0 is the value of the affinity constant at infinite temperature, Q a measure of the isosteric heat of adsorption, t_0 the value of the heterogeneity parameter at a reference temperature T_0, and B the slope of the plot of t versus $-1/T$.

It is worth noting that the Tóth model is much more suitable for modeling supercritical rather than subcritical adsorption equilibria. Although the Tóth model returns a value of q for any arbitrarily large value of P, for subcritical adsorption as is the case here it makes no sense to go above the saturation pressure, P_s, of the adsorptive at the adsorption temperature. In fact, in this case the parameter q_∞ should be regarded as a fictitious saturation capacity that allows the model to satisfy the condition $q(T, P_s) = q_s \equiv v_p/v_a$. For this condition to be met q_∞ must be defined as

$$q_\infty = \frac{q_s[1 + (bP_s)^t]^{\frac{1}{t}}}{bP_s} \quad 4.6.14$$

and in this case the Tóth model can be expressed in the following dimensionless form that relates the fractional loading and the reduced pressure:

$$\theta = \left[\frac{1 + (b')^t}{1 + (b'x)^t}\right]^{1/t} x \quad 4.6.15$$

where $b' = bP_s$. Given that the representations of θ as a function of x for the studied AC/F-gas combinations result in (nearly) temperature-independent curves, eqn. 4.6.15 can be fitted directly to those data with just two temperature-independent parameters (b' and t) this is quite convenient.

Away from the critical temperature and not too high vapor pressures of the adsorptive, the temperature-dependence of P_s is given by the simplified form of the Clausius-Clapeyron equation

$$P_s = P_s^\infty \exp\left(\frac{-\Delta H_v}{RT}\right) \quad 4.6.16$$

where ΔH_v is the specific enthalpy of vaporization. Combining this expression with eqn. 4.6.11, it is concluded that the parameter Q in eqn. 4.6.12 must be equal to ΔH_v for $b' \equiv bP_s$ to be independent of temperature.

Another useful single-component adsorption equilibrium model is the multi-site Langmuir model,[41] which can be written as

$$q = \sum\nolimits_{k=1}^{n_s} \frac{H_k P}{1 + b_k P} \quad 4.6.17$$

where H_k is the contribution of sites (or pores) of type k to the overall Henry constant, $H = \sum H_k$, and b_k the corresponding Langmuir equilibrium constant. Since the model must satisfy the constraint $q(P_s, T) = q_s(T)$, it is convenient to rearrange it in dimensionless form as follows

$$\theta = \sum\nolimits_{k=1}^{n_s} \frac{\theta_k(1 + b_k)x}{1 + b_k x}, \qquad \theta_1 + \cdots \theta_{n_s} = 1 \quad 4.6.18$$

where the Henry constants have been replaced by the fractional site distributions, θ_k. In particular, for $n_s = 2$ the above expression reduces to the dual-site (or bi-) Langmuir model

$$\theta = \theta_1 \frac{(1+b_1)x}{1+b_1 x} + (1-\theta_1)\frac{(1+b_2)x}{1+b_2 x} \qquad 4.6.19$$

This three-parameter model is the simplest of the series capable of describing the heterogeneity of an activated carbon, in which, for example, θ_1 and b_1 characterize the contribution of the smaller pores and $1-\theta_1$ and $b_2 \ll b_1$ that of the larger ones.

Under the ATP framework the experimental characteristic curve, $W(\tilde{\phi})$, is commonly fitted to the Dubinin–Astakhov (D–A) equation [80,82,83].

$$W = W_s \exp\left(-\gamma \tilde{\phi}^n\right) \qquad 4.6.20$$

where γ and n are fitting parameters related to the characteristic energy for the given adsorbent and to the pore size distribution, respectively. However, we have found that the alternative approach of fitting $W(\tilde{\phi})$ to a low-order polynomial expansion [82],

$$\ln\left(\frac{W}{W_s}\right) = \gamma_1 \tilde{\phi} + \gamma_2 \tilde{\phi}^2 + \gamma_3 \tilde{\phi}^3 + \cdots \qquad 4.6.21$$

where the γ's are fitting parameters, usually describes better the experimental data.

To obtain the isosteric heat of adsorption, Q_{st}, for a given adsorption isotherm model, one uses the relationship $Q_{st} = RT^2(\partial \ln P / \partial T)_q$, analogous to the well-known Clausius–Clapeyron equation for a one-component gas-liquid system. The result for the dimensionless Toth model defined by eqn. 4.6.15 is

$$Q_{st} = \Delta H_v - R\gamma \frac{1+b^n}{1+b^n-(b\theta)^n} \qquad 4.6.22$$

where ΔH_v and $\gamma \equiv \mathrm{d}\ln v_a / \mathrm{d}(1/T)$ are constants if the explored temperature range is not too wide. Since $\gamma < 0$, eqn. 4.6.22 defines Q_{st} as a monotonically increasing function of θ limited between $Q_{st}(0) = \Delta H_v + R|\gamma|$ and $Q_{st}(1) = \Delta H_v + R|\gamma|(1+b^n)$.

The isosteric heat of adsorption for the dimensionless dual-site Langmuir model, given by eqn. 4.6.4, is very well (though not exactly) approximated by

$$Q_{st} = \Delta H_v - R\gamma \frac{1+\theta_1 b_1 + (1-\theta_1)b_2}{1+[\theta_1 b_1 + (1-\theta_1)b_2](1-\theta)} \qquad 4.6.23$$

which is as a monotonically increasing function of θ from $Q_{st}(0) = \Delta H_v + R|\gamma|$ to $Q_{st}(1) = \Delta H_v + R|\gamma|[1+\theta_1 b_1 + (1-\theta_1)b_2]$.

Finally, for the APT model given by eqn. 6 the isosteric heat of adsorption is

$$Q_{st} = \Delta H_v + \frac{\phi}{\xi} + \frac{\gamma}{\xi}\frac{\theta}{T}\frac{\mathrm{d}\phi}{\mathrm{d}\theta} \qquad 4.6.24$$

where $\xi \equiv \mathrm{d}\ln(f_s/f) / \mathrm{d}\ln(P_s/P)$, which is slightly smaller than 1, can be taken as constant with very good approximation if the explored temperature range is not too wide. Although T appears explicitly in eqn. 4.6.24, it is worth noting that the latter expresses Q_{st} as a function of θ because $\phi/T = -R\ln x$,

where x is the reduced pressure, and it was observed that $\theta = \theta(x)$ for the solid-fluid systems studied. According to eqn. 4.6.24, at low fractional loadings Q_{st} is approximately given by $Q_{\mathrm{st}} = \Delta H_{\mathrm{v}} + \phi/\xi$, which is a monotonically decreasing function of θ starting from the limiting value $Q_{\mathrm{st}}(0) \equiv \lim_{\theta \to 0} Q_{\mathrm{st}} = +\infty$, whereas at high fractional loadings $Q_{\mathrm{st}} = \Delta H_{\mathrm{v}} + (\gamma/\xi T)(\mathrm{d}\phi/\mathrm{d}\ln\theta)$, which is an increasing function of θ. The overall result is that $Q_{\mathrm{st}}(\theta)$ will have a more or less convex shape.

The dimensionless Tóth parameters that best fit the experimental adsorption data for each AC/F-gas pair are listed in Table 4.6.3 and the corresponding fittings are plotted in Figure 4.6.4 – 4.6.6 as dashed lines. The experimental adsorption data for each AC/F-gas pair were also successfully fitted to the dimensionless dual-site Langmuir model (the parameters are listed in Table 4.6.4 and the corresponding fittings plotted in Figure 4.6.14 – 4.6.16), as well as to the APT model in the form of eqn. 4.6.21 (Table 4.6.5 and Figure 4.6.14 – 4.6.16). These models have been chosen because they correlate well adsorption equilibrium data at low and high pressures on heterogeneous adsorbents such as activated carbons. The good agreement between the fittings of the three different adsorption equilibrium models and the experimental adsorption data shows that these models describe well the thermodynamics of the studied AC/F-gas systems and are therefore suitable for use in modeling and simulation of adsorption-based separation processes. Additionally, it was observed that replacing the fractional site-distribution parameter, $\theta_{i,1}$, for adsorption of F-gas i in a given AC, by a single adsorbate-independent parameter, θ_1, did not change the quality of the fitting but increased its robustness. Table 4.6.6 lists the best-fit parameter values of this model for each of the twelve solid-fluid systems. Overall, both Tóth's and the dual-site Langmuir model fit equally well the experimental adsorption data; they are, however, slightly outperformed by the APT model when it is formulated in the form of eqn. 4.6.21.

Table 4.6.3 Best-fit parameter values of the dimensionless Toth model (eqn. 4.6.15) for each AC/F-gas pair.

		b'	t	r^2
Ecosorb	R-32	6.945	0.892	0.996
	R-125	211.6	0.414	0.998
	R-134a	49.46	0.563	0.996
BAC	R-32	9.091	1.050	0.998
	R-125	187.9	0.518	0.999
	R-134a	76.85	0.660	0.997
AC1	R-32	6.937	0.825	0.998
	R-125	160.0	0.428	0.993
	R-134a	61.71	0.529	0.998
AC2	R-32	0.438	0.313	0.999
	R-125	80.44	0.208	0.999
	R-134a	24.91	0.170	0.997

Table 4.6.4 Best-fit parameter values of the dimensionless dual-site Langmuir model (eqn. 4.6.19) with adsorbate-dependent θ_1 for each AC/F-gas pair.

		θ_1	b_1	b_2	r^2
Ecosorb	R-32	0.046	91.61	5.708	0.995
	R-125	0.590	115.8	4.165	0.996
	R-134a	0.544	62.11	4.767	0.996
BAC	R-32	0.000	9.465	0.000	0.998
	R-125	0.699	115.0	4.931	0.997
	R-134a	0.701	73.34	5.456	0.998
AC1	R-32	0.038	855.1	5.345	0.999
	R-125	0.429	196.1	7.262	0.992
	R-134a	0.437	101.1	6.466	0.998
AC2	R-32	0.209	10.21	0.471	0.999
	R-125	0.359	64.46	1.537	0.999
	R-134a	0.344	36.75	0.902	0.999

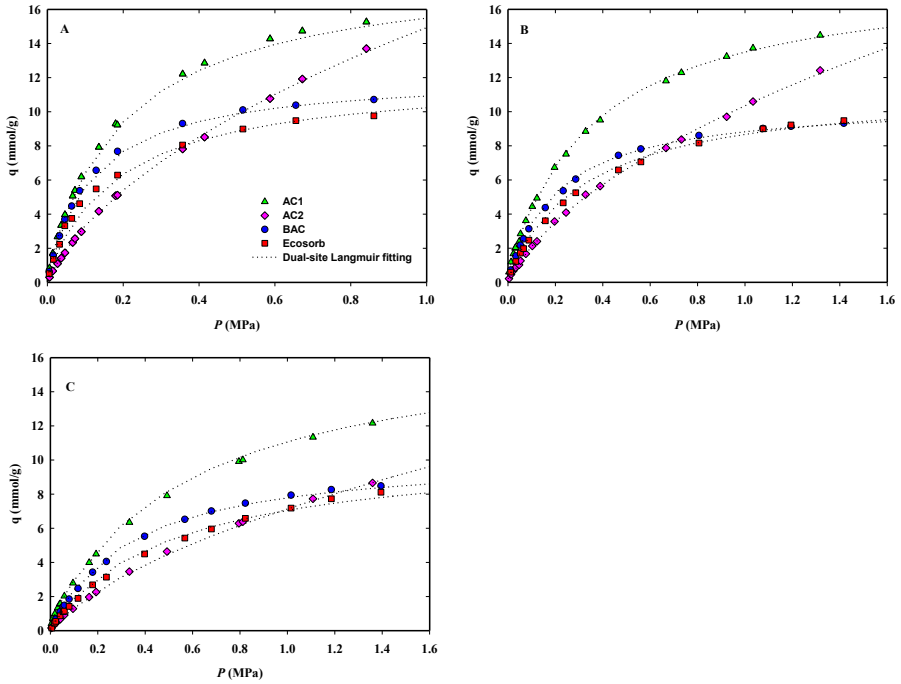


Figure 4.6.14 Adsorption equilibrium isotherms of R-32 on AC1 (green triangles), AC2 (pink diamonds), BAC (blue circles), and Ecosorb (red squares), at 283.15 K (A), 303.15 K (B), and 323.15 K (C). The dashed lines represent the fittings with the dimensionless dual-site Langmuir isotherm model (eqn. 4.6.19).

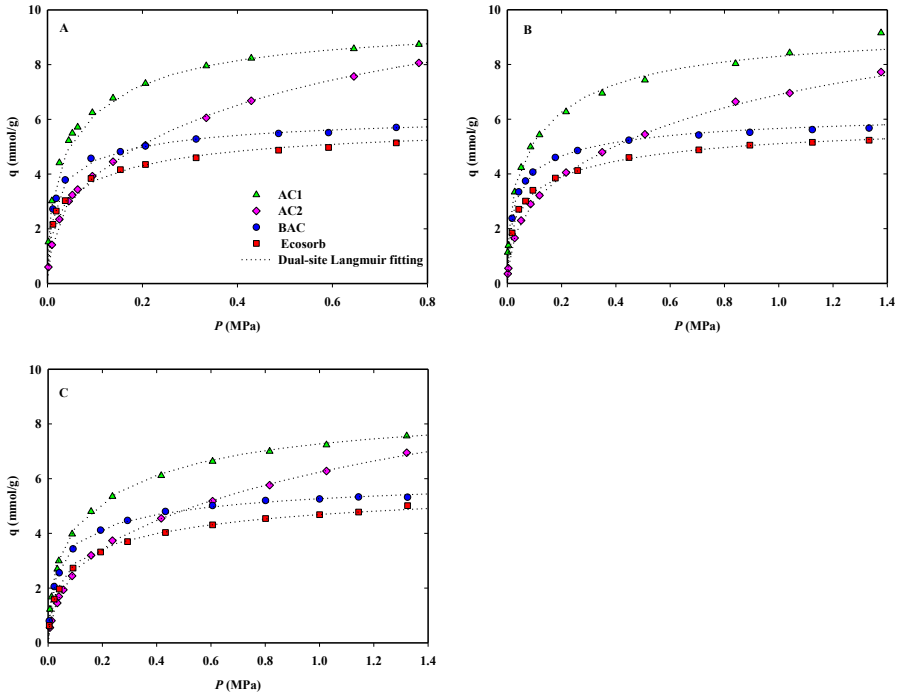


Figure 4.6.15 Adsorption equilibrium isotherms of R-125 on AC1 (green triangles), AC2 (pink diamonds), BAC (blue circles), and Ecosorb (red squares), at 283.15 K (A), 303.15 K (B), and 323.15 K (C). The dashed lines represent the fittings with the dimensionless dual-site Langmuir isotherm model (eqn. 4.6.19).

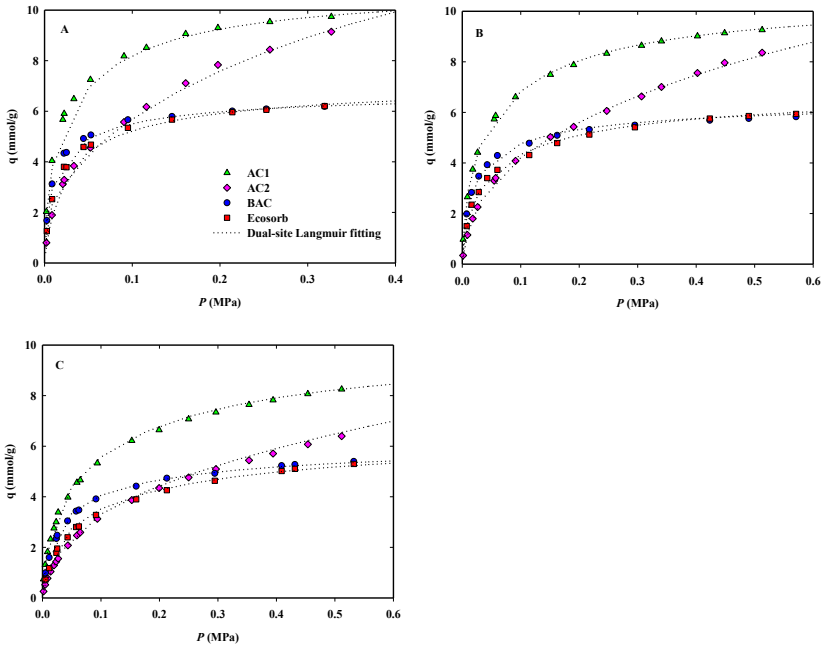


Figure 4.6.16 Adsorption equilibrium isotherms of R-134a on AC1 (green triangles), AC2 (pink diamonds), BAC (blue circles), and Ecosorb (red squares), at 283.15 K (A), 303.15 K (B), and 323.15 K (C). The dashed lines represent the fittings with the dimensionless dual-site Langmuir isotherm model (eqn. 4.6.19).

Table 4.6.5 Best-fit parameter values of the APT model (eqn.4.6.21) for each AC/F-gas system. The γ_i's are expressed in J/mol.

		$-10^5\gamma_1$	$-10^{10}\gamma_2$	$-10^{13}\gamma_3$	$-10^{18}\gamma_4$	r^2
Ecosorb	R-32	6.104	201.5	−5.111		0.996
	R-125	5.085	25.47	1.528		0.998
	R-134a	3.284	80.92			0.995
BAC	R-32	2.268	210.7	4.342		0.999
	R-125	3.248	24.53	1.937		0.998
	R-134a	2.266	42.78	2.097		0.996
AC1	R-32	1.468	109.3	−4.032	4.993	0.999
	R-125	4.499	53.95			0.995
	R-134a	4.120	65.79			0.998
AC2	R-32	28.33	9.631			0.998
	R-125	12.68	38.67			0.998
	R-134a	15.08	36.47			0.998

Table 4.6.6 Best-fit parameter values of the dimensionless dual-site Langmuir model (eqn. 4.6.21) with adsorbate-independent θ_1 for each AC/F-gas pair.

$\boldsymbol{\theta_1 \pm \sigma^2}$	$\boldsymbol{b_1 \pm \sigma^2}$	$\boldsymbol{b_2 \pm \sigma^2}$
0.574 ± 0.002	Ecosorb	
	9.763 ± 0.05	3.465 ± 0.03
	123.1 ± 0.97	4.475 ± 0.04
	57.36 ± 0.31	4.308 ± 0.03
0.427 ± 0.003	BAC	
	9.462 ± 0.04	9.467 ± 0.04
	8.690 ± 0.08	172.4 ± 1.70
	146.2 ± 1.50	13.14 ± 0.08
0.421 ± 0.001	AC1	
	12.66 ± 0.07	3.380 ± 0.02
	204.6 ± 1.60	7.445 ± 0.04
	108.1 ± 0.71	6.737 ± 0.03
0.348 ± 0.001	AC2	
	5.941 ± 0.03	0.201 ± 0.00
	68.41 ± 0.53	1.610 ± 0.01
	36.04 ± 0.24	0.884 ± 0.01

Each adsorption isotherm (Figure 4.6.4 –4.6.6) exhibits the classical Type I behavior [84] of gaseous adsorbates in microporous solids, with progressive pore filling due to the polydisperse PSD. At the highest pressures tested at 303.15K the adsorption capacity for R-32 is 9.48 mmol/g on Ecosorb, 9.32 mmol/g on BAC, 14.5 mmol/g on AC1, and 12.4 mmol/g on AC2. For R-134a in the same conditions, the adsorption capacity is 5.95 mmol/g on Ecosorb, 5.83 mmol/g on BAC, 9.26 mmol/g on AC1, and 8.36 mmol/g on AC2. For R-125 in the same conditions, the adsorption capacity is 5.23 mmol/g on Ecosorb, 5.67 mmol/g on BAC, 9.15 on AC1, and 7.72 mmol/g on AC2. The two noncommercial ACs (AC1 and AC2) have larger adsorption capacities at higher pressures, which is in accordance with their higher surface area and pore volume.

All ACs have similar Q_{st} values for each gas (see Figure 4.6.7.), with slightly larger values for R-125 and R-134a than for R-32, and all of them strongly correlated with the respective heats of vaporization. The isosteric heats of adsorptions calculated from the dimensionless Tóth, dimensionless dual-site Langmuir, and APT models are plotted and compared with the experimental calorimetric data in Figure 4.6.17 and 4.6.18. The predicted Q_{st} values are in fairly good qualitative if not quantitative agreement with the measurements, but far from the fine quality by which the equilibrium loadings are described by the same thermodynamic models. In accordance with the observations on the fittings of the

adsorption measurements, the APT model seems to describe the measured Q_{st} data better than the other two models. This is not surprising, given that the APT model is the only one of the three capable of describing the monotonically decreasing or concave shapes of the experimental Q_{st} curves.

In order to evaluate the adsorption capacities of each AC, the adsorption isotherms of R-32, R-125, and R-134a at 303.15 K on the four ACs were compared (Figure 4.6.18). At the highest pressures, R-32 is the most adsorbed F-gas on all ACs, followed by R-134a, and then by R-125. This results from the adsorption of a vapor close to conditions of complete pore filling being governed by the entropy of its liquid-like adsorbed phase and, therefore, the saturation capacity, $q_s = v_p/v_a$, being approximately inversely proportional to the molar volume, v_m, of the condensed adsorptive at the adsorption temperature, due to the dependence of q_s on v_a. This is indeed the case given than the ordering of the v_m's is R-32 < R-134a < R-125.

Since the four ACs have different PSDs, the experimental adsorption data were interpreted taking the specific surface area and pore volume of each AC (listed in Table 4.6.1) into account. Figure 4.6.19 compares the experimental adsorption equilibria of R-134a at 323.15 K on the different ACs, expressed as the amount adsorbed per unit weight of solid (mmol/g), unit surface area of solid (mmol/m^2), and unit pore volume of solid (mmol/cm^3). On a weight basis, the noncommercial AC1 carbon has much higher adsorption capacity at higher pressures than the commercial BAC and Ecosorb carbons, followed by AC2. However, when the results are compared per unit surface area or unit pore volume of solid, the performance difference between the carbons clearly decreases, as expected. The best results, obtained at high pressures, for AC1 and AC2 are due to their larger porous volumes, which lead to a higher adsorption capacity. Similar observations can be made for the other AC/F-gas pairs at 298.15 K, 303.15 K, and 323.15 K (data not shown).

On the other hand, in the low-pressure region the free energy of the AC/F-gas system is totally governed by enthalpic effects, as the Henry constant is solely a function of the solid-fluid interaction potential. The latter is a strong function of pore width, decreasing with increasing pore size in the micropore range and then levelling off at the value for the interaction with a single flat carbon wall. Additionally, the contribution of a given pore width to the total amount adsorbed in the low-pressure region will be proportional to the contribution of that pore size to the specific surface area of the solid. Hence, the importance of the PSD for analysis of the low-pressure F-gas adsorption data on the ACs. Indeed, such an analysis shows that the AC with larger pores in the micropore range (AC2) has lower adsorption capacity in the low-pressure region than the other ACs with smaller pore sizes.

The APT has two attributes especially useful for predicting single-component adsorption equilibrium from a limited set of experimental measurements. The first one, which has been amply demonstrated above, is that according to the theory the characteristic curve is temperature independent. Therefore, only adsorption equilibrium measurements at one temperature are necessary to obtain the characteristic curve, and this is sufficient to describe the adsorption at all temperatures for the same gas-solid system. The second feature, despite being of more limited applicability, is also very useful: in many

cases the theory can be generalized if an adsorbate-dependent affinity coefficient, β, is used as a shifting factor to bring the characteristic curves of all gases on the same adsorbent into a single curve. This has been observed to hold for a series of systems [76,85,86] and it is demonstrated here that it can also be generalized with excellent accuracy to the twelve solid-fluid systems studied.

Introducing an adsorbate-dependent affinity coefficient, β_i, as a scaling factor of the adsorption potential for the *i* the F-gas leads to

$$W_i \equiv (qv_a)_i = W\left(\tilde{\phi}_i\right), \frac{\tilde{\phi}_i \equiv \phi_i}{\beta_i} \qquad 4.6.25$$

where $W(\tilde{\phi})$ is a function supposed to be adsorbate independent. Following previous work [87,88], the affinity coefficient is assumed to be a power function of the molecular parachor, $\mathcal{P}$ (a measure of molecular volume), that is

$$\frac{\beta_i}{\beta_j} = \left(\frac{\mathcal{P}_i}{\mathcal{P}_j}\right)^n \qquad 4.6.26$$

where $n = 0.9$ is the most suggested exponent. Following the usual convention of setting $\beta = 1$ for benzene ($\mathcal{P} = 199.0$), the previous equation takes the form $\beta_i = (\mathcal{P}_i/199.0)^{0.9}$.

In the present work $\mathcal{P}$ is approximated by the simple formula $\mathcal{P} = 8.0 + 0.707V_c$ [75], where V_c is the critical volume (taken from the NIST Chemistry Webbook) [65].

The APT was successfully applied to the adsorption equilibrium data of R-32, R-125, and R-134a on the four ACs, to obtain a single temperature-independent characteristic curve for each solid-fluid system. Moreover, by employing the β coefficient it was possible to collapse the characteristic curves of the different F-gases on the same AC into a single characteristic curve (Figure 4.6.20). It should be highlighted that these characteristic curves were generated without any fitting of the β parameters—they are among the multi-adsorbate characteristic curves with the lowest data dispersion reported in the literature since Dubinin's pioneering work in the mid-1940s [82]. These characteristic curves were fitted to eqn. 4.6.21with very good precision (Figure 4.6.21); the fitted parameters are listed in Table 4.6.5.

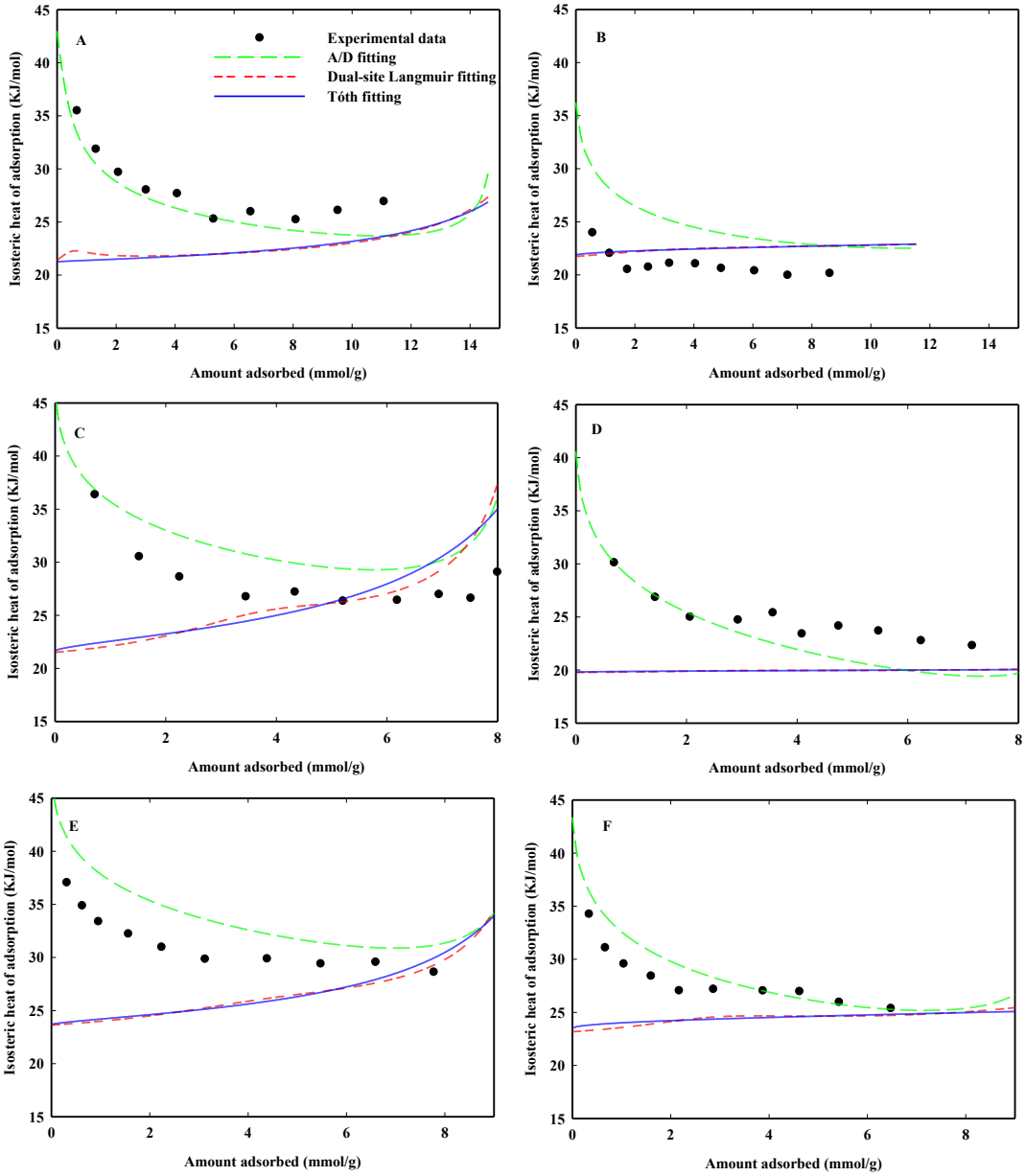


Figure 4.6.17 Isosteric heats of F-gas adsorption on AC1 and AC2, determined experimentally (black dots) at 323.15 K and calculated by applying the Clausius-Clapeyron equation to the APT (long-dashed green line), dual-site Langmuir (short-dashed red line), and Toth (solid blue line) models, and the values. A, R-32/AC1; B, R-32/AC2; C, R-125/AC1; D, R-125/AC2; E, R-134a/AC1; F, R-134a/AC2.

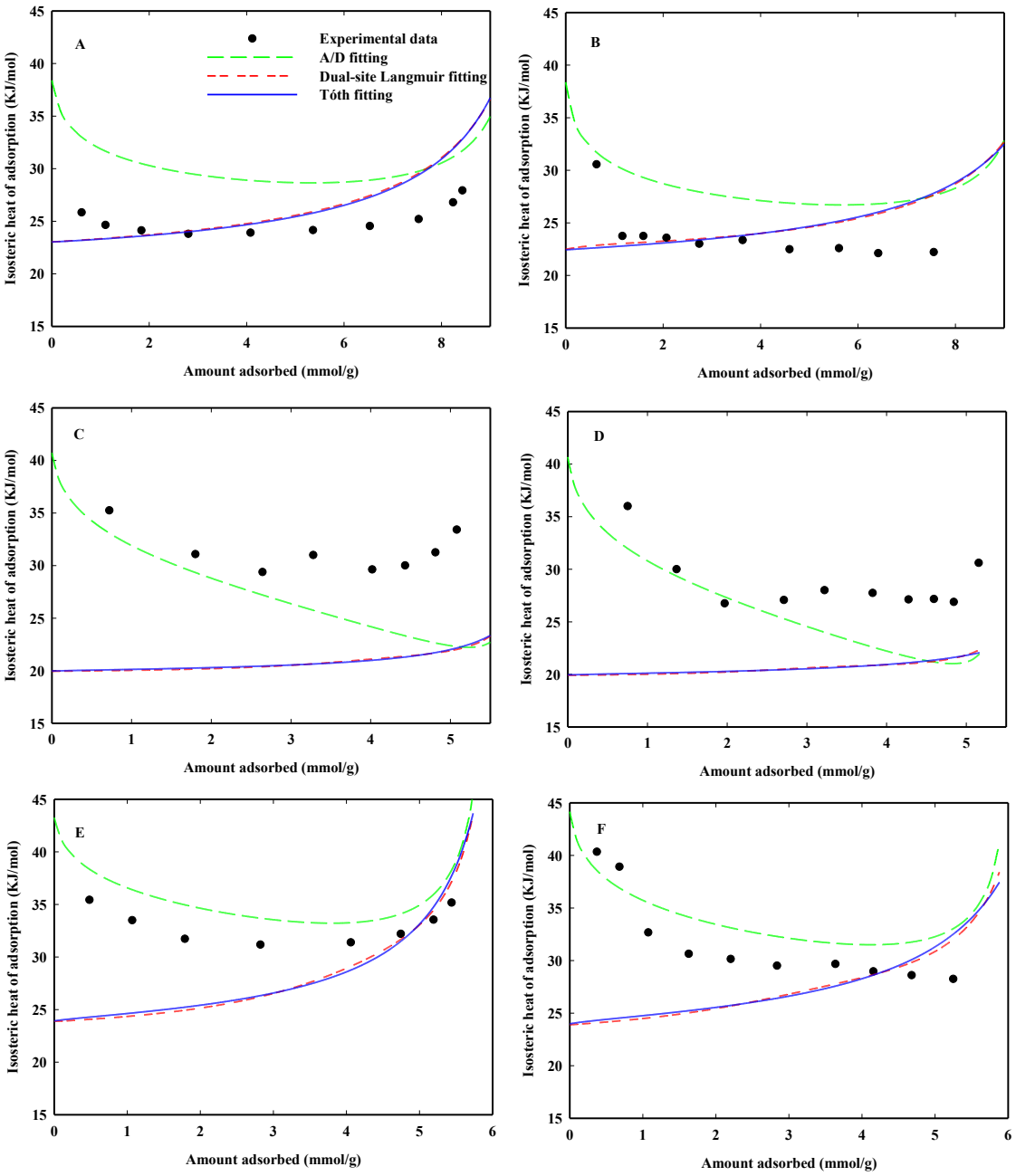


Figure 4.6.18 Isosteric heats of F-gas adsorption of BAC and Ecosorb, determined experimentally (black dots) at 323.15 K and calculated by applying the Clausius-Clapeyron equation to the APT (long-dashed green line), dual-site Langmuir (short-dashed red line), and Toth (solid blue line) models. A, R-32/BAC; B, R-32/Ecosorb; C, R-125/BAC; D, R-125/Ecosorb; E, R-134a/BAC; F, R-134a/Ecosorb.

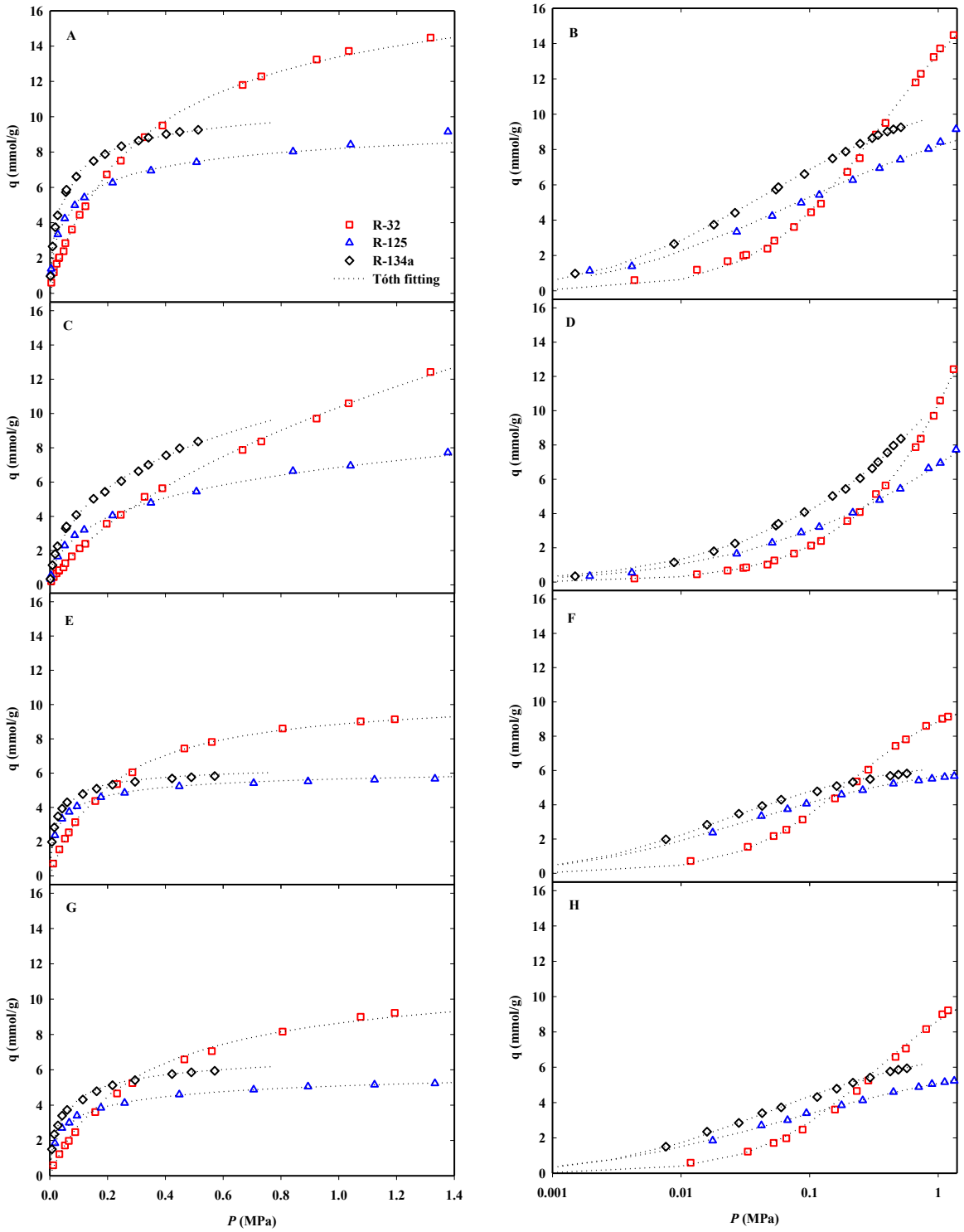


Figure 4.6.19 Isosteric heats of F-gas adsorption of BAC and Ecosorb, determined experimentally (black dots) at 323.15 K and calculated by applying the Clausius-Clapeyron equation to the APT (long-dashed green line), dual-site Langmuir (short-dashed red line), and Toth (solid blue line) models. A, R-32/BAC; B, R-32/Ecosorb; C, R-125/BAC; D, R-125/Ecosorb; E, R-134a/BAC; F, R-134a/Ecosorb.

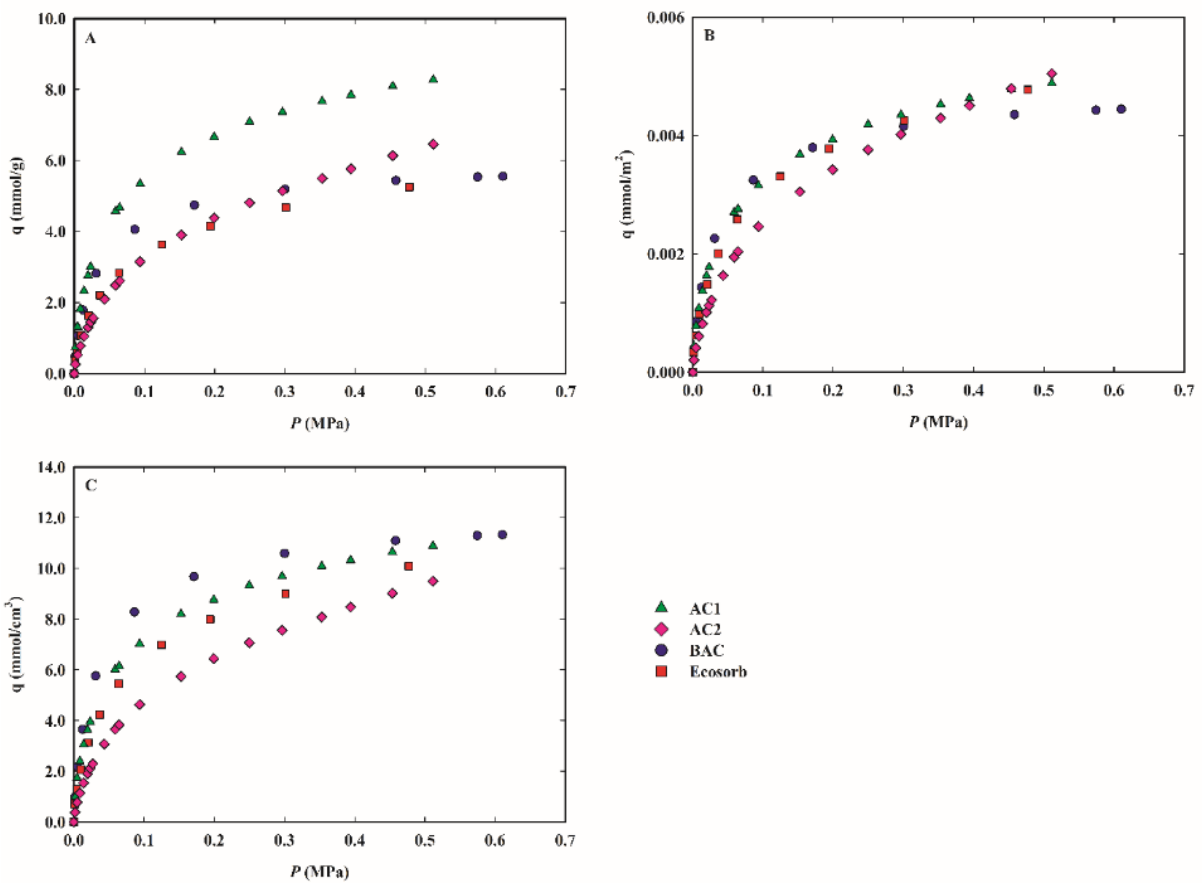


Figure 4.6.20 Comparison of experimental R-134a adsorption data on AC1 (green triangles), AC2 (pink diamonds), BAC (blue circles), and Ecosorb (red squares) carbons at 323.15 K. Data are compared per unit (A) weight (mmol/g), (B) surface area (mmol/m^2), and (C) pore volume (mmol/cm^3) of adsorbent.

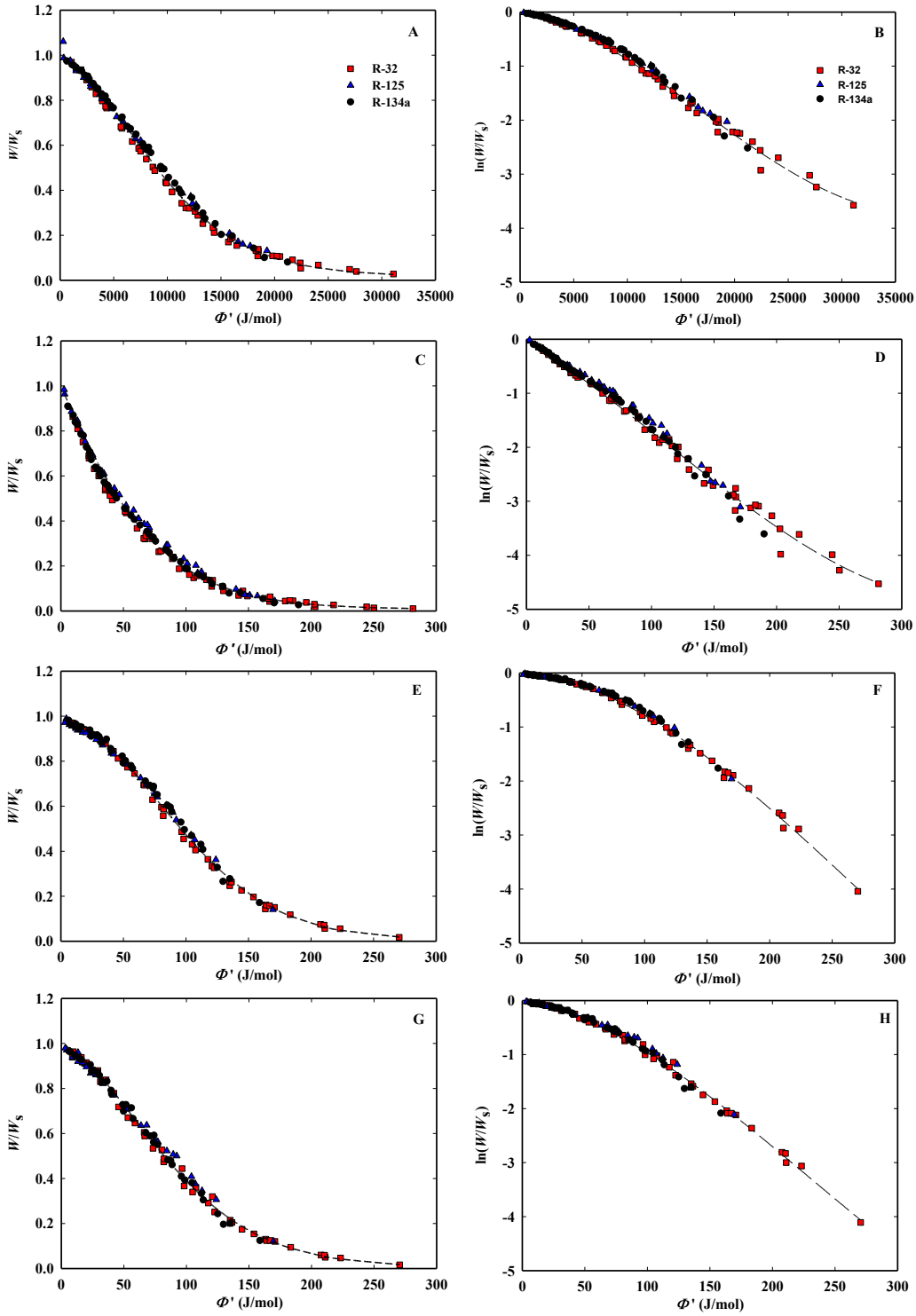


Figure 4.6.21 Characteristic curves obtained by superimposing the experimental adsorption data of R-32, R-125, and R-134a at 283.15 K, 303.15 K and 323.15 K on AC1 (A, B), AC2 (C, D), BAC (E, F), and Ecosorb (G, H) into a single temperature-independent curve. The characteristic curves were fitted to eqn. 23 (represented as dashed lines). The right-hand-side plots use a logarithmic scale of fractional volume filling.

4.6.2.3 Prediction of mixed-Gas Adsorption using the Ideal Adsorption Solution Theory

Near azeotropic mixtures of F-gases, such as the commercial refrigerants R-410A and R-407F, are not easily separated into their individual components by distillation. The selectivity of an adsorbent towards one component from a gas mixture is critical to develop highly efficient adsorbent-based gas separation processes.

From the fittings of the Tóth model to the single-component adsorption equilibrium data of the three F-gases, the Ideal Adsorption Solution theory (IAST) [89] was used to predict the multicomponent adsorption equilibrium of R-410A (R-32/R-125, 50/50 wt %) and R-410F (R-32/R-125/R-134a, 30/30/40 wt %), and also the mole-fraction composition of their adsorbed phases. It should be noted that a similar procedure based on the fittings of the dual-site Langmuir or APT models could very well have been adopted the choice of Tóth's model was a simple matter of convenience and the IAST mathematical model is described in Section 4.5.

The adsorption equilibria of R-410A and R-407F in the four ACs at 303.15 K were simulated for a pressure range between 0.01 and 0.8 MPa. The equilibrium mole fractions of the gas phase (y) correspond to the bulk compositions of the two commercial F-gases ($y_{\text{R-32}}^{(0)} = 0.7$ and $y_{\text{R-125}}^{(0)} = 0.3$ for R-410A, and $y_{\text{R-32}}^{(0)} = 0.47$, $y_{\text{R-125}}^{(0)} = 0.21$, and $y_{\text{R-134a}}^{(0)} = 0.32$ for R-407F). The results are plotted in Figure 4.6.22, the highest R-410A adsorption capacities were obtained for AC1 while the lowest adsorption capacities at the highest pressures were obtained for BAC and Ecosorb.

Simulations at four different total pressures (0.05, 0.1, 0.3, and 0.5 MPa) and varying the gas-phase equilibrium molar fractions were also performed for R-410A. The IAST predictions of the amounts of R-410A and its two components (R-32, R-125) adsorbed on the four ACs were performed as a function of $y_{\text{R-32}}$ (Figure 4.6.23–4.6.26). As expected, the R-125 amount adsorbed decreases while the R-32 amount adsorbed increases when $y_{\text{R-32}}$ is increased. Moreover, the equilibrium mole fraction of R-32 at which equal amounts of the two gases are adsorbed is always higher than 0.5 for all ACs, decreasing when the total pressure increases. This behavior indicates that the four ACs are more selective for R-125 than for R-32 and that this selectivity decreases with increasing pressure.

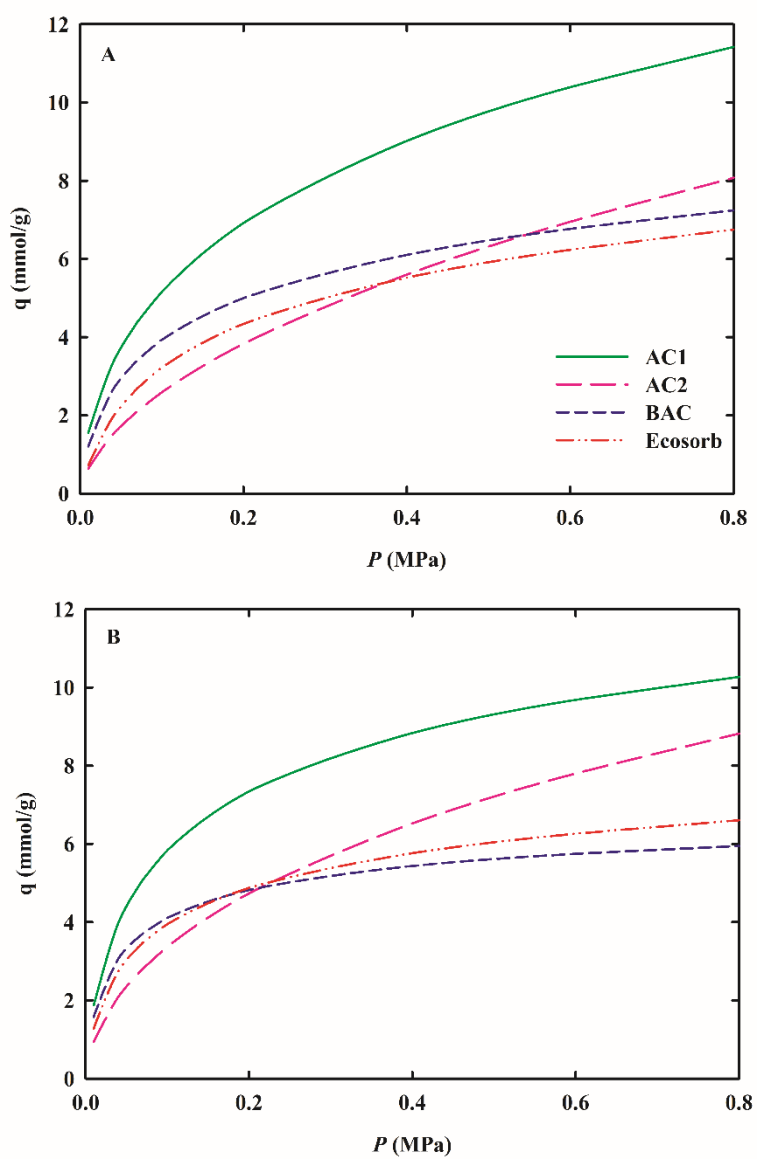


Figure 4.6.22 IAST prediction of the adsorbed amounts of (A) R-410A and (B) R-407F as function of pressure at the equilibrium gas-phase mole fractions corresponding to the bulk composition of R-410A ($y_{\text{R-32}} = 0.7$ and $y_{\text{R-125}} = 0.3$) and R-407F ($y_{\text{R-32}} = 0.47$, $y_{\text{R-125}} = 0.21$, and $y_{\text{R-134a}} = 0.32$) and 303.15 K.

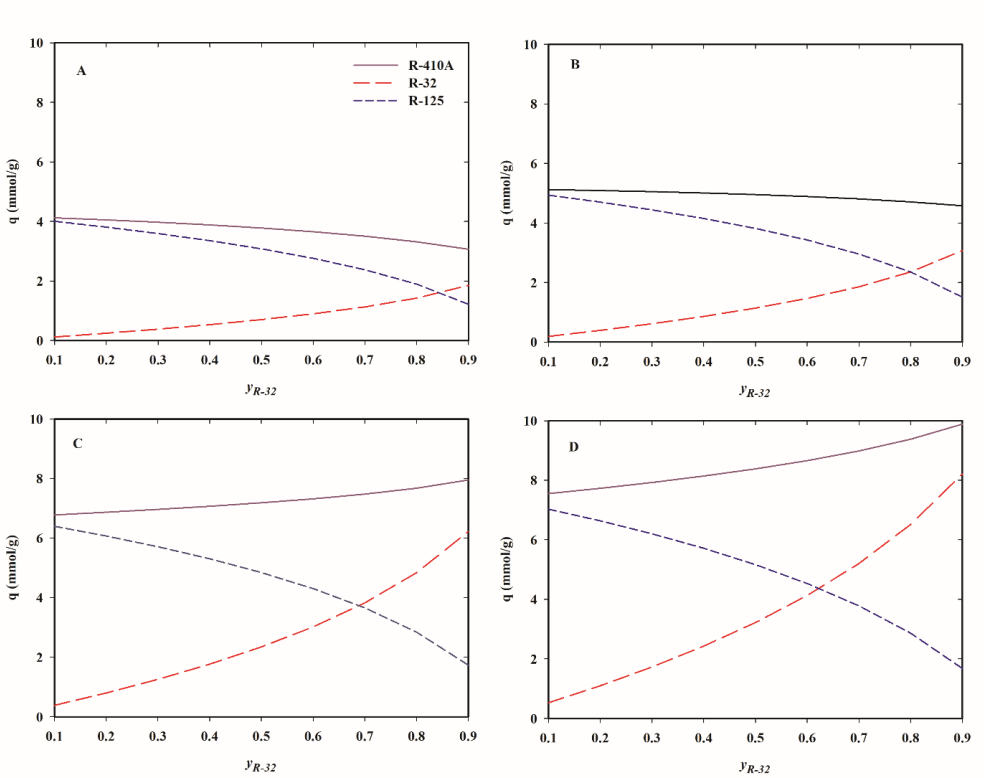


Figure 4.6.23 IAST prediction of the adsorbed amounts of (A) R-410A and (B) R-407F as function of pressure at the equilibrium gas-phase mole fractions corresponding to the bulk composition of R-410A ($y_{\text{R-32}} = 0.7$ and $y_{\text{R-125}} = 0.3$) and R-407F ($y_{\text{R-32}} = 0.47$, $y_{\text{R-125}} = 0.21$, and $y_{\text{R-134a}} = 0.32$) and 303.15 K.

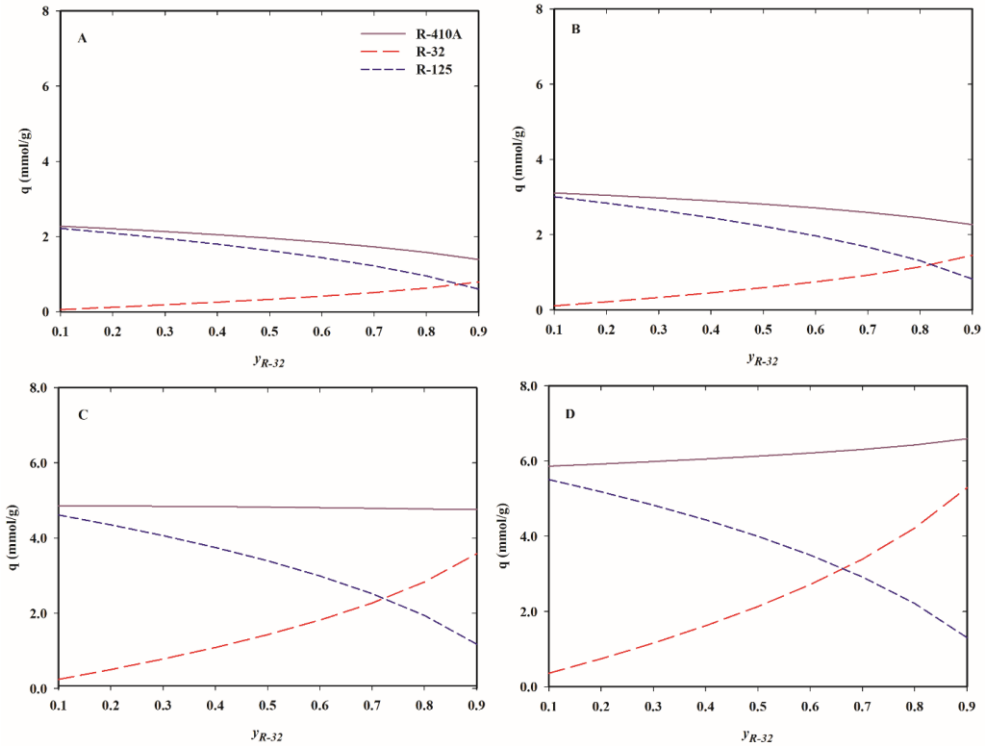


Figure 4.6.24 IAST prediction of the adsorbed amount of R-410A (purple circles), and of each of its components, R-32 (red squares) and R-125 (blue circles), on AC2 as a function of $y_{\text{R-32}}$, at 303.15 K and 0.05 MPa (A), 0.1 MPa (B), 0.3 MPa (C), and 0.5 MPa (D).

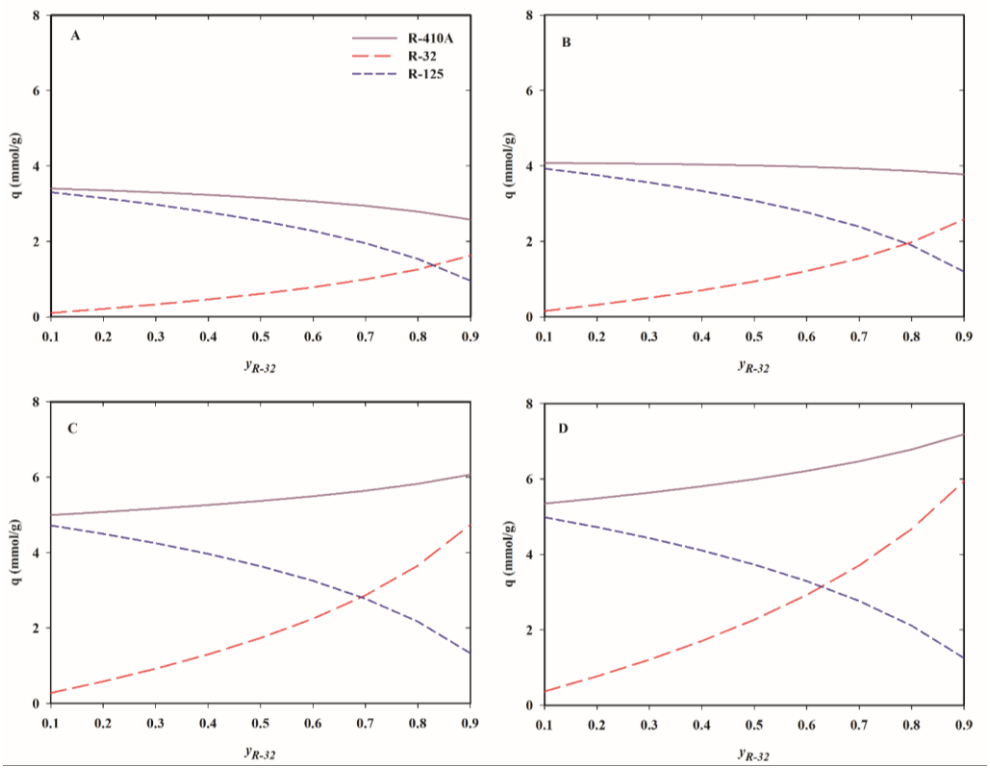


Figure 4.6.25 IAST prediction of the adsorbed amount of R-410A (purple circles), and of each of its components, R-32 (red squares) and R-125 (blue circles), on BAC as a function of $y_{R\text{-}32}$, at 303.15 K and 0.05 MPa (A), 0.1 MPa (B), 0.3 MPa (C), and 0.5 MPa (D).

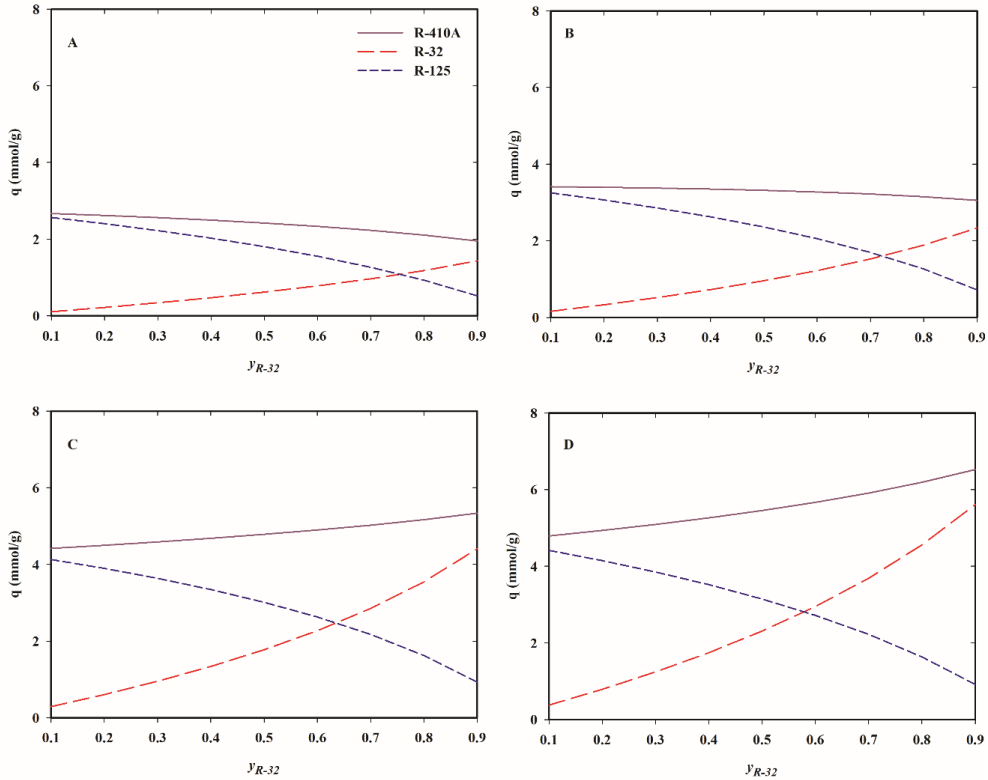


Figure 4.6.26 IAST prediction of the adsorbed amount of R-410A (purple circles), and of each of its components, R-32 (red squares) and R-125 (blue circles), on Ecosorb as a function of $y_{R\text{-}32}$, at 303.15 K and 0.05 MPa (A), 0.1 MPa (B), 0.3 MPa (C), and 0.5 MPa (D).

4.6.2.4 Selectivity of the ACs for F-gases in Binary and Ternary Mixtures

If the amount of free, unabsorbed gas in the pore volume of the adsorbent is negligible compared to the amount adsorbed, which is the case for the solid-fluid systems under consideration, the selectivity, S_{ij}, of the solid for gas *i* over gas *j*, is described by the mathematical model provided in Section 4.

Using the IAST results, the selectivity, S_{12}, of each carbon for R-125 ($i = 1$) over R-32 ($i = 2$) of the commercial refrigerant R-410A was determined. Therefore, if $S_{12} > 1$, R-125 is preferentially adsorbed, but if $S_{12} < 1$, R-32 is preferentially adsorbed. In Figure 4.6.27 S_{12} is plotted as a function of $y_{\text{R-32}}$ for each activated carbon at 303.15 K. All ACs are more selective to R-125 than to R-32 at all tested pressures, and S_{12} increases at lower pressures. Moreover, at a given fixed pressure, S_{12} increases with increasing $y_{\text{R-32}}$ for all carbons. The value of S_{12} was also determined as a function of pressure for the equilibrium gas-phase composition corresponding to that of bulk R-410A (Figure 4.6.28). The results reinforce the observation that all ACs are selective to R-125, with the noncommercial ACs, AC1 and AC2, presenting the best selectivities. Although all ACs were selective to R-125 at all tested pressures, the highest S_{12} values were obtained at the lowest pressures.

In the case of the R-407F ternary mixture, the selectivities to R-134a ($i = 3$) over R-125 ($j = 1$) and R-32 ($j = 2$), S_{31} and S_{32}, and to R-125 over R-32, S_{12}, were determined as a function of pressure at 303.15 K for the equilibrium gas-phase composition of the bulk R-407F (Figure 4.6.29). All ACs are more selective to R-125 or R-134a than to R-32 and more selective to R-134a than to R-125. The highest selectivities were obtained for BAC (S_{12} and S_{32}) and Ecosorb (S_{31}). In general, all ACs are more selective to R-134a and R-125 than to R-32 and their selectivity is favored at lower pressures.

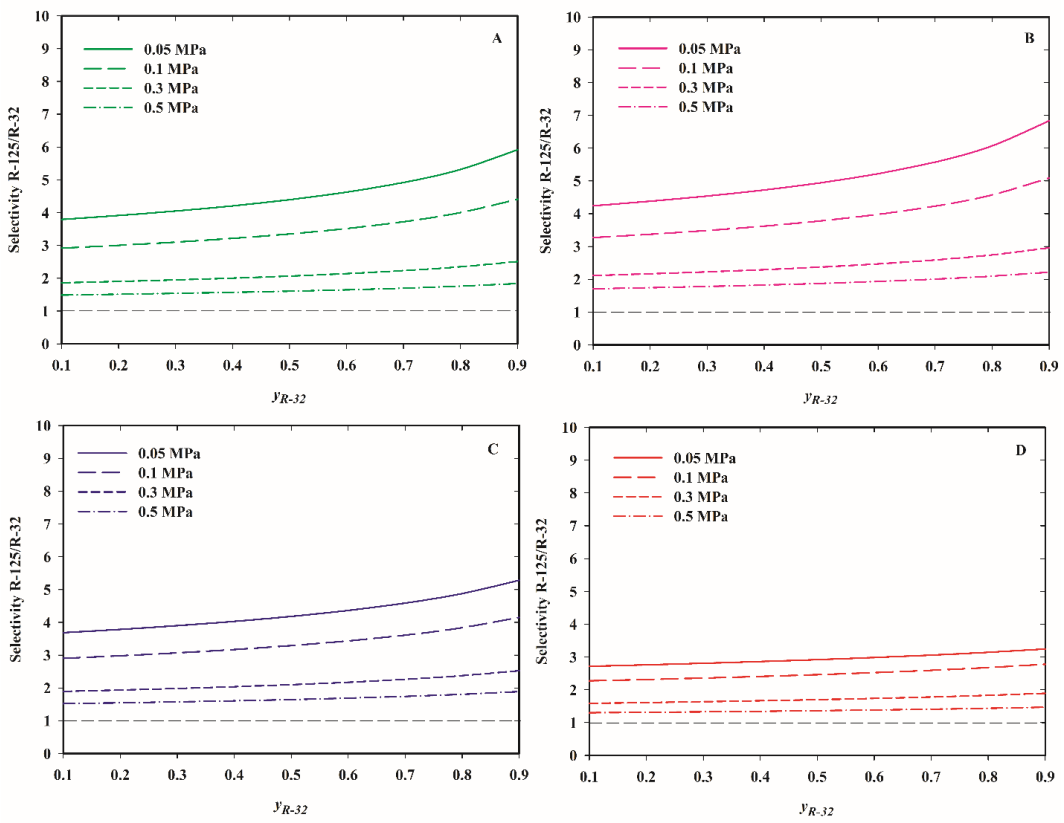


Figure 4.6.27 Selectivities to R-125 over R-32 for AC1 (A), AC2 (B), BAC (C), and Ecosorb (D) activated carbons, for the commercial R-410A gas mixture, as a function of $y_{R\text{-}32}$, at 0.05 MPa, 0.1 MPa, 0.3 MPa, and 0.5 MPa, and 303.15 K

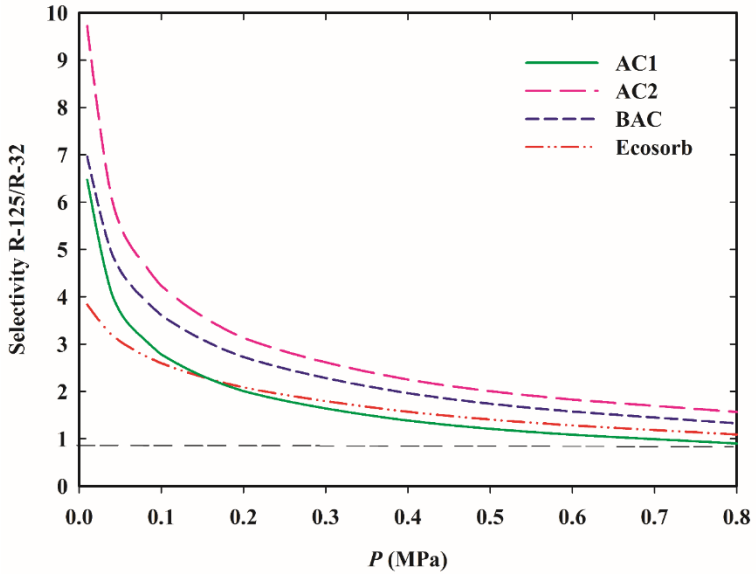


Figure 4.6.28 Selectivity of AC1 (green triangles), AC2 (pink diamonds), BAC (blue circles), and Ecosorb (red squares) to R-125 over R-32 as function of pressure at 303.15 K, for the equilibrium gas phase composition of bulk the R-410A mixture ($y_{R\text{-}32} = 0.7$ and $y_{R\text{-}125} = 0.3$).

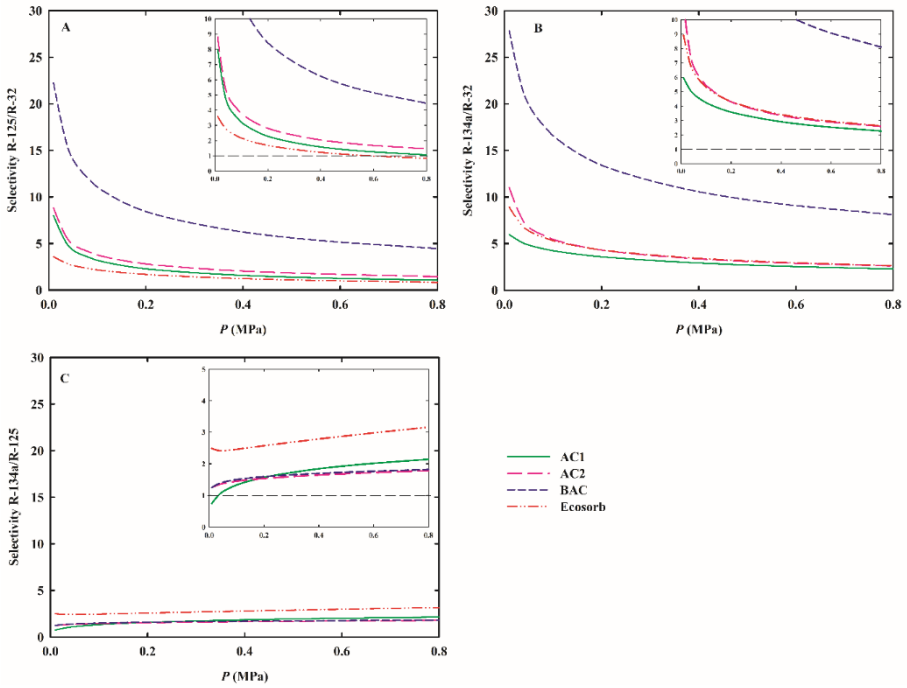


Figure 4.6.29 Selectivities to R-125 over R-32 (A), R-134a over R-32 (B), and R-134a over R-125 (C) for AC1 (green triangles), AC2 (pink diamonds), BAC (blue circles), and Ecosorb (red squares) carbons, for the commercial R-407F gas mixture ($y_{\text{R-32}} = 0.47$, $y_{\text{R-125}} = 0.21$, and $y_{\text{R-134a}} = 0.32$), as a function of pressure at 303.15 K. For a better visualization, the inset on each graph shows a zoomed-in view of the curves for the lowest values of the selectivity.

4.6.3 Conclusions

In the present work, the adsorption equilibrium of three of the most used F-gases in refrigeration was studied in four different types of activated carbon. The isosteric heats of adsorption were determined for each AC/F-gas. The adsorption data were successfully correlated with the Tóth, dual-site Langmuir, and APT models. The adsorption data of the three F-gases in each AC were successfully collapsed into a single temperature-independent characteristic curve. The experimental results show that the noncommercial activated carbons AC1 and AC2 have the highest adsorption capacities for the three pure F-gases studied at the highest pressures tested. Moreover, R-32 is the most adsorbed F-gas in all ACs.

Using the Ideal Adsorption Solution theory (IAST), the adsorption of two commercial gaseous refrigerant mixtures R-410A and R-407F was predicted at four different pressures and at different equilibrium gas compositions. The selectivity to each component of the mixtures was determined for the four activated carbons. All ACs are selective to R-125 in the R-410A commercial refrigerant, specially at low pressures, with one of the noncommercial ACs yielding the best selectivity. Additionally, all ACs are more selective to R-125 and R-134a than R-32 in the R407-F commercial refrigerant, with the commercial ACs presenting the best selectivities, specially at low pressures.

This work provides important insights into the fundamental understanding of the performance of different activated carbons for the capture and separation of F-gases from binary mixtures, such as the commercial refrigerant R-410A, and ternary mixtures, such as refrigerant R-407F. The use of

activated carbons with different porous characteristics allows the selective adsorption of different F-gases from different F-gas mixtures. This information is of vital importance to understand which properties control the adsorption capacity of these materials. With this knowledge, the best material can be selected for application in the design and scale-up of a given separation process.

4.7 Exploring the potential of biomass-derived carbons for the separation of fluorinated gases with high global warming potential

The development of advanced and innovative biomaterials with porous structural characteristics for the capture of fluorinated gases (F-gases) is important to contribute to the reduction of emissions of these gases with very high global warming potential. In this work, four biocarbons (CC-1:3H_3PO_4, CC-1:1H_3PO_4, CC-K_2CO_3 and CC-CO_2) were produced by chemical and physical activation of corn cob biomass (CC). The adsorption equilibria of difluoromethane (R-32), pentafluoroethane (R-125), 1,1,1-tetrafluoroethane (R-125), 1,1,2-tetrafluoroethane (R-134a), sulphur hexafluoride (SF_6), and nitrogen (N_2) on these biocarbons were determined at 303.15 K. The highest adsorption capacities were obtained for CC-K_2CO_3 and CC-CO_2 and a full characterization was also performed for these biomaterials at 283.15 and 323.15 K. On the other hand, the selectivities of SF_6/N_2 and the commercial refrigerants R-410A, R-407C, and R-407F were estimated using the Ideal Adsorption Solution theory (IAST). The results obtained for SF_6/N_2 show that the biocarbon CC-K_2CO_3 stands out from the other materials. In addition, the CC-CO_2 shows a preference for R-32 over R-125 for the separation of the R-410A. Finally, CC-K_2CO_3 has a greater preference for R-134a over R-32 and R-125 in the R-407C and R-407F blends. Overall, these novel biocarbons improve the separation and purification of the F-gases under study, facilitating their application on a pilot scale.

4.7.1 Experimental section

4.7.1.1 Material

Difluoromethane, R-32 (wt % purity ≥ 99.9) and pentafluoroethane, R-125 (wt % purity ≥ 99.8) were supplied by Polo Zero (Lisbon, Portugal). 1,1,1,2-tetrafluoroethane, R-134a (wt % purity ≥ 99.8) and SF_6 (wt % purity ≥ 99.8) were supplied by Air Liquid (Lisbon, Portugal). The designation and chemical structure of these F-gases are shown in Table 1.1.1. Nitrogen (N_2) (wt % purity ≥ 99.9999) was supplied by Air Liquid (Lisbon, Portugal) and Helium (wt % purity ≥ 99.999) was supplied by Praxair (Lisbon, Portugal).

4.7.1.2 Synthesis of biomass-derived porous carbons

Porous biomaterials were prepared using CC residual biomass with 3 different activation agents: CO_2, K_2CO_3 and H_3PO_4. The preparation of the biocarbons was carried out following the methodology reported in previous works [46,47,58,90]. The CC was placed in a quartz reactor placed inside a furnace within a vertical configuration and the temperature inside the furnace was measured using a thermocouple connected to the programmable PID controller (RKC, REX-P96). In the physical activation with CO_2, the CC was heated up in the furnace up to 1073.15 K, at a heating rate of 5 K/min, under an N_2 flow of 150 cm^3/min. When the target temperature was achieved, the N_2 flow was switched to CO_2 flow (150 cm^3/min) and kept for one hour. Then, it was cooled down under N_2 flow, and the carbon material was collected. The chemical activation with H_3PO_4 consisted of wet impregnation of the biomass with the acid using two impregnation mass ratios biomass: H_3PO_4 of 1:1 and 1:3. After impregnation at 323.15 K for 5 h, samples were dried at 378.15 K and thermally treated in the furnace at 773.15 K for two hours (heating rate of 5 $K \cdot min^{-1}$) under an N_2 flow of 150 cm^3/min. Afterwards, the obtained carbons were thoroughly washed with deionized water until neutral pH and dried at 378.15 K. The chemical activation with K_2CO_3 consisted of the dry impregnation of the biomass and the salt in a mortar using the mass ratio biomass: K_2CO_3 of 1:1. The mixture was placed in the furnace and heated up to 1073.15 K, at a heating rate of 5 K/min, and kept for one hour at this temperature, under an N_2 flow of 150 cm^3/min. After cooling, the obtained carbons were subsequently washed with deionized water until neutral pH and dried at 378.15 K.

4.7.2 Results and discussion

4.7.2.1 Materials characterisation

The methodology for the equipment used in the characterization of the materials is described in Section 4.2, While Table 4.7.1 presents the textural information of the 4 biomaterials used for F-gas adsorption, taking into account the distribution of micropores (≤ 20 Å), mesopores (between 20-500 Å) and macropores (≥ 500 Å) defined by IUPAC [84,91]. CC-1:3H_3PO_4 has a BET surface area of 1060 m^2/g and a micro/mesoporosity in the range of 7 to 60 Å (see Figure 4.7.1). The standard N_2 adsorption isotherm (77 K) for this biomaterial is characteristic of micro/mesoporous materials. In addition, CC-1:1H_3PO_4 presents a specific BET surface area of 1073 m^2/g and a micro/mesoporosity in the range of 5 to 45 Å (see Figure 4.7.1). Its N_2 adsorption isotherm is characteristic of materials with wider micropores and narrower mesopores (≤ 25 Å, see Figure 4.7.1). CC-K_2CO_3 has a BET surface area of 1286 m^2/g, a microporosity in the range of 5 to 15 Å (see Figure 4.7.1), characteristic of microporous materials with mainly narrow micropores of width < 10 Å (see Figure 4.7.1) [84,91]. Finally, CC-CO_2 has a BET

surface area of 820 m²/g and a microporosity in the range of 6 to 20 Å (see Figure 4.7.1) and its respective N_2 isotherm (see Figure 4.7.1) is characteristic of materials with narrow micropores [84,91].

Table 4.7.1 Textural parameters of biomaterials studied in this work.

Carbon sample	Parameter				
	S_{BET} (m²/g)	v_{total} (cm^3g^{-1})	v_{micro}(cm^3g^{-1})	v_{meso}(cm^3g^{-1})	**Ref**
CC-1:3H_3PO_4	1060	1.10	0.15	0.96	This work
CC-1:1H_3PO_4	1073	0.59	0.34	0.25	This work
CC-K_2CO_3	1286	0.51	0.46	0.05	This work
CC-CO_2	820	0.38	0.31	0.07	[40, 53]

The results demonstrated that the chemical treatment of the biomaterials CC-1:1H_3PO_4 and CC-1:3H_3PO_4 have an important influence on the textural properties. Although both carbons have similar BET surface areas (1073 and 1060 m2/g), the pores size distribution is quite different since CC-1:1H_3PO_4 presented a higher micropore volume and smaller micropores while CC-1:3H_3PO_4 presented higher mesopore volume and larger micropores [47] (see Table 4.7.1 and Figure 4.7.1). CC-K_2CO_3 is the carbon with the highest surface area and CC-CO_2 presented the smallest one. Nevertheless, both carbons have similar micropore volumes although CC-K_2CO_3 also presented mesoporosity. This carbon presented the smallest micropore size distribution, see Figure 4.7.1.

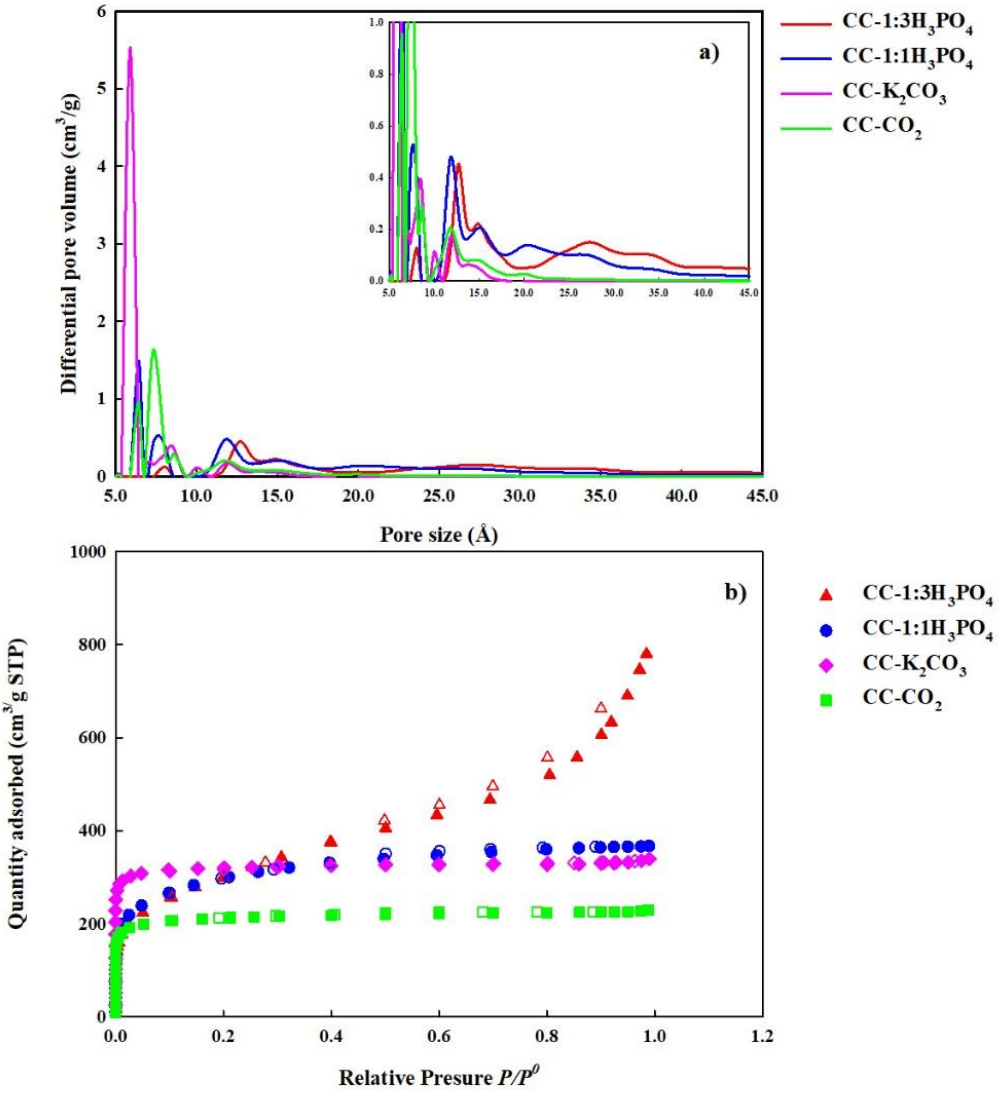


Figure 4.7.1 Pore size distribution of the biomaterials studied in this work: a) CC-1:3H_3PO_4 (red line), CC-1:1H_3PO_4 (blue line), CC-K_2CO_3 (pink line) and CC-CO_2 (green line); b) nitrogen adsorption (full symbols) and desorption (empty symbols) equilibrium isotherms at 77 K for CC-1:3H_3PO_4 (red up triangles), CC-1:1H_3PO_4 (blue circles), CC-K_2CO_3 (pink diamond) and CC-CO_2 (green square).

XPS spectroscopy was used to determine the elemental composition of the sample surface. The results obtained on the four biomaterials are given in Tables 4.7.2-4.7.3 and the corresponding spectra for the main regions are shown in Figure 4.7.2-4.7.4.

Table 4.7.2 Atomic concentrations (%) of relevant elements in carbon samples.

Carbon sample	C	O	P	N	Si	S	Cl	K	C/O
CC-1:3H_3PO_4	80.7	14.07	2.99	1.33	0.7	0.2	0	0	5.74
CC-1:1H_3PO_4	79.85	14.57	3.08	1.19	1.3	0	0	0	5.48
CC-K_2CO_3	89.44	9.88	-	0.45	-	0.22	0	0	9.05
CC-CO_2	91.0	5.64	0.53	0.98	0.37	0	0.25	1.23	16.1

The activation agent H_3PO_4 produces subtle changes in the oxygen present on the biomaterial surface. Table 4.7.3 demonstrates that the 1:3 ratio obtained 14.07% oxygen while the 1:1 ratio presented a value of 14.57%. In addition, the presence of phosphorus can be seen in these two samples due to their respective chemical treatments. However, the oxygen ratio in the other two activated biomaterials (with K_2CO_3 and CO_2 treatment) is lower (see Table 4.7.3.). Not surprisingly, the sample with the lower amount of oxygen functional groups is CC-CO_2. It is important to note that a lower carbon/oxygen ratio corresponds to a higher oxygen content on the material surface. Sample CC-K_2CO_3 does not seem to have Si, probably due to the washing performed after the activation, reducing the mineral content.

The characteristic peak at the binding energy of C1S is present in all samples. The C1S peak corresponds to the C sp2, followed by a smaller contribution of oxidized carbon forms. These oxidized forms include alcohol/ether (–COH, –COC–, O C(O–C*)), carbonyl (–C=O), and carboxyl (COOH) functional groups. The calculated atomic concentration (%) of carbon % bonded to oxygen, concerning the total percentage of carbon on the surface, also revealed that the samples activated with phosphoric acid have a higher relative amount of oxygen. CC-1:1H_3PO_4 and CC-1:3H_3PO_4 have 3.71 and 3.64 % respectively and CC-K_2CO_3 and CC-CO_2 3.2 and 2.2%.

Furthermore, CC-CO_2 is only biomaterial with an ester component. A relevant result is the identification of the presence of P in the samples CC-1:1 H_3PO_4 and CC-1:3 H_3PO_4. The XPS P2p peak could be fitted to account for 3 components, revealing three discernible peaks at 133.2 eV, 134.3 eV and 136 eV. These contributions within the P2p zone can be attributed to P groups such as C-PO_3 or C_2-PO_2 group directly bonded to a carbon site or C-O-PO_3H_2, incorporated in the carbon surface [92–94].

Table 4.7.3 Peak positions (eV), atomic concentrations (%) and assignments for the XPS detailed regions.

	CC-1:3H_3PO_4		**CC-1:1H_2PO_4**		**CC-K_2CO_3**		**CC-CO_2**		**Assignments**
	BE(eV)	**at. %**	**BE(eV)**	**at. %**	**BE(eV)**	**at. %**	**BE(eV)**	**at. %**	
C1S	-	-	-	-	-	-	283.5	7.7	
C1S	284.8	72.43	284.8	74.45	284.8	67.44	284.8	60.95	C-C/C=C/CHx Aromatic-Aliphatic
C1S	286.08	11.97	286.21	13.1	286.25	19.33	286.17	19.73	C-N / C-OH/C-O-C
C1S	287.56	6.7	288.00	6.7	288.7	9.86	-	-	Carbonyl C=O, Amide N-C=O
C1S	-	-	-	-	-	-	289.3	11.62	Ester O-C=O
C1S	289.98	8.91	290.36	5.74	290.75	3.37	-	-	Carbonate
O1S	531.08	19.86	531.0	21.46	531.49	25.62	531	43.44	C=O / O=C-O
O1S	532.94	68.29	533.12	71.48	533.05	68.06	532.42	45.54	Organic C-O
O1S	534.96	7.06	535.5	11.85	536.7	6.31	533.9	11.02	C-0-C
P2p	133.16	21.74	133.22	29.35	-	-	-	-	$(PO_4)_3$, $(P_2O_7)_4$
P2p	134.24	62.15	134.15	56.78	-	-	-	-	C-O-PO_3H_2 / H_3PO_3
P2p	136.94	16.11	136.8	13.87	-	-	-	-	

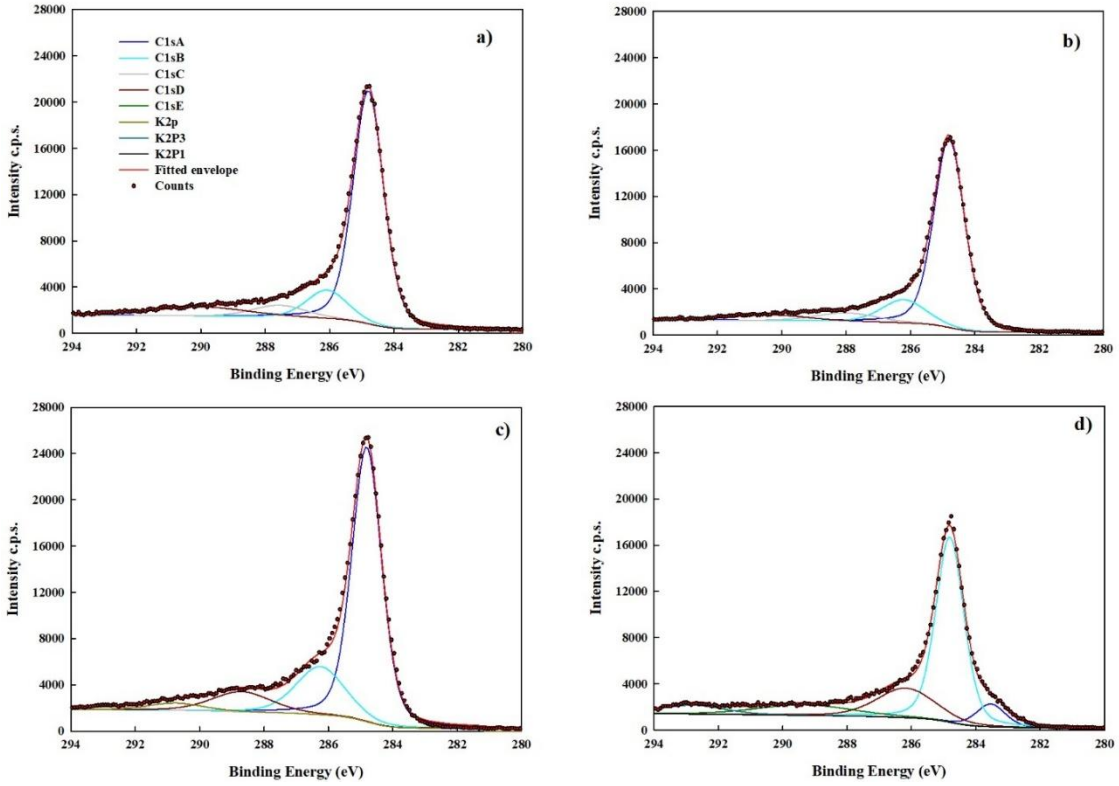


Figure 4.7.2 For the four biomaterials investigated in this work, XPS detailed regions C1s of: a) CC-1:3(H_3PO_4); b) CC-1:1(H_3PO_4); c) CC-K_2CO_3; d) CC-CO_2.

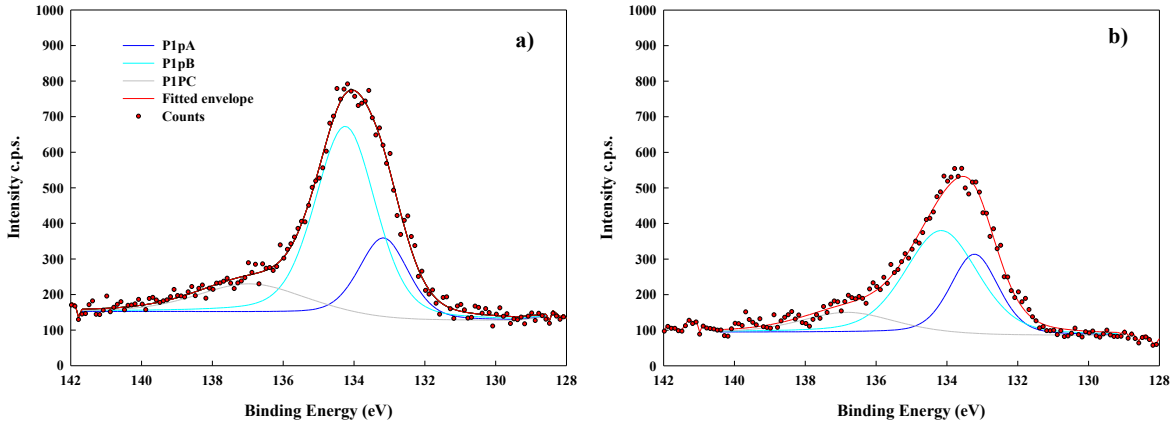


Figure 4.7.3 For the four biomaterials investigated in this work, XPS detailed regions P2p of: a) CC-1:3(H_3PO_4); and b) CC-1:1(H_3PO_4).

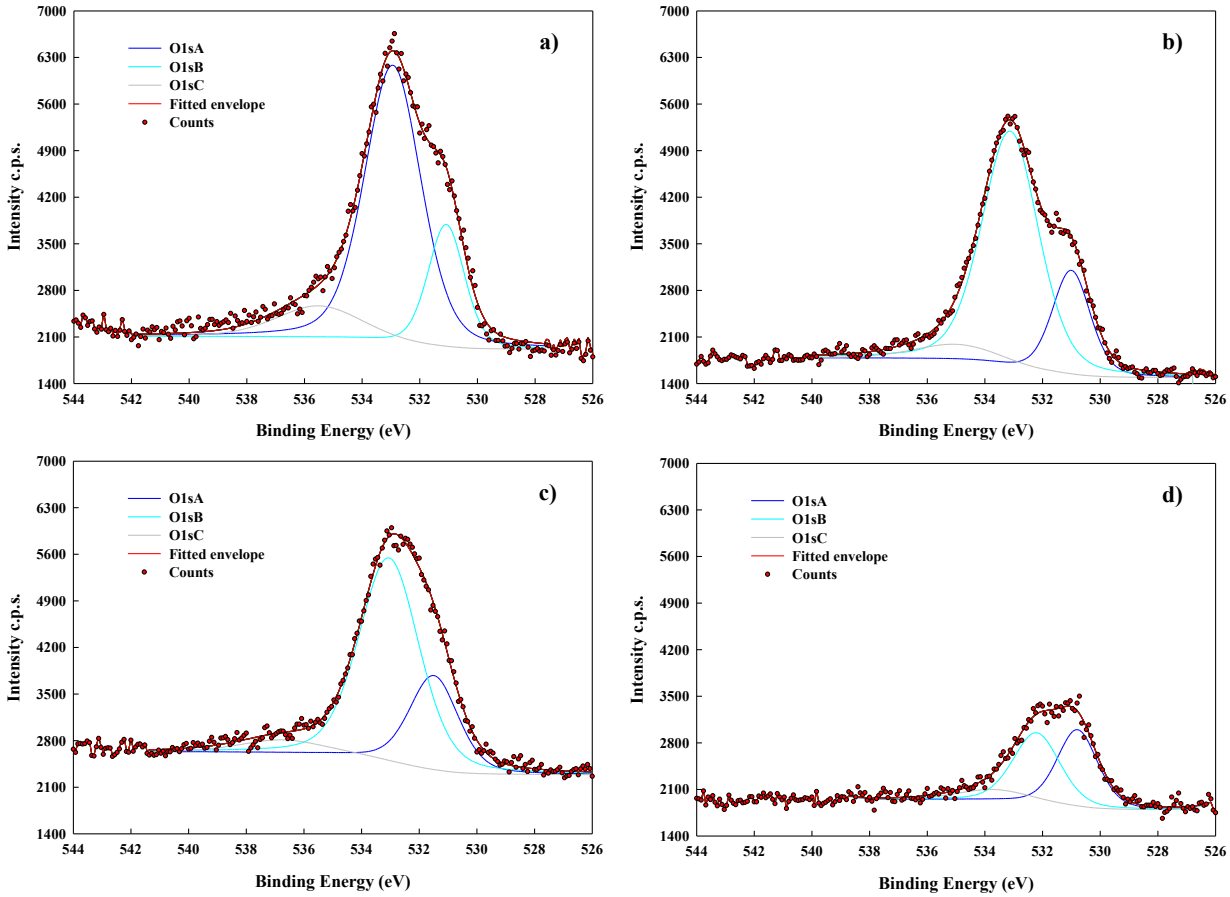


Figure 4.7.4 For the four biomaterials investigated in this work, XPS detailed regions O1s of: a) CC-1:3(H_3PO_4); b) CC-1:1(H_3PO_4); c) CC-K_2CO_3; and d) CC-CO_2.

The FTIR spectra of the activated carbons studied in this work are shown in Figure 4.7.5. The peak at 3444 cm^{-1} is typical of the H-O vibration of hydroxyl functional groups with hydrogen bonds, which originate at the frequency where O-H functional groups are present. Additionally, the peak at 2928 cm^{-1} is characteristic of the C-C vibrations of the alkyl groups. The peak in the band within the range of 1560-1627 cm^{-1} is attributed to the stretching vibrations of the C=C bonds of the alkene groups. The peak in the 1385 cm^{-1} band is assigned to the stretching of the C-C bonds of aromatic rings polarised by the oxygen atoms bound close to the C atoms. The bands between 1075-1180 cm^{-1} are assigned to the vibration of C-O stretches of esters [47,95].

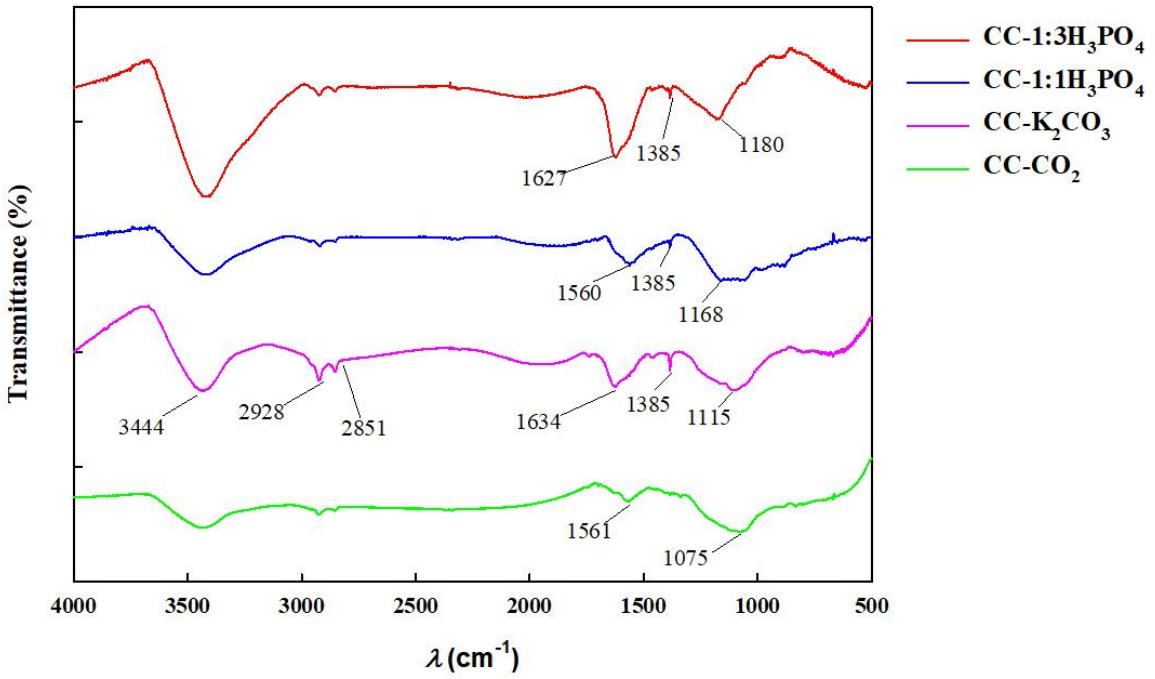


Figure 4.7.5 FTIR spectra for the biomaterials studied in this work: a) CC-1:3H_3PO_4 (red line); b) CC-1:1H_3PO_4 (blue line); c) CC-K_2CO_3 (pink line) and CC-CO_2 (green line).

The thermogravimetric analysis illustrated in Figure 4.7.6 displays the thermal stability of the biomaterials studied in this work. The activated carbons obtained by chemical activation are less stable than the carbon obtained by physical activation with CO_2. Figure 4.7.6 shows that CC-1:3H_3PO_4, CC-1:1H_3PO_4 and CC-K_2CO_3 have a mass loss of 5% at the temperature of 341.15 K. However, CC-CO_2 has a mass loss of 5% only at 484 K which corresponds to a residual mass loss. This initial mass loss until 380 K may be attributed to the water evaporation adsorbed in the carbon surface. The regeneration process of these biomaterials was carried out at 373.15 K because the percentage mass loss is less than 8% and is related to the evaporation of the amount of water adsorbed by the materials. If this temperature is exceeded, the structural characteristics of the materials and the functional groups that are present on the surface of the material can be affected. The weight loss is much more pronounced for the biomaterials with chemical treatment, suggesting that these materials have a more hydrophilic nature, probably related to the functional groups present in these materials. All biomaterials are reasonably stable up to approximately 800 K. From this temperature, an accentuated loss of mass was observed up to 1050 K, attributed to a possible decomposition of minerals in the solid matrix or the decomposition of functional groups on the surface of the materials.

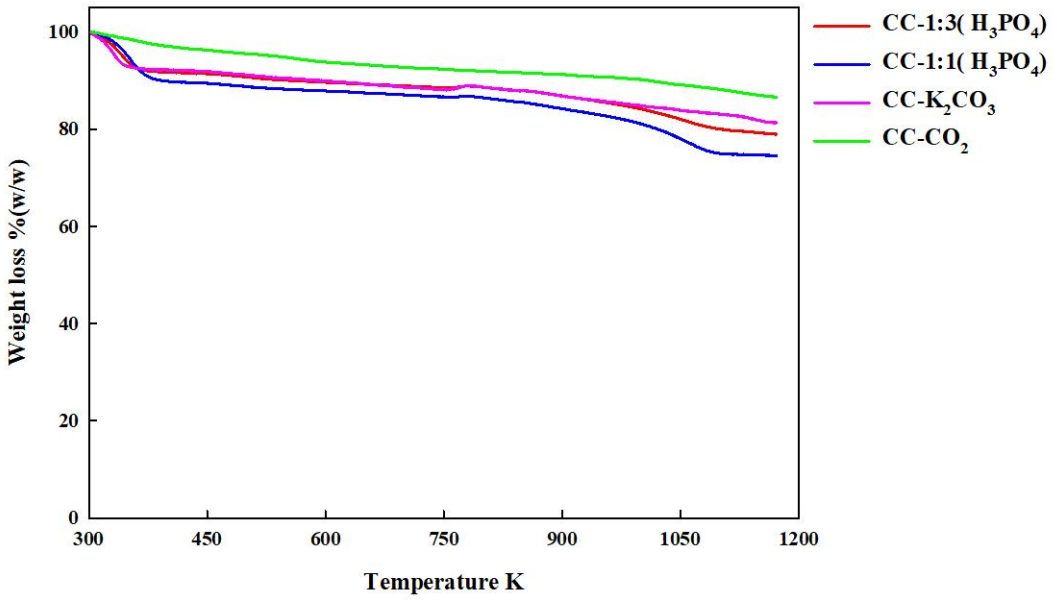


Figure 4.7.6 Thermogravimetric analysis (TGA) of the biomaterials studied in this work: a) CC-1:3H_3PO_4 (red line); b) CC-1:1H_3PO_4 (blue line); c) CC-K_2CO_3 (pink line) and CC-CO_2 (green line).

The results of the elemental analysis are given in Table 5. These biomaterials have a high carbon content, as expected for materials derived from biomass rich in carbohydrates, cellulose and hemicellulose. The biomaterial with the highest carbon content is CC-CO_2. This difference can be attributed to the type of activation and the reduction of oxygen groups on the material surface [46].

Table 4.7.4 Elemental analysis of the biomaterials studied in this work.

	CC-1:3H_3PO_4	**CC-1:1H_3PO_4**	**CC-K_2CO_3**	**CC-CO_2**
C (*wt.*%)	66.6	72.2	65.1	74.82
H (*wt.*%)	1.43	1.33	1.97	0.74
N (*wt.*%)	0.31	0.42	0.120	1.59
S (*wt.*%)	0	0	0	0
O[a] (*wt.*%)	31.7	26.05	32.8	22.85

[a] Calculated as follows: O = 100 – (C + H + N + S)

The SEM analysis (see Figure 4.7.7) was used to analyse the morphology of the samples. This analysis supports the results discussed in Table 4.7.1, confirming that the material CC-1:3H_3PO_4 has the highest mesoporosity. This biomaterial retains very little of its initial biomass due to the chemical activation with H_3PO_4. This process affects the material walls, resulting in an increment of the porosity. Then, micropores are formed, some collapse, and some walls become thinner. In addition, this biomaterial has a well-developed pore structure, indicating a high surface area. The results shown in Table 4.7.1 demonstrated that CC-1:1H_3PO_4 exhibits both micro and mesoporosity, as confirmed in Figure 4.7.7. The 1:1 ratio generates micro and mesoporosity although maintaining its morphology. However, the chemical activation with K_2CO_3 collapses the biomass structure, generating visible smaller porosity. This

behaviour is related to K_2CO_3 which has a more aggressive chemical effect on the biomass structure. Finally, the physical activation with CO_2 attacks the walls of the biomass, generating greater porosity and thinner structures, as verified in Figure 4.7.7. However, the porosity obtained using K_2CO_3 is greater than that obtained using CO_2.

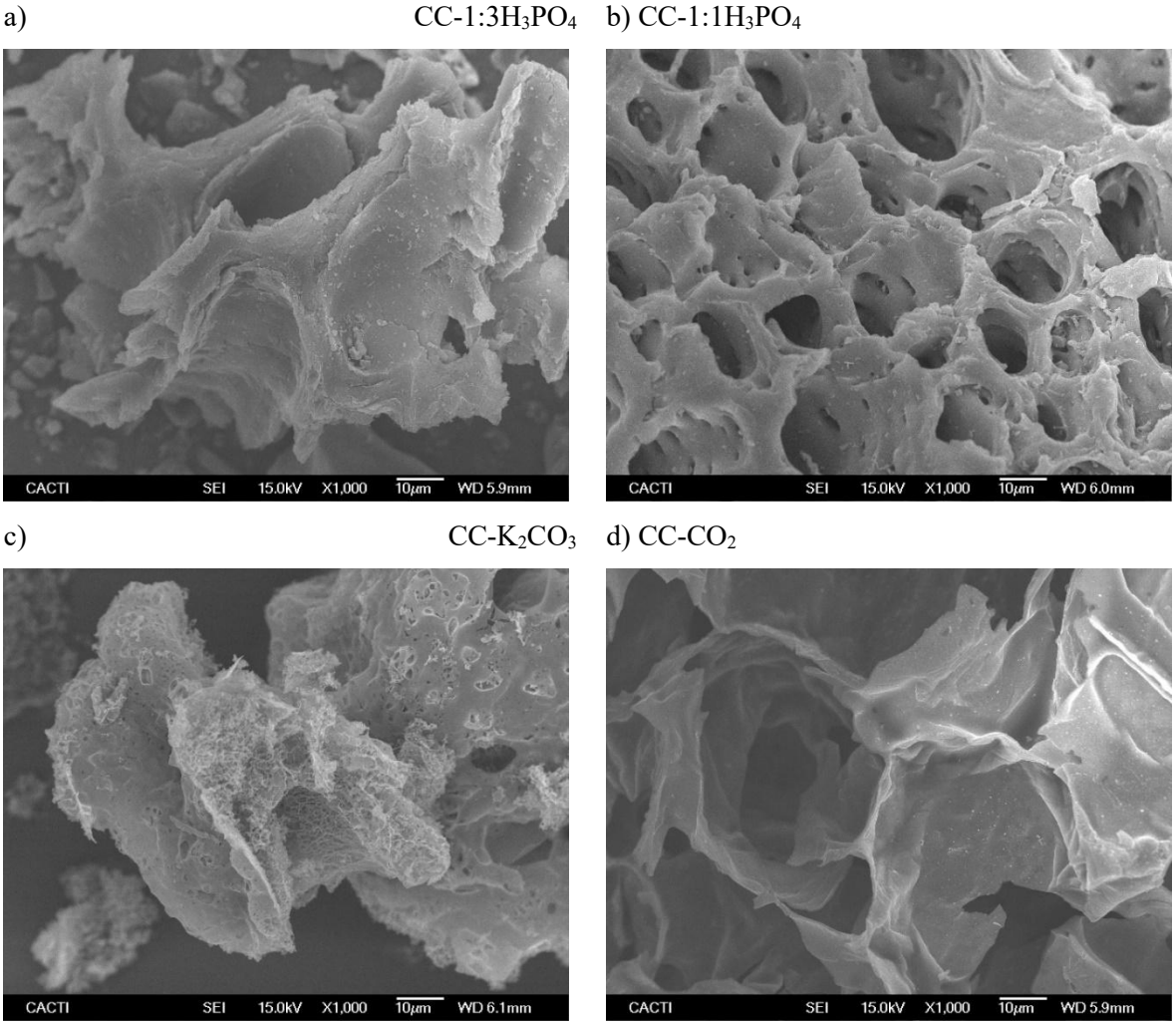


Figure 4.7.7 SEM images of the biomaterials studied in this work: a) CC-1:3H_3PO_4; b) CC-1:1H_3PO_4, c) CC-K_2CO_3; and d) CC-CO_2.

4.7.2.2 Adsorption equilibrium of R-32, R-125, R-134a, SF_6 and N_2

In this work, an initial screening at 303.15 K was performed between the 4 biomaterials (CC-1:3H_3PO_4, CC-1:1H_3PO_4, CC-K_2CO_3 and CC-CO_2) and the 5 gases studied in this work (R-32, R-125, R-134a, SF_6 and N_2) to determine which of the materials might be promising for the separation processes, with the methodology for determining the adsorption equilibrium described in Section 4.3. The total adsorbed amount, q, for all biocarbons, is shown in Figure 4.7.8 at 303.15 K. The DSL model successfully describes the adsorption equilibria on all biomaterials studied in this work. Taking into account the results obtained in the initial screening, CC-K_2CO_3 and CC-CO_2 were selected to perform a complete characterization at 283.15, 303.15 and 323.15 K (see results also in Figure 4.7.9-4.7.11). In addition, their structural characteristics have been considered since both materials are predominantly microporous. These micropores can help to favour the F-gases adsorption. The equilibria data were measured up to 80% below the saturation pressure of each gas to avoid condensation of the adsorbate. The adsorption is superimposable to the desorption, i.e. these systems do not have hysteresis. This adsorption is governed by the accessible volume of the micropore rather than by the surface area [84,91]. Besides, this type of equilibria is related to materials with wider micropore size distributions and narrower mesopores [84,91]. However, the adsorption equilibria for the F-gases on the biomaterial CC-1:3H_3PO_4 are characteristic of mesoporous materials with a significant amount of overlap of monolayer and the onset of multilayer adsorption. Finally, all biomaterials with N_2 have an almost linear isotherm, with low adsorption capacity because N_2 can be considered an inert gas in many separation processes.

As expected, all the biomaterials studied in this work have higher adsorption for F-gases than nitrogen. The adsorption capacities of F-gases have the following trend: R-32 > R-125 ≈ R-134a > SF_6 [96]. This order in the adsorption equilibria between F-gas and biomaterials can be related to the characteristics of the pores, and the physicochemical properties of the F-gas. Depending on the nature of the available adsorption sites, electrostatic or van der waals interactions may be favoured [97]. The adsorption isotherms studied in this work have different behaviour at pressures below 0.2 MPa and pressures above this value. The adsorption equilibria of R-125, R134a and SF_6 in the pressure range $P < 0.2$ MPa have the following behaviour: CC-K_2CO_3 > CC-1:1H_3PO_4 ≥ CC-1:3H_3PO_4 > CC-CO_2, see Fig. S6. The adsorption capacities for the F-gases (R-125, R-134a and SF_6) follow the same trend as the surface area of these biomaterials (see Figure 4.7.12) [98]. This behaviour is related to the high porosity (see Figure 4.7.7) and surface area developed through their chemical or physical treatment, which directly favours adsorption.

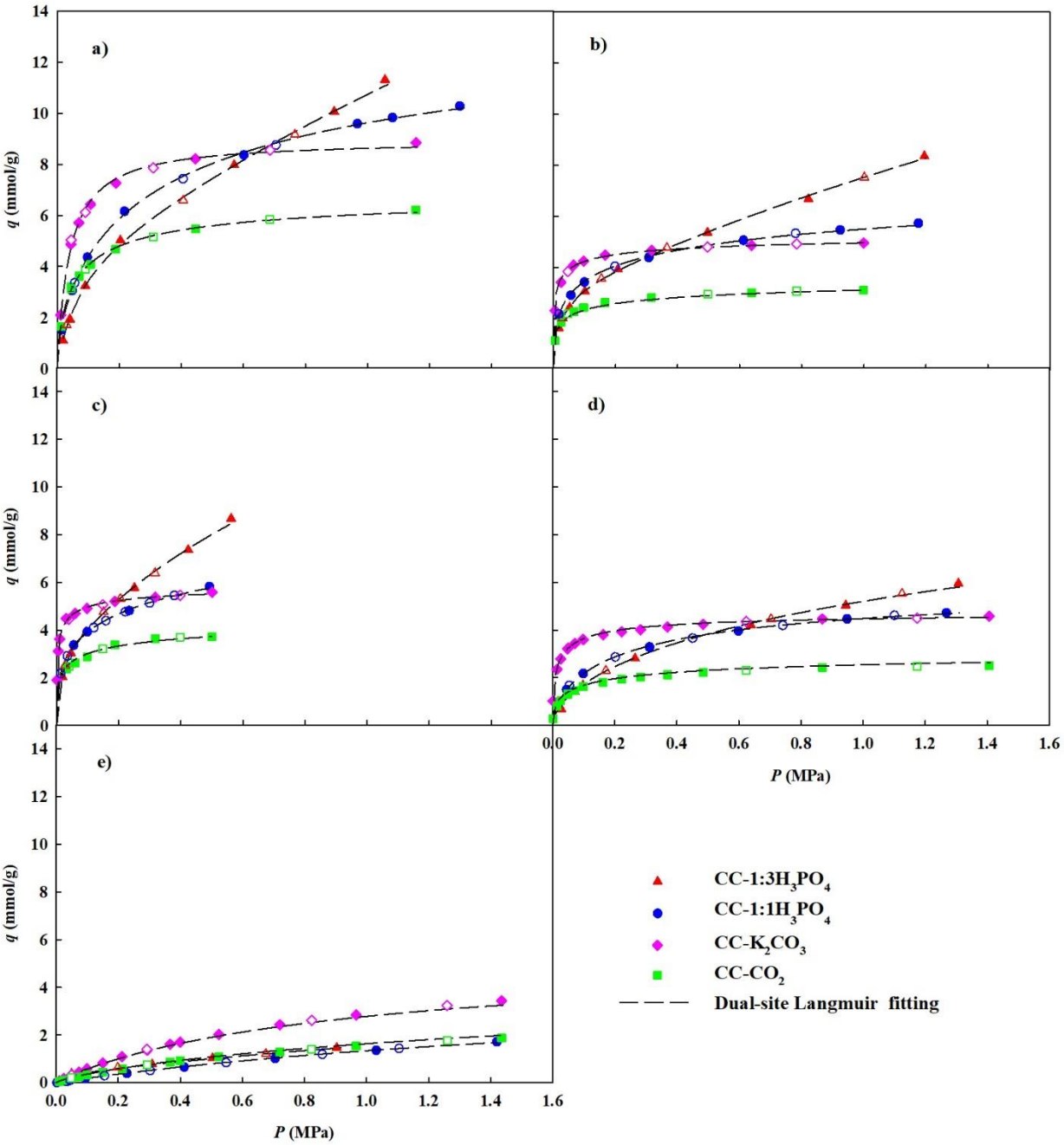


Figure 4.7.8 Adsorption (full symbols) and desorption (empty symbols) equilibrium isotherms: a) R-32; b) R-125; c) R-134a; d) SF_6; e) N_2 on CC-1:3H_3PO_4 (red up triangles), CC-1:1H_3PO_4 (blue circles), CC-K_2CO_3 (pink diamond) and CC-CO_2 (green square) at 303.15 K.

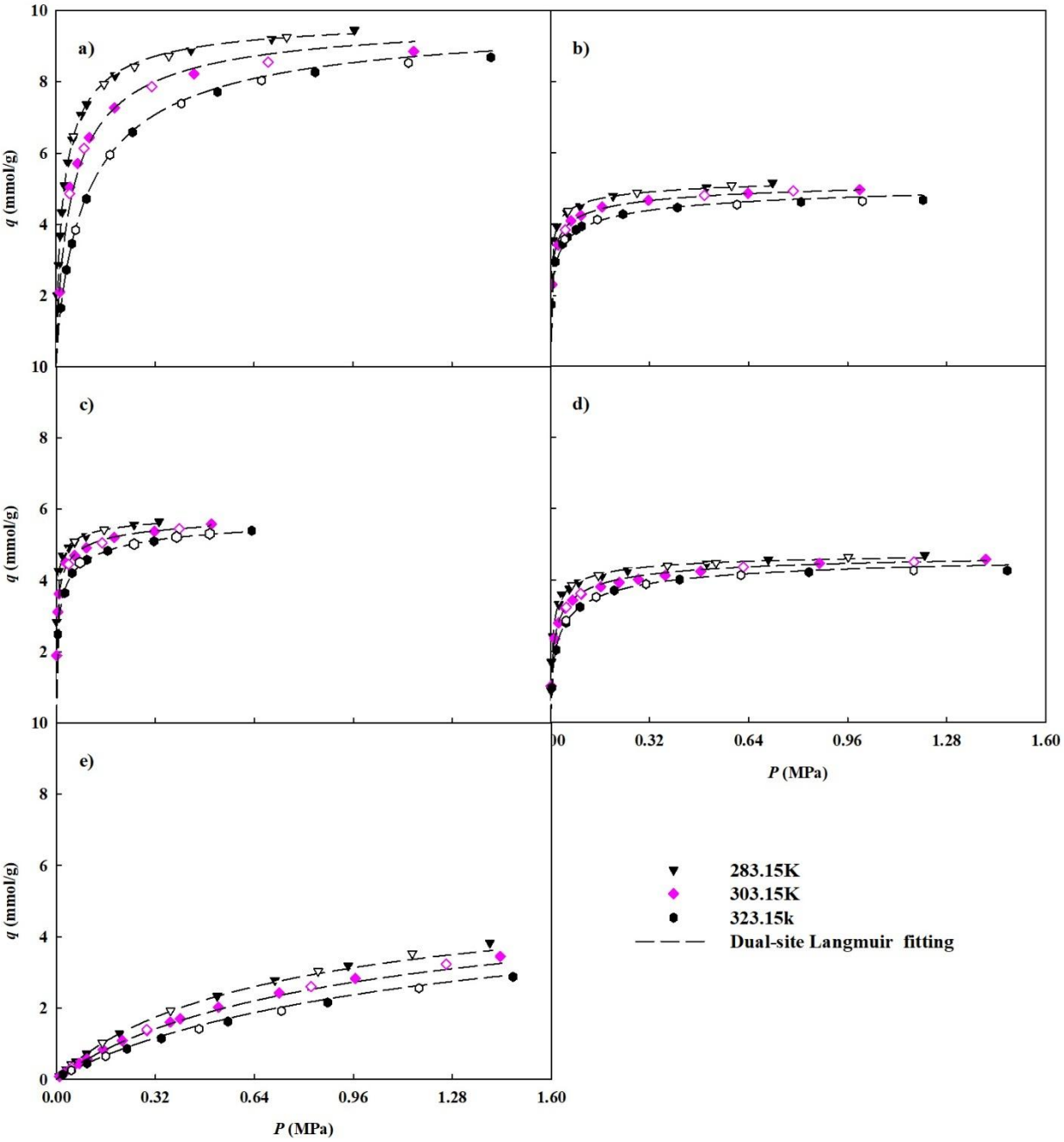


Figure 4.7.9 Adsorption (full symbols) and desorption (empty symbols) equilibrium isotherms of: a) R-32; b) R-125; c) R-134a; d) SF_6; and e) N_2 on CC-K_2CO_3.

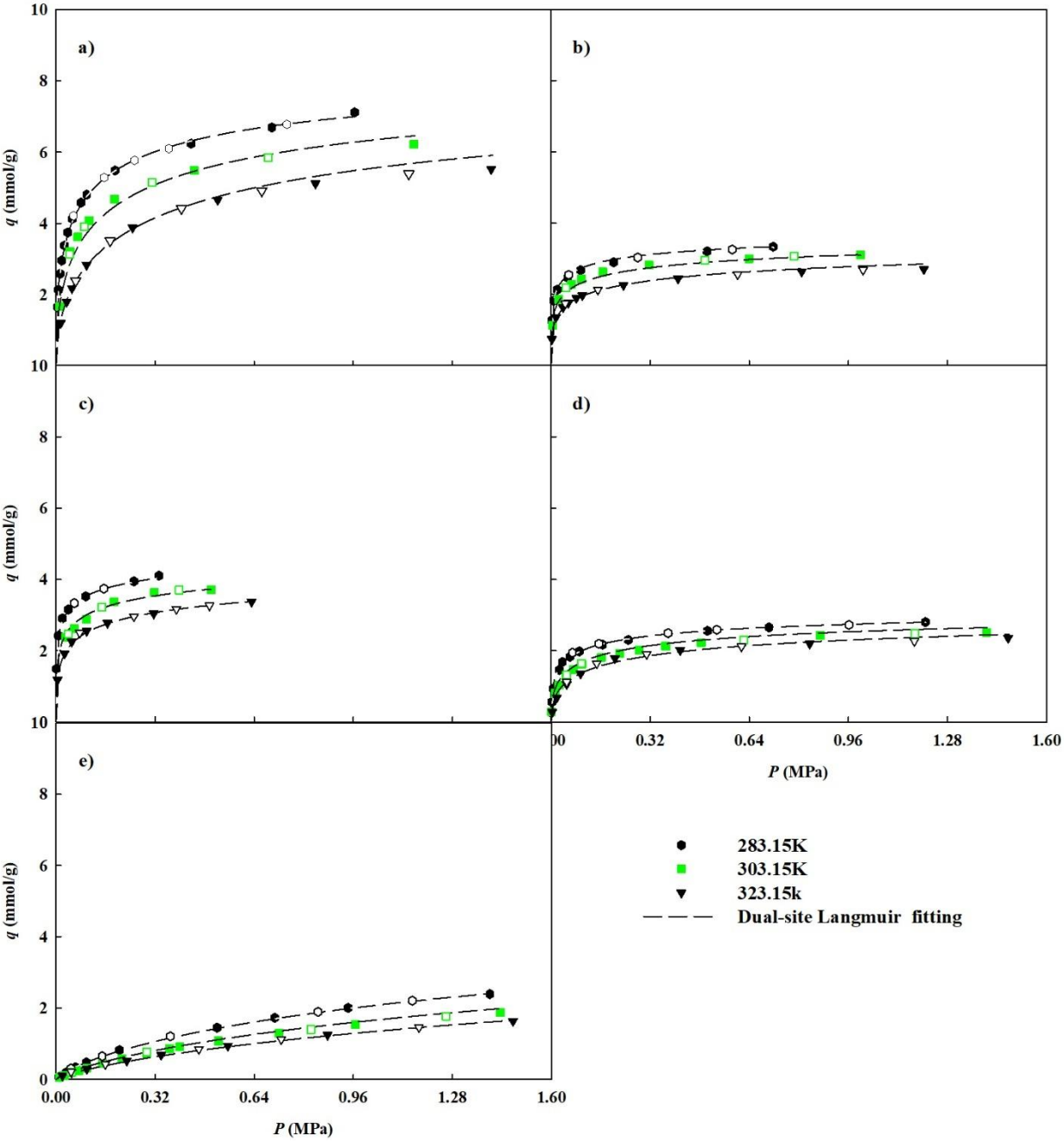


Figure 4.7.10 Adsorption (full symbols) and desorption (empty symbols) equilibrium isotherms of: a) R-32; b) R-125; c) R-134a; d) SF_6; and e) N_2 on CC-CO_2.

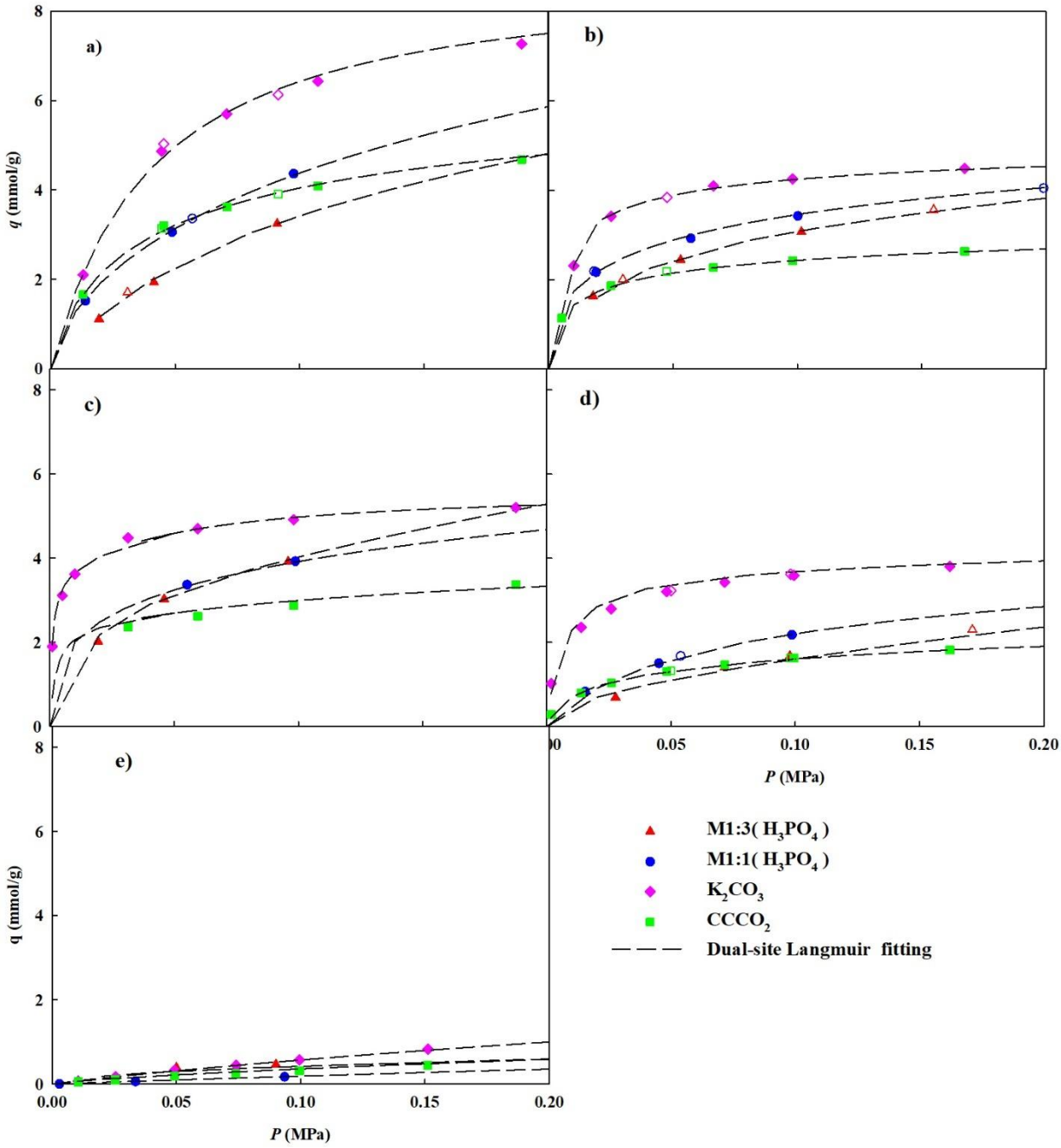


Figure 4.7.11 Adsorption (full symbols) and desorption (empty symbols) equilibrium isotherms of: a) R-32; b) R-125; c) R-134a; d) SF_6; e) N_2 on CC-1:3H_3PO_4 (red up triangles), CC-1:1H_3PO_4 (blue circles), CC-K_2CO_3 (pink diamond) and CC-CO_2 (green square) at 303.15 K.

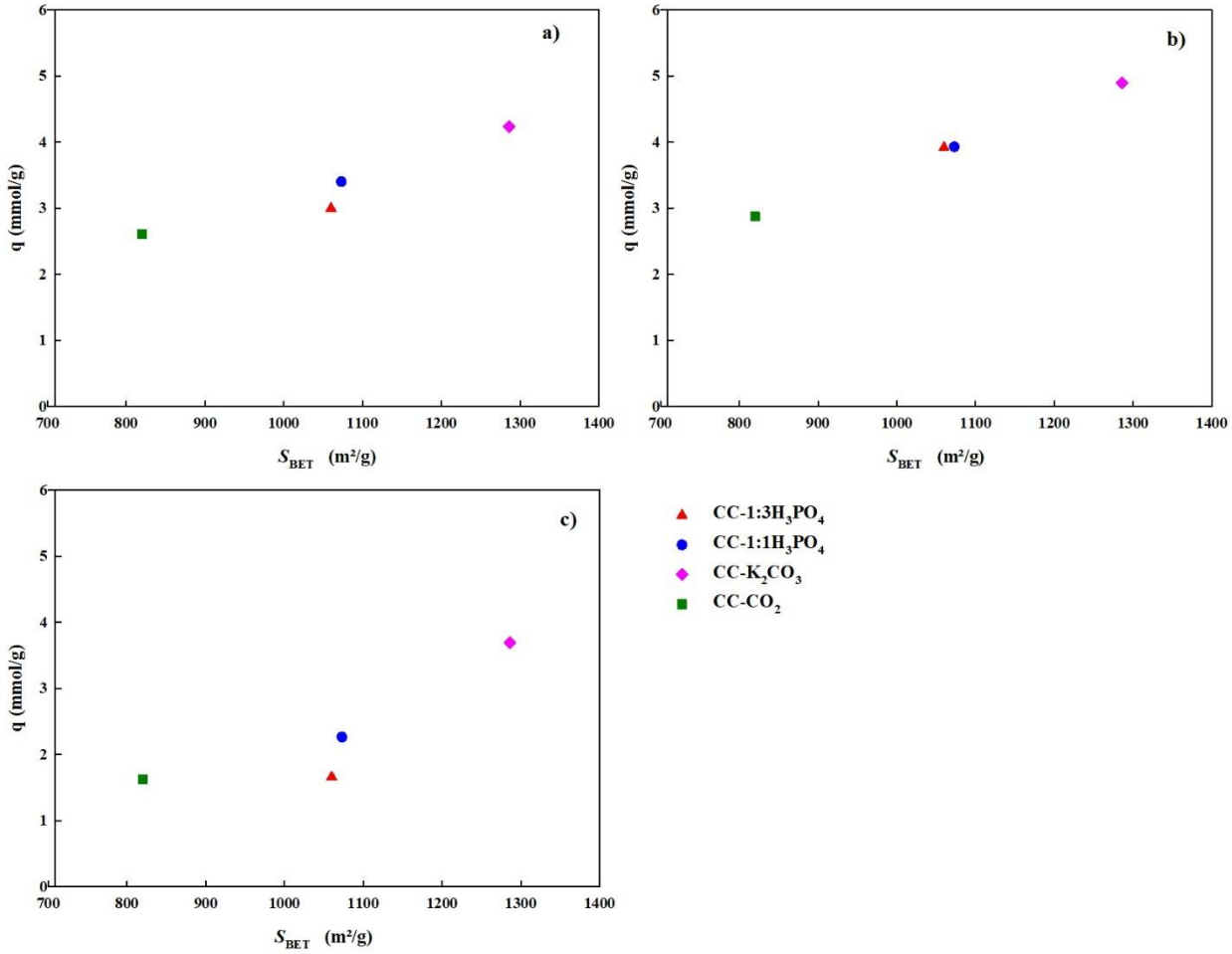


Figure 4.7.12 Relationship of adsorption uptakes versus SBET of: a) R-125; b) R-134a; c) SF_6 at 303.15 K and 0.1 MPa.

On the other hand, the functional groups on the surface of CC-K_2CO_3 (carbonyl oxygen groups (C=O), see Table 4.7.3) have facilitated interactions with the acidic hydrogen atoms of the F-gases [99] because these functional groups are good hydrogen bond acceptors [99]. On the other hand, the bio-material surface functional groups increase in the order of C-OH/C-O-C > Carbonyl C=O (see Table 4.7.3). These functional groups may also interact with the F-gases, promoting adsorption [100]. For R-32 gas at pressures below $P < 0.2$ MPa, the adsorption equilibria exhibit distinct behaviour as follows: CC-K_2CO_3 > CC-1:1H_3PO_4 > CC-CO_2 > CC-1:3H_3PO_4, as observed in Figure 4.7.11. This trend follows exactly the microporous volume trend. The presence of the C-OH/C-O-C functional group (see Table 4.7.3) also facilitate interactions between the two hydrogens in the R-32, improving its adsorption capacity.

At higher pressures, $P > 0.2$ MPa, the adsorption of all F-gases on all biocarbons presents the following trend: CC-1:3H_3PO_4 > CC-1:1H_3PO_4 ≥ CC-K_2CO_3 > CC-CO_2. In this case, the total pore volume of the biomaterials influences the adsorption capacities. However, in the case of nitrogen, the

behaviour is: CC-K_2CO_3 > CC-CO_2 ≈ CC-1:3H_3PO_4 ≈ CC-1:1H_3PO_4, because this gas can be considered inert.

The adsorption is influenced by the surface chemistry of the carbons. H_3PO_4 carbons present a very acidic character (pHpzc = 2.0 – 3.0) with acidic oxygenated groups at their surface [101], while CC-K_2CO_3 (pHpzc = 6.5) and CC-CO_2 (pHpzc = 9.6) have a more basic surface. Additionally, the biomaterials activated with H_3PO_4 have phosphorous groups incorporated in the surface as detected by XPS which favoures the adsorption at lower pressures. At higher pressures, the mesopore content of these carbons led to higher gas uptake. In addition, taking into account the electric dipole polarizability of the F-gases (R-125 > R-134a > R-32 with values of 4.623, 4.549 and 2.761 $Å^3$ respectively) [102–104], the adsorption affinity correlates inversely with the polarizability [96,105]. Therefore, van de Waals's interactions can be also strong in F-gases with lower polarizability as can be seen in Figure 4.7.13. Finally, in the case of SF_6 and N_2, polarizability does not play an important role because these gases do not have a dipole moment which could favour the interactions between the gas and the biomaterial [105].

A comparison with the adsorption data reported in the literature was carried out at a pressure of 0.1 MPa and temperatures near 303.15 K. The results are presented in Figure 4.7.14-4.7.17 and Table 4.7.5. Figure 4.7.14 shows that the best adsorbent for R-32 is the MOF MIL-101, rather than our biomaterial CC-K_2CO_3. This MOF has mesoporous cage structures connected through microporous windows, which facilitates adsorption [96]. Furthermore, the small size of CC-K_2CO_3 micropores and low oxygen content (see Table 4.7.2.) could decrease the interactions with F-gases. In the case of R-125, the most effective adsorbent is the MOF Cu-BTC as shown in Figure 4.7.15. This behaviour could be related to the interactions between the gas molecules and the adsorbent [29]. However, CC-K_2CO_3 exhibits a good adsorption capacity related to the textural characteristics and interaction between the material and this F-gas. In the adsorption of R-134a (see Figure 4.7.16), CC-K_2CO_3 has a lower adsorption capacity compared to the commercial activated carbon GAC II [106]. Finally, Figure 4.7.17 shows that activated carbon Ph_6M_4Cs11 obtained excellent SF_6 adsorption due to its ultramicroporosity [107]. However, the CC-K_2CO_3 adsorption is considerable when compared to other materials in the literature due to its favourable structural characteristics. Some literature materials have shown better adsorption than the biomaterials studied in this work, however, economic factors must be considered. MOFs are much more expensive than our materials. Furthermore, biocarbons are produced from waste biomass residues, which are available in large quantities and have higher sustainability compared to other commercial materials.

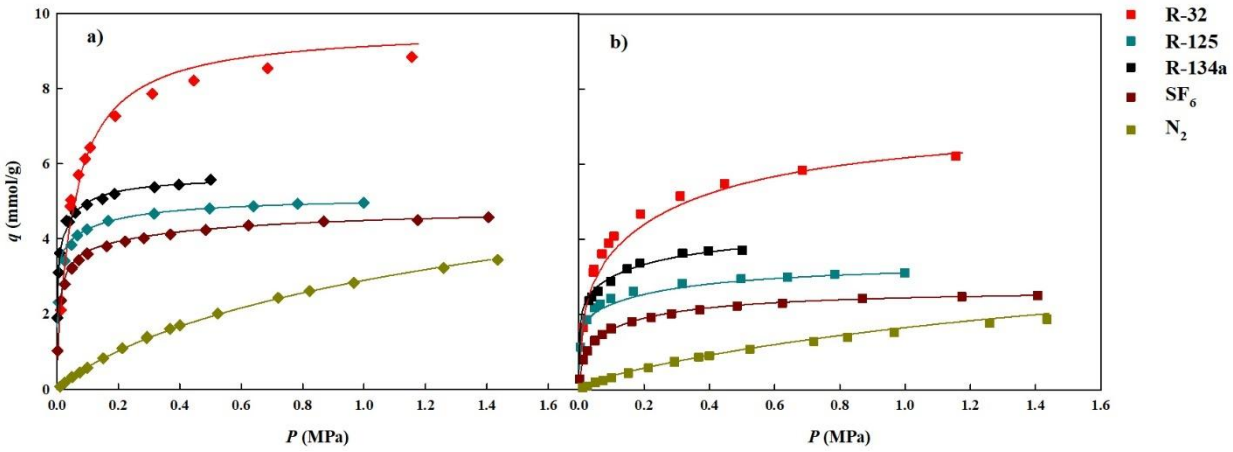


Figure 4.7.13 Relationship of adsorption uptakes versus SBET of: a) R-125; b) R-134a; c) SF_6 at 303.15 K and 0.1 MPa.

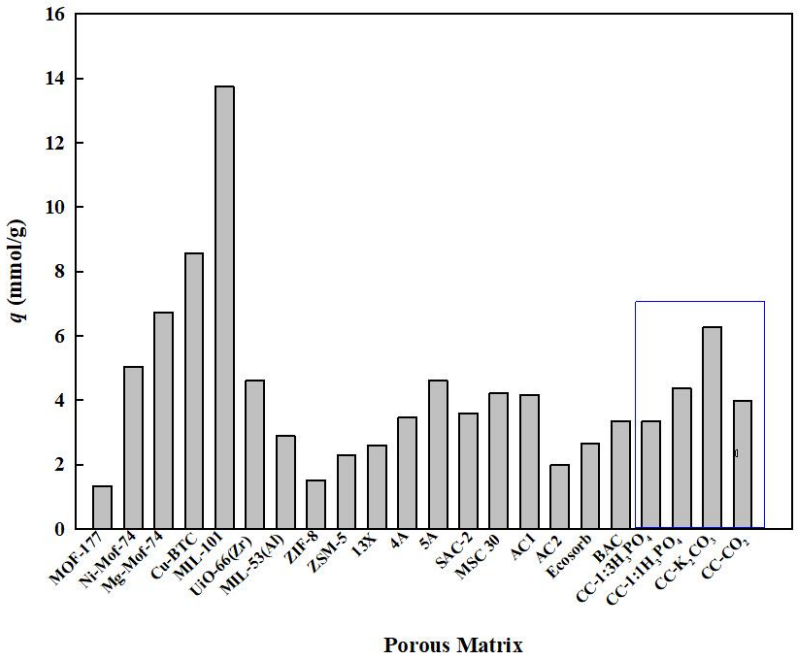


Figure 4.7.14 The adsorption of R-32 on porous matrices at 0.1 MPa and 303.15 K.

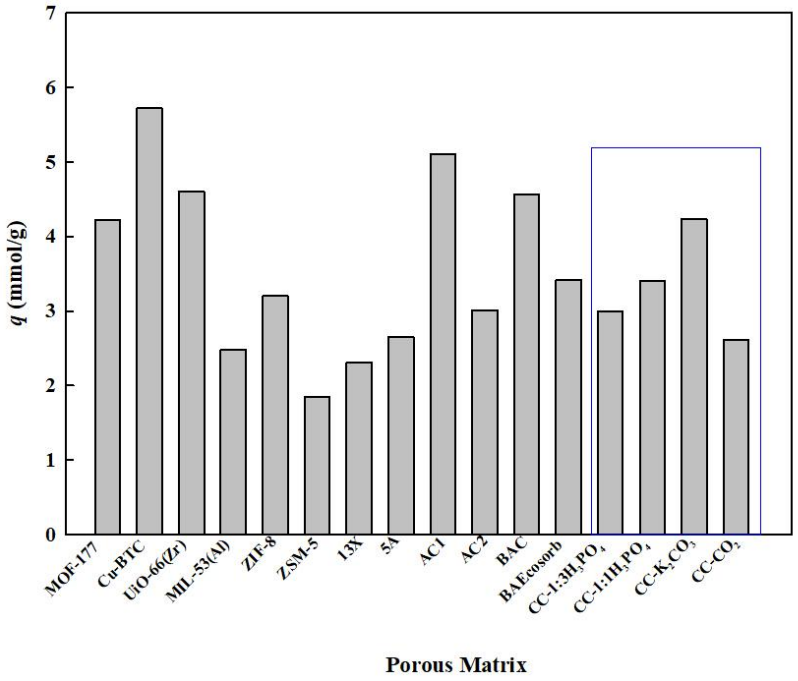


Figure 4.7.15 The adsorption of R-32 on porous matrices at 0.1 MPa and 303.15 K

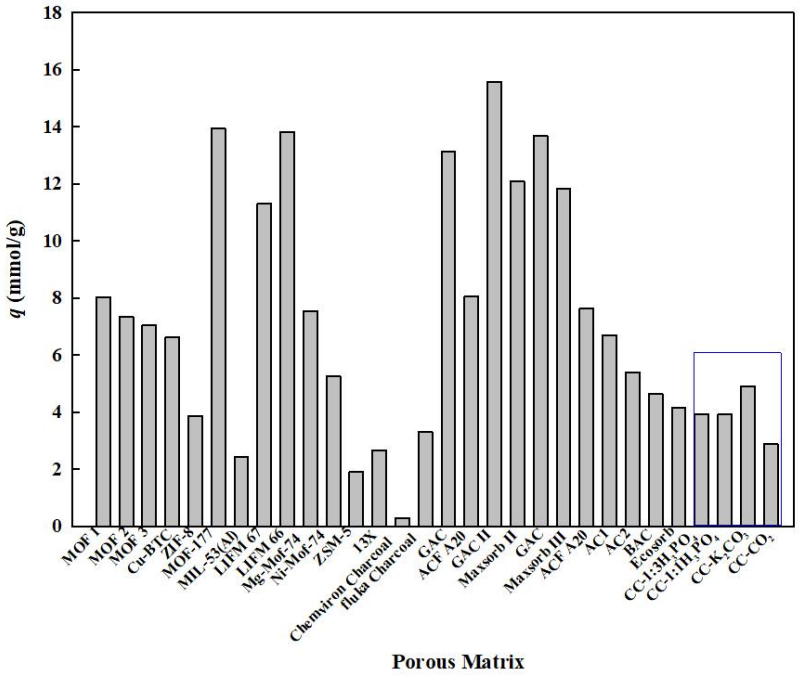


Figure 4.7.16 The adsorption of R-134a on porous matrices at 0.1 MPa and 303.15 K.

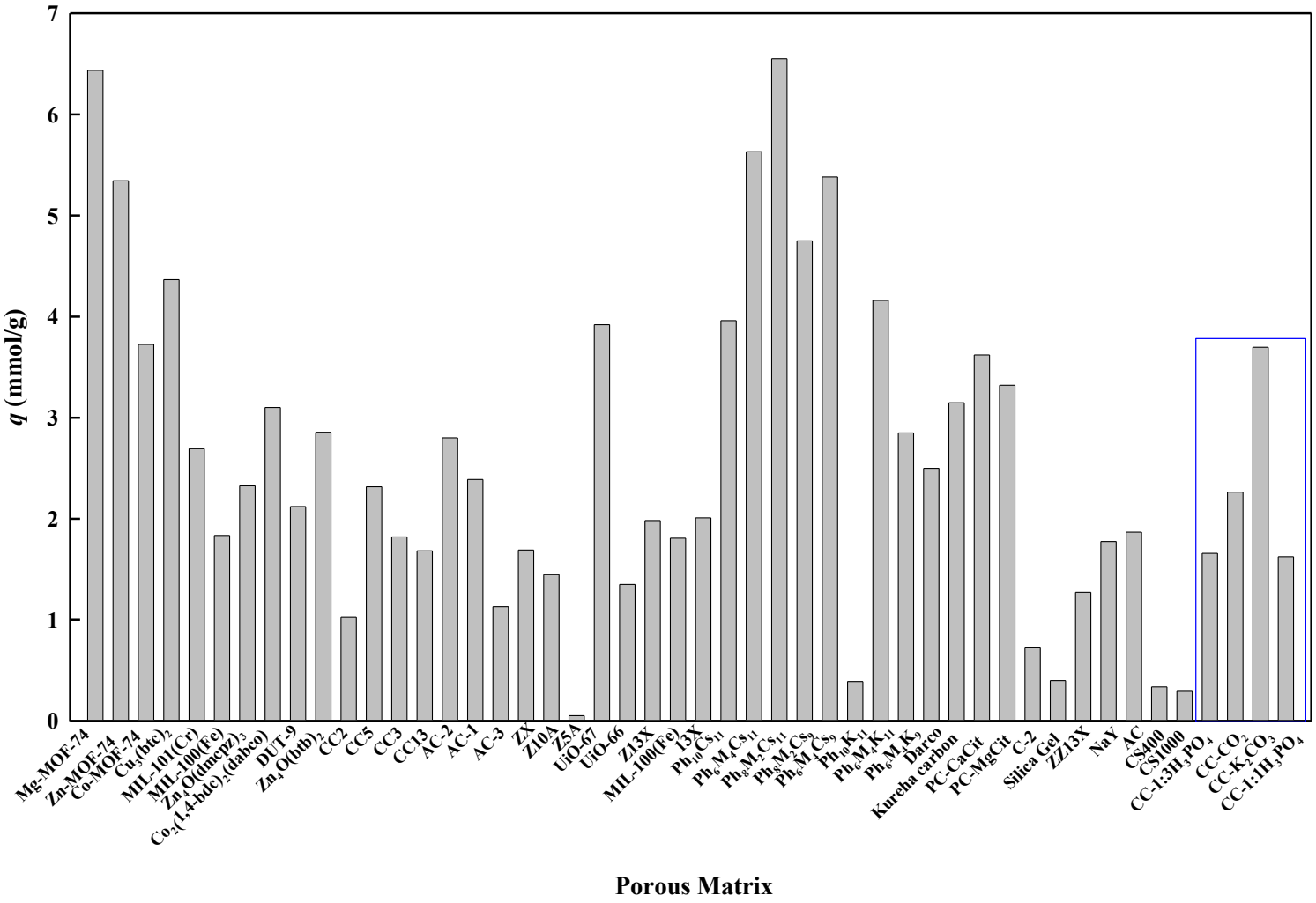


Figure 4.7.17 The adsorption of SF_6 on porous matrices at 0.1 MPa and 303.15 K.

Table 4.7.5 The comparison between the literature data and experimental data of this work for F-gases (R-32, R-125, R-134a, and SF_6) on porous matrices.

R-32					
Porous Solid	**Component**	***q*(mmol/g)**	***P*(Mpa)**	***T*(K)**	**Reference**
MOF	MOF-177	1.33	0.1	303.15	[108]
MOF	Ni-Mof-74	5.05	0.1	293.15	[109]
MOF	Mg-Mof-74	6.72	0.1	293.15	[109]
MOF	Cu-BTC	8.56	0.1	303.15	[108]
MOF	MIL-101	13.75	0.1	298.15	[96]
MOF	UiO-66(Zr)	4.60	0.1	293.15	[39]
MOF	MIL-53(Al)	2.90	0.1	303.15	[108]
MOF	ZIF-8	1.50	0.1	303.15	[108]
MOF	ZSM-5	2.28	0.1	303.15	[108]
Zeolite	13X	2.60	0.1	293.15	[39]
Zeolite	4A	3.46	0.1	293.15	[20]
Zeolite	5A	4.60	0.1	293.15	[20]
Activated carbon	SAC-2	3.59	0.1	303.15	[110]
Activated carbon	MSC 30	4.23	0.1	303.15	[111]
Activated carbon	AC1	4.16	0.1	303.15	[112]
Activated carbon	AC2	1.99	0.1	303.15	[112]
Activated carbon	Ecosorb	2.66	0.1	303.15	[108]
Activated carbon	BAC	3.34	0.1	303.15	[112]
Activated carbon	CC-1:3H_3PO_4	3.34	0.1	303.15	This work
Activated carbon	CC-1:1H_3PO_4	4.38	0.1	303.15	This work

Activated carbon	CC-K_2CO_3	6.27	0.1	303.15	This work
Activated carbon	CC-CO_2	3.99	0.1	303.15	This work

R-125

Porous Solid	**Component**	***q*(mmol/g)**	***P*(Mpa)**	***T*(K)**	**Reference**
MOF	MOF-177	4.22	0.1	303.15	[108]
MOF	Cu-BTC	5.72	0.1	303.15	[108]
MOF	UiO-66(Zr)	4.60	0.1	293.15	[39]
MOF	MIL-53(Al)	2.48	0.1	303.15	[108]
MOF	ZIF-8	3.20	0.1	30315	[108]
Zeolite	ZSM-5	1.85	0.1	303.15	[108]
Zeolite	13X	2.31	0.1	293.15	[19]
Zeolite	5A	2.65	0.1	293.15	[20]
Activated carbon	AC1	5.11	0.1	303.15	[112]
Activated carbon	AC2	3.01	0.1	303.15	[112]
Activated carbon	BAC	4.57	0.1	303.15	[112]
Activated carbon	Ecosorb	3.42	0.1	303.15	[112]
Activated carbon	CC-1:3H_3PO_4	3.00	0.1	303.15	This work
Activated carbon	CC-1:1H_3PO_4	3.40	0.1	303.15	This work
Activated carbon	CC-K_2CO_3	4.24	0.1	303.15	This work
Activated carbon	CC-CO_2	2.61	0.1	303.15	This work

R-134a

Porous Solid	**Component**	***q*(mmol/g)**	***P*(Mpa)**	***T*(K)**	**Reference**

MOF	MOF 1	8.04	0.1	298.15	[113]
MOF	MOF 2	7.35	0.1	298.15	[113]
MOF	MOF 3	7.06	0.1	298.15	[113]
MOF	Cu-BTC	6.61	0.1	303.15	[108]
MOF	ZIF-8	3.86	0.1	303.15	[108]
MOF	MOF-177	13.9	0.1	303.15	[108]
MOF	MIL-53(Al)	2.44	0.1	303.15	[108]
MOF	LIFM 67	11.3	0.1	298.15	[114]
MOF	LIFM 66	13.8	0.1	298.15	[114]
MOF	Mg-Mof-74	7.53	0.1	298.15	[109]
MOF	Ni-Mof-74	5.26	0.1	298.15	[109]
Zeolite	ZSM-5	1.92	0.1	303.15	[108]
Zeolite	13X	2.66	0.1	293.15	[19]
Activated carbon	Chemviron Charcoal	0.294	0.1	293.15	[115]
Activated carbon	fluka Charcoal	3.29	0.1	293.15	[115]
Activated carbon	GAC	13.1	0.1	293.15	[116]
Activated carbon	ACF A20	8.06	0.1	293.15	[42]
Activated carbon	GAC II	15.6	0.1	293.15	[117]
Activated carbon	Maxsorb II	12.1	0.1	298.15	[106]
Activated carbon	GAC	13.7	0.1	298.15	[42]
Activated carbon	Maxsorb III	11.8	0.1	298.15	[116]
Activated carbon	ACF A20	7.64	0.1	298.15	[117]
Activated carbon	AC1	6.70	0.1	303.15	[112]

Activated carbon	AC2	5.39	0.1	303.15	[112]
Activated carbon	BAC	4.63	0.1	303.15	[112]
Activated carbon	Ecosorb	4.14	0.1	303.15	[112]
Activated carbon	CC-1:3H_3PO_4	3.93	0.1	303.15	This work
Activated carbon	CC-1:1H_3PO_4	3.92	0.1	303.15	This work
Activated carbon	CC-K_2CO_3	4.90	0.1	303.15	This work
Activated carbon	CC-CO_2	2.88	0.1	303.15	This work

SF_6

Porous Solid	Component	*q*(mmol/g)	*P*(Mpa)	*T*(K)	Reference
MOF	Mg-MOF-74	6.44	0.1	298.15	[118]
MOF	Co-MOF-74	5.34	0.1	298.15	[118]
MOF	Zn-MOF-74	3.72	0.1	298.15	[118]
MOF	Cu3(btc)2	4.37	0.1	298.15	[119]
MOF	MIL-100(Fe)	2.69	0.1	298.15	[119]
MOF	MIL-101(Cr)	1.84	0.1	298.15	[119]
MOF	Zn4O(dmcpz)3	2.33	0.1	298.15	[119]
MOF	Co_2(1,4-bdc)$_2$(dabco)	3.10	0.1	298.15	[119]
MOF	DUT-9	2.12	0.1	298.15	[119]
MOF	$Zn_4O(btb)_2$	2.86	0.1	298.15	[120]
MOF	CC2 α	1.03	0.1	298.15	[120]
MOF	CC3 α	2.32	0.1	298.15	[120]
MOF	CC5 α	1.82	0.1	298.15	[120]
MOF	CC13 β	1.68	0.1	298.15	[120]

Activated carbon	AC-1	2.80	0.1	303.65	[121]
Activated carbon	AC-2	2.39	0.1	303.65	[121]
Activated carbon	AC-3	1.13	0.1	303.65	[121]
Zeolite	ZX	1.69	0.1	303.65	[121]
Zeolite	Z10A	1.45	0.1	303.65	[121]
Zeolite	Z5A	0.05	0.1	303.65	[121]
MOF	UiO-67	3.92	0.1	298.15	[122]
MOF	UiO-66	1.35	0.1	298.15	[122]
Zeolite	zeolite-13X	1.98	0.1	298.15	[122]
MOF	MIL-100(Fe)	1.81	0.1	298.15	[123]
Zeolite	Zeolite 13X	2.01	0.1	298.15	[123]
Activated carbon	Ph10Cs11	3.96	0.1	298.15	[107]
Activated carbon	$Ph_8M_2Cs1_1$	5.63	0.1	298.15	[107]
Activated carbon	$Ph_6M_4Cs_{11}$	6.55	0.1	298.15	[107]
Activated carbon	$Ph_8M_2Cs_9$	4.75	0.1	298.15	[107]
Activated carbon	$Ph_6M_4Cs_9$	5.38	0.1	298.15	[107]
Activated carbon	$Ph_{10}K_{11}$	0.39	0.1	298.15	[107]
Activated carbon	$Ph_6M_4K_{11}$	4.16	0.1	298.15	[107]
Activated carbon	$Ph_6M_4K_9$	2.85	0.1	298.15	[107]
Activated carbon	Darco	2.50	0.1	298.15	[107]
Activated carbon	Kureha carbon	3.15	0.1	298.15	[124]

Activated carbon	PC-CaCit	3.62	0.1	298.15	[125]
Activated carbon	PC-MgCit	3.32	0.1	298.15	[125]
Activated carbon	C-2	0.73	0.1	298.15	[126]
Sílice	Silica gel	0.40	0.1	298.15	[127]
Zeolite	13x	1.27	0.1	298.15	[127]
Zeolite	NaY	1.78	0.1	298.15	[127]
Zeolite	AC	1.87	0.1	298.15	[127]
Activated carbon	CS400	0.34	0.1	300.15	[128]
Activated carbon	CS1000	0.30	0.1	300.15	[128]
Activated carbon	CC-1:3H_3PO_4	1.66	0.1	303.15	This work
Activated carbon	CC-1:1H_3PO_4	2.26	0.1	303.15	This work
Activated carbon	CC-K_2CO_3	3.70	0.1	303.15	This work
Activated carbon	CC-CO_2	1.63	0.1	303.15	This work

4.7.2.3 Henry Law's constant

In this work, the determination of the K_H, as described in Section 4.4, was carried out to select the most suitable biomaterials for the separation and purification of F-gases. constant has been carried out to select the best biomaterials for the separation and purification of F-gases. The Henry's constants of all gases on the 4 biocarbons studied in this work are represented in Figure 4.7.18. CC-1:1H_3PO_4 presents higher values than CC-1:3H_3PO_4 where the gases present the following trend: R-125 > R32 > R-134a > SF_6 > N_2. However, CC-K_2CO_3 obtained higher values than CC-CO_2, and the gas order for CC-K_2CO_3 is R-125 > R-134a > SF_6 > R-32 >N_2. The K_H values for CC-1:1H_3PO_4 and CC-1:3H_3PO_4 are relatively smaller than for the other two biomaterials, as expected. This behaviour can be associated with the pore size distribution of these biomaterials [129]. In addition, the carbon surfaces with different geometries, pore width and average surface curvature play essential roles in the determination of Henry's law constants [130]. Finally, the affinity between the selected biomaterials, CC-K_2CO_3 and CC-

CO_2, and gases is due to the strong interactions promoted both by micropore sizes and surface chemistry [96,105].

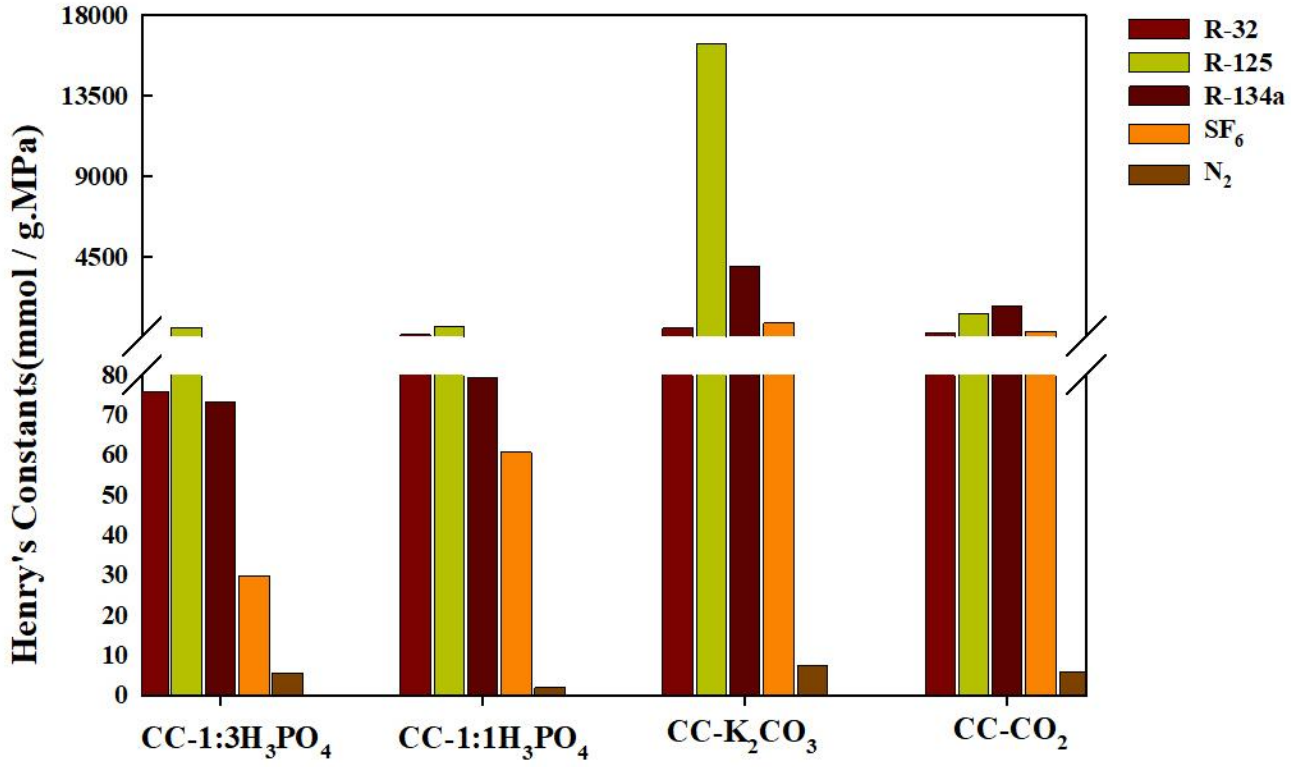


Figure 4.7.18 Henry's law constants at 303.15 K for the biomaterials studied in this work.

4.7.2.4 Isosteric heat of adsorption

The two best carbon materials, CC-K_2CO_3 and CC-CO_2, for F-gases adsorption were also selected for full characterization. The theoretical heat of adsorption, Q_{st}, are plotted in Figure 4.7.19 and were determined for q = 0.2, 0.4, 1, 2, …n mmol/kg (see Figure 4.7.20-4.7.21). The heats of adsorption for the gases R-32, R-125 and R-134a on CC-K_2CO_3 and CC-CO_2 are in the range of 20-30 kJ/mol. However, the values for N_2 are over 10 kJ/mol. The isosteric heat of adsorption is slightly higher for high loading than for low loading due to the heterogeneous nature of the biomaterial surfaces. In addition, in the pores of the biomaterials, the gases occupy the energetically more stable sites first until the pores are saturated. Consequently, the excess gas molecules interact with one another and occupy the available structural sites, resulting in a slight increase in the heat of adsorption [61,66]. Finally, the isosteric heat of adsorption for SF_6 is in a range between 20-30 kJ/mol. At lower load values, this heat of adsorption is higher because the gas occupied places where they have more interaction. However, a minimum is observed at 1.5 mmol/g and after this value, the isosteric heat of adsorption for SF_6 increases again. This behaviour could be associated with the interaction between the gas and biomaterial surface after the saturation of the pore, generating forces of attraction and increasing the isosteric heat of adsorption [131,132].

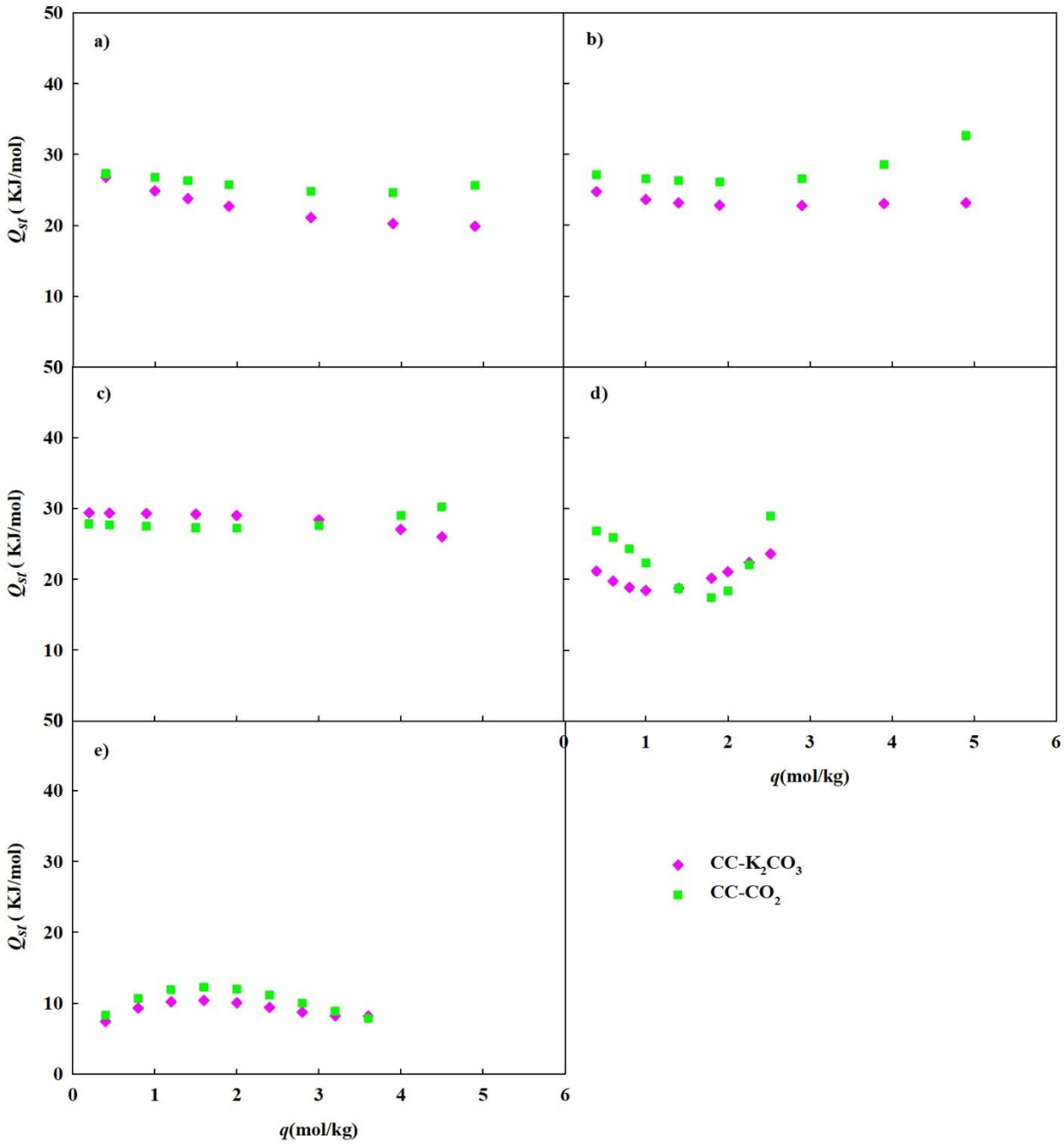


Figure 4.7.19 Isosteric heat of adsorption: a) R-32; b) R-125; c) R-134a; d) SF_6; and e) N_2 on CC-K_2CO_3 and CC-CO_2.

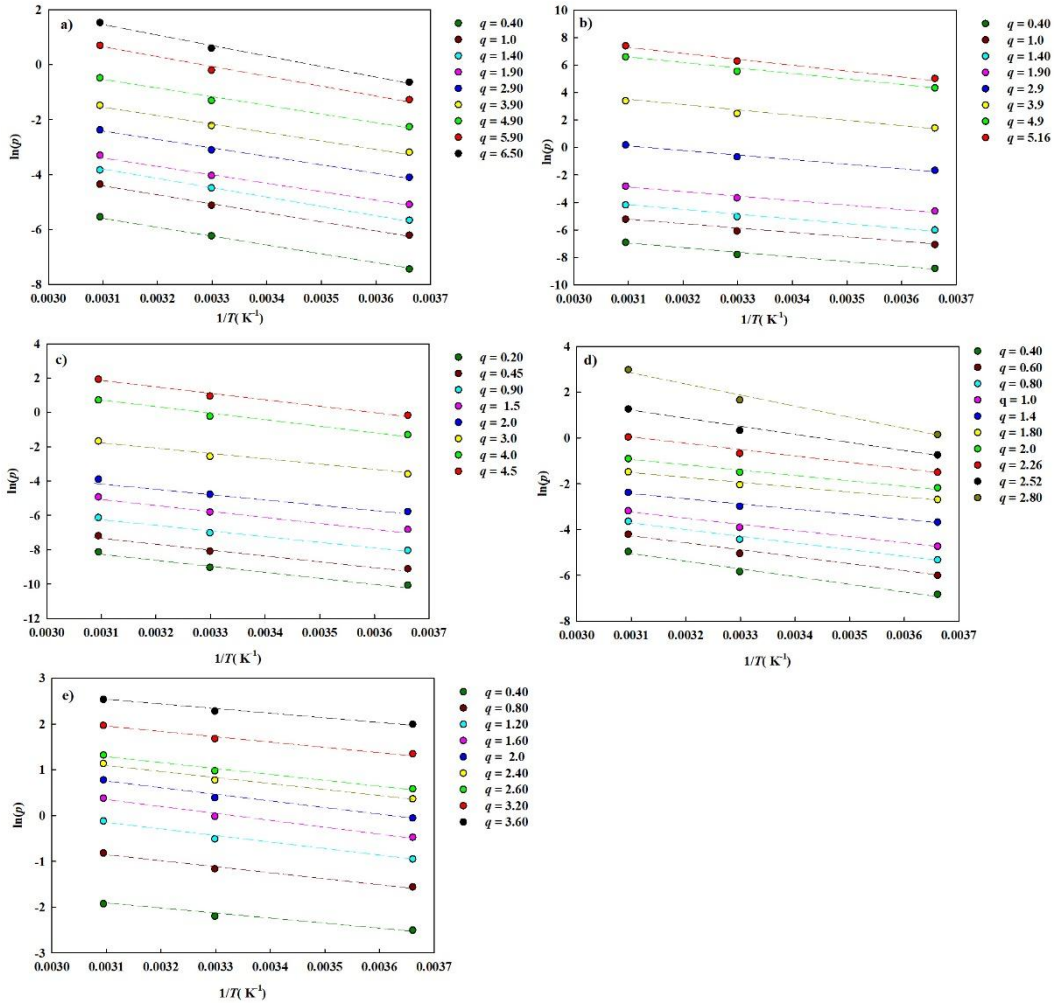


Figure 4.7.20 Adsorption isosteres on CC-K_2CO_3 of: a) R-32; b) R-125; c) R-134a; d) SF_6; and e) N_2 in the temperature range 283.15-323.15 K

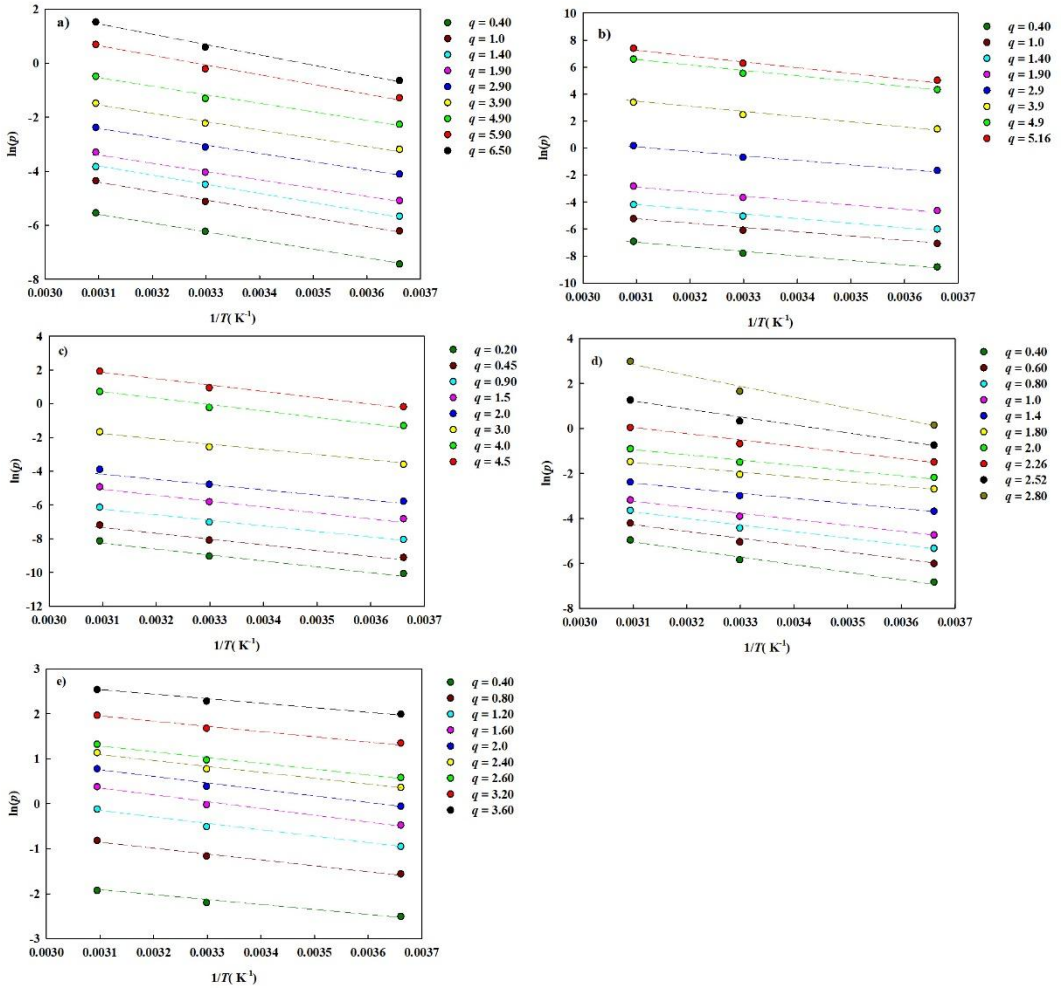


Figure 4.7.21 Adsorption isosteres on CC-CO_2 of: a) R-32; b) R-125; c) R-134a; d) SF_6 and E) N_2 in the 283.15-323.15 K temperature range.

4.7.2.5 Adsorption of R-410A, R-407C and R-407F using the Ideal Adsorption Solution Theory (IAST)

In the refrigeration sector, there is a clear interest in the separation of commercial blends for recovery of added value compounds. In this work, the separation of the following commercial refrigerants R-410A (R-32/R-125, 50/50 wt %), R-407F (R-32/R-125/R-134a, 30/30/40 wt %) and R-407C (R-32/R-125/R-134a, 23/25/52 wt %) was studied because these blends have high GWP. Furthermore, SF_6 is the greenhouse gas with the highest GWP and is widely used as an insulating gas in electrical transformers and semiconductor manufacturing processes [122,133]. The SF_6/N_2 mixture (35/65 wt %) is used in the sectors mentioned above to eliminate some dielectric strength problems. The recovery of pure SF_6 is very important for the different applications of this F-gas [122,133,134].

Separations of the F-gases are not easy because these mixtures are azeotropic or nearly azeotropic. In this work, the IAST allows us to predict the multicomponent behaviour of the equilibrium isotherms of the blends studied in this work. The estimated equilibria in the multi-component mixture were determined from 0.01 to 1 MPa for R-410A and SF_6/N_2 (see Figure 4.7.22- 4.7.24). In addition,

the pressure range selected for R-407C and R-407F was from 0.01 to 0.6 MPa (see Figure 4.7.25- 4.7.26. The selectivity for R-410A is illustrated in Figure 4.7.22 and 4.7.23. In the pressure range 0.01-0.1 MPa, all biomaterials have a higher selectivity for R-125 with the following trend: CC-K_2CO_3 > CC-1:1H_3PO_4 ≈ CC-1:3H_3PO_4 > CC-CO_2. This behaviour is related to the influence of the F-gas sizes that are competing for the available adsorption sites. However, the maximum selectivity values are achieved for the separation R-32/R-125 at high pressures, with the following tendency: CC-CO_2 > CC-K_2CO_3 > CC-1:1H_3PO_4 > CC-1:3H_3PO_4. This trend is probably influenced by the pore volume and pore size distribution. CC-CO_2 and CC-K_2CO_3 are mostly microporous where the smaller gas molecules (R-32) are more easily packed, increasing considerably its adsorption. While CC-1:1H_3PO_4 and CC-1:3H_3PO_4 materials have more than 40% of their porous volume attributed to mesoporosity, providing access for the adsorption sites to larger gases (R-125). Furthermore, the functional groups present in CC-K_2CO_3 contribute to lower selectivity to R-32, due to positive interactions of R-125 with the surface of the material. Finally, all biomaterials facilitate the recovery of R-32 at a P > 0.1 MPa because R-125 remain adsorbed on the biomaterial, see Figure 4.7.22.

In the case of the SF_6/N_2 separation, the most widely used composition in the electrical industry is y_{SF6} = 0.10 and y_{N2} = 0.90. Figure 4.7.24 represents the performance of all biocarbons studied in this work to the capture of SF_6. Figure 4.7.8 shows that the adsorption isotherms of these two gases have a characteristic performance linear for N_2 and favourable for SF_6 in all biomaterials. This different behaviour in the adsorption isotherms facilitates the separation and increases the selectivity (see Figure 4.7.24.). Besides, the selectivity increases at P < 0.1 MPa following this trend: CC-K_2CO_3 > CC-1:1H_3PO_4 > CC-CO_2 > CC-1:3H_3PO_4. At low pressures, the selectivity of the biomaterials is directly influenced by the pore size distribution. Then, the pore size distribution of the biomaterials exerts a greater effect on the competitive adsorption performance at low pressure directly favouring the selectivity of SF_6 over N_2 [35].

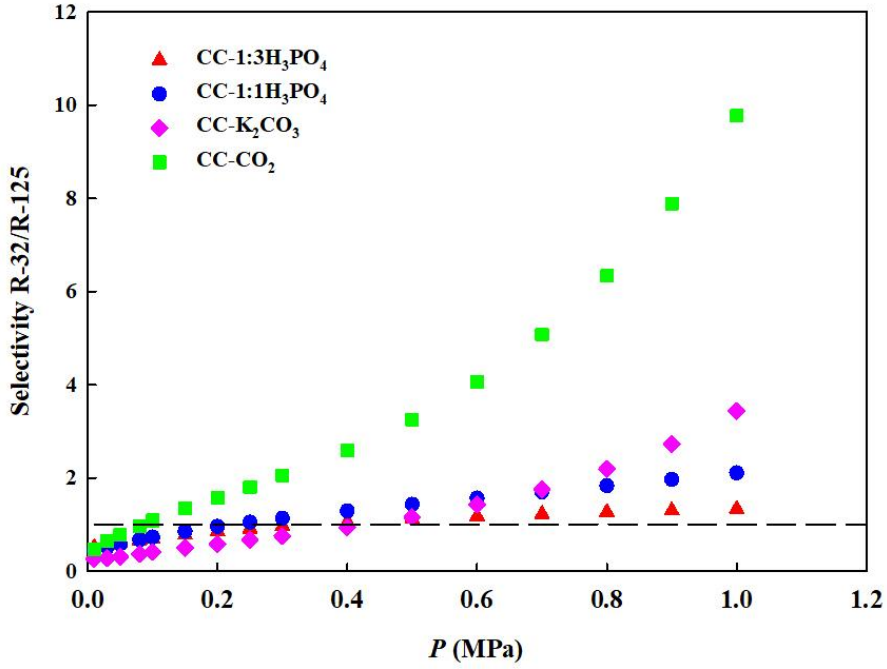


Figure 4.7.22 Selectivity of CC-1:3H_3PO_4 (red up triangles), CC-1:1H_3PO_4 (blue circles), CC-K_2CO_3 (pink diamond) and CC-CO_2 (green square) to R-32 over R-125 as a function of pressure at 303.15 K for the equilibrium gas phase composition of the R-410A mixture ($y_{R\text{-}32}$ = 0.7 and $y_{R\text{-}125}$ = 0.3).

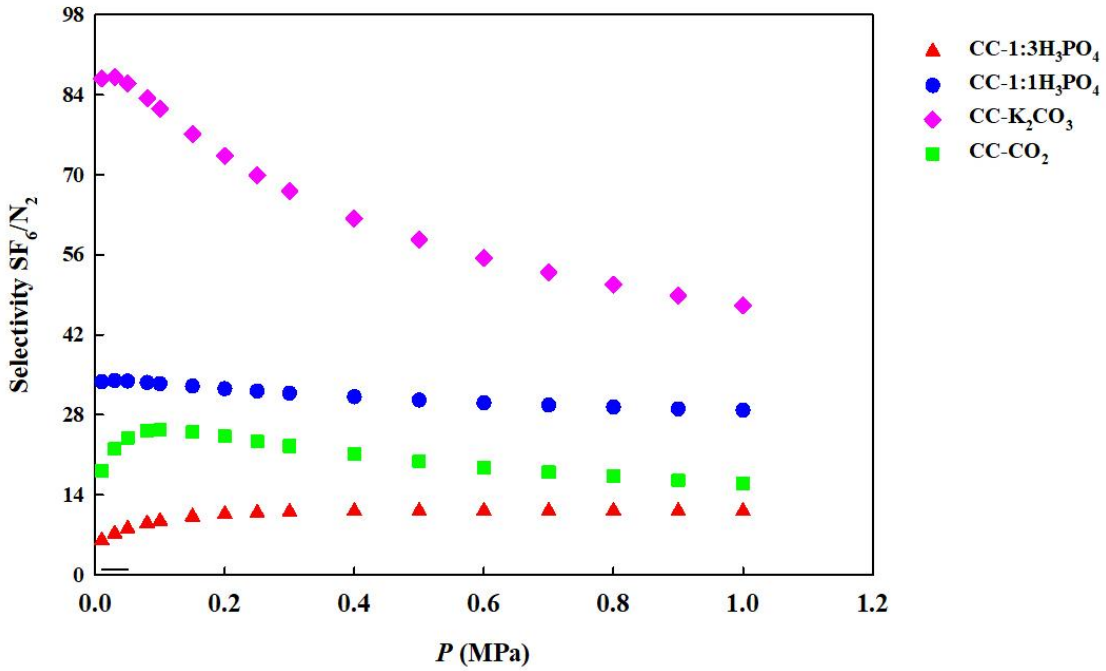


Figure 4.7.23 Selectivity of CC-1:3H_3PO_4 (red up triangles), CC-1:1H_3PO_4 (blue circles), CC-K_2CO_3 (pink diamond) and CC-CO_2 (green square) to SF_6 over N_2 as a function of pressure at 303.15 K, for the equilibrium gas phase composition of the SF_6/N_2 mixture (y_{SF6} = 0.10 and y_{N2} = 0.90).

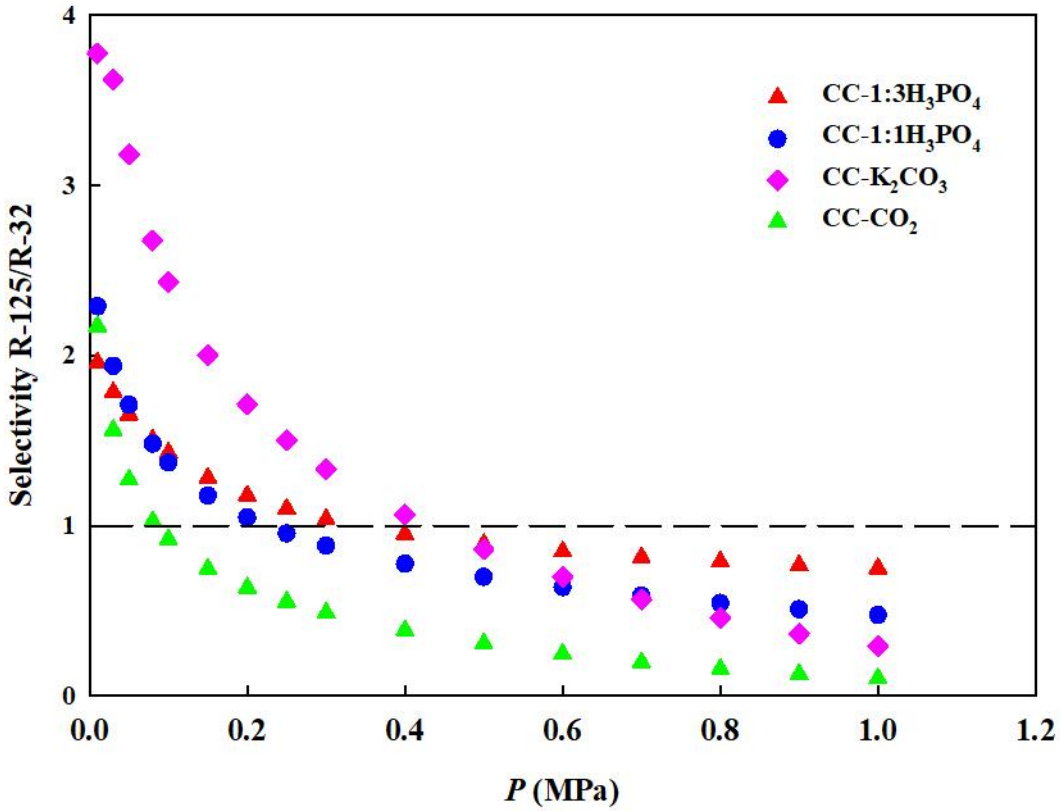


Figure 4.7.24 Selectivity of CC-1:3H_3PO_4 (red up triangles), CC-1:1H_3PO_4 (blue circles), CC-K_2CO_3 (pink diamond) and CC-CO_2 (green square) to R-125 over R-32 as a function of pressure at 303.15 K, for the equilibrium gas phase composition of the R-410A mixture ($y_{R\text{-}32}$ = 0.7 and $y_{R\text{-}125}$ = 0.3).

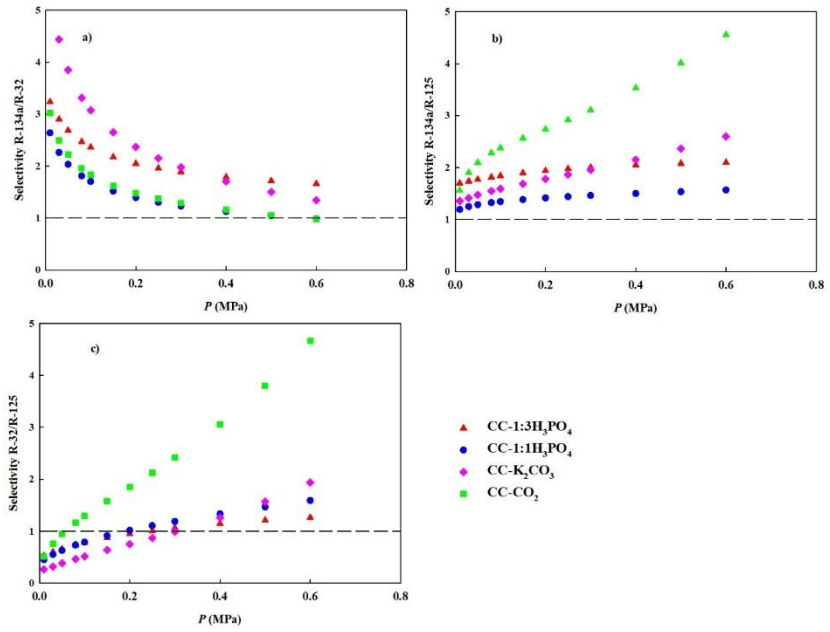


Figure 4.7.25 Selectivity of CC-1:3H_3PO_4 (red up triangles), CC-1:1H_3PO_4 (blue circles), CC-K_2CO_3 (pink diamond) and CC-CO_2 (green square) to: a) R-134a over R-32; b) R-134a over R-125; and c) R-32 over R-125, for the commercial R-407C gas mixture ($y_{R\text{-}32}$ = 0.38, $y_{R\text{-}125}$ = 0.18, and $y_{R\text{-}134a}$ = 0.44, as a function of pressure at 303.15 K.

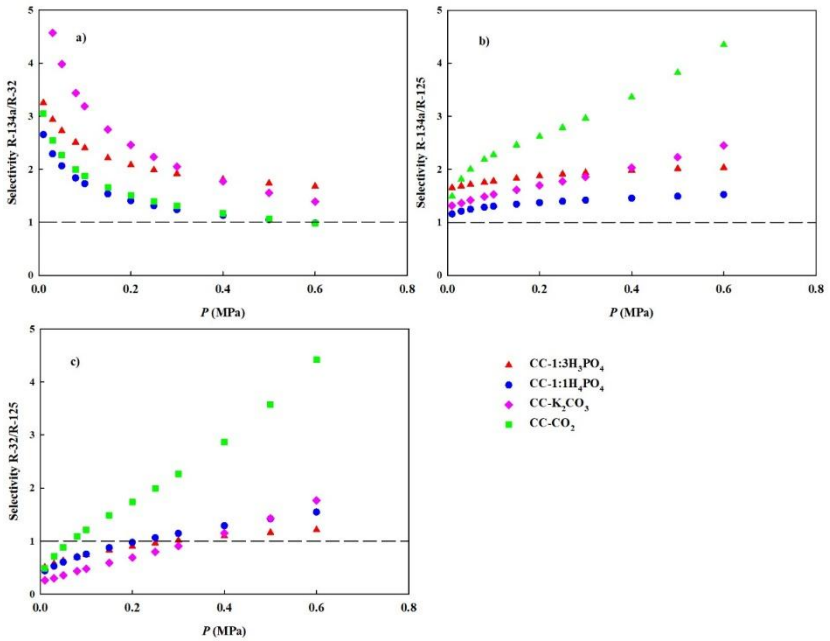


Figure 4.7.26 Selectivity of CC-1:3H_3PO_4 (red up triangles), CC-1:1H_3PO_4 (blue circles), CC-K_2CO_3 (pink diamond) and CC-CO_2 (green square) to: a) R-134a over R-32; b) R-134a over R-125; and c) R-32 over R-125, for the commercial R-407F gas mixture ($y_{R\text{-}32}$ = 0.47, $y_{R\text{-}125}$ = 0.21, and $y_{R\text{-}134a}$ = 0.32), as a function of pressure at 303.15 K

In Figure 4.7.25 and 4.7.26, the selectivity of the separation of the commercial ternary refrigerant blends R-407C ($y_{R\text{-}32}$ = 0.38, $y_{R\text{-}125}$ = 0.18, and $y_{R\text{-}134a}$ = 0.44) and R-407F ($y_{R\text{-}32}$ = 0.47, $y_{R\text{-}125}$ = 0.21, and $y_{R\text{-}134a}$ = 0.32) with the biomaterials studied in this work are represented. The results for the R-407C separation demonstrate that the biocarbons studied in this work have a greater affinity for R-134a. The selectivity of R-134a/R-32 presents the following order: CC-K_2CO_3 > CC-1:3H_3PO_4 > CC-CO_2 > CC-1:1H_3PO_4. Figure 4.7.1 demonstrates that the material is structurally microporous. In addition, at low pressure, the electrostatic interactions are favoured by the polarizability of the gases: R-134a has higher polarizability than R-32. The structural diversity in the pore size distribution of the biomaterials influences the selectivity at low-pressure [35,36]. The adsorption equilibria are also controlled by molecular interactions with the pore walls, favouring the selectivity for R-134a over R-32.

In the case of the R134a/R125 separation, the selectivity at high pressures is influenced by two factors: i) the size of the molecule where R-134a is smaller than R-125, favouring the packing of more molecules in the materials [135,136]; ii) the electronegativity generated by the fluorine atoms, generating repulsion, preventing H-bonding between the hydrogens present in the F-gas with the carbonyl (C=O) functional groups present in the materials. Then, adsorption equilibria are thus favoured for R-134a > R-125 and this factor directly affects the selectivity.

In the separation of R-32/R-125, the order of the materials at maximum pressure is CC-CO_2 > CC-K_2CO_3 ≥ CC-1:1H_3PO_4 > CC-1:3H_3PO_4. This separation is influenced by the size of the F-gas since the size of the R-32 molecule is smaller than R-125 and more F-gas molecules can be packed in the biomaterials [135,136]. Finally, the separation of the commercial refrigerant R-407F is represented in Figure 4.7.26. The behaviour presented in this ternary blend is the same as the commercial refrigerant R-407C. Therefore, these results demonstrated that for these mixtures the percentages of each component do not have a significant influence on these separations

4.7.3 Conclusions

The preparation of biomaterials is a green alternative to provide solutions to the amount of waste that is generated worldwide from different biomass sources. In this work, four different biocarbons (CC-1:3H_3PO_4, CC-1:1H_3PO_4, CC-K_2CO_3 and CC-CO_2) were prepared with different structural characteristics and the adsorption equilibria were determined with the five different F-gases at 303.15 K. These biomaterials possess different textural characteristics, including micropores, mesopores, and surface area, which have the most important influence in the F-gases adsorption. Furthermore, the different physical and chemical treatments produce biomaterials with an acidic or basic nature and different functional groups on the material surface. The interactions of these functional groups, depending on the hydrogens of the F-gas, promote adsorption and aid in the selectivity for F-gas separation. The biocarbons with the best performance, CC-K_2CO_3 and CC-CO_2, were selected to carry out a complete characterization at 283.15 K and 323.15 K. The diversity of isotherms is due to the type of

microporosity/mesoporosity present in these biomaterials. Then, a Dual Langmuir site adsorption model was selected because this model allows to describe of different behaviours at low and high pressure for the systems studied.

On the other hand, this work demonstrated that the different separation processes of the different commercial refrigerants can be designed taking into account the target gas. For example, the CC-CO_2 must be used to recover R-32. However, if the target gas is R-134a or R-125, the selected biomaterials must be CC-K_2CO_3. Furthermore, the best performance for the SF_6/N_2 separation is with the biomaterial CC-K_2CO_3. These neoteric and novel biomaterials open the door to future separation and capture processes for the different blends: R-410A, R-407C, R-407F and SF_6/N_2. The results of these separations demonstrated that biocarbons are promising for their use at pilot or industrial scale in the purification of pure F-gases. In addition, this work provides key fundamental information for the design and development of novel, advanced and neoteric biomaterials with different structural modifications with improved properties and performances.

4.8 Coconut shell derived activated carbon for effective separation of greenhouse gases

The development of efficient adsorbent materials for the selective capture of greenhouse gases (GHGs) is crucial. The porosity and surface area of the materials are key factors for the GHGs separation. This study demonstrates how waste from coconut shell (CS) biomass can be used to design novel biomaterials (C_S-CO_2, CS-$ZnCl_2$) with enhanced GHG selectivity. A comparison with activated carbon monoliths (ACM) and a metal-organic framework (Fe-BTC) was carried out to assess the impact of different porous matrices on GHGs capture. The adsorption equilibrium of R-32, R-125, R-134a, R-143a, CO_2, and CH_4 on these materials was measured between 283.15-323.15 K. The adsorption isotherms obtained were fitted using the dual-site Langmuir model. For R-32, R-125, R-134a and R-143a, the adsorption capacity follows ACM > CS-$ZnCl_2$ > Fe-BTC > CS-CO_2 due to the decrease of the surface area. The CO_2 adsorption capacity is ACM > Fe-BTC > CS-$ZnCl_2$ > CS-CO_2, which is related to the micropore volume. In this case, CS-CO_2 has a smaller adsorption capacity but is similar to ACM and outperforms Fe-BTC at $P < 0.4$ MPa. The selectivity of R-410A, R-407C, R-404A, and CO_2/CH_4 blends was determined with the Ideal Adsorbed Solution Theory (IAST). CS-$ZnCl_2$ shows a higher selectivity for R-125 over R-32 in R-410A and R-407C separations due to its larger pore volume. CS-CO_2 predominantly adsorbs R-134a and R-143a over R-125 in R-404A separation. ACM preferentially adsorbs CO_2 over CH_4 due to its large, elongated micropores. This study introduces innovative materials that improve GHGs separation and help reduce emissions.

4.8.1 Experimental Section

4.8.1.1 Materials

Difluoromethane, R-32 (purity ≥ 99.9 wt %) and pentafluoroethane, R-125 (purity ≥ 99.8 wt %), 1,1,1,2-tetrafluoroethane, R-134a (purity ≥ 99.8 wt %), and 1,1,1-trifluoroethane, R-143a (purity ≥ 99.9 wt %), were supplied by Polo Zero (Lisbon, Portugal). Carbon dioxide, CO_2 (purity ≥ 99.9 wt %) and methane, CH_4 (purity ≥ 99.9 wt %), were supplied by Air Liquid (Lisbon, Portugal) and helium (purity ≥ 99.9 wt %) was supplied by Praxair (Lisbon, Portugal). Activated carbon monolith, ACM, was developed and produced by Sutcliffe Speakman Carbons Ltd (Bristol, UK), and MOF-Fe-BTC was supplied by Basolite F300, Sigma-Aldrich, Portugal.

4.8.1.2 Synthesis of biomass-derived porous carbons

The biomaterials used in this work were prepared from residual coconut shell (CS) biomass from the Maceio industries, AL, Brazil. The biomaterials were treated by chemical activation with $ZnCl_2$, CS-$ZnCl_2$, and by physical activation with CO_2, CS-CO_2. In the chemical activation, the CS was impregnated with $ZnCl_2$ using an impregnation ratio of 2:5 (w/w) and was kept at 353.15 K for 4 h. Then, the impregnated sample was submitted to pyrolysis under constant nitrogen flow (5 L/h). The temperature was raised at 5 K/min up to 873.15 K and maintained for 3 h. Subsequently, the obtained biomaterial was pre-washed with an HCl solution (2 M) to remove the excess $ZnCl_2$. Then, the sample was washed with deionized water until neutral pH and dried at 378.15 K. In the physical activation using CO_2, the CS biomass was first carbonized at 1073.15 K under a constant nitrogen flow of 5 L/h and maintained for 4 hours. After cooling down to room temperature, the obtained biomaterial was activated under a CO_2 flow (1 L/h) at 1073 K for 4 hours, followed by cooling down to room temperature.

4.8.2 Results and discussion

4.8.2.1 Materials characterisation

The details of the equipment used for the characterization of the materials are described in Section 4.2, Table 1 shows the results of the nitrogen adsorption-desorption isotherms at 77 K for the four porous solid matrices, including their surface area (S_{BET}), total volume (v_{total}), micropore volume (v_{micro}), and mesopore volume (v_{meso}). The pore classification is defined by the IUPAC as micropores ≤ 20 Å, mesopores, between 20-500 Å, and macropores ≥ 500 Å [84,137]. CS-CO_2 has a S_{BET} of 602 m²/g (see Table 4.8.1) and microporosity in the 5–15 Å range (Figure 4.8.1). The N_2 adsorption-desorption isotherm for this material corresponds to a type I(a) with negligible hysteresis, characteristic of highly microporous materials with mainly narrow micropores, width ≤ 1 nm [84,137].

Table 4.8.1 Textural parameters of the adsorbents studied in this work.

Adsorbent	S_{BET} (m^2/g)	v_{total} (cm^3g^{-1})[a]	v_{micro}(cm^3g^{-1})[b]	v_{meso}(cm^3g^{-1})[c]
CS-CO_2	602	0.245	0.211	0.034
CS-$ZnCl_2$	1391	0.859	0.240	0.619
ACM	1446	0.779	0.692	0.088
Fe-BTC	1213	0.625	0.487	0.139

[a] evaluated by the amount of N_2 adsorbed at $P/P^0 = 0.95$
[b] determined by the t-plot method
[c] determined by the difference between v_{total} and v_{micro}.

CS-$ZnCl_2$ has a S_{BET} of 1391 m²/g (see Table 4.8.1) and micro/mesoporosity in the 5–60 Å range (see Figure 4.8.1). The N_2 adsorption-desorption isotherm of this material is the type I(b), which has pore size distributions over a broader range, including large micropores and narrow mesopores (≤ 25 Å). Finally, ACM and Fe-BTC have micro/mesoporosity distributions in the 5–40 Å and 5–30 Å ranges, respectively, as shown in Figure 4.8.1. Their surface areas are 1446 and 1213 m²/g, respectively (see Table 4.8.1). The N_2 adsorption-desorption isotherms for these two materials are also type I(b) with negligible hysteresis. Fe-BTC is reported in the literature with a small surface area (480 m^2/g) and total pore volume of 0.27 cm^3/g [138]. These differences in structural characteristics can be attributed to the material preparation conditions [139]. For example, in the literature, doped bimetallic materials have shown that the improvement in their structural properties is primarily due to the absence of charge-balancing anions [140] resulting in structures with larger surface area and pore volume.

The FTIR spectra of CS-CO_2, CS-$ZnCl_2$, ACM, and Fe-BTC are shown in Figure 4.8.2. All materials have a common band around 3440 cm^{-1} attributed to stretching vibration of the hydroxyl groups of water, phenols and alcohols. Additionally, the bands located around 2923-2844 cm^{-1} correspond to the C-H stretching vibrations in the -CH_3 and -CH_2- functional groups. The bands around 1634-1619 cm^{-1} are assigned to the stretching vibrations of the C=C aromatic ring. The peak observed at 1382 cm^{-1} can also be attributed to the O-H bend frequency of phenol, while the ether structures present in the material cause stretching vibrations at 1130 cm^{-1}. In the FTIR spectrum of Fe-BTC, the bands at 1564-1372 cm^{-1} are due to the asymmetric and symmetric stretching vibrations of the carboxylate groups present in Fe-BTC [141]. Additionally, the band at the 767 cm^{-1} is due to the bending of aromatic CH bonds.

The stability of these materials was determined by thermogravimetric analysis (TGA). Furthermore, TGA also allows determination of the decomposition temperature and evaluates if the degassing process affects the structural characteristics of the adsorbents. Figure 4.8.2 shows that the CS-CO_2 and CS-$ZnCl_2$ experience a 5 % mass loss at temperatures around 350 K, which may be due to adsorbed water or gases in their microporosity. Additionally, there is a 15 % mass loss for CS-$ZnCl_2$ at temperatures above 900 K due to the decomposition of the material. Biomaterials (CS-CO_2 and CS-$ZnCl_2$) are the most stable materials studied in this work [142,143]. On the other hand, ACM experiences a significant mass loss of 25 % at temperatures below 370 K, which is attributed to water or gases adsorbed in

the material's porosity. Then, the mass loss remains constant up to a temperature of 600 K, from which this material presents a continuous decomposition until a temperature above 1200 K. This mass loss may be due to the decomposition of organic material or mineral matter present in the material. Fe-BTC experiences a 10 % mass loss at temperatures below 400 K, caused by the water from its framework. In the range of 500-700 K, a 40 % mass loss was observed due to the decomposition of its organic material [141,144]. Finally, at temperatures above 700 K, the material undergoes its ultimate decomposition.

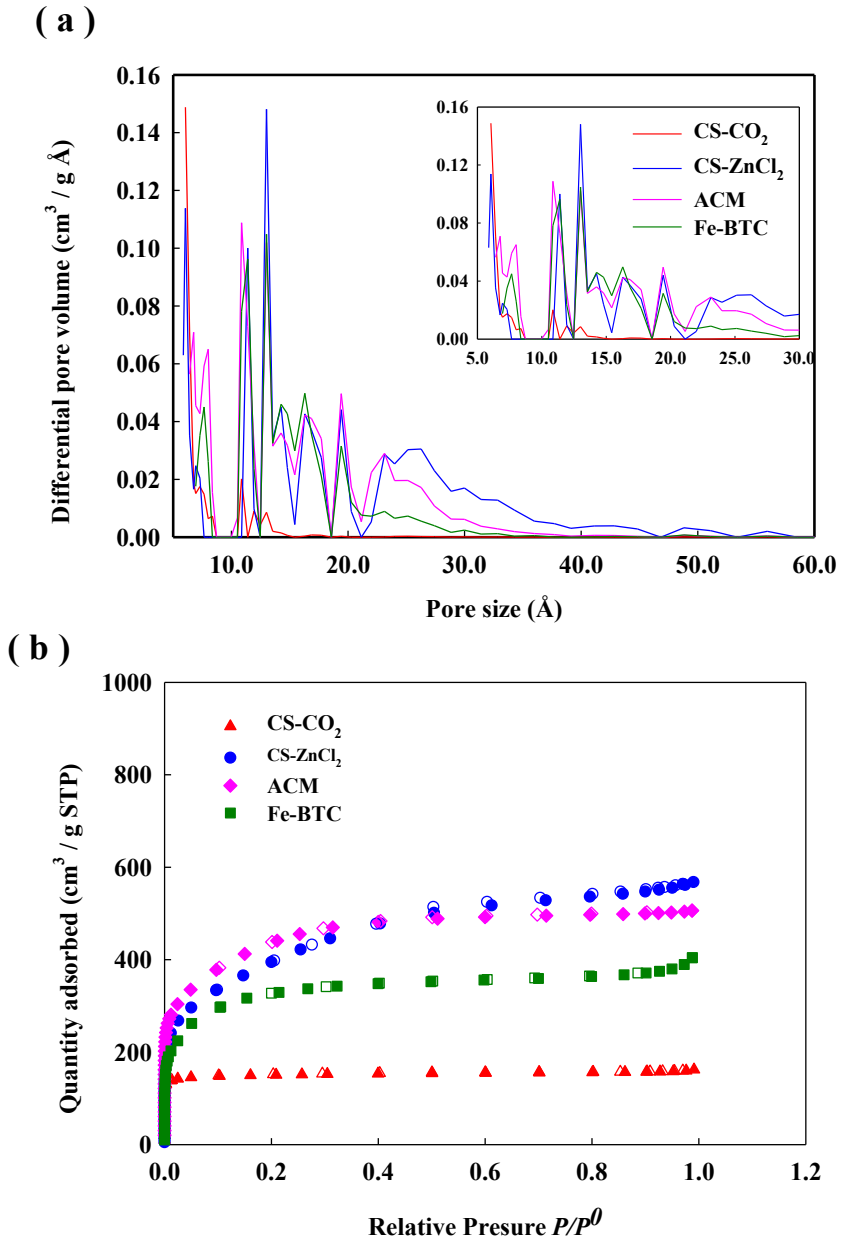


Figure 4.8.1 Pore size distribution of the adsorbents studied in this work of: (a) CS-CO_2 (red line), CS-$ZnCl_2$ (blue line), ACM (pink line) and Fe-BTC(green line); (b) nitrogen adsorption (full symbols) and desorption (empty symbols) equilibrium isotherms at 77 K for CS-CO_2 (red up triangles), CS-$ZnCl_2$ (blue circles), ACM (pink diamond) and Fe-BTC(green square).

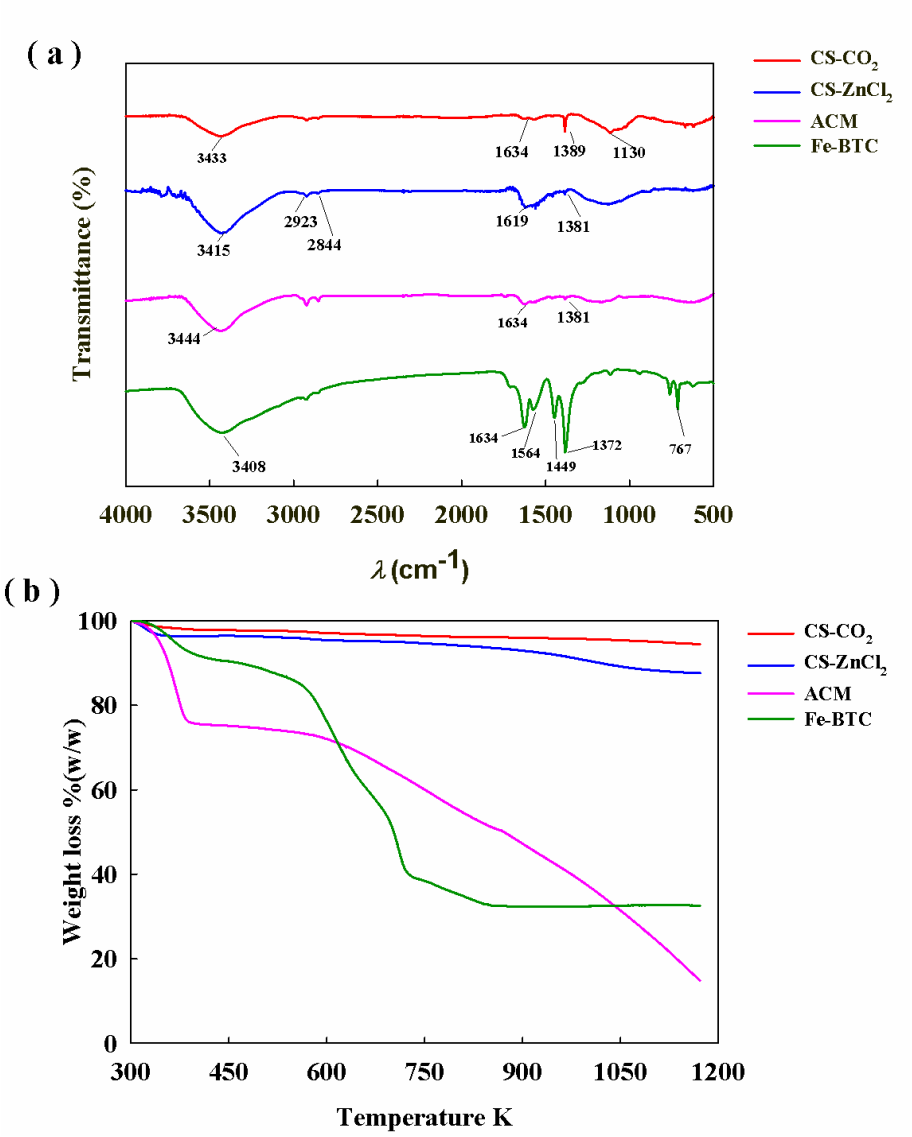


Figure 4.8.2 Characterizations of (a) FTIR spectra and (b) thermogravimetric analysis (TGA) for the adsorbents studied in this work: CS-CO_2 (red line), CS-$ZnCl_2$ (blue line), ACM (pink line) and Fe-BTC (green line).

The results of the elemental analysis are given in Table 4.8.2. As expected, CS-CO_2 and CS-$ZnCl_2$ have a high carbon content, which can be related to their origin from residual biomass rich in cellulose and hemicellulose. The variation in elemental content between these biomaterials can be explained by differences in residence time during the preparation or the different activation compounds used. On the other hand, all porous solids also exhibit high carbon and hydrogen content, which may enhance the interactions with the GHGs, favouring the adsorption.

Table 4.8.2 Elemental analysis of the materials.

	CS-CO_2	CS-$ZnCl_2$	ACM	Fe-BTC
C (wt%)	73.5	80.6	54.6	32.8
H (wt%)	0.96	1.22	2.37	3.17
N (wt%)	0.12	0.85	0.23	0.2
S (wt%)	<L.D.	<L.D.	<L.D.	<L.D.

L.D. - limit of detection

4.8.2.2 Adsorption equilibrium of GHGs

The details of the adsorption equilibrium determination are provided in Section 4.3, while adsorption equilibria of R-32, R-125, R-134a, R-143a, CO_2 and CH_4 on the four different porous solids (CS-CO_2, CS-$ZnCl_2$, ACM and Fe-BTC) are shown in Figures 4.8.3-4.8.8. These equilibria were measured at 283.15, 303.15 and 323.15 K. The adsorption equilibria of R-32, R-125, R-134a, and R-143a were measured below 80 % of the saturation pressure of each gas to prevent capillary condensation in the adsorbents. The temperature dependence of the adsorption equilibria is evaluated because it is needed for an efficient design of any adsorption and separation process. No hysteresis was observed in all adsorption equilibria, indicating only physical adsorption.

The adsorption-desorption equilibria of the pure components were initially fitted using the Toth adsorption model (see Figure 4.8.9), which did not provide a satisfactory fit. Therefore, the Dual Site Langmuir (DSL) model was selected because it accurately describes the adsorption process. The use of the DSL model is necessary due to the heterogeneity of the porous solid matrix surface, the variety of functional groups, and the development of porosity that produces multiple adsorption sites with varying affinities between the adsorbent and adsorbate [145–147] The dual-site Langmuir (DSL) model is described as follows:

$$q_t = q_{m1,i}\frac{b_{1i}p_i}{1+b_{1i}p_i} + q_{m2,i}\frac{b_{2i}p_i}{1+b_{2i}p_i} \qquad 4.8.1$$

where $q_{m1,i}$ and $q_{m2,i}$ are the maximum adsorption capacity of component *i* in each of the two locations, b_{1i} and b_{2i} are the affinity constant (MPa^{-1}) of component *i* in the two locations, and *p* is the partial pressure [28]. The affinity parameters, b_{1i} and b_{2i}, can be expressed in the form of a temperature-dependent equation and can be obtained by Van't Hoff equation:

$$b_{\mathrm{ji}} = b_{j\infty}\,\exp\left(\frac{-\Delta H_{\mathrm{i}}}{R_{\mathrm{g}}T}\right) \qquad 4.8.2$$

where b_∞ is the adsorption affinity constant at an infinite temperature, *T* is the temperature, R_{g} is the ideal gas constant and $-\Delta H_{ji}$ is the isosteric heat of adsorption of gas *i* on site *j*. On the other hand, Tables 4.8.3 shows the parameters obtained from the DLS model, while the fittings are displayed in Figures 4.8.3-4.8.8. The average relative error (ARE) obtained from the experimental data was determined using the following equation:

$$ARE(\%) = \frac{100}{N_{exp}} \sum \frac{[q_{fit} - q_{exp}]}{q_{exp}} \quad 4.8.3$$

where N_{exp} is the number of experimental points and q_{fit} and q_{exp} are the fit and experimental adsorbed quantity.

At pressures below 1.2 MPa, the order of adsorption capacity of R-32, R-125, R-134a and R-143a on the studied materials is ACM > CS-$ZnCl_2$ > Fe-BTC > CS-CO_2, directly related to the decrease of these materials' surface area (see Table 4.8.1). The surface area or the specific microporous volume controls the adsorption capacity of these materials. Then, materials with larger pore volumes and surface areas have greater GHG saturation capacities. ACM has the highest micropore volume and shows the extreme adsorption slope at low pressure. However, CS-$ZnCl_2$ surpasses it at mid-pressures due to the larger pore volumes associated with its mesoporosity. Then, the adsorption data are in agreement with the structural properties listed in Table 4.8.1.

The CO_2 adsorption capacity of the materials follows the order of: ACM > Fe-BTC > CS-$ZnCl_2$ > CS-CO_2 (see Figure 4.8.3). This behaviour agrees with the decrease of the total specific micropore volume. Although CS-CO_2 has a smaller saturation capacity than the other materials, this biomaterial has a CO_2 adsorption capacity similar to ACM and larger than the MOF at P < 0.4 MPa.

At pressures below 0.1 MPa, the order of methane adsorption is CS-CO_2 > CS-$ZnCl_2$ > ACM > Fe-BTC. This order is consistent with the increment of the surface area and total micropore volume of these activated carbons. Moreover, Fe-BTC is not favoured in the adsorption process due to the repulsive interactions of the iron present in this MOF structure. At pressures above 0.8 MPa, the order of the materials is ACM > CS-$ZnCl_2$ > CS-CO_2 > Fe-BTC and at pressures above 1.4 MPa presents the same order of the S_{BET}: ACM > CS-$ZnCl_2$ > Fe-BTC > CS-CO_2. If Fe-BTC is excluded once more, the order is favoured by the surface area and volume of micropores. In the case of Fe-BTC, this material generates repulsion between the iron III present in its structure and the methane, which can hinder the adsorption process [148].

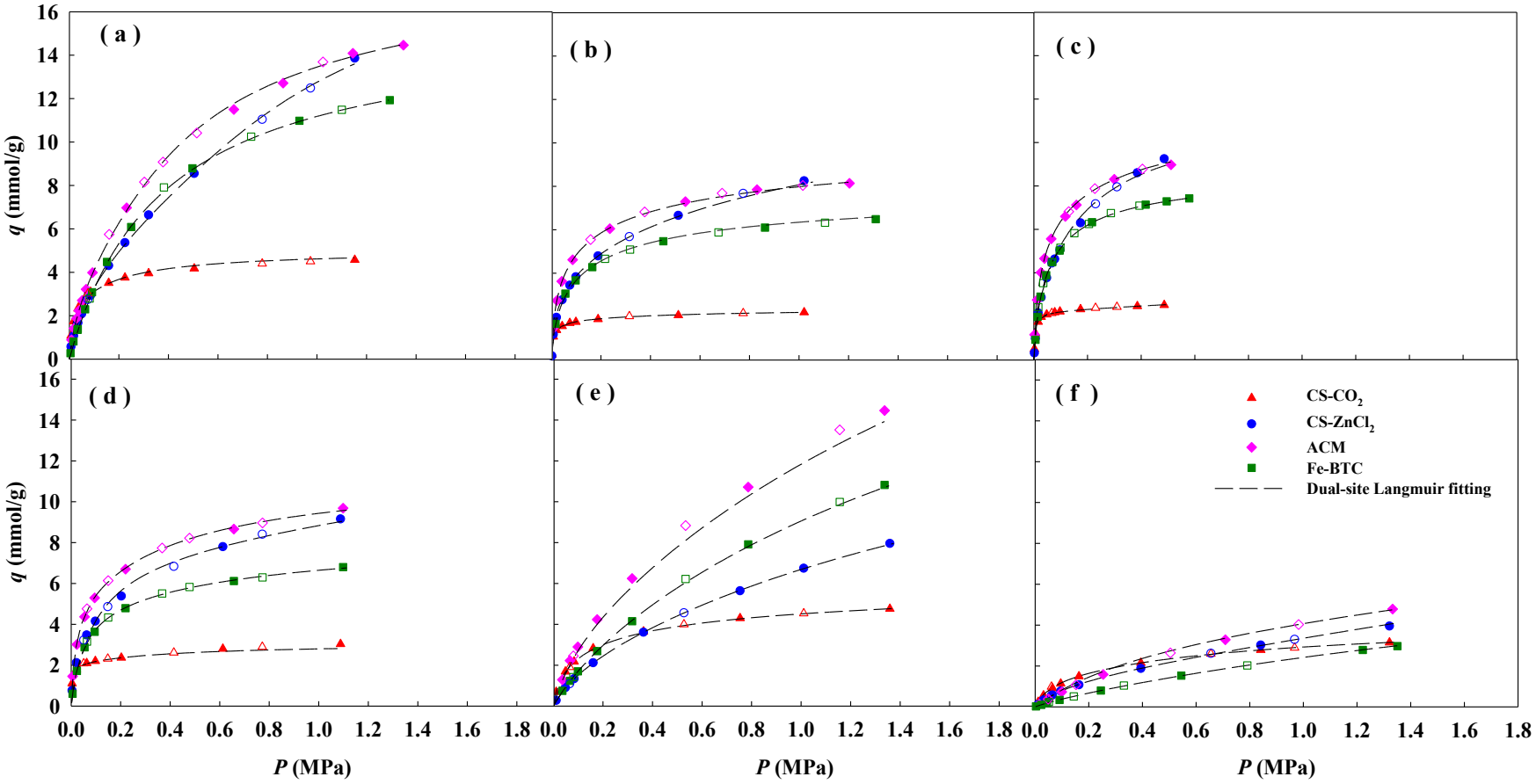


Figure 4.8.3 Characterizations of (a) FTIR spectra and (b) thermogravimetric analysis (TGA) for the adsorbents studied in this work: CS-CO_2 (red line), CS-$ZnCl_2$ (blue line), ACM (pink line) and Fe-BTC (green line).

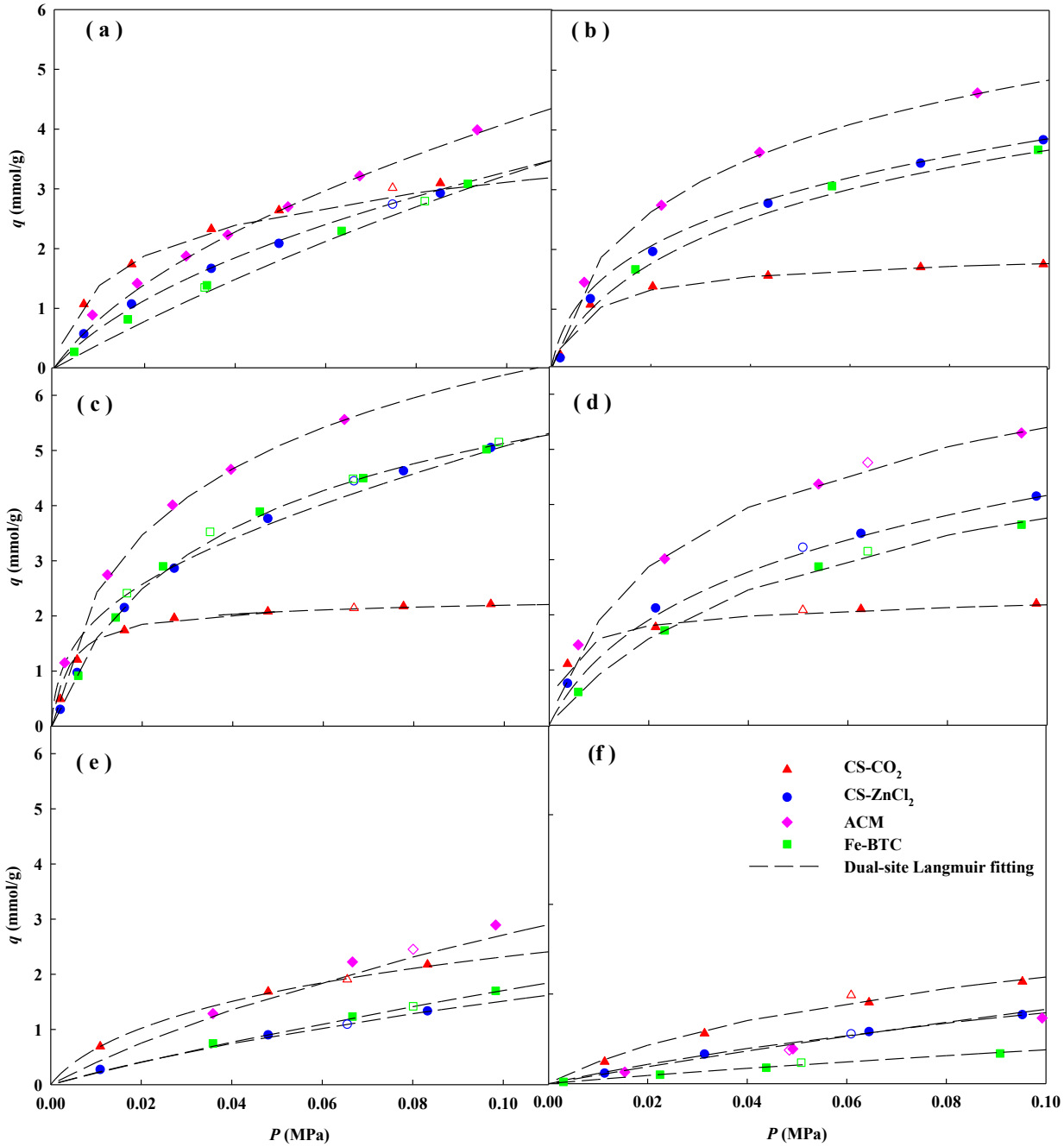


Figure 4.8.4 Adsorption (full symbols) and desorption (empty symbols) equilibrium in the pressure range 0 – 0.1 MPa of: (a) R-32; (b) R-125; (c) R-134a; (d) R-143a; (e) CO_2 and (f) CH_4 at 303.15 K

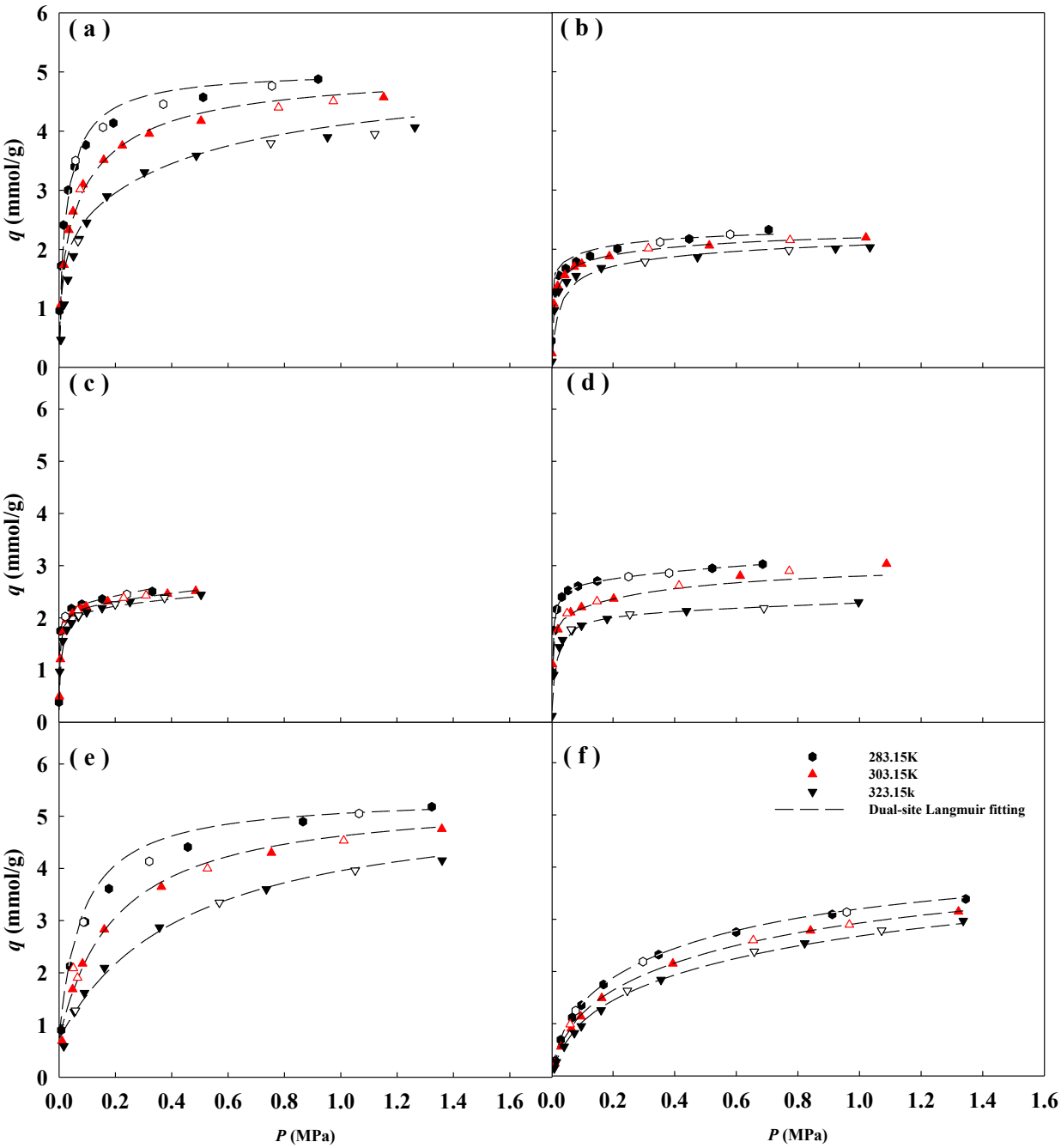


Figure 4.8.5 Adsorption (full symbols) and desorption (empty symbols) equilibrium isotherms on CS-CO_2 of: (a) R-32; (b) R-125; (c) R-134a; (d) R-143a; (e) CO_2 and (f) CH_4.

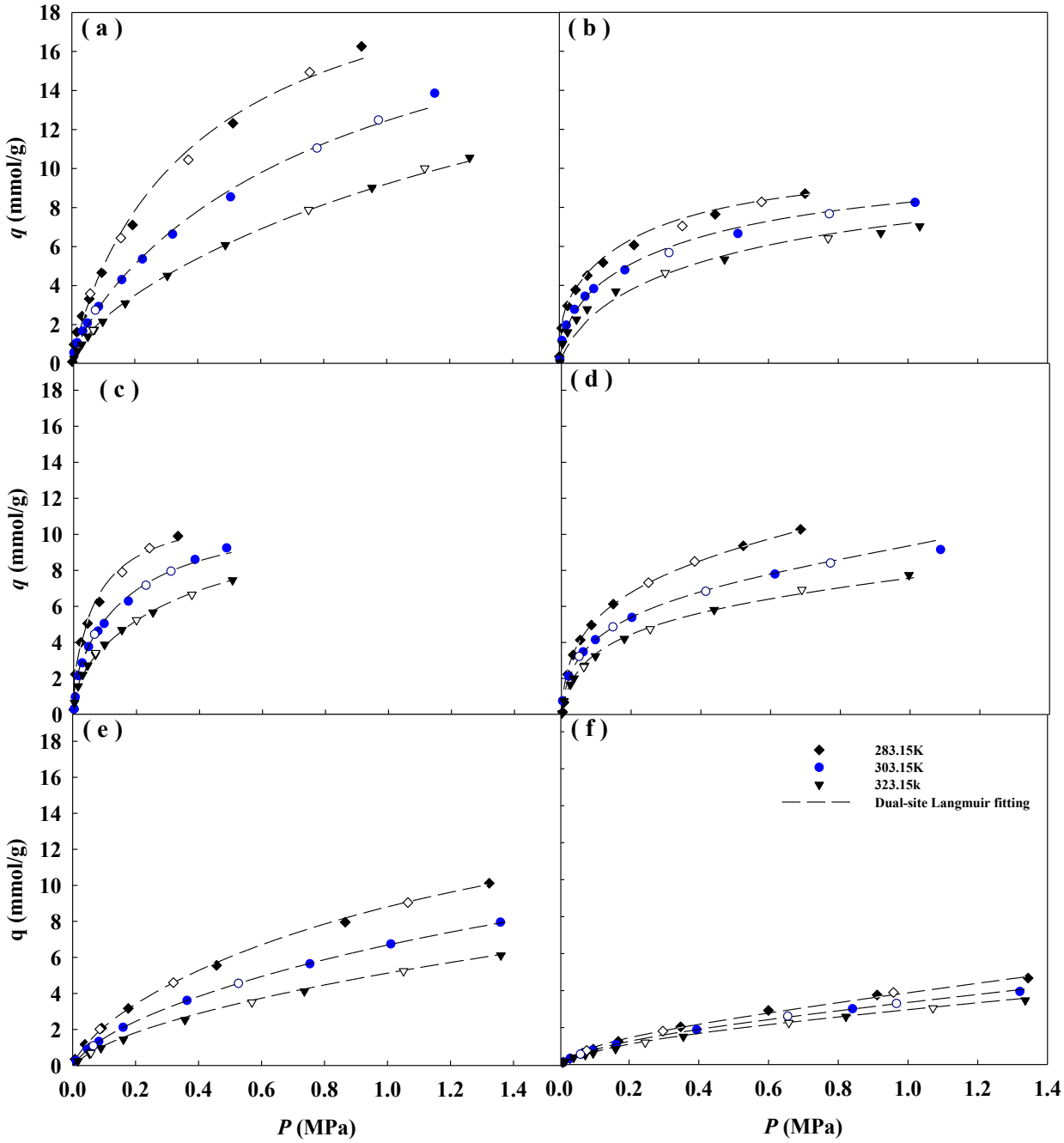


Figure 4.8.6 Adsorption (full symbols) and desorption (empty symbols) equilibrium isotherms on CS-$ZnCl_2$ of: (a) R-32; (b) R-125; (c) R-134a; (d) R-143a; (e) CO_2; and (f) CH_4.

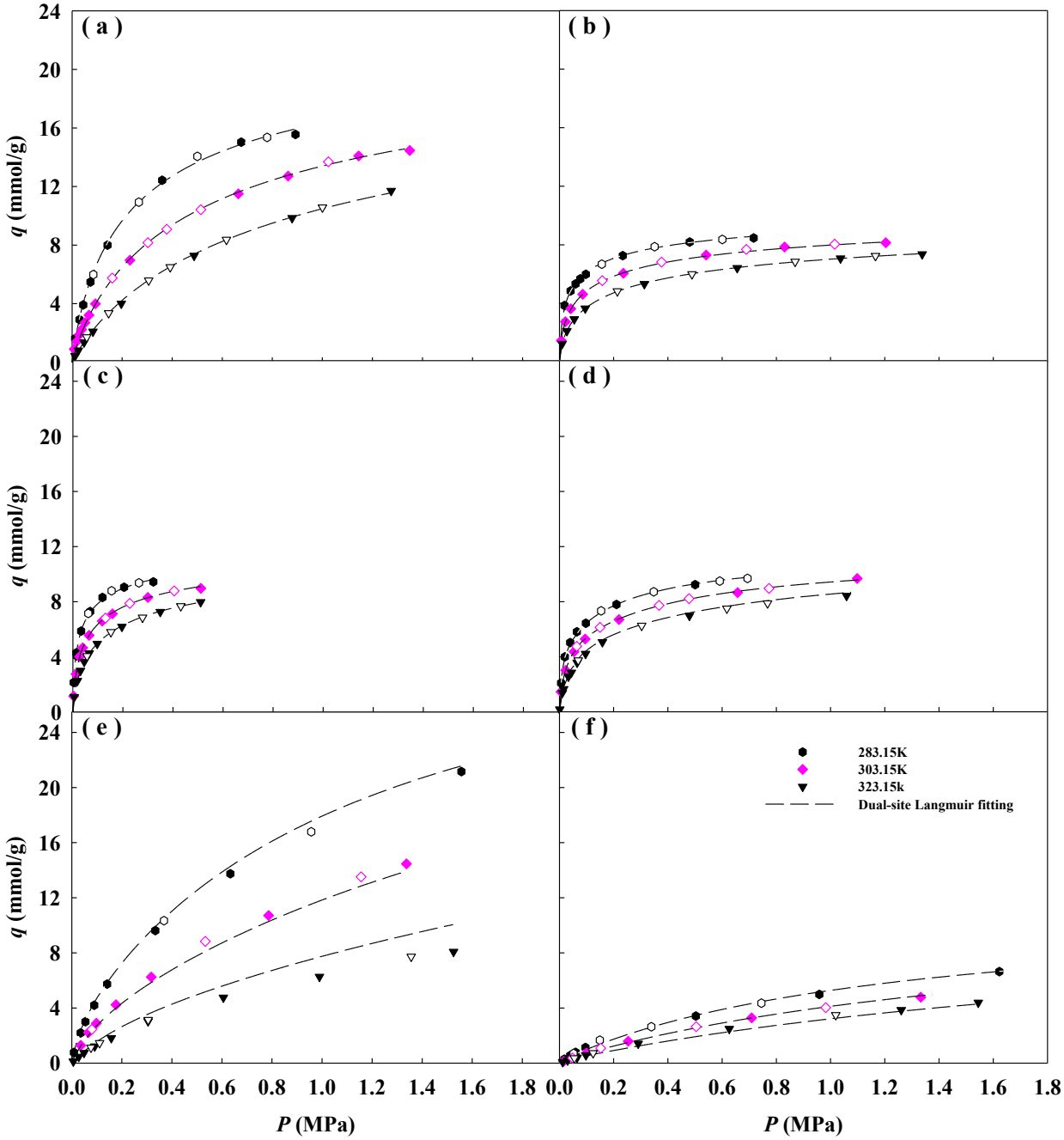


Figure 4.8.7 Adsorption (full symbols) and desorption (empty symbols) equilibrium isotherms on ACM of: (a) R-32; (b) R-125; (c) R-134a; (d) R-143a; (e) CO_2; and (f) CH_4.

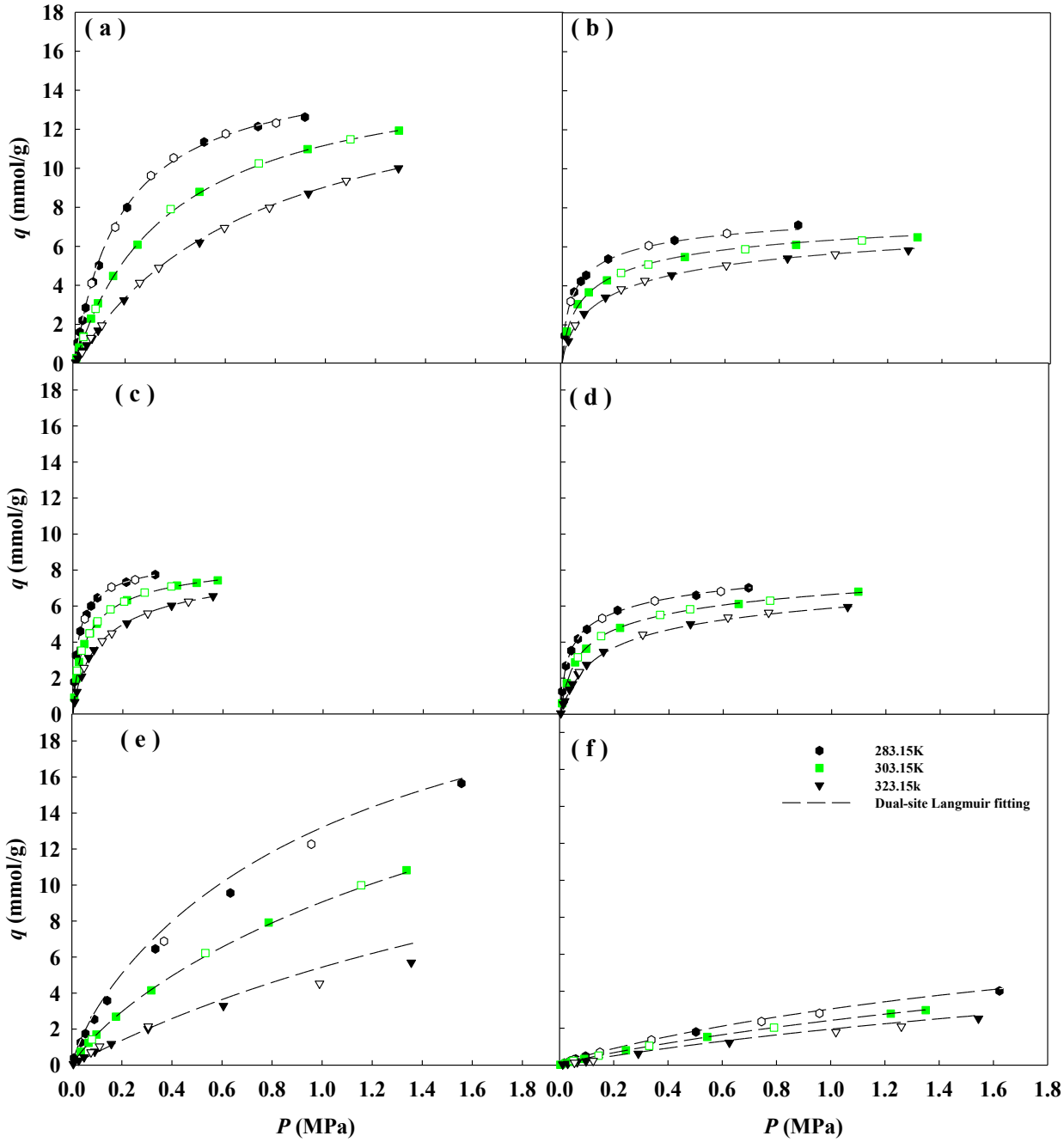


Figure 4.8.8 Adsorption (full symbols) and desorption (empty symbols) equilibrium isotherms on Fe-BTC of: (a) R-32; (b) R-125; (c) R-134a; (d) R-143a; (e) CO_2; and (f) CH_4.

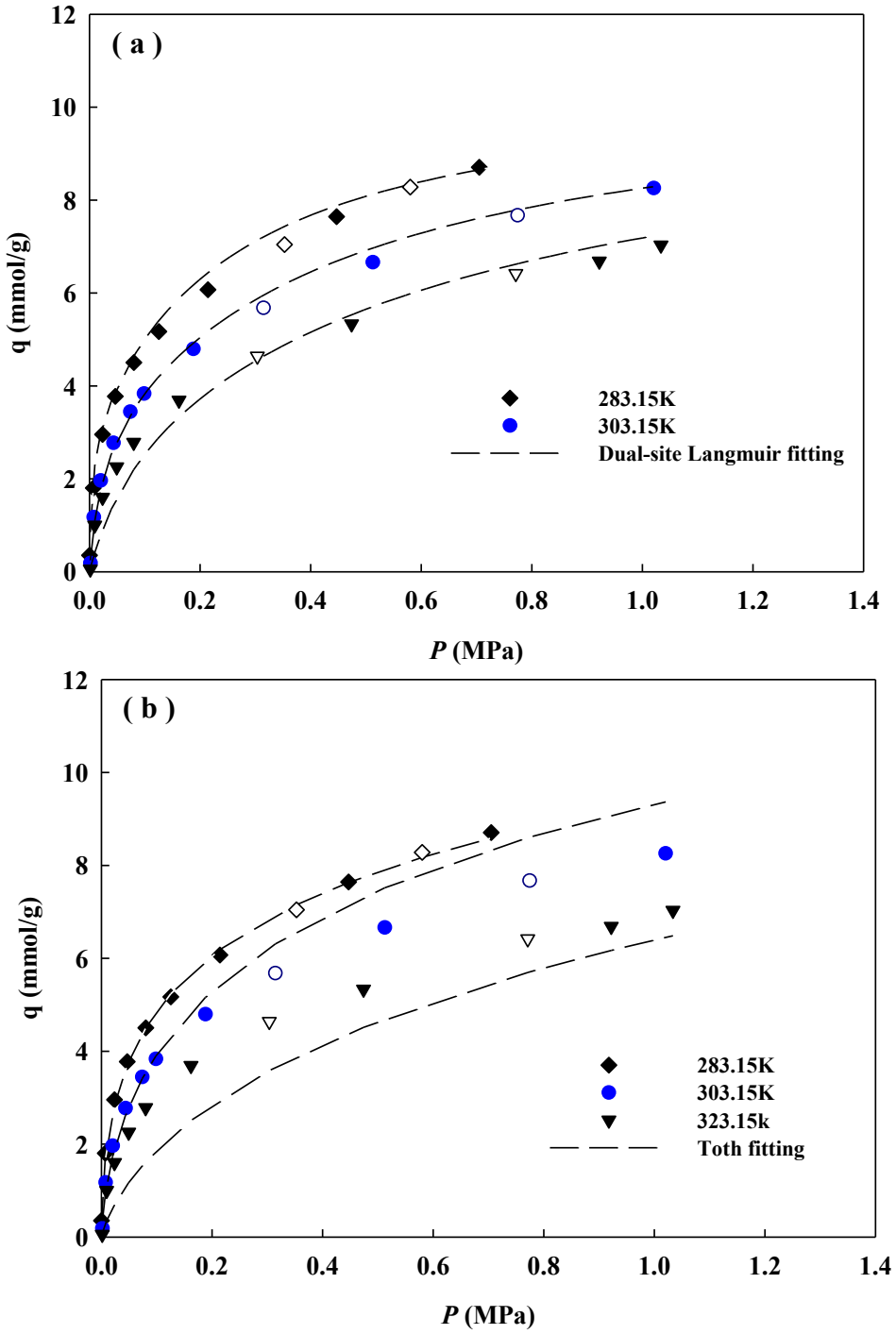


Figure 4.8.9 Comparison of the fitting obtained for CS-$ZnCl_2$ with the adsorption models: (a) Dual site Langmuir; and (b) Toth.

Table 4.8.3 DSL model parameters for sorption of R-32, R-125, R-134a, R-143a, CO_2 and CH_4 at 283.15 K, 303.15 K, and 323.15 K.

Adsorbents	Gases	q_m (mol·kg^{-1})		b (M·Pa^{-1})		ΔH_i (kJ·mol^{-1})		ARE
		q_{m1}	q_{m2}	b_1	b_2	$(\Delta H_i)_1$	$(\Delta H_i)_2$	
CS-CO_2	R-32	2.99	2.21	1.85E-07	123	43.6	4.35E-03	3.18
	R-125	0.633	1.76	4.43E-05	2.68E-06	27.3	44.7	3.87
	R-134a	9.78	1.85	6.96E-05	2.32E-06	28.4	48.3	3.45
	R-143a	2.36	1.20	2.544E-06	2.711E-09	44.1	48.5	4.88
	CO_2	4.67	0.728	9.70E-06	25.2	33.2	140	5.44
	CH_4	1.36	3.05	0.261	8.92E-03	10.7	12.3	3.82
CS-$ZnCl_2$	R-32	20.8	1.62	3.79E-05	23.0	25.9	3.27E-03	5.61
	R-125	2.89	7.85	1.20E-08	6.77E-04	55.7	20.4	4.39
	R-134a	2.20	2.38	8.04E-03	4.25E-04	26.1	16.9	3.73
	R-143a	7.67	25.4	2.026	3.68E-08	4.21	36.7	4.56
	CO_2	1.68	17.7	1.66E-02	2.71E-04	16.0	18.5	3.48
	CH_4	1.37	48.9	0.161	2.24E-03	9.54	7.63	5.83
ACM	R-32	18.2	41.6	6.07E-05	1.40E-02	26.9	4.01E-03	5.57
	R-125	4.12	5.56	7.62E-06	2.96E-05	41.2	28.7	2.29
	R-134a	6.97	3.35	2.90E-05	3.67E-04	31.7	32.4	1.82
	R-143a	5.03	3.56	9.17E-05	6.73E-05	31.1	24.4	2.28
	CO_2	2.96	32.7	2.83E-05	5.37E-06	32.2	28.2	4.81
	CH_4	11.4	0.126	1.34E-03	1.34E-06	15.1	42.6	5.66
Fe-BTC	R-32	14.9	0.632	5.73E-05	1.35	27.1	3.27E-02	4.33
	R-125	3.23	5.60	3.68E-06	2.79E-03	30.0	22.2	3.77
	R-134a	3.60	6.69	2.83E-05	3.63E-04	26.0	28.4	2.91
	R-143a	5.00	6.59	1.98E-03	4.70E-04	25.7	21.3	2.54
	CO_2	23.7	1.84E-11	9.34E-09	1.30	45.4	3.27E-03	5.94
	CH_4	10.1	0.178	3.11E-03	8.41E-07	11.4	41.4	5.74

4.8.2.3 Henry Law's constant

In the design of separation processes, it is important to consider the isosteric heat of adsorption (Q_{st}) because the separation can present temperature peaks that affect the capacity of the materials. Therefore, the theoretical Q_{st} was calculated from the experimental adsorption equilibria. First, the experimental data were fitted to the virial equation, following the methodology described in Section 4.4. The parameters obtained from this fitting are presented in Tables 4.8.4. In addition, by linearizing the Clausius–Clapeyron equation, linear isosteric plots for different adsorbed quantities were generated, allowing the determination of Q_{st} (see Figure 4.8.10- 4.8.13).

The Q_{st} for R-32, R-125, R-134a, and CO_2 is in the range of 20-60 kJ/mol (see Figure 4.8.14), while for CH_4 it varies between 8-18 kJ/mol. The Q_{st} of GHGs on ACM, Fe-BTC, and CS-$ZnCl_2$ materials tends to have a line shape and a gentle slope. Initially, the adsorbate adheres to the narrow pores of the adsorbent, generating strong interactions and high isosteric heat. Once these high-energy sites are saturated, the adsorbate molecules begin to occupy lower-energy pores, reducing the isosteric heat [67,149–151]. However, the Q_{st} of R-134a, CO_2 and CH_4 on CS-CO_2 increases and then begins to decrease. This is because gas molecules must occupy energetically stable locations, which allow them to interact and generate heat release [149–151]. The Q_{st} of R-32, R-125, and R-143a on CS-CO_2 exhibit unusual behaviour due to their structural characteristics. This material has a well-developed porosity (see Figure 4.8.1a), with pores of different energy levels. These pores fill up and the available energy decreases, reducing the Q_{st}. However, once these sites are occupied, the adsorbed molecules interact with others, promoting adsorption and gradually increasing the heat release during the process [67,151–153].

Table 4.8.4 Viral model parameters obtained for R-32, R-125, R-134a, R-134a, CO_2 and CH_4.

CS-CO_2						
Parameters	**R-32**	**R-125**	**R-134a**	**R-143a**	**CO_2**	**CH_4**
A_0 (kg/mol)	-4.69	-1.12	-1.96E-02	-16.3	0.210	1.20
A_1 (kg·K/mol)	1583	-730	-174	4314	54.9	-308
B_0 ((kg/mol)^2)	2.16	3.59E-02	-1.68E-02	23.5	0.244	-0.492
B_1 ((kg·K/mol)^2)	-704	1336	352	-6578	-93.6	188
C_0 ((kg/mol)^3)	-2.39E-01	0.316	-2.83E-03	-5.73	-5.71E-02	5.53E-02
C_1 ((kg/mol)^3)	84.2	-388	-23.6	1663	21.3	-22.5
K_∞ (mol/(kg·MPa))	2.35E-08	6.98E-05	1.58E-03	2.67E-02	2.60E-03	0.741
-ΔH (kJ/mol)	59.3	33.9	35.3	18.7	26.7	8.61
ARE (%)	0.331	7.65	6.71	3.13	0.100	0.228
CS-$ZnCl_2$						
Parameters	**R-32**	**R-125**	**R-134a**	**R-143a**	**CO_2**	**CH_4**
A_0 (kg/mol)	0.360	-0.539	0.715	-0.191	0.291	3.06
A_1 (kg·K/mol)	-52.8	292	-0.318	105	-16.1	-807

B_0 ((kg/mol)^2)	-7.76E-02	-3.62E-02	-0.176	0.193	-0.160	-1.63
B_1 ((kg·K/mol)^2)	17.4	-1.62	13.9	-54.7	35.7	454
C_0 ((kg/mol)^3)	3.92E-03	1.28E-02	7.26E-03	-1.63E-02	1.62E-02	0.237
C_1 ((kg/mol)^3)	-0.962	-3.33	-0.111	4.50	-4.09	-67.0
K_∞ (mol/(kg·MPa))	5.88E-03	4.10E-05	4.03E-03	6.41E-02	4.79E-03	12.2
-ΔH (kJ/mol)	24.1	40.9	31.7	20.0	6.82E-02	22.2
ARE (%)	1.46	4.23	7.81	6.16	21.8	1.22

ACM

Parameters	R-32	R-125	R-134a	R-143a	CO_2	CH_4
A_0 (kg/mol)	-0.562	2.23	2.05	-0.143	0.405	-1.21
A_1 (kg·K/mol)	220	-603	-447	94.2	-92.3	393
B_0 ((kg/mol)^2)	8.28E-02	-0.533	-0.538	1.27E-02	-4.41E-02	0.684
B_1 ((kg·K/mol)^2)	-31.0	157	128	-2.46	11.5	-203
C_0 ((kg/mol)^3)	-2.61E-03	3.62E-02	4.11E-02	5.17E-05	6.85E-04	-7.39E-02
C_1 ((kg/mol)^3)	1.06	-10.3	-9.82	-2.30E-02	-0.173	21.7
K_∞ (mol/(kg·MPa))	4.91E-05	0.658	1.04	6.68E-04	1.42E-04	1.90E-02
-ΔH (kJ/mol)	36.7	16.9	18.5	33.5	31.7	15.7
ARE (%)	0.537	5.31	1.04	0.321	1.402	0.540

Fe-BTC

Parameters	R-32	R-125	R-134a	R-143a	CO_2	CH_4
A_0 (kg/mol)	-0.756	0.190	1.25	-1.18	0.414	-0.832
A_1 (kg·K/mol)	266	-66.8	-359	383	-93.7	339
B_0 ((kg/mol)^2)	0.168	5.15E-02	-0.148	0.190	-6.28E-02	0.429
B_1 ((kg·K/mol)^2)	-56.4	2.24	49.1	-49.7	16.2	-161
C_0 ((kg/mol)^3)	-8.94E-03	3.08E-03	8.02E-04	3.34E-04	1.55E-03	-5.62E-02
C_1 ((kg/mol)^3)	3.07	-1.31	7.47E-02	2.58E-02	-0.381	20.7
K_∞ (mol/(kg·MPa))	8.29E-05	3.98E-03	0.157		2.12E-04	3.12E-03
-ΔH (kJ/mol)	33.8	25.2	18.6	35.4	29.1	18.4
ARE (%)	0.289	1.06	0.505	1.71	1.25	0.940

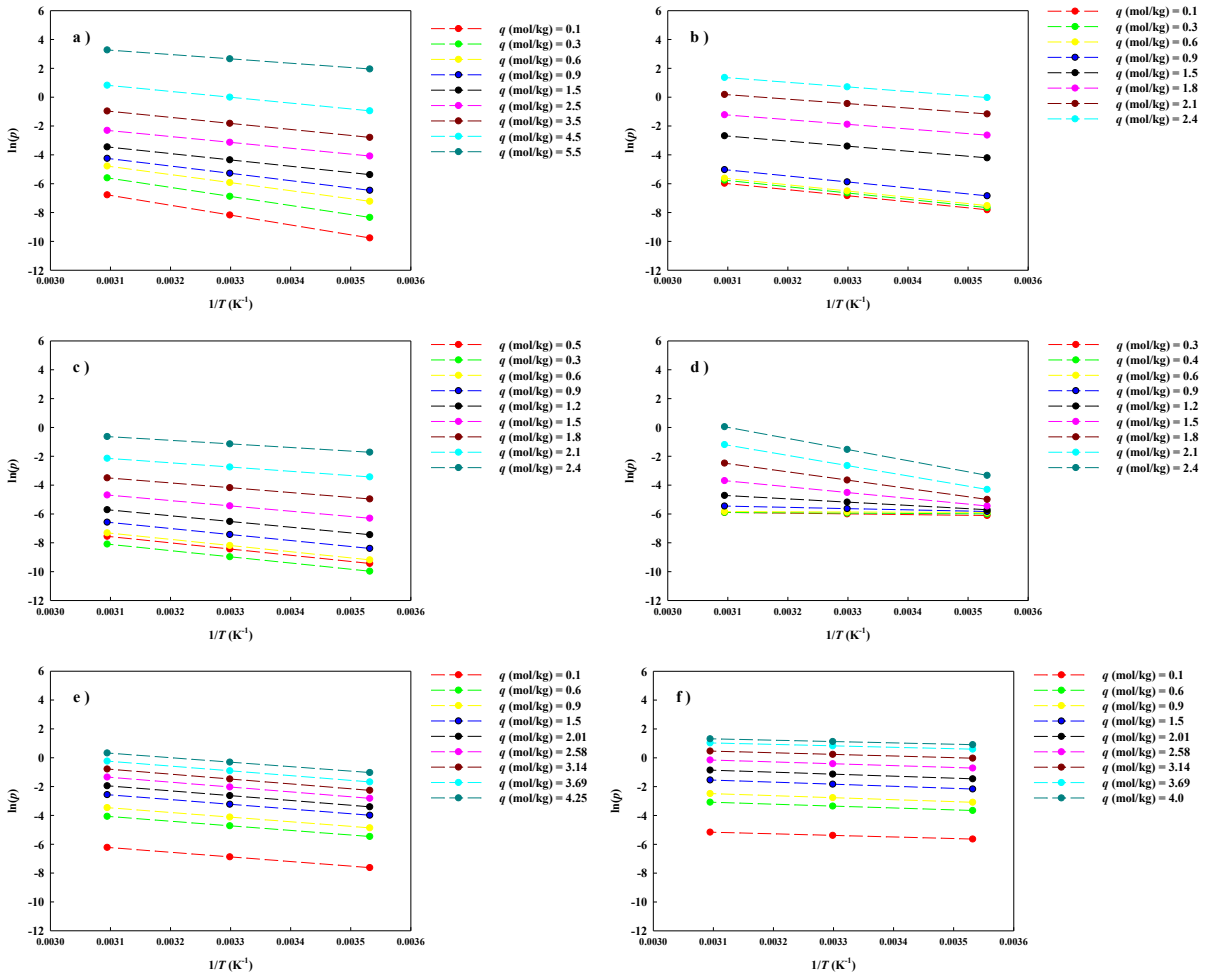


Figure 4.8.10 Adsorption isosteres on CS-CO_2 of: (a) R-32; (b) R-125; (c) R-134a; (d) R-143a; (e) CO_2 and (f) CH_4 in the temperature range 283.15-323.15 K.

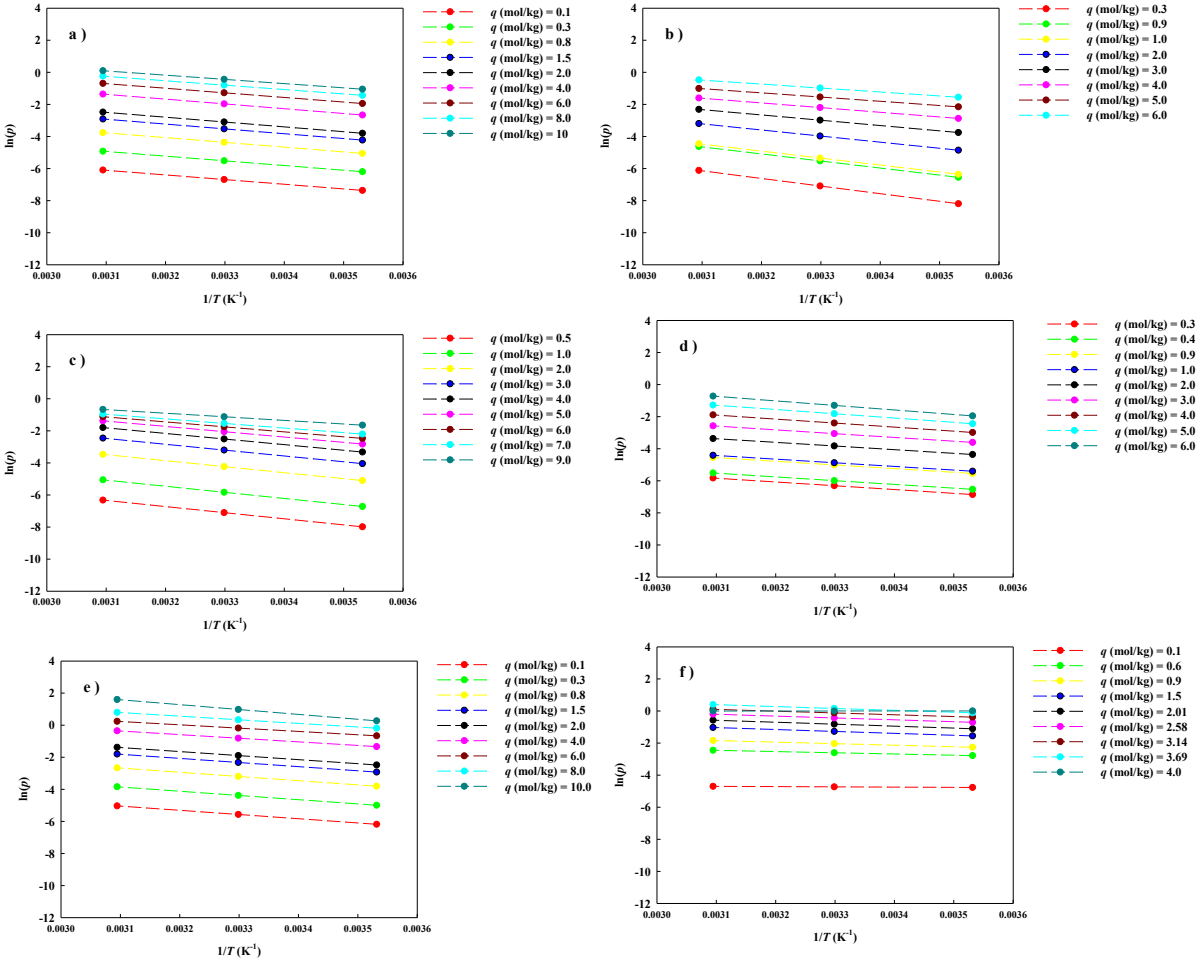


Figure 4.8.11 Adsorption isosteres on CS-$ZnCl_2$ of: (a) R-32; (b) R-125; (c) R-134a; (d) R-143a; (e) CO_2 and (f) CH_4 in the temperature range 283.15-323.15 K.

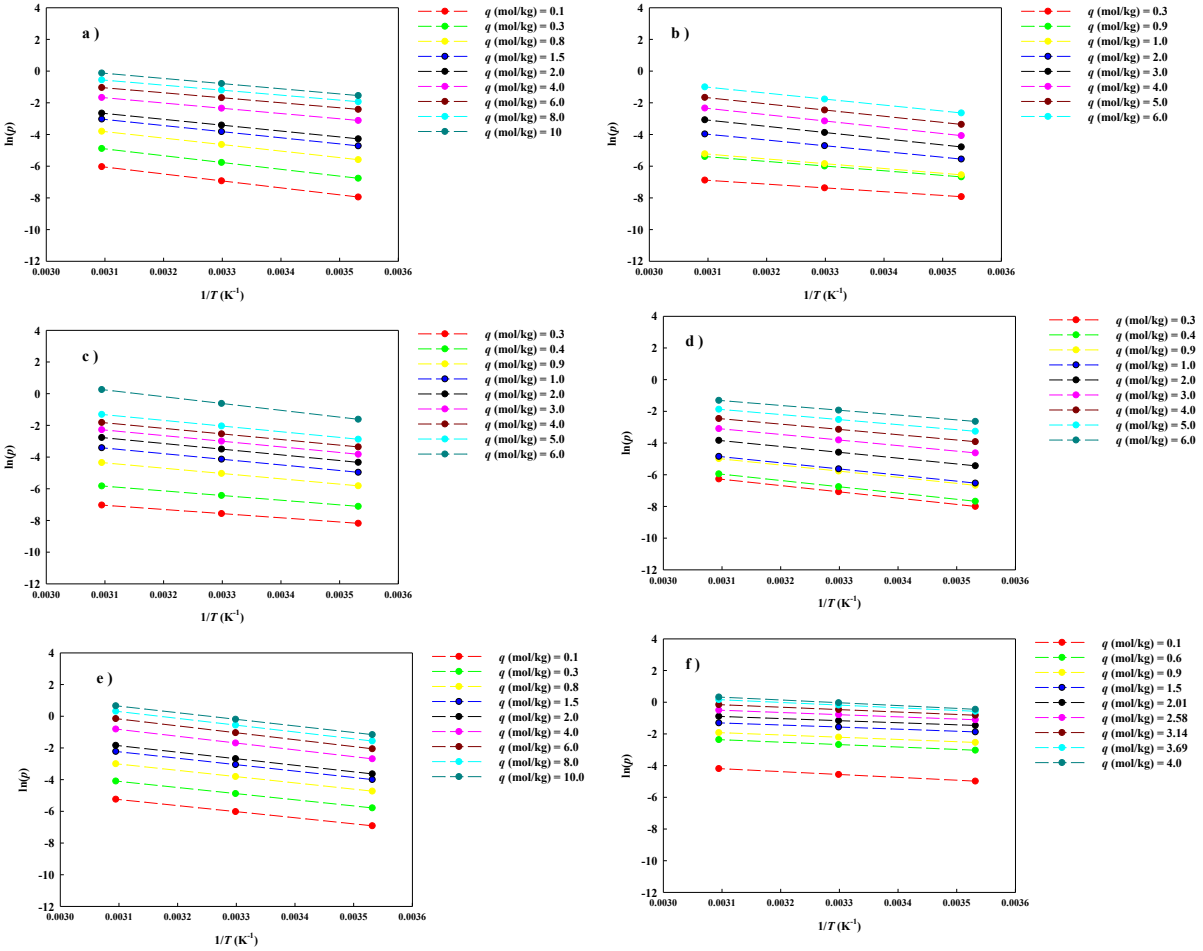


Figure 4.8.12 Adsorption isosteres on ACM of: (a) R-32; (b) R-125; (c) R-134a; (d) R-143a; (e) CO_2 and (f) CH_4 in the temperature range 283.15-323.15 K.

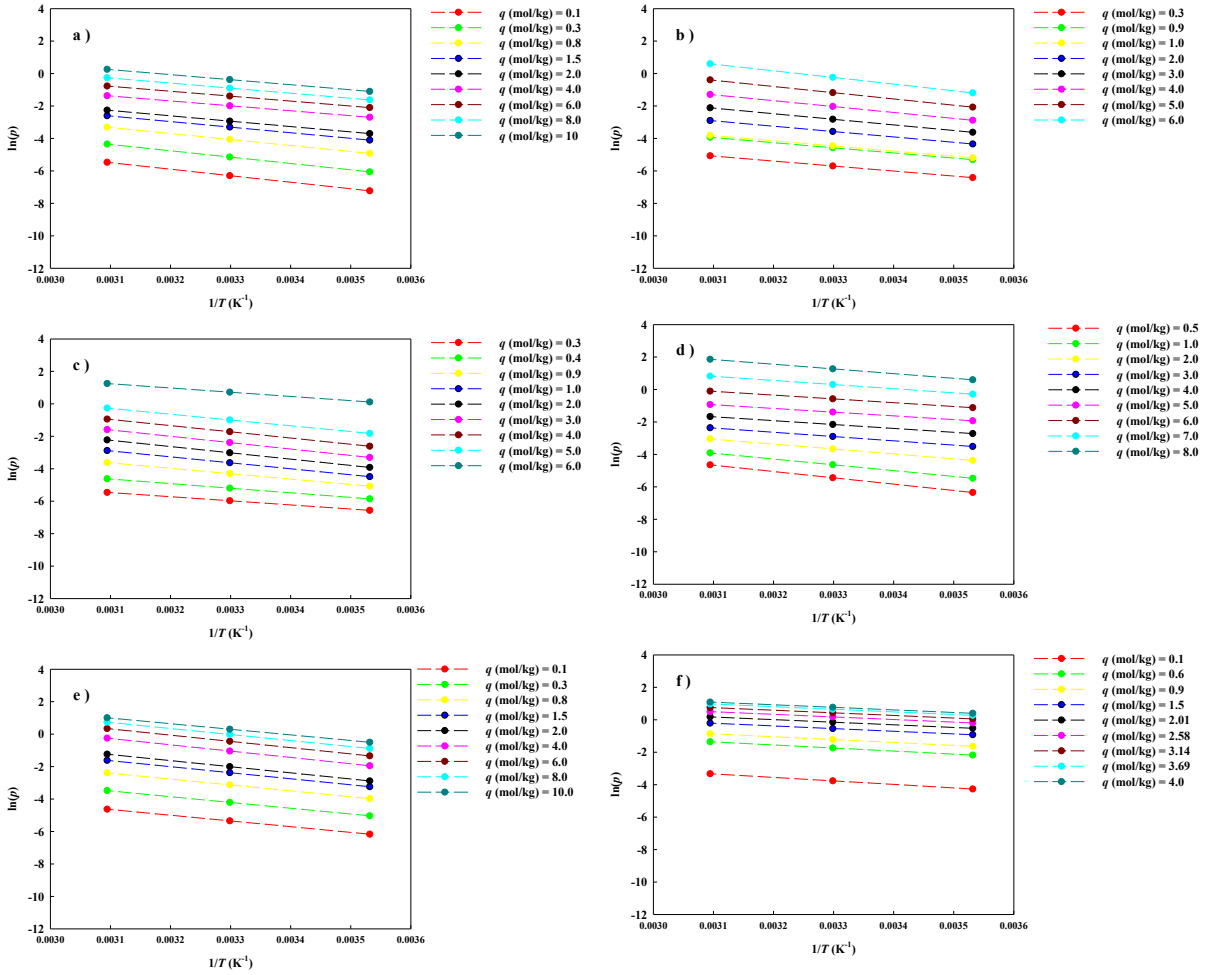


Figure 4.8.13 Adsorption isosteres on Fe-BTC of: (a) R-32; (b) R-125; (c) R-134a; (d) R-143a; (e) CO_2 and (f) CH_4 in the temperature range 283.15-323.15 K.

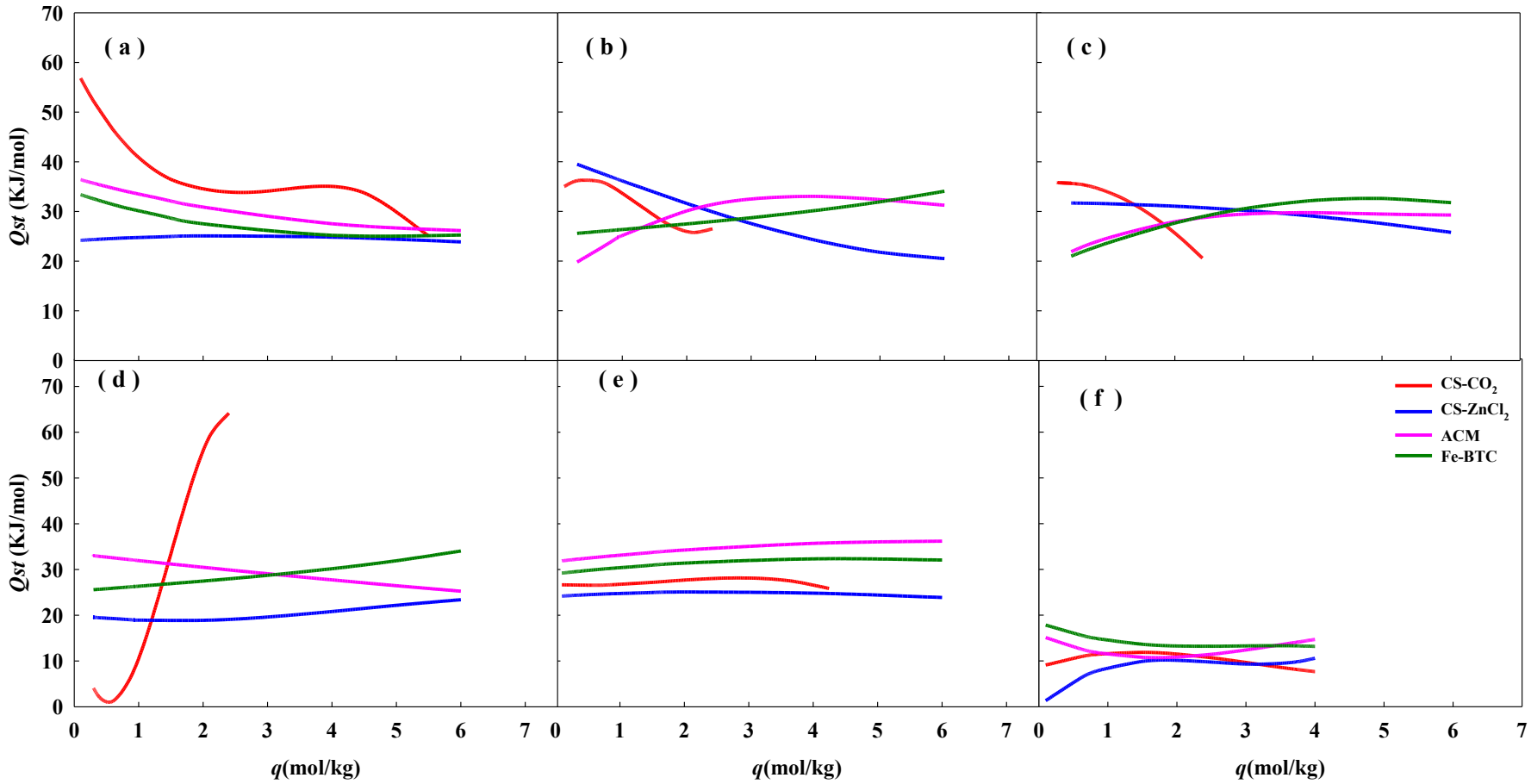


Figure 4.8.14 Isosteric heat of adsorption of: (a) R-32; (b) R-125; (c) R-134a; (d) R-143a; (e) CO_2; and (f) CH_4 at 303.15 K.

4.8.2.4 Prediction of the GHG separation using the Ideal Adsorption Solution Theory (IAST)

The design and optimisation of efficient technology to separate and purify the commercial mixtures of GHGs, most used in European industries, has aroused great interest. In some cases, there is no standardised technology to capture and separate these GHGs at the end of the life cycle of the equipment containing them. The performance of the different separations for commercial blends can be theoretically calculated through selectivity. The prediction of the multicomponent composition of the adsorbed phase was determined using Ideal Adsorption Solution Theory (IAST) [27,72,89,154], for the following commercial blends of GHGs: R-410A (R-32/R-125, 50/50 wt %, data in Figure 4.8.15 , R-407C (R-32/R-125/R-134a, 23/25/52 wt %, data in Figure 4.8.16), R-404A (R-125/R-143a/R-134a, 44/52/4 wt %, data in Figure 4.8.17) at 303.15 K in the pressure ranges of 0.1-1.0 MPa. A pressure limitation in these commercial blends was applied to avoid capillary condensation by saturation. The CO_2/CH_4 mixture (65/35 wt %) was determined at 303.15 K in the pressure range of 0.1- 1 MPa (see Figure 4.8.17). The selectivity for the solid–fluid system was evaluated in accordance with the methodology outlined in Section 4.5.

The selectivity for the commercial blend R-410A is shown in Figure 4.8.15 for the four porous solid matrices. At $P < 0.1$, the order of the materials is CS-$ZnCl_2$ > ACM > Fe-BTC > CS-CO_2, which coincides with the decrease in the total pore volume of the materials (see Table 1). In this case, the R-125 size is higher than the R-32, which plays an important role in separating this commercial refrigerant blend R-410A. Then, a larger number of molecules can be packed into the materials that have a larger volume. However, at $P > 0.1$ MPa, the best performance is obtained for commercial activated carbon ACM with values similar to CS-$ZnCl_2$. Under these pressures, materials with a higher surface area allow for the storage of a greater number of molecules. On the other hand, in the separation of R-32 over R-125, the CS-CO_2 material is more favoured because this material has the smallest pores, facilitating the adsorption of small gases.

The selectivity of the commercial blend R-407C is displayed in Figure 4.8.16. To understand the selectivity of this refrigerant blend, it was divided into the binary mixtures R-125/R-32, R-134a/R-125 and R-134a/R-32. The binary mixtures R-125/R-32 and R-134a/R-32 tend to have similar behaviour. At $P < 0.1$ MPa, the order of the binary mixtures is given by CS-$ZnCl_2$ > ACM > Fe-BTC > CS-CO_2, which corresponds again to the decrease of the total pore volume of the materials. The molecules of R-125 and R-134a are larger than R-32 and it is easier to adsorb in materials with high total pore volume and larger pores, as expected. However, for $P > 0.1$ MPa, the selectivity tends to decrease in the following order: ACM > CS-$ZnCl_2$ > Fe-BTC > CS-CO_2. This order corresponds to the decreasing order of the surface area of the materials because a greater surface area can store more gas molecules.

However, it is important to note that the activated carbons ACM and CS-$ZnCl_2$ have similar values over the range of pressures studied in this work.

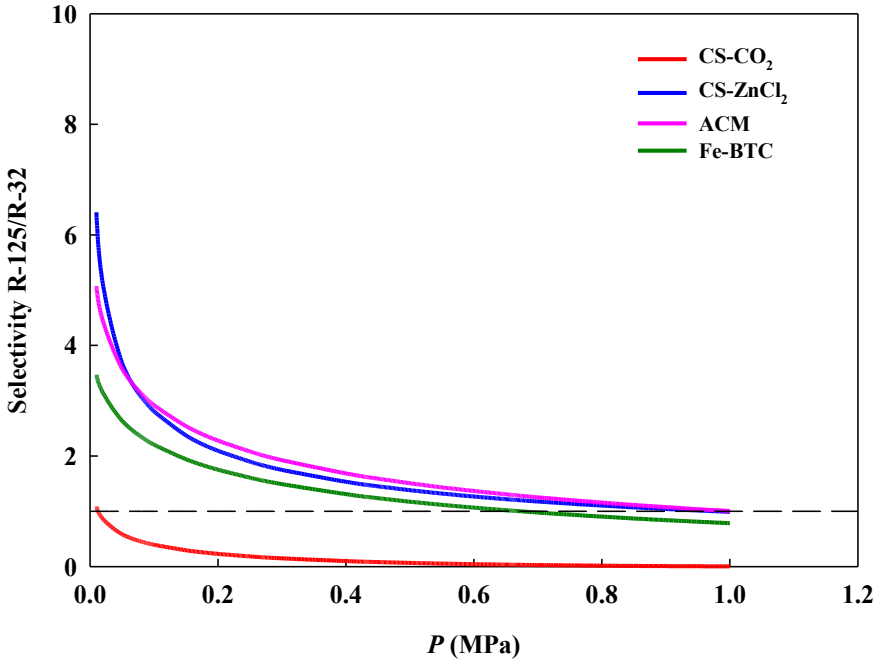


Figure 4.8.15 Selectivity of CS-CO_2 (red line), CS-$ZnCl_2$ (blue line), ACM (pink line) and Fe-BTC (green line) to R-32 over R-125 as a function of pressure at 303.15 K, for R-410A blend ($y_{R-32} = 0.7$ and $y_{R-125} = 0.3$).

Figure 4.8.16. present the selectivity of the binary mixture R-134a/R-125. In this separation, the order of the materials is given by CS-CO_2 > Fe-BTC > ACM ≈ CS-$ZnCl_2$ and this order coincides with the increasing order of the total pore volume of the materials (see Table 4.8.1). In this case, the hydrogen atoms of F-gases can form hydrogen bonds with the oxygens present in the oxygenated functional groups at the CS-CO_2 surface (see Figure 4.8.2a), favouring the separation in the mixture R-134a/R-125.

In Figure 4.8.17, the separation of the ternary mixture R-404A is presented. The possible separation was analysed taking into account the binary mixtures R-134a/R-143a, R-134a/R-125 and R-143a/R-125. The order of materials in the separation of the binary mixture R-134a/R-143a at high pressures is: Fe-BTC > CS-$ZnCl_2$ > ACM > CS-CO_2. The order of selectivity for all materials, except Fe-BTC, follows the decrease in total pore volume (see Table 4.8.1). This total volume allows the separation and storage of gases. However, the structure and metallic centre of Fe-BTC generate a greater number of preferential adsorption sites for R-134a than for R-143a. The difference between these F-gases is in the number of fluorine atoms (R-134a has 4 fluorine atoms and R-143a has 3 atoms), which are highly electronegative. The negatively charged fluorine atoms of R-134a generate stronger interactions with the positively charged metallic centre of Fe-BTC, favouring the separation [105]. Furthermore, Figure 4.8.17 represents the selectivity of the binary mixture R-134a/R-125 and R-143a/R-125. The separation of these mixtures is influenced by the dipolar moment of the F-gases (R-143a > R-134a > R-125 with values of 2.32, 2.06, and 1.54 Debye, respectively) [105]. The dipolar moment generates greater

interactions with the functional groups on the surface of materials, improving pore filling and increasing competitive adsorption by the adsorbent [105,155]. On the other hand, in the separation of the mixture R-134a over R-125, the order of materials is CS-CO_2 > Fe-BTC > ACM > CS-$ZnCl_2$, and this order respects the increment of the total volume of the pores of the materials (see Table 4.8.1).

The separation of CO_2 and CH_4 is illustrated in Figure 4.8.18, and the selectivity values are presented. In this case, the order of selectivity is as follows: ACM > Fe-BTC > CS-CO_2 > CS-$ZnCl_2$. The selectivity of the material favours the CO_2 separation over the CH_4 molecule. ACM exhibits a higher microporosity and surface area (see Table 4.8.2 and Table 4.8.1), which allows the packing of a greater number of molecules.

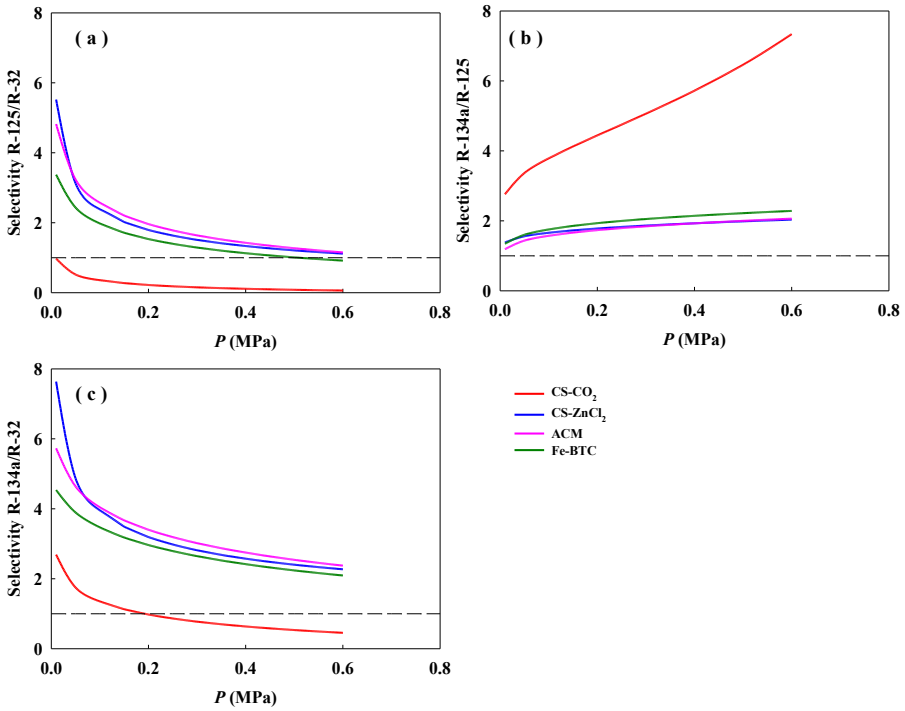


Figure 4.8.16 Selectivity of CS-CO_2 (red line), CS-$ZnCl_2$ (blue line), ACM (pink line) and Fe-BTC (green line) to: (a) R-125 over R-32; (b) R-134a over R-125 and (c) R-134a over R-32, as a function of pressure at 303.15 K for the commercial R-407C blend ($y_{R-32} = 0.38$, $y_{R-125} = 0.18$, and $y_{R-134a} = 0.44$).

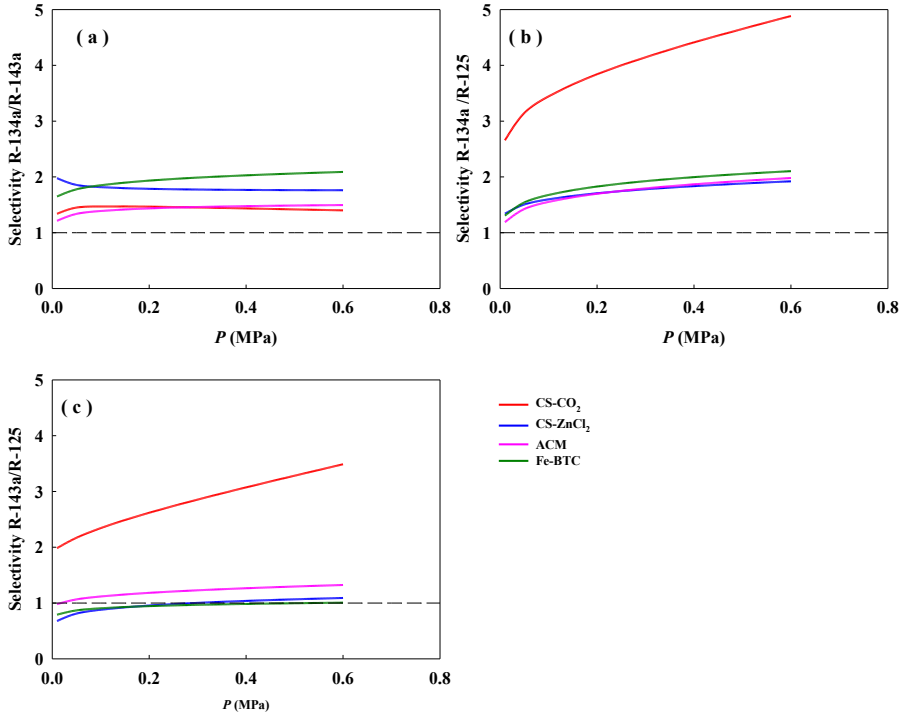


Figure 4.8.17 Selectivity of CS-CO_2 (red line), CS-$ZnCl_2$ (blue line), ACM (pink line) and Fe-BTC (green line) to: (a) R-134a over R-143a, (b) R-134a over R-125 and (c) R-143a over R-125, as a function of pressure at 303.15 K for the commercial R-404A blend ($y_{R-125} = 0.44$, $y_{R-143a} = 0.56$, and $y_{R-134a} = 0.04$).

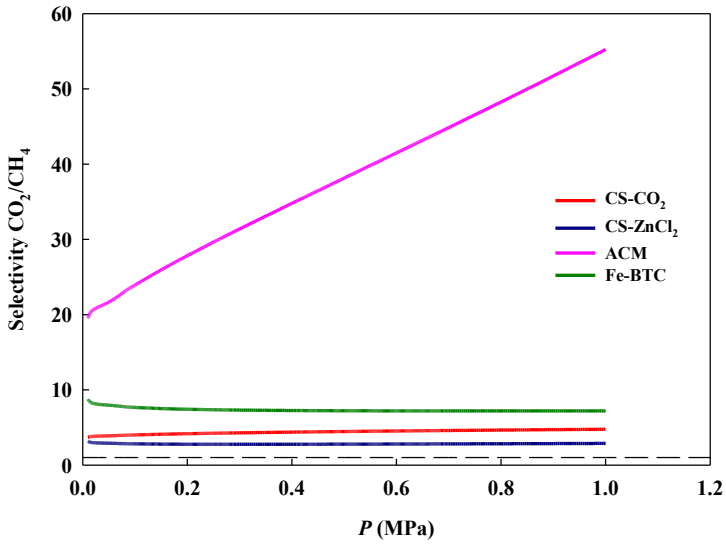


Figure 4.8.18 Selectivity of CS-CO_2 (red line), CS-$ZnCl_2$ (blue line), ACM (pink line) and Fe-BTC (green line) to CO_2 over CH_4 as a function of pressure at 303.15 K, for the CO_2/CH_4 mixture ($y_{CO_2} = 0.4$ and y $y_{CH_4} = 0.6$).

4.8.3 Conclusions

Biomaterials can be an efficient alternative to provide solutions for the capture and separation of GHGs. These novel alternatives have structural characteristics such as porosity and surface area that allow them to selectively adsorb GHGs gases. Besides, these biomaterials can be prepared using residual biomass to minimise production costs and to make them more attractive for their industrial application. In this work, two activated carbons were prepared from coconut shell biomass residues (CS-CO_2 and CS-$ZnCl_2$), using chemical activation with $ZnCl_2$ and physical activation with CO_2. The activation processes play a key role in developing stable and functional structures for adsorption applications. Both activation methods significantly contributed to the formation of a well-developed porous network, enhancing these biomaterials' stability.

In addition, two other solid porous materials, a commercial activated carbon ACM and a MOF Fe-BTC, were used to compare the performance of these biomaterials for the capture and separation of different GHGs studied in this work. All materials were characterised to understand how the textual properties can benefit the selective adsorption of GHGs. The nitrogen isotherms are characteristic of materials with large surface areas and are highly micro-mesoporous. In addition, adsorption equilibria of GHGs (R-32, R-125, R-134a, R-143a, CO_2 and CH_4) on two prepared biomaterials, CS-CO_2 and CS-$ZnCl_2$, and two commercial porous solid materials, ACM and Fe-BTC, were determined at 283.15, 303.15 and 323.15 K. The experimental adsorption equilibria were adjusted using the Dual Langmuir site adsorption model because this adsorption model allows us to describe the diversity of behaviours that are present in these systems. On the other hand, the IAST adsorption model was used to predict the separations of the mixtures R-410A, R-407C, R-404A and CO_2/CH_4. The results demonstrated that CS-$ZnCl_2$ is the most effective material for the separation of R-410A and R-407C blends at atmospheric pressure. This material has a large surface area, which allows it to store a notable number of GHGs molecules. Besides, CS-$ZnCl_2$ has large mesopores that allow these molecules to enter in the smallest micropores. On the other hand, CS-CO_2 obtained the highest selectivity for the separation of the R-404A blend. This behaviour may be related to the oxygens present on the material surface that interact with the hydrogens present in the F-gas molecules.

Then, biomaterials prepared in this work (CS-CO_2, CS-$ZnCl_2$) offer higher selectivity compared to ACM and Fe-BTC, making them ideal for industrial applications where the separation of F-gases is crucial. Although their adsorption capacity is lower, their superior selectivity enables more efficient separation processes. Then, these biomaterials are the better choice for industrial applications that require high purity and efficiency. Finally, the activated carbon ACM is the material with the highest selectivity in the separation of the CO_2/CH_4 mixture. In this case, the GHGs molecules are preferentially adsorbed in micropores and large surface areas, which benefits the packing of these molecules. Finally, this work provides vital information to design novel capture and separation processes of GHGs using novel activated carbons prepared with waste biomass. Then, the results of this work are essential for

developing efficient alternative materials for the implementation of the separation of commercial refrigerants and other GHGs mixtures on a pilot scale.

4.9 Exploring the Potential of Metal–Organic Frameworks for the Separation of Blends of Fluorinated Gases with High Global Warming Potential

The research on porous materials for the selective capture of fluorinated gases (F-gases) is key to reduce their emissions. Here, the adsorption of difluoromethane (R-32), pentafluoroethane (R-125), and 1,1,1,2-tetrafluoroethane (R-134a) is studied in four metal–organic frameworks (MOFs: Cu-benzene-1,3,5-tricarboxylate, zeolitic imidazolate framework-8, MOF-177, and MIL-53(Al)) and in one zeolite (ZSM-5) with the aim to develop technologies for the efficient capture and separation of high global warming potential blends containing these gases. Single-component sorption equilibria of the pure gases are measured at three temperatures (283.15, 303.15, and 323.15 K) by gravimetry and correlated using the Tóth and Virial adsorption models, and selectivities toward R-410A and R-407F are determined by ideal adsorption solution theory. While at lower pressures, R-125 and R-134a are preferentially adsorbed in all materials, at higher pressures there is no selectivity, or it is shifted toward the adsorption R-32. Furthermore, at high pressures, MOF-177 shows the highest adsorption capacity for the three F-gases. The results presented here show that the utilization of MOFs, as tailored made materials, is promising for the development of new approaches for the selective capture of F-gases and for the separation of blends of these gases, which are used in commercial refrigeration.

4.9.1 Experimental section

4.9.1.1 Materials

Difluoromethane, R-32 (wt % purity ≥ 99.9) and pentafluoroethane, R-125 (wt % purity ≥ 99.8) were supplied by Polo Zero (Portugal). 1,1,1,2-tetrafluoroethane, R-134a (wt % purity ≥ 99.8), was supplied by Air liquid (Portugal). The designation and chemical structure of these F-gases are shown in Table 1.1.1. Nitrogen (N_2) (wt % purity ≥ 99.9999) was supplied by Linde Gas (France) and Helium (wt % purity ≥ 99.999) by Praxair (Portugal). For this work one zeolite and four MOFs were purchased: zeolite ZSM-5 (Alfa Aesar, Germany); ZIF-8 (Basolite Z1200, Sigma-Aldrich, Portugal); MIL-53(Al) (Basolite A100, Sigma-Aldrich, France), Cu-BTC (HKUST-1 or MOF-199, MOF Technologies, UK); and MOF-177 (Basolite Z377, Sigma-Aldrich, France).

4.9.2 Results and discussion

4.9.2.1 Materials characterisation

F-gas adsorption was studied on four MOFs and one zeolite (ZSM-5) with different textural characteristics. The specific Brunauer–Emmett–Teller (BET) surface area, S_{BET}, and specific pore volume, v_p, of each adsorbent are listed in Table 4.9.1. The pore size distributions (PSDs) for each material are depicted in Figure 4.9.1. In addition, details of the equipment used for material characterization are provided in Section 4.2.

Table 4.9.1 BET surface area, $\boldsymbol{S_{BET}}$, and specific pore volume, $\boldsymbol{v_p}$, of the zeolite and MOFs.

	Cu-BTC	ZIF-8	MOF-177	MIL-53(Al)	ZSM-5
S_{BET} (m^2/g)	1172	1302	4190	1043	434
v_p (cm^3/g)	0.56	0.65	1.75	0.79	0.26

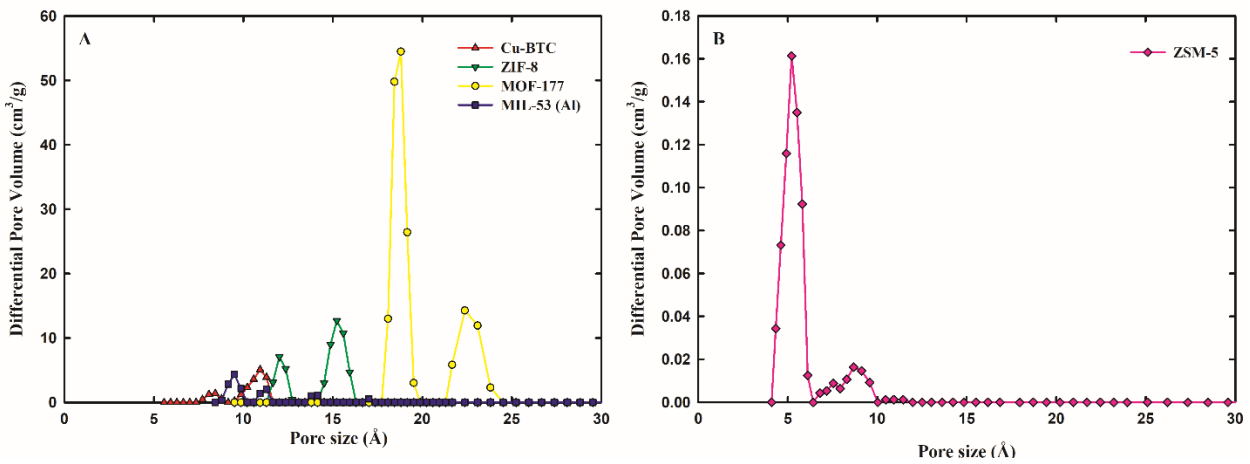


Figure 4.9.1 Pore size distribution of the studied adsorbents, determined by deconvolution of the N_2 (77K) or Ar (87K) adsorption isotherms using standard methods based on the Non-Localized Density Functional theory (NLDFT). Panel A: Cu-BTC (red up triangles), ZIF-8 (green down triangles), MOF-177 (yellow circles), and MIL-53 (Al) (blue squares). Panel B: Zeolite ZSM-5 (pink diamond).

Gas sorption in porous materials is governed by different processes, according to the operating conditions and the characteristics of both the adsorbate (sub- or supercritical adsorption) and the adsorbent. Adsorption in microporous materials takes place in the porous network of the adsorbent and therefore is dependent on its textural properties (see Figure 4.9.2), morphology, and pore size distribution. MOF-177 is the adsorbent with the highest value of both S_{BET} and v_p (4190 $m^2\ g^{-1}$ and 1.75 $cm^3\ g^{-1}$, respectively), substantially different from the values for the other MOFs (S_{BET} values ranging from 1043 to 1303 $m^2\ g^{-1}$, and v_p values ranging from 0.56 to 0.79 $cm^3\ g^{-1}$) and from the zeolite, which present the lowest values for all materials (S_{BET} of 434 $m^2\ g^{-1}$ and v_p of 0.26 $cm^3\ g^{-1}$).

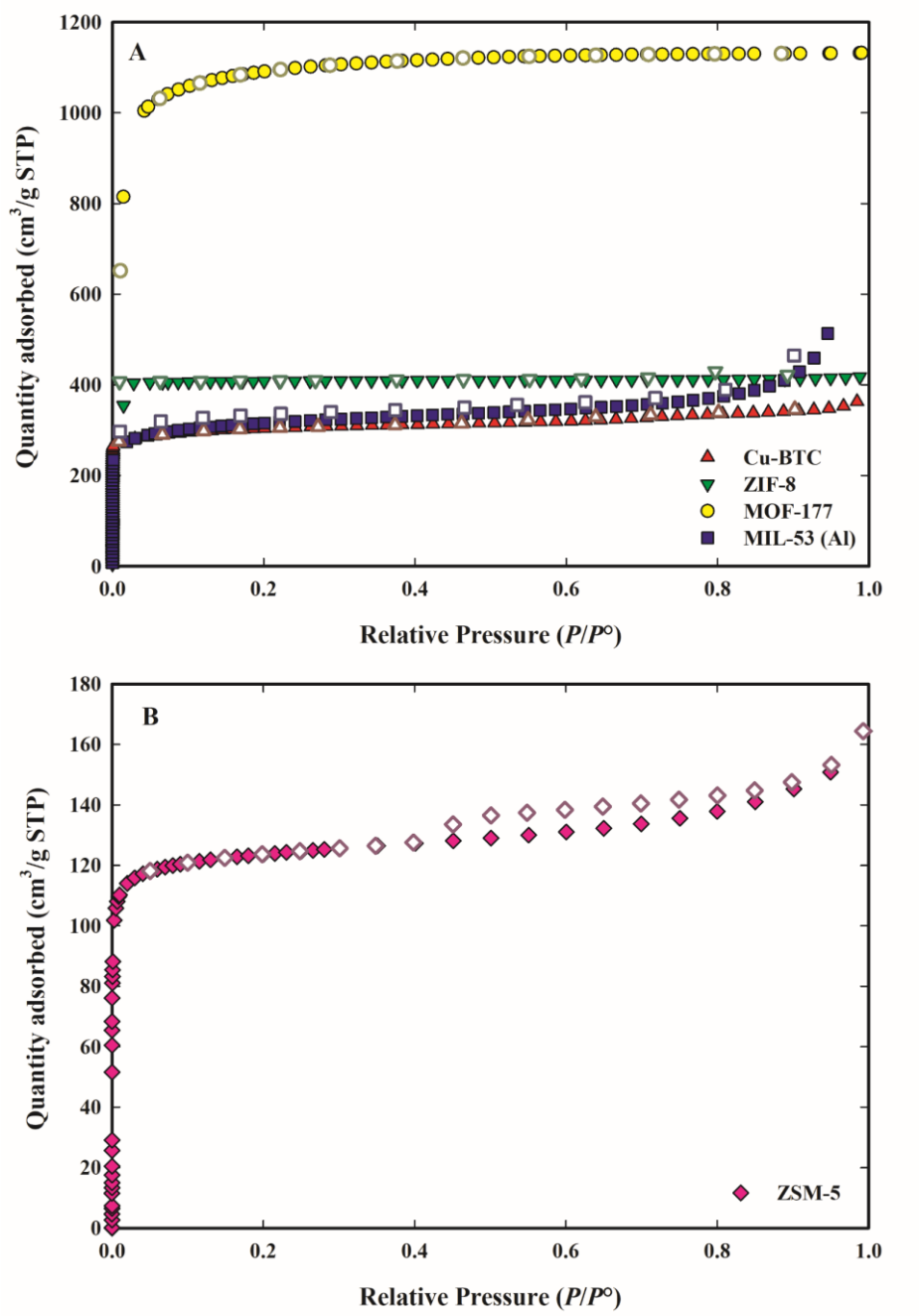


Figure 4.9.2 Adsorption isotherms of nitrogen at 77 K for Cu-BTC, ZIF-8, MOF 177 and MIL 53 (Al) (panel A), and of argon at 87 K for zeolite ZSM5 (panel B).

All materials are clearly distinguishable by their PSD profiles (see Figure 4.9.1). The PSDs of all materials present two main peaks. While MOF-177 has both micropores (pores size 17–20 Å) and mesopores (pores size 20–25 Å), zeolite ZSM-5 (pores size range: 5–10 Å), MOFs Cu-BTC (pores size range: 7–12 Å), MIL-53 (Al) (pores size range: 8–10 Å), and ZIF-8 (pores size range: 12–17 Å) only have micropores (pore size <20 Å). In the case of ZSM-5, a large fraction of the pores is in the ultramicropore region (bellow 5 Å). These differences in textural properties, together with the differences in the chemical properties of the adsorbents, impact gas adsorption and separation because the physical and chemical processes governing adsorption in mesopores are different from those in micropores.

4.9.2.2 Adsorption Equilibrium of R-32, R-125, and R-134a

The details of the adsorption equilibrium determination are provided in Section 4.3. Following this methodology, the experimental adsorption equilibrium data at 283.15, 303.15, and 323.15 K, expressed as millimoles of adsorbed gas per gram of adsorbent (mmol g^{-1}), are plotted in Figure 4.9.3-4.9.5 as a function of the equilibrium gas pressure. The maximum adsorption pressure for each studied F-gas was at least 10 % lower than its vapor pressure at each measured temperature. Figure 4.9.6 presents the isotherms at 303.15 K for the three F-gases as a function of equilibrium pressure up to 0.15 MPa, to ease the discussion of gas adsorption at low pressures.

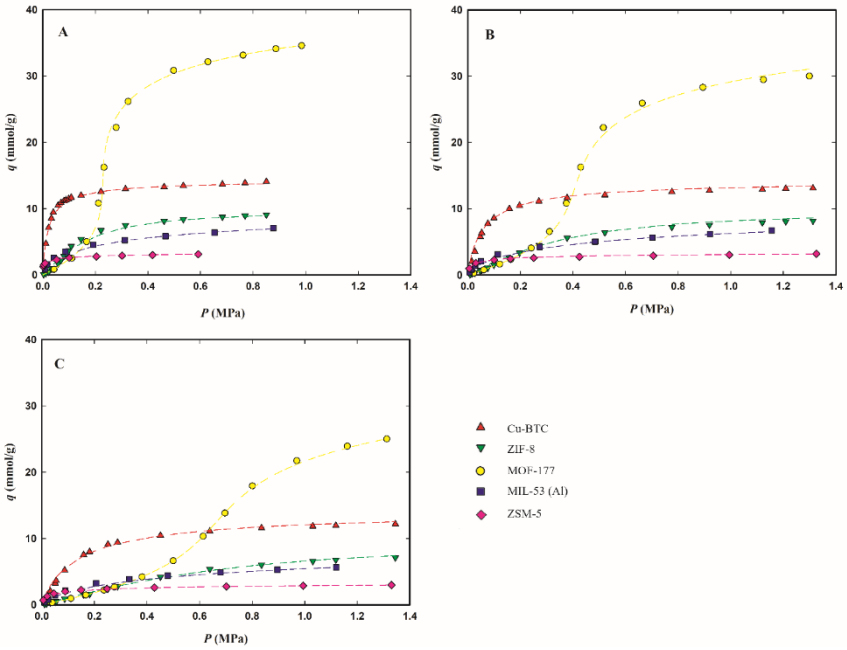


Figure 4.9.3 Adsorption equilibrium isotherms of R-32 on Cu-BTC (red up triangles), ZIF-8 (green down triangles), MOF-177 (yellow circles), MIL-53(Al) (blue squares), and zeolite ZSM-5 (pink diamond), at 283.15 K (panel A), 303.15 K (panel B), and 323.15 K (panel C). The dashed lines represent the data fittings with the Toth's model for Cu-BTC, ZIF-8, ZSM-5, and MIL-53(Al) or the Virial model for MOF-177.

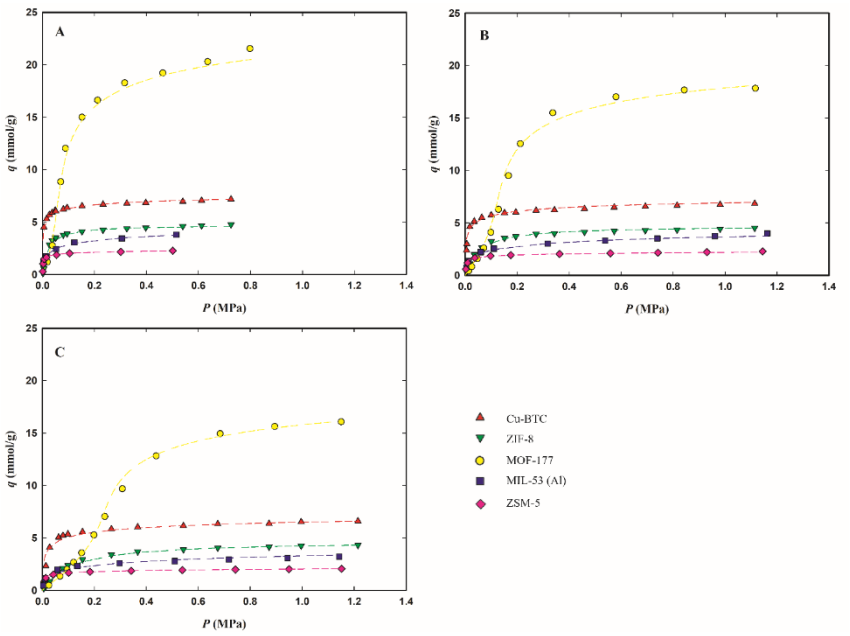


Figure 4.9.4 Adsorption equilibrium isotherms of R-125 on Cu-BTC (red up triangles), ZIF-8 (green down triangles), MOF-177 (yellow circles), MIL-53 (Al) (blue squares), and zeolite ZSM-5 (pink diamond), at 283.15 K (panel A), 303.15 K (panel B), and 323.15 K (panel C). The dashed lines represent the data fittings with the Toth's model for Cu-BTC, ZIF-8, ZSM-5, and MIL-53(Al) or the Virial model for MOF-177.

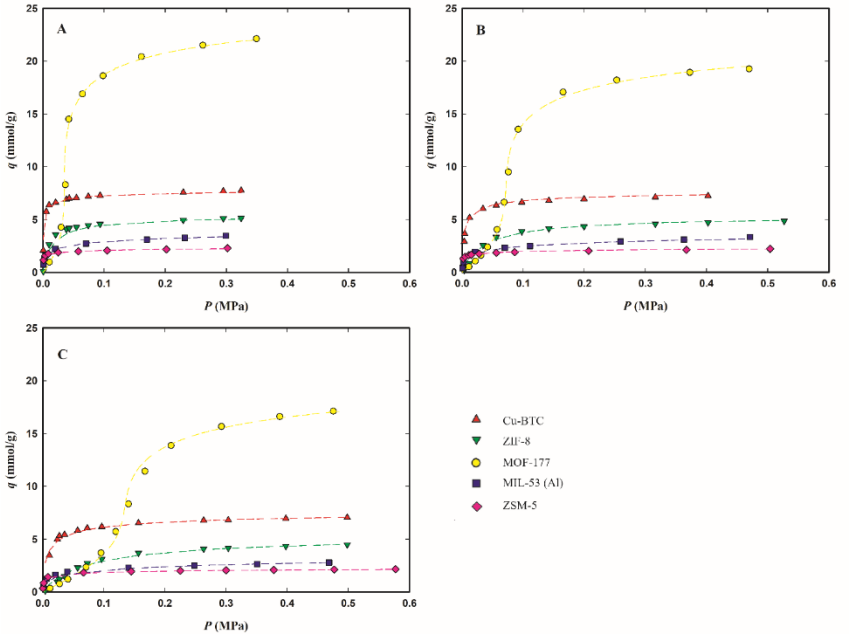


Figure 4.9.5 Adsorption equilibrium isotherms of R-134a on Cu-BTC (red up triangles), ZIF-8 (green down triangles), MOF-177 (yellow circles), MIL-53 (Al) (blue squares), and zeolite ZSM-5 (pink diamond), at 283.15 K (panel A), 303.15 K (panel B), and 323.15 K (panel C). The dashed lines represent the data fittings with the Toth's model for Cu-BTC, ZIF-8, ZSM-5, and MIL-53(Al) or the Virial model for MOF-177.

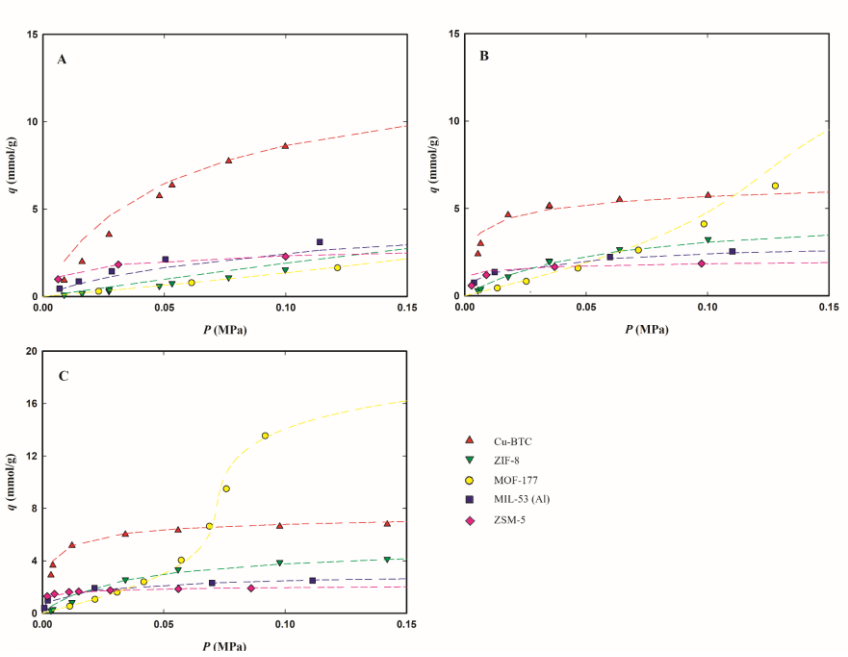


Figure 4.9.6 Adsorption equilibrium isotherms at 303.15 K of R-32 (panel A), R-125 (panel B), and R-134a (panel C) on Cu-BTC (red up triangles), ZIF-8 (green down triangles), MOF-177 (yellow circles), MIL-53 (Al) (blue squares), and zeolite ZSM-5 (pink diamond). The dashed lines represent the fittings with the Toth's or Virial models.

Almost no data on the adsorption of F-gases in the materials studied in this work are available in the literature. Figure 4.9.7 compares the adsorption of R-32 and R-125 in Cu-BTC at the three studied temperatures (283.15, 303.15, and 323.15 K) and the data available in the literature obtained at 293.15 K; it is shown that there is good agreement and trends between studies [156].

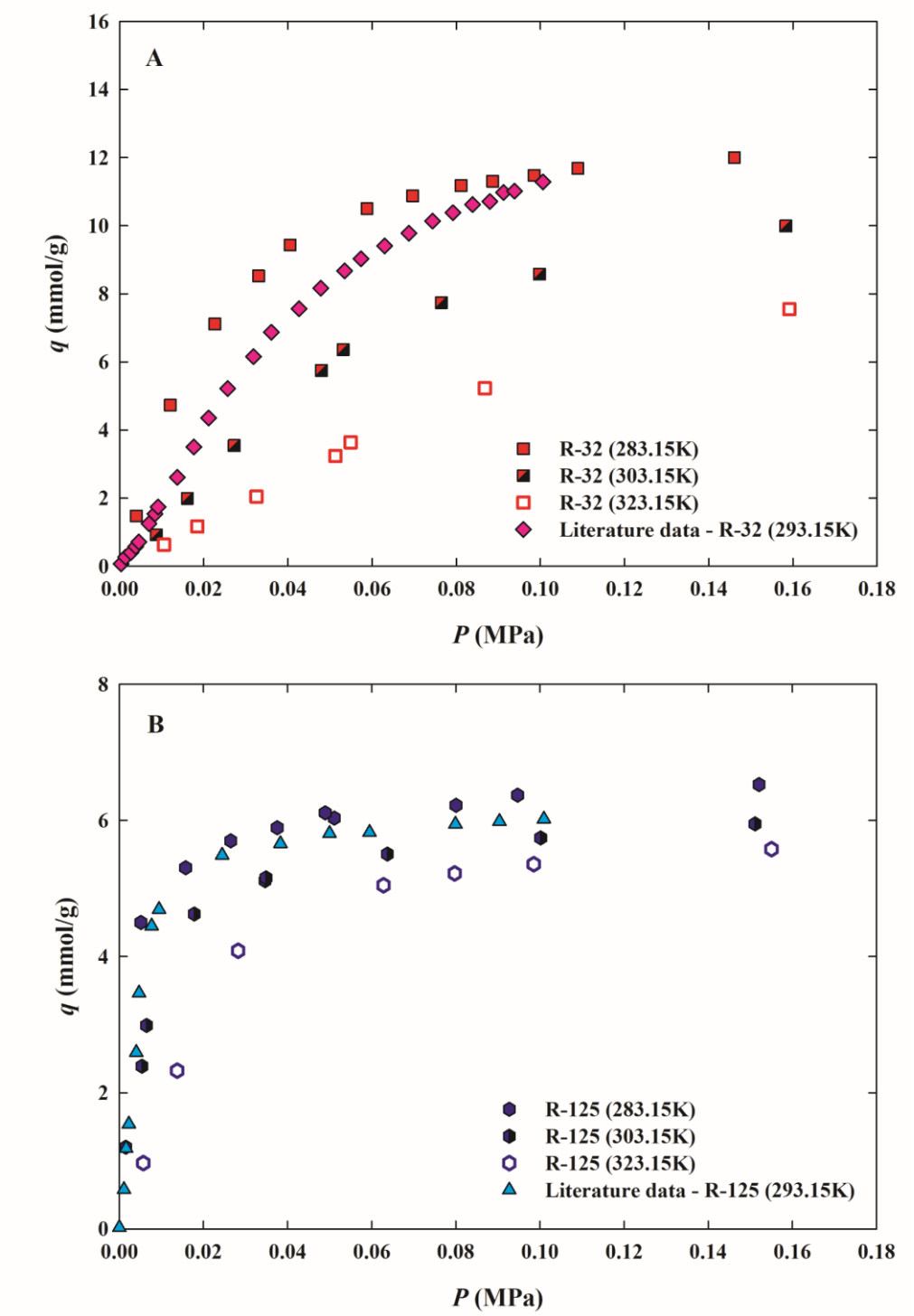


Figure 4.9.7 Comparison between the adsorption of R-32 (panel A) and R-125 (panel B) in Cu-BTC at 283.15, 303.15, and 323.15 K, studied in this work, and literature data available at 293.15 K [97].

All isotherms, except those of MOF-177, present a classical Type I behavior [84], corresponding to progressive pore filling of gas molecules in microporous adsorbents (see Figure 4.9.1). Type V isotherms according to the isotherm classification of International Union of Pure and Applied Chemistry [157–160], observed for the MOF-177 (see Figure 4.9.1), are typical of mesoporous adsorbents in which the adsorption process is governed by both adsorbent–adsorbate interactions and interactions between

the adsorbate molecules in the condensed state [84]. The adsorption data were fitted by isotherm models, with good agreement between calculated and experimental data. Considering the behavior of the isotherms, two different adsorption equilibrium models were employed. Experimental adsorption data were fitted using the Tóth's model for the zeolite ZSM-5 and the MOFs Cu-BTC, MIL-53(Al), and ZIF-8. MOF-177 has a type V isotherm [158–160], and therefore cannot be fitted by a Tóth model (comparison of the Tóth and Virial fittings for R-32 adsorption in MOF-177 are shown in Figure 4.9.8). In this case the experimental adsorption data for MOF-177 were fitted with the Virial isotherm model [159,161]. This model is very flexible to adjust isotherms with different degrees of inclination and inflexion points and allows predicting multicomponent adsorption using the virial coefficients of the mixture [157,162,163].

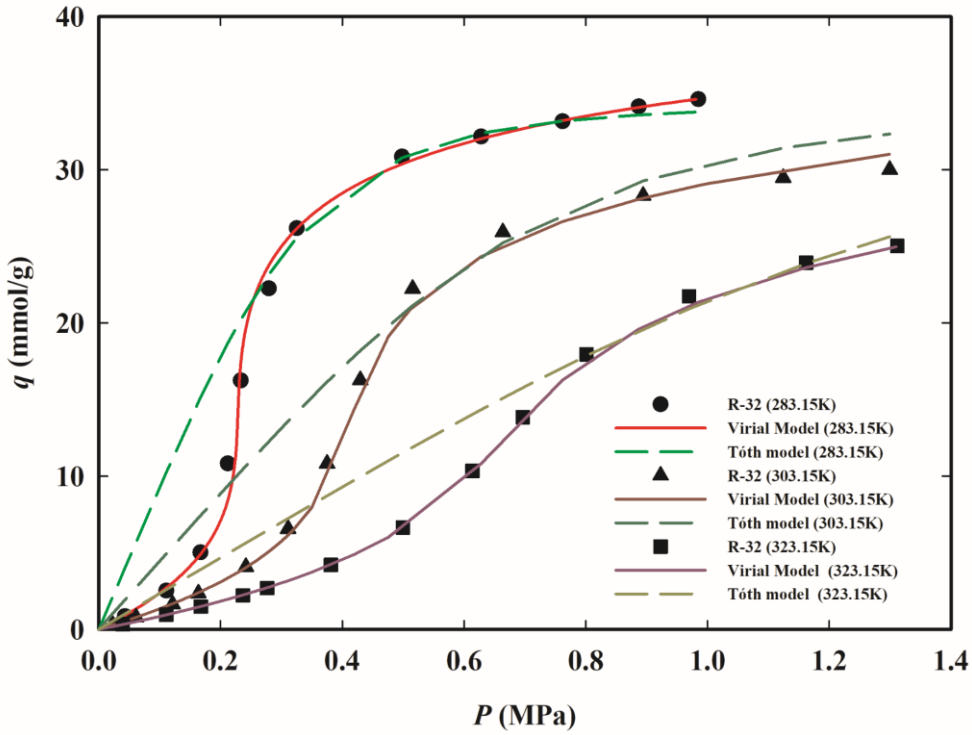


Figure 4.9.8 Comparison of the Toth's and Virial models fitting to the adsorption of R-32 in MOF-177.

The Toth model[81] is described by:

$$q = \frac{q_{\infty} bP}{[1 + (bP)^t]^{1/t}} \quad 4.9.1$$

where $q_{\infty} = \log_{P \to \infty} q$; $b = K_H / q_{\infty}$ is an affinity constant (MPa^{-1}); K_H (mmol g^{-1} MPa^{-1}) is the Henry constant; and t is a dimensionless heterogeneity parameter. The parameters b and t depend on temperature as follows:

$$b = b_0 \exp\left(\frac{Q}{RT}\right) \quad 4.9.2$$

$$t = t_0 + B\left(1 - \frac{T_0}{T}\right) \quad 4.9.3$$

where b_0 is the affinity constant at infinite temperature; Q is the isosteric heat of adsorption; t_0 is the heterogeneity parameter at a reference temperature T_0; and B the slope of the plot of t versus $-1/T$.

The Virial isotherms [159,161], truncated after the third virial coefficient, can be expressed as

$$P = \frac{q}{K_H} exp\left(2Aq + \frac{3}{2}Bq^2 + \frac{4}{3}Cq^3\right) \quad 4.9.4$$

where q is the amount adsorbed; p is the partial pressure of the adsorbate; K_H is Henry's constant; and A, B and C are the viral coefficients. The Henry's constant is temperature-dependent and is determined by the van't Hoff equation as follows:

$$K_H = K_{\infty} \exp\left(\frac{\Delta H}{RT}\right) \quad 4.9.5$$

where K_{∞} is the constant at infinite temperature, R the ideal gas constant, ΔH the isosteric heat of adsorption, and T the temperature. Viral coefficients A, B and C have temperature dependence and are truncated after the second term.

$$A = \sum_{m}^{\infty} \frac{A_m}{T^m} \quad 4.9.6$$

$$B = \sum_{m}^{\infty} \frac{B_m}{T^m} \quad 4.9.7$$

$$C = \sum_{m}^{\infty} \frac{C_m}{T^m} \quad 4.9.8$$

The Tóth and Virial parameters that best fit the experimental adsorption data for each adsorbent/F-gas pair are listed in Tables 4.9.2-4.9.3 corresponding fittings are plotted in Figure 4.9.3-4.9.6 as dashed lines. The chosen models correlate well with the adsorption equilibrium data at low and high pressures on the studied materials, describing well the thermodynamics of the studied F-gas/adsorbent systems. Therefore, these models are suitable for use in the modeling and simulation of adsorption-based separation processes.

Table 4.9.2 Best-fit parameter values of the Toth model for each adsorbent/F-gas pair.

		b	*t*	Error (%)
Cu-BTC	**R-32**	55.29	0.851	6.7
	R-125	8747	0.353	1.2
	R-134a	3713	0.520	6.0
ZIF-8	**R-32**	4.274	1.66	5.3
	R-125	43.79	1.01	6.5
	R-134a	43.62	1.09	5.7
MIL-53(Al)	**R-32**	12.22	0.481	1.5
	R-125	2629	0.256	0.56
	R-134a	7348	0.267	1.3
ZSM-5	**R-32**	3079	0.340	0.73
	R-125	4465	0.240	3.4
	R-134a	2260	0.254	0.67

Table 4.9.3 Viral model parameters obtained for the system MOF-177 + F-gas.

	R-32	**R-134a**	**R-125**
A_0 (Kg/mol)	-0.065	0.34	0.46
A_1 (Kg·K/mol)	7.747	-110.5	-144.6
B_0 ((Kg/mol)^2)	0.010	-0.066	-0.11
B_1 ((Kg·K/mol)^2)	-3.106	17.01	30.87
C_0 ((Kg/mol)^3)	0.000	0.004	0.006
C_1 ((Kg/mol)^3)	0.059	-0.89	-1.6
K_∞ (mol/(Kg·bar))	1.28E-02	3.61E-03	5.82E-03
$-\Delta H$ (KJ/mol)	17.260	19.380	21.869
Error (%)	0.107	1.06	1.33

The micro-mesoporous MOF-177 has the highest adsorption capacity of the three studied HFCs, adsorbing more than double the amount of each gas, when compared with the other four microporous materials (see Figure 4.9.3-4.9.6). At 303.15 K and the maximum tested pressure for each F-gas, this material adsorbs around 30 mmol g^{-1} of R-32 (at 1.30 MPa), 19 mmol g^{-1} of R-134a (at 0.47 MPa), and 18 mmol g^{-1} of R-125 (at 1.11 MPa). On the other hand, at low pressures, MOF-177 adsorbs similar or lower amounts of all F-gases, compared to the other materials (see Figure 4.9.9). This peculiar behavior of MOF-177 may be explained by a primary interaction of the gas molecules with the adsorbent pore walls at lower pressures, followed by interactions between gas molecules that allow the accommodation of more gas molecules in the mesopores at higher pressures.

While for all materials the highest adsorption capacities were achieved for R-32, at low pressures most of the studied materials adsorb fewer R-32, when compared to the other two studied gases (see Figure 4.9.9). This discrepancy in the R-32 adsorption behavior at low and at high pressures is more remarkable for ZIF-8 and MOF-177, which are the materials that adsorb the lowest amount of R-32 at low pressures (below 0.15 MPa in Figure 4.9.6) and the ones with the widest pores and with the highest superficial areas of all studied materials. At low pressures, adsorption is typically governed by enthalpic processes where the strength of the solid–fluid interaction decreases with increasing micropore size. At low amounts of adsorbed gas, ZIF-8 and MOF-177 have the lowest values of isosteric heat (see Figure 4.9.10), indicating a low degree of interaction between the gas molecules and these two adsorbents. At high pressures and conditions close to pore filling, the entropy of the condensed adsorbed phase controls gas adsorption. Therefore, the saturation capacity, q_{∞}, is inversely proportional to the molar volume, v_m, of each HFC ($v_{m:}$ R-32 < R-134a < R-125) and directly proportional to pore volume and superficial area available for gas adsorption. MIL-53(Al) and ZSM-5, the materials with the lowest superficial areas and with the narrower micropores (<10 Å), have the lowest adsorption capacity for the three studied gases. Interestingly, Cu-BTC has higher gas adsorption capacity than ZIF-8 and MIL-53(Al) (see Figure 4.9.3), despite having the smallest v_p of all MOFs and the second smallest superficial area of all MOFs (see Figure 4.9.1). This indicates that for this material, Cu-BTC, other factors control the gas adsorption capacity.

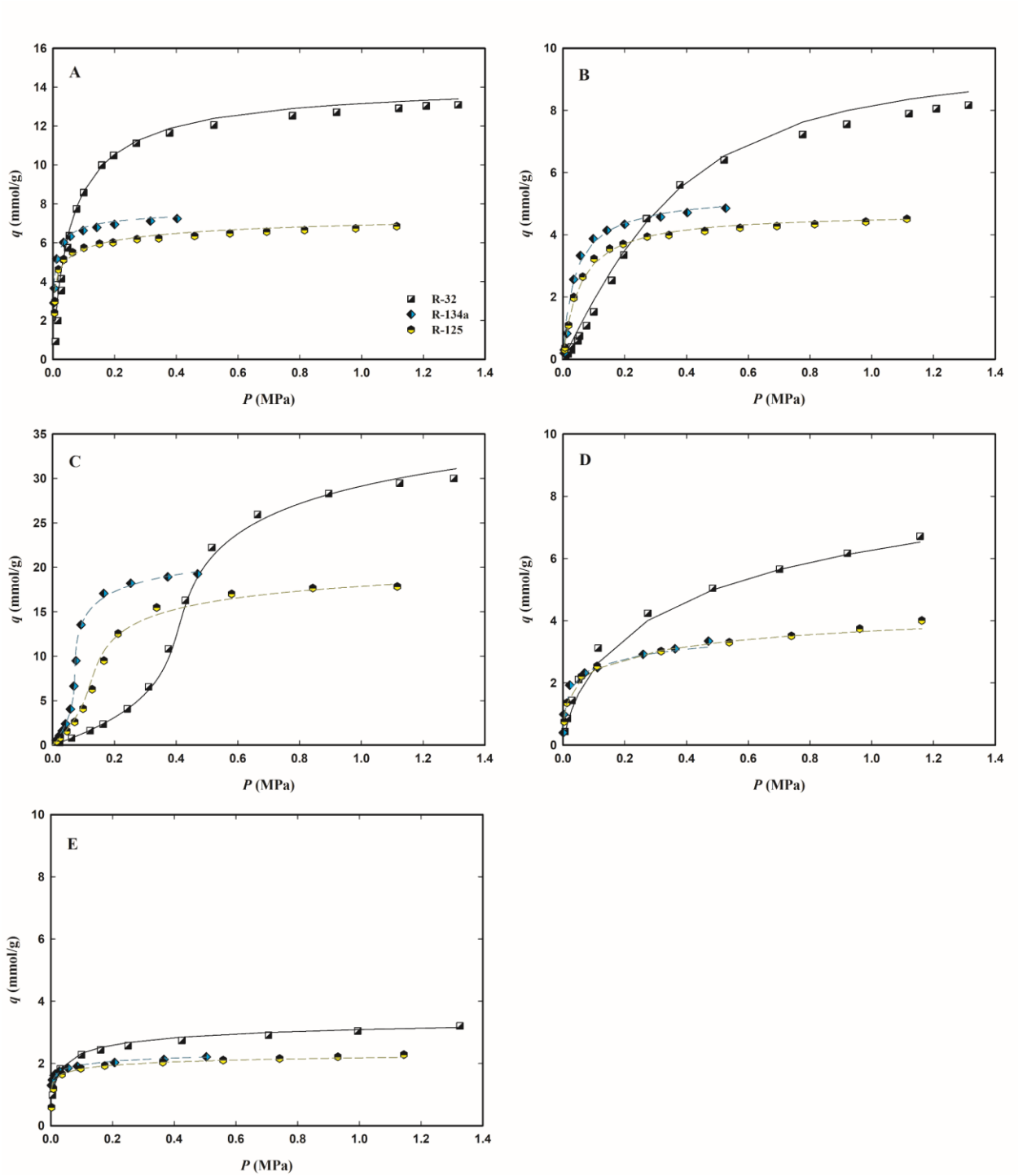


Figure 4.9.9 Adsorption equilibrium isotherms at 303.15 K of R-32 (squares), R-134a (diamond), and R-125 (hexagon) on Cu-BTC (panel A), ZIF-8 (panel B), MOF-177 (panel C), MIL-53(Al) (panel D), and ZSM-5 (panel E). The dashed lines represent the fittings with the Toth's (panels A, B, D, and E) or the Virial models (panel C).

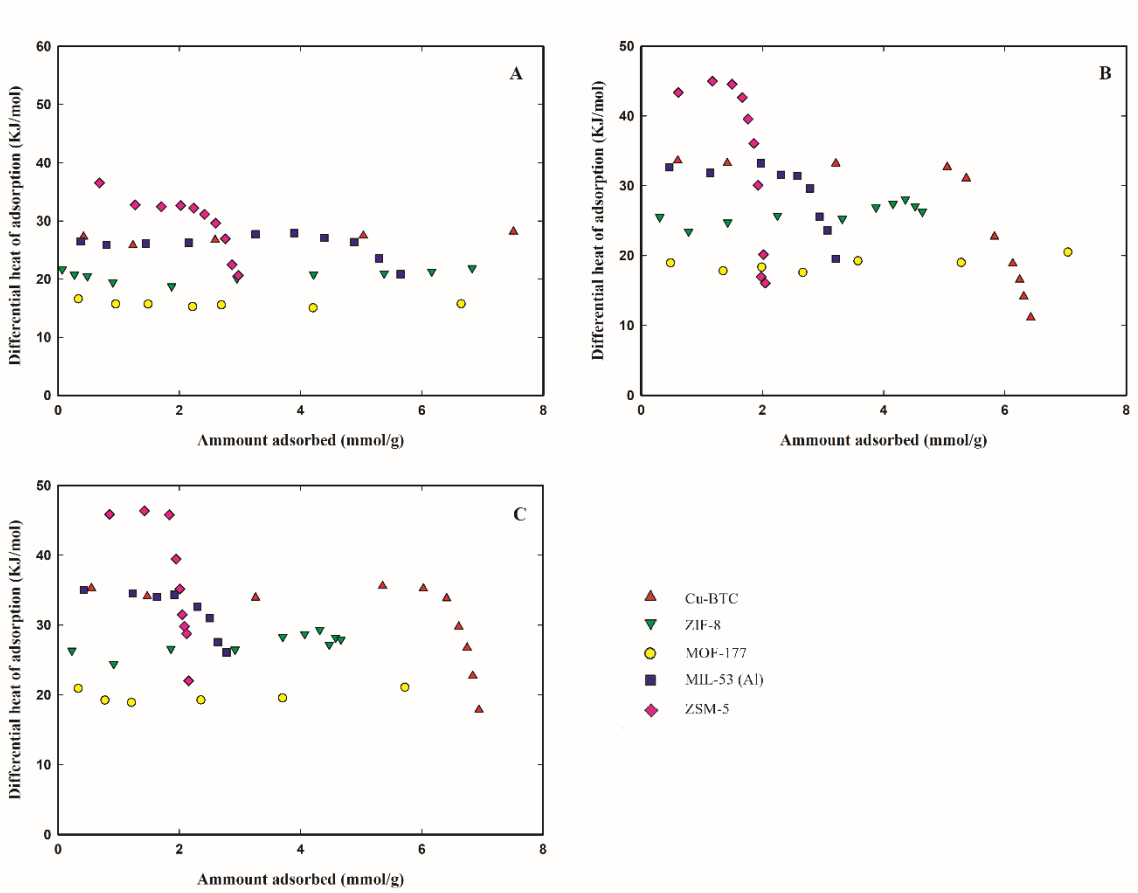


Figure 4.9.10 Differential heats of adsorption of R-32 (panel A), R-125 (panel B), and R-134a (panel C) at 323.15 K on Cu-BTC (red up triangles), ZIF-8 (green down triangles), MOF-177 (yellow circles), MIL-53 (Al) (blue squares), and Zeolite ZSM-5 (pink diamond).

The differential heats of adsorption (determined for each HFC/adsorbent at 323.15 K) for R-134a and R-125 (see Figure 4.9.10) are higher than for R-32, in accordance with the higher heats of vaporization of R-134a and R-125. These results may also indicate a lower degree of interaction between R-32 molecules and the adsorbents, probably because of the existence of fewer hydrogen and fluorine atoms available for interactions. This behavior may explain why R-32 is preferentially adsorbed at higher pressures. On the other hand, for low sorbate adsorbed amount, the heat of adsorption for the zeolite ZSM-5 is higher than the other materials, exceeding 30 kJ mol^{-1} for R-32 and 40 kJ mol^{-1} for R-125. In this material electrostatic interactions are likely to dominate over weaker dispersive interactions, such as van der Waals forces [17].

4.9.2.3 Prediction of the GHG separation using the Ideal Adsorption Solution Theory (IAST)

The commercial refrigerants R-410A (R-32/R-125, 50/50 wt %; $y_{\text{R-32}}^{(0)} = 0.7$, $y_{\text{R-125}}^{(0)} = 0.3$) and R-407F (R-32/R-125/R-134a, 30/30/40 wt %; $y_{\text{R-32}}^{(0)} = 0.47$, $y_{\text{R-125}}^{(0)} = 0.21$, and $y_{\text{R-134a}}^{(0)} = 0.32$) are near azeotropic blends of HFCs. Therefore, these refrigerants are not easily separated into their individual components by conventional methods, such as distillation. In this work we explored the adsorption of R-32, R-125, and R-134a in five porous materials, aiming at evaluating their capability to split R-410A and R-407F into their components. The multicomponent adsorption equilibrium data of R-410A, R-407F, and their components were predicted using the IAST [72,154] from the Tóth and Virial fittings to the single-component adsorption equilibrium data of R-32, R-125, and R-134a at 303.15 K. The adsorption equilibria of the gas blends were predicted for pressures up to 1.0 MPa for R-410A and up to 0.6 MPa for R-407F, to not exceed the saturation pressure of the individual pure F-gas at 303.15 K. The results are plotted in Figure 4.9.11. The adsorption of both gas blends in all materials increases with increasing pressure and at the highest tested pressures, the highest adsorption capacities were obtained for MOF-177, which is the studied material with the highest value for S_{BET} and v_{p} as well as the one with the widest pores. On the other hand, at the lowest tested pressures (P < 0.1 MPa), MOF-177 is the material with the lowest adsorption capacity and Cu-BTC is the one with the highest capacity. The lowest adsorption capacity for both gas blends, at the highest tested pressures, was obtained for zeolite ZSM-5, which is the studied material with the lowest values for S_{BET} and v_{p} as well as the one with the narrowest pores.

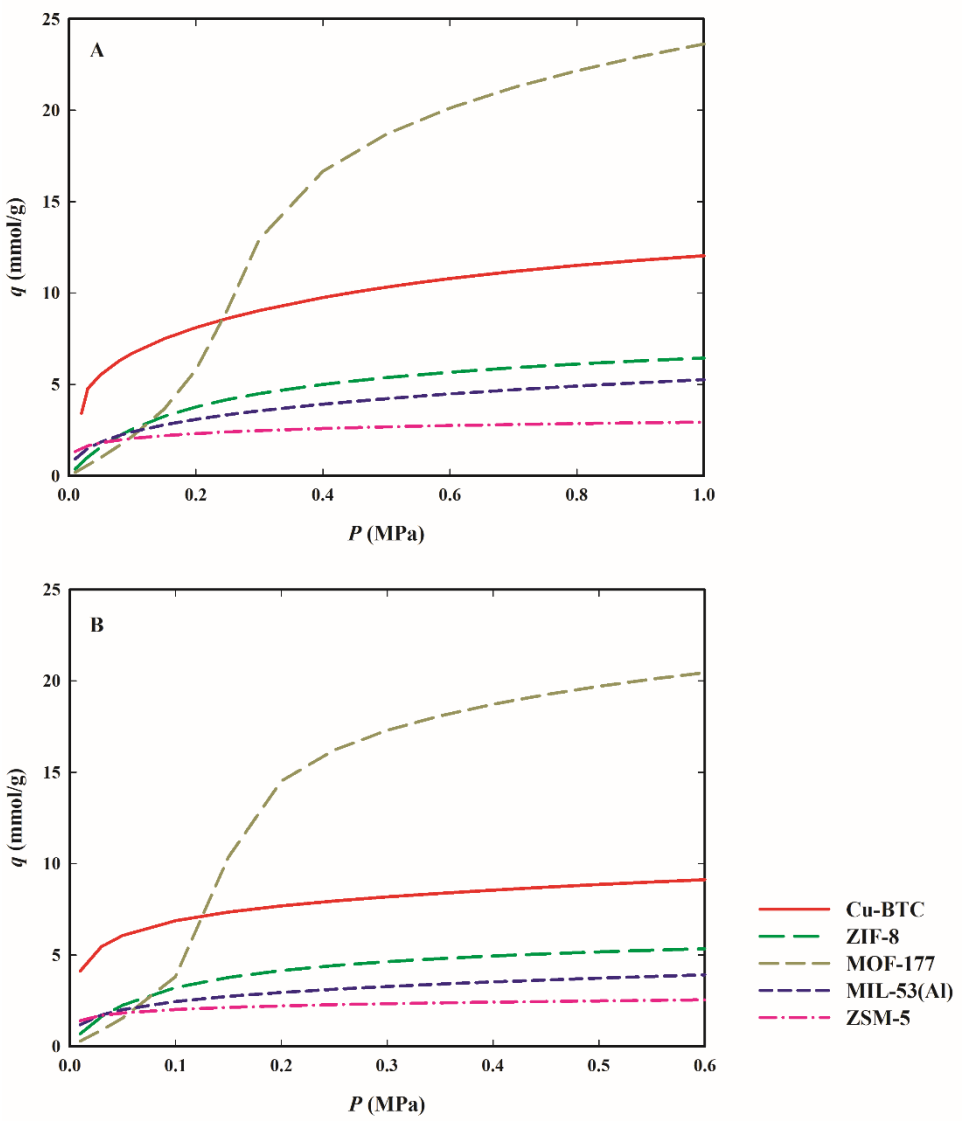


Figure 4.9.11 IAST prediction of the adsorbed amounts of R-410A (panel A) and R-407F (panel B) as a function of pressure at the equilibrium gas-phase mole fractions corresponding to the bulk composition (R-410A: $y_{\text{R-32}} = 0.7$ and $y_{\text{R-125}} = 0.3$; and R-407F: $y_{\text{R-32}} = 0.47$, $y_{\text{R-125}} = 0.21$, and $y_{\text{R-134a}} = 0.32$) at 303.15 K.

4.9.2.4 Prediction of the GHG separation using the Ideal Adsorption Solution Theory (IAST)

The selectivity of the materials for the separation of the pure components (R-32, R-125, and R-134a) of the two commercial refrigerants, R-410A and R-407F, was calculated using the predictions determined by IAST. The gas selectivity (S_{ij}) at 303.15 K of each material for the separation of a gas *i* from the mixture with a gas *j* was determined following the methodology described in Section 4.5.

In the case of R-410A, the selectivity of each material toward R-125 over R-32 was determined. The selectivity was determined as a function of pressure for the equilibrium gas-phase composition corresponding to that of bulk R-410A (see Figure 4.9.12). If $S > 1$, R-125 is preferentially adsorbed but if $S < 1$, R-32 is preferentially adsorbed.

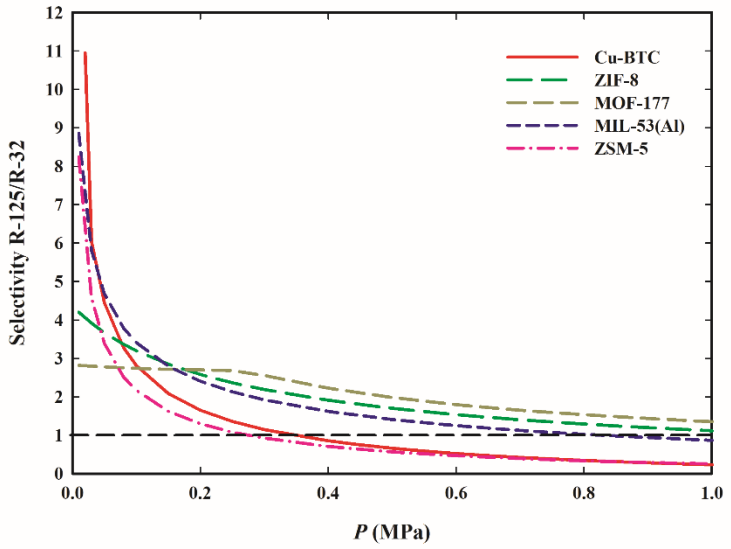


Figure 4.9.12 Selectivity of Cu-BTC (red line), ZIF-8 (green line), MOF-177 (yellow line), MIL-53 (Al) (blue line), and zeolite ZSM-5 (pink line) to R-32 over R-125 as a function of pressure at 303.15 K, for the equilibrium gas phase composition of bulk the R-410A mixture ($y_{\text{R-32}} = 0.7$ and $y_{\text{R-125}} = 0.3$).

At pressures below 0.3 MPa, all materials are selective toward R-125, with Cu-BTC, MIL-53(Al), and ZSM-5 achieving selectivities of around 11, 9, and 8, respectively, at the lowest studied pressures. Interestingly, at higher pressures (above 0.4 MPa), the selectivity of Cu-BTC and ZSM-5 is shifted toward R-32 (reaching selectivities for R-32 of around 2 at 1.0MPa). On the other side, MOF-177, ZIF-8, and MIL-53(Al) have no significant selectivity toward any of the two gases at high pressures. In this case, the dimensions of the pores seem to play an important role in the selectivity. The materials with the narrowest pores have higher selectivity toward R-125 at low pressures, probably as a result of higher interaction of the R-125 molecules (which have a higher number of fluorine atoms to establish interactions) with the pore walls. At high pressures, the selectivity of Cu-BTC and ZSM-5 is shifted toward R-32, possibility due to the smaller size of this molecule, which facilitates its packing at the smaller pores.

In the case of the R-407F blend (ternary mixture of R-32, R-125, and R-134a), the selectivities for the separations of R-125/R-32, R-134a/R-125, and R-134a/R-32 were determined as a function of pressure at 303.15 K for the equilibrium gas-phase composition of the bulk R-407F (see Figure 4.9.13).

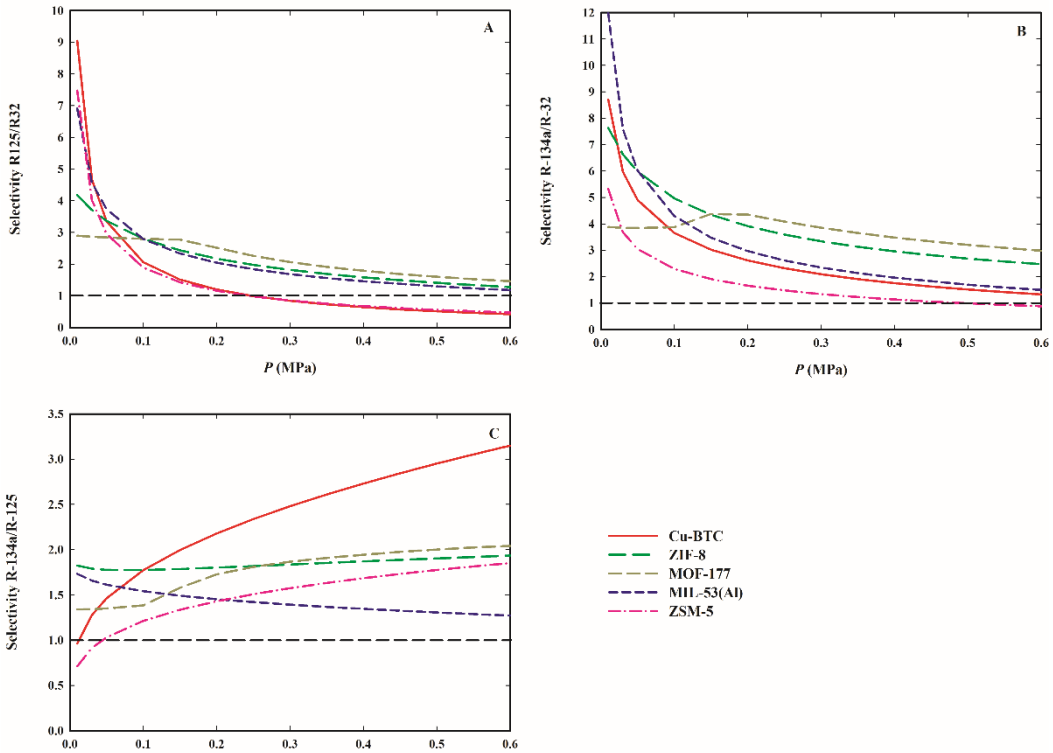


Figure 4.9.13 Selectivities of Cu-BTC, ZIF-8, MOF-177, MIL-53(Al), and ZSM-5 to: R-125 over R-32 (panel A); R-134a over R-32 (panel B); and R-134a over R-125 (panel C), for the commercial R-407F gas mixture ($y_{\text{R-32}} = 0.47$, $y_{\text{R-125}} = 0.21$, and $y_{\text{R-134a}} = 0.32$), as a function of pressure at 303.15 K.

In general, all materials are selective for the separation of R-134a from mixtures with the other two gases ($S_{R134a/R32} > 1$ and $S_{R134a/R125} > 1$). While $S_{R\text{-}134a/R\text{-}32}$ decreases with pressure for all materials, $S_{134a/R\text{-}125}$ increases with the pressure for Cu-BTC, MOF-177, and ZMS-5; decreases with pressure for MIL-53(Al); and is kept almost constant for ZIF-8. Concluding, the textural properties of materials play an important role in defining the selectivity toward the different studied F-gases, with all materials being selective toward R-125 and R-134a over R-32 at low pressures. For Cu-BTC and ZSM-5, the results show that R-125/R-32 selectivity (in the binary and ternary blends) can be shifter either toward R-125 or to R-32 by changing the pressure.

4.9.3 Conclusions

The emergence of new materials, such as MOFs, brings new and promising perspectives for the separation of refrigerant blends. Since they are excellent tailor-made materials, thousands of different MOFs can be designed and prepared.

In this work, four MOFs with different metal sites, chemical compositions, and textural properties, and one zeolite were selected and studied for the selective adsorption of three pure F-gases (R-32, R-125, and R-134a) at three different temperatures (283.15, 303.15, and 323.15 K) at a range of pressures up to 1.4 MPa. For the four tested microporous materials (three MOFs and one zeolite), the type I isotherms were successfully correlated with the Tóth equation, while for the micro-mesoporous MOF-177 the obtained type V isotherms were successfully correlated with the Virial model. At lower pressures, R-125 and R-134a are preferentially adsorbed in all materials, probably due to enthalpic factors resulting from a higher degree of interactions between the gas molecules and the adsorbent. However, at higher pressures, entropic factors may be involved in the gas adsorption process and therefore the selectivity is shifted toward the adsorption of the gas with the lowest molar volume (R-32), or toward a value of 1 (no selectivity). Furthermore, MOF-177 is the material with the highest adsorption capacity at higher pressures for the three studied F-gases, resulting from its mesoporous nature, which allows the packing of more gas molecules in its pores at high pressures.

The results presented in this work show that the utilization of MOFs, as tailored made materials, is promising for the development of new approaches for the selective capture of F-gases and for the separation of blends of these gases, which are used in commercial refrigeration. Moreover, this work contributes to the fundamental understanding of the behavior of these novel materials and the different interactions and mechanisms involved in gas adsorption. Finally, this work opens possibilities for the development of improved materials.

4.10 Porous Organic Polymers for the adsorption of fluorinated gases

The development of advanced materials exhibiting self-assembling and selective adsorption properties for the capture of fluorinated gases (F-gases) has attracted substantial attention, driven by the urgent need to mitigate the impacts of climate change. For the use of these materials at an industrial scale, the preparation of these materials must be both effective and economically accessible. Porous Organic Polymers (POPs) represent a broad and versatile class of materials entirely constructed from organic building blocks linked through covalent bonds. Their intrinsic porosity, high surface area, and tuneable functionality, including both crystalline and amorphous structures, make them attractive for a wide range of applications. Some of these properties can facilitate strong and selective interactions with F-gas molecules. These textual properties can facilitate strong and selective interactions with F-gas molecules. These advanced materials offer promising alternatives to support the circular economy initiatives in the refrigeration sector, as encouraged by the European Union. In this study, the adsorption equilibria of difluoromethane (R-32), pentafluoroethane (R-125), 1,1,1-tetrafluoroethane (R-134a), sulphur hexafluoride (SF_6), and nitrogen (N_2) were experimentally determined on four distinct POPs: RIO-55, RIO-23, RIO-20, and RIO-12. The experimental data were fitted using the Dual-Site Langmuir adsorption model to capture the diversity of adsorption behaviors observed in these systems. Furthermore, competitive selectivity for representative commercial blends, R-410A, R-407C, and SF_6/N_2, was evaluated through Ideal Adsorbed Solution Theory (IAST) calculations. Among the materials investigated, RIO-55 demonstrated the highest selectivity, particularly under low-pressure conditions, due to its optimal balance between microporosity and mesoporosity. This intrinsic ionic character further enhances interactions, making it the most promising candidate for the selective capture of F-gases.

4.10.1 Experimental section

4.10.1.1 Materials

All reagents and chemicals were acquired and used as received, without further purification. Melamine (purity > 98 wt %), triformyl resorcinol (purity > 98 wt %), acetic acid (purity > 99 wt %), dimethyl sulfoxide (DMSO, ACS reagent grade, purity > 99 wt %), and ethanol (ACS reagent grade, purity > 99.5 wt %) were purchased from Sigma-Aldrich (Lisbon, Portugal). Difluoromethane (R-32, purity ≥ 99.9 wt %) and pentafluoroethane (R-125, purity ≥ 99.8 wt %) were supplied by Polo Zero (Lisbon, Portugal). 1,1,1,2-Tetrafluoroethane (R-134a, purity ≥ 99.8 wt %), sulphur hexafluoride (SF_6,

purity ≥ 99.8 wt %), and nitrogen (N_2, purity ≥ 99.9 wt %) were obtained from Linde Gas (Lisbon, Portugal). Helium (He, purity ≥ 99.9 wt %) was provided by Praxair (Lisbon, Portugal).

4.10.1.2 Synthesis of POPs

RIO-55, RIO-12, and RIO-20 were synthesised following previously established procedures [164–167]. In the final step, RIO-55 was not subjected to supercritical CO_2 ($scCO_2$) drying to intentionally reduce its porosity and surface area in order to improve selective adsorption. The synthesis of RIO-23 was carried out by introducing 75 mg of melamine (0.6 mmol) and 135 mg of triformyl resorcinol (TFRe, 0.7 mmol) into a 48 mL high-pressure reaction vessel (ChemGlass; 38 mm O.D. × 114 mm length). Subsequently, 8 mL of DMSO and 3 mL of 6 M acetic acid were added. The mixture was stirred and heated at 438 K for 72 hours. The product was a gelatinous solid, which was filtered, washed with ethanol, and dried using $scCO_2$. The final POP was obtained as an orange, extremely lightweight powder.

4.10.2 Results and discussion

4.10.2.1 Materials characterisation

The details of the equipment used for material characterization are provided in Section 4.2, where Table 4.10.1 summarises the textural properties of the four POPs investigated for the adsorption of fluorinated gases (F-gases). According to the IUPAC classification, the nitrogen adsorption/desorption isotherms expose distinct pore structures among the POPs. RIO-12 exhibits a Type I isotherm, characteristic of microporous materials, while RIO-55 and RIO-20 show Type II and RIO-23 presents a Type IV isotherm, typically associated with microporous/mesoporous materials. Moreover, RIO-55, RIO-20, and RIO-12 confirm H4-type hysteresis, and RIO-23 exhibits H3-type hysteresis, suggesting larger pores. Despite exhibiting microporosity, RIO-23 also presents larger pores, which generate “false pores” as detected by porosimetry. These larger pores can function as additional adsorption sites and facilitate gas diffusion. The hysteresis observed in all RIO materials can be attributed to the self-assembly-driven generation of porosity, which may lead to capillary condensation effects within the pore network, as illustrated Figure 4.10.1 [31,84,91,168,169].

The nitrogen adsorption/desorption isotherm profiles observed for the RIO materials are consistent with the textural characteristics typically associated with layered or lamellar structures [168,170,171]. The presence of hysteresis in these materials is indicative of the micro/mesoporosity, which arises both within individual particles and in the interparticle voids created during self-assembly processes [31,168,170,171]. The pore size distribution was assessed based on the IUPAC classification

system [84,91,169], where pores with diameters ≤ 20 Å are considered micropores, those between 20–500 Å as mesopores, and pores ≥ 500 Å as macropores. The BET method was employed to determine the specific surface area of the POPs from nitrogen adsorption isotherms [172]. RIO-55 exhibited a relatively low surface area of 55 m²/g and mesoporosity in the range of 23–45 Å. In contrast, RIO-23 presented a significantly higher surface area of 518 m²/g and exhibited a dual micro/mesoporous structure with pores ranging from 11–35 Å (see Table 4.10.1 and Figure 4.10.1). RIO-20 and RIO-12 exhibited S_{BET} values of 170 m²/g and 985 m²/g, respectively. Their pore size distributions revealed micro/mesoporosity within the range of 12–45 Å for RIO-20 and 5–30 Å for RIO-12 (see Table 4.10.1 and Figure 4.10.1). The substantial reduction in the surface area of RIO-55 (see Figure 4.10.2) is attributed to the absence of $scCO_2$ drying during synthesis, a critical step in preserving ionic lamellar POPs [31,32,37]. This reduction is also reflected in the diminished micropore volume, which may be advantageous for enhancing the selective adsorption of larger F-gases due to restricted diffusion in narrower micropores.

Table 4.10.1 Textural parameters of POPs studied in this work obtained from N_2 adsorption isotherms.

POPs	S_{BET}(m²/g)	v_{total} (cm³g⁻¹)	v_{micro}(cm³g⁻¹)	v_{meso}(cm³g⁻¹)
RIO-55	55	0.08	0.04	0.04
RIO-23	518	0.69	0.34	0.35
RIO-20	170	0.23	0.12	0.11
RIO-12	985	0.49	0.42	0.07

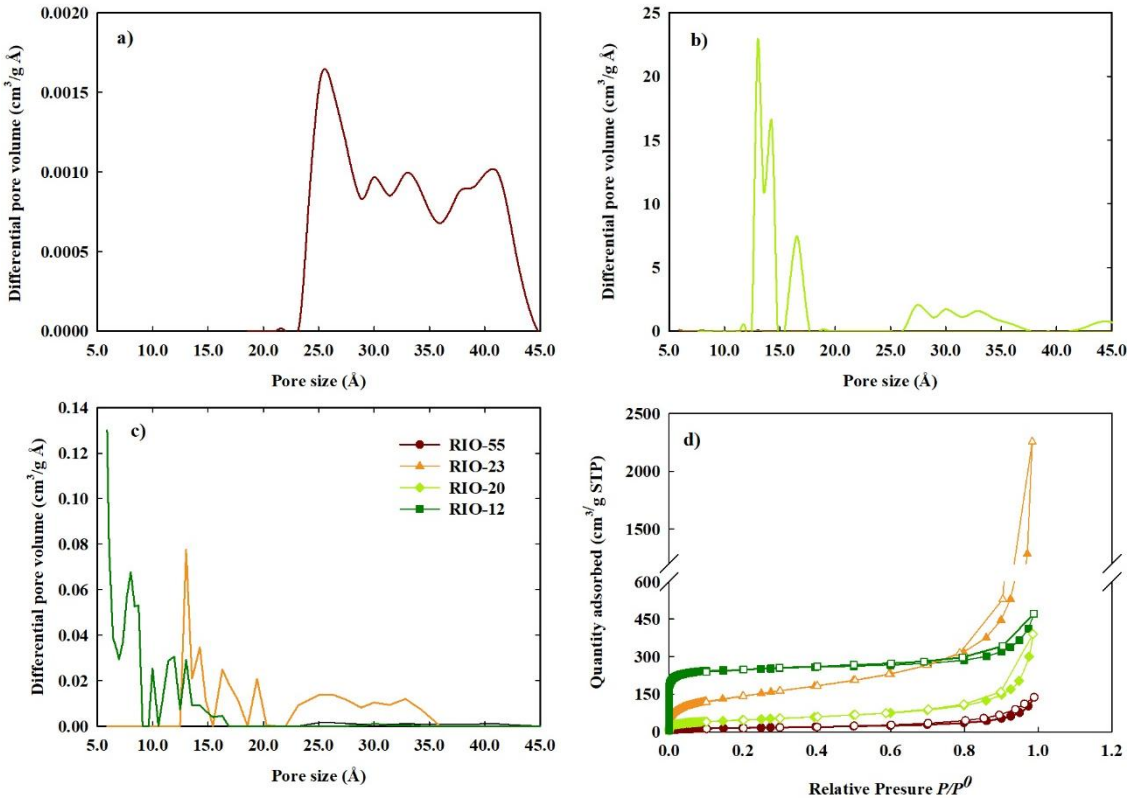


Figure 4.10.1 Pore size distribution of the POPs studied in this work: a) RIO-55 (dark red line), b) RIO-20 (green line), c) RIO-23 (orange line) and RIO-12 (dark green line), and d) nitrogen adsorption (full symbols) and desorption (empty symbols) equilibrium isotherms at 77 K for RIO-55 (dark red), RIO-23 (orange), RIO-20 (green) and RIO-12 (dark green).

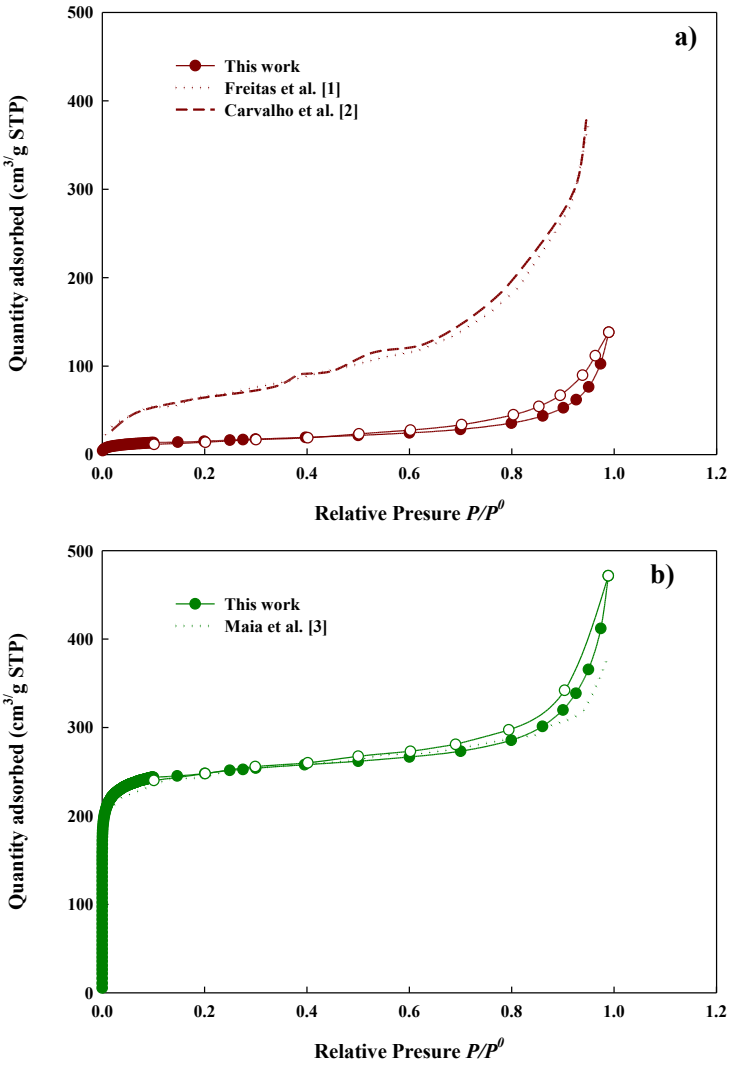


Figure 4.10.2 Equilibrium isotherms at 77 K for: a) RIO-55 (dark red) and RIO-12 (dark green).

Figure 4.10.3 presents the FTIR spectra of the POPs investigated in this study. Characteristic bands associated with aldehyde carbonyl (C=O) stretching vibrations are observed at approximately 1563 cm-¹ for RIO-55, 1549 cm-¹ for both RIO-23 and RIO-20, and 1623 cm-¹ for RIO-12. In addition, vibrational bands observed at 1455 cm-¹ (RIO-55 and RIO-23), 1474 cm-¹ (RIO-20), and 1445 cm⁻¹ (RIO-12) are attributed to C–N=N stretching modes, which likely originate from dye-derived moieties retained within the structures. Furthermore, distinct bands at 1626 cm-¹ (RIO-55) and 1645 cm-¹ (RIO-23) are assigned to C=N stretching vibrations, suggesting enhanced intermolecular hydrogen bonding interactions within the POPs matrices, which can influence the material's crystallinity and chemical stability [32,173].

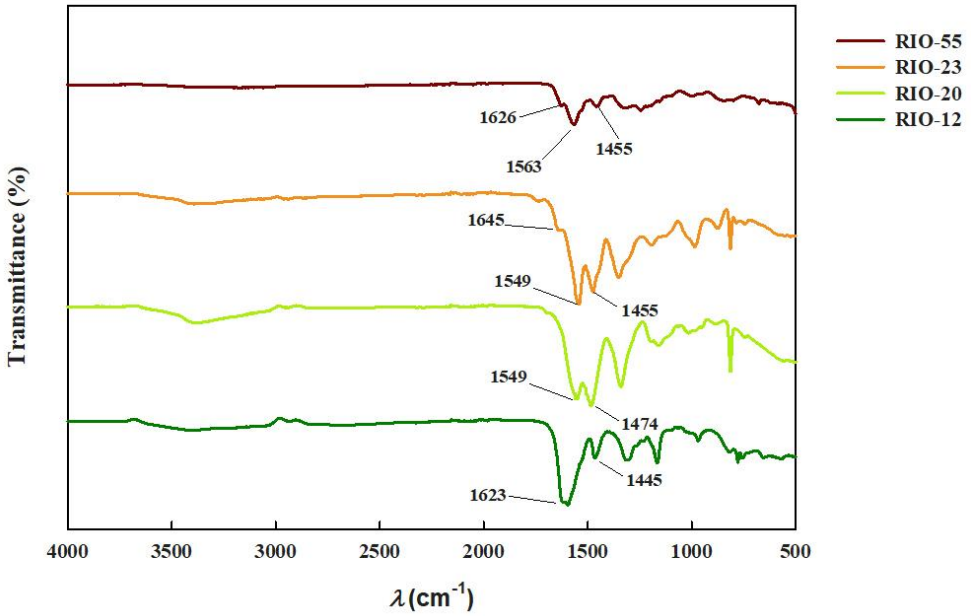


Figure 4.10.3 FTIR spectra for the POPs studied in this work: RIO-55 (dark red line), RIO-23 (orange line), RIO-20 (green line), and RIO-12 (dark green line).

Thermogravimetric analysis of the RIO materials reveals three distinct regions of mass loss, as depicted in Figure 4.10.4. In the first region, a minor weight loss of approximately 5 - 10 % occurs around 400 K, which is attributed to the desorption of residual solvents entrapped within the porous structure of the materials. Then, a gradual mass loss is observed up to approximately 615 K, beyond which significant thermal decomposition of these RIO materials occurs. RIO-55 exhibits an initial mass loss of ~ 20 %, ultimately reaching a total weight loss of 47 % upon heating to 1200 K. Similarly, RIO-23 and RIO-20 suffer major thermal degradation ≈ 45 - 48 % beyond 615 K, finishing in total mass losses of approximately 87 % by 1200 K. In contrast, RIO-12 demonstrates a relatively lower mass loss of ~ 35 % above 615 K, with decomposition proceeding progressively up to 1200 K, resulting in a total weight loss of around 60 %. In summary, the thermal behaviour of these POPs indicates that they are thermally stable up to at least 400 - 450 K. These results highlight their potential for regeneration and reuse in GHG capture and separation processes. Furthermore, all materials employed in this study required at least 8 - 10 regeneration cycles. After these cycles, the materials preserved their structural integrity as well as their adsorption performance. These results confirm the high stability of the POPs.

Table 4.10.2 presents the results of the elemental analysis for the synthesised POPs, revealing high contents of carbon, nitrogen, and oxygen, consistent with the chemical composition of the POPs. The elevated nitrogen and oxygen content is particularly relevant, as these heteroatoms contribute to the presence of polar functional groups (e.g., amines, imines, hydroxyls) on the POPs surfaces. These functionalities can serve as active sites for specific interactions with GHGs, thereby enhancing adsorption performance.

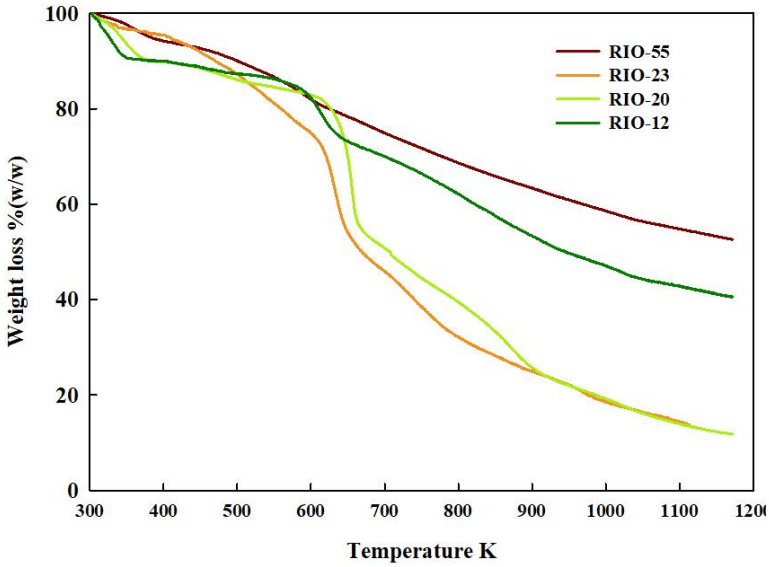


Figure 4.10.4 TGA of the POPs studied in this work: RIO-55 (dark red line), RIO-23 (orange line), RIO-20 (green line) and RIO-12 (dark green line).

Table 4.10.2 Elemental analysis of the POPs studied in this work.

	RIO-55	**RIO-23**	**RIO-20**	**RIO-12**
C (*wt.*%)	54.8	42.6	44.7	33.4
H (*wt.*%)	4.2	4.6	4.5	4.9
N (*wt.*%)	16.7	29.4	14	43.6
S (*wt.*%)	0	4.5	0	1.7
O[a] (*wt.*%)	24.3	18.8	36.9	16.4

[a] Calculated as follow: O = 100 – (C + H + N + S)

The XPS analysis was carried out to determine the elemental atomic composition (%). RIO-20 and RIO-23 possess high nitrogen content (43.12 % and 28.65 %, respectively), suggesting that their molecular networks are built from precursors rich in nitrogen-containing functional groups. RIO-20 exhibits a very low oxygen content (3.79 %), whereas RIO-23 shows a higher oxygen percentage (11.79 %). In the latter, it was also detected 2.17 % atomic sulphur and 0.24 % chlorine, which are believed not to be structural elements but rather residues from the synthesis process or other external sources. In the case of RIO-12 and IO-55, a higher carbon content (70.54 % and 72.66 %, respectively) and a more moderate nitrogen concentration (12.66 % and 15.68 %) were detected. Both samples contain significant amounts of oxygen (16.64 % and 9.98 %). RIO-55 is the only sample with a relevant chlorine concentration (1.20 %), which is part of its structure. Additionally, fluorine (0.48 %) was detected in this sample, likely originating from a fluorinated salt and considered to be a residual contaminant.

Concerning the XRPD analysis, RIO-12 showed a crystalline material with diffraction peaks at 6.9°, 11.9° and 27.2°, corresponding to the lattice planes (100), (210) and (002), respectively, [174]. RIO-55 also presented a crystalline behaviour with diffraction peaks at 4.7° and 26.9°, corresponding

to the lattice planes (100) and (002), respectively. It is important to consider that RIO-20 and RIO-23 do not show crystalline behaviour, indicating an amorphous character.

The SEM analysis (see Figure 4.10.5) was used to analyse the morphology of the materials studied in this work. The RIO-55 morphology consists of highly agglomerated particles with rugged and poorly defined surfaces (see Figure 4.10.5a). This characterisation demonstrates the low surface area and minimal total and microporous volumes of this material (see Table 4.10.1.), indicating severely limited pore accessibility. In contrast, RIO-23 (see Figure 4.10.5b) exhibits more open particles, with greater surface development, consistent with its surface area and increased microporous volume (see Table 4.10.1.) [175]. This more expanded morphology promotes a network of accessible pores. On the other hand, RIO-20 presents larger aggregates and relatively compact crystalline blocks (see Figure 4.10.5c), with an intermediate surface area and microporous volume (see Table 4.10.1.). These values suggest a balance between crystalline growth and microporosity preservation, indicating that dense morphology does not entirely hinder access to the porous network. Finally, RIO-12 is characterised by well-defined spherical particles distributed throughout the aggregates [33,175]. This morphology indicates a controlled nucleation mechanism that generates higher porosity than RIO-23 and RIO-20, making RIO-12 the most promising with respect to structural properties. In summary, highly collapsed structures (RIO-55) significantly reduce surface area, whereas more open morphologies (RIO-12) maximise accessible surface and microporosity, highlighting that surface texture and pore distribution directly influence adsorptive performance and selectivity of F-gases on these POPs.

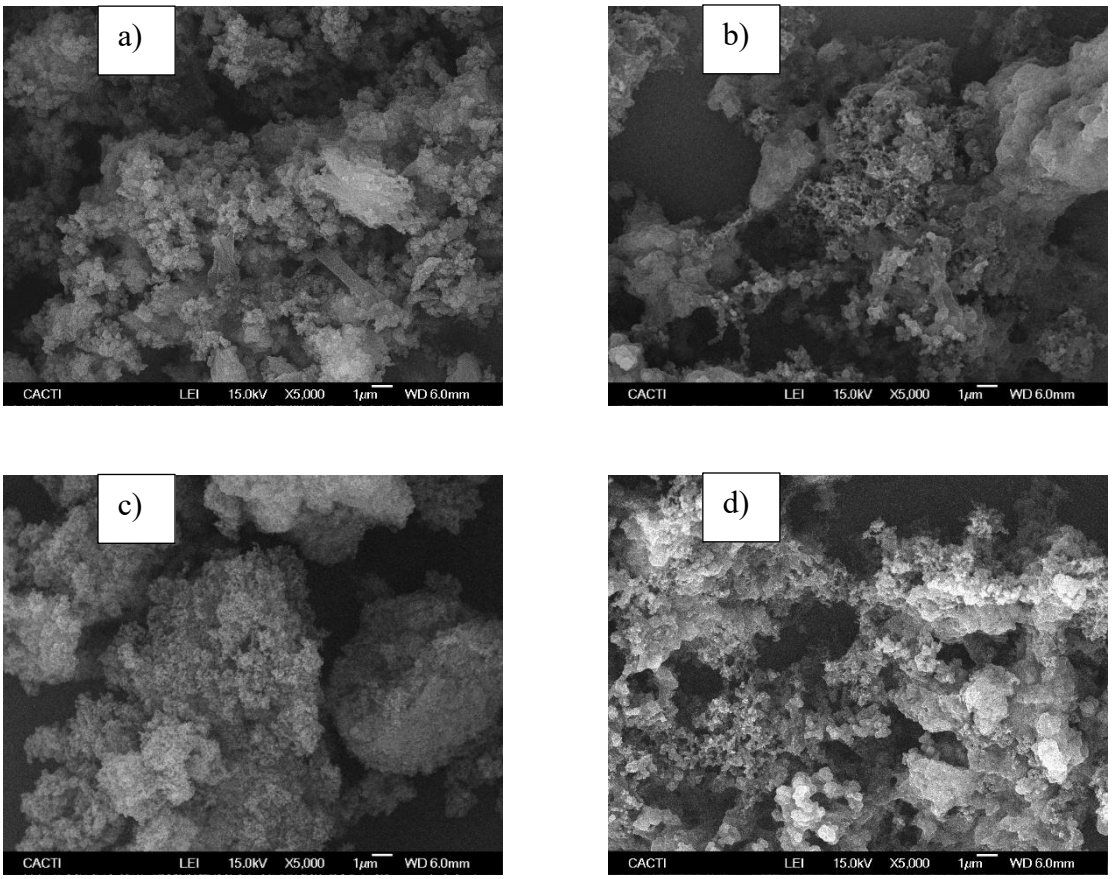


Figure 4.10.5 SEM images of the POPs studied in this work: a) RIO-55, b) RIO-23, c) RIO-20, and d) RIO-12.

4.10.2.2 Adsorption equilibrium of GHGs on POPs

The methodology and equipment used for the determination of adsorption equilibria are described in Section 4.3. The adsorption-desorption equilibrium data for GHGs on the synthesised POPs exhibit negligible hysteresis, suggesting complete reversibility of the adsorption process and efficient material regeneration upon desorption. This behaviour indicates that the interactions between the POPs and GHGs are predominantly physical. The shape and type of the isotherms obtained are primarily governed by the intrinsic structural features of the adsorbents, such as specific surface area, pore volume, and pore size distribution. The dual-site Langmuir (DSL) model was applied to fit the experimental isotherm data. This model was selected to capture heterogeneous adsorption characteristics, providing insights into the competitive and thermodynamically favorable interactions between the POPs and the GHGs.

The adsorption equilibria were fitted with the dual-site Langmuir model (DSL) [176,177]:

$$q = q_{m1,i}\frac{b_{1i}p_i}{1+b_{1i}p_i} + q_{m2,i}\frac{b_{2i}p_i}{1+b_{2i}p_i} \qquad 4.10.1$$

where $q_{m1,i}$ and $q_{m2,i}$ are the maximum adsorption capacity of component *i* in each of the two adsorption sites, b_{1i} and b_{2i} are the affinity constants (MPa^{-1}) of component *i* in each of the adsorption sites, and *P* is the partial pressure. The fitting parameters for the Dual-Site Langmuir (DSL) model are summarised in Table 4.10.3. The accuracy of the model was evaluated using the Average Relative Error (ARE), calculated as follows:

$$ARE(\%) == \frac{100}{N_{exp}} \sum \frac{[q_{fit} - q_{exp}]}{q_{exp}} \quad 4.10.2$$

where N_{exp} is the number of experimental points, and q_{fit} and q_{exp} are the fit and experimental adsorbed quantity.

Table 4.10.3 Adsorption equilibrium model parameters for sorption of R-32, R-125, R-134a, SF_6 and N_2 on POPs at 303.15 K.

POPs	Gases	q_m (mmol/g)		b (MPa^{-1})		ARE (%)
		q_{m1}	q_{m2}	b_1	b_2	
RIO-55	R-32	5.39	0.956	0.476	72.7	2.17
	R-125	5.09	0.227	0.154	78.7	1.80
	R-134a	4.76	0.903	0.251	24.5	0.698
	SF_6	4.52	0.0405	0.106	45.9	3.04
	N_2	2.46	0.0552	0.158	45.5	8.44
RIO-23	R-32	15.2	0.810	0.532	43.8	5.36
	R-125	9.17	0.973	0.675	97.2	2.33
	R-134a	12.5	0.910	1.07	331	3.14
	SF_6	9.24	0.358	0.346	33.7	1.25
	N_2	3.31	0.0629	0.238	95.2	4.22
RIO-20	R-32	8.65	1.47	0.289	25.8	2.81
	R-125	8.89	0.800	0.151	25.4	2.42
	R-134a	5.16	0.794	0.689	84.8	0.987
	SF_6	8.57	0.374	0.101	12.0	2.39
	N_2	2.86	0.0228	0.199	55.5	6.60
RIO-12	R-32	7.72	4.80	0.294	22.9	1.63
	R-125	6.44	2.66	0.243	109	0.904
	R-134a	3.34	2.62	1.66	354	0.306
	SF_6	5.35	2.09	0.201	46	1.24
	N_2	5.96	0.0952	0.219	11.6	5.46

The adsorption behaviour of R-32, R-125, and R-134a on the POPs is depicted in Figure 4.10.6 with two primary factors: the presence and nature of functional groups on the POPs surfaces, and the intrinsic structural characteristics of each material. The adsorption process can be delineated into two distinct pressure-dependent regimes: a low-pressure region and a high-pressure region. For R-32, this transition occurs at approximately 1 MPa, for R-125 at around 0.5 MPa, and for R-134a at roughly 0.2 MPa. In the low-pressure regime, the adsorption capacities follow the order: RIO-12 > RIO-23 > RIO-20 > RIO-55. This trend correlates well with the corresponding micropore volumes and specific surface areas of the POPs, as reported in Table 4.10.1. These results suggest that at low pressures, microporosity and accessible surface area are the dominant factors controlling gas uptake.

RIO-12 exhibits the highest specific surface area and a predominantly mesoporous structure among the POPs analyzed (see Figure 4.10.1), which significantly contributes to its enhanced adsorption capacity. In general, materials with larger surface areas demonstrate superior gas uptake due to the increased availability of adsorption sites [36,151]. Moreover, the adsorption of F-gases is also driven by electrostatic interactions, as these molecules possess highly electronegative fluorine atoms. The adsorption in RIO-12 is further enhanced by the presence of surface functional groups such as hydroxyl (-OH) and aldehyde carbonyl (C=O), which can engage in hydrogen bonding with the F-gases. Additionally, the tubular structure of RIO-12 may enable molecular diffusion into confined pores, reinforcing adsorption at low pressures.

However, at higher pressures, the adsorption capacity order shifts to RIO-23 > RIO-12 > RIO-20 > RIO-55. This change can be attributed to the total pore volume, which becomes increasingly influential as pressure rises. RIO-23 possesses the highest pore volume among the POPs (see Table 4.10.1), facilitating denser molecular packing and thus higher adsorption at elevated pressures. Furthermore, the adsorption affinity for individual F-gases follows the trend: R-32 > R-134a > R-125. This is primarily due to the molecular structure and degree of fluorination. As the number of fluorine atoms increases, the overall electronegativity of the molecule reduces the strength of interactions with the POPs surface functional groups. Consequently, F-gases with fewer fluorine atoms exhibit stronger specific interactions with the POPs, thereby enhancing adsorption performance.

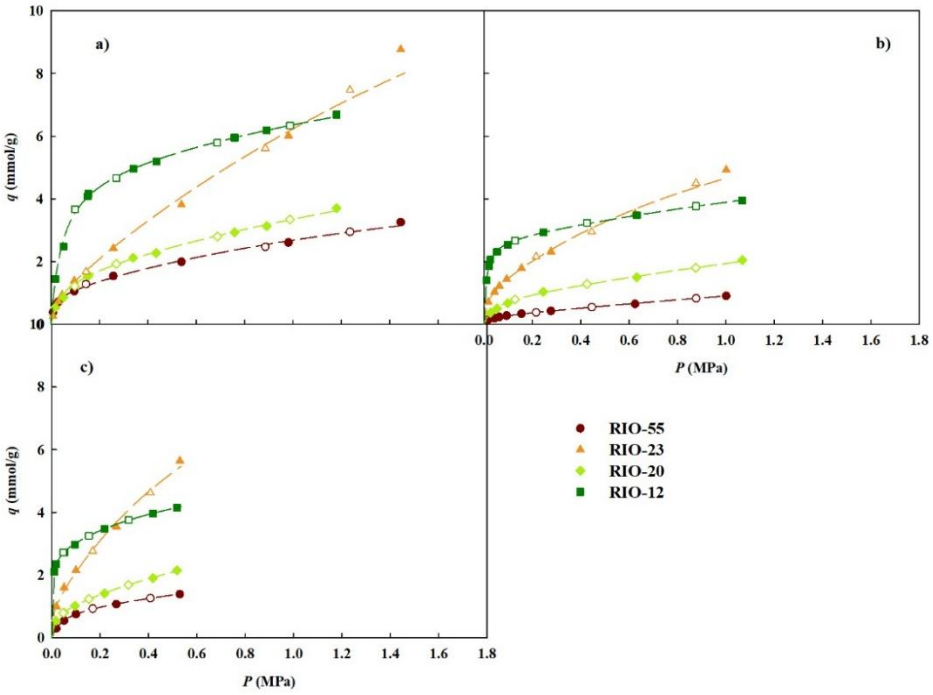


Figure 4.10.6 Adsorption (full symbols) and desorption (empty symbols) equilibrium isotherms of: a) R-32; b) R-125; and c) R-134a on RIO-55 (dark red), RIO-23 (orange), RIO-20 (green) and RIO-12 (dark green) at 303.15 K.

The adsorption behaviour of SF_6 on the POPs, depicted in Figure 4.10.7a, is primarily governed by the structural properties of the adsorbents rather than specific electrostatic interactions. Due to its geometry and high molecular symmetry, SF_6 has a net dipole moment of zero, effectively nullifying any directional electrostatic interactions with the functional groups present on the POPs surfaces. The observed adsorption capacities of the POPs follow the order: RIO-12 > RIO-23 > RIO-20 > RIO-55, which correlates with both the mesoporous volume and the overall surface area (see Table 4.10.1). RIO-12, with its high specific surface area and well-developed mesoporosity, exhibits the greatest SF_6 uptake. However, at higher pressures, RIO-23 slightly surpasses RIO-12. This is attributed to RIO-23 possessing a larger total pore volume, which enhances its ability to accommodate and pack SF_6 molecules under pressure. These findings underscore the importance of pore volume and distribution when adsorbing highly symmetric, nonpolar gases, such as SF_6.

On the other hand, N_2 adsorption is primarily influenced by the structural characteristics of the POPs, particularly micropore volume and specific surface area, as detailed in Table 4.10.1. As illustrated in Figure 4.10.7b, the adsorption capacities follow the order: RIO-12 > RIO-23 > RIO-20 > RIO-55. This trend reflects the decreasing microporosity and surface area, which are critical parameters for the physisorption of small, non-polar molecules such as N_2. Given that N_2 possesses a linear, homonuclear structure with a dipole moment of zero, it is incapable of engaging in significant electrostatic interactions with the functional groups of the POPs. As a result, adsorption is predominantly governed by physical confinement effects.

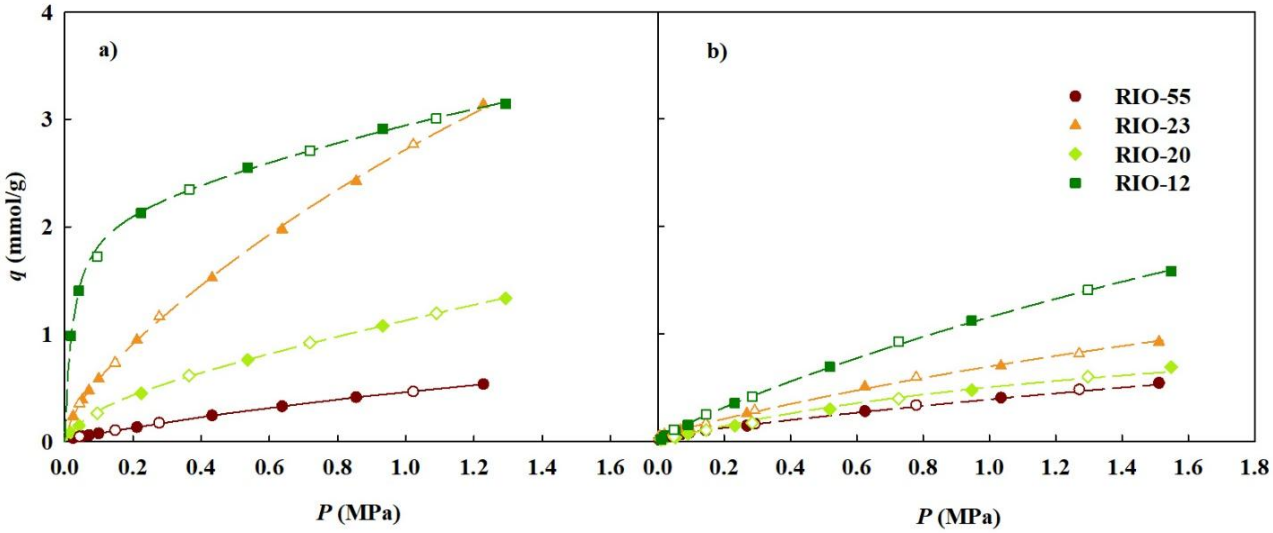


Figure 4.10.7 Adsorption (full symbols) and desorption (empty symbols) equilibrium isotherms of: a) SF_6; b) N_2 on RIO-55 (dark red), RIO-23 (orange), RIO-20 (green) and RIO-12 (dark green) at 303.15 K.

4.10.2.3 Determination of Henry's law constant

Henry's constants were determined by applying the virial equation, as described in Section 4.4. These constants were subsequently calculated for each gas–POPs pair to quantitatively assess the intrinsic adsorption affinity in the low-pressure region (see Figure 4.10.8). Adsorption is predominantly governed by the strength of the gas–surface interactions rather than by pore-filling phenomena. The results show a consistent trend across all studied gases following the order: RIO-12 > RIO-23 > RIO-20 > RIO-55. These trends correlate strongly with the micropore volume of the materials (see Table 4.10.1). Gas molecules preferentially occupy the most energetically favourable adsorption sites. Therefore, materials with greater microporosity enhance the initial uptake and affinity as quantified by Henry's constants.

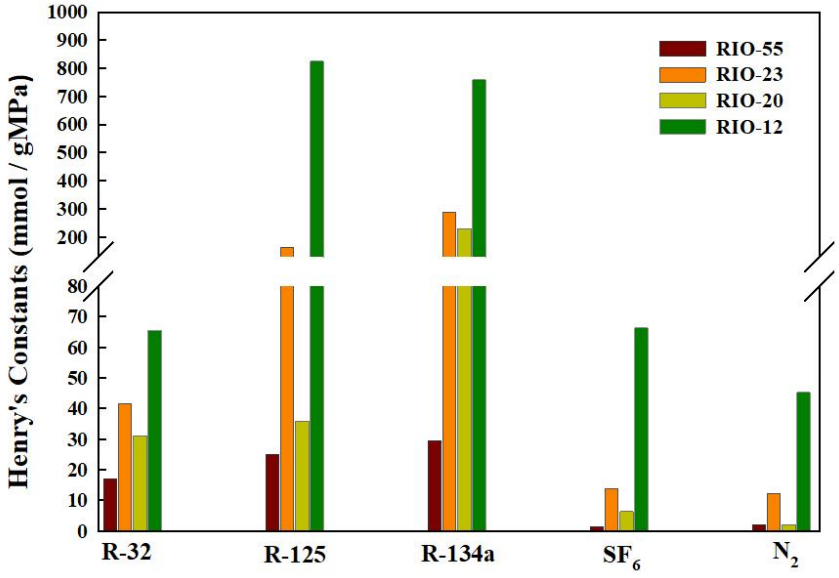


Figure 4.10.8 Henry's law constants at 303.15 K for the POPs studied in this work.

4.10.2.4 Separations of the F-gases mixtures

The increasing increasing industrialization and the resulting emission of F-gases necessitate the development of efficient technologies for the separation and capture of mixtures into their pure components. The selective separation of multicomponent gas mixtures remains a significant challenge due to the complexity of competitive adsorption phenomena. A widely adopted approach to evaluate such separations involves deriving multicomponent adsorption behaviour from single-component isotherms using thermodynamic models. Among these, the Ideal Adsorbed Solution Theory (IAST) is the most extensively employed method for predicting multicomponent adsorption equilibria [69,70,178–180]. IAST assumes that the adsorbed phase behaves as an ideal solution, following Raoult's law, and formulates a system of nonlinear equations to describe the composition of the adsorbed phase at equilibrium [179]. The predictive accuracy of IAST relies heavily on the suitability and quality of the adsorption model used to describe the single-component adsorption behaviour. In the present study, IAST was applied to estimate the adsorption equilibria of F-gases mixtures on POPs, utilising the Dual-Site Langmuir (DSL) model.

The gas mixtures investigated in this study were selected based on their industrial relevance and representativeness of commonly used F-gases. These mixtures exhibit a high level of complexity due to the presence of azeotropic or quasi-azeotropic behaviour, which poses significant challenges for their separation using conventional techniques. In particular, two commercially important refrigerant blends were analysed: R-410A, composed of R-32 and R-125 with molar fractions $y_{R-32} = 0.7$ and $y_{R-125} = 0.3$ and R-407C, a ternary mixture of R-32, R-125, and R-134a with molar fractions $y_{R-32} = 0.38$, $y_{R-125} = 0.18$ and $y_{R-134a} = 0.44$. Additionally, the study addresses gas mixtures relevant to the electrical insulation and semiconductor industries, specifically a binary blend of SF_6 and N_2 ($y_{SF_6} = 0.10$ and $y_{N_2} = 0.90$). The inclusion of these mixtures enables a comprehensive assessment of the adsorption-based separation performance of POPs in technologically significant applications involving complex gas systems.

The multicomponent adsorption equilibria of F-gases on the POPs materials were evaluated at 303.15 K within a pressure range of 0.01 to 1.0 MPa for the binary gas mixtures R-410A and SF_6/N_2). For the ternary mixture R-407C, equilibrium measurements were conducted between 0.01 and 0.6 MPa to mitigate the capillary condensation within the POPs. Based on the obtained multicomponent adsorption data, the selectivity of gas component *i* over component *j* was calculated following the methodology described in Section 4.5.

The commercial refrigerant blend R-410A consists of two components, R-32 and R-125, which differ in both the number of fluorine atoms and carbon chain length. These structural differences significantly influence their interactions with the functional groups present in the POPs. The high electronegativity of fluorine atoms induces electrostatic repulsions with the functional groups on the POPs surfaces. Experimental results (see Figure 4.10.6) demonstrate that R-32 exhibits a higher adsorption

capacity than R-125 across all studied POPs. Then, RIO-55 and RIO-20 show enhanced selectivity toward R-32. In contrast, RIO-23 displays the highest preference for the selectivity of R-125 over R-32 across the entire pressure range. The selectivity trend for the R-410A, shown in Figure 4.10.9, follows the order: RIO-55 > RIO-20 > RIO-12 > RIO-23. This observed trend correlates with the total pore volume of the POPs (see Table 4.10.1). RIO-55, which has the lowest surface area and total pore volume among the studied materials [35], favours the preferential adsorption of the smaller R-32 molecules due to stronger confinement effects. This molecular sieving effect enhances the selectivity for R-32 over R-125, underscoring the critical role of textural properties in the competitive adsorption behaviour of F-gases mixtures [35].

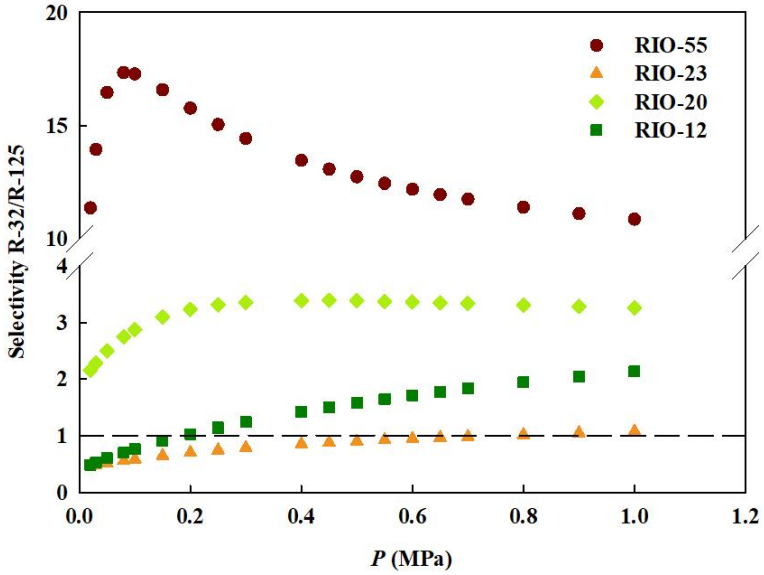


Figure 4.10.9 Selectivity of RIO-55 (dark red), RIO-23 (orange), RIO-20 (green) and RIO-12 (dark green) to R-32 over R-125 as a function of pressure at 303.15 K, for the equilibrium gas phase composition of the R-32/R-125 mixture ($y_{R-32} = 0.7$ and $y_{R-125} = 0.3$). The dotted line represents the point where selectivity is equal to $y = 1$.

In the separation of SF_6 from N_2, the contribution of electrostatic interactions between these gases and the functional groups on the surface of the POPs is negligible, due to the nonpolar nature and zero dipole moment of both molecules. Then, the adsorption behaviour is governed by the textural properties of the materials. In all studied POPs, SF_6 exhibits a greater affinity for adsorption compared to N_2, as illustrated in Figure 4.10.7. The competitive selectivity for SF_6 over N_2 follows the order: RIO-12 > RIO-23 > RIO-20 > RIO-55 (see Figure 4.10.10). This trend correlates closely with the micropore volume and specific surface area of the materials, as presented in Table 4.10.1. This trend correlates with the micropore volume and specific surface area of the materials, as presented in Table 4.10.1. Then, materials with higher microporosity and accessible surface area facilitate more effective molecular packing of SF_6, enhancing the adsorption capacity and improving separation selectivity. Furthermore, a larger mesoporous volume contributes to accommodating a greater number of SF_6 molecules under equilibrium conditions, favouring the overall adsorption process and competitive selectivity in these POPs.

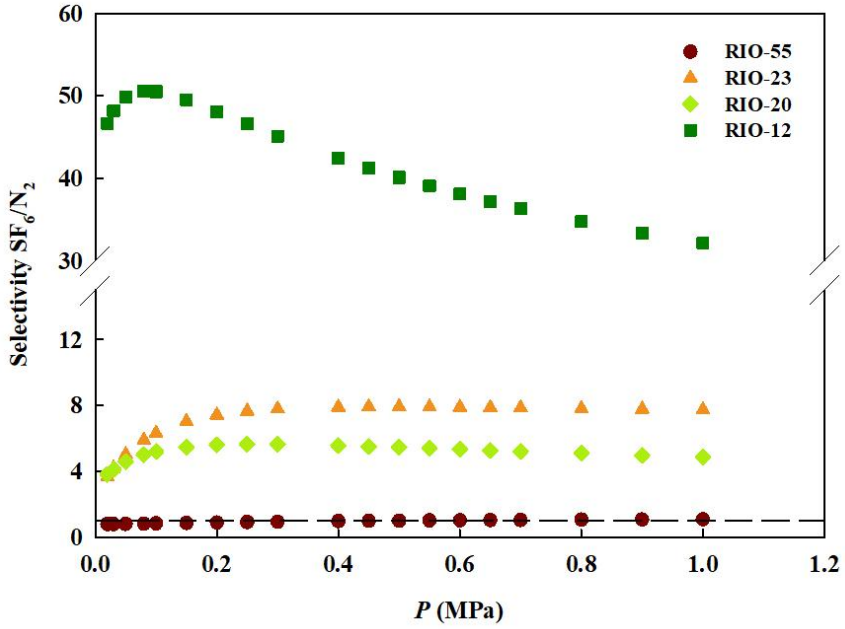


Figure 4.10.10 Selectivity of RIO-55 (dark red), RIO-23 (orange), RIO-20 (green) and RIO-12 (dark green) (green square) to SF_6 over N_2 as a function of pressure at 303.15 K, for the equilibrium gas phase composition of the SF_6/N_2 mixture ($y_{SF_6} = 0.10$ and $y_{N_2} = 0.90$). The dotted line represents the point where selectivity is equal to $y = 1$.

Fig. 4.10.11 present the selective separation behaviour of the commercial refrigerant blend R-407C, which comprises three F-gases: R-32, R-125, and R-134a. These components exhibit distinct properties in terms of molecular size and fluorine content, which influence their interactions with the POPs. The number of fluorine atoms impacts their electrostatic interactions with the functional groups on the surface of the POPs, where higher fluorine content enhances electron density and induces repulsive interactions, influencing adsorption selectivity.

The Fig. 4.10.11 illustrates the binary competitive adsorption scenarios within the ternary mixture. For the binary system R-32/R-125, the selectivity trend is as follows: RIO-55 > RIO-20 > RIO-12 > RIO-23. This behaviour is attributed to the smaller diameter of R-32, which allows it to be preferentially adsorbed in the narrower pores of materials like RIO-55, which possesses the lowest total pore volume (see Table 1). The confinement effect in small pores, along with subtle interactions with surface functional groups, enhances selectivity for R-32 over R-125.

In the binary separation of R-134a over R-125 (See Figure 4.10.11b), the selectivity follows the order: RIO-55 > RIO-12 > RIO-20 > RIO-23. The greater number of fluorine atoms in R-125 increases its electrostatic repulsion with the functional groups, disfavouring its adsorption. The moderate polarity and molecular size of R-134a make it more amenable to adsorption within the smaller micropores, particularly in RIO-55 and RIO-12. This trend also aligns with increasing micropore volume, favouring adsorption of relatively smaller or less fluorinated species (from smallest to largest, as shown in Table 4.10.10 and Figure 4.10.6).

Finally, in the binary separation of R-134a over R-32 (see Fig. 4.10.11c), the observed selectivity order is: RIO-12 > RIO-23 > RIO-20 > RIO-55 In this case, POPs with a larger micropore volume, especially RIO-12, enhance the packing efficiency of the slightly larger R-134a molecules, thus promoting competitive adsorption over the smaller R-32 species. These results highlight the critical role of pore size distribution, total pore volume, and surface in determining the selective adsorption behaviour of complex gas mixtures.

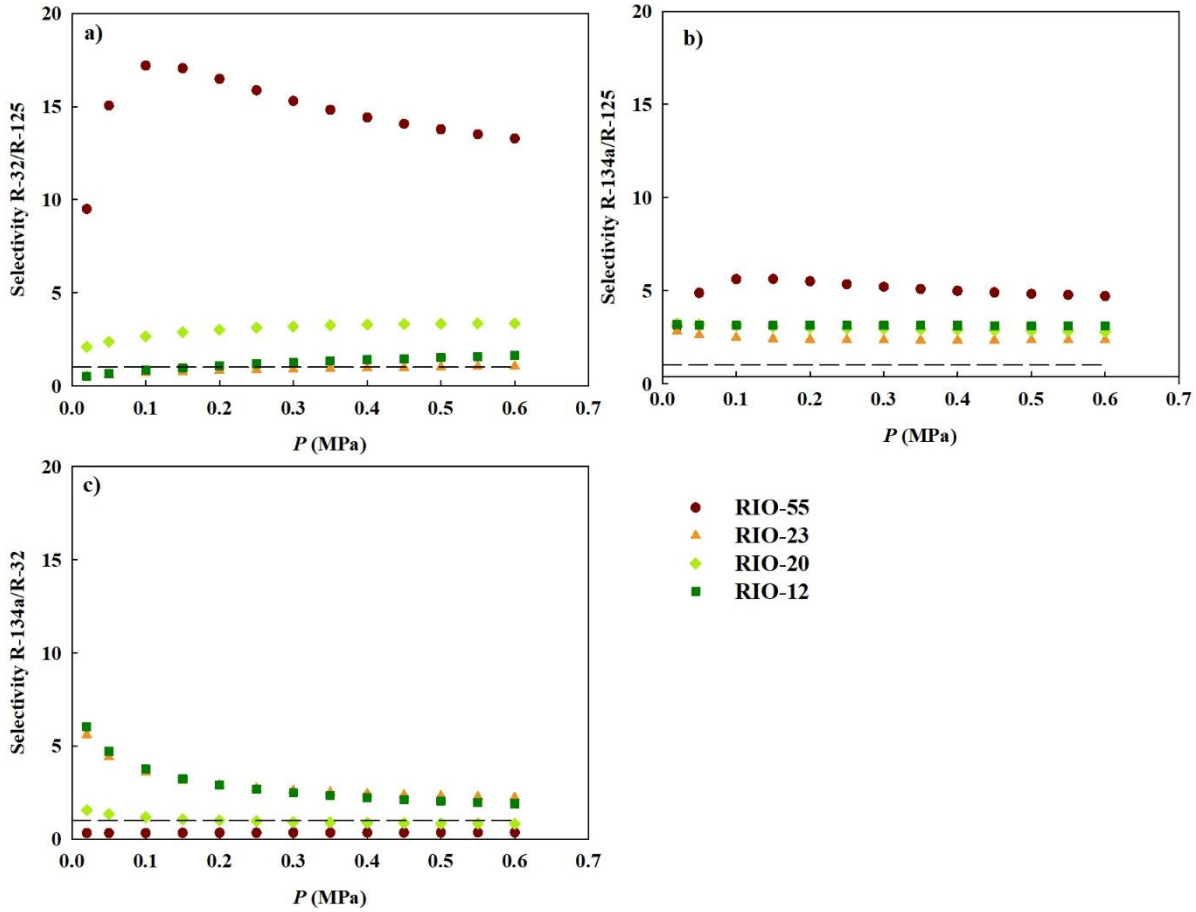


Figure 4.10.11 Selectivity of RIO-55 (dark red circles), RIO-23 (orange triangles), RIO-20 (green diamonds) and RIO-12 (dark green squares) to: a) R-32 over R-125; b) R-134a over R-125; and c) R-134a over R-32 as a function of pressure at 303.15 K, for the commercial R-407C gas mixture ($y_{R-32} = 0.38$, $y_{R-125} = 0.18$ and $y_{R-134a} = 0.44$). The dotted line represents the point where selectivity is equal to $y = 1$.

The performance of our materials was compared with the materials reported in the literature under identical conditions (303.15 K and 0.1 MPa) with the same gases studied in this work. These conditions, which are close to atmospheric pressure, allow for the separation of binary mixtures R-410A, SF_6/N_2 (see Figure 4.10.12- 4.10.13) without additional energy input.

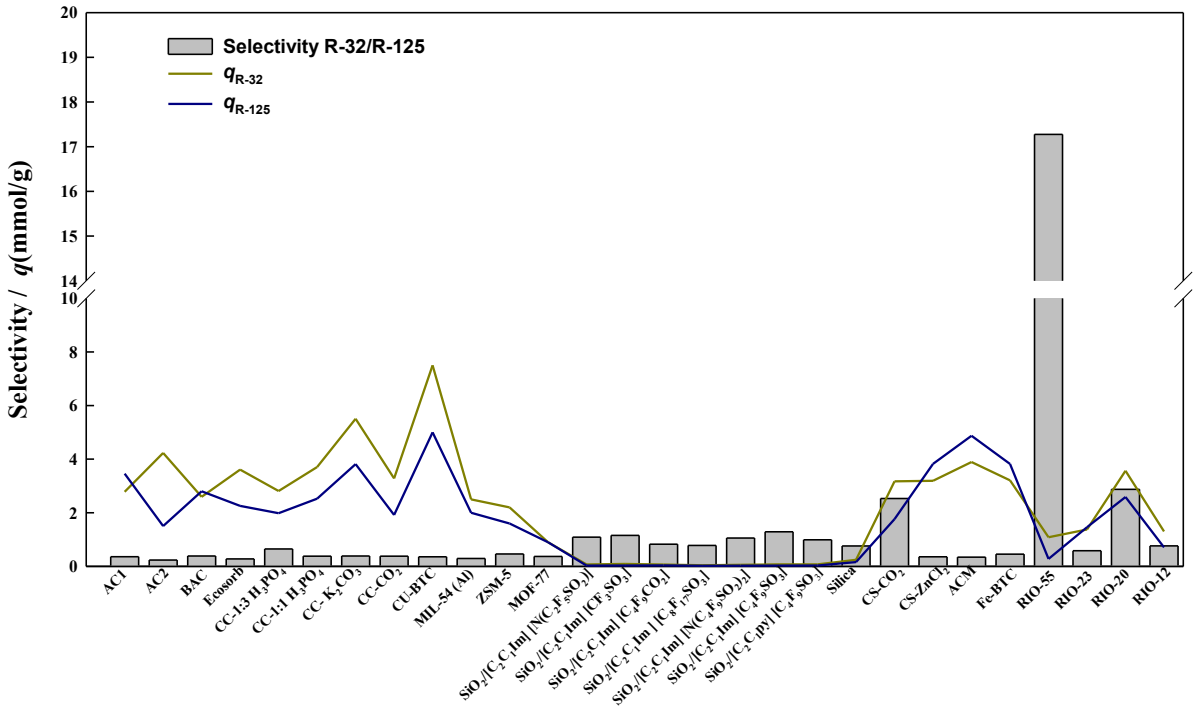


Figure 4.10.12 Comparison of the adsorption capacity of R-32 and R-125, and the selectivity of the R-410A mixture ($y_{R-32} = 0.7$ and $y_{R-125} = 0.3$) for the materials studied in this work and those reported in the literature at a pressure of 0.1 MPa and 303.15 K [19,27,29,30,38,181–191].

Different families of materials were evaluated, including MOFs, zeolites, AC, Bio-AC, and hybrid composite materials for the binary separation of R-410A (R-32/R-125). Some MOFs and zeolites exhibit high adsorption capacities, but their low selectivity limits their effectiveness in the separation of R-32 from R-125. Hybrid composites show higher selectivity, although their low adsorption capacity reduces the total amount of gas that can be separated and purified. Similarly, AC and Bio-AC exhibit high capacity, but their moderate selectivity decreases the overall efficiency of the process [192–194]. In contrast, the RIO materials studied in this work achieve a well-balanced performance, combining moderate to high adsorption capacity with high selectivity, allowing preferential adsorption for the target gas. Furthermore, these materials maintain stable performance, and their structural characteristics (tuned pore size and the presence of functional groups) favour interaction with the components of interest [192–194]. In summary, RIO materials show superior potential compared to other studied adsorbents for the separation of R-410A [38–40].

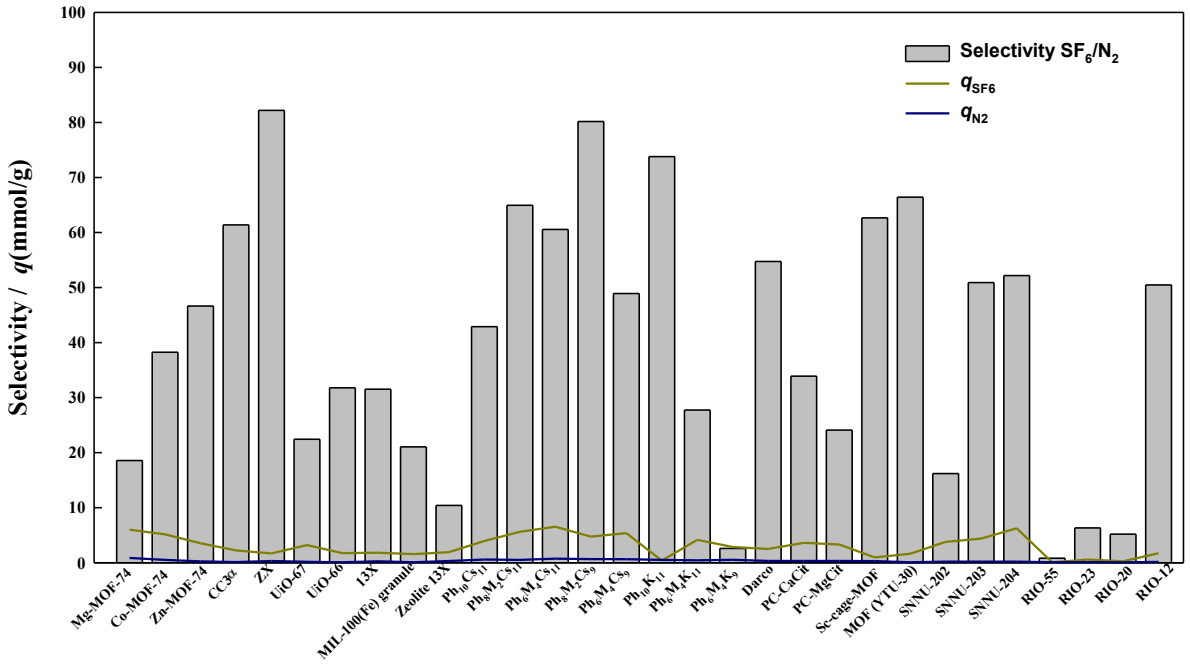


Figure 4.10.13 Comparison of the adsorption capacity of SF_6 and N_2, and the selectivity of the SF_6/N_2 mixture ($y_{SF_6} = 0.10$ and $y_{N_2} = 0.90$) for the materials studied in this work and those reported in the literature at a pressure of 0.1 MPa and 303.15 K [107,120–122,195–200].

In the case of SF_6/N_2 separation (see Figure 4.10.13), microporosity and surface area are crucial, improving selectivity toward SF_6 [119,122,196–198]. This behaviour explains the superior performance of zeolites ZX and 13X, some MOFs and activated carbons, compared to the POPs studied in this work. However, RIO-12 stands out due to its high microporosity and large surface area, which significantly enhances both parameters: its adsorption capacity and selectivity toward SF_6.

4.10.3 Conclusions

Porous Organic Polymers (POPs), including crystalline and amorphous materials, represent a promising and versatile platform for the selective separation of fluorinated gases (F-gases), due to their tuneable structures and functional surfaces. In this study, four POPs, RIO-55, RIO-23, RIO-20, and RIO-12, were synthesised from precursors including natural dyes, melamine, and hydrazine. These materials exhibit diverse structural features, including variations in surface area, microporosity, and mesoporosity, which are critical parameters that influence their adsorption performance and selectivity.

Adsorption equilibria were experimentally determined at 303.15 K for R-32, R-125, R-134a, and SF_6, as well as N_2. The adsorption data exhibited a wide range of isotherm behaviours, which were effectively described using the Dual-Site Langmuir (DSL) model. This model was selected due to its capacity to capture heterogeneous adsorption sites and competitive interactions. The presence of surface functional groups, notably aldehyde carbonyls (C=O) and hydroxyl groups (–OH), facilitates specific electrostatic interactions with the F-gas molecules. However, adsorption capacity was also strongly

influenced by the structural characteristics of the POPs. Among the materials studied, RIO-12 demonstrated superior adsorption performance due to its high surface area and substantial micropore volume, enhancing its gas uptake.

The selectivity of these materials for industrially relevant F-gas mixtures was determined using the Ideal Adsorbed Solution Theory (IAST). The POPs were evaluated for the separation of the most important refrigeration blends at a commercial level, namely R-410A (R-32/R-125) and R-407C (R-32/R-125/R-134a), as well as SF6/N2 mixture. The competitive adsorption behaviour revealed that RIO-55 exhibited the highest selectivity for separating R-410A and R-407C, due to its lower total pore volume and smaller pore sizes. In contrast, RIO-12 was the most effective in separating SF_6 from N_2, attributed to its larger surface area, which facilitates the packing and retention of larger SF_6 molecules. These materials demonstrate a well-balanced performance, offering competitive separation of F-gases and SF_6/N_2 mixtures compared to conventional zeolites, POPs, and activated carbons, while also providing advantages in economic viability and scalability. Overall, functionalized POPs represent a promising alternative where selectivity can be maximised without substantially compromising adsorption capacity. In summary, this work underscores the potential of rationally designed POPs for F-gas separation, offering a pathway toward more efficient and sustainable processes in industrial applications involving refrigerants and electrical insulators.

4.11 References

[1] Z. Wang, Y. Wang, J. Li, S. Henne, B. Zhang, J. Hu, J. Zhang, Impacts of the Degradation of 2,3,3,3-Tetrafluoropropene into Trifluoroacetic Acid from Its Application in Automobile Air Conditioners in China, the United States, and Europe, Environ Sci Technol 52 (2018) 2819–2826. https://doi.org/10.1021/acs.est.7b05960.

[2] S. Henne, D.E. Shallcross, S. Reimann, P. Xiao, D. Brunner, S. O'Doherty, B. Buchmann, S. O'Doherty, B. Buchmann, Future emissions and atmospheric fate of HFC-1234yf from mobile air conditioners in europe, Environ Sci Technol 46 (2012) 1650–1658. https://doi.org/10.1021/es2034608.

[3] A. Mota-Babiloni, P. Makhnatch, R. Khodabandeh, Études récentes sur la substitution des HFC par des frigorigènes synthétiques alternatifs à faible GWP : performances énergétiques et impacts environnementaux, International Journal of Refrigeration 82 (2017) 288–301. https://doi.org/10.1016/j.ijrefrig.2017.06.026.

[4] B.J. Cardoso, F.B. Lamas, A.R. Gaspar, J.B. Ribeiro, Frigorigènes utilisés dans l'industrie alimentaire portugaise: Statut actuel, International Journal of Refrigeration 83 (2017) 60–74. https://doi.org/10.1016/j.ijrefrig.2017.07.013.

[5] J.L.C. Fannou, C. Rousseau, L. Lamarche, S. Kajl, A comparative performance study of a direct expansion geothermal evaporator using R410A and R407C as refrigerant alternatives to R22, Appl Therm Eng 82 (2015) 306–317. https://doi.org/10.1016/j.applthermaleng.2015.02.079.

[6] M. Bortolini, M. Gamberi, R. Gamberini, A. Graziani, F. Lolli, A. Regattieri, Retrofitting of R404a commercial refrigeration systems using R410a and R407f refrigerants, International Journal of Refrigeration 55 (2015) 142–152. https://doi.org/10.1016/j.ijrefrig.2015.02.015.

[7] B.J. Cardoso, F.B. Lamas, A.R. Gaspar, J.B. Ribeiro, J.L.C. Fannou, C. Rousseau, L. Lamarche, S. Kajl, M. Bortolini, M. Gamberi, R. Gamberini, A. Graziani, F. Lolli, A. Regattieri, The European FluoroCarbons Technical Committee is a Cefic Sector Group, https://www.fluorocarbons.org/hfcs-hfos-hcfos, (accessed: October 2022), International Journal of Refrigeration 82 (2015) 306–317. https://doi.org/10.1016/j.ijrefrig.2015.02.015.

[8] N.D. Miranda, P. Giovani Palafox-Alcantar, R. Khosla, M.D. McCulloch, Metrics for the emissions of F-gas refrigerants, Sustainable Energy Technologies and Assessments 58 (2023) 103348. https://doi.org/https://doi.org/10.1016/j.seta.2023.103348.

[9] A. Jordan, H. Frank, Trifluoroacetate in the environment. Evidence for sources other than HFC/HCFCs, Environ Sci Technol 33 (1999) 522–527. https://doi.org/10.1021/es980674y.

[10] R. Holland, M.A.H. Khan, I. Driscoll, R. Chhantyal-Pun, R.G. Derwent, C.A. Taatjes, A.J. Orr-Ewing, C.J. Percival, D.E. Shallcross, Investigation of the Production of Trifluoroacetic Acid from Two Halocarbons, HFC-134a and HFO-1234yf and Its Fates Using a Global Three-Dimensional Chemical

Transport Model, ACS Earth Space Chem 5 (2021) 849–857. https://doi.org/10.1021/acsearthspacechem.0c00355.

[11] P.J. Castro, J.M.M. Aráujo, G. Martinho, A.B. Pereiro, Waste Management Strategies to Mitigate the Effects of Fluorinated Greenhouse Gases on Climate Change, Applied Sciences 11 (2021). https://doi.org/10.3390/app11104367.

[12] X. Tang, S.R. Wilson, K.R. Solomon, M. Shao, S. Madronich, Changes in air quality and tropospheric composition due to depletion of stratospheric ozone and interactions with climate, Photochem. Photobiol. Sci. 10 (2011) 280–291. https://doi.org/10.1039/C0PP90039G.

[13] K.R. Solomon, G.J.M. Velders, S.R. Wilson, S. Madronich, J. Longstreth, P.J. Aucamp, J.F. Bornman, Sources, fates, toxicity, and risks of trifluoroacetic acid and its salts: Relevance to substances regulated under the Montreal and Kyoto Protocols, J Toxicol Environ Health B Crit Rev 19 (2016) 289–304. https://doi.org/10.1080/10937404.2016.1175981.

[14] J.C. Boutonnet, P. Bingham, D. Calamari, C. de Rooij, J. Franklin, T. Kawano, J.-M. Libre, A. McCul-loch, G. Malinverno, J.M. Odom, G.M. Rusch, K. Smythe, I. Sobolev, R. Thompson, J.M. Tiedje, Environmental Risk Assessment of Trifluoroacetic Acid, Human and Ecological Risk Assessment: An International Journal 5 (1999) 59–124. https://doi.org/10.1080/10807039991289644.

[15] J.C. Ball, T.J. Wellington, Formation of Trifluoroacetic Acid from the Atmospheric Degradation of Hydrofluorocarbon 134a: A Human Health Concern?, Air & Waste 43 (1993) 1260–1262. https://doi.org/10.1080/1073161X.1993.10467204.

[16] D. Jovell, S. B. Gómez, M.E. Zakrzewska, A.V.M. Nunes, J.M.M. Araújo, A.B. Pereiro, F. Llovell, Insight on the Solubility of R134a in Fluorinated Ionic Liquids and Deep Eutectic Solvents, J Chem Eng Data 65 (2020) 4956–4969. https://doi.org/10.1021/acs.jced.0c00588.

[17] A.D. Yancey, S.J. Terian, B.J. Shaw, T.M. Bish, D.R. Corbin, M.B. Shiflett, A review of fluorocarbon sorption on porous materials, Microporous and Mesoporous Materials 331 (2022) 111654. https://doi.org/10.1016/j.micromeso.2021.111654.

[18] A.D. Yancey, D.R. Corbin, M.B. Shiflett, Difluoromethane (HFC-32) and Pentafluoroethane (HFC-125) Sorption on Linde Type A (LTA) Zeolites for the Separation of Azeotropic Hydrofluorocarbon Refrigerant Mixtures, Langmuir 38 (2022) 1937–1953. https://doi.org/10.1021/acs.langmuir.1c02904.

[19] D.K.J.A. Wanigarathna, B. Liu, J. Gao, Adsorption separation of R134a, R125, and R143a fluorocarbon mixtures using 13X and surface modified 5A zeolites, AIChE Journal 64 (2018) 640–648. https://doi.org/10.1002/aic.15955.

[20] D.K.J.A. Wanigarathna, J. Gao, T. Takanami, Q. Zhang, B. Liu, Adsorption Separation of R-22, R-32 and R-125 Fluorocarbons using 4A Molecular Sieve Zeolite, ChemistrySelect 1 (2016) 3718–3722. https://doi.org/10.1002/slct.201600689.

[21] S. Asensio-Delgado, F. Pardo, G. Zarca, A. Urtiaga, Machine learning for predicting the solubility of high-GWP fluorinated refrigerants in ionic liquids, J Mol Liq 367 (2022) 120472. https://doi.org/10.1016/j.molliq.2022.120472.

[22] M.-B. Kim, T.-U. Yoon, D.-Y. Hong, S.-Y. Kim, S.-J. Lee, S.-I. Kim, S.-K. Lee, J.-S. Chang, Y.-S. Bae, High SF6/N2 selectivity in a hydrothermally stable zirconium-based metal–organic framework, Chemical Engineering Journal 276 (2015) 315–321. https://doi.org/https://doi.org/10.1016/j.cej.2015.04.087.

[23] C.Y. Chuah, S. Yu, K. Na, T.-H. Bae, Enhanced SF6 recovery by hierarchically structured MFI zeolite, Journal of Industrial and Engineering Chemistry 62 (2018) 64–71. https://doi.org/https://doi.org/10.1016/j.jiec.2017.12.045.

[24] C.Y. Chuah, K. Goh, T.-H. Bae, Hierarchically Structured HKUST-1 Nanocrystals for Enhanced SF6 Capture and Recovery, The Journal of Physical Chemistry C 121 (2017) 6748–6755. https://doi.org/10.1021/acs.jpcc.7b00291.

[25] A. Parthiban, A.A.R. Gopal, P. Siwayanan, K.W. Chew, Disposal methods, health effects and emission regulations for sulfur hexafluoride and its by-products, J Hazard Mater 417 (2021) 126107. https://doi.org/10.1016/j.jhazmat.2021.126107.

[26] A.D. Yancey, D.P. Broom, M.G. Roper, M.J. Benham, D.R. Corbin, M.B. Shiflett, Separation of Azeotropic Hydrofluorocarbon Refrigerant Mixtures: Thermodynamic and Kinetic Modeling for Binary Adsorption of HFC-32 and HFC-125 on Zeolite 5A, Langmuir 38 (2022) 10836–10853. https://doi.org/10.1021/acs.langmuir.2c01491.

[27] J.E. Sosa, C. Malheiro, R.P.P.L. Ribeiro, P.J. Castro, M.M. Piñeiro, J.M.M. Araújo, F. Plantier, J.P.B. Mota, A.B. Pereiro, Adsorption of fluorinated greenhouse gases on activated carbons: evaluation of their potential for gas separation, Journal of Chemical Technology & Biotechnology 95 (2020) 1892–1905. https://doi.org/https://doi.org/10.1002/jctb.6371.

[28] R.P.P.L. Ribeiro, J.E. Sosa, J.M.M. Araújo, A.B. Pereiro, J.P.B. Mota, Vacuum swing adsorption for R-32 recovery from R-410A refrigerant blend, International Journal of Refrigeration 150 (2023) 253–264. https://doi.org/https://doi.org/10.1016/j.ijrefrig.2023.01.020.

[29] J.E. Sosa, C. Malheiro, P.J. Castro, R.P.P.L. Ribeiro, M.M. Piñeiro, F. Plantier, J.P.B. Mota, J.M.M. Araújo, A.B. Pereiro, Exploring the Potential of Metal–Organic Frameworks for the Separation of Blends of Fluorinated Gases with High Global Warming Potential, Global Challenges 7 (2023) 2200107. https://doi.org/https://doi.org/10.1002/gch2.202200107.

[30] J.E. Sosa, R.P.P.L. Ribeiro, P.J. Castro, J.P.B. Mota, A.B. Pereiro, J.M.M. Araújo, Sorption of fluorinated greenhouse gases in silica-supported fluorinated ionic liquids, J Environ Chem Eng 10 (2022) 108580. https://doi.org/https://doi.org/10.1016/j.jece.2022.108580.

[31] S.K.S. Freitas, F.L. Oliveira, C. Merlini, E.P.S. Justo, A. Gioda, P.M. Esteves, Dye-based covalent organic networks, Journal of Physics: Materials 3 (2020) 025011. https://doi.org/10.1088/2515-7639/ab854b.

[32] R. A. Maia, F. L. Oliveira, M. Nazarkovsky, P. M. Esteves, Crystal Engineering of Covalent Organic Frameworks Based on Hydrazine and Hydroxy-1,3,5-Triformylbenzenes, Crystal Growth & Design 18 (2018) 5682–5689. https://doi.org/10.1021/acs.cgd.8b01110.

[33] R.A. Maia, F. Lopes Oliveira, V. Ritleng, Q. Wang, B. Louis, P. Mothé Esteves, CO2 Capture by Hydroxylated Azine-Based Covalent Organic Frameworks, Chemistry – A European Journal 27 (2021) 8048–8055. https://doi.org/https://doi.org/10.1002/chem.202100478.

[34] B. Petrovic, M. Gorbounov, S. Masoudi Soltani, Influence of surface modification on selective CO2 adsorption: A technical review on mechanisms and methods, Microporous and Mesoporous Materials 312 (2021) 110751. https://doi.org/https://doi.org/10.1016/j.micromeso.2020.110751.

[35] S. Wang, L. Lu, D. Wu, X. Lu, W. Cao, T. Yang, Y. Zhu, Molecular Simulation Study of the Adsorption and Diffusion of a Mixture of CO2/CH4 in Activated Carbon: Effect of Textural Properties and Surface Chemistry, J Chem Eng Data 61 (2016) 4139–4147. https://doi.org/10.1021/acs.jced.6b00554.

[36] F. Anwar, M. Khaleel, K. Wang, G.N. Karanikolos, Selectivity Tuning of Adsorbents for Ethane/Ethylene Separation: A Review, Ind Eng Chem Res 61 (2022) 12269–12293. https://doi.org/10.1021/acs.iecr.2c02438.

[37] A. Carvalho, L.C. Branco, L.R.C. Corrêa, A.B. Paninho, P.M. Esteves, H. Cruz, S.K.S. Freitas, Impregnation of different lanthanides in a covalent organic framework (RIO-55) to a chemical determination of dopants substances, Heliyon 10 (2024) e36181. https://doi.org/https://doi.org/10.1016/j.heliyon.2024.e36181.

[38] J.E. Sosa, R.P.P.L. Ribeiro, I. Matos, M. Bernardo, I.M. Fonseca, J.P.B. Mota, J.M.M. Araújo, A.B. Pereiro, Exploring the potential of biomass-derived carbons for the separation of fluorinated gases with high global warming potential, Biomass Bioenergy 188 (2024) 107323. https://doi.org/https://doi.org/10.1016/j.biombioe.2024.107323.

[39] D.K.J.A. Wanigarathna, J. Gao, B. Liu, Fluorocarbon Separation in a Thermally Robust Zirconium Carboxylate Metal–Organic Framework, Chem Asian J 13 (2018) 977–981. https://doi.org/10.1002/asia.201800337.

[40] A.A. Askalany, B.B. Saha, Experimental and theoretical study of adsorption kinetics of Difluoromethane onto activated carbons, International Journal of Refrigeration 49 (2015) 160–168. https://doi.org/https://doi.org/10.1016/j.ijrefrig.2014.10.009.

[41] Y. Peng, F. Zhang, X. Zheng, H. Wang, C. Xu, Q. Xiao, Y. Zhong, W. Zhu, Comparison Study on the Adsorption of CFC-115 and HFC-125 on Activated Carbon and Silicalite-1, Ind Eng Chem Res 49 (2010) 10009–10015. https://doi.org/10.1021/ie1010806.

[42] K.A.R.K.C.N.B.B.S.S.K. Wai Soong Loh M. Kumja, I.I. El-Sharkawy, Adsorption Parameter and Heat of Adsorption of Activated Carbon/HFC-134a Pair, Heat Transfer Engineering 31 (2010) 910–916. https://doi.org/10.1080/01457631003603949.

[43] B.S. Akkimaradi, M. Prasad, P. Dutta, K. Srinivasan, Adsorption of 1,1,1,2-Tetrafluoroethane on Activated Charcoal, J Chem Eng Data 46 (2001) 417–422. https://doi.org/10.1021/je000277e.

[44] R. Gonzalez-Olmos, F. Llovell, Life cycle assessment of fluorinated gas recovery from waste refrigerants through vacuum swing adsorption, Sustainable Materials and Technologies 39 (2024) e00811. https://doi.org/https://doi.org/10.1016/j.susmat.2023.e00811.

[45] KET4F-Gas Project, KET4F-Gas Project 2022, (2022). http://www.ket4f-gas.eu/?page_id=1537 (accessed January 8, 2024).

[46] E. Surra, M. Costa, M. Bernardo, N. Lapa, I. Esteves, I. Fonseca, New adsorbents from maize cob wastes and anaerobic digestate for H 2 S removal from biogas, Waste Management 94 (2019) 136–145. https://doi.org/10.1016/j.wasman.2019.05.048.

[47] V.O. Njoku, B.H. Hameed, Preparation and characterization of activated carbon from corncob by chemical activation with H3PO4 for 2,4-dichlorophenoxyacetic acid adsorption, Chemical Engineering Journal 173 (2011) 391–399. https://doi.org/https://doi.org/10.1016/j.cej.2011.07.075.

[48] M.K. Al Mesfer, C. Goel, S. Mohan, P. Dinesha, Synthesis and characterization of high-performance activated carbon from walnut shell biomass for CO2 capture, Science of The Total Environment 27 (2021) 15020–15028. https://doi.org/10.1007/s11356-020-07934-x.

[49] Y. Zhang, A.E. Ghaly, B. Li, Physical Properties of Corn Residues, Am J Biochem Biotechnol 8 (2012) 44–53. https://doi.org/10.3844/ajbbsp.2012.44.53.

[50] S. Deng, Y. Nie, Z. Du, Q. Huang, P. Meng, B. Wang, J. Huang, G. Yu, Enhanced adsorption of perfluorooctane sulfonate and perfluorooctanoate by bamboo-derived granular activated carbon, J Hazard Mater 282 (2015) 150–157. https://doi.org/https://doi.org/10.1016/j.jhazmat.2014.03.045.

[51] C. Goel, S. Mohan, P. Dinesha, CO2 capture by adsorption on biomass-derived activated char: A review, Science of the Total Environment 798 (2021) 149296. https://doi.org/10.1016/j.scitotenv.2021.149296.

[52] D. Duan, Y. Zhang, Y. Wang, H. Lei, Q. Wang, R. Ruan, Production of renewable jet fuel and gasoline range hydrocarbons from catalytic pyrolysis of soapstock over corn cob-derived activated carbons, Energy 209 (2020) 118454. https://doi.org/https://doi.org/10.1016/j.energy.2020.118454.

[53] X. Wang, W. Zeng, C. Xin, X. Kong, X. Hu, Q. Guo, The development of activated carbon from corncob for CO2 capture, RSC Adv. 12 (2022) 33069–33078. https://doi.org/10.1039/D2RA05979G.

[54] S. Agustina, A. Yulianto, A. Kamil, A. Saepudin, Fajriyan, S.E.R. Manurung, Budiyanto, A. Majid, A. Fitrina, Corn cob usage as activated carbon using KOH as activator, IOP Conf Ser Earth Environ Sci 1266 (2023) 12082. https://doi.org/10.1088/1755-1315/1266/1/012082.

[55] A. Medhat, H.H. El-Maghrabi, A. Abdelghany, N.M. Abdel Menem, P. Raynaud, Y.M. Moustafa, M.A. Elsayed, A.A. Nada, Efficiently activated carbons from corn cob for methylene blue adsorption, Applied Surface Science Advances 3 (2021) 100037. https://doi.org/https://doi.org/10.1016/j.apsadv.2020.100037.

[56] M. Song, B. Jin, R. Xiao, L. Yang, Y. Wu, Z. Zhong, Y. Huang, The comparison of two activation techniques to prepare activated carbon from corn cob, Biomass Bioenergy 48 (2013) 250–256. https://doi.org/https://doi.org/10.1016/j.biombioe.2012.11.007.

[57] E. Surra, R.P.P.L. Ribeiro, T. Santos, M. Bernardo, J.P.B. Mota, N. Lapa, I.A.A.C. Esteves, Evaluation of activated carbons produced from Maize Cob Waste for adsorption-based CO2 separation and biogas upgrading, J Environ Chem Eng 10 (2022) 107065. https://doi.org/https://doi.org/10.1016/j.jece.2021.107065.

[58] N. V Sych, S.I. Trofymenko, O.I. Poddubnaya, M.M. Tsyba, V.I. Sapsay, D.O. Klymchuk, A.M. Puziy, Porous structure and surface chemistry of phosphoric acid activated carbon from corncob, Appl Surf Sci 261 (2012) 75–82. https://doi.org/https://doi.org/10.1016/j.apsusc.2012.07.084.

[59] E. Surra, R.P.P.L. Ribeiro, T. Santos, M. Bernardo, J.P.B. Mota, N. Lapa, I.A.A.C. Esteves, Evaluation of activated carbons produced from Maize Cob Waste for adsorption-based CO2 separation and biogas upgrading, J Environ Chem Eng 10 (2022). https://doi.org/10.1016/j.jece.2021.107065.

[60] R.P.P.L. Ribeiro, C.L. Antunes, A.U. Garate, A.F. Portela, M.G. Plaza, J.P.B. Mota, I.A.A.C. Esteves, Binderless shaped metal-organic framework particles: Impact on carbon dioxide adsorption, Microporous and Mesoporous Materials 275 (2019) 111–121. https://doi.org/https://doi.org/10.1016/j.micromeso.2018.08.002.

[61] B.C.R. Camacho, R.P.P.L. Ribeiro, I.A.A.C. Esteves, J.P.B. Mota, Adsorption equilibrium of carbon dioxide and nitrogen on the MIL-53(Al) metal organic framework, Sep Purif Technol 141 (2015) 150–159. https://doi.org/10.1016/j.seppur.2014.11.040.

[62] R. Coupan, F. Plantier, J.P. Torré, C. Dicharry, P. Sénéchal, F. Guerton, P. Moonen, A. Khoukh, S.A. Kessas, M. Hemati, Creating innovative composite materials to enhance the kinetics of CO2 capture by hydroquinone clathrates, Chemical Engineering Journal 325 (2017) 35–48. https://doi.org/10.1016/j.cej.2017.05.038.

[63] F. Khaddour, A. Knorst-Fouran, F. Plantier, M.M. Piñeiro, B. Mendiboure, C. Miqueu, A fully consistent experimental and molecular simulation study of methane adsorption on activated carbon, Adsorption 20 (2014) 649–656. https://doi.org/10.1007/s10450-014-9611-2.

[64] D.D. Do, Adsorption Analysis: Equilibria and Kinetics, 1998.

[65] P.J. Linstrom, W.G. Mallard, The NIST Chemistry WebBook: A Chemical Data Resource on the Internet, J Chem Eng Data 46 (2001) 1059–1063. https://doi.org/10.1021/je000236i.

[66] R.P.P.L. Ribeiro, J. Barreto, M.D. Grosso Xavier, D. Martins, I.A.A.C. Esteves, M. Branco, T. Tirolien, J.P.B. Mota, G. Bonfait, Cryogenic neon adsorption on Co3(ndc)3(dabco) metal-organic framework, Microporous and Mesoporous Materials 298 (2020). https://doi.org/10.1016/j.micromeso.2020.110055.

[67] R.P.P.L. Ribeiro, B.C.R. Camacho, A. Lyubchyk, I.A.A.C. Esteves, F.J.A.L. Cruz, J.P.B. Mota, Experimental and computational study of ethane and ethylene adsorption in the MIL-53(Al) metal

organic framework, Microporous and Mesoporous Materials 230 (2016) 154–165. https://doi.org/10.1016/j.micromeso.2016.05.006.

[68] J.E. Sosa, R.P.P.L. Ribeiro, I. Matos, M. Bernardo, I.M. Fonseca, J.P.B. Mota, J.M.M. Araújo, A.B. Pereiro, Exploring the potential of biomass-derived carbons for the separation of fluorinated gases with high global warming potential, Biomass Bioenergy 188 (2024) 107323. https://doi.org/https://doi.org/10.1016/j.biombioe.2024.107323.

[69] J. A. O'Brien, A. L. Myers, A comprehensive technique for equilibrium calculations in adsorbed mixtures: the generalized FastIAS method, Industrial & Engineering Chemistry Research 27 (2002) 2085–2092. https://doi.org/10.1021/ie00083a021.

[70] A.L. Myers, J.M. Prausnitz, Thermodynamics of mixed-gas adsorption, AIChE Journal 11 (1965) 121–127. https://doi.org/10.1002/aic.690110125.

[71] J.A. O'brien, A.L. Myers, Rapid Calculations of Multicomponent Adsorption Equilibria from Pure Isotherm Data, Industrial and Engineering Chemistry Process Design and Development 24 (1985) 1188–1191. https://doi.org/10.1021/I200031A049.

[72] A.L. Myers, D. Valenzuela, Computer Algorithm And Graphical Method For Calculating Adsorption Equilibria Of Gas Mixtures, JOURNAL OF CHEMICAL ENGINEERING OF JAPAN 19 (1986) 392–396. https://doi.org/10.1252/JCEJ.19.392.

[73] J.A. O'Brien, A.L. Myers, A Comprehensive Technique for Equilibrium Calculations in Adsorbed Mixtures: The Generalized FastIAS Method, Ind Eng Chem Res 27 (1988) 2085–2092. https://doi.org/10.1021/IE00083A021.

[74] A. Mouahid, D. Bessieres, F. Plantier, G. Pijaudier-Cabot, A thermostated coupled apparatus for the simultaneous determination of adsorption isotherms and differential enthalpies of adsorption at high pressure and high temperature, J Therm Anal Calorim 109 (2012) 1077–1087. https://doi.org/10.1007/s10973-011-1820-2.

[75] I.A. de A.C. Esteves, Gas separation processes by integrated adsorption and permeation technologies, Universidade NOVA de Lisboa (Portugal), 2005.

[76] I.A.A.C. Esteves, M.S.S. Lopes, P.M.C. Nunes, J.P.B. Mota, Adsorption of natural gas and biogas components on activated carbon, Sep Purif Technol 62 (2008) 281–296. https://doi.org/https://doi.org/10.1016/j.seppur.2008.01.027.

[77] F.G. Helfferich, Principles of adsorption & adsorption processes, by D. M. Ruthven, John Wiley & Sons, 1984, xxiv + 433 pp, AIChE Journal 31 (1985) 523–524. https://doi.org/https://doi.org/10.1002/aic.690310335.

[78] M.M. Dubinin, Adsorption in micropores, J Colloid Interface Sci 23 (1967) 487–499. https://doi.org/https://doi.org/10.1016/0021-9797(67)90195-6.

[79] M.M. Dubinin, The Potential Theory of Adsorption of Gases and Vapors for Adsorbents with Energetically Nonuniform Surfaces., Chem Rev 60 (1960) 235–241. https://doi.org/10.1021/cr60204a006.

[80] M.M. DUBININ, Physical Adsorption of Gases and Vapors in Micropores, in: D.A. CADENHEAD, J.F. DANIELLI, M.D. ROSENBERG (Eds.), Progress in Surface and Membrane Science, Elsevier, 1975: pp. 1–70. https://doi.org/https://doi.org/10.1016/B978-0-12-571809-7.50006-1.

[81] J. Tóth, Uniform interpretation of gas/solid adsorption, Adv Colloid Interface Sci 55 (1995) 1–239. https://doi.org/https://doi.org/10.1016/0001-8686(94)00226-3.

[82] S. Ozawa, S. Kusumi, Y. Ogino, Physical adsorption of gases at high pressure. IV. An improvement of the Dubinin—Astakhov adsorption equation, J Colloid Interface Sci 56 (1976) 83–91. https://doi.org/https://doi.org/10.1016/0021-9797(76)90149-1.

[83] M.M. DUBININ, V.A. ASTAKHOV, Description of Adsorption Equilibria of Vapors on Zeolites over Wide Ranges of Temperature and Pressure, in: Molecular Sieve Zeolites-II, AMERICAN CHEMICAL SOCIETY, 1971: pp. 69–85. https://doi.org/doi:10.1021/ba-1971-0102.ch044.

[84] M. Thommes, K. Kaneko, A. V. Neimark, J.P. Olivier, F. Rodriguez-Reinoso, J. Rouquerol, K.S.W. Sing, Physisorption of gases, with special reference to the evaluation of surface area and pore size distribution (IUPAC Technical Report), Pure and Applied Chemistry 87 (2015) 1051–1069. https://doi.org/10.1515/pac-2014-1117.

[85] B.C.R. Camacho, R.P.P.L. Ribeiro, I.A.A.C. Esteves, J.P.B. Mota, Adsorption equilibrium of carbon dioxide and nitrogen on the MIL-53(Al) metal organic framework, Sep Purif Technol 141 (2015) 150–159. https://doi.org/https://doi.org/10.1016/j.seppur.2014.11.040.

[86] A.R. Nabais, R.P.P.L. Ribeiro, J.P.B. Mota, V.D. Alves, I.A.A.C. Esteves, L.A. Neves, CO2/N2 gas separation using Fe(BTC)-based mixed matrix membranes: A view on the adsorptive and filler properties of metal-organic frameworks, Sep Purif Technol 202 (2018) 174–184. https://doi.org/https://doi.org/10.1016/j.seppur.2018.03.028.

[87] G.O. Wood, Affinity coefficients of the Polanyi/Dubinin adsorption isotherm equations: A review with compilations and correlations, Carbon N Y 39 (2001) 343–356. https://doi.org/https://doi.org/10.1016/S0008-6223(00)00128-7.

[88] G. Odell Wood, Activated carbon adsorption capacities for vapors, Carbon N Y 30 (1992) 593–599. https://doi.org/https://doi.org/10.1016/0008-6223(92)90177-X.

[89] A.L. Myers, J.M. Prausnitz, Thermodynamics of Mixed-Gas Adsorption, AIChE J. 11 (1965) 121.

[90] M. Bernardo, S. Rodrigues, N. Lapa, I. Matos, F. Lemos, M.K.S. Batista, A.P. Carvalho, I. Fonseca, High efficacy on diclofenac removal by activated carbon produced from potato peel waste, International Journal of Environmental Science and Technology 13 (2016) 1989–2000. https://doi.org/10.1007/s13762-016-1030-3.

[91] K.S.W. Sing, Reporting physisorption data for gas/solid systems with special reference to the determination of surface area and porosity (Recommendations 1984), 57 (1985) 603–619. https://doi.org/doi:10.1351/pac198557040603.

[92] M. Godino-Ojer, V.R. Morales, A.J. López Peinado, M. Bernardo, N. Lapa, A.M. Ferraria, A.M.B. do Rego, I.M. Fonseca, I. Matos, E. Pérez-Mayoral, P-Doped carbon catalyst highly efficient for benzodiazepine synthesis. Tires valorisation, Catal Today 419 (2023) 114160. https://doi.org/https://doi.org/10.1016/j.cattod.2023.114160.

[93] A. V. Naumkin, A. Kraut-Vass, S. W. Gaarenstroom, A. V. Naumkin, NIST X-ray Photoelectron Spectroscopy Database, NIST Standard Reference Database Number 20, National Institute of Standards and Technology, (2012). https://doi.org/https://dx.doi.org/10.18434/T4T88K.

[94] J. Bedia, R. Ruiz-Rosas, J. Rodríguez-Mirasol, T. Cordero, Kinetic study of the decomposition of 2-butanol on carbon-based acid catalyst, AIChE Journal 56 (2010) 1557–1568. https://doi.org/https://doi.org/10.1002/aic.12056.

[95] A. Mokhati, O. Benturki, A. Benturki, R. Fennouh, Z. Kecira, M. Bernardo, I. Matos, N. Lapa, M. Ventura, O.S.G.P. Soares, A.M.B. Do Rego, I. Fonseca, Conversion of Argan Nutshells into Novel Porous Carbons in the Scope of Circular Economy: Adsorption Performance of Emerging Contaminants, Applied Sciences 12 (2022). https://doi.org/10.3390/app12157607.

[96] R.K. Motkuri, H.V.R. Annapureddy, M. Vijaykumar, H.T. Schaef, P.F. Martin, B.P. McGrail, L.X. Dang, R. Krishna, P.K. Thallapally, Fluorocarbon adsorption in hierarchical porous frameworks, Nat Commun 5 (2014) 1–6. https://doi.org/10.1038/ncomms5368.

[97] D.K.J.A. Wanigarathna, J. Gao, B. Liu, Fluorocarbon Separation in a Thermally Robust Zirconium Carboxylate Metal–Organic Framework, Chem Asian J 13 (2018) 977–981. https://doi.org/10.1002/asia.201800337.

[98] S.M.W. Wilson, F. Al-Enzi, V.A. Gabriel, F.H. Tezel, Effect of pore size and heterogeneous surface on the adsorption of CO2, N2, O2, and Ar on carbon aerogel, RF aerogel, and activated carbons, Microporous and Mesoporous Materials 322 (2021) 111089. https://doi.org/10.1016/j.micromeso.2021.111089.

[99] S. Ohtani, K. Onishi, K. Wada, T. Hirohata, S. Inagi, J. Pirillo, Y. Hijikata, M. Mizuno, K. Kato, T. Ogoshi, Size-Selective Capture of Fluorocarbon Gases and Storage of Volatile Halogenated Organic Vapors with Low Boiling Points by Molecular-Scale Cavities of Crystalline Pillar[n]quinones, Adv Funct Mater n/a (n.d.) 2312304. https://doi.org/https://doi.org/10.1002/adfm.202312304.

[100] G. Li, P. Xiao, X. Dong, P.A. Webley, Dual Mode Roll-up Effect in Multicomponent Non-Isothermal Adsorption Processes with Multilayered Bed Packing, Chem. Eng. Sci. 66 (2011) 1825.

[101] M. Godino-Ojer, R. Blazquez-García, I. Matos, M. Bernardo, I.M. Fonseca, E. Pérez Mayoral, Porous carbons-derived from vegetal biomass in the synthesis of quinoxalines. Mechanistic insights, Catal Today 354 (2020) 90–99. https://doi.org/https://doi.org/10.1016/j.cattod.2019.06.043.

[102] National Institute of Standards and Technology (NIST), Experimental data for CF3CHF2 (pentafluoroethane), (n.d.). https://cccbdb.nist.gov/exp2x.asp?casno=354336&charge=0#2015Tha/Wu:144302 (accessed March 22, 2023).

[103] National Institute of Standards and Technology (NIST), Experimental data for CH2F2 (Methane, difluoro-), (n.d.). https://cccbdb.nist.gov/exp2x.asp?casno=75105&charge=0 (accessed March 22, 2023).

[104] National Institute of Standards and Technology (NIST), Experimental Polarizabilites, 2023-03-22 (n.d.). https://cccbdb.nist.gov/pollistx.asp#2015Tha/Wu:144302.

[105] D.K.J.A. Wanigarathna, J. Gao, B. Liu, Metal organic frameworks for adsorption-based separation of fluorocompounds: a review, Mater Adv 1 (2020) 310–320. https://doi.org/10.1039/d0ma00083c.

[106] M. Attalla, S. Sadek, Experimental Investigation of Granular Activated Carbon/R-134a Pair for Adsorption Cooling System Applications, Journal of Power and Energy Engineering 02 (2014) 11–20. https://doi.org/10.4236/jpee.2014.22002.

[107] Y. Yang, K. Goh, C.Y. Chuah, H.E. Karahan, Ö. Birer, T.-H. Bae, Sub-Ångström-level engineering of ultramicroporous carbons for enhanced sulfur hexafluoride capture, Carbon N Y 155 (2019) 56–64. https://doi.org/https://doi.org/10.1016/j.carbon.2019.08.034.

[108] J.E. Sosa, C. Malheiro, P.J. Castro, R.P.P.L. Ribeiro, M.M. Piñeiro, F. Plantier, J.P.B. Mota, J.M.M. Araújo, A.B. Pereiro, Exploring the Potential of Metal – Organic Frameworks for the Separation of Blends of Fluorinated Gases with High Global Warming Potential, 2200107 (2022). https://doi.org/10.1002/gch2.202200107.

[109] S. Cai, S. Tian, Y. Lu, G. Wang, Y. Pu, K. Peng, Molecular Simulations of Adsorption and Energy Storage of R1234yf, R1234ze(z), R134a, R32, and their Mixtures in M-MOF-74 (M = Mg, Ni) Nanoparticles, Sci Rep 10 (2020) 1–11. https://doi.org/10.1038/s41598-020-64187-x.

[110] F. Shabir, M. Sultan, T. Miyazaki, B.B. Saha, A. Askalany, I. Ali, Y. Zhou, R. Ahmad, R.R. Shamshiri, Recent updates on the adsorption capacities of adsorbent-adsorbate pairs for heat transformation applications, Renewable and Sustainable Energy Reviews 119 (2020) 109630. https://doi.org/https://doi.org/10.1016/j.rser.2019.109630.

[111] Z. Yang, M. Sultan, K. Thu, T. Miyazaki, Experimental investigation and thermodynamic modeling of adsorption equilibria of MSC30 with R32 for supercritical adsorption cooling systems, Int J Heat Mass Transf 219 (2024) 124873. https://doi.org/https://doi.org/10.1016/j.ijheatmasstransfer.2023.124873.

[112] J.E. Sosa, C. Malheiro, R.P.P.L. Ribeiro, P.J. Castro, M.M. Piñeiro, J.M.M. Araújo, F. Plantier, J.P.B. Mota, A.B. Pereiro, Adsorption of fluorinated greenhouse gases on activated carbons: evaluation of their potential for gas separation, Journal of Chemical Technology and Biotechnology (2020). https://doi.org/10.1002/jctb.6371.

[113] Z.-W. Mo, H.-L. Zhou, D.-D. Zhou, R.-B. Lin, P.-Q. Liao, C.-T. He, W.-X. Zhang, X.-M. Chen, J.-P. Zhang, Mesoporous Metal–Organic Frameworks with Exceptionally High Working Capacities for Adsorption Heat Transformation, Advanced Materials 30 (2018) 1704350. https://doi.org/https://doi.org/10.1002/adma.201704350.

[114] Y.-Y. Xiong, R. Krishna, T. Pham, K.A. Forrest, C.-X. Chen, Z.-W. Wei, J.-J. Jiang, H.-P. Wang, Y. Fan, M. Pan, C.-Y. Su, Pore-Nanospace Engineering of Mixed-Ligand Metal–Organic Frameworks for High Adsorption of Hydrofluorocarbons and Hydrochlorofluorocarbons, Chemistry of Materials 34 (2022) 5116–5124. https://doi.org/10.1021/acs.chemmater.2c00601.

[115] B.S. Akkimaradi, M. Prasad, P. Dutta, K. Srinivasan, Adsorption of 1,1,1,2-Tetrafluoroethane on Activated Charcoal, J Chem Eng Data 46 (2001) 417–422. https://doi.org/10.1021/je000277e.

[116] A.A. Askalany, M. Salem, I.M. Ismail, A.H.H. Ali, M.G. Morsy, Experimental study on adsorption–desorption characteristics of granular activated carbon/R134a pair, International Journal of Refrigeration 35 (2012) 494–498. https://doi.org/https://doi.org/10.1016/j.ijrefrig.2011.04.002.

[117] W.S. Loh, A. Bin Ismail, B. Xi, K.C. Ng, W.G. Chun, Adsorption Isotherms and Isosteric Enthalpy of Adsorption for Assorted Refrigerants on Activated Carbons, J Chem Eng Data 57 (2012) 2766–2773. https://doi.org/10.1021/je3008099.

[118] M.-B. Kim, S.-J. Lee, C.Y. Lee, Y.-S. Bae, High SF6 selectivities and capacities in isostructural metal-organic frameworks with proper pore sizes and highly dense unsaturated metal sites, Microporous and Mesoporous Materials 190 (2014) 356–361. https://doi.org/https://doi.org/10.1016/j.micromeso.2014.02.028.

[119] I. Senkovska, E. Barea, J.A.R. Navarro, S. Kaskel, Adsorptive capturing and storing greenhouse gases such as sulfur hexafluoride and carbon tetrafluoride using metal–organic frameworks, Microporous and Mesoporous Materials 156 (2012) 115–120. https://doi.org/https://doi.org/10.1016/j.micromeso.2012.02.021.

[120] T. Hasell, M. Miklitz, A. Stephenson, M.A. Little, S.Y. Chong, R. Clowes, L. Chen, D. Holden, G.A. Tribello, K.E. Jelfs, A.I. Cooper, Porous Organic Cages for Sulfur Hexafluoride Separation, J Am Chem Soc 138 (2016) 1653–1659. https://doi.org/10.1021/jacs.5b11797.

[121] W.-S. Cho, K.-H. Lee, H.-J. Chang, W. Huh, H.-H. Kwon, Evaluation of pressure-temperature swing adsorption for sulfur hexafluoride (SF6) recovery from SF6 and N2 gas mixture, Korean Journal of Chemical Engineering 28 (2011) 2196–2201. https://doi.org/10.1007/s11814-011-0104-7.

[122] M.B. Kim, T.H. Kim, T.U. Yoon, J.H. Kang, J.H. Kim, Y.S. Bae, Efficient SF6/N2 separation at high pressures using a zirconium-based mesoporous metal–organic framework, Journal of Industrial and Engineering Chemistry 84 (2020) 179–184. https://doi.org/10.1016/j.jiec.2019.12.032.

[123] P.-J. Kim, Y.-W. You, H. Park, J.-S. Chang, Y.-S. Bae, C.-H. Lee, J.-K. Suh, Separation of SF6 from SF6/N2 mixture using metal–organic framework MIL-100(Fe) granule, Chemical Engineering Journal 262 (2015) 683–690. https://doi.org/https://doi.org/10.1016/j.cej.2014.09.123.

[124] W. Zhu, J.C. Groen, F. Kapteijn, J.A. Moulijn, Adsorption of Butane Isomers and SF6 on Kureha Activated Carbon: 1. Equilibrium, Langmuir 20 (2004) 5277–5284. https://doi.org/10.1021/la030264+.

[125] R. Sun, C.-W. Tai, M. Strømme, O. Cheung, Hierarchical Porous Carbon Synthesized from Novel Porous Amorphous Calcium or Magnesium Citrate with Enhanced SF6 Uptake and SF6/N2 Selectivity, ACS Appl Nano Mater 2 (2019) 778–789. https://doi.org/10.1021/acsanm.8b02005.

[126] J. Jagiełło, T.J. Bandosz, K. Putyera, J.A. Schwarz, Micropore structure of template-derived carbons studied using adsorption of gases with different molecular diameters, J. Chem. Soc., Faraday Trans. 91 (1995) 2929–2933. https://doi.org/10.1039/FT9959102929.

[127] S. Chen, Y. Shen, Z. Guan, B. Liu, Z. Tang, D. Zhang, B. Fu, Adsorption Properties of SF6 on Zeolite NaY, 13X, Activated Carbon, and Silica Gel, J Chem Eng Data 65 (2020) 4044–4051. https://doi.org/10.1021/acs.jced.0c00348.

[128] X. Peng, J.M. Vicent-Luna, Q. Jin, Separation of CF4/N2, C2F6/N2, and SF6/N2 Mixtures in Amorphous Activated Carbons Using Molecular Simulations, ACS Appl Mater Interfaces 12 (2020) 20044–20055. https://doi.org/10.1021/acsami.0c01043.

[129] J. Liu, M.D. Levan, Henry's law constants and isosteric heats of adsorption at zero loading for multi-wall carbon surfaces with different geometries, Carbon N Y 48 (2010) 3454–3462. https://doi.org/10.1016/j.carbon.2010.05.042.

[130] S. Builes, S.I. Sandler, R. Xiong, Isosteric heats of gas and liquid adsorption, Langmuir 29 (2013) 10416–10422. https://doi.org/10.1021/la401035p.

[131] A. Lyubchyk, I.A.A.C. Esteves, F.J.A.L. Cruz, J.P.B. Mota, Experimental and theoretical studies of supercritical methane adsorption in the mil-53(al) metal organic framework, Journal of Physical Chemistry C 115 (2011) 20628–20638. https://doi.org/10.1021/jp207326d.

[132] R. Babarao, Z. Hu, J. Jiang, S. Chempath, S.I. Sandler, Storage and separation of CO2 and CH4 in silicalite, C168 schwarzite, and IRMOF-1: A comparative study from Monte Carlo simulation, Langmuir 23 (2007) 659–666. https://doi.org/10.1021/la062289p.

[133] E.K. Lee, J.D. Lee, H.J. Lee, B.R. Lee, Y.S. Lee, S.M. Kim, H.O. Park, Y.S. Kim, Y. Do Park, Y. Do Kim, Pure SF6 and SF6-N2 mixture gas hydrates equilibrium and kinetic characteristics, Environ Sci Technol 43 (2009) 7723–7727. https://doi.org/10.1021/es901350v.

[134] K.H. Kim, P.G. Ingole, J.H. Kim, H.K. Lee, Experimental investigation and simulation of hollow fiber membrane process for SF6 recovery from GIS, Polym Adv Technol 24 (2013) 997–1004. https://doi.org/10.1002/pat.3175.

[135] F. Pardo, G. Zarca, A. Urtiaga, Effect of feed pressure and long-term separation performance of Pebax-ionic liquid membranes for the recovery of difluoromethane (R32) from refrigerant mixture R410A, J Memb Sci 618 (2021) 118744. https://doi.org/https://doi.org/10.1016/j.memsci.2020.118744.

[136] F. Pardo, G. Zarca, A. Urtiaga, Separation of Refrigerant Gas Mixtures Containing R32, R134a, and R1234yf through Poly(ether- block-amide) Membranes, ACS Sustain Chem Eng 8 (2020) 2548–2556. https://doi.org/10.1021/acssuschemeng.9b07195.

[137] K.S.W. Sing, Reporting physisorption data for gas/solid systems with special reference to the determination of surface area and porosity (Recommendations 1984), 57 (1985) 603–619. https://doi.org/doi:10.1351/pac198557040603.

[138] A.R. Nabais, R.P.P.L. Ribeiro, J.P.B. Mota, V.D. Alves, I.A.A.C. Esteves, L.A. Neves, CO2/N2 gas separation using Fe(BTC)-based mixed matrix membranes: A view on the adsorptive and filler

properties of metal-organic frameworks, Sep Purif Technol 202 (2018) 174–184. https://doi.org/https://doi.org/10.1016/j.seppur.2018.03.028.

[139] M. Sanchez-Sanchez, I. de Asua, D. Ruano, K. Diaz, Direct Synthesis, Structural Features, and Enhanced Catalytic Activity of the Basolite F300-like Semiamorphous Fe-BTC Framework, Cryst Growth Des 15 (2015) 4498–4506. https://doi.org/10.1021/acs.cgd.5b00755.

[140] T.H. Rupam, T. Steenhaut, M.L. Palash, Y. Filinchuk, S. Hermans, B.B. Saha, Thermochemical energy applications of green transition metal doped MIL–100(Fe), Chemical Engineering Journal 448 (2022) 137590. https://doi.org/https://doi.org/10.1016/j.cej.2022.137590.

[141] G.R. Delpiano, D. Tocco, L. Medda, E. Magner, A. Salis, Adsorption of Malachite Green and Alizarin Red S Dyes Using Fe-BTC Metal Organic Framework as Adsorbent, Int J Mol Sci 22 (2021). https://doi.org/10.3390/ijms22020788.

[142] M. Safa Gamal, N. Asikin-Mijan, M. Arumugam, U. Rashid, Y.H. Taufiq-Yap, Solvent-free catalytic deoxygenation of palm fatty acid distillate over cobalt and manganese supported on activated carbon originating from waste coconut shell, J Anal Appl Pyrolysis 144 (2019) 104690. https://doi.org/https://doi.org/10.1016/j.jaap.2019.104690.

[143] M. Parsa, Y. Qi, J.J. Di Nuzzo, Y. Moussakhani, A. Tirto, A.L. Chaffee, Regenerable carbon honeycomb monoliths directly prepared from brown coal: A novel carbon product, Chemical Engineering Journal 471 (2023) 144699. https://doi.org/https://doi.org/10.1016/j.cej.2023.144699.

[144] A. Karami, A. Ahmed, R. Sabouni, G.A. Husseini, M. Al Sharabati, N. AlSawaftah, V. Paul, Hybrid liposome/metal–organic framework as a promising dual-responsive nanocarriers for anticancer drug delivery, Colloids Surf B Biointerfaces 217 (2022) 112599. https://doi.org/https://doi.org/10.1016/j.colsurfb.2022.112599.

[145] J. Jung, H. Do, K. Chung, M. Cho, C.-H. Lee, Adsorption equilibria and kinetics of CO2, CH4, CO, N2, O2, and H2 on silica-based adsorbents for H2 enhancement processes from steel off-gas for the direct reduced iron process, Chemical Engineering Journal 479 (2024) 147678. https://doi.org/https://doi.org/10.1016/j.cej.2023.147678.

[146] L.-K. Lee, D.M. Ruthven, Analysis of thermal effects in adsorption rate measurements, J. Chem. Soc., Faraday Trans. 1 75 (1979) 2406–2422. https://doi.org/10.1039/F19797502406.

[147] D.M. Ruthven, L.-K. Lee, H. Yucel, Kinetics of non-isothermal sorption in molecular sieve crystals, AIChE Journal 26 (1980) 16–23. https://doi.org/https://doi.org/10.1002/aic.690260104.

[148] A.F. Sapnik, C.W. Ashling, L.K. Macreadie, S.J. Lee, T. Johnson, S.G. Telfer, T.D. Bennett, Gas adsorption in the topologically disordered Fe-BTC framework, J Mater Chem A Mater 9 (2021) 27019–27027. https://doi.org/10.1039/D1TA08449F.

[149] T.H. Rupam, Md.A. Islam, A. Pal, A. Chakraborty, B.B. Saha, Thermodynamic property surfaces for various adsorbent/adsorbate pairs for cooling applications, Int J Heat Mass Transf 144 (2019) 118579. https://doi.org/https://doi.org/10.1016/j.ijheatmasstransfer.2019.118579.

[150] M.L. Palash, T.H. Rupam, A. Pal, A. Chakraborty, B.B. Saha, R. Wang, Design principles for synthesizing high grade activated carbons for adsorption heat pumps, Chemical Engineering Journal Advances 6 (2021) 100086. https://doi.org/https://doi.org/10.1016/j.ceja.2021.100086.

[151] J. Jia, Y. Xing, B. Li, Y. Wu, D. Wang, Molecular simulation study of adsorption-diffusion of CH4, CO2 and H2O in gas-fat coal, Sci Rep 14 (2024) 24131. https://doi.org/10.1038/s41598-024-74647-3.

[152] R. Babarao, Z. Hu, J. Jiang, S. Chempath, S.I. Sandler, Storage and Separation of CO2 and CH4 in Silicalite, C168 Schwarzite, and IRMOF-1: A Comparative Study from Monte Carlo Simulation, Langmuir 23 (2007) 659–666. https://doi.org/10.1021/la062289p.

[153] A. Lyubchyk, I.A.A.C. Esteves, F.J.A.L. Cruz, J.P.B. Mota, Experimental and Theoretical Studies of Supercritical Methane Adsorption in the MIL-53(Al) Metal Organic Framework, The Journal of Physical Chemistry C 115 (2011) 20628–20638. https://doi.org/10.1021/jp207326d.

[154] A.L. Myers, ADSORPTION OF GAS MIXTURES-A THERMODYNAMIC APPROACH, Ind Eng Chem 60 (1968) 45–49. https://doi.org/10.1021/ie50701a007.

[155] S.H. Madani, M.J. Biggs, F. Rodríguez-Reinoso, P. Pendleton, Decoding gas-solid interaction effects on adsorption isotherm shape: II. Polar adsorptives, Microporous and Mesoporous Materials 278 (2019) 232–240. https://doi.org/https://doi.org/10.1016/j.micromeso.2018.11.039.

[156] G. Calleja, J. Pau, J.A. Calles, Pure and multicomponent adsorption equilibrium of carbon dioxide, ethylene, and propane on ZSM-5 zeolites with different Si/Al ratios, J Chem Eng Data 43 (1998) 994–1003. https://doi.org/10.1021/je9702100.

[157] Z.A. ALOthman, A Review: Fundamental Aspects of Silicate Mesoporous Materials, Materials 5 (2012) 2874–2902. https://doi.org/10.3390/ma5122874.

[158] R.D. Harter, The Little Adsorption Book: A Practical Guide for Engineers and Scientists, 1998. https://doi.org/10.1097/00010694-199802000-00010.

[159] R.P.P.L. Ribeiro, C.A. Grande, A.E. Rodrigues, Adsorption of water vapor on carbon molecular sieve: Thermal and electrothermal regeneration study, Ind Eng Chem Res 50 (2011) 2144–2156. https://doi.org/10.1021/ie101133g.

[160] R.T. Yang, Gas separation by adsorption processes, Butterworths, 1987.

[161] R.M. Barrer, Sorption in Porous Crystals: Equilibria and Their Interpretation., Journal of Chemical Technology and Biotechnology 31 (1981) 71–85. https://doi.org/10.1002/jctb.503310111.

[162] A.M. Ribeiro, T.P. Sauer, C.A. Grande, R.F.P.M. Moreira, J.M. Loureiro, A.E. Rodrigues, Adsorption equilibrium and kinetics of water vapor on different adsorbents, Ind Eng Chem Res 47 (2008) 7019–7026. https://doi.org/10.1021/ie701732x.

[163] S.M. Taqvi, M.D. LeVan, A Simple Way To Describe Nonisothermal Adsorption Equilibrium Data Using Polynomials Orthogonal to Summation, Ind Eng Chem Res 36 (1997) 419–423. https://doi.org/10.1021/ie960366d.

[164] S.K.S. Freitas, R.S. Borges, C. Merlini, G.M.O. Barra, P.M. Esteves, Thermal Conductivity of Covalent Organic Frameworks as a Function of Their Pore Size, The Journal of Physical Chemistry C 121 (2017) 27247–27252. https://doi.org/10.1021/acs.jpcc.7b10487.

[165] S.K.S. Freitas, F.L. Oliveira, C. Merlini, E.P.S. Justo, A. Gioda, P.M. Esteves, Dye-based Covalent Organic Networks (CONs), Journal of Physics: Materials (2020).

[166] S.K.S. Freitas, F.L. Oliveira, T.C. Dos Santos, D. Hisse, C. Merlini, C. Machado, P.M. Esteves, A Carbocationic Triarylmethane-based Porous Covalent Organic Network, Chem. Eur. J. 27 (2020) 2342. https://doi.org/10.1002/chem.202003554.

[167] R.A. Maia, F.L. Oliveira, M. Nazarkovsky, P.M. Esteves, Crystal Engineering of Covalent Organic Frameworks Based on Hydrazine and Hydroxy-1,3,5-Triformylbenzenes, Cryst Growth Des 18 (2018) 5682–5689.

[168] W.J. Roth, B. Gil, W. Makowski, B. Marszalek, P. Eliášová, Layer like porous materials with hierarchical structure, Chem. Soc. Rev. 45 (2016) 3400–3438. https://doi.org/10.1039/C5CS00508F.

[169] S. Zhang, J. Fu, G. Xing, W. Zhu, T. Ben, Recent advances in porous adsorbent assisted atmospheric water harvesting: a review of adsorbent materials, Chemical Synthesis 3 (2023). https://doi.org/10.20517/cs.2022.40.

[170] S. Mitra, S. Kandambeth, B.P. Biswal, A. Khayum M., C.K. Choudhury, M. Mehta, G. Kaur, S. Banerjee, A. Prabhune, S. Verma, S. Roy, U.K. Kharul, R. Banerjee, Self-Exfoliated Guanidinium-Based Ionic Covalent Organic Nanosheets (iCONs), J Am Chem Soc 138 (2016) 2823–2828. https://doi.org/10.1021/jacs.5b13533.

[171] S. Chandra, S. Kandambeth, B.P. Biswal, B. Lukose, S.M. Kunjir, M. Chaudhary, R. Babarao, T. Heine, R. Banerjee, Chemically Stable Multilayered Covalent Organic Nanosheets from Covalent Organic Frameworks via Mechanical Delamination, J Am Chem Soc 135 (2013) 17853–17861. https://doi.org/10.1021/ja408121p.

[172] S. Brunauer, P.H. Emmett, E. Teller, Adsorption of Gases in Multimolecular Layers, J Am Chem Soc 60 (1938) 309–319. https://doi.org/10.1021/ja01269a023.

[173] G. Das, D. Balaji Shinde, S. Kandambeth, B.P. Biswal, R. Banerjee, Mechanosynthesis of imine, β-ketoenamine, and hydrogen-bonded imine-linked covalent organic frameworks using liquid-assisted grinding, Chem. Commun. 50 (2014) 12615–12618. https://doi.org/10.1039/C4CC03389B.

[174] R. A. Maia, F.L. Oliveira, M. Nazarkovsky, P.M. Esteves, Crystal Engineering of Covalent Organic Frameworks Based on Hydrazine and Hydroxy-1,3,5-Triformylbenzenes, Cryst Growth Des 18 (2018) 5682–5689. https://doi.org/10.1021/acs.cgd.8b01110.

[175] S. Wang, Z. Zhang, H. Zhang, A.G. Rajan, N. Xu, Y. Yang, Y. Zeng, P. Liu, X. Zhang, Q. Mao, Y. He, J. Zhao, B.-G. Li, M.S. Strano, W.-J. Wang, Reversible Polycondensation-Termination Growth of Covalent-Organic-Framework Spheres, Fibers, and Films, Matter 1 (2019) 1592–1605. https://doi.org/10.1016/j.matt.2019.08.019.

[176] J. A. Ritter, S. J. Bhadra, A. D. Ebner, On the Use of the Dual-Process Langmuir Model for Correlating Unary Equilibria and Predicting Mixed-Gas Adsorption Equilibria, Langmuir 27 (2011) 4700–4712. https://doi.org/10.1021/la104965w.

[177] S. García, J. J. Pis, F. Rubiera, C. Pevida, Predicting Mixed-Gas Adsorption Equilibria on Activated Carbon for Precombustion CO2 Capture, Langmuir 29 (2013) 6042–6052. https://doi.org/10.1021/la4004998.

[178] J.A. O'brien, A.L. Myers, Rapid Calculations of Multicomponent Adsorption Equilibria from Pure Isotherm Data, Industrial and Engineering Chemistry Process Design and Development 24 (1985) 1188–1191. https://doi.org/10.1021/i200031a049.

[179] G. Santori, M. Luberti, H. Ahn, Ideal adsorbed solution theory solved with direct search minimisation, Comput Chem Eng 71 (2014) 235–240. https://doi.org/https://doi.org/10.1016/j.compchemeng.2014.07.027.

[180] K.S. Walton, D.S. Sholl, Predicting multicomponent adsorption: 50 years of the ideal adsorbed solution theory, AIChE Journal 61 (2015) 2757–2762. https://doi.org/https://doi.org/10.1002/aic.14878.

[181] J.E. Sosa, Rui.P.P.L. Ribeiro, I. Matos, M. Bernardo, I.M. Fonseca, J.P.B. Mota, J.M.M. Araújo, A.B. Pereiro, Coconut shell derived activated carbon for effective separation of greenhouse gases, International Journal of Refrigeration 176 (2025) 66–78. https://doi.org/https://doi.org/10.1016/j.ijrefrig.2025.04.022.

[182] B.B. Saha, K. Habib, I.I. El-Sharkawy, S. Koyama, Adsorption characteristics and heat of adsorption measurements of R-134a on activated carbon, International Journal of Refrigeration 32 (2009) 1563–1569. https://doi.org/https://doi.org/10.1016/j.ijrefrig.2009.03.010.

[183] A.A. Askalany, B.B. Saha, K. Uddin, T. Miyzaki, S. Koyama, K. Srinivasan, I.M. Ismail, Adsorption Isotherms and Heat of Adsorption of Difluoromethane on Activated Carbons, J Chem Eng Data 58 (2013) 2828–2834. https://doi.org/10.1021/je4005678.

[184] M. Sultan, T. Miyazaki, B.B. Saha, S. Koyama, H.-S. Kil, K. Nakabayashi, J. Miyawaki, S.-H. Yoon, Adsorption of Difluoromethane (HFC-32) onto phenol resin based adsorbent: Theory and experiments, Int J Heat Mass Transf 127 (2018) 348–356. https://doi.org/https://doi.org/10.1016/j.ijheatmasstransfer.2018.07.097.

[185] B.B. Saha, I.I. El-Sharkawy, R. Thorpe, R.E. Critoph, Accurate adsorption isotherms of R134a onto activated carbons for cooling and freezing applications, International Journal of Refrigeration 35 (2012) 499–505. https://doi.org/https://doi.org/10.1016/j.ijrefrig.2011.05.002.

[186] J. Zheng, D. Barpaga, B.A. Trump, M. Shetty, Y. Fan, P. Bhattacharya, J.J. Jenks, C.-Y. Su, C.M. Brown, G. Maurin, B.P. McGrail, R.K. Motkuri, Molecular Insight into Fluorocarbon Adsorption in Pore Expanded Metal–Organic Framework Analogs, J Am Chem Soc 142 (2020) 3002–3012. https://doi.org/10.1021/jacs.9b11963.

[187] S. Wang, L. Zhou, H. Qin, Z. Dong, H. Li, B. Liu, Z. Wang, L. Zhang, Q. Fu, X. Chen, Study of CHF3/CH2F2 Adsorption Separation in TIFSIX-2-Cu-i, Molecules 29 (2024). https://doi.org/10.3390/molecules29081721.

[188] Q. Wang, Z. Huang, S. Ou, R. Zhang, The Energy Storage Properties of Refrigerants (R170, R134a, R143a, and R152a) in Mof-5 Nanoparticles: A Molecular Simulation Approach, Materials 12 (2019). https://doi.org/10.3390/ma12213577.

[189] R. Jerozal, J. Kim, J.-H. Lee, P. Milner, Enhancing Selective Hydrofluorocarbon Greenhouse Gas Capture via Halogenation of Metal-Organic Frameworks, (2024). https://doi.org/10.26434/chemrxiv-2024-bck4q.

[190] Q. Wang, S. Tang, Energy storage analysis of R125 in UIO-66 and MOF-5 nanoparticles: A molecular simulation study, 17 (2019) 229–234. https://doi.org/doi:10.1515/chem-2019-0026.

[191] M. Frere, K. Berlier, J. Bougard, R. Jadot, Adsorption of Dichlorodifluoromethane, Chlorodifluoromethane, Chloropentafluoroethane, 1,1-Difluoroethane, and 1,1,1,2-Tetrafluoroethane on Silica Gel, J Chem Eng Data 39 (1994) 697–699. https://doi.org/10.1021/je00016a012.

[192] X. Li, H. Bian, W. Huang, B. Yan, X. Wang, B. Zhu, A review on anion-pillared metal–organic frameworks (APMOFs) and their composites with the balance of adsorption capacity and separation selectivity for efficient gas separation, Coord Chem Rev 470 (2022) 214714. https://doi.org/https://doi.org/10.1016/j.ccr.2022.214714.

[193] L. Paz, S. Gentil, V. Fierro, A. Celzard, Assessing the performance of adsorbents for CO2/CH4 separation in pressure swing adsorption units: A review, J Environ Chem Eng 12 (2024) 114870. https://doi.org/https://doi.org/10.1016/j.jece.2024.114870.

[194] N. Kumar, S. Mukherjee, N.C. Harvey-Reid, A.A. Bezrukov, K. Tan, V. Martins, M. Vandichel, T. Pham, L.M. van Wyk, K. Oyekan, A. Kumar, K.A. Forrest, K.M. Patil, L.J. Barbour, B. Space, Y. Huang, P.E. Kruger, M.J. Zaworotko, Breaking the trade-off between selectivity and adsorption capacity for gas separation, Chem 7 (2021) 3085–3098. https://doi.org/https://doi.org/10.1016/j.chempr.2021.07.007.

[195] M.-B. Kim, S.-J. Lee, C.Y. Lee, Y.-S. Bae, High SF6 selectivities and capacities in isostructural metal-organic frameworks with proper pore sizes and highly dense unsaturated metal sites, Microporous and Mesoporous Materials 190 (2014) 356–361. https://doi.org/https://doi.org/10.1016/j.micromeso.2014.02.028.

[196] M. Toyoda, H. Murase, T. Imai, H. Naotsuka, A. Kobayashi, K. Takano, K. Ohkuma, SF6 reclaimer from SF6/N2 mixtures by gas separation with molecular sieving effect, IEEE Trans. Power Delivery 18 (2003) 442.

[197] R. Sun, C.-W. Tai, M. Strømme, O. Cheung, Hierarchical Porous Carbon Synthesized from Novel Porous Amorphous Calcium or Magnesium Citrate with Enhanced SF6 Uptake and SF6/N2 Selectivity, ACS Appl Nano Mater 2 (2019) 778–789. https://doi.org/10.1021/acsanm.8b02005.

[198] H. Wang, L. Shi, Z. Xiong, S. Ma, H. Cao, S. Cai, Z. Qiao, J. Pan, Z. Chen, A two-dimensional metal–organic framework assembled from scandium-based cages for the selective capture of sulfur hexafluoride, Chem. Commun. 60 (2024) 2397–2400. https://doi.org/10.1039/D3CC05087D.

[199] Y.-P. Li, X.-J. Zhang, J.-J. Ni, W.-J. Ji, S. Li, Y.-L. Li, W. Wen, J. Wang, Z.-Y. Sui, X.-F. Xu, Design of a highly-stable cobalt (II) porous framework based on aromatic stacking strategy for efficient SF6 capture and SF6/N2 mixture separation, Sep Purif Technol 343 (2024) 126995. https://doi.org/https://doi.org/10.1016/j.seppur.2024.126995.

[200] Y.-P. Li, J.-J. Ni, S. Li, J. Wang, Z.-Y. Sui, X.-F. Xu, Rational pore-window size control in three Cu-MOFs with different pore environments for efficient capture of the greenhouse gas SF6, J Solid State Chem 329 (2024) 124443. https://doi.org/https://doi.org/10.1016/j.jssc.2023.124443.

CHAPTER 5

POROUS MATERIALS FOR THE CAPTURE AND SEPARATION OF SF_6, THE MOST POTENT GHG

5.1 Introduction

Climate change presents a pressing global challenge with serious and potentially irreversible consequences [1]. These effects are primarily driven by elevated concentrations of greenhouse gases (GHGs) in the atmosphere, which disrupt temperature and weather systems [1]. One illustrative example is the decreasing water levels in the Amazon River, which threaten regional biodiversity, including plant species critical for GHGs capture [1–3]. The global average temperature has already increased, intensifying the frequency and severity of extreme weather events around the world. These temperature extremes are also linked to increased incidence of cardiovascular disorders and the spread of climate-sensitive diseases [4].

Current GHG emissions are largely composed of: carbon dioxide (79.7 %), methane (11.1 %), nitrous oxide (6.1 %), and fluorinated gases (F-gases, 3.1 %) [5]. Although F-gases contribute with a relatively small fraction of total emissions, they are classified as super pollutants due to their disproportionately high global warming potential (GWP) [6]. Among them, sulphur hexafluoride (SF_6) stands out, with a GWP approximately 22,800 times greater than that of CO_2 [6]. SF_6 is widely utilized in the electrical and electronics industries for its excellent insulating properties [7] often in mixtures containing 10 to 50 wt% of nitrogen (N_2) to minimize the environmental risk of full release [8]. However, its atmospheric concentration has risen from 3.67 ppt in 1994 to 10.5 ppt in 2020 and continues to increase [9–11]. To address this, countries have implemented emission control measures [6,9], including voluntary reduction programs in the U.S. since 1999 and stricter emission limits [12], reaching 1% in 2020 [13]. California and the EU aim to reduce SF_6 use gradually, with the EU targeting two-thirds of 2014 levels by 2030 and evaluating replacement in industrial and high-voltage equipment [9,14]. The Paris Agreement sets a global temperature limit of 2 °C above pre-industrial levels [9], and some governments have imposed SF_6 taxes to encourage reductions (Spain: 66 €/kg; Quebec: 239 $/kg) [9,15]. Controlling SF_6 emissions is thus essential for achieving greenhouse gas reduction goals and net-zero targets.

The main sources of SF_6 emissions are linked to inadequate maintenance of equipment containing the gas or to improper handling during recovery operations. To address this, international organizations have incorporated Leak Detection and Repair (LDAR) programs as a key measure to prevent losses before the recovery process [9,16–18]. The extensive use of SF_6 as a dielectric and insulating gas in the electrical sector particularly in high-voltage circuit breakers, switchgear, and transformers accounts for more than 80 % of global emissions [18–20]. Additional, though smaller yet relevant, contributions arise from the semiconductor industry, where SF_6 is employed in plasma etching and chamber cleaning during microelectronics manufacturing [21,22]. Historically, SF_6 was also used in magnesium and aluminum smelting to prevent oxidation of molten metals; however, its use in metallurgy has significantly declined due to regulatory restrictions and the adoption of alternative gases [20,23].

In response to its environmental persistence and extremely high global warming potential, different strategies have been investigated to mitigate SF_6 emissions. One pathway focuses on degradation

and safe conversion. Traditional incineration at high temperatures (~1100 °C) can achieve substantial removal rates, but it presents drawbacks such as the generation of toxic byproducts and additional CO_2 emissions [18,24,25]. To overcome these limitations, catalytic thermal degradation using metal phosphates such as $AlPO_4$ and $CePO_4$ has been developed, enabling operation at lower temperatures with greater product selectivity [26,27]. More recently, innovative approaches have been reported, including the use of graphitic carbon to transform SF_6 into reusable fluorinated materials [28], and catalytic conversion into chemical precursors with potential applications in the medical field [29]. These advances highlight the potential to integrate SF_6 degradation into circular economy strategies or into the development of substitute gases.

Another important line of research focuses on exploring alternative gases to SF_6 to reduce the environmental impact of gas-insulated electrical equipment (GIS and GCB) while maintaining their insulating and arc-extinguishing capabilities [30]. Promising candidates include mixtures of CO_2, N_2, CF_3I, and fluorinated compounds such as C_4F_7N/CO_2, $C_5F_{10}O$, and hydrofluoroolefins (HFOs), which have shown dielectric properties comparable or even superior to those of SF_6 under certain pressure ranges [7,31–33]. These gases have been studied in terms of their performance under partial discharges and electric arcs. However, challenges remain regarding arc-quenching capability, compatibility with solid materials, toxicity, formation of byproducts, and adaptation to industrial designs [34]. In parallel, computational chemistry and artificial intelligence are being applied to design new molecules with enhanced stability and improved environmental safety, offering a promising avenue for the future [31].

The recovery and purification of SF_6 represent the most direct and effective strategy for reducing its emissions, as they are closely tied to the gas's life cycle. Since the 1990s, companies such as Solvay have developed industrial-scale recycling processes involving washing, adsorption, and compression, achieving purities of up to 98.5 %, which allow reuse in the electrical industry and in magnesium smelting [18,35]. More advanced technologies including cryogenic distillation, liquefaction, hydrate formation, and adsorption on porous materials such as metal-organic frameworks (MOFs), activated carbons (ACs), zeolites, and silica-based adsorbents have been shown to reach purities above 99.9 % [36–49]. Nevertheless, these methods still face economic and energy limitations that hinder their large-scale implementation [18,50,51].

Porous solid matrices such as MOFs have gained attention for SF_6/N_2 separation due to their adjustable structures, where studies on M-MOF-74 (M = Mg, Co, Zn) showed that unsaturated metal sites selectively enhance SF_6 adsorption through gas–gas interactions [45]. Key structural parameters, including surface area, pore volumes and pore size, have been extensively studied in relation to their impact on SF_6 adsorption performance. MOFs with narrow pores typically favour selective separation at low pressures, whereas those with larger pores are more suitable for SF_6 storage applications [39]. Moreover, the incorporation of functional groups onto MOF surfaces has been explored to enhance specific interactions with SF_6, thereby improving separation efficiency [39]. Two-dimensional MOFs (2D-MOFs) are proposed as a highly selective and sensitive platform for the filtration and detection of

fluorinated gases, demonstrating efficacy and stability even under extreme industrial conditions [52]. Furthermore, the influence of pressure on SF_6/N_2 adsorption has been investigated in UIO-66 and UIO-67, with the latter exhibiting superior selectivity due to its pore size [36]. More recently, advanced MOFs such as Sc-cage-MOF and YTU-30 have been developed, in which tailored architectures and functional groups promote strong interactions with SF_6, either through cage confinement or via SF–π and CH–F interactions [46,47]. In addition, the SNNU-202, 203, and 204 series incorporate dinuclear building blocks and aromatic rings that enhance selective adsorption along the pore walls [39]. Additionally, BUT-53 has demonstrated the ability to recover high-purity SF_6 (>99.9 %) even under humid conditions, proving to be a promising approach for sustainable SF_6 capture [53]. Furthermore, GNU-3, a cobalt-based MOF with nanomolecular traps and well-defined pores, efficiently captures SF_6 from N_2 mixtures due to strong supramolecular interactions, exhibiting high selectivity and excellent regeneration capacity [54]. Nevertheless, despite their advantages, the high cost of MOF precursors and synthesis remains a major barrier to their industrial-scale implementation.

In contrast, ACs offer a more economically viable and scalable alternative due to their structural diversity, low production cost, and ease of preparation [38,40,41]. Recent efforts have focused on optimizing activation processes using various precursors to enhance pore structure and surface functionality, resulting in materials with improved selectivity for SF_6 [38,41]. The presence of mesopores facilitates faster diffusion and enhances adsorption capacities [38,40,41], whereas the well-defined microporous structure of ultramicroporous carbon materials, combined with imine and aromatic functional groups, promotes the capture and separation of SF_6 by creating a hydrophobic environment that favors specific interactions with large, nonpolar molecules [48], making CC3 a highly promising adsorbent for the efficient separation of SF_6/N_2 mixtures [48]. Similarly, porous carbons derived from CaCit and MgCit exhibit very high surface areas and optimized porosity, enhancing both adsorption capacity and selectivity toward SF_6 in separation processes [49]. Their stability, moisture resistance, and low synthesis cost further support the potential of PC-CaCit and PC-MgCit as adsorbents for greenhouse gas capture [49]. Furthermore, the balance between surface area and microporosity enhances SF6 adsorption capacity, allowing a greater amount of gas to be stored on the material's surface, as observed in activated carbon AC-1[44]. Finally, ultramicroporous carbons such as $Ph_{10}Cs_{11}$, $Ph_8M_2Cs_{11}$, $Ph_6M_4Cs_{11}$, $Ph_8M_2Cs_9$, $Ph_6M_4Cs_9$, $Ph_{10}K_{11}$, $Ph_6M_4K_{11}$, and Darco, obtained via nitrogen doping and alkali-ion activation, allow precise pore size control (5.8–7.7 Å) to optimize SF_6 adsorption [37], and pore tuning with melamine increased SF_6 uptake more than 16-fold and achieved high SF_6/N_2 selectivity (78.8), while also demonstrating good stability and recyclability over multiple adsorption-desorption cycles [37]. Carbon adsorbents (CAK) synthesized from citric acid and KOH via a one-step carbonization-activation method exhibit finely tuned micropores (0.73–0.88 nm) and mesopores that enhance SF_6/N_2 separation [38], with micropores ≤ 0.9 nm controlling SF_6 adsorption at low pressure and mesopores improving diffusion. Among them, CAK2 achieved the highest uptake [38], and these results provide valuable insights for the design of high-performance porous materials for SF_6 capture and recovery [38]. The

activation process used in the production of activated carbon is crucial in enhancing its structural and textural properties [38]. Selecting appropriate activation methods can significantly increase surface area and microporosity, while also creating larger mesopores that enhance adsorption capacity for gases such as SF_6 [38]. To ensure economic viability, choosing low-cost, sustainable biomass precursors is essential for the development of bio-based activated carbons (Bio-ACs), aligning with the principles of the circular economy. In this context, coconut shell (CS) waste has emerged as a promising and cost-effective feedstock for Bio-AC production, offering favorable characteristics for industrial-scale gas adsorption applications

ACs not only demonstrate outstanding SF_6 adsorption and separation performance but also offer significant practical advantages. They can be produced from abundant and inexpensive precursors—such as coal, biomass, or petroleum residues which is critical for scalable implementation in industrial settings [55]. Furthermore, their cost-effectiveness is clear when compared with other adsorbents; for instance, activated carbon and zeolites can cost as little as 0.4 USD g^{-1}, considerably lower than amine-based or MOF materials [56]. These attributes highlight the innovative contribution of this study, demonstrating activated carbons as feasible and competitive alternatives for SF_6 separation. Altogether, these properties indicate that these materials represent a promising alternative for industrial-scale application, as their porous structures can be reproduced at larger scales and their structural features such as high microporosity, SF_6 affinity, and chemical stability make them suitable for large-volume gas capture and separation processes. Finally, activated carbons demonstrate remarkable SF_6 adsorption and separation capabilities, making them an economically viable and easily prepared alternative for industrial-scale applications due to their reproducible structure, high microporosity, and chemical and thermal stability.

The objective of this chapter is to comprehensively evaluate the adsorption performance, capture capacity, working capacity, regenerability, and selectivity of SF_6 from its mixture with N_2 using a range of porous solid matrices. Two biomass-derived activated carbons (BIO-ACs) prepared from coconut shell waste were investigated, one obtained by physical activation with CO_2 and the other by chemical activation with $ZnCl_2$. Physical activation mainly promoted the development of microporosity in the CS–CO_2 material, whereas chemical activation enhanced both micro- and mesoporosity in CS–$ZnCl_2$, thus improving accessibility to the adsorption sites.

In addition, three commercial activated carbons (AC1, AC2, and AC3), a commercial activated carbon monolith (ACM), an activated carbon honeycomb monolith (ACHM), and a metal–organic framework (Fe-BTC) were included. The selection of these adsorbents provided a robust comparative framework to assess SF_6/N_2 separation across materials of different structural and chemical nature.

Adsorption equilibria of SF_6 and N_2 were measured for all materials at 283.15, 303.15, and 323.15 K, and the experimental data were fitted using the Toth model, which is well recognized for accurately describing adsorption behavior over wide pressure ranges. From these fits, working capacities were calculated to elucidate the effects of pressure and temperature on separation efficiency.

Furthermore, the competitive selectivity of the SF_6/N_2 mixture was assessed using the Ideal Adsorbed Solution Theory (IAST).

The performance of the studied materials was further benchmarked against literature data under industrially relevant conditions (303.15 K and 0.1 MPa), considering not only selectivity but also key textural parameters such as surface area and pore volume in relation to SF_6 uptake. Finally, advanced evaluation criteria were applied, namely the Figures of Merit (FOMs) proposed by Yang and Ackley, which integrate working capacity, selectivity, and regenerability, thereby providing a more realistic and comprehensive assessment of material performance for industrial applications.

Overall, this study represents a significant contribution to advancing the understanding of SF_6/N_2 separation mechanisms, offering not only fundamental insights into the performance of materials with diverse structural origins, but also practical perspectives for the design of more efficient, sustainable, and industrially scalable separation processes.

This chapter is adapted from the following publications:

Section 5.4

J.E. Sosa, R. P. P. L. Ribeiro, S. Kolakovic, I. Matos, M. Bernardo, J. P. B. Mota, J. M. M. Araújo, Ana B. Pereiro, *Solid Porous Materials for Selective Capture and Separation of Sulfur Hexafluoride (SF_6)*, ChemPlusChem (2025). https://doi.org/10.1002/cplu.202500376.

Section 5.5

J. E. Sosa, R. P. P. L. Ribeiro, S. Kolakovic, J. P. B. Mota, J. M. M. Araújo, A. B. Pereiro, *Capture and separation of sulphur hexafluoride: the most powerful greenhouse gas*, J. Mol. Liq. (2025), (**under revision**).

5.2 Toth Isotherm Model

Adsorption isotherm models are essential for describing how a gas interacts with the surface of a porous solid. Classical models such as Langmuir and Freundlich provide an initial approximation but are often insufficient to capture the complexity of heterogeneous surfaces or wide ranges of pressure and temperature.

In this context, the Toth model emerges as a more advanced and flexible tool. This model incorporates a heterogeneity parameter (t) that accounts for deviations from ideal adsorption on uniform surfaces, providing a more realistic representation of gas–solid interactions in complex porous materials. Moreover, its mathematical formulation allows precise fitting of experimental data under both low and high-pressure conditions, making it particularly useful for the simulation and optimization of cyclic adsorption–desorption processes. For these reasons, the Toth model has been widely employed to

analyze the adsorption equilibria, ensuring a reliable and consistent fit with the experimental data [57–59]. The Toth isotherm model is mathematically expressed as follows:

$$q = \frac{q_s bP}{[1 + (bP)^t]^{1/t}} \quad 5.2.1$$

$$b = b_0 \exp\left(\frac{Q_{st}^0}{RT_0}\left(\frac{T_0}{T} - 1\right)\right) \quad 5.2.2$$

$$t = t_0 + \alpha\left(1 - \frac{T_0}{T}\right) \quad 5.2.3$$

where q is the equilibrium concentration of the adsorbed phase, q_s is the maximum amount of adsorption, b_0 is the adsorption affinity constant at the reference temperature T_0, and Q^0_{st} represents the isosteric heat of adsorption at zero charges. The parameter t is the heterogeneity parameter, which accounts for deviations from ideal homogeneous adsorption. Additionally, t_0 and α are empirical constants used to describe the temperature dependence of the heterogeneity parameter t. The average relative error (ARE) between the experimental and fitted data was calculated using the following equation:

$$ARE(\%) = \frac{100}{N_{exp}} \sum \frac{[q_{fit} - q_{exp}]}{q_{exp}} \quad 5.2.4$$

where N_{exp} is the number of experimental points and q_{fit} and q_{exp} are the fitted and experimental data of the adsorbed quantity.

5.3 Performance Criteria for the Selection of Adsorbent Materials

The reliable evaluation of adsorbent materials for SF_6/N_2 separation requires more than a simple assessment of equilibrium selectivity. While selectivity provides valuable insight into the preferential uptake of one component over another, it does not account for the impact of operating conditions, such as pressure and temperature, nor does it reflect the effective amount of gas that can be adsorbed and subsequently desorbed. For this reason, complementary performance indicators such as working capacity, regenerability, and figure-of-merit (FOM) criteria proposed by Ackley and Yang are essential [60]. These metrics provide a more realistic measure of the efficiency, sustainability, and long-term feasibility of materials in cyclic adsorption–desorption processes, enabling the identification of adsorbents not only with high selectivity, but also with operational robustness, energy efficiency, and industrial scalability.

Building on this framework, the application of these performance criteria requires first fitting the equilibrium data of the pure components, followed by the use of predictive models to evaluate gas mixture behavior. In this work, the equilibrium data of both the studied materials and those reported in the literature were fitted using the Toth model [38,39,43–46,48,49,61–64]. Then, the IAST was used to predict the composition of the SF_6/N_2 mixture and the selectivity at the feed composition of $y_{SF6} = 0.02$ and $y_{N2} = 0.98$. However, there is a limitation with selectivity, since it does not consider the differences due to pressure and temperature variation in the adsorption process. This aspect is critical in an

adsorption process because it does not consider the effective amount of gas adsorbed and desorbed in a material [60]. For this reason, the work capacity criterion Δq_{SF_6} and Δq_{N_2} has been studied. This criterion is determined by the difference in the equilibrium quantities at high pressures ($q^*_{ads,pure}$) and equilibrium quantities at low pressures ($q^*_{des,pure}$), calculated as follows [60]:

$$\Delta q_{SF_6} = \left(q^*_{ads,pure} - q^*_{des,pure}\right)|_{feed} \quad 5.3.1$$

$$\Delta q_{N_2} = \left(q^*_{ads,pure} - q^*_{des,pure}\right)|_{feed} \quad 5.3.2$$

In addition, it is crucial to assess the differential capacity for work between adsorption and desorption. The Ackley's FOM ($\propto_{\boldsymbol{A}}$) metric is proportional to the adsorption capacity and is defined by [60]:

$$\propto_{\boldsymbol{A}} = \Delta q_{SF_6}\left(\frac{\Delta q_{SF_6}}{\Delta q_{N_2}}\right) \quad 5.3.3$$

Finally, the Yang's FOM metric ($\propto_{\propto}$) correlates selectivity with the difference in work capacity and is expressed as follows:

$$\propto_{\propto} = S_{\left(\boldsymbol{SF_6}/_{N_2}\right)}\left(\frac{\Delta q_{SF_6}}{\Delta q_{N_2}}\right) \quad 5.3.4$$

The economic and operational viability of a material is critical to any process, but equally important is its sustainability and efficiency for industrial applications. For this reason, regeneration capacity plays a key role in ensuring the long-term functionality and reusability of the material. In this work, the regeneration capacity is determined by the following equation:

$$\text{Regenerability (\%)}: \left(\frac{\Delta q_{SF_6}}{q_{SF_6}}\right) \quad 5.3.5$$

5.4 Porous Materials for Selective Capture and Storage of Sulphur Hexafluoride (SF_6)

Developing technologies to capture, purify, and reuse potent greenhouse gases such as sulfur hexafluoride (SF_6) is crucial because of their high global warming potential. Porous solid matrices are promising candidates for this purpose, due to their high surface areas and pore volumes. In this study, two coconut shell–derived activated carbons (CS-CO_2 and CS-$ZnCl_2$), obtained through physical and chemical activation, were evaluated and compared with two commercial adsorbents: an activated carbon monolith (ACM) and a metal-organic framework (Fe-BTC). The adsorption capacities for SF_6 and nitrogen (N_2) were measured gravimetrically at three temperatures: 283.15, 303.15, and 323.15 K. The experimental data were fitted using the Toth model, and the impact of temperature and pressure on the adsorption performance was analyzed. The order of SF_6 adsorption capacity was ACM > CS-$ZnCl_2$ > Fe-BTC > CS-CO_2, reflecting dependence on surface area. Selectivity for SF_6/N_2 separation was evaluated using Ideal Adsorbed Solution Theory (IAST), with ACM exhibiting the highest adsorption

capacity due to its selective separation properties. These findings contribute to the understanding and selection of efficient adsorbent materials for SF_6 separation and recovery, providing valuable insights for their future implementation in industrial gas treatment and environmental management applications.

5.4.1 Experimental section

5.4.1.1 Materials

Sulphur hexafluoride, SF_6 (≥ 99.99 wt % purity) and N_2 (≥ 99.99 wt % purity) were supplied by Air Liquide (Lisbon, Portugal). Activated carbon monolith, ACM, was produced by Sutcliffe Speakman Carbons Ltd (Bristol, UK), and MOF-Fe-BTC was supplied by Sigma-Aldrich (Lisbon, Portugal).

5.4.2 Results and discussion

5.4.2.1 Adsorption Equilibrium of SF_6 and N_2

Table 5.4.1 provides the characterizations of the materials studied in this work: surface area, pore size distribution (calculated using the NLDFT model), and pore volume. This characterization was obtained using N_2 adsorption isotherms at 77 K, and the data were published in a previous work [65]. This table presents the surface area of the four porous solid matrices studied, which follow the trend: ACM > CS-$ZnCl_2$ > Fe-BTC > CS-CO_2. This order correlates with the adsorption capacity of SF_6 at pressures below 1.5 MPa (see Figure 5.4.1a), which is controlled by both the pore size distributions of the materials and the stronger interactions with this F-gas. SF_6 has a diameter of ~ 5.15 Å and a polarizability of 4.49 $Å^3$ [66–68], whereas N_2 has a smaller diameter of ~ 3.64 Å and a lower polarizability of 1.710 $Å^3$ [66–68]. These differences significantly influence their interactions with the pore surfaces. Then, SF_6 experiences stronger interactions with the material surfaces due to its higher polarizability and larger size, which explains the adsorption capacity trend. CS-$ZnCl_2$ has a broader micro/mesoporosity of 5–60 Å, including both wide and narrow pores (≤ 25 Å) [65], allowing more efficient accommodation of SF_6. In contrast, CS-CO_2 exhibits high microporosity with narrow pores mainly in the 5–15 Å range [65], which restricts the accessibility of the larger and more polarizable SF_6 molecules. ACM and Fe-BTC display intermediate micro/mesoporosity distributions of 5–40 Å and 5–30 Å [65], respectively. Therefore, the observed surface area ranking reflects not only the textural properties of the materials but also the suitability of their pores for interacting with SF_6, explaining the highest uptake capacity of ACM. N_2 is a smaller-sized and lower polarizability molecule. Then, N_2 adsorption is influenced by micropore accessibility, as demonstrated in Figure 5.4.1a. However, the mesopore volume plays a more dominant role, which accounts for the deviations in adsorption trends observed with this gas.

The adsorption equilibria of SF_6 and N_2 on these materials at 283.15, 303.15, and 323.15 K are detailed in Section 4.3 (see Figures 5.4.2–5.4.3). The experimental data were fitted using the Toth adsorption model (the model is described in Section 5.2), with the corresponding parameters and fitting errors summarised in Table 5.4.2. These results further support the relationship between textural properties and adsorption behavior for both gases. The adsorption trend observed for SF_6 is not mirrored in the case of N_2. At pressures below 0.5 MPa, the order of N_2 adsorption capacity is CS-CO_2 > ACM > CS-$ZnCl_2$ > Fe-BTC (Figure 5.4.1b). This sequence does not fully align with the structural characteristics of the materials, primarily due to the deviation of Fe-BTC. One plausible explanation is that the nitrogen molecule, possessing a zero dipole moment, has limited interaction with the Fe (III) active site present in Fe-BTC [69]. When Fe-BTC is excluded, the trend among the remaining materials, CS-CO_2 > ACM > CS-$ZnCl_2$, can be attributed to the increasing mesopore volume, as shown in Table 5.4.1. However, at higher pressures (P > 1 MPa), the order of adsorption capacity shifts to ACM > CS-$ZnCl_2$ > CS-CO_2 > Fe-BTC. Again, Fe-BTC fails to follow the expected trend based on its structural characteristics, as observed by the other materials. When Fe-BTC is excluded, the adsorption behavior of the other materials corresponds to a decreasing order in surface area and micropore volume, as detailed in Table 5.4.1. These results highlight the complex interplay between pore structure, surface area, and the nature of the adsorbate in determining adsorption performance.

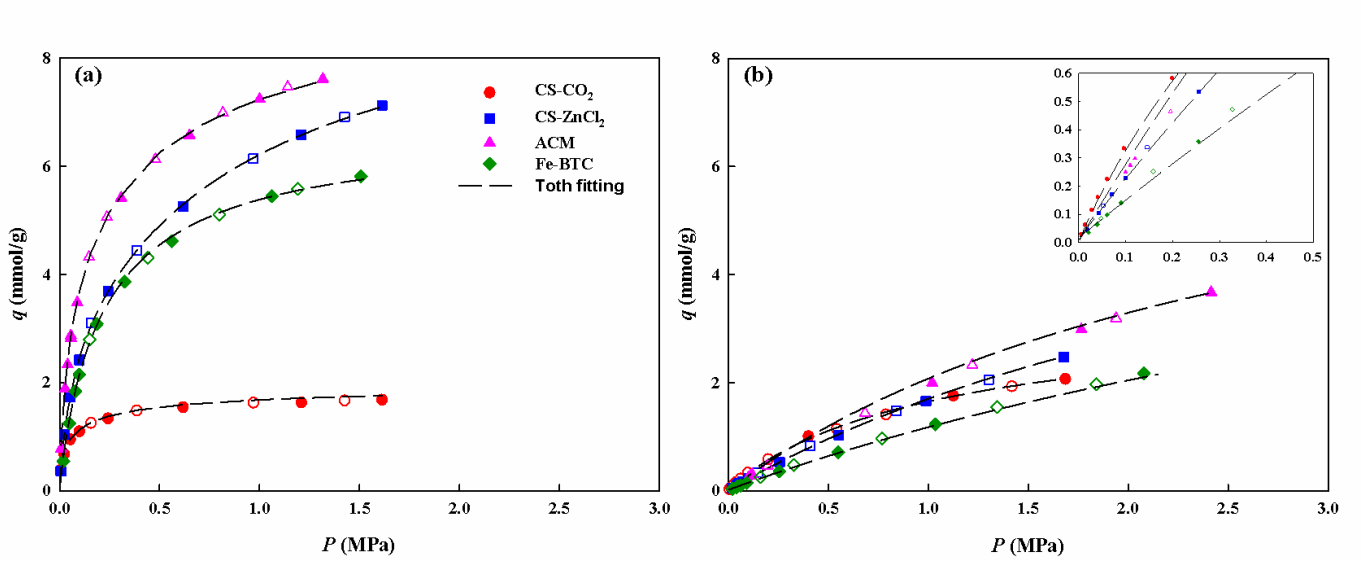


Figure 5.4.1 Adsorption (full symbols) and desorption (empty symbols) equilibrium isotherms on: (a) SF_6 and (b) N_2 at 303.15 K.

Table 5.4.1 Textural parameters of materials studied in this work obtained from N_2 adsorption-desorption isotherms.

Carbon sample	Parameter				Ref.
	S_{BET} (m^2/g)	v_{total} (cm^3g^{-1})	v_{micro}(cm^3g^{-1})	v_{meso}(cm^3g^{-1})	
$CS\text{-}CO_2$	602	0.245	0.211	0.034	[70]
$CS\text{-}ZnCl_2$	1391	0.859	0.240	0.619	
ACM	1446	0.779	0.692	0.088	
Fe-BT	1213	0.625	0.487	0.139	

Table 5.4.2 Toth adsorption model parameters for sorption of SF_6 and N_2 at 283.15 K, 303.15 K, and 323.15 K.

Adsorbents	**Gases**	q_s **(mmol/g)**	b_0 **(MPa^{-1})**	α	t_0	T_0**(K)**	Q_{st}^0 **(kJ/mol)**	**ARE (%)**
$CS\text{-}CO_2$	SF_6	2.05	335	0.328	0.436	303.15	47.9	4.17
	N_2	5.80	1.37	0.214	0.564	303.15	16.5	0.01
$CS\text{-}ZnCl_2$	SF_6	13.1	13.4	0	0.449	303.15	19.8	5.04
	N_2	18.1	0.193	0.706	0.595	303.15	12.6	0.01
ACM	SF_6	10.5	38.6	0.054	0.525	303.15	27.8	4.17
	N_2	15.8	0.272	0.076	0.655	303.15	10.8	0.10
Fe-BTC	SF_6	7.23	11.5	0	0.791	303.15	25.7	1.04
	N_2	12.8	0.158	0.078	0.713	303.15	9.27	0.10

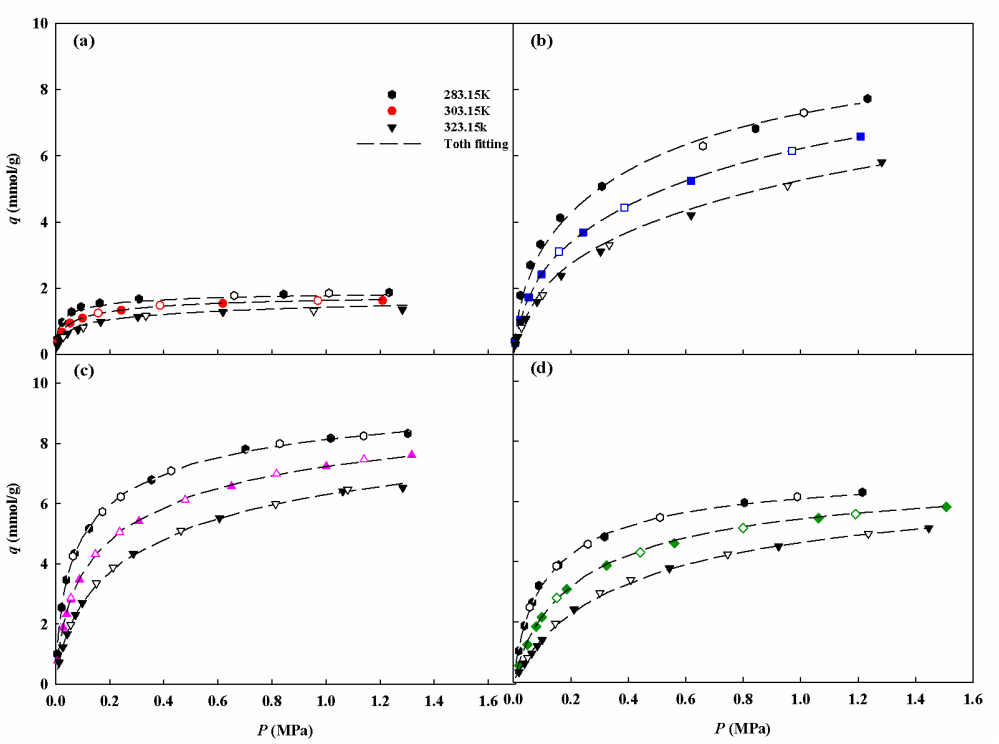


Figure 5.4.2 Adsorption (full symbols) and desorption (empty symbols) equilibrium isotherms of SF_6 on: (a) CS-CO_2, (b) CS-$ZnCl_2$, (c) ACM and (d) Fe-BTC.

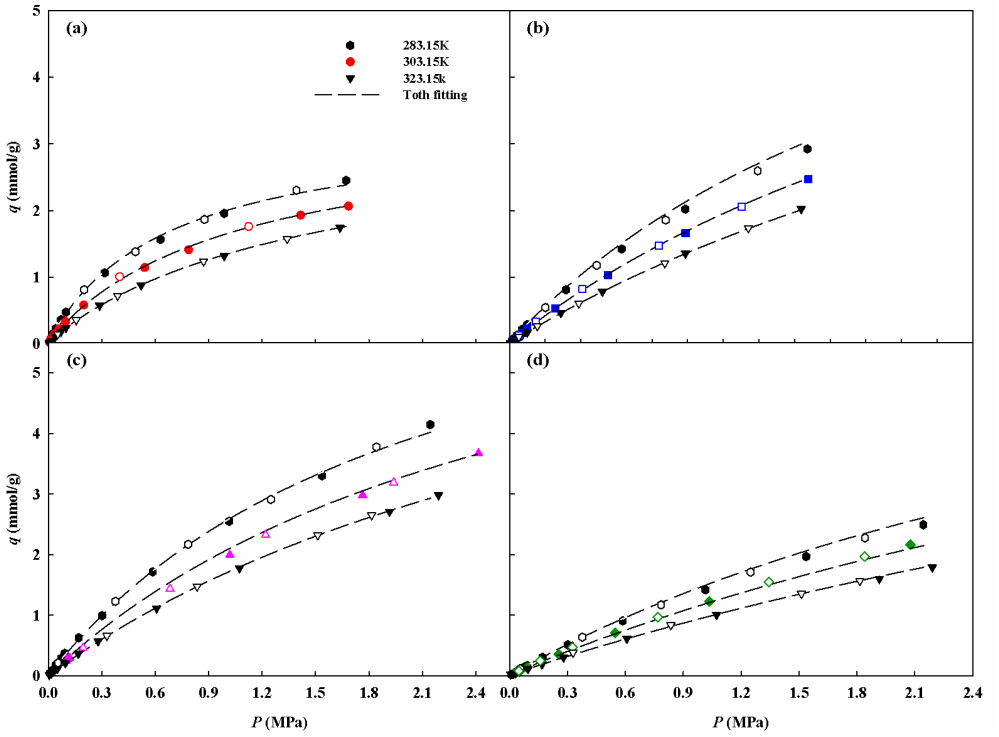


Figure 5.4.3 Adsorption (full symbols) and desorption (empty symbols) equilibrium isotherms of N_2 on: (a) CS-CO_2, (b) CS-$ZnCl_2$, (c) ACM and (d) Fe-BTC.

The adsorption equilibria are accompanied by desorption, indicating that they do not exhibit hysteresis and that the interactions between adsorbents and adsorbates are purely physical. Such behavior is advantageous for practical separation processes involving multiple adsorption-desorption cycles, as it allows for complete regeneration of the porous materials at room temperature without leaving undesirable residues. To assess the practical applicability of the materials, the working capacity was evaluated as a function of the desorption temperature T_H (ranging from 313.15 - 373.15 K) at a desorption pressure of 0.010 MPa and a feed temperature T_L of 303.15 K [71,72]. This pressure reflects the partial pressure of the commercial SF_6/N_2 mixture (with molar fractions y_{SF6}= 0.02 and y_{N2} = 0.98) commonly used in the electrical industry [8]. As shown in Figure 5.4.4, ACM material outperforms the other materials in both SF_6 adsorption at low temperatures and higher working capacity $\Delta_q = q_{T_L} - q_{T_H}$ across the evaluated regeneration temperature range. For instance, at a regeneration temperature of 313.15 K, the working capacity follows the order: ACM (0.60 mmol/g) > CS-$ZnCl_2$ (0.34 mmol/g) > CS-CO_2 (0.23 mmol/g) > Fe-BTC (0.22 mmol/g). This trend remains consistent at higher regeneration temperatures. Although all materials show promising adsorption–regeneration performance, Fe-BTC consistently exhibits the lowest S_{F6} adsorption capacity. This limitation is attributed to its structural characteristics, such as lower porosity and less favorable distribution of adsorption sites, which hinder its performance in SF_6/N_2 separation under the studied conditions.

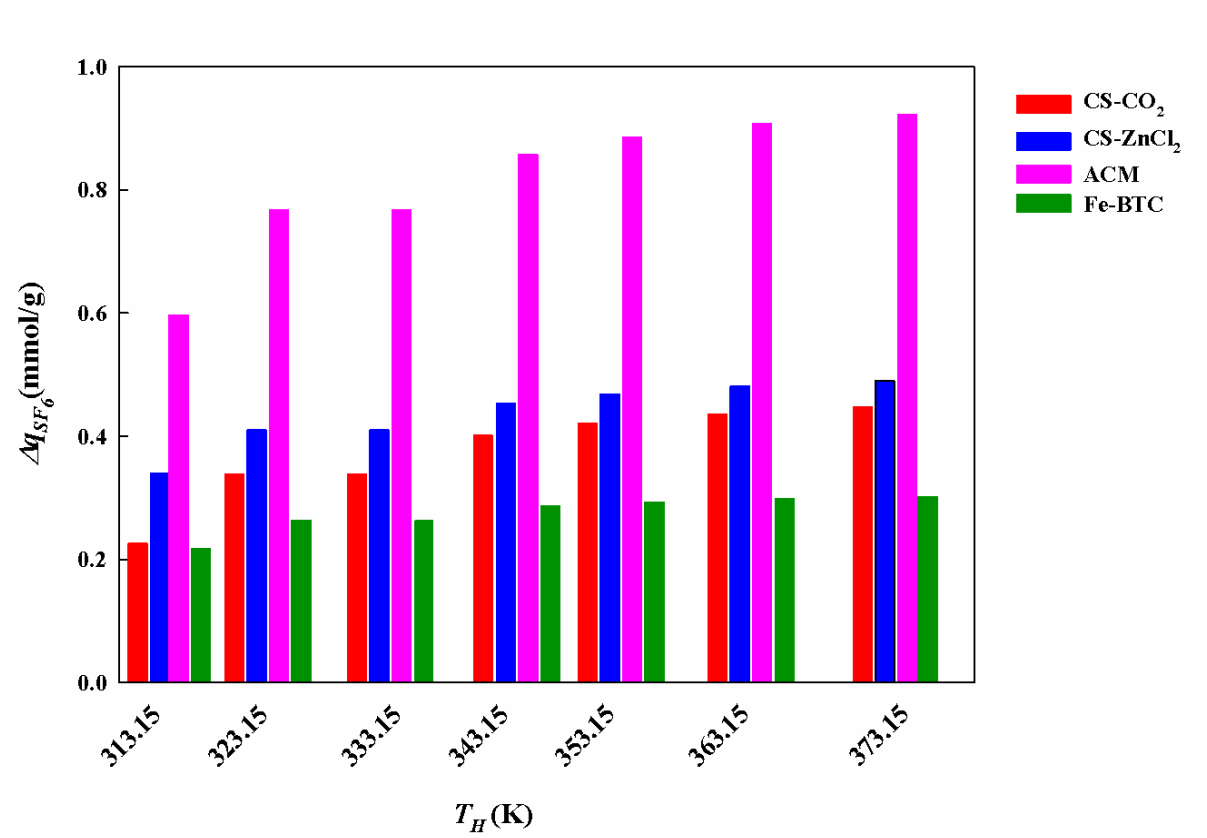


Figure 5.4.4 SF_6 working capacity (Δq_{SF_6}) as a function of desorption temperature T_H for isobaric operation at the pressure of 0.010 MPa and temperature of 303.15 K.

In the gas separation process, the effects of the feed pressure and desorption temperature are key parameters influencing adsorption performance. To explore this, the feed pressure varied between 0.1 and 1 MPa, and the T_H ranged from 303.15 to 373.15 K. Figure 5.4.5 presents contour plots illustrating the impact of pressure on the amount of SF_6 absorbed by the materials. For instance, at a desorption temperature of 373.15 K and a feed pressure of $P_{SF6,feed}$ = 0.1 MPa, the working capacity follows the order: ACM (3.92 mmol/g) > CS-$ZnCl_2$ (2.56 mmol/g) > Fe-BTC (2.39 mmol/g) > CS-CO_2 (1.12 mmol/g). Increasing the feed pressure to 0.5 MPa at the same desorption temperature results in higher working capacities: ACM (6.46 mmol/g) > CS-$ZnCl_2$ (5.14 mmol/g) > Fe-BTC (4.82 mmol/g) > CS-CO_2 (1.52 mmol/g). Although the absolute uptake increases with pressure, the ranking of materials remains unchanged. This consistent trend correlates with the surface area of the materials, which decreases in the same order. A larger surface area facilitates the adsorption of a greater number of gas molecules, thereby enhancing performance. These findings confirm that the porous solid matrices studied here are promising candidates for SF_6 separation processes, particularly under controlled pressure and temperature conditions.

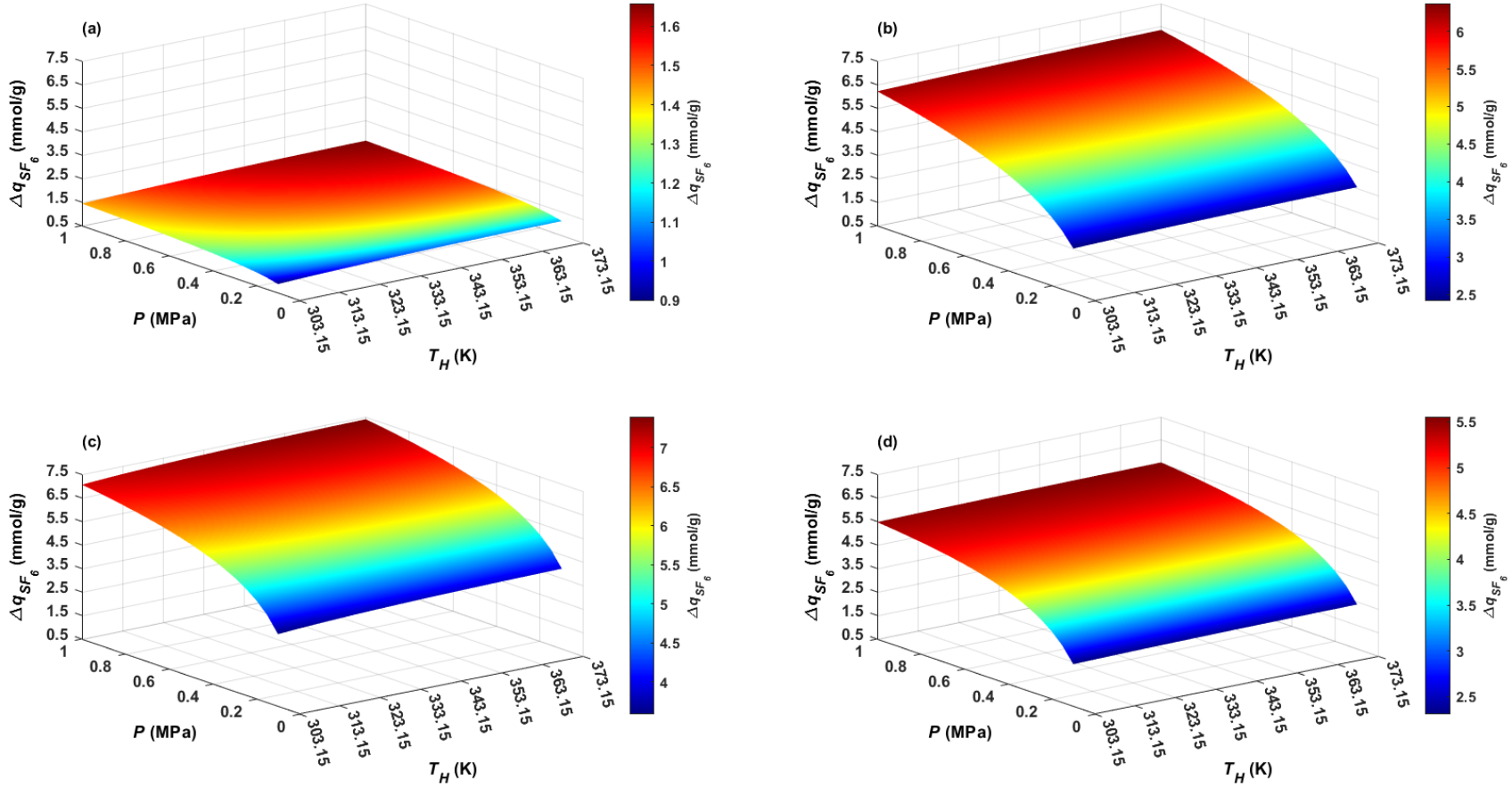


Figure 5.4.5 Contour plots of the working capacity (mmol/g) as a function of the degassing temperature, T_H, and the feed pressure, P on: (a) CS-CO_2, (b) CS-$ZnCl_2$, (c) ACM and (d) Fe-BTC.

5.4.2.2 Isosteric Heat of Adsorption and Henry's Law Constant

In the design of gas separation processes, the isosteric heat of adsorption Q_{st} is a key parameter, as it accounts for approximately 30 % of the total electrical energy consumed during the degassing process [73,74]. As such, Q_{st} is a critical variable for evaluating adsorption efficiency. It serves as an indicator of the strength of interactions between the adsorbent and adsorbate, and it is directly relevant to applications in gas separation, capture and storage [73,75–77]. In this study, Q_{st} was determined from the experimental adsorption data using the Clausius-Clapeyron equation, according to established methodologies [58,75,76,78]:

$$(\log_e P)_q = constant - \frac{Q_{st}}{RT} \qquad 5.4.1$$

where R is the universal gas constant, P is the equilibrium pressure, and T is the temperature.

The experimental adsorption equilibria were fitted using a virial model and subsequently converted to the linear isosteric plots of $(\log_e P)_{q=const}$ *versus* $1/T$ for different q values: 0.1, 0.45, 0.65, 0.85…n mmol/g, corresponding to the maximum adsorption loading of each material. The isosteric heat of adsorption (Q_{st}) for SF_6 across all porous solid matrices lies within the theoretical range of 25 to 35 KJ/mol (see Figure 5.4.6a) [75,79]. For a consistent comparison across all materials, the analysis was limited to adsorption capacities up to 2 mol·kg^{-1}, corresponding to the maximum adsorption loading of CS-CO_2, the material with the lowest adsorption capacity. Within this range, Q_{st} remains relatively uniform and linear, reflecting the consistent energetic interactions across the adsorbents. N_2 does not follow the same SF_6 trend, mainly due to its much lower polarizability (1.710 Å^3) and its smaller diameter (~ 3.64 Å) [66–68]. These properties lead to weaker interactions with the adsorbent surfaces, making N_2 adsorption more dependent on micropore accessibility and mesopore volume than surface area or specific adsorbent–adsorbate interactions. In contrast, SF_6 possesses high polarizability and a larger size (~ 5.15 Å) [66–68]. These properties provide stronger interactions with the material surfaces, which explains the adsorption capacity trend: ACM > CS-CO_2 > CS-$ZnCl_2$ > Fe-BTC. The adsorption of SF_6 molecules leads to significant heat generation due to the strong interactions with energetically favorable adsorption sites located within the pore walls.[80] This results in a linear increase of Q_{st} with increasing uptake. In contrast, N_2 exhibits a linear Q_{st} profile with significantly lower values ranging from 6 to 15 KJ/mol across all materials (see Figure 5.4.6b). This behavior reflects the limited interaction of N_2 with the porous matrices. As N_2 loading increases, the available adsorption sites become saturated, leading to a gradual reduction in adsorption enthalpy and thus a decline in Q_{st} [81].

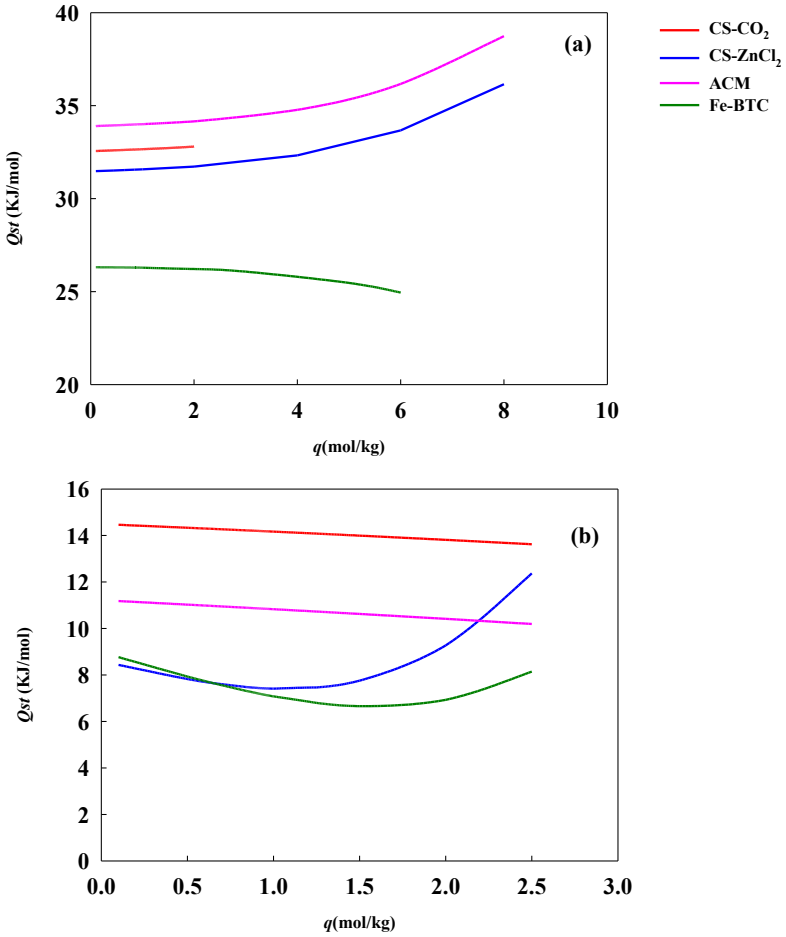


Figure 5.4.6 Isosteric heat of adsorption of: (a) SF_6 and (b) N_2.

In addition, Henry's constants, K_H, are essential for understanding the interactions between the four porous solid matrices (CS-CO_2, CS-$ZnCl_2$, ACM, and Fe-BTC) and the two gases under study (SF_6 and N_2). Both Q_{st} and K_H provide insight into the affinity between the gas molecules and the surface of the adsorbent materials [73,77,80]. Stronger adsorbate–absorbent interactions typically result in higher values of both Q_{st} and K_H. Henry's constants were calculated using the virial equation as described in Section 4.4. For the initial screening metric, K_H serves as a key indicator for selecting the most suitable materials for SF_6/N_2 separation and purification processes. For SF_6, the K_H values follow the order: ACM > CS-CO_2 > CS-$ZnCl_2$ > Fe-BTC. In contrast, for N_2, the order is: CS-CO_2 > ACM > CS-$ZnCl_2$ > Fe-BTC (see Figure 5.4.7.). These trends in K_H are consistent with the patterns observed for Q_{st}, further supporting the conclusion that the nature and strength of adsorbate/adsorbent interactions are governed by the structural characteristics of the pores and the presence of energetically favorable adsorption sites. This relationship also accounts for the observed linear dependence of Q_{st} on increasing gas loading [82–84].

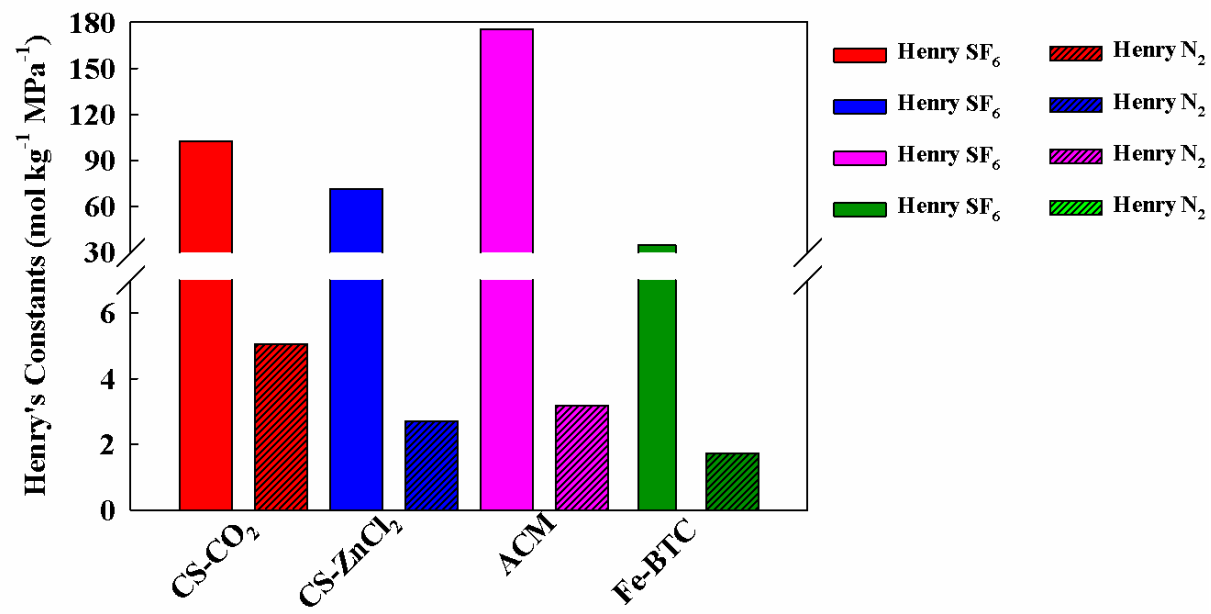


Figure 5.4.7 Henry's Law constants at 303.15 K.

5.4.2.3 Selectivity of SF_6/N_2 Mixture Predicted Using IAST Theory

Sulfur hexafluoride (SF_6) is extensively used in the electrical industry as an insulating gas, often blended with nitrogen in concentrations ranging from 0.1-50 wt % to mitigate its environmental impact [8]. However, there is currently no standardized method for capturing SF_6 at the end of its life cycle. To evaluate the potential of various porous solid matrices for separating SF_6/N_2 mixtures, the selectivity of each material was assessed based on its preferential adsorption behavior. The Toth model parameters (see Table 5.4.3.), determined using the adsorption equilibria of pure SF_6 and N_2, were combined with the Ideal Adsorption Solution Theory (IAST) to predict the composition of the adsorbed phase in the industrially relevant gas mixture (y_{SF6} = 0.02, y_{N2} = 0.98). The mathematical details of IAST are described in Section 4.5. The calculated selectivity values, shown in Figure 5.4.8, indicate that all materials favor SF_6 over N_2, following the trend: ACM > $CS\text{-}ZnCl_2$ > Fe-BTC > $CS\text{-}CO_2$. This order correlates with the decreasing surface area of the materials (see Table 5.4.1.), because larger surface areas and favorable pore structures can accommodate more adsorbate molecules, enhancing SF_6/N_2 separation. Moreover, when a material is selective towards SF_6 and evaluated under dynamic conditions with diluted SF_6/N_2 feeds, the retention of SF_6 in the adsorption column is significantly prolonged, enabling the production of N_2 with purities exceeding 99.999 % [53]. These findings are consistent with the working capacity results previously discussed (see Figure 5.4.4). An important factor influencing separation is the shape of the adsorption isotherms for each pure component [85]. As shown in Figures Figure 5.4.2. -5.4.3, the SF_6 isotherm exhibits a steeper slope at low pressures, while the N_2 isotherm is more linear. This behavior confirms that SF_6 adsorption is favored, whereas N_2 remains in the gas phase, supporting the observed selectivity results.

Table 5.4.3 Toth adsorption model parameters for sorption of SF_6 and N_2 at 283.15 K, 303.15 K, and 323.15 K.

Adsorbents	Gases	q_s (mmol/g)	b_0 (MPa^{-1})	α	t_0	T_0(K)	Q_{st}^0 (kJ/mol)	ARE (%)
$CS\text{-}CO_2$	SF_6	2.05	335	0.328	0.436	303.15	47.9	4.17
	N_2	5.80	1.37	0.214	0.564	303.15	16.5	0.01
$CS\text{-}ZnCl_2$	SF_6	13.1	13.4	0	0.449	303.15	19.8	5.04
	N_2	18.1	0.193	0.706	0.595	303.15	12.6	0.01
ACM	SF_6	10.5	38.6	0.054	0.525	303.15	27.8	4.17
	N_2	15.8	0.272	0.076	0.655	303.15	10.8	0.10
Fe-BTC	SF_6	7.23	11.5	0	0.791	303.15	25.7	1.04
	N_2	12.8	0.158	0.078	0.713	303.15	9.27	0.10

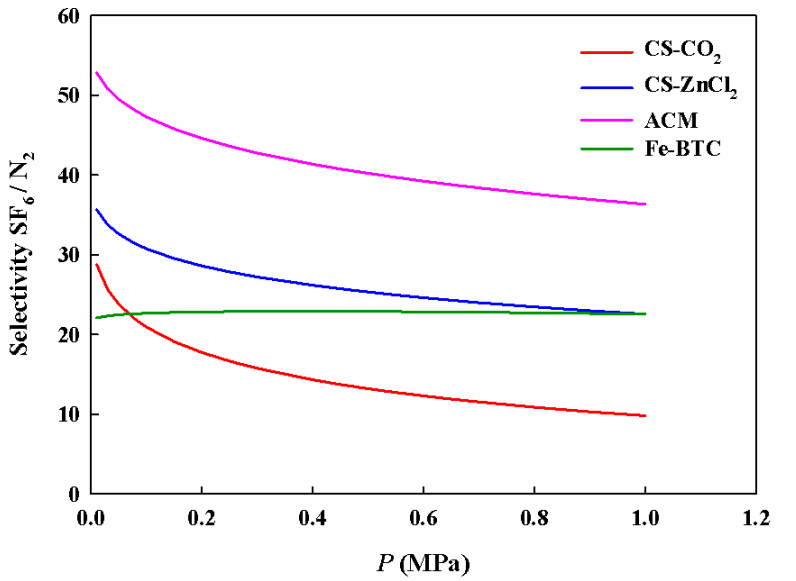


Figure 5.4.8 Selectivity of $CS\text{-}CO_2$, $CS\text{-}ZnCl_2$, ACM, Fe-BTC to SF_6 over N_2 as a function of pressure at 303.15 K for the equilibrium gas phase composition of the SF_6/N_2 mixture (y_{SF6}= 0.02 and y_{N2} = 0.98).

To gain a deeper understanding of the dominant factors influencing the separation of the SF_6/N_2 mixture, the results obtained in this study were compared with those reported in the literature under similar conditions (0.1 MPa and temperatures of 298.15 and 303.15 K) [38,39,43–49,53,54,61,62,64,86–90]. This comparative analysis focused on key structural properties (surface area (S_{BET}) and total pore volume (v_{total}), along with SF_6 adsorption capacity (q_{SF6}) and selectivity, as presented in Figure 5.4.9. The most representative materials in Figure 5.4.9a–5.4.9b include Ph_6M_4Cs11, Mg-MOF-74, CO-MOF-74, $Ph_8M_2Cs_{11}$, $Ph_6M_4Cs_9$, CAK1, CAK2, CAK3, CAK4, PC-800, Kureha carbon, $Ph_8M_2Cs_9$ and ACM (see Figure 5.4.10). The materials exhibiting the highest adsorption capacity typically possess S_{BET} values in the range of 1500–2000 m^2/g and v_{total} values of approximately 0.5–1.1 cm^3/g. Among them, $Ph_6M_4Cs_{11}$, $Ph_8M_2Cs_{11}$ and $Ph_6M_4Cs_9$ are synthetic activated carbons derived from

phenolic carboxylic resins, melamine and various heavy metals [62]. Their enhanced adsorption capacity can be attributed to the structural properties developed during chemical activation, which foster large surface areas, high pore volumes, and abundant microporosity. Additionally, larger total pore volumes facilitate the diffusion of gas molecules into micropores, allowing a greater number of molecules to be stored in the structure of the material, increasing their adsorption capacity [62]. The MOFs Mg-MOF-74 and CO-MOF-74 are characterized by their highly porous frameworks and the presence of dense unsaturated metal sites, which facilitate strong interactions with SF6 molecules, thereby improving adsorption performance [45]. The ACM material studied in this work also performed strongly (highlighted in the demarcated region of Figure 5.4.9a–5.4.9b) alongside several commercial materials such as AC, BIO-AC, and synthetic ACs (CAK1, CAK2, CAK4, PC-800, Kureha carbon, and $Ph_8M_2Cs_9$). These materials are distinguished by their high porosity and elongated micropores, which are significantly influenced by the chemical agents employed during activation [62,64,87].

As shown in Figure 5.4.9c–5.4.9d, BTU-53 exhibits the highest SF_6/N_2 selectivity, despite not possessing the largest surface area or total pore volume. This outstanding performance is attributed to the presence of optimally sized pores together with aromatic and metal sites [53], which generate strong supramolecular interactions with SF_6 while reducing the affinity for N_2 [53]. These results highlight that selectivity is favored by the functional groups present within the pores, which establish adsorbent–adsorbate interactions that, in combination with structural features, facilitate SF_6 separation. Therefore, an efficient material must balance its selectivity and structural properties to optimize SF_6 capture [91]. On the other hand, it is remarkable that ACs such as AC PC-800 and PC-750 demonstrate superior selectivity, a result of their tailored microporous structure [64]. The materials investigated in this work also exhibit promising selectivity values. Importantly, they are derived from residual biomass, offering a more sustainable and cost-effective alternative compared to conventional synthetic or commercial materials. Nevertheless, when selecting adsorbents for industrial applications, a range of factors must be considered, including the adsorption capacity for gas mixtures, selectivity, material renderability, adsorption/desorption kinetics, compatibility, regeneration capacity, and overall production cost.

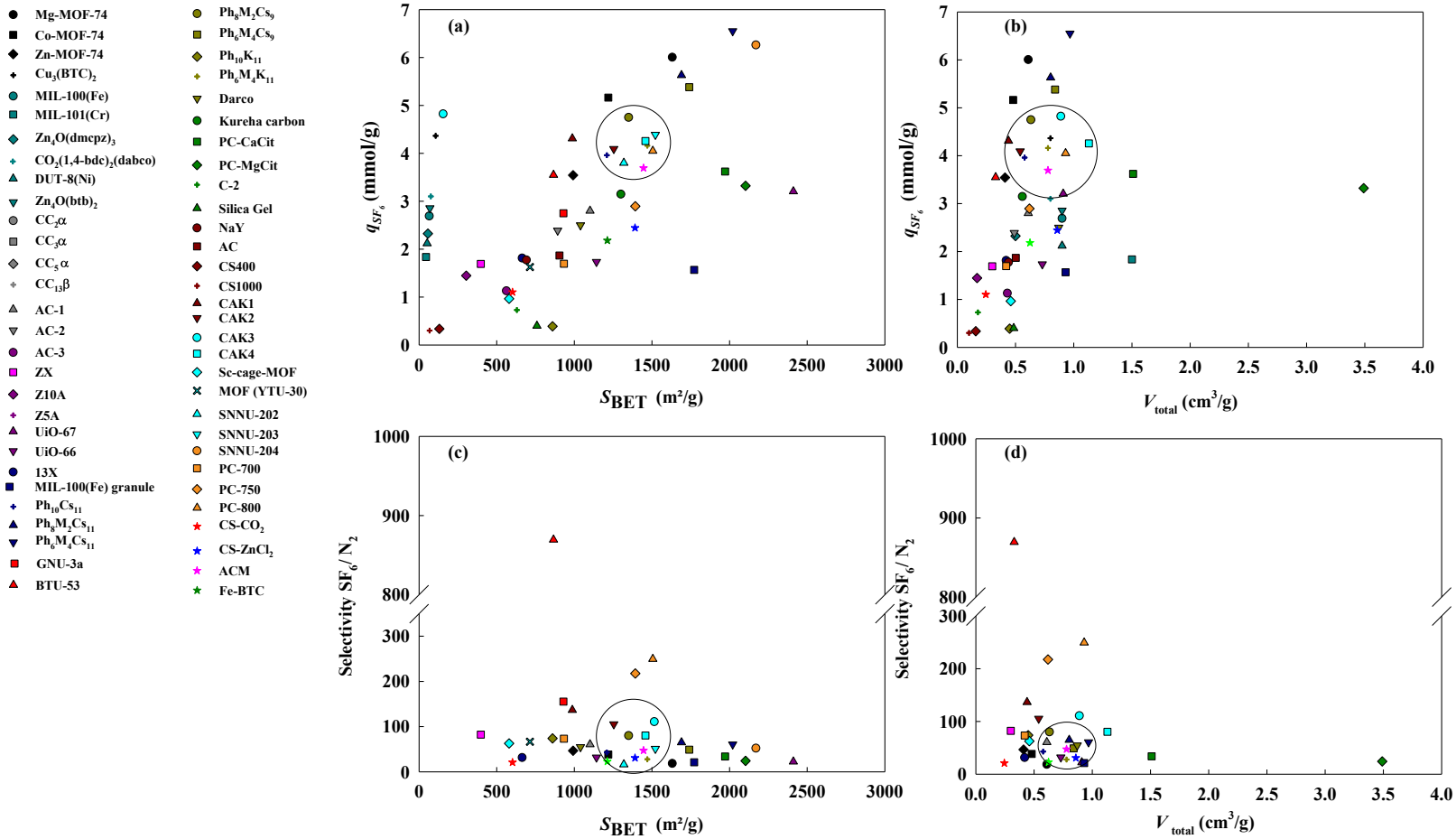


Figure 5.4.9 Comparison of materials studied in this work and literature, taking into account: (a) q_{SF_6} *versus* S_{BET}; (b) q_{SF_6} *versus* v_{total}; (c) SF_6/N_2 selectivity *versus* S_{BET}; and (d) SF_6/N_2 selectivity *versus* v_{total} at 303.15 K and 0.1 MPa for the equilibrium gas phase composition of y_{SF6}= 0.02 and y_{N2} = 0.98 [38,39,43–46,48,49,53,54,62–64].

5.4.2.4 Criteria for Material Selection

Material selection plays a crucial role in the separation of complex gas mixtures, requiring comparative analysis based on adsorption of equilibrium data and selectivity. To identify optimal adsorbents, Yang's and Ackley's FOM metrics are often employed, as they provide a comprehensive evaluation of working capacity, selectivity, and regeneration capacity [92–94]. These performance indicators significantly influence process efficiency, gas purity, and material lifespan [95]. In this study, both metrics were applied to compare the four porous materials developed herein with 36 benchmark materials reported in the literature for the separation of SF_6/N_2 mixture (y_{SF_6} = 0.02 and y_{N_2} = 0.98), under the conditions of 0.1 MPa and 303.15 K, with a desorption pressure of 0.001 MPa at the same temperature. The comparative results are sum-marized in Figure 5.4.12. According to Ackley's FOM, which focuses on working capacity (see Figure 5.4.13), ACM ranks 13th among the evaluated materials, following the order: $Ph_6M_4K_{11}$ > SNNU-204 > $Ph_8M_2Cs_{11}$ > UiO-66 > SNNU-203 > $Ph_6M_4Cs_{11}$ > Zn-MOF-74 > Darco > SNNU-202 > CAK4 > UiO-67 > PC-800 > ACM. These top-performing materials can be broadly classified into three categories:

(i) Metal-organic frameworks (MOFs) such as SNNU-204, SNNU-203, Zn-MOF-74, and UiO-67;

(ii) Activated carbons (ACs) derived from phenolic resins, including $Ph_6M_4K_{11}$, $Ph_8M_2Cs_{11}$, and $Ph_6M_4Cs_{11}$;

(iii) Commercial and biomass-based ACs, such as Darco, CAK4, PC-800, and ACM.

Despite their high performance, MOFs may pose scalability and cost challenges at an industrial level. Conversely, ACM demonstrates a balance of performance and processability, with favorable structural characteristics particularly its microporosity that make it a promising candidate for gas separation applications.

Regarding the Yang's FOM metric (see Figure 5.4.14), which relates working capacity to pure component selectivity, the highest-ranking materials were mostly commercial ACs (PC-800, PC-750, CAK1, CAK3, CAK4 and ACM), MOFs (SNNU-204, SNNU-203, Zn-MOF-74, YTU-30-MOF and UiO-66), phenolic resin ACs ($Ph_6M_4K_{11}$, $Ph_8M_2Cs_{11}$), and porous organic cages (CC3α). The performance of the different materials is ordered as follows: PC-800 > SNNU-204 > $Ph_6M_4K_{11}$ > PC-750 > $Ph_8M_2Cs_{11}$ > CAK4 > YTU-30-MOF > CAK1 > UiO-66 > SNNU-203 > CAK3 > CC3α > Zn-MOF-74 > $Ph_6M_4Cs_{11}$ > ACM. While many of the top performers are acti-vated carbons, their highly microporous structure, though advantageous for adsorption, may hinder regeneration, thereby increasing operational costs. This trade-off highlights the need for a more targeted approach in adsorbent selection. To this end, the materials were further evaluated under conditions more representative of industrial operation, considering a broader range of pressures and temperatures:

- **Condition 1:** Feed pressure of 1 MPa at 303.15 K and desorption pressure of 0.1 MPa at 303.15 K.

- **Condition 2:** Feed pressure of 1 MPa at 303.15 K and desorption pressure of 0.1 MPa at 313.15 K.
- **Condition 3:** Feed pressure of 1 MPa at 303.15 K and desorption pressure of 0.001 MPa at 323.15 K.

This multi-scenario analysis allows for a more comprehensive evaluation of material performance, particularly in terms of robustness, operational versatility, and industrial applicability.

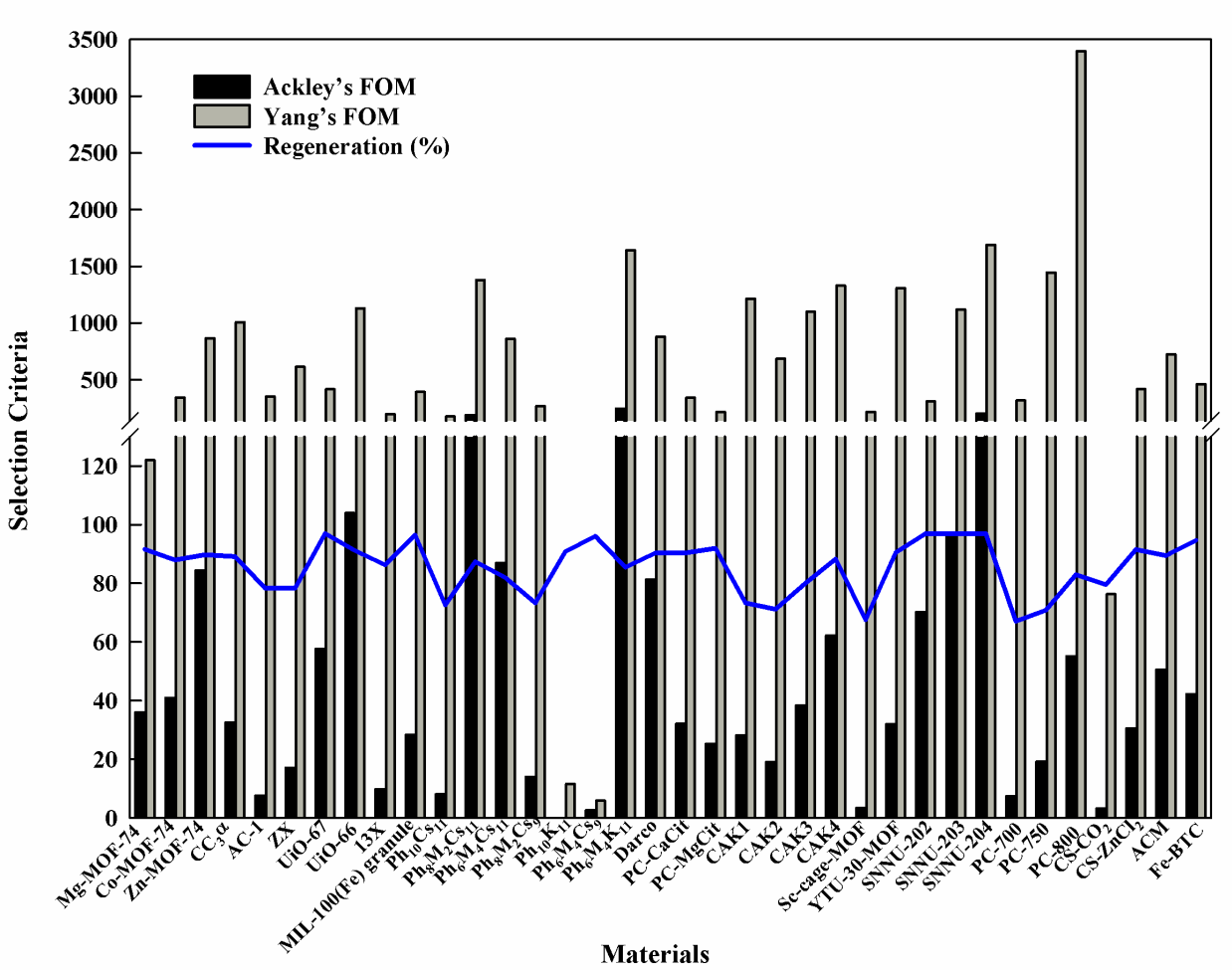


Figure 5.4.10 Selection criteria of porous solid matrices using Ackey's FOM, Yang's FOM, and regeneration capacity at an adsorption pressure of 0.1 MPa and 303.15 K, with desorption at 0.001 MPa and 303.15 K.

Under these operating conditions, the limited availability of experimental data in the literature reduces the number of comparable materials. For the first condition, the materials are ranked as follows: MIL-100(Fe) granulated > Fe-BTC > ACM > CS-ZnC_{l2} > UIO-67 > UIO-66 > 13X > CS-CO_2 (see Figure 5.4.16a). While most materials exhibit good working capacities, the pore structure strongly influences their regeneration performance. In this scenario, the regeneration efficiency for 13X and CS-CO_2 lies in the range of 20-25 %, whereas for the other materials, it is approximately 55 %. These findings suggest that although a substantial amount of gas is adsorbed, the limited regeneration restricts the materials' overall efficiency and hampers their long-term reusability. Under the second condition, an increase in desorption temperature significantly improves the regeneration: MIL-100(Fe) granulated > Fe-BTC > ACM > CS-$ZnCl_2$ > 13X > CS-CO_2 (see Figure 5.4.17b). Here, the regeneration capacity improves to 25–50% for 13X and CS-CO_2 and reaches 90–95% for the other materials, thereby markedly increasing their working capacities. Finally, in the third condition, full regeneration is achieved due to the elevated desorption temperature and lower pressure. The performance order shifts slightly to: MIL-100(Fe) granulated > ACM > Fe-BTC > CS-$ZnCl_2$ > 13X > CS-CO_2 (see Figure 5.4.18c). Importantly, ACM exhibits a significant improvement, outperforming Fe-BTC under these harsher desorption conditions. This suggests that ACM's porous architecture supports more efficient desorption at elevated temperatures. Such enhanced regeneration not only increases working capacity but also provides ACM with a clear advantage in terms of stability and long-term operational reusability in gas separation processes.

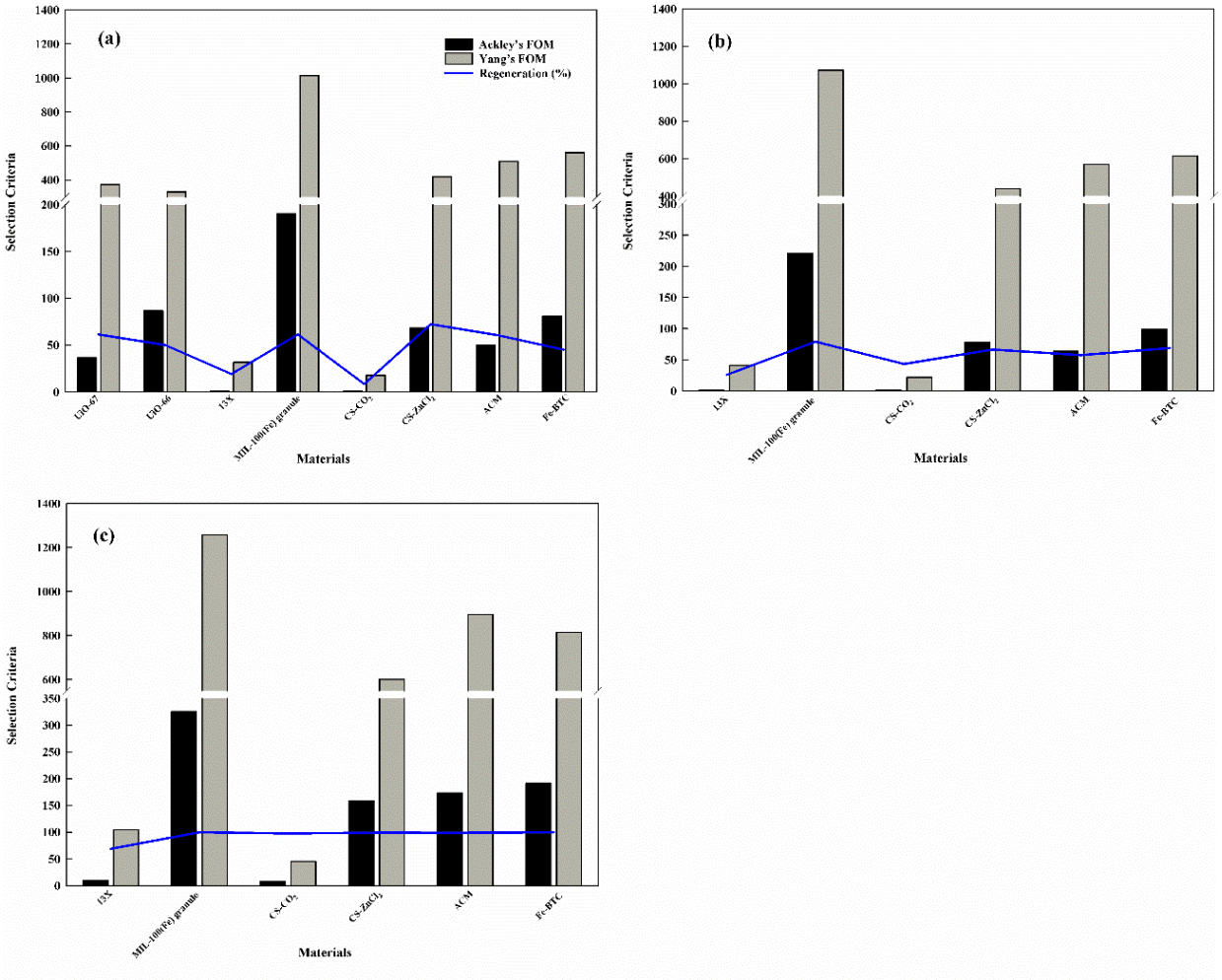


Figure 5.4.11 Selection criteria for porous solid matrices using Ackey's FOM, and Yang's FOM for: (a) condition 1 - feed pressure of 1 MPa at 303.15 K and desorption pressure of 0.1 MPa at 303.15 K, (b) Condition 2 - feed pressure of 1 MPa at 303.15 K and desorption pressure of 0.1 MPa at 313.15 K and (c) Condition 3 - feed pressure of 1 MPa at 303.15 K and desorption pressure of 0.001 MPa at 323.15 K.

5.4.3 Conclusions

The materials investigated in this study, ACM, CS-$ZnCL_2$, Fe-BTC and CS-CO_2, demonstrate significant potential for the capture and separation of SF_6 from SF_6/N_2 mixtures, owing to their diverse structural characteristics that enhance SF_6 selectivity. Across the entire pressure range evaluated, SF_6 adsorption is favored in all porous solid matrices due to the well-developed microporosity and high surface areas, which enable efficient gas packing. At high pressures, this structural advantage significantly boosts the adsorption capacity for SF_6. In contrast, N_2 adsorption is more pronounced at low pressures, particularly in CS-CO_2, as evidenced by higher Henry's law constants, indicating stronger interactions at initial loadings. The efficiency of the materials was further assessed through working capacity calculations under varying pressure and temperature conditions. The results underscore the critical role of surface area not only in maximizing capacity but also in improving regeneration and overall separation performance. Additionally, the interplay between selectivity and working capacity was examined, highlighting the importance of achieving a balance between adsorption strength and desorption ease. A comparative analysis with state-of-the-art materials from the literature confirms the competitive performance of the studied materials, particularly ACM, which stands out due to its excellent working capacity and regeneration behavior. ACM exhibits the highest SF_6 adsorption capacity among the materials studied, due to its high surface area, well-distributed pore volume across micro- and mesopores, and favorable polarity of its active sites. This combination enables stronger interactions with SF_6 molecules, explaining its high selectivity over N_2 and its efficiency in SF_6/N_2 separation. The correlation between the diameter of SF_6, the pore distribution of ACM, and its polarity makes this material a particularly promising adsorbent for the SF_6 capture and storage applications. In summary, this work provides valuable insights for the design and optimization of SF_6 capture and separation processes, reinforcing the potential of these materials for pilot-scale implementation. The findings pave the way for the development of cost-effective and efficient solid porous adsorbents for industrial gas separation applications.

5.5 Capture and separation of sulphur hexafluoride: the most powerful greenhouse gas

Sulphur hexafluoride (SF_6) is a potent greenhouse gas (GHG), possessing the highest global warming potential among commonly monitored GHGs, making its mitigation a critical environmental priority. Numerous porous solid matrices have been developed for SF_6 capture; however, large-scale industrial deployment remains hindered primarily by high production costs. In this study, the adsorption and separation of SF_6 from SF_6/N_2 mixtures were investigated using four activated carbon materials

(ACs), selected for their low cost, ease of fabrication and suitability for industrial applications. The adsorption equilibria of SF_6 and N_2 on the four ACs (designated AC1, AC2, AC3 and ACHM) were measured using a gravimetric method at three temperatures: 283, 303 and 323 K. The experimental data were fitted using the Toth adsorption model, which accurately described the system behaviour across both low and high-pressure regions. Additionally, the selectivity of the SF_6/N_2 was evaluated using Ideal Adsorption Solution Theory (IAST). Among the tested materials, ACHM exhibited superior selectivity of the SF_6/N_2 mixture, attributed to its high microporosity. Finally, a comparative analysis with materials reported in the literature under industrially relevant conditions highlighted the strong potential of these ACs, particularly in terms of working capacity, selectivity and regeneration capacity.

5.5.1 Experimental section

5.5.1.1 Materials

Sulphur hexafluoride, SF_6 (≥ 99.99 wt % purity) and N_2 (≥ 99.99 wt % purity) were supplied by Air Liquide (Portugal). AC1, AC2, and AC3 were produced by Sutcliffe Speakman Carbons Ltd (United Kingdom). Activated carbon honeycomb monolith, ACHM, was supplied by Mast Carbon (United Kingdom).

5.5.2 Results and discussion

5.5.2.1 Materials characterization

Table 5.5.1 and Figure 5.5.1 show the nitrogen adsorption–desorption isotherms at 77 K for the materials investigated in this study. Details of the characterization equipment are provided in Section 4.2. The data for AC1 and AC2 were previously reported in a prior publication [96]. According to the IUPAC classification, pore sizes are categorized as micropores (≤ 20 Å), mesopores (20-500 Å) and macropores (≥ 500 Å) [97,98]. Materials AC1, AC2 and AC3 exhibit microporosity in the range of 5 to 20 Å and mesoporosity between 20 to 40 Å as shown in Figure 5.5.1. The total pore volume is listed in Table 5.5.1. On the other hand, these three-materials display type I(b) nitrogen isotherms according to the IUPAC classification [97,98], which is indicative of micro-mesoporous structures. Corresponding surface area values are also provided in Table 5.5.1. Notably, the nitrogen isotherms of AC2 and AC3 are nearly identical, resulting in comparable surface areas and similar adsorption equilibria with the target gases. In contrast, the ACHM material displays microporosity in the 5-15 Å range and a type I(a) nitrogen isotherm characteristic of highly microporous materials. The total pore volume and surface area for ACHM material are also reported in Table 5.5.1. All materials investigated in this study were

submitted to at least 8–10 regeneration cycles, after which they retained both their structural properties and adsorption capacity. These experimental results demonstrate the excellent stability of the materials.

Table 5.5.1 Textural parameters of activated carbons obtained from N_2 adsorption at 77 K**.**

Carbon sample	Parameter				Ref
	S_{BET} (m^2/g)	v_{total} (cm^3g^{-1})	v_{micro} (cm^3g^{-1})	v_{meso} (cm^3g^{-1})	
AC1	1695	0.760	0.620	0.140	Sosa *et al*. [96]
AC2	1280	0.680	0.362	0.360	Sosa *et al*. [96]
AC3	1229	0.749	0.320	0.387	This work
ACHM	1153	0.454	0.454	1.48E-04	This work

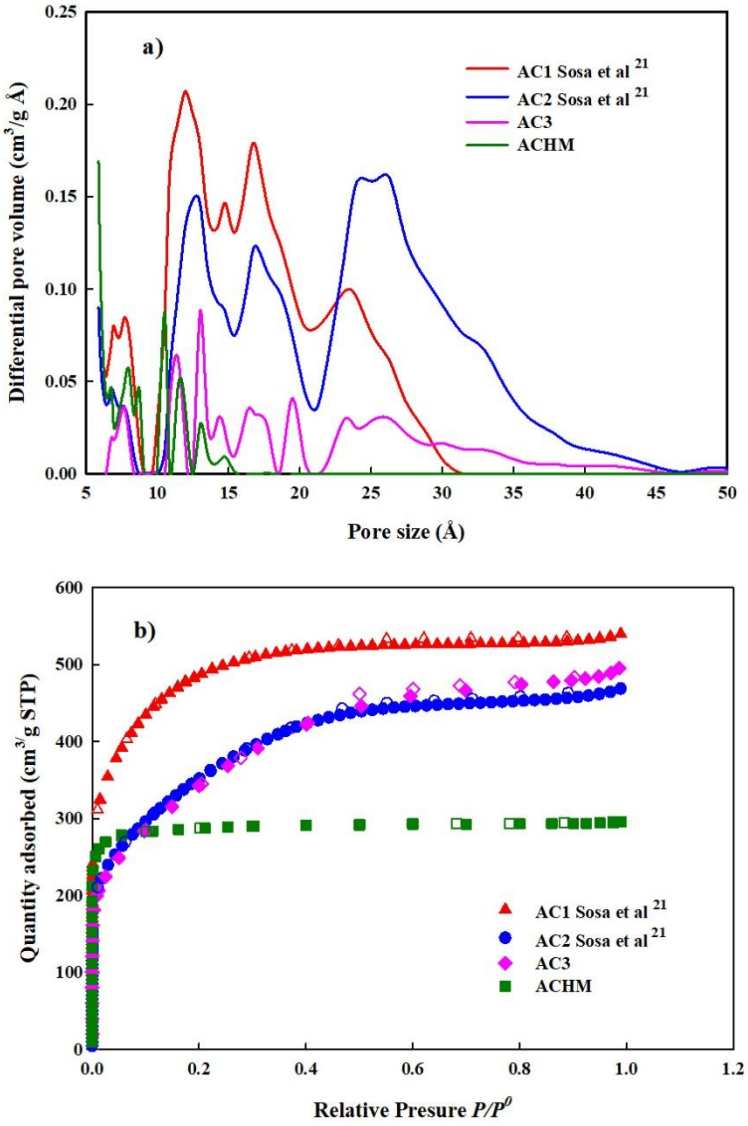


Figure 5.5.1 Characterisation of the carbon samples studied in this work: a) pore size distribution (calculated using the DFT adsorption model) and b) the nitrogen adsorption (full symbols) and desorption (empty symbols) equilibrium isotherms at 77 K for AC1, AC2, AC3 and ACHM.

5.5.2.2 Adsorption equilibrium of SF_6 and N_2

The adsorption equilibria of SF_6 and N_2 on AC1, AC2, AC3 and ACHM are shown in Figure. 5.5.2-5.5.3, with the details of the equilibrium determination provided in Section 4.3. The adsorption and desorption equilibrium points of SF_6 and N_2 practically overlap, indicating the absence of hysteresis and confirming that the adsorption process is fully reversible [99]. SF_6 exhibits a favourable adsorption equilibrium isotherm (see Figure 5.5.2), while N_2 shows more linear behavior (see Figure. 5.5.3). At the highest pressure, the SF_6 adsorption capacity follows the trend: AC1 > AC2 > AC3 > ACHM (see Figure. 5.5.3), which corresponds to the decreasing surface area of these materials (see Table 5.5.1). A higher surface area enhances gas adsorption by providing more available sites for molecule interaction and storage [100]. The change in the adsorption order between SF_6 and N_2 is attributed to the different relationship between molecular size, polarisability, and the pore size distribution of the materials. SF_6 has a larger diameter (5.15 Å) and high polarisability (4.49 Å^3)[67,101], Then, adsorption is strongly governed by van der waals interactions, which are maximised when the molecule is confined in intermediate pores (see Figure 5.5.1, 10–25 Å). These favourable interactions explain the highest adsorption capacities of AC1 and AC2, followed by AC3 and finally ACHM, which lacks suitable microporosity.

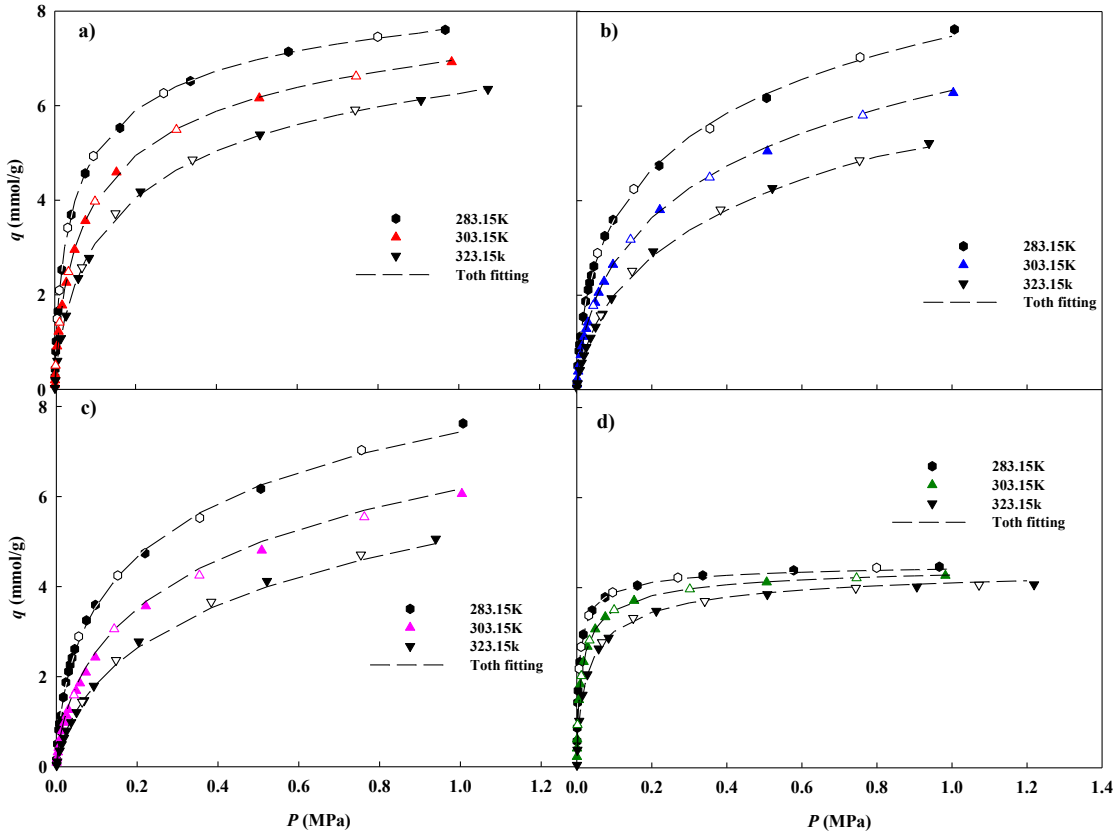


Figure 5.5.2 Adsorption (full symbols) and desorption (empty symbols) equilibrium isotherms of SF_6 on a) AC1 and b) AC2.

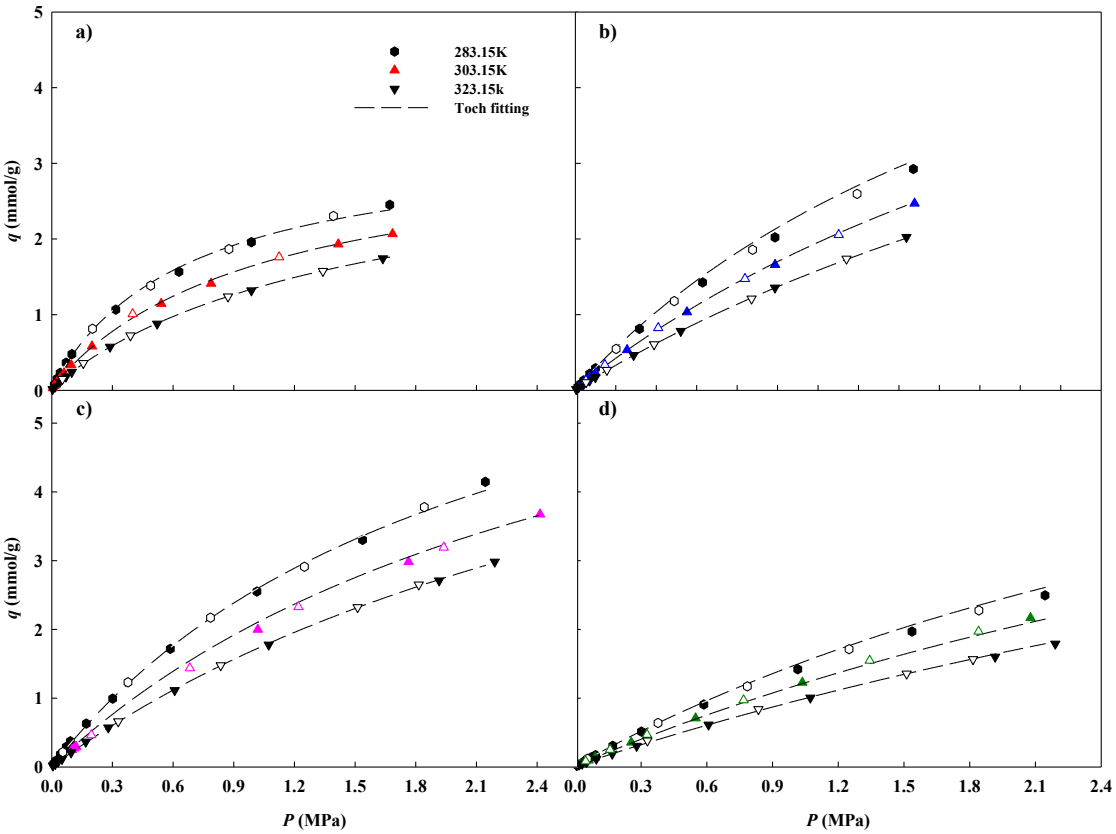


Figure 5.5.3 Adsorption (full symbols) and desorption (empty symbols) equilibrium isotherms of N_2 on a) AC1, b) AC2, AC3 and c) ACHM.

Across the entire pressure range, the N_2 adsorption equilibria follow the order: ACHM > AC1 > AC3 ≈ AC2 (see Figure. 5.5.3). This trend does not directly correlate with the textual properties, such as surface area, but is consistent with the degree of microporosity in the <10 Å range, as shown in Figure 5.5.1. Enhanced microporosity in this range significantly increases the N_2 adsorption capacity [100,102]. For the observed trend of materials AC1 > AC3 ≈ AC2, the order is attributed to differences in micropore volume, ranging from the largest to the smallest (see Table 5.5.1). In contrast, N_2 is smaller (3.64 Å) and less polarizable (1.71 $Å^3$) [67,101], so van der waals forces in larger pores are weaker. In this case, adsorption is dominated by confinement in ultramicropores (<10 Å), where proximity to the pore walls enhances interactions that would otherwise be weak. Thus, ACHM, with a higher fraction of ultramicropores, becomes the most efficient material for N_2, followed by AC1, while AC2 and AC3, dominated by larger pores, show lower capacities. Overall, these results demonstrate that the adsorption order arises from the interplay between molecular size, polarizability, and pore structure, with van der waals interactions serving as the primary driving force, whose effectiveness depends on the degree of molecular confinement within the pores [103,104].

In the context of the gas separation process, selecting an adsorption model that accurately describes the experimental equilibrium data is essential. In this study, the adsorption–desorption equilibria of SF_6 and N_2 on activated carbons (ACs) were analyzed using the Toth adsorption model, as described in Section 5.2. This limitation is critical because inadequate fittings can lead to erroneous estimations.

In contrast, the Toth adsorption model provided an excellent fit for both gases (Figure 5.5.2-5.3), making it suitable for process simulation and optimization of adsorption-based separations. The validity of the model was confirmed by calculating the ARE using Equation 5.2.4, with errors consistently below 1 %, as reported in Table 5.5.2.

Table 5.5.2 Toth adsorption model parameters for adsorption of SF_6 and N_2 at 283, 303, and 323 K.

Adsorbents	Gases	q_s (mmol/g)	b_0 (MPa^{-1})	α	t_0	T_0(K)	Q_{st}^0 (kJ/mol)	ARE (%)
AC1	SF_6	9.60	63.8	2.16E-02	0.504	303.15	25.8	0.138
	N_2	10.4	0.546	0	0.712	303.15	10.1	0.150
AC2	SF_6	15.9	29.6	5.14E-02	0.351	303.15	25.4	0.222
	N_2	11.7	0.326	0	0.659	303.15	12.0	0.027
AC3	SF_6	15.1	25.8	2.19E-02	0.371	303.15	26.8	0.720
	N_2	6.90	0.483	0	0.927	303.15	11.2	0.100
ACHM	SF_6	4.61	416	0	0.601	303.15	31.4	0.211
	N_2	15.5	1.12	1.28	0.405	303.15	29.2	0.244

Evaluating materials solely based on storage capacity can be misleading, as a material with high uptake may not necessarily perform well in separation processes. Therefore, the working capacity (Δq_{SF6}) was assessed under two conditions: 1) varying the degassing temperature (T_H) while maintaining constant feed temperature (T_L) and feed pressure; and 2) varying both feed pressure and T_H while keeping T_L constant. The working capacity was calculated as the difference between the adsorption capacity at feed and regeneration conditions: $\Delta q_{SF_6} = q_{T_L} - q_{T_H}$ [71,72,105].

Figure 5.5.4 presents the working capacity in the desorption temperature range of 313-373 K, at a degassing pressure of 0.001 MPa, feed pressure of 0.01 MPa and feed temperature T_L of 303 K. Across all T_H values, the working capacity follows the order: ACHM > AC1 > AC2 > AC3. This trend corresponds to the distribution of microporosity in the < 10 Å range (see Figure 5.5.1), where higher microporosity enhances the adsorption due to stronger electrostatic interactions between gas molecules and surface functional groups [46,47,86,103,104]. Despite ACHM has a lower specific surface area (1153 m^2/g) and total pore volume (0.454 cm^3/g) compared to AC1, AC2, and AC3 (see Table 5.5.1), its narrow micropores in the 5–15 Å range provide an optimal confinement effect for SF_6 molecules. This confinement maximises interactions, which are further enhanced by the large diameter (~ 5.15 Å) and high polarisability (4.49 $Å^3$) of SF_6. In contrast, AC1, AC2, and AC3 possess higher surface areas and total pore volumes but broader micropore distributions (5–20 Å) combined with mesopores (20–40 Å), which reduce the confinement effect and the adsorbate–adsorbent interactions at low pressures. Consequently, ACHM achieves a higher working capacity, highlighting that the matching of micropore

size with molecular dimensions and polarizability of the adsorbate is more critical than the total surface area or pore volume for low-pressure adsorption performance.

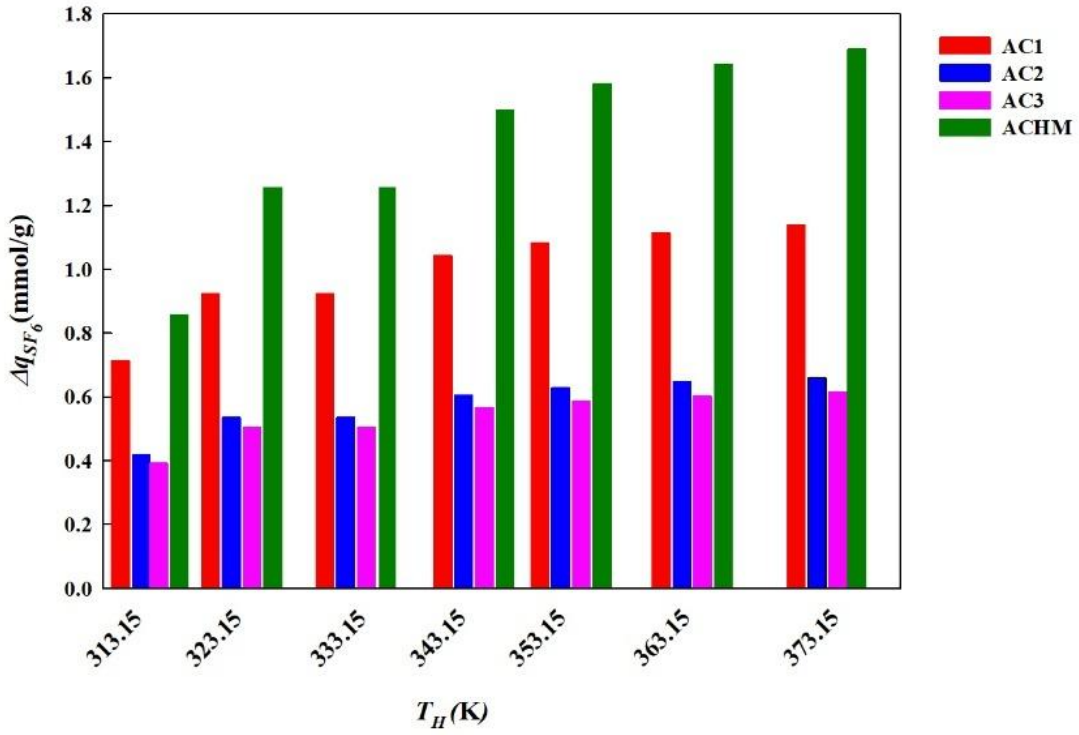


Figure 5.5.4 SF_6 working capacity (Δq_{SF6}) as a function of desorption temperature (T_H) for isobaric operation at 0.01 MPa and an adsorption temperature of 303 K.

Figure 5.5.5 illustrates the working capacity of the materials under varying feed pressures (0.1-1 MPa), degassing temperatures T_H = 303-373 K, a fixed feed temperature T_L = 298 K, and a degassing pressure of 0.001 MPa. The results clearly show that feed pressure has a crucial role in determining the working capacity. For instance, at a feed pressure of 0.1 MPa and T_H = 303 K, the working capacity of SF_6 follows the order: AC1 (3.67 mmol/g) > ACHM (2.59 mmol/g) = AC3 (2.59 mmol/g) > AC2 (2.52 mmol/g). However, when the feed pressure increases to 0.5 MPa at the same degassing temperature (303 K), the trend shifts to: AC1 (5.84 mmol/g) > AC2 (5.07 mmol/g) > AC3 (4.99 mmol/g) > ACHM (3.17 mmol/g). This increase in feed pressure results in an approximate 40% enhancement in the working capacity for the AC materials. Interestingly, ACHM material exhibits a decrease in working capacity with this increment of pressure when it is regenerated at 303 K. In contrast, AC1, AC2 and AC3 facilitate desorption, enhancing regeneration performance across all feed pressures and degassing temperatures studied. Therefore, AC1, AC2 and AC3 show greater potential for continuous SF_6/N_2 separation processes, particularly those involving pressure and temperature variations.

The observed shift in the working capacity trend with increasing feed pressure can be explained by considering both pore structure and textural properties. At low pressures (0.1 MPa), ACHM's narrow micropores (see Figure 5.5.1, 5–15 Å) provide an optimal match with the SF_6 kinetic diameter (~5.15

Å), resulting in strong van der waals interactions and relatively high working capacity despite its lower surface area and total pore volume. However, at higher pressures (0.5 MPa), these narrow micropores in ACHM saturate quickly, and its limited total surface area (see Figure 5.5.1**,** 1153 m^2/g) and pore volume (see Figure 5.5.1, 0.454 cm^3/g) restrict further adsorption. In contrast, AC1, AC2, and AC3 have broader micro-mesoporous structures (see Figure 5.5.1, 5–20 Å micropores, 20–40 Å mesopores) with higher total surface areas and pore volumes, allowing them to accommodate more SF_6 molecules at elevated pressures. Consequently, ACHM shows a lower working capacity at high pressures, while AC1–AC3 display substantial increases (~40 %), highlighting their superior performance in cyclic SF_6/N_2 separation processes.

These results, as shown in Figure 5.5.4 and further analyzed in Figure. 5.5.5, highlight the combined influence of degassing temperature, applied vacuum pressure, and feed pressure on the working capacity. Regeneration conditions control the removal of residual molecules from micropores and the recovery of adsorption sites, while the microporosity of the materials determines the efficiency of gas adsorption. Together, these factors explain the observed trends in working capacity across different temperatures and pressures, providing a comprehensive understanding of how the materials respond under varying operational conditions.

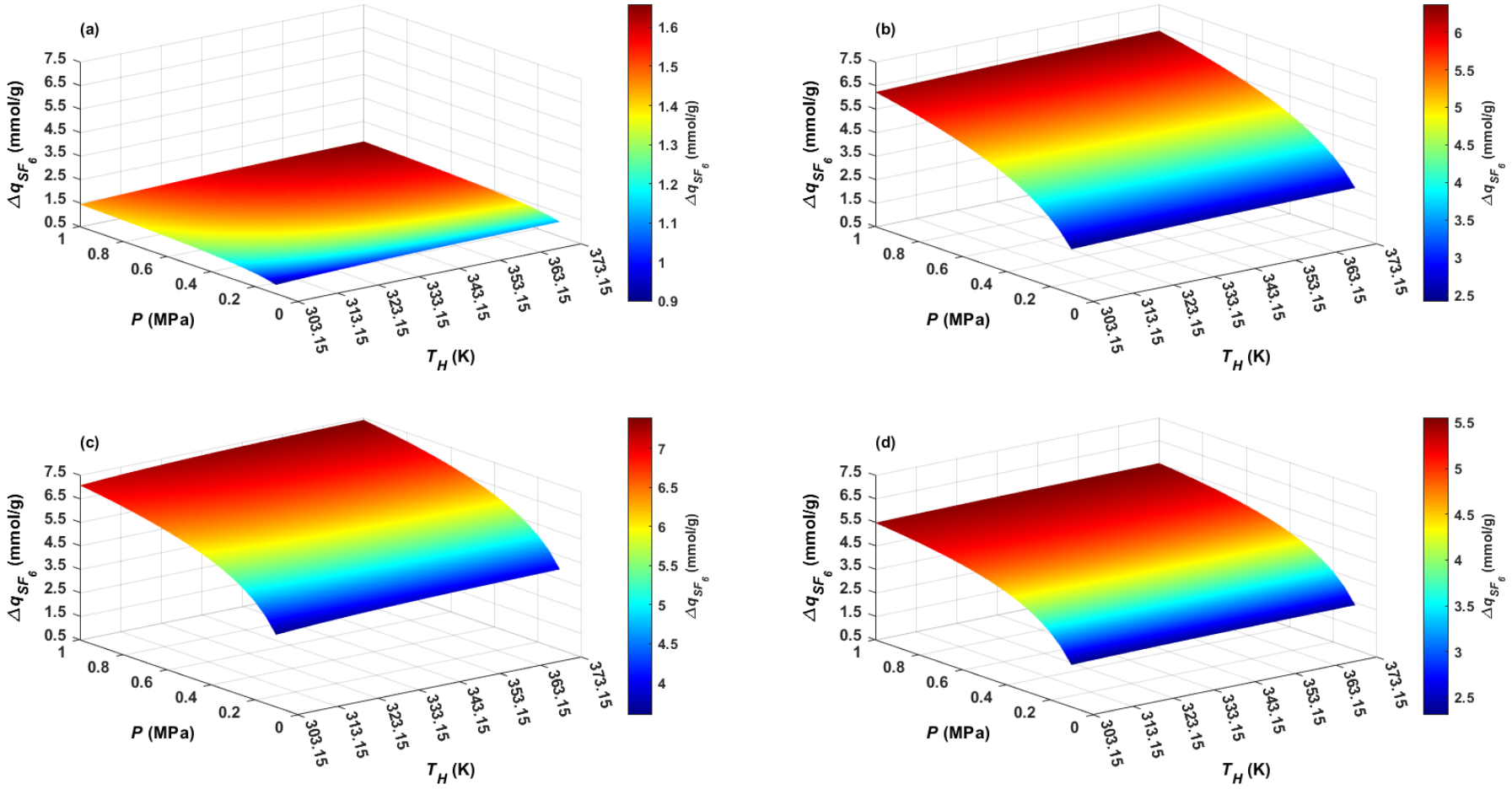


Figure 5.5.5 Contour plots of the working capacity (mmol/g) as a function of the degassing temperature, T_H, and the feed pressure, P on: a) AC1, b) AC2, AC3 and c) ACH.

5.5.2.3 Determination of Determination of Henry's law constant

In separation processes, the isosteric heat of adsorption (Q_{st}) is a critical parameter for evaluating and selecting adsorbent materials. During adsorption, heat is released as gas molecules interact with the adsorbent [106]. A high Q_{st} indicates strong interactions between the adsorbent and the adsorbate. However, excessive heat generation can lead to localised heating of the adsorption bed during the adsorption step of a separation process, which may reduce working capacity and process efficiency [106]. Furthermore, it will influence the ease of adsorbent regeneration. For these reasons, materials with moderate Q_{st} values are generally preferred to maintain optimal performance in separation applications. Q_{st} was calculated from pure component data collected at different temperatures using the Clausius-Clapeyron equation [58,75,76]:

$$(\log_e P)_q = constant - \frac{Q_{st}}{RT} \qquad 5.5.1$$

Experimental data were first fitted using the virial equation, as described in Section 4.4, and the resulting parameters were used to generate linear isosteric plots of $(\log_e P)_{q=\text{const}}$ *vs* $1/T$ for different values of q (mmol/g): 0.1, 0.45, 0.65, 0.85. The Q_{st} values for SF_6 adsorption range from 20 to 33 kJ/mol across all materials, while those for N_2 fall between 8 and 30 kJ/mol (Fig. 6). For SF_6, a linear Q_{st} profile is observed for AC1, AC2 and AC3, suggesting that adsorption occurs on energetically stable and available structural sites within the materials [73,80,107]. In contrast, ACHM material displays a concave Q_{st} curve, attributed to competition among gas molecules for the most energetically stable micropores. As these sites become saturated, Q_{st} initially decreases. (see Figure 5.5.6). A subsequent increase is observed with higher loadings, likely due to new adsorbate–adsorbate interactions forming within confined spaces [84]. For nitrogen, all materials except AC1 exhibit concave adsorption heats for all isotherms, except in the case of AC1, where continued linear behaviour was observed. This behaviour again reflects competitive adsorption in stable micropores, with a decrease in isosteric heat as saturation is approached. The later increase in Q_{st} is attributed to intermolecular interactions among adsorbed N_2 molecules. In contrast, the linear Q_{st} trend observed for AC1 indicates a non-significant adsorbate-adsorbent effect as loading increases [84].

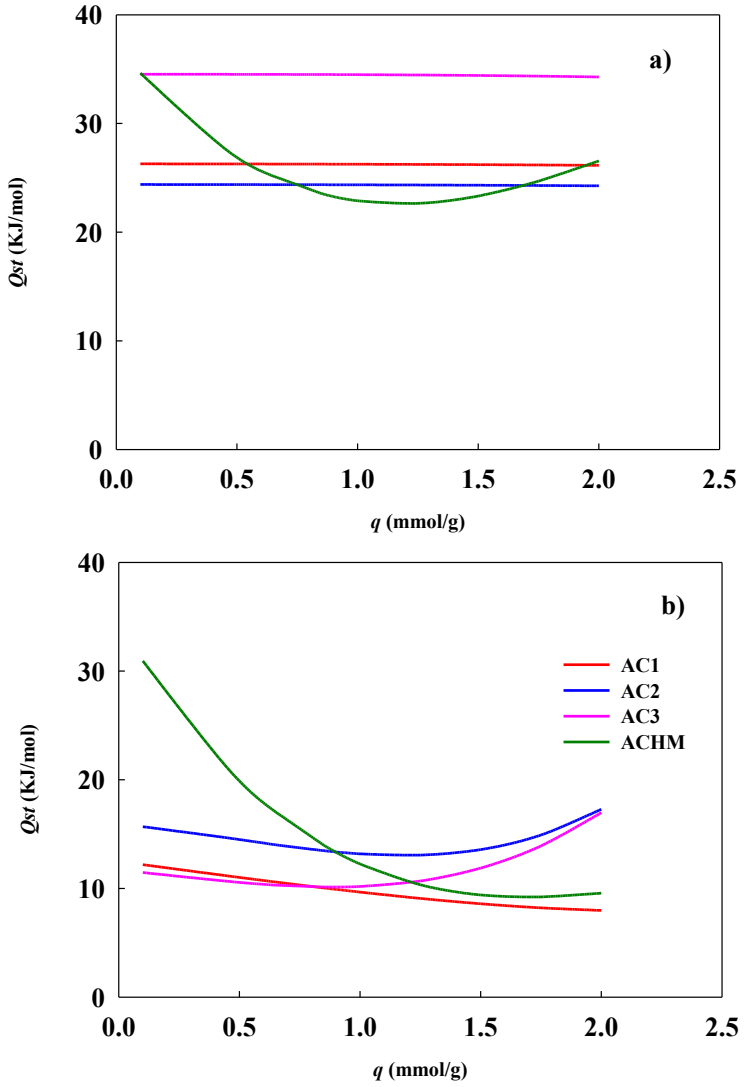


Figure 5.5.6 Isosteric heat of adsorption of: a) SF_6 and b) N_2 at 303 K.

One of the most effective approaches for evaluating adsorbate–adsorbent affinity in separation processes is through the determination of Henry's constant (K_H). This parameter reflects the strength of interaction between the adsorbate and the adsorbent, with higher K_H values indicating greater affinity. In this study, Henry's constants were calculated at 303 K, using parameters obtained from fitting the experimental data to the virial equation.[73,77,80].

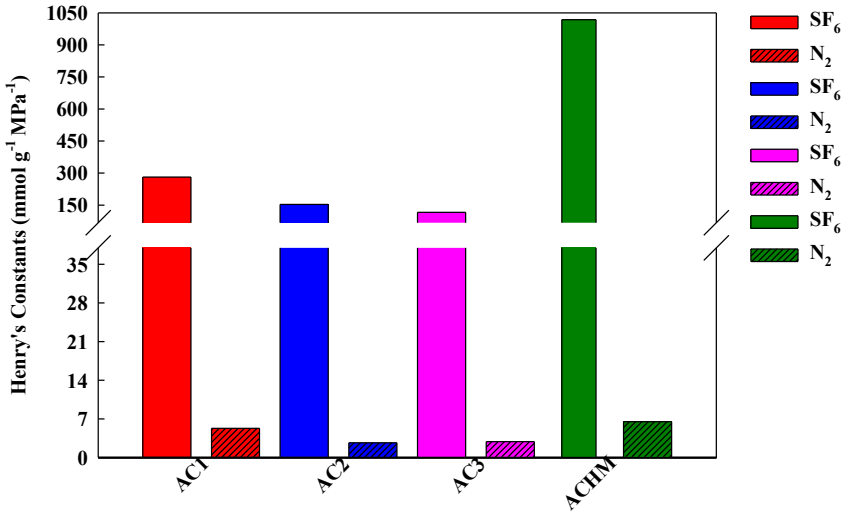


Figure 5.5.7 Henry's law constants for all adsorbents at 303 K.

At 303 K, the Henry's constant (K_H) for the adsorption of SF_6 and N_2 follows the order: ACHM > AC1 > AC2 > AC3 (Figure 5.5.7). The observed order correlates with the amount of micropores smaller than 10 Å, as shown in Figure 5.5.11. Furthermore, K_H primarily reflects the adsorption behaviour in the low-pressure region, where electrostatic interactions between the adsorbate molecules and the energetically favourable microporous sites dominate.

5.5.2.4 Prediction of the adsorption of SF6/N2 using the Ideal Adsorption Solution Theory (IAST).

In gas-insulated electrical equipment, sulphur hexafluoride is frequently used alongside nitrogen to preserve performance while reducing environmental concerns [8]. Currently, no commercial technology exists for the efficient capture or separation of SF_6, prompting the evaluation of suitable adsorbent materials [108]. In this study, we assess the selectivity of various porous materials to separate SF_6 from SF_6/N_2 mixtures. The pure-component adsorption equilibria of SF_6 and N_2 were fitted using Toth's model, and the Ideal Adsorption Solution Theory (IAST), whose mathematical model is described in Section 4.5, was applied to predict the adsorbed phase composition of an industrially relevant SF_6/N_2 mixture with gas-phase mole fractions of $y_{SF6} = 0.02$ and $y_{N2} = 0.98$ [96,109–111] .

Adsorption equilibrium data for this mixture, obtained with the four porous solid matrices at 303 K over a pressure range of 0.01-1.0 MPa. The IAST method assumes an ideal adsorbed solution and does not account for adsorbate–adsorbate interactions. However, this method provides a reliable and widely accepted approach to predict multicomponent adsorption [112–114]. The IAST method has been validated against both experimental measurements and molecular simulations for gases with similar interactions [112–114],ensuring that the calculated selectivity values reflect realistic trends in industrially relevant SF_6/N_2 mixtures.

The selectivity of the mixture (S_{ij}) was determined using the multicomponent adsorbed phase compositions according to the following expression:

$$S_{ij} = \frac{x_i/x_j}{y_i/y_j} \quad 5.5.2$$

where x_i and x_j are the adsorbed mole fractions of gas i and j, respectively, and y_i and y_j are the mole fractions of gas i of gas j, respectively, in the gas phase at equilibrium.

The selectivity results for the commercial SF_6/N_2 mixture are presented in Figure 5.5.8. A key factor influencing the predicted selectivity is the type of pure-component isotherm. In all materials studied, N_2 exhibits nearly linear isotherms, while SF_6 shows non-linear behaviour, an advantage for selective adsorption of SF_6 over N_2. The observed selectivity order is ACHM > AC1 > AC2 > AC3 and can be explained by considering both the micropore size distribution and the intrinsic properties of the adsorbates. This trend indicates that stronger adsorbent–adsorbate affinity enhances the selectivity toward SF_6. ACHM exhibits a narrow microporosity in the range of 5–15 Å (see Figure 5.5.1), which matches the diameter of SF_6 (~ 5.15 Å) [67]. This microporosity promotes greater overlap between the adsorbed molecules and the pore walls, maximizing interactions. The effect is further reinforced by the higher polarizability of SF_6 (4.49 Å³) compared with N_2 (1.71 Å³) [101], which increases interactions and explains the higher adsorption capacity and selectivity toward SF_6 in ACHM.

In contrast, AC1, AC2, and AC3 exhibit broader micro-mesoporous structures (micropores of 5–20 Å and mesopores of 20–40 Å, see Figure 5.5.1). These pores reduce the interactions compared with ACHM. At the same time, the smaller N_2 molecules (~ 3.64 Å diameter) interact less effectively with pore walls [67], and their lower polarisability limits the adsorption. Consequently, variations in pore size distribution have a minor influence on N_2 adsorption, whereas SF_6 adsorption is markedly dependent on the match between pore dimensions and molecular size. Overall, these results demonstrate that selectivity depends not only on total micropore volume or surface area but, more critically, on the match between pore size distribution, gas diameter, and molecular polarisability of the adsorbates. Then, the narrow microporosity of ACHM explains the favourable confinement conditions to outperform AC1–AC3 in the separation of SF_6 from N_2.

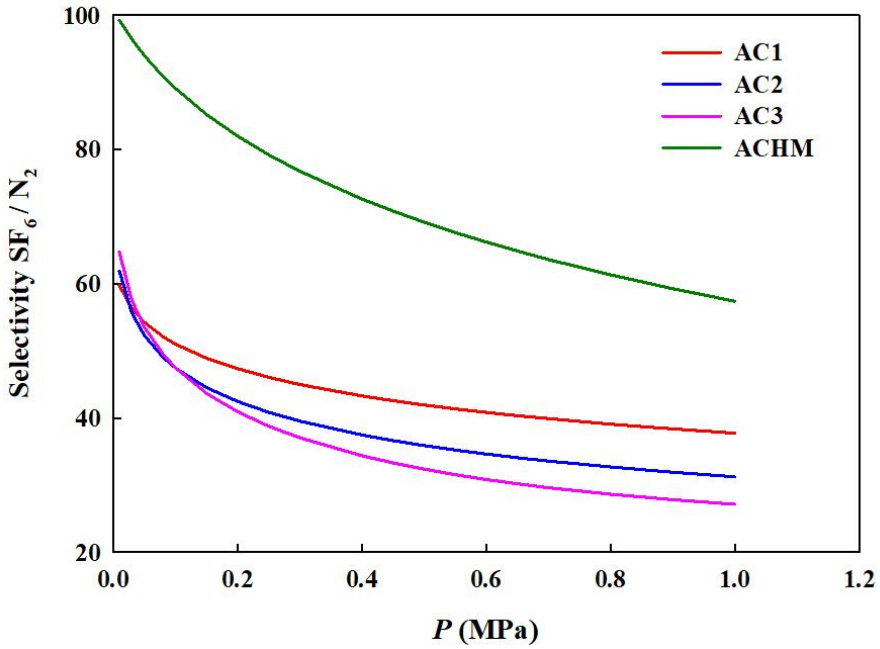


Figure 5.5.8 Selectivity of AC1, AC2, AC3, and ACHM to SF_6 over N_2 as a function of pressure at 303 K for the equilibrium gas phase composition of the SF_6/N_2 mixture (y_{SF6}= 0.02 and y_{N2} = 0.98).

To assess the relationship between adsorption capacity and selectivity, Figure 5.5.9 shows the SF_6/N_2 performance of our materials and those reported in the literature. SF_6 (~5.15 Å kinetic diameter and 4.49 Å³ polarizability) interacts more strongly with the pores than N_2 (~3.64 Å kinetic diameter and 1.71 Å³ polarizability) [67,101], promoting molecular selectivity; however, the adsorption of N_2 can also be favored by its own polarizability, especially in materials with accessible pores or polar cavities. M-MOF-74 MOFs exhibit high capacities (>5 mmol·g⁻¹) due to their large surface areas and one-dimensional channels that accommodate large, polarizable molecules like SF_6, although selectivity decreases due to N_2 co-adsorption [45]. In contrast, MOFs such as UiO-67 or MIL-100(Fe) and zeolites show higher selectivity by favoring preferential interactions with SF_6 through narrow micropores and polar cavities, limiting N_2 adsorption; however, their overall capacities are lower [36,43]. Conventional ACs achieve moderate capacities (2–3 mmol·g⁻¹) and lower selectivity's (<60), as their heterogeneous porosity allows adsorption of SF_6 but also of N_2 due to its polarizability [37,44,49]. Other materials, such as $Ph_{10}Cs_{11}$, $Ph_8M_2Cs_{11}$, Ph_6M4Cs_{11}, Ph_8M_2Cs9, $Ph_6M_4Cs_9$, $Ph_{10}K_{11}$, and $Ph_6M_4K_{11}$, show good adsorption capacities but lower selectivity's (<65), indicating that while their porosity allows SF_6 capture, interactions with N_2 are not fully restricted [37]. Our activated carbon ACHM and the CAK1–CAK4 family combine moderate-to-high capacities (~3–4 mmol·g⁻¹) with high selectivity (>90), thanks to optimized microporosity that maximizes SF_6 adsorption and controlled mesoporosity that facilitates diffusion, achieving a favorable structural balance between capacity and selectivity [38]. However, the limited information on adsorption capacities under varying temperatures and pressures restricts comprehensive evaluation under industrial conditions.

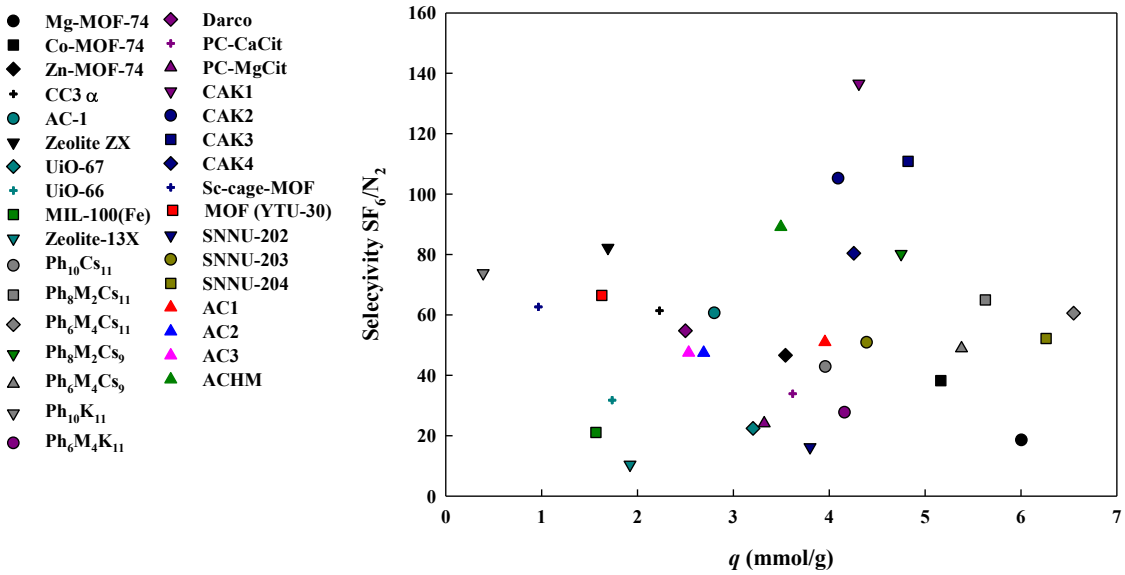


Figure 5.5.9 Comparison of the SF_6 adsorption capacity (q, mmol·g^{-1}) and SF_6/N_2 selectivity of the materials in this work (AC1, AC2, AC3, and ACHM) with materials reported in the literature at 303.15 K [36–39,43–49].

5.5.2.5 Evaluation of materials for the separation and capture of SF_6.

Material selection for separation processes depends not only on selectivity and affinity between the adsorbent and adsorbate but also on several additional factors, including working capacity, regeneration efficiency, and operational stability [45,60,115]. To comprehensively evaluate the materials studied in this work, the Yang and Ackley Figures of Merit (FOMs) were employed, as they provide insight into performance under varying pressure and temperature conditions [45,60,115] (The mathematical models for the selection criteria are described in Section 5.3). Two case studies were designed to simulate different industrial scenarios for separating an SF_6/N_2 mixture (y_{SF6} = 0.02 and y_{N2} = 0.98) at 303 K. The first case considered a feed pressure of 0.5 MPa with a desorption pressure of 0.1 MPa, while the second considered a feed pressure of 0.1 MPa and a desorption pressure of 0.01 MPa. To assess the performance of the materials developed in this study, a comparison was made with experimental data from the literature under similar industrial conditions. Specifically, materials such as Zeolite-13X, Zeolite ZX, AC-1, and MIL-100(Fe) were examined within the same pressure range used in the case studies [43,44]. Their adsorption data were fitted using the Toth model to ensure consistent and rigorous evaluation. Additionally, relevant pressure and temperature conditions for this and previous studies were considered to evaluate the performance of these adsorbents [43,44], and the corresponding results for each criterion are presented in Figure 5.5.10.

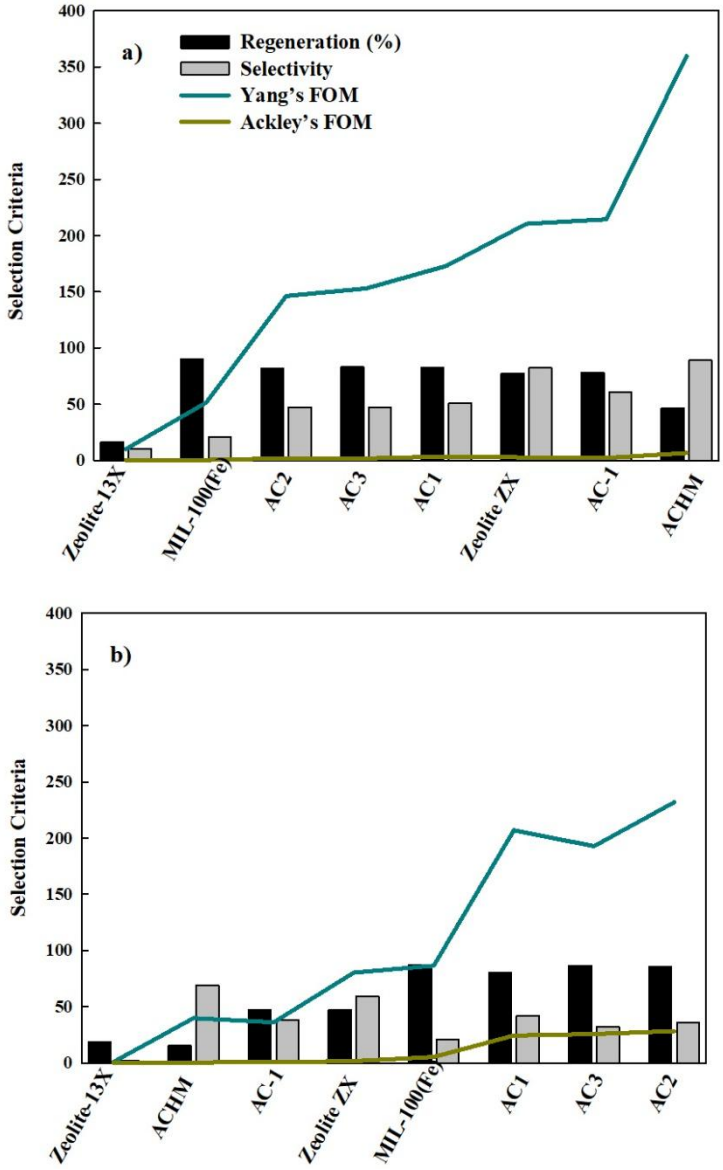


Figure 5.5.10 The selection criteria for the selection of materials at 303 K for: a) 0.1 MPa and b) 0.5 MPa.

Figure 5.5.10a illustrates case 1, representing the operation conditions for the SF_6/N_2 mixture (y_{SF6} = 0.02 and y_{N2} = 0.98) at a feed pressure is 0.1 MPa and a desorption pressure of 0.01 MPa at 303 K. Based on Yang's FOM and Ackley's FOM criteria, the materials are ranked as follows: ACHM > AC-1 > Zeolite ZX > AC1 > AC2 > AC3 > MIL-100(Fe) > Zeolite-13X. These criteria incorporate both the working capacity and selectivity, indicating that ACHM is a promising candidate for pilot-scale applications. However, the regeneration capacity is a decisive parameter for practical separation processes, as it strongly affects process efficiency, operational stability, and overall economics. In cyclic adsorption–desorption operations, materials with low regeneration capacity, such as ACHM (~ 36 %), retain a significant portion of adsorbed SF_6 after each cycle, which reduces the effective working capacity, increases the frequency and duration of regeneration steps, and can necessitate larger or more complex equipment to maintain throughput [116,117]. In contrast, the other materials (MIL-100(Fe), AC2,

AC3, AC1, Zeolite ZX, and AC-1) exhibit high selectivity and competitive working capacities, together with regeneration efficiencies in the range of 60–80 %. These properties enable robust cyclic adsorption–desorption performance with negligible efficiency losses, resulting in lower overall energy and economic costs [118]. Furthermore, the high regeneration stability of the adsorbents ensures efficient cyclic operation and pilot-scale feasibility [67]. Similarly, it has been noted that regeneration performance constitutes a critical parameter for maintaining separation efficiency over multiple cycles [117].

In the second case study (Figure 5.5.10b), at a feed pressure of 0.5 MPa, a desorption pressure of 0.1 MPa, and 303 K, the ranking based on Yang's FOM, Ackley's FOM, and the degassing percentage is: AC2 > AC3 > AC1 > Zeolite-13X > Zeolite ZX > AC-1 > ACHM (Figure 5.5.10b). Under these high-pressure conditions, AC1, AC2 and AC3 maintain high regeneration capacities between 80-87 %, ensuring stable working capacity over multiple cycles, reducing material consumption, and minimizing operational interruptions [116–118]. These combined criteria - selectivity, working capacity, and regeneration - offer a comprehensive basis for identifying the most suitable materials for pilot-scale implementation.

5.5.3 Conclusion

In this work, the adsorption equilibria of AC1, AC2, AC3, and ACHM were systematically investigated. The results revealed nearly linear isotherms for N_2 and concave isotherms for SF_6, indicating differing adsorption behaviours. All materials were carefully selected based on their high adsorption capacity and selectivity. The temperature-dependent study showed that ACHM exhibited the highest working capacity among the tested materials, attributed to its well-developed microporosity. However, under combined temperature and pressure variations, AC1 demonstrated the highest working capacity owing to its greater surface area and total pore volume, which enhances gas storage and adsorption efficiency. This highlights the importance of working capacity evaluation for identifying key parameters in process design and material selection for industrial applications. Nevertheless, a comprehensive study of the adsorbate-adsorbent systems must also consider additional factors such as isosteric heat of adsorption, Henry's constant, selectivity and regeneration capacity. ACHM exhibited the highest Henry's constant, indicating a strong affinity for SF_6. These results reaffirm that materials with high microporosity are promising candidates for SF_6 mixture separation.

5.6 References

[1] B.M. Flores, E. Montoya, B. Sakschewski, N. Nascimento, A. Staal, R.A. Betts, C. Levis, D.M. Lapola, A. Esquível-Muelbert, C. Jakovac, C.A. Nobre, R.S. Oliveira, L.S. Borma, D. Nian, N. Boers, S.B. Hecht, H. ter Steege, J. Arieira, I.L. Lucas, E. Berenguer, J.A. Marengo, L. V Gatti, C.R.C. Mattos, M. Hirota, Critical transitions in the Amazon forest system, Nature 626 (2024) 555–564. https://doi.org/10.1038/s41586-023-06970-0.

[2] Andreoni A, Climate Change Drove Drought in the Amazon, (2024). https://www.nytimes.com/2024/01/24/climate/amazon-drought-low-water.html (accessed February 18, 2025).

[3] Ionova A, A Changing Climate Is Scorching the World's Biggest River, (2024). https://www.nytimes.com/2024/10/06/world/americas/amazon-river-climate-change-brazil.html (accessed February 18, 2025).

[4] M. Kiehbadroudinezhad, A. Merabet, H. Hosseinzadeh-Bandbafha, Chapter Twelve - Health impacts of greenhouse gases emissions on humans and the environment, in: M.R. Rahimpour, M.A. Makarem, M. Meshksar (Eds.), Advances and Technology Development in Greenhouse Gases: Emission, Capture and Conversion, Elsevier, 2024: pp. 265–291. https://doi.org/https://doi.org/10.1016/B978-0-443-19231-9.00011-9.

[5] U.S. Environmental Protection Agency | US EPA, Overview of Greenhouse Gases., (n.d.). https://www.epa.gov/ghgemissions/overview-greenhouse-gases / (accessed on 21 June 2024) (accessed June 25, 2024).

[6] B.K. Sovacool, S. Griffiths, J. Kim, M. Bazilian, Climate change and industrial F-gases: A critical and systematic review of developments, sociotechnical systems and policy options for reducing synthetic greenhouse gas emissions, Renewable and Sustainable Energy Reviews 141 (2021) 110759. https://doi.org/https://doi.org/10.1016/j.rser.2021.110759.

[7] M. Rabie, C.M. Franck, Assessment of Eco-friendly Gases for Electrical Insulation to Replace the Most Potent Industrial Greenhouse Gas SF6, Environ Sci Technol 52 (2018) 369–380. https://doi.org/10.1021/acs.est.7b03465.

[8] E.K. Lee, J.D. Lee, H.J. Lee, B.R. Lee, Y.S. Lee, S.M. Kim, H.O. Park, Y.S. Kim, Y.-D. Park, Y. Do Kim, Pure SF6 and SF6−N2 Mixture Gas Hydrates Equilibrium and Kinetic Characteristics, Environ Sci Technol 43 (2009) 7723–7727. https://doi.org/10.1021/es901350v.

[9] S. Shi, Y. Li, Z. Cui, Y. Yan, X. Zhang, J. Tang, S. Xiao, Recent advances in degradation of the most potent industrial greenhouse gas sulfur hexafluoride, Chemical Engineering Journal 470 (2023) 144166. https://doi.org/https://doi.org/10.1016/j.cej.2023.144166.

[10] Global Monitoring Laboratory, Sulfur hexafluoride (SF6) - Combined Dataset, (2023). https://gml.noaa.gov/hats/combined/SF6.html (accessed September 3, 2025).

[11] Global Monitoring Laboratory, US Emission Tracker for Potent GHGs, (2023). https://gml.noaa.gov/hats/US_emissiontracker/emission.html?gas=SF6 (accessed September 3, 2025).

[12] P.G. Simmonds, M. Rigby, A.J. Manning, S. Park, K.M. Stanley, A. McCulloch, S. Henne, F. Graziosi, M. Maione, J. Arduini, S. Reimann, M.K. Vollmer, J. Mühle, S. O'Doherty, D. Young, P.B. Krummel, P.J. Fraser, R.F. Weiss, P.K. Salameh, C.M. Harth, M.-K. Park, H. Park, T. Arnold, C. Rennick, L.P. Steele, B. Mitrevski, R.H.J. Wang, R.G. Prinn, The increasing atmospheric burden of the greenhouse gas sulfur hexafluoride (SF_6), Atmos Chem Phys 20 (2020) 7271–7290. https://doi.org/10.5194/acp-20-7271-2020.

[13] T.M.L. Wigley, S.J. Smith, M.J. Prather, Radiative Forcing Due to Reactive Gas Emissions, J Clim 15 (2002) 2690–2696. https://doi.org/10.1175/1520-0442(2002)015<2690:RFDTRG>2.0.CO;2.

[14] climate and Clean Air Coalition, Primer on Short-Lived Climate Pollutants, (2013). https://www.ccacoalition.org/resources/primer-short-lived-climate-pollutants (accessed September 3, 2025).

[15] J. Hanoteau, D. Talbot, Impacts of the Québec carbon emissions trading scheme on plant-level performance and employment, Carbon Manag 10 (2019) 287–298. https://doi.org/10.1080/17583004.2019.1595154.

[16] U.S. Environmental Protection Agency | US EPA, State and Regional Regulations Related to SF6 Emissions from Electric Transmission and Distribution, (n.d.). https://www.google.com/search?q=Epa&rlz=1C1GCEA_enPT1054PT1054&oq=Epa&gs_lcrp=EgZjaHJvbWUyBggAEEUYOTIGCAEQRRg8MgYIAhBFGDwyBggDEEUYPDIGCAQQRRg8MgYIBRBFGDwyBggGEEUYQTIGCAcQRRhB0gEIMTI5MGowajeoAgCwAgA&sourceid=chrome&ie=UTF-8 (accessed August 25, 2025).

[17] United States Environmental Protection Agency, Overview of SF6 Emissions Sources and Reduction Options in Electric Power System, (2018). https://19january2021snapshot.epa.gov/f-gas-partnership-programs/overview-sf6-emissions-sources-and-reduction-options-electric-power_.html (accessed September 3, 2025).

[18] Z. Cui, Y. Li, S. Xiao, S. Tian, J. Tang, Y. Hao, X. Zhang, Recent progresses, challenges and proposals on SF6 emission reduction approaches, Science of The Total Environment 906 (2024) 167347. https://doi.org/https://doi.org/10.1016/j.scitotenv.2023.167347.

[19] M.-B. Kim, K.-M. Kim, T.-H. Kim, Highly selective adsorption of SF6 over N2 in a bromine-functionalized zirconium-based metal-organic framework, Chem. Eng. J. 339 (2018) 223.

[20] S. Bartos, C. Laush, J. Scharfenberg, R. Kantamaneni, Reducing greenhouse gas emissions from magnesium die casting, J Clean Prod 15 (2007) 979–987. https://doi.org/https://doi.org/10.1016/j.jclepro.2006.01.008.

[21] J.-H. Cheng, S.C. Bartos, W.M. Lee, S.-N. Li, J. (Ching-H. Lu, SF6 usage and emission trends in the TFT-LCD industry, International Journal of Greenhouse Gas Control 17 (2013) 106–110. https://doi.org/https://doi.org/10.1016/j.ijggc.2013.04.003.

[22] V.T.H. Nguyen, E. Shkondin, F. Jensen, J. Hübner, P. Leussink, H. Jansen, Ultrahigh aspect ratio etching of silicon in SF6-O2 plasma: The clear-oxidize-remove-etch (CORE) sequence and chromium

mask, Journal of Vacuum Science & Technology A 38 (2020) 053002. https://doi.org/10.1116/6.0000357.

[23] S. Bartos, J. Marks, R. Kantamaneni, C. Laush, california measured sf 6 emissions from magnesium die casting operations, 2003.

[24] L.G. Christophorou, J.K. Olthoff, R.J. Van Brunt, Sulfur hexafluoride and the electric power industry, IEEE Electrical Insulation Magazine 13 (1997) 20–24. https://doi.org/10.1109/57.620514.

[25] M. Maiss, C.A.M. Brenninkmeijer, Atmospheric SF6: Trends, Sources, and Prospects, Environ Sci Technol 32 (1998) 3077–3086. https://doi.org/10.1021/es9802807.

[26] N.-K. Park, H.-G. Park, T.J. Lee, W.-C. Chang, W.-T. Kwon, Hydrolysis and oxidation on supported phosphate catalyst for decomposition of SF6, Catal Today 185 (2012) 247–252. https://doi.org/https://doi.org/10.1016/j.cattod.2011.08.008.

[27] D. Kashiwagi, A. Takai, T. Takubo, H. Yamada, T. Inoue, K. Nagaoka, Y. Takita, Catalytic activity of rare earth phosphates for SF6 decomposition and promotion effects of rare earths added into AlPO4, J Colloid Interface Sci 332 (2009) 136–144. https://doi.org/https://doi.org/10.1016/j.jcis.2008.12.003.

[28] H. Xu, Y. Tang, Y. Wang, H. Meng, Y. Lu, H. Fan, C. Li, Mechanochemical Degradation of SF6 for Realizing Simultaneous Disposal of Super Greenhouse Gas and Manufacture of Fluorinated Graphite Materials, Ind Eng Chem Res 62 (2023) 7921–7930. https://doi.org/10.1021/acs.iecr.3c00629.

[29] A. Taponard, T. Jarrosson, L. Khrouz, M. Médebielle, J. Broggi, A. Tlili, Metal-Free SF6 Activation: A New SF5-Based Reagent Enables Deoxyfluorination and Pentafluorosulfanylation Reactions, Angewandte Chemie International Edition 61 (2022) e202204623. https://doi.org/https://doi.org/10.1002/anie.202204623.

[30] X. Li, H. Zhao, A.B. Murphy, SF6-alternative gases for application in gas-insulated switchgear, J Phys D Appl Phys 51 (2018) 153001. https://doi.org/10.1088/1361-6463/aab314.

[31] M. Rabie, C.M. Franck, Computational screening of new high voltage insulation gases with low global warming potential, IEEE Transactions on Dielectrics and Electrical Insulation 22 (2015) 296–302. https://doi.org/10.1109/TDEI.2014.004474.

[32] C. Zhang, H. Shi, L. Cheng, K. Zhao, X. Xie, H. Ma, First principles based computational scheme for designing new SF6 replacements, IEEE Transactions on Dielectrics and Electrical Insulation 23 (2016) 2572–2578. https://doi.org/10.1109/TDEI.2016.7736814.

[33] D.C. Kothe, V. Hinrichsen, K. Ermeler, A. Kalter, Experimental investigation of dielectric properties of alternative insulation gases for medium voltage switchgear, in: VDE High Voltage Technology 2020; ETG-Symposium, 2020: pp. 1–6.

[34] B. Zhang, L. Chen, X. Li, Z. Guo, Y. Pu, N. Tang, Evaluating the dielectric strength of promising SF6 alternatives by DFT calculations and DC breakdown tests, IEEE Transactions on Dielectrics and Electrical Insulation 27 (2020) 1187–1194. https://doi.org/10.1109/TDEI.2020.008906.

[35] D.C. Lauzon, The SF 6 ReUse Program-A Case Study International Conference on SF 6 and the Environment: Emission and Reduction Strategies, 2002.

[36] M.B. Kim, T.H. Kim, T.U. Yoon, J.H. Kang, J.H. Kim, Y.S. Bae, Efficient SF6/N2 separation at high pressures using a zirconium-based mesoporous metal–organic framework, Journal of Industrial and Engineering Chemistry 84 (2020) 179–184. https://doi.org/10.1016/j.jiec.2019.12.032.

[37] Y. Yang, K. Goh, C.Y. Chuah, H.E. Karahan, Ö. Birer, T.-H. Bae, Sub-Ångström-level engineering of ultramicroporous carbons for enhanced sulfur hexafluoride capture, Carbon N Y 155 (2019) 56–64. https://doi.org/https://doi.org/10.1016/j.carbon.2019.08.034.

[38] W. Fu, J. Wang, Y. Li, Z. Sui, X. Xu, Investigation on the pore structure-performance relationship of porous carbon adsorbents for SF6/N2 separation via fine pore modulation, Sep Purif Technol 348 (2024) 127788. https://doi.org/https://doi.org/10.1016/j.seppur.2024.127788.

[39] Y.-P. Li, J.-J. Ni, S. Li, J. Wang, Z.-Y. Sui, X.-F. Xu, Rational pore-window size control in three Cu-MOFs with different pore environments for efficient capture of the greenhouse gas SF6, J Solid State Chem 329 (2024) 124443. https://doi.org/https://doi.org/10.1016/j.jssc.2023.124443.

[40] J. Serafin, B. Dziejarski, Activated carbons—preparation, characterization and their application in CO2 capture: A review, Environmental Science and Pollution Research 31 (2024) 40008–40062. https://doi.org/10.1007/s11356-023-28023-9.

[41] Y. Li, J. Mei, L. Wu, Q. Xu, Z. Li, Ultrahigh surface area hierarchical porous carbon derived from biomass via a new KOH activation strategy for high-performance supercapacitor, Int J Hydrogen Energy 49 (2024) 67–80. https://doi.org/https://doi.org/10.1016/j.ijhydene.2023.10.319.

[42] E. Jo, S. Yang, D.W. Kim, D.W. Kang, Greenhouse sulfur hexafluoride gas capture and separation using emerging porous solids, Coord Chem Rev 515 (2024) 215958. https://doi.org/https://doi.org/10.1016/j.ccr.2024.215958.

[43] P.-J. Kim, Y.-W. You, H. Park, J.-S. Chang, Y.-S. Bae, C.-H. Lee, J.-K. Suh, Separation of SF6 from SF6/N2 mixture using metal–organic framework MIL-100(Fe) granule, Chemical Engineering Journal 262 (2015) 683–690. https://doi.org/https://doi.org/10.1016/j.cej.2014.09.123.

[44] W.-S. Cho, K.-H. Lee, H.-J. Chang, W. Huh, H.-H. Kwon, Evaluation of pressure-temperature swing adsorption for sulfur hexafluoride (SF6) recovery from SF6 and N2 gas mixture, Korean Journal of Chemical Engineering 28 (2011) 2196–2201. https://doi.org/10.1007/s11814-011-0104-7.

[45] M.-B. Kim, S.-J. Lee, C.Y. Lee, Y.-S. Bae, High SF6 selectivities and capacities in isostructural metal-organic frameworks with proper pore sizes and highly dense unsaturated metal sites, Microporous and Mesoporous Materials 190 (2014) 356–361. https://doi.org/https://doi.org/10.1016/j.micromeso.2014.02.028.

[46] H. Wang, L. Shi, Z. Xiong, S. Ma, H. Cao, S. Cai, Z. Qiao, J. Pan, Z. Chen, A two-dimensional metal–organic framework assembled from scandium-based cages for the selective capture of sulfur hexafluoride, Chem. Commun. 60 (2024) 2397–2400. https://doi.org/10.1039/D3CC05087D.

[47] Y.-P. Li, X.-J. Zhang, J.-J. Ni, W.-J. Ji, S. Li, Y.-L. Li, W. Wen, J. Wang, Z.-Y. Sui, X.-F. Xu, Design of a highly-stable cobalt (II) porous framework based on aromatic stacking strategy for efficient SF6 capture and SF6/N2 mixture separation, Sep Purif Technol 343 (2024) 126995. https://doi.org/https://doi.org/10.1016/j.seppur.2024.126995.

[48] T. Hasell, M. Miklitz, A. Stephenson, M.A. Little, S.Y. Chong, R. Clowes, L.J. Chen, D. Holden, G.A. Tribello, K.E. Jelfs, A.I. Cooper, Porous Organic Cages for Sulfur Hexafluoride Separation, J. Am. Chem. Soc. 138 (2016) 1653.

[49] R. Sun, C.-W. Tai, M. Strømme, O. Cheung, Hierarchical Porous Carbon Synthesized from Novel Porous Amorphous Calcium or Magnesium Citrate with Enhanced SF6 Uptake and SF6/N2 Selectivity, ACS Appl Nano Mater 2 (2019) 778–789. https://doi.org/10.1021/acsanm.8b02005.

[50] C.Y. Chuah, S. Yu, K. Na, T.-H. Bae, Enhanced SF6 recovery by hierarchically structured MFI zeolite, Journal of Industrial and Engineering Chemistry 62 (2018) 64–71. https://doi.org/https://doi.org/10.1016/j.jiec.2017.12.045.

[51] G. Xu, F. Liang, Y. Yang, Y. Hu, K. Zhang, W. Liu, An Improved CO2 Separation and Purification System Based on Cryogenic Separation and Distillation Theory, Energies (Basel) 7 (2014) 3484–3502. https://doi.org/10.3390/en7053484.

[52] P. Wu, Y. Li, Y. Luo, Y. Yan, R. Zhuo, D. Wang, J. Tang, H. Yuan, X. Zhang, S. Xiao, 2D MOF-Based Filtration-Sensing Strategy for Trace Gas Sensing Under Intense F-Gas Interference at Room Temperature, Adv Funct Mater 35 (2025) 2415517. https://doi.org/https://doi.org/10.1002/adfm.202415517.

[53] X. Zhang, Y.-L. Zhao, X.-Y. Li, X. Bai, Q. Chen, J.-R. Li, Recovery of High-Purity SF6 from Humid SF6/N2 Mixture within a Co(II)-Pyrazolate Framework, J Am Chem Soc 146 (2024) 19303–19309. https://doi.org/10.1021/jacs.4c05075.

[54] S.-M. Li, Q. Zhang, H.-C. Jiang, Q.-L. Ni, L.-C. Gui, X.-J. Wang, T.-L. Hu, Constructing local nanomolecular trap in a scalable, low-cost, and ultramicroporous metal–organic framework for efficient capture of greenhouse gases SF6 and CO2, Chemical Engineering Journal 496 (2024) 154026. https://doi.org/https://doi.org/10.1016/j.cej.2024.154026.

[55] M.J. Prauchner, S. da C. Oliveira, F. Rodríguez-Reinoso, Tailoring Low-Cost Granular Activated Carbons Intended for CO2 Adsorption, Front Chem Volume 8-2020 (2020). https://doi.org/10.3389/fchem.2020.581133.

[56] A. Rana, J.M. Andino, A Review of Materials for Carbon Dioxide Capture, Catalysts 15 (2025). https://doi.org/10.3390/catal15030273.

[57] B.C.R. Camacho, R.P.P.L. Ribeiro, I.A.A.C. Esteves, J.P.B. Mota, Adsorption equilibrium of carbon dioxide and nitrogen on the MIL-53(Al) metal organic framework, Sep Purif Technol 141 (2015) 150–159. https://doi.org/10.1016/j.seppur.2014.11.040.

[58] R.P.P.L. Ribeiro, B.C.R. Camacho, A. Lyubchyk, I.A.A.C. Esteves, F.J.A.L. Cruz, J.P.B. Mota, Experimental and computational study of ethane and ethylene adsorption in the MIL-53(Al) metal

organic framework, Microporous and Mesoporous Materials 230 (2016) 154–165. https://doi.org/10.1016/j.micromeso.2016.05.006.

[59] D.D. Do, Adsorption Analysis: Equilibria and Kinetics, published by imperial college press and distributed by world scientific publishing CO., 1998. https://doi.org/10.1142/p111.

[60] A.K. Rajagopalan, A.M. Avila, A. Rajendran, Do adsorbent screening metrics predict process performance? A process optimisation based study for post-combustion capture of CO2, International Journal of Greenhouse Gas Control 46 (2016) 76–85. https://doi.org/https://doi.org/10.1016/j.ijggc.2015.12.033.

[61] M.-B. Kim, T.-H. Kim, T.-U. Yoon, J.H. Kang, J.-H. Kim, Y.-S. Bae, Efficient SF6/N2 separation at high pressures using a zirconium-based mesoporous metal–organic framework, Journal of Industrial and Engineering Chemistry 84 (2020) 179–184. https://doi.org/https://doi.org/10.1016/j.jiec.2019.12.032.

[62] Y. Yang, K. Goh, C.Y. Chuah, H.E. Karahan, Ö. Birer, T.-H. Bae, Sub-Ångström-level engineering of ultramicroporous carbons for enhanced sulfur hexafluoride capture, Carbon N Y 155 (2019) 56–64. https://doi.org/https://doi.org/10.1016/j.carbon.2019.08.034.

[63] Y.-P. Li, X.-J. Zhang, J.-J. Ni, W.-J. Ji, S. Li, Y.-L. Li, W. Wen, J. Wang, Z.-Y. Sui, X.-F. Xu, Design of a highly-stable cobalt (II) porous framework based on aromatic stacking strategy for efficient SF6 capture and SF6/N2 mixture separation, Sep Purif Technol 343 (2024) 126995. https://doi.org/https://doi.org/10.1016/j.seppur.2024.126995.

[64] W. Fu, J. Wang, Y. Li, Z. Sui, B. Xiao, X. Xu, Highly-efficient separation of SF6/N2 and NF3/N2 with record selectivity on one-step synthesized carbon nanosheet, Sep Purif Technol 330 (2024) 125496. https://doi.org/https://doi.org/10.1016/j.seppur.2023.125496.

[65] J.E. Sosa, Rui.P.P.L. Ribeiro, I. Matos, M. Bernardo, I.M. Fonseca, J.P.B. Mota, J.M.M. Araújo, A.B. Pereiro, Coconut shell derived activated carbon for effective separation of greenhouse gases, International Journal of Refrigeration 176 (2025) 66–78. https://doi.org/https://doi.org/10.1016/j.ijrefrig.2025.04.022.

[66] National Institute of Standards and Technology (NIST), Experimental Polarizabilites, (2022). https://cccbdb.nist.gov/pollistx.asp#2015Tha/Wu:144302 (accessed August 25, 2025).

[67] J. Li, Y. Chen, T. Ke, Y. Jin, R. Fan, G. Xu, L. Yang, Z. Zhang, Z. Bao, Q. Ren, Q. Yang, Efficient continuous SF6/N2 separation using low-cost and robust metal-organic frameworks composites, Nat Commun 16 (2025) 632. https://doi.org/10.1038/s41467-025-56031-5.

[68] I. Matito-Martos, J. Álvarez-Ossorio, J.J. Gutiérrez-Sevillano, M. Doblaré, A. Martin-Calvo, S. Calero, Zeolites for the selective adsorption of sulfur hexafluoride, Phys. Chem. Chem. Phys. 17 (2015) 18121–18130. https://doi.org/10.1039/C5CP02407B.

[69] T. Maihom, S. Choomwattana, S. Wannakao, M. Probst, J. Limtrakul, Ethylene Epoxidation with Nitrous Oxide over Fe–BTC Metal–Organic Frameworks: A DFT Study, ChemPhysChem 17 (2016) 3416–3422. https://doi.org/https://doi.org/10.1002/cphc.201600836.

[70] Julio E. Sosa, Rui. P. P. L. Ribeiro, Inês Matos, Maria Bernardo, Isabel M. Fonseca, José P. B. Mota, João M. M. Araújo, Ana B. Pereiro, Innovative Porous Solid Matrices for the Separation of Greenhouse Gases, SCI TOTAL ENVIRON (n.d.).

[71] R.P.P.L. Ribeiro, J.P.B. Mota, Surface Area and Porosity of Co3(ndc)3(dabco) Metal–Organic Framework and Its Methane Storage Capacity: A Combined Experimental and Simulation Study, The Journal of Physical Chemistry C 125 (2021) 2411–2423. https://doi.org/10.1021/acs.jpcc.0c09362.

[72] D.N.D.L. Mendes, A. Gaspar, I. Ferreira, J.P.B. Mota, R.P.P.L. Ribeiro, 3D-printed hybrid zeolitic/carbonaceous electrically conductive adsorbent structures, Chemical Engineering Research and Design 174 (2021) 442–453. https://doi.org/https://doi.org/10.1016/j.cherd.2021.08.020.

[73] D.W. Siderius, H.W. Hatch, V.K. Shen, Temperature Extrapolation of Henry's Law Constants and the Isosteric Heat of Adsorption, J Phys Chem B 126 (2022) 7999–8009. https://doi.org/10.1021/acs.jpcb.2c04583.

[74] D. Ramirez, S. Qi, M.J. Rood, K.J. Hay, Equilibrium and Heat of Adsorption for Organic Vapors and Activated Carbons, Environ Sci Technol 39 (2005) 5864–5871. https://doi.org/10.1021/es048144r.

[75] R.P.P.L. Ribeiro, J. Barreto, M.D. Grosso Xavier, D. Martins, I.A.A.C. Esteves, M. Branco, T. Tirolien, J.P.B. Mota, G. Bonfait, Cryogenic neon adsorption on Co3(ndc)3(dabco) metal-organic framework, Microporous and Mesoporous Materials 298 (2020). https://doi.org/10.1016/j.micromeso.2020.110055.

[76] S. Builes, S.I. Sandler, R. Xiong, Isosteric heats of gas and liquid adsorption, Langmuir 29 (2013) 10416–10422. https://doi.org/10.1021/la401035p.

[77] L. Sarkisov, Toward Rational Design of Metal–Organic Frameworks for Sensing Applications: Efficient Calculation of Adsorption Characteristics in Zero Loading Regime, The Journal of Physical Chemistry C 116 (2012) 3025–3033. https://doi.org/10.1021/jp210633w.

[78] Y. Li, H. Yi, X. Tang, F. Li, Q. Yuan, Adsorption separation of CO2/CH4 gas mixture on the commercial zeolites at atmospheric pressure, Chemical Engineering Journal 229 (2013) 50–56. https://doi.org/https://doi.org/10.1016/j.cej.2013.05.101.

[79] F.N. Ridha, P.A. Webley, Anomalous Henry's law behavior of nitrogen and carbon dioxide adsorption on alkali-exchanged chabazite zeolites, Sep Purif Technol 67 (2009) 336–343. https://doi.org/10.1016/j.seppur.2009.03.045.

[80] H. Xu, L. Prasetyo, D.D. Do, D. Nicholson, The Henry constant and isosteric heat at zero loading for adsorption on energetically heterogeneous solids absolute versus excess, Chemical Engineering Journal 395 (2020) 125035. https://doi.org/https://doi.org/10.1016/j.cej.2020.125035.

[81] A. V Palodkar, K. Anupam, Z. Roy, B.B. Saha, G.N. Halder, High pressure adsorption isotherms of nitrogen onto granular activated carbon for a single bed pressure swing adsorption refrigeration system, Heat and Mass Transfer 53 (2017) 3155–3166. https://doi.org/10.1007/s00231-017-2057-9.

[82] J. Liu, M.D. LeVan, Henry's law constants and isosteric heats of adsorption at zero loading for multi-wall carbon surfaces with different geometries, Carbon N Y 48 (2010) 3454–3462. https://doi.org/https://doi.org/10.1016/j.carbon.2010.05.042.

[83] M.L. Palash, T.H. Rupam, A. Pal, A. Chakraborty, B.B. Saha, R. Wang, Design principles for synthesizing high grade activated carbons for adsorption heat pumps, Chemical Engineering Journal Advances 6 (2021) 100086. https://doi.org/https://doi.org/10.1016/j.ceja.2021.100086.

[84] J. Jia, Y. Xing, B. Li, Y. Wu, D. Wang, Molecular simulation study of adsorption-diffusion of CH4, CO2 and H2O in gas-fat coal, Sci Rep 14 (2024) 24131. https://doi.org/10.1038/s41598-024-74647-3.

[85] M. Mozaffari Majd, V. Kordzadeh-Kermani, V. Ghalandari, A. Askari, M. Sillanpää, Adsorption isotherm models: A comprehensive and systematic review (2010−2020), Science of The Total Environment 812 (2022) 151334. https://doi.org/https://doi.org/10.1016/j.scitotenv.2021.151334.

[86] I. Senkovska, E. Barea, J.A.R. Navarro, S. Kaskel, Adsorptive capturing and storing greenhouse gases such as sulfur hexafluoride and carbon tetrafluoride using metal–organic frameworks, Microporous and Mesoporous Materials 156 (2012) 115–120. https://doi.org/https://doi.org/10.1016/j.micromeso.2012.02.021.

[87] W. Zhu, J.C. Groen, F. Kapteijn, J.A. Moulijn, Adsorption of Butane Isomers and SF6 on Kureha Activated Carbon: 1. Equilibrium, Langmuir 20 (2004) 5277–5284. https://doi.org/10.1021/la030264+.

[88] J. Jagiełło, T.J. Bandosz, K. Putyera, J.A. Schwarz, Micropore structure of template-derived carbons studied using adsorption of gases with different molecular diameters, J. Chem. Soc., Faraday Trans. 91 (1995) 2929–2933. https://doi.org/10.1039/FT9959102929.

[89] S. Chen, Y. Shen, Z. Guan, B. Liu, Z. Tang, D. Zhang, B. Fu, Adsorption Properties of SF6 on Zeolite NaY, 13X, Activated Carbon, and Silica Gel, J Chem Eng Data 65 (2020) 4044–4051. https://doi.org/10.1021/acs.jced.0c00348.

[90] X. Peng, J.M. Vicent-Luna, Q. Jin, Separation of CF4/N2, C2F6/N2, and SF6/N2 Mixtures in Amorphous Activated Carbons Using Molecular Simulations, ACS Appl. Mater. Interfaces 12 (2020) 20044.

[91] J.-R. Li, R.J. Kuppler, H.-C. Zhou, Selective gas adsorption and separation in metal–organic frameworks, Chem. Soc. Rev. 38 (2009) 1477–1504. https://doi.org/10.1039/B802426J.

[92] R.T. Yang, PREFACE AND ACKNOWLEDGMENTS, in: R.T. Yang (Ed.), Gas Separation by Adsorption Processes, Butterworth-Heinemann, 1987: pp. ix–x. https://doi.org/https://doi.org/10.1016/B978-0-409-90004-0.50003-9.

[93] C. Tien, ed., Copyright, in: Introduction to Adsorption, Elsevier, 2019: p. iv. https://doi.org/https://doi.org/10.1016/B978-0-12-816446-4.09994-2.

[94] F. Rouquerol, J. Rouquerol, K.S.W. Sing, P. Llewellyn, G. Maurin, eds., Preface to the First Edition, in: Adsorption by Powders and Porous Solids (Second Edition), Second Edition, Academic Press, Oxford, 2014: pp. xiii–xiv. https://doi.org/https://doi.org/10.1016/B978-0-08-097035-6.09988-5.

[95] R.P.P.L. Ribeiro, J.E. Sosa, J.M.M. Araújo, A.B. Pereiro, J.P.B. Mota, Vacuum Swing Adsorption for R-32 recovery from R-410A refrigerant blend, International Journal of Refrigeration (2023). https://doi.org/https://doi.org/10.1016/j.ijrefrig.2023.01.020.

[96] J.E. Sosa, C. Malheiro, R.P.P.L. Ribeiro, P.J. Castro, M.M. Piñeiro, J.M.M. Araújo, F. Plantier, J.P.B. Mota, A.B. Pereiro, Adsorption of fluorinated greenhouse gases on activated carbons: evaluation of their potential for gas separation, Journal of Chemical Technology & Biotechnology 95 (2020) 1892–1905. https://doi.org/https://doi.org/10.1002/jctb.6371.

[97] K.S.W. Sing, Reporting physisorption data for gas/solid systems with special reference to the determination of surface area and porosity (Recommendations 1984), 57 (1985) 603–619. https://doi.org/doi:10.1351/pac198557040603.

[98] M. Thommes, K. Kaneko, A. V. Neimark, J.P. Olivier, F. Rodriguez-Reinoso, J. Rouquerol, K.S.W. Sing, Physisorption of gases, with special reference to the evaluation of surface area and pore size distribution (IUPAC Technical Report), Pure and Applied Chemistry 87 (2015) 1051–1069. https://doi.org/10.1515/pac-2014-1117.

[99] M. Chen, S.A. Masum, S. Sadasivam, H.R. Thomas, A.C. Mitchell, Modeling Gas Adsorption–Desorption Hysteresis in Energetically Heterogeneous Coal and Shale, Energy & Fuels 37 (2023) 2149–2163. https://doi.org/10.1021/acs.energyfuels.2c03441.

[100] S. Wang, L. Lu, D. Wu, X. Lu, W. Cao, T. Yang, Y. Zhu, Molecular Simulation Study of the Adsorption and Diffusion of a Mixture of CO2/CH4 in Activated Carbon: Effect of Textural Properties and Surface Chemistry, Journal of Chemical & Engineering Data 61 (2016) 4139–4147. https://doi.org/10.1021/acs.jced.6b00554.

[101] National Institute of Standards and Technology (NIST), Experimental Polarizabilites, 2023-03-22 (n.d.). https://cccbdb.nist.gov/pollistx.asp#2015Tha/Wu:144302.

[102] F. Anwar, M. Khaleel, K. Wang, G. N. Karanikolos, Selectivity Tuning of Adsorbents for Ethane/Ethylene Separation: A Review, Industrial & Engineering Chemistry Research 61 (2022) 12269–12293. https://doi.org/10.1021/acs.iecr.2c02438.

[103] R. Haul, S. J. Gregg, K. S. W. Sing: Adsorption, Surface Area and Porosity. 2. Auflage, Academic Press, London 1982. 303 Seiten, Preis: $ 49.50, Berichte Der Bunsengesellschaft Für Physikalische Chemie 86 (1982) 957. https://doi.org/https://doi.org/10.1002/bbpc.19820861019.

[104] M. Eskandari-Ghadi, Y. Zhang, Mechanics of shrinkage-swelling transition of microporous materials at the initial stage of adsorption, Int J Solids Struct 222–223 (2021) 111041. https://doi.org/https://doi.org/10.1016/j.ijsolstr.2021.111041.

[105] R.P.P.L. Ribeiro, J.P.B. Mota, Adsorption of Carbon Dioxide and Nitrogen in Co3(ndc)3(dabco) Metal–Organic Framework, Int J Mol Sci 25 (2024). https://doi.org/10.3390/ijms25189951.

[106] D. Saha, M.J. Kienbaum, Role of oxygen, nitrogen and sulfur functionalities on the surface of nanoporous carbons in CO2 adsorption: A critical review, Microporous and Mesoporous Materials 287 (2019) 29–55. https://doi.org/https://doi.org/10.1016/j.micromeso.2019.05.051.

[107] R. Babarao, Z. Hu, J. Jiang, S. Chempath, S.I. Sandler, Storage and Separation of CO2 and CH4 in Silicalite, C168 Schwarzite, and IRMOF-1: A Comparative Study from Monte Carlo Simulation, Langmuir 23 (2007) 659–666. https://doi.org/10.1021/la062289p.

[108] S. Ga, S. Lee, G. Park, J. Kim, M. Realff, J.H. Lee, New model for S-shaped isotherm data and its application to process modeling using IAST, Chemical Engineering Journal 420 (2021). https://doi.org/10.1016/j.cej.2020.127580.

[109] J. A. O'Brien, A. L. Myers, A comprehensive technique for equilibrium calculations in adsorbed mixtures: the generalized FastIAS method, Industrial & Engineering Chemistry Research 27 (2002) 2085–2092. https://doi.org/10.1021/ie00083a021.

[110] A.L. Myers, J.M. Prausnitz, Thermodynamics of mixed-gas adsorption, AIChE Journal 11 (1965) 121–127. https://doi.org/10.1002/aic.690110125.

[111] J.A. O'brien, A.L. Myers, Rapid Calculations of Multicomponent Adsorption Equilibria from Pure Isotherm Data, Industrial and Engineering Chemistry Process Design and Development 24 (1985) 1188–1191. https://doi.org/10.1021/i200031a049.

[112] R. Krishna, J.M. van Baten, How Reliable Is the Ideal Adsorbed Solution Theory for the Estimation of Mixture Separation Selectivities in Microporous Crystalline Adsorbents?, ACS Omega 6 (2021) 15499–15513. https://doi.org/10.1021/acsomega.1c02136.

[113] K.S. Walton, D.S. Sholl, Predicting multicomponent adsorption: 50 years of the ideal adsorbed solution theory, AIChE Journal 61 (2015) 2757–2762. https://doi.org/https://doi.org/10.1002/aic.14878.

[114] M. Ismail, M.A. Bustam, N.E.F. Kari, Y.F. Yeong, Ideal Adsorbed Solution Theory (IAST) of Carbon Dioxide and Methane Adsorption Using Magnesium Gallate Metal-Organic Framework (Mg-gallate), Molecules 28 (2023). https://doi.org/10.3390/molecules28073016.

[115] Y.-S. Bae, R.Q. Snurr, Development and Evaluation of Porous Materials for Carbon Dioxide Separation and Capture, Angewandte Chemie International Edition 50 (2011) 11586–11596. https://doi.org/https://doi.org/10.1002/anie.201101891.

[116] C. Wen, G. Wei, M. Hu, H. Yin, J. Yang, C. Li, H. Zhang, Regeneration Technology of Ex-service SF6 Adsorbent Using Vacuum Heat Treatment, IOP Conf Ser Mater Sci Eng 486 (2019) 12024. https://doi.org/10.1088/1757-899X/486/1/012024.

[117] Cheng Wei, Zhu Feng, Hang Chen, Xu ZhengJie, Study on regeneration performance of carbon fluoride adsorbent in SF6 gas, E3S Web Conf. 441 (2023) 1023. https://doi.org/10.1051/e3sconf/202344101023.

[118] M.A. Alsharif, Understanding Adsorption: Theories, Techniques, and Applications, in: T.I. Shabatina, Y. Gromova (Eds.), Adsorption, IntechOpen, Rijeka, 2025. https://doi.org/10.5772/intechopen.1008865.

CHAPTER 6

CONCLUDING REMARKS AND FUTURE PERSPECTIVES

6.1 General conclusion

The doctoral thesis demonstrates the importance of designing and selecting advanced adsorbents and solvents for the capture and selective separation of F-gases and other GHGs. The research encompassed ILs, DES, composites, ACs, biocarbons, zeolites, MOFs, and POFs, providing a comprehensive perspective on how the structure and properties of these materials directly influence the performance and selectivity of sorption processes.

In the case of ILs and DES, it was clearly observed that FILs containing alkyl-fluorinated chains up to four carbons exhibit significantly higher absorption capacities for F-gases such as R-32, R-125, and R-134a when compared to conventional ILs with longer hydrogenated chains, which are generally more toxic and less efficient. The experimental results confirm that both solubility and selectivity of F-gases are strongly dependent on the chemical structure of the IL cation and anion, as well as on the molar ratio of components in DES and the operating temperature. In particular, R-134a demonstrated the highest solubility in all evaluated DES. In this last case, the selectivity can be effectively tuned by modifying both the operating conditions and the composition of the DES, opening the possibility of tailoring solvents for specific separation tasks. Additionally, the incorporation of FILs into porous silica matrices proved to be a promising strategy to enhance the contact surface and mass transfer, while still preserving the intrinsic selective behaviour of ILs. This behaviour was especially relevant for R-134a in commercial mixtures R-410A and R-407F, where the composites maintained the advantages of the IL phase but improved material handling and operational stability.

On the other hand, COSMO-RS was used to explore the interactions between ILs and greenhouse gases, providing valuable insights for a rational pre-selection of suitable ILs before experimental testing. Furthermore, process-scale simulations based on COSMO/Aspen Plus calculations confirmed both the technical feasibility and the economic competitiveness of these absorption processes under industrial conditions. Among the different candidates, $[C_2C_1Im][CF_3SO_3]$, $[C_2C_1Im][N(CF_3SO_3)_2]$, and $[C_8C1Im][N(CF_3SO_3)_2]$ were identified as the most promising absorbents, capable of achieving hydrofluorocarbon (HFC) recoveries above 90 % under optimised absorption column operating conditions. Taken together, these results provide not only a deeper fundamental understanding of the thermodynamic and kinetic mechanisms governing F-gas absorption but also a clear demonstration of their scalability and practical viability for industrial implementation.

Regarding ACs and biocarbons, the AC1 and AC2 exhibited the highest adsorption capacities for pure F-gases, with R-32 being the most adsorbed gas across all activated carbons. Selectivity in commercial mixtures R-410A and R-407F was higher toward R-125 and R-134a, with commercial ACs, showing better selectivity in R-407F at low pressures. The biocarbons CC-K_2CO_3 and CC-CO_2 demonstrated excellent performance. CC-CO_2 is recommended for R-32 recovery, while CC-K_2CO_3 is suitable for R-125 and R-134a, as well as SF_6/N_2 separation. Additionally, activated carbons derived from coconut shell biomass, CS-CO_2 and CS-$ZnCl_2$, showed high selectivity and stability, with CS-$ZnCl_2$ being

most effective for separating R-410A and R-407C mixtures. Besides, CS-CO_2 shows the highest selectivity for R-404A. ACM stood out in CO_2/CH_4 separation, highlighting the importance of microporosity, pore distribution, and surface chemistry for adsorption and selectivity. These results confirm that biocarbons prepared from residual biomass are sustainable and cost-effective alternatives for industrial gas purification applications.

Porous organic polymers RIO-55 and RIO-12 showed outstanding performance in F-gas separation. RIO-55 exhibited the highest selectivity for components of R-410A and R-407C, favoured by its lower total pore volume and smaller pore sizes, optimising the adsorption of small fluorinated molecules. RIO-12, with a high surface area and substantial micropore volume, was more effective for SF_6 capture from SF_6/N_2 mixtures. Electrostatic interactions provided by surface functional groups significantly contributed to adsorption capacity and selectivity, highlighting the potential of POPs for sustainable industrial applications in refrigeration and electrical insulation.

Specific studies on SF_6 adsorption in AC1–AC3 and ACHM demonstrated that microporosity and high surface area are crucial for capacity and selectivity, while regeneration and working capacity evaluation are essential to ensure efficient and sustainable cyclic operation. ACHM showed the highest Henry's constant and strong affinity for SF_6, although its limited regeneration (~ 36 %) could restrict sustained cyclic operations. In contrast, AC1–AC3 achieved an optimal balance between selectivity and regeneration (80–87 %) at higher pressures (0.5 MPa), emerging as promising candidates for industrial SF_6 separation processes.

Overall, these studies provide essential information for the design, optimisation, and scale-up of F-gases and GHGs separation processes, showing that both fluorinated ILs/DES and ACs, biocarbons, and POPs can be tailored to maximise capacity, selectivity, and operational efficiency. The integration of structural characteristics such as microporosity, mesoporosity, surface area, and surface functionalization enables the selective separation of complex gas mixtures, paving the way for sustainable and economically viable applications in refrigeration, electrical insulation, and GHG capture.

6.2 Future work

The results collected in this work open several directions in future research for the separation, capture and storage of F-gases. Firstly, the optimisation of ILs and DES should be pursued to enhance both solubility and selectivity for specific F-gases in pure and mixed streams. Future studies could focus on the systematic design of new ILs with tailored cations and anions to increase gas solubility, selectivity at room pressures and temperatures. Efforts should also be directed toward reducing viscosity to improve mass transfer in industrial-scale absorption processes. Additionally, coupling thermodynamic and kinetic studies may allow the identification of optimal operational parameters for the selective separation of more complex F-gases mixtures. Long-term stability and the regeneration capacity of ILs and DES under repeated absorption–desorption cycles should be assessed to ensure industrial viability. Secondly, the incorporation of ILs or DES in porous solid matrices presents a promising avenue to enhance the stability, mass transfer and contact efficiency. Future research should explore advanced composite materials with optimised pore structures, surface areas, and homogeneous IL or DES distribution. Surface functionalization strategies may be investigated to further improve the selective uptake of target F-gases. Scale-up studies are essential to evaluate pressure drop, flow distribution, and overall column performance in industrial processes.

Thirdly, activated carbons and biocarbons derived from biomass sources offer environmentally friendly alternatives for F-gases and GHGs separation. Future studies should explore a wider variety of biomass precursors and activation methods to produce carbons with tailored micro- and mesoporosity for enhanced selectivity and adsorption capacity. Surface functionalization to target specific gases could further improve performance. Long-term cyclic adsorption studies, including thermal and pressure swing regeneration, are essential to evaluate material stability. Pilot-scale implementation and testing of these materials in real industrial conditions are of vital importance to validate their practical industrial application. Fourthly, POPs offer a versatile platform for selective F-gases separation due to their tunable porosity and functional surfaces. Future work should focus on the rational design of POPs with tailored pore sizes and surface chemistries to maximise adsorption selectivity for specific F-gases mixtures. Additionally, studies on competitive adsorption in multi-component mixtures and the stability of POPs under repeated cycles are necessary to establish their industrial feasibility.

Fifthly, advanced thermodynamic models should be extended to predict multi-component F-gases behaviour. The incorporation of the study of kinetic effects using process simulations will allow more accurate predictions of industrial sorption column performance. Process optimisation studies using tools such as Aspen Plus or gPROMS should aim to minimise energy consumption, solvent loss, and operational costs. Sixthly, the capture and separation of high global warming potential gases require dedicated research. Future investigations should focus on the design of high-capacity, high-selectivity adsorbents that leverage microporosity, mesoporosity, and surface chemistry to maximise uptake while maintaining effective regeneration.

Finally, sustainability considerations should guide future work. A complete assessment of technology performances & integrated sustainability, environmental life cycle assessment (E-LCA), life cycle costing (LCC) and social life cycle assessment (S-LCA) is essential to ensure replication of the proposed solutions and the most promising technologies. Scaling up promising materials from laboratory to pilot and industrial scale, along with the development of hybrid separation processes, may further enhance energy efficiency and overall process performance. Besides, the valorisation of residual biomass for the production of high-performance biomaterials can minimise environmental impact and reduce material costs, making these solutions more attractive for industrial applications. In summary, the directions outlined above provide a roadmap for advancing the design, optimisation, and industrial implementation of novel materials and processes for the selective capture and separation of F-gases and other greenhouse gases, contributing to more sustainable and efficient environmental technologies.

2025

JULIO EDUARDO SOSA PARRA

NEW ADVANCED HYBRID MATERIALS FOR SEPARATION OF FLUORINATED GREENHOUSE GASES